Springer Proceedings in Physics 158

Gongtian Shen
Zhanwen Wu
Junjiao Zhang *Editors*

Advances in Acoustic Emission Technology

Proceedings of the World Conference on Acoustic Emission–2013

Springer

Springer Proceedings in Physics

Volume 158

For further volumes:
http://www.springer.com/series/361

Gongtian Shen • Zhanwen Wu • Junjiao Zhang
Editors

Advances in Acoustic Emission Technology

Proceedings of the World Conference on Acoustic Emission–2013

Springer

Editors
Gongtian Shen
China Special Equipment Inspection and Research Institute
Beijing, China

Zhanwen Wu
China Special Equipment Inspection and Research Institute
Beijing, China

Junjiao Zhang
China Special Equipment Inspection and Research Institute
Beijing, China

ISSN 0930-8989 ISSN 1867-4941 (electronic)
ISBN 978-1-4939-1238-4 ISBN 978-1-4939-1239-1 (eBook)
DOI 10.1007/978-1-4939-1239-1
Springer New York Heidelberg Dordrecht London

Library of Congress Control Number: 2014947351

Printed on acid-free paper

Springer is part of Springer Science+Business Media (www.springer.com)

Preface

This volume includes the papers selected from the World Conference on Acoustic Emission—2013 (WCAE-2013) that was held on Oct. 30th–Nov. 2nd in Shanghai, China. WCAE was the formal conference of the International Society on Acoustic Emission (ISAE). WCAE-2013 was jointly organized by Chinese Society for Non-destructive Testing (ChSNDT) and China Special Equipment Inspection and Research Institute (CSEI). This was the second of such event of ISAE following its inaugural one in 2011 in Beijing, China. WCAE is aimed at providing a platform to scientists and practitioners in both academia and industry in the field of acoustic emission and exchanging research and application information, with particular emphasis on scientific and technical development and cooperation worldwide.

The WCAE-2013 consisted of four invited keynote lectures, and nine oral and one poster sessions. It covered all major the areas of acoustic emission applications, including Instrumentation, Signal processing and analysis, Material characteristics, Structure, Condition Monitoring and diagnosis, and Miscellaneous.

WCAE-2013 received 84 submissions, which were documented in the extended abstracts of WCAE-2013. 67 full papers were submitted for the consideration of achieved formal proceeding. After peer reviews, 61 were included in this volume.

We are grateful to all the members of the committees who contributed their efforts to review the manuscripts. We would also like to express our sincere gratitude to Chinese Society for Non-destructive Testing (ChSNDT) and China Special Equipment Inspection and Research Institute (CSEI) for their enormous supports. Last, but not the least, we thank the contributions of all the delegates who participated in WCAE-2013.

Beijing, China — Gongtian Shen
Beijing, China — Zhanwen Wu
Beijing, China — Junjiao Zhang

Committees

Organization committee

Chair Gongtian Shen, China Special Equipment Inspection and Research Institute

Co-chair Allen Green, Acoustic Emission Technology Consulting
Rongsheng Geng, Beijing Aeronautical Technology Research Center

Member Yongchang Xu, Chinese Society for Non-destructive Testing
Zhen Huo, Wuhan Institute of Boiler and Pressure Vessel Inspection
Guang Dai, Northeast Petroleum University
Weihe Guan, Hefei General Machinery Research Institute
Bangxian Li, China Special Equipment Inspection and Research Institute
Shifeng Liu, Beijing Shenghua Industrial Co. Ltd.
Gary Qi, University of Memphis
Fengjing Xu, Physical Acoustics Corporation (PAC) Beijing Representative Office
Zhanwen Wu, China Special Equipment Inspection and Research Institute

Paper and program committee

Chair Gongtian Shen, China Special Equipment Inspection and Research Institute

Co-chair Gary Qi, University of Memphis

Members Allen Theodore Green, Acoustic Emission Technology Consulting
Manabu Enoki, University of Tokyo
Oswaldo Santos Filho, Technology Center, Eletronorte
Karen Margaret Holford, Cardiff University
Oh Yang Kwon, Inha University

Andy C. C. Tan, Queensland University of Technology
Peter Tscheliesnig, TÜV Austria Services GmbH
Bangxian Li, China Special Equipment Inspection and Research Institute
Cherdpong Jomdecha, King Mongkut's University of Technology
Boris Muravin, Association of Engineers and Architects in Israel

Secretary committee

Chair Bangxian Li, China Special Equipment Inspection and Research Institute

Members Zhanwen Wu, China Special Equipment Inspection and Research Institute
Yaqing Zhu, Chinese Society for Non-destructive Testing
Yingyun Wang, Chinese Society for Non-destructive Testing
Jingyuan Ji, Chinese Society for Non-destructive Testing
Guanghai Li, China Special Equipment Inspection and Research Institute
Wei Li, Northeast Petroleum University

Advisory committee

Ozan Akkus, Purdue University, USA.
Athanasios Anastasopoulos, Envirocoustics, Greece.
Alan A. Barhorst, Texas Tech University, USA.
Martin Browne, University of Southampton, UK.
Mark Carlos, Physical Acoustics Corporation, USA.
Phil Cole, Physical Acoustics Limited, UK.
Alberto Carpinteri, Politecnico di Torino, Italy.
Guang Dai, Northeast Petroleum University, China.
Manabu Enoki, University of Tokyo, Japan.
Oswaldo Goncalves dos Santos Filho, Eletronorte Technology Center, Brazil.
Pedro Feres Filho, Physical Acoustics South America, Brazil.
Mochen Ge, Missouri University of Science and Technology, USA.
Rongsheng Geng, Beijing Aeronautical Technology Research Center, China.
Allen Green, Acoustic Technology Group, USA.
Janez Grum, University of Ljubljana, Slovenia.
Christian U. Grosse, Technische Universität München, Germany.
Weihe Guan, Hefei General Machinery Research Institute, China.
Hajime Hatano, University of Tokyo, Japan.
Karen M. Holford, Cardiff University, UK.
Zhen Huo, Wuhan Boiler and Pressure Vessel Inspection Institute, China.
Cherdpong Jomdecha, King Mongkut's University of Technology Thonburi, Thailand.
Yilan Kang, Tianjin University, China.
Oh-Yang Kwon, Inha University, Korea.
Joseph F. Labuz, University of Minnesota, USA.

Jean-Claude Lenain, Euro Physical Acoustics, France.
Bangxian Li, China Special Equipment Inspection and Research Institute, China.
Shifeng Liu, Soundwel Technology Co. Ltd., China.
Zhenjun Liu, Aerospace Research Institute of Materials and Processing Technology, China.
Gerd Manthei, University of Applied Sciences, Germany.
Antolino Gallego Molina, University of Granada, Spain.
Boris Muravin, Margan Physical Dianostics Ltd., Israel.
Gary Qi, University of Memphis, USA.
Robert Reuben, Heriot-Watt University, UK.
Victor Shemyakin, Diapac, Russia.
Gongtian Shen, China Special Equipment Inspection and Research Institute, China.
Tomoki Shiotani, Kyoto University, Japan.
Svetlana Alex Stragnefors, Non-destructive Testing and Technical Diagnostic Association, Kazakhstan.
Vaclav Svoboda, Preditest, Czech.
Guiyun Tian, University of Newcastle, UK.
Andy C.C. Tan, Queensland University of Technology, Australia.
Peter Tscheliesnig, TÜV Austria Services GmbH, Austria.
Sotirios Vahaviolos, MISTRAS Group Inc., USA.
Hartmut Vallen, Vallen System, Germany.
Shuichi Wakayama, Tokyo Metropolitan University, Japan.
Steven F. Wayne, The University of Memphis, USA.
Jason Weiss, Purdue University, USA.
Shigenori Yuyama, Nippon Physical Acoustics, Ltd., Japan.

Contents

Part I
Instrumentation

Development of High-Speed Wi-Fi Wireless Acoustic Emission System

Gongtian Shen, Yajing Zhang, Yibiao Dong, and Shifeng Liu

Abstract In order to satisfy the requirement of AE testing and monitoring for pipeline, large pressure vessel, large crane and amusement device, a new 16-channel high-speed Wi-Fi wireless acoustic emission system based on GPS and Wi-Fi techniques was developed. The test results indicate that this system possesses very high function and can satisfy common AE applications. The theoretical maximum distance between wireless controller and wireless AE acquisition units is up to 10 km. Three kilometers testing has been carried out at present. The transmitting rate is 7,000 hits/s or 3.6 Mbps between wireless controller and wireless AE acquisition units. The clock synchronization accuracy based on GPS can be up to 3 μs. It realizes time difference AE source location in real time. The system maximum error for steel plate is 77 mm. This accuracy can meet the requirements of most AE testing applications.

1 Introduction

Acoustic emission (AE) technique has been widely applied in materials testing, structure testing and evaluation of integrity for pressure equipment, bridges, cranes, buildings, and condition monitoring and fault diagnosis for bearings [1, 2]. As the transmission of AE signals needs cables for common commercial AE instruments, it is very inconvenient for the AE testing and monitoring of bridges, pipelines, large

G. Shen (✉)
China Special Equipment Inspection and Research Institute, Beijing 100013, China
e-mail: shengongtian@csei.org.cn

Y. Zhang • Y. Dong • S. Liu
Beijing Soundwel Technology Co. Ltd., Beijing 100012, China
e-mail: sliu@soundwel.cn

G. Shen et al. (eds.), *Advances in Acoustic Emission Technology: Proceedings of the World Conference on Acoustic Emission-2013*, Springer Proceedings in Physics 158,
DOI 10.1007/978-1-4939-1239-1_1,

steel structures, railway tunnels, buildings, amusement rides, etc. In recent years, some papers have reported the development of wireless AE instruments and applications [3–5]. A few wireless AE instruments have been offered for sale in the market. But so far, the wireless acoustic emission instruments in the market have not the function of time difference source location due to low transmitting rate and lack of synchronous clock.

In order to satisfy the requirement of AE testing and monitoring for pipeline, large pressure vessel, large crane and amusement device, China Special Equipment Inspection and Research Institute and Beijing Soundwel Technology Corporation Ltd. have jointly developed a new multichannel wireless acoustic emission system with large transmitting rate and synchronous clock based on the Wi-Fi and GPS technique. This paper reports the details of the developed wireless acoustic emission system.

2 Design of the New Wireless Acoustic Emission System

2.1 General Design

In order to satisfy the requirement of AE testing and monitoring for large structure, the new developing wireless AE system must possess the following functions:

1. Wireless transmitting distance of AE signals is longer than 1,000 m.
2. The channels are at least 12 in number.
3. It can make time difference source location.
4. The transmitting rate of AE signals can insure the real time analysis and display of AE parameters and source location for all channels.
5. The transmitting rate of AE signals can insure the real time analysis and display of waveforms of AE signals for at least one channel.

Figure 1 shows the functional block diagram of the new wireless acoustic emission system. It includes sensors, wireless acoustic emission acquisition units

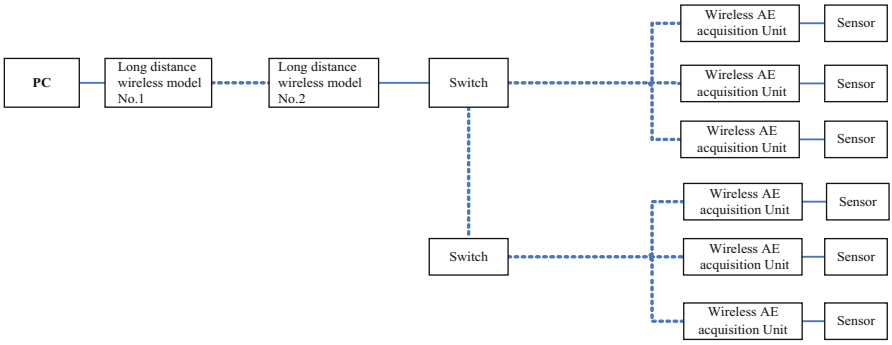

Fig. 1 Functional block diagram of new wireless acoustic emission system

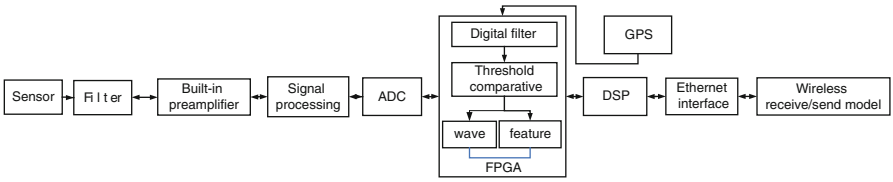

Fig. 2 Function block diagram of the wireless AE signal acquisition unit

(built-in GPS antenna), switch, two Wi-Fi long distance wireless models, and one PC. The dotted line in Fig. 1 means double-way wireless communication and solid line, cable connection. In order to extend the transmitting distance and increase the transmitting rate of AE signals, a new high-speed Wi-Fi wireless communication system is applied here. Transmission of the operating instruction parameters from PC to the wireless AE acquisition unit includes five steps. First, set operating parameters of data acquisition for the wireless AE acquisition units in PC. Second, transmit the operating parameters of the units to No. 1 Wi-Fi wireless model by network cable. Third, the No. 1 Wi-Fi wireless model transmits the operating parameters to No. 2 Wi-Fi wireless model. Fourth, the No. 2 Wi-Fi wireless model transmits the operating parameters to a switch via a network cable. Fifth, the switch transmits the operating parameters to the wireless AE acquisition units. If the wireless AE acquisition units locate to a far place from the switch, another switch or more are required. The switches can transmit data to each other.

Transmission of AE Data from the wireless AE acquisition unit to PC includes six steps. First, AE signals detected by sensor are sent to the AE acquisition unit by a signal cable. Second, the unit acquires the AE signal according to the operating parameters set by PC software. Third, the unit transmits the AE data to a switch wirelessly. Fourth, the switch transmits the AE data to the No. 2 Wi-Fi wireless model. Fifth, the No. 2 Wi-Fi wireless model transmits the AE data to the No. 1 Wi-Fi wireless model. Sixth, the No. 1 Wi-Fi wireless model transmits the AE data to the PC by network cable.

2.2 Design of the Wireless AE Signal Acquisition Unit

Figure 2 shows the function block diagram of the wireless AE signal acquisition unit. The unit includes a box and a few connecting devices including one AE sensor, one GPS antenna, one Wi-Fi transmitting antenna, and one external parameter input interface. There are nine modules inside the box. These modules respectively are filter, preamplifier, signal processing, ADC, FPGA, GPS, DSP, ethernet interface, and wireless receiving and sending module. In order to implement clock synchronization, GPS technology is employed.

The working procedures in the wireless AE acquisition unit from AE signal detection to sending out include eight steps. First, the acoustic emission signal

detected by the sensor is sent to an analog filter. Second, the AE signal filtered by the analog filter is transmitted to the built-in preamplifier for amplifying. Third, the signal amplified by the preamplifier is initially processed to satisfy the requirement of ADC. Fourth, ADC transforms the analog AE signal to digital AE signal according to the time given by the GPS and transmits it to the FPGA chip. Fifth, the FPGA chip carries out digital filter, threshold comparative, waveform drawing, AE feature parameters producing for the digital wave according to the setup of the PC software and transmits data to DSP chip. Sixth, the DSP chip converts the data to the format which can be identified by ethernet interface, and transmits the data to the ethernet circuit. Seventh, the ethernet interface converts the data to signals which can be received and sent by the wireless module. Eighth, the data is transmitted to the switch wirelessly.

2.3 Selection of Wireless Data Communication Technique

Bluetooth, Wi-Fi, IrDA, and Zigbee are all near distance wireless communication techniques which are widely used at present. Bluetooth technique uses a frequency range of 2.4 GHz and only provides maximum 1 Mbps transmitting rate and 10 m transmitting distance. Wi-Fi technique uses a frequency range of 2.4 GHz. Its maximum transmitting rate is 54 Mb/s and maximum transmitting distance of the basic module is 100 m, and the remote module can be up to 10 km. IrDA is used only to communicate between two devices. Its transmitting rate is only 115.2 kb/s and transmitting distance is 1 m. The transmitting rate of Zigbee technique is only 10 ~ 250 kb/s and its effective transmitting distance is from 10 to 75 m.

For most of acoustic emission testing applications such as pipelines, bridges, and large steel structures, the data transmitting rate needs several hundreds of AE hits per channel per second and wireless communication distance requires at least a few hundreds of meters. This equals to a data transmitting rate of several Mb/s. For this reason, the Wi-Fi technique was selected to be applied for the newly developed wireless acoustic emission system.

3 Development and Testing of the New Wireless Acoustic Emission System

3.1 The Developed New Wireless Acoustic Emission System

Finally, a high-speed Wi-Fi wireless acoustic emission system with 16 channels was developed. Figure 3 shows the photograph of the developed wireless AE signal acquisition unit. Figure 4 shows the switch and No. 2 long distance wireless model. Figure 5 shows No. 1 long distance wireless model and PC.

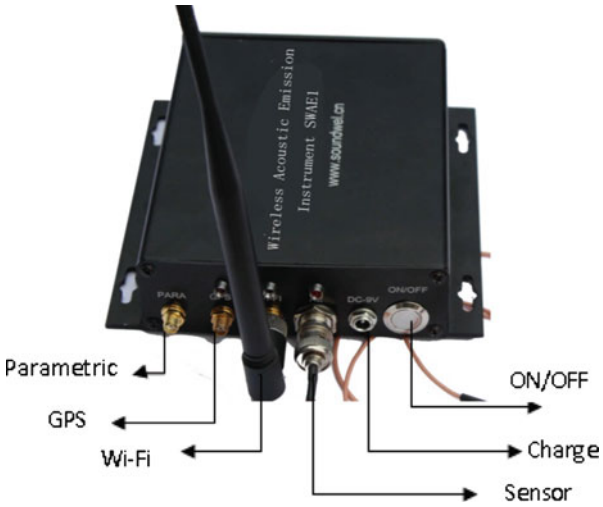

Fig. 3 The wireless AE signal acquisition unit

Fig. 4 The switch and long distance wireless model

3.2 Communication Distance Testing

In the open field without any barrier, four sensors were coupled on one steel plate. The communication distance was tested by using broken lead as AE simulation source, as shown in the Fig. 6. The test distances between PC and the four wireless AE signal acquisition units are respectively 100, 200, 500, 1,000, 2,000, and 3,000 m. The testing results show that the PC could receive the broken-lead signals for every distance. Due to the limit of the testing site, further distance testing has not been carried out.

Fig. 5 The long distance wireless model and PC

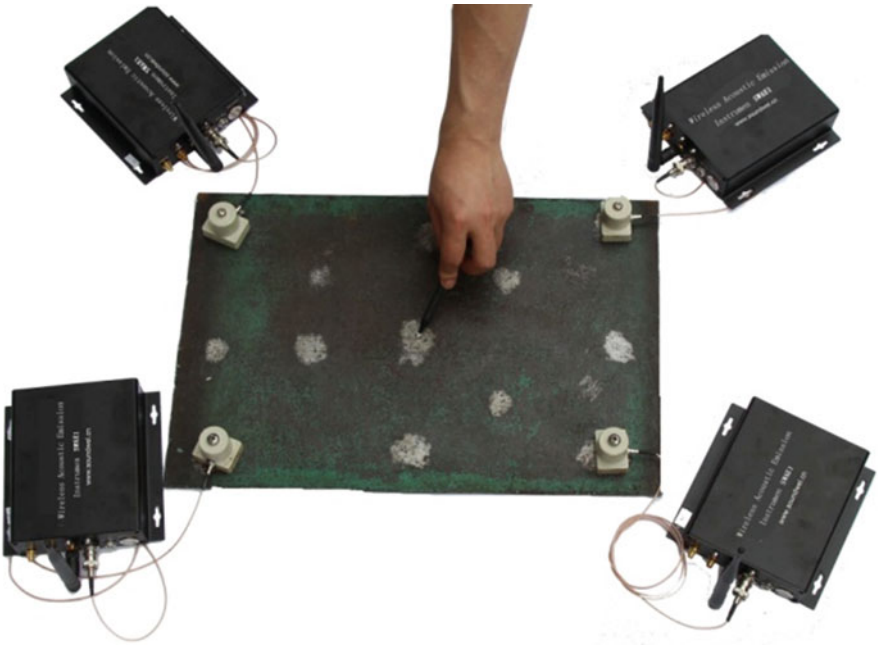

Fig. 6 Broken-lead testing

3.3 Data Transmitting Rate Testing

Using the same equipment in Fig. 6, the data transmitting rate was tested by use of an AE standard signal generator. The operating parameters of the AE signal acquisition units were set such that sampling rate was 10 MHz, sampling length (points) was 2,048, Hit Definition Time (HDT) was 0, and Hit Lockout Time (HLT) was 0. AE standard signal generator emitted continuous sine signal with 150 kHz to the excitation sensor. The testing results show that the continuous data transferring rate of wireless acoustic emission system can be over 7,000 hits/s or 3.6 Mbps for 300 m communication distance and 6,000 hits/s or 3.1 Mbps for 3,000 m communication distance.

3.4 Time-Difference Location Testing

The testing devices were the same as above in Fig. 6. An emitting sensor of simulation AE signals was put in the center of the steel plate. It was first confirmed that the four wireless acoustic emission acquisition units can receive GPS signals. Then, the simulation AE signals were emitted by an AE sensor excited by a sine signal per second generated by an AE standard signal generator. Four sensors detected the AE signals and separately transmitted them to the four wireless acoustic emission acquisition units. The test was carried out in one hour. The arrival time and time differences of AE hits from the four units were observed. The testing results show that the time differences of two different channels were between 5 and 24 μs. As the acoustic velocity is about 3,200 m/s for the steel plate, the maximum location error of the system is 77 mm. This location error is the same level for the common AE instrument.

4 Testing in Pressure Vessel

In order to test the comprehensive performance of the newly developed wireless AE system, a scrapped 10 m^3 petroleum liquefied gas (LPG) tank was tested by hydraulic test. The size of the tank is $\Phi 1{,}600 \times 5{,}000 \times 12$ mm. The material of the tank is 16 MnR carbon steel. The design pressure of the tank is 1.6 MPa. Figure 7 is the photograph of the AE testing of the LPG tank by use of the newly developed 16-channel wireless AE system. A total of 16 sensors were mounted on the tank and divided into two groups for time-difference source location. Triangle source location was used. Figure 8 shows the placement of the sensors. One place was mounted with two sensors.

Fig. 7 The AE testing of LPG tank

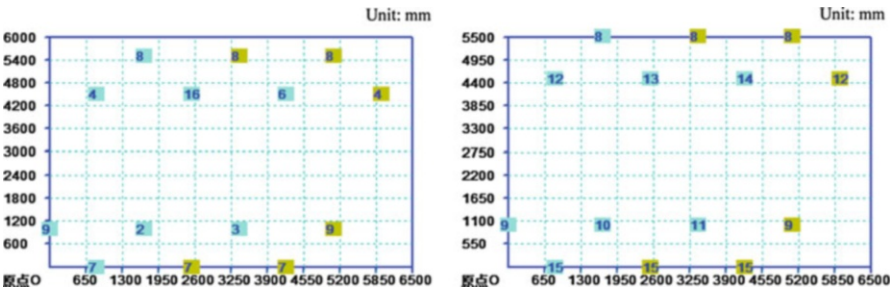

Fig. 8 Placement of the sensors

4.1 The Setup of Operating Status for the AE Unit

Sampling frequency is set to 10 M. Sampling length is 2,048. Peak Definition Time (PDT) is 1,000 μs. Hit Definition Time (HDT) is 2,000 μs. Hit Lockout Time (HLT) is 20,000 μs. Location HLT is 1,000 μs. Hit-data threshold is 40 dB. Analog and digital filter were all ignored.

4.2 Sensitivity Testing of Channels

2H Φ0.3 mm pencil lead breaking was used as the simulation AE signal source to test the sensitivity of the channels. Table 1 lists the testing results of the sensitivity for the 16 channels. The minimum is 96.7 dB, the maximum is 98.5 dB, and the average is 97.8 dB. The result is very good.

Table 1 Sensitivity testing of channels

Channel No.	Sensitivity (dB)	Channel No.	Sensitivity (dB)
1	98.2	9	98.1
2	97.6	10	96.7
3	98.0	11	98.5
4	96.7	12	98.1
5	98.4	13	97.2
6	97.4	14	97.8
7	96.9	15	98.4
8	97.2	16	97.6

Table 2 Attenuation testing of the tank

Distance of AE source (mm)	Distance of AE source (mm)	Distance of AE source (mm)	Distance of AE source (mm)
100	98	3,000	63
500	87	4,000	61
1,000	73	5,000	59
2,000	66		

4.3 Attenuation Testing

The AE attenuation of the tank was tested for channel No. 3. The simulation AE signal source is the same as above. The maximum distance between sensors in one triangle group is 4,500 mm. The attenuation of maximum 5,000 mm distance was tested. Table 2 lists the testing result. According to this result, the threshold was set to 40 dB for all channels.

4.4 Source Location Testing

The sound velocity tested by this wireless AE system was 3,180 m/s. The time-difference source location testing was performed by use of this sound velocity. We got one lead breaking and one source location. Figure 9 gives the testing results of source location for channel Nos. 2, 4, 9, 10 and 12.

4.5 Background Noise Testing

The background noise was tested by gradually decreasing threshold. The background noise levels were between 30 and 34 dB for the 16 channels. According to this and attenuation testing result, the threshold was set to 40 dB for all channels.

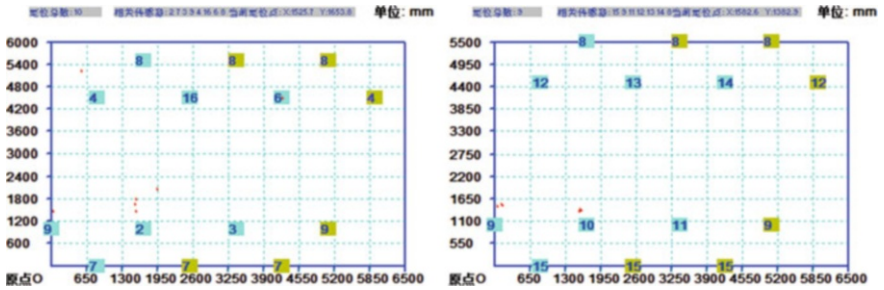

Fig. 9 Source location testing

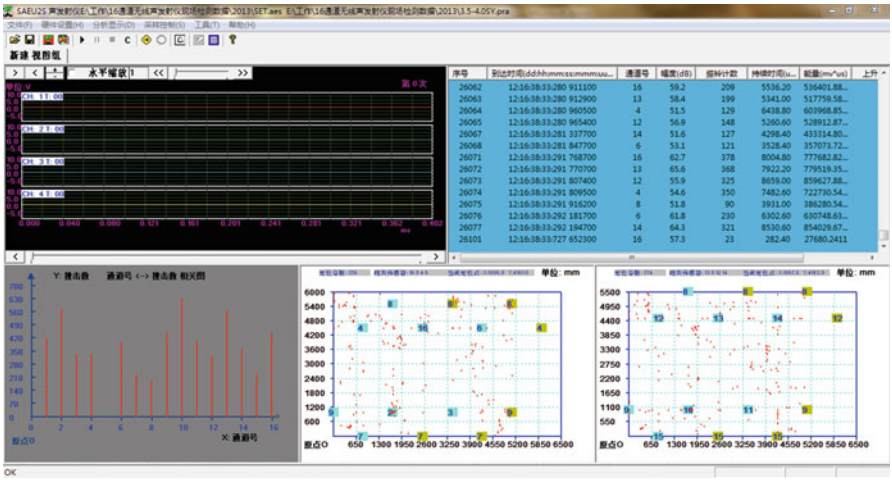

Fig. 10 Display of AE signals between 3.5 and 4.0 MPa pressurization

4.6 AE Testing During Pressurization

The pressurization from 0 to 4.0 MPa was carried out with 5 min pressure hold for each 0.5 MPa step. The list of AE parameters, waveform of AE signals, correlation diagrams of the AE parameters, and time difference of AE source location could be observed in real time during the test. Figure 10 gives the example of display of AE signals between 3.5 and 4.0 MPa pressurization.

5 Conclusion

A new high-speed Wi-Fi wireless acoustic emission system with 16 channels was developed. The test results indicate that this system possesses very high level and can satisfy common AE applications. The key function and parameters of the system are as follows:

1. The theoretical maximum distance between wireless controller and wireless AE acquisition unit is up to 10 km. Three kilometers testing has been carried out at present.
2. Point to multi-point Wi-Fi communication speed between wireless controller and wireless AE acquisition units is 7,000 hits/s or 3.6 Mbps. When the communication distance is 3,000 m, continuous data transferring rate can be over 6,000 hits/s or 3.1 Mbps.
3. The clock synchronization accuracy based on GPS can be up to 3 μs. It realizes time difference AE source location in real time. The system maximum error for steel plate is 77 mm. This accuracy can meet the requirements of most AE testing applications.

Acknowledgment This study was financially supported by Chinese 12th five-year science and technology supporting project No. 2011BAK06B01

References

1. G. Shen, G. Dai, S. Liu. *Review of acoustic emission in China*. Proceedings of 6th International Conference on Acoustic Emission, South Lake Tahoe, Nevada, USA, 28 October to 2 November 2007
2. G. Shen, G. Dai, Z. Huo. *Progress of acoustic emission in China.* Proceedings of World Conference on Acoustic Emission-2011, Beijing, China, 24–26 August 2011
3. C.U. Gross, S.D. Glaser, M. Kruger, Initial development of wireless acoustic emission sensor motes for civil infrastructure state monitoring. Smart. Struct. Syst. **6**(3), 197–209 (2010)
4. G. Shen, S. Liu, W. Wang, Development of a pipeline leakage location instrument based on acoustic waves. Non-destructive Testing **32**, 53–56 (2010)
5. D.J. Yoon, S. Lee, C.Y. Kim, D.C. Seo. Acoustic emission diagnosis system and wireless monitoring for damage assessment of concrete structures. *NDT for safety*, 7–9 November 2007

State-of-the-Art Wireless Acoustic Emission System for Structural Health Monitoring

Jason Dong, Ed Lowenhar, Valery Godinez, and Mark Carlos

Abstract In recent years, there has been an increasing demand for wireless operation and sensor fusion for structural health monitoring on aged infrastructures. Although advanced wireless and sensor fusion technologies have made it possible to develop equipment for such an application, there are some critical issues for such equipment to be effectively and reliably used in infrastructure sites. This paper addresses these critical issues and introduces solutions and state-of-the-art features implemented in a wireless AE system. Laboratory and field tests have been conducted to prove the necessity and effectiveness of the measures taken in the design of wireless AE systems.

1 Introduction

Wireless techniques have been intensively used in a wide variety of areas of civilian life, science academy, and industry. Accordingly, there is also a demand and desire for wireless technology to be used in acoustic emission (AE) structural health monitoring. This demand is very obvious as wiring and powering are big and time-consuming issues in any online structural health monitoring projects. Certainly, wireless is an ideal solution for resolving many structural health monitoring problems. Several researchers [1–5] have conducted projects to develop wireless AE systems for structural health monitoring. Although each development has its own unique features, it lacks functional consolidation and robust design for a sensor fusion system to be effectively and reliably used in actual structural sites.

J. Dong (✉) • E. Lowenhar • V. Godinez • M. Carlos
Mistras Group Inc., Princeton Junction, NJ 08536, USA
e-mail: jason.dong@mistrasgroup.com

G. Shen et al. (eds.), *Advances in Acoustic Emission Technology: Proceedings of the World Conference on Acoustic Emission-2013*, Springer Proceedings in Physics 158,
DOI 10.1007/978-1-4939-1239-1_2,

Actually, there are many critical issues that have to be resolved before a wireless system can be effectively used in structural health monitoring sites. Valery et al. [6, 7] have reported a NIST sponsored project on an energy harvesting wireless AE system for structural health monitoring (NIST-TIP Grant #70NANB9H007), this paper extends Godinez et al.'s [6] work to address the critical issues of developing a wireless AE system and introduces the state-of-the-art features used in a commercially available wireless AE system. Specifically, the system powering, data storage, sensor fusion, preamplifier power, front end data filtering, AE event location, auto sensor checking, alarm, wireless protocol, data transfer rate, data transfer distance, system interface and wireless base station, etc. are discussed. Finally, laboratory and field test results are given to demonstrate the success of using the developed wireless AE system for structural health monitoring.

2 Configuration of Wireless AE System

Configuration of a simple four-channel wireless AE system is shown in Fig. 1. It consists of four sensors, a four-channel wireless AE node (model number 1284), a base station, and a control laptop. The wireless AE node does signal conditioning, amplification, data acquisition, AE feature extraction, signal processing, data storage, and wireless communication and data transfer with the base station. The control software of the wireless system, e.g., AEwin, is installed in the laptop which controls the data acquisition and wireless data transfer through the base station.

The core of the wireless system is a four-channel wireless AE board as shown in Fig. 2. It consists of microprocessor, data storage SD card, wireless signal transmitter and receiver module, power module, filters, amplifiers, parametric signal conditioners, FPGA based AE feature extraction and signal processing module, etc. In considering of the needs for crack detection and event location in 2D, e.g., welds, or 3D, e.g., concrete beam, structures, four AE channels are integrated into one wireless AE node which allows time synchronization between the four AE channels so that accurate location can be performed. Actually, each of the channels includes

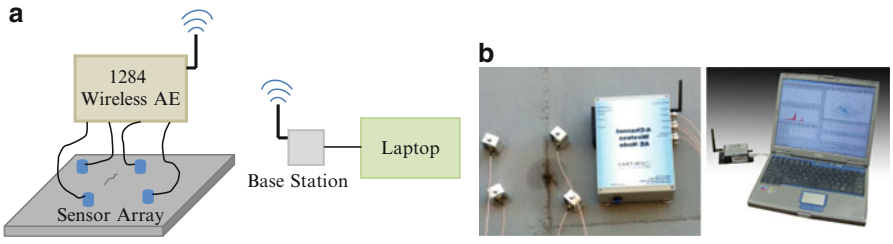

Fig. 1 Configuration of one node wireless AE system (**a**) Block diagram of a wireless AE system, (**b**) illustration photos of a wireless AE system

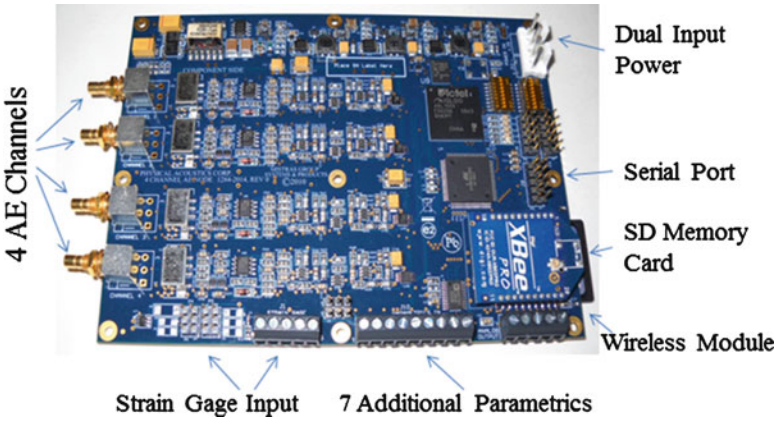

Fig. 2 Photo of a four-channel wireless AE board

signal conditioning, analog high pass and low pass filters, digital filters, and data acquisition or A/D module.

Though it is a wireless AE system, there is a necessity to use wired AE sensors which should be located around the monitoring area. In the 1284 wireless AE system, each channel is designed to be able to support both internal and external preamplifiers. With the internal preamplifier setup, general AE sensors can be used. Amplification circuit in the wireless AE board is used to amplify the signal with 26 dB gain. In the case that sensor location is very far from the wireless AE node, an external preamplifier or a sensor with integral preamplifier can be used. The wireless AE node provides 5 V DC power to the external preamplifier so that the sensor cable can be driven longer distances, e.g., over 100 m. The DC power and the AE signal share the same coaxial cable in this case.

Besides the four AE channels, the wireless AE board has also integrated eight parametric channels; one of them is a dedicated strain gauge channel with full bridge circuit so that a strain gauge can be connected to the system directly without having an external conditioner. Another parametric input is also used to monitor the battery level when an internal battery pack is used. The remaining six parametrics can be used for monitoring load, pressure, temperature, wind, etc.

The wireless AE board is enclosed in an IP-67 NEMA box so that it can be used in outdoor environments.

The base station is a wireless signal receiver module and is connected to a control laptop or PC through a USB port. Zigbee wireless protocol is used for wireless communication. Wireless data receiving and signal processing software (AEwin) is installed in the laptop which can control the start and stop of data acquisition of the wireless AE node.

The hardware setup of the 1284 wireless AE node can also be remotely controlled from the laptop. The wireless AE node can be set to allow AE features and waveforms to be transferred to the laptop and displayed in real time. In considering

the speed limit of the Zigbee wireless data transfer, the 1284 wireless AE node allows waveform data to be stored in the local SD card so that to avoid congestion of wireless data transfer.

In Fig. 1, no power connection is shown. Both 1284 and laptop can be run with internal battery power. The powering mechanism of the 1284 is specifically optimized to prolong battery life and to use self-powered energy, e.g., portable solar or portable wind power generator, whenever it is possible.

3 State-of-the-Art Features

In structural health monitoring, although AE is the most important method integrated into a wireless sensor network, other signals, e.g., strain, temperature, load, pressure, and tilt, are also important for correlation analysis and structure integrity assessment. Some critical issues, e.g., sensor fusion, power consumption, sensor self-diagnosis, local data storage, wireless communication, have to be properly considered in the design so that a functionally consolidated reliable system can be used at the structural health monitoring site. Bear these in mind, the design and development of the 1284 wireless AE system has integrated some state-of-the-art technological features as summarized below.

- Sensor fusion. The 1284 is actually a wireless sensor fusion network; not only it includes four AE channels but it also integrates totally eight parametric channels that can measure strain, temperature, load, battery power, pressure, vibration, and tilt signals in the same time with AE.
- Strain gauge conditioner. Besides direct voltage input from parametric channels, the 1284 has included a specific built-in strain gauge conditioner, and a full bridge circuit has been built into the system. It made doing wireless strain measurement without using any other conditioner or instrument convenient.
- Low power consumption design. Power consumption of the unit depends on the acoustic emission activity being detected, the rate at which external parametrics, particularly the strain gauge channel, are recorded, and whether the captured data is being transferred to the base station or just saved into the SD card. To optimize the system power performance, not only the 1284 wireless system was designed to use minimum power, but also several strategies are adopted to minimize the use of power, such as sleeping mode with parametric triggering wakeup, using low power sensor and user definable front end filters etc. The power consumption could be as low as 36 mW in the sleeping mode and 360 mW in low rate (4 hit/s) monitoring and data transfer.
- Dual power inputs. Low power consumption, extended battery life, and self-power harvest are critical for sustained use of the wireless sensor network in the field. The 1284 uses two power sources: One is the internal battery pack which is functional when no external power is available. Another one is external power source which can be either from a constant AC/DC source or a self-power

harvest device, e.g., portable solar or wind power generator. The dual power sources can be automatically switched whenever a power source is stronger than the other. For the internal battery pack, either a rechargeable battery pack or a non-rechargeable battery pack can be used. Since the system was designed with extreme low power consumption, a battery pack with 8 D-Cell battery has enough power to perform one-month continuous monitoring. Additionally, one parametric input is dedicated to monitor the remaining battery power so that an alarm will be sent out in low power status.

- Automated sensor checking. During long term structural health monitoring, it is very important to assure that sensors are always properly attached and AE channels are functioning well. This can be done through the auto sensor testing function built within the 1284. Each channel of the 1284 is equipped with a tone burst signal output circuit. When required, a tone burst, at a selected frequency and number of cycles can be sent out to the sensors in a regular time interval to verify the performance of the sensors and related channel paths. In addition, this function can also be used for acousto-ultrasonic test; when a high energy tone burst signal is sent out from any one of the channels, all three other channels can serve as receivers, and therefore any change between the cross sensor paths of the material structure can be monitored.
- Use of sensor types. The 1284 can use two types of sensors, i.e., a sensor without integral preamplifier and a sensor with integral preamplifier. This is achieved with a design of an internal preamplifier and a phantom power output circuit. A jumper is available to select either internal preamplifier or external preamplifier which allows very long signal cable from the sensor to the 1284.
- Real time waveform capture and feature extraction. The 1284 can not only do real time waveform capture but also extract the following AE features simultaneously, i.e., Time of Arrival, Peak Amplitude, Energy, Rise Time, Duration, Counts, ASL, RMS, Absolute Energy, and Time to Peak.
- Data storage. In order to buffer the possible large amount AE data, an SD memory card is available in the 1284. The capacity of the data storage depends on the capacity of the SD card. So far, up to 32 GB SD cards have been tested.
- Optimization of data saving and wireless data transfer. Due to the bandwidth limit of the Zigbee protocol used in the wireless sensor network, it is not possible to transfer all AE data including AE features and waveform data to remote computer in real time. Some of the data, especially the waveform data, have to be saved in local storage or SD card. Therefore, data transfer mechanism has been optimized in the 1284 to allow AE feature data to be transferred to the remote computer in real time, but all AE feature data and waveform data are actually saved in the local SD memory card simultaneously. The data files can be wirelessly or physically transferred to the base station computer later when the system is not busy.
- Event based front end filtering. In order to effectively remove noises and to reduce the amount of data stored or transferred, digital filtering and hit based front end filters are available in the 1284, as well as a special event based front

end filter is employed. This filter only allows saving and/or transfer of a sequence of AE hits or waveform data, resulting from an AE event.

- Data Logger. The 1284 can not only be used as a remote wireless sensor network but also as a data logger. The data acquisition can be started in two ways, i.e., controlled by a remote computer or self-start with power on. In the second case, no computer control is needed so that the unit can be left on test site to collect data as a data logger. Additionally, even if a start of data acquisition is initiated by the remote laptop, a discontinuation of the remote wireless connection between the 1284 and the laptop shall not affect the work of the 1284 which will continuously work as a data logger.
- Zigbee wireless protocol. Many wireless protocols are available in the market. However, considering power consumption, data transmission distance, capability of creating a mesh network and reasonable data transmission speed, Zigbee wireless protocol is used in the 1284. This made the 1284 to have very low power consumption (<0.5 W in continuous data collection and transmission), high hit transmission rate (250 hits/s), and long distance communication (up to 500 m depending on the site condition).
- Alarm output. The 1284 wireless system provides the capability of alarming based on user defined criteria obtained after careful review of AE data captured from a baseline response of damage detection and other system parameters like strain, load, temperature, and other quantities recorded by the instrument. Whenever the alarm criterion is met, the 1284 sends an alarm message to the base station wirelessly in conjunction with AE data.
- Weather protection. The 1284 has been designed to operate in a wide temperature range, −35 to +65 °C. All electronic circuit components are enclosed in an IP-67 NEMA box. So it can be used in varying weather environments without degrading the performance.

4 Examples of AE Test Results

The 1284 wireless AE system has now been substantially tested by some users in both laboratories and structural health monitoring sites. Here are two graphic examples of the test results.

The first example is a hit vs. time graph (Fig. 3) in a four-point bending test of a reinforced concrete structure. Cyclic load was applied to the structure, and it shows continued AE signal when the load is up. The AE hit activity is quiet when the load is at low level.

The second example is a waveform capture in crack detection test of steel material. Figure 4 shows a waveform and its spectrum acquired by the 1284 wireless system and transferred to the wireless base station. Since the sensor used is a 150 kHz low power integral preamplifier type, the spectrum clearly shows the peak frequency around the 150 kHz.

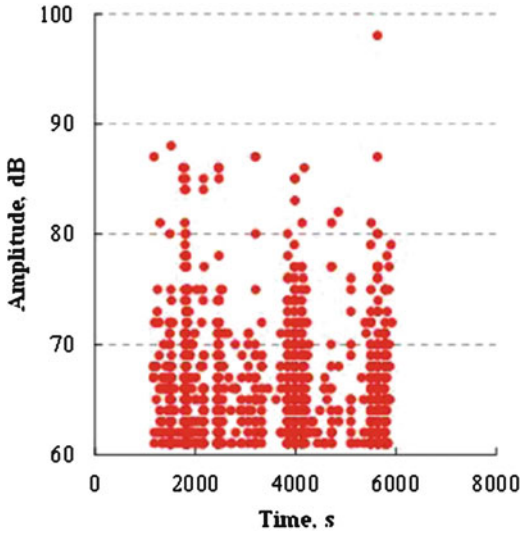

Fig. 3 Amplitude vs. time plot of a four-point bending test [7]

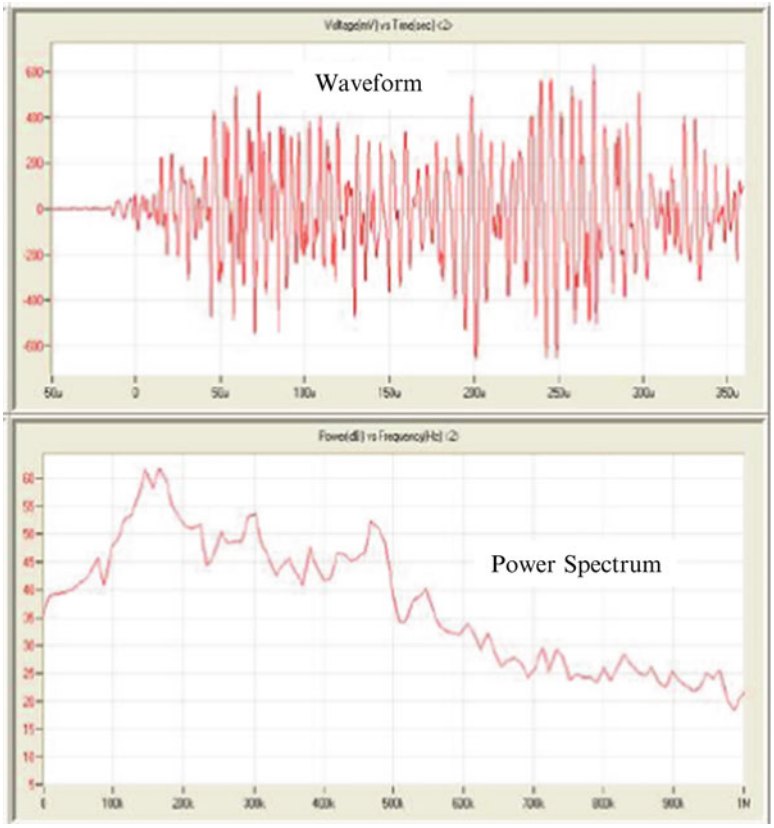

Fig. 4 AE waveform and power spectrum acquired by 1284 [6]

5 Conclusions

Though wireless AE system is very attractive in structural health monitoring because of its advantages in no cabling, there are many challenges before a wireless system can be reliably used in actual field sites. Sensor fusion, power availability and management, self-sensor checking, data storage, front end filtering, wireless communication and data transmission, etc. are of major concerns. This paper has addressed solutions to these concerns and described state-of-the-art technological features that have been implemented in a commercial wireless AE system. With the added state-of-the-art features, the developed wireless AE system has passed some laboratory and field tests conducted by several institutes and industrial users, and it has proven to be sustainable in field use.

References

1. C.U. Grosse, S.D. Glaser, M. Kruger, Initial development of wireless acoustic emission sensor motes for civil infrastructure state monitoring. Smart Struct. Syst. **6**(3), 197–209 (2010)
2. D.J. Yoon, S. Lee, C.Y. Kim, D.C. Seo. Acoustic emission diagnosis system and wireless monitoring for damage assessment of concrete structures. *NDT for Safety*, 7–9 November 2007
3. Y. Lu, J. Tang, Prototyping a wireless sensing platform for acoustic emission signals collected by microphone arrays. Sensors and smart structures technologies for civil, mechanical and aerospace systems. Proc. SPIE **7292** (2009)
4. Report on Wireless sensor networks using MEMS for acoustic emission analysis including other monitoring tasks. (Sustainable Bridges, SB-5.5, 2007) http://www.sustainablebridges.net/main.php/SB5.5.pdf?fileitem=22708623. Accessed 30 November 2007
5. A. Carpinteri, G. Lacidogna, A. Manuello, G. Niccolini. Acoustic emission wireless transmission system for structural and infrastructural networks. *VIII International Conference on Fracture Mechanics of Concrete and Concrete Sstructures*, *FraMCos-8*, 2013
6. V.F. Godinez, D.J. Inman, P.H. Ziehl, V. Giurgiutiu, A. Nanni, Recent advances in the development of a self-powered wireless sensor network for structural health prognosis. Nondestructive characterization for composite materials, aerospace engineering, civil infrastructure and homeland security. Proc. SPIE **7983** (2011)
7. V.F. et al. Self powered wireless sensor network for structural health prognosis. (NIST Technology innovation program final report, 2013) http://www.nist.gov/tip/proj_briefs/upload/tip_project_brief_080011_9h9007.pdf

Some Benefits of Storing AE Data in a Modern Database Format

Hartmut Vallen, Thomas Thenikl, and Gabriel Corneanu

Abstract During the development of our first AE system in the mid-1980s, we decided to store AE data in a binary file format. Back then, this was the best solution since data could be accessed randomly, not only sequentially, and stored to disk at highest speed and compactness. Several tasks can read the data simultaneously for online analysis. Since then the raw hit and parametric data are stored to a file with extension PRI. Waveform data and features extracted from it are stored to files with extension TRA and TRF, respectively. The fact that this format is still in use today speaks for its advantages. Its capability of simultaneously storing and reading of over hundred thousand hits per second during online analysis is still unsurpassed. A bottleneck is caused by the complexity of managing rather different kinds of data, such as hit driven and time driven features, waveforms, external parameters, labels, and others. This bottleneck makes it difficult to add new features and functions, and to give other parties' software read-access to all kinds of AE data in real time. Meanwhile the development in PC technology as well as in data management presents some nice alternatives in storing and organizing acquired AE data. The most flexible way in overcoming the limitations of the current file format and to address the upcoming challenges lies in using a database engine that organizes and manages measurement data. Trials have proven that performance of certain database engines satisfies our expectations and requirements with regard to speed, safety, and efficiency. These results as well as the upcoming challenges convinced us to start with the development of a new file format based on a modern SQL (Structured Query Language) database engine. SQLite is now implemented in our latest software release (R2013.0809) with excellent stability and maturity. Online analysis of over 100,000 hits per second is ongoing supported. It was never before so easy to support new features and functions by an AE data file format. The update to the new file format is included in the normal yearly update rate. Interested parties are invited to request an evaluation key that allows trying out the new software.

H. Vallen (✉) • T. Thenikl • G. Corneanu
Vallen Systeme GmbH, Icking 82057, Germany
e-mail: sales@vallen.de

G. Shen et al. (eds.), *Advances in Acoustic Emission Technology: Proceedings of the World Conference on Acoustic Emission-2013*, Springer Proceedings in Physics 158,
DOI 10.1007/978-1-4939-1239-1_3,

1 Introduction

The data acquisition unit of an acoustic emission (AE) system receives and measures AE signals from any number of AE sensors, converts the measurement results into digital data sets, and transfers them to the memory of the PC that controls the data acquisition. From the memory, data is stored to a permanent storage device, usually a hard disk, and also used by online analysis software, that performs a number of steps like data rejection based on filter criteria, AE source location, clustering statistical data processing, and data visualization in graphical and numerical form.

Only data stored on file can be processed during post analysis. The data format, written during data acquisition, determines important performance parameters, e.g., speed of data storage and analysis in terms of hits and waveforms per second, accuracy, resolution and dynamic range of measurements and time stamps, data volume in terms of bytes per hit and waveform, the versatility of using AE data in many different applications, and the accessibility of AE data by third-party software.

2 Previous Binary Data Format

Using the previous binary data format and a modern PC one can store, analyze, and visualize the results of more than hundred thousand hits per second in real time. The binary format creates very compact data files, compared to readable text format, and allows for fastest random access to any data set on the file, e.g., to start an analysis process at any desired data set.

2.1 Requirements on the AE Data Format

The data format must be able to store and read different kinds of data, e.g.,

- Hit driven AE feature data
- Time driven AE status data
- External parameter data
- System driven labels
- User entered labels
- Hit or time driven AE waveforms
- Features derived from AE waveforms after data acquisition.

Furthermore, the data format must allow for simultaneous access of data by different analysis tasks during data acquisition.

All these requirements lead to a considerable complexity that makes it difficult to extend the functional range and to implement new features and new kind of data, for example external data from a weather station.

2.2 *Limitations of the Previous Binary AE Data Format*

The main limitations of the previous data format were:

- Either "True Energy" (from squared AE signal) or "Signal Strength" (from rectified AE signal) must be selected prior to data acquisition.
- Only eight external parametric inputs were supported.
- Only 26 characters user-text per Label (unlimited numbers of labels) were supported.
- Dynamic range of time stamp was limited to about 280 days at 100 ns resolution (70 days at 25 ns resolution).
- Same waveform record time for short and long hits.

2.3 *Consequences*

A new modern AE data format would significantly shorten the efforts for the implementation of new functions and features.

A more flexible data format could accelerate the progress in AE technology!

The implementation of a new data format was one of our essential objectives over the past few years. It has already been implemented in the current software release R2013.0809 issued in August 2013.

3 Online Data Processing and Data File Types

Figure 1 shows the interrelation between real-time processes and involved types of data files in previous software versions:

After installing the new software release all data processing output file extensions have "dB" appended to it. This is the main difference the user will encounter.

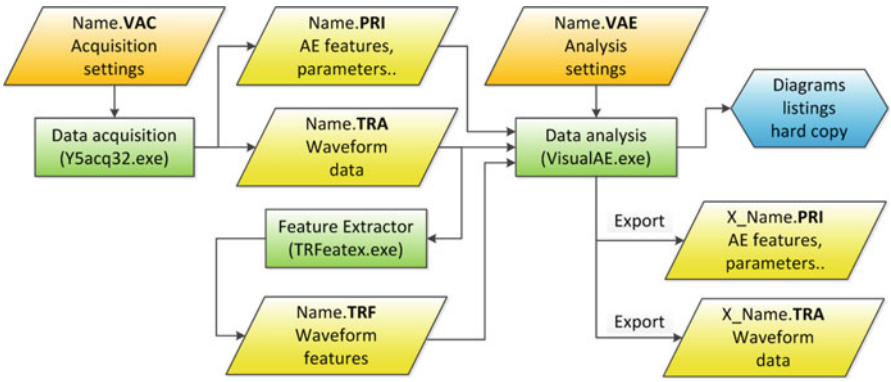

Fig. 1 Online data processing and data file types (previous versions)

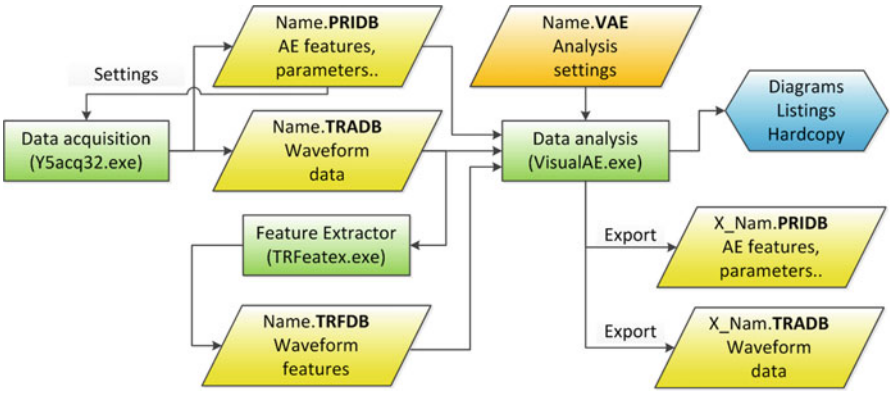

Fig. 2 Online data processing and data file types (new database version)

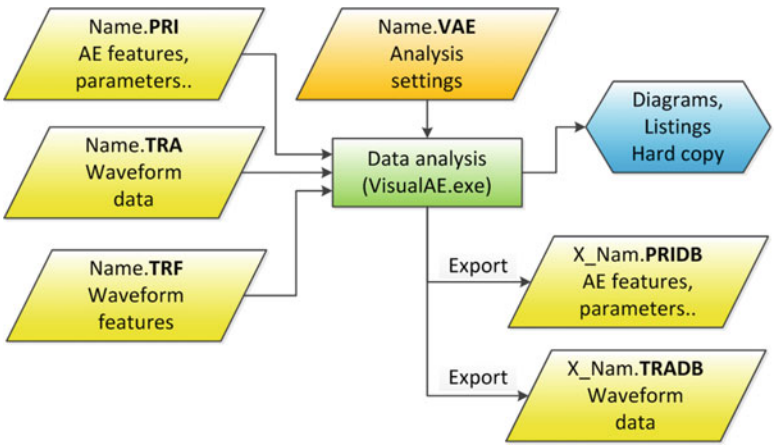

Fig. 3 In offline mode VisualAE can still process the previous binary format and export filtered data in new database format

Figure 2 shows the changed file extensions in their context. Each file with extension PRIDB, TRADB, and TRFDB contains a complete self-describing database structure which can be easily modified to match the requirements of new challenges. VisualAE, VisualTR, and VisualClass are still able to read and process the previous file format as shown in Fig. 3, as well as the new format. For projects in which TRF files are exchanged among the partners, we recommend all partners either to change to the new file format at the same time or to postpone the installation of the new version until the project is completed.

For the convenient conversion of any number of data files acquired by a previous software version to the database format, the conversion tool PRI2DB is provided.

4 Alternative Data File Formats

In the course of our analysis of the alternative data formats, we selected two as most promising: SQLite and HDF5.

4.1 Library and Data File Format HDF5

HDF5 is a multipurpose data file format and a software library for the storage of all kinds of scientific data (see [2]). But we recognized two essential limitations with HDF5 in the tested version:

First, the internal structure works with constant data set lengths, meaning that it would not become possible with HDF5 to store short compact waveforms of short hits and long waveforms of long hits.

Second, HDF 5 does not support the access of multiple simultaneously running analysis tasks to the file currently written by a data acquisition task.

4.2 Database Engine SQLite and Data File Format SQLite3

According to [1] SQLite is the most widely deployed "Structured Query Language" (SQL) database engine in the world. The source code for SQLite is in the public domain.

SQLite offers following advantages over the previous format:

- The language SQLite is very powerful, easy to learn and makes a self-describing data structure possible.
- Access is easier, compared to HDF5.
- There are a lot of free-of-cost tools available that let one examine the data structure and contents.
- SQL is used in thousands of applications, means it is very stable and mature.

We found very few disadvantages of SQLite:

- SQLite requires more data processing power than the binary file; however, hundred thousand hits per second online data analysis performance is still possible when using a Dual Core CPU.
- SQLite data files are a little bigger than the previous binary files.

5 Benefits of SQLite in Favor of AE Technology

Data transparency: Data can be read and analyzed by proven and widespread tools like MATLAB without the need of a prior conversion. Free-of-cost tools make it possible to examine the structure and contents of internal tables. Figure 4 shows

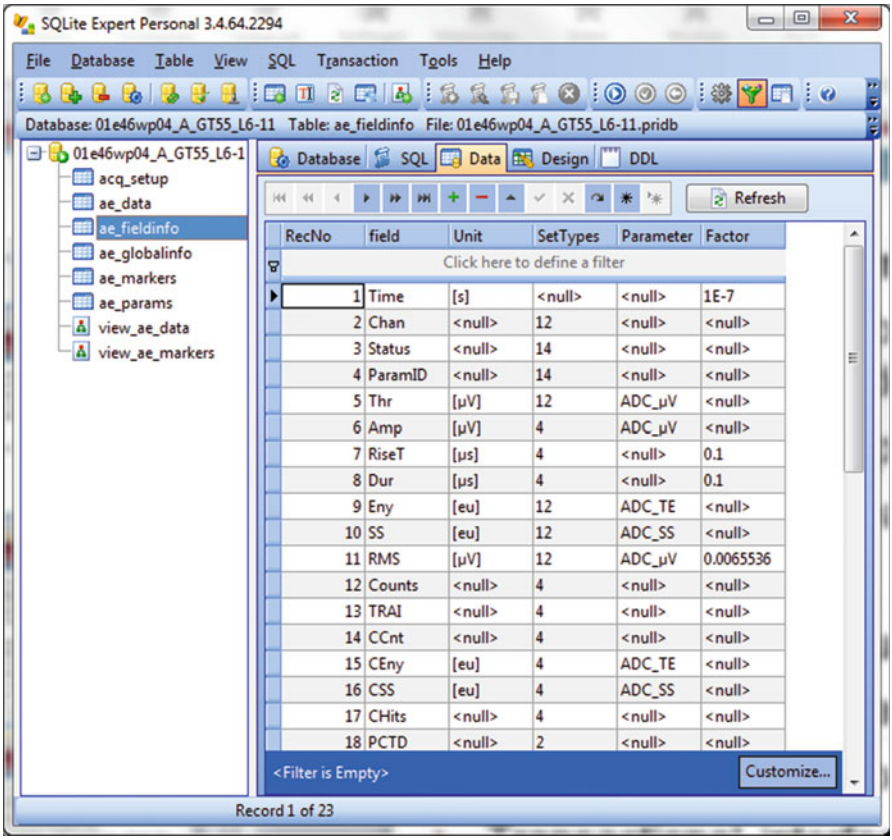

Fig. 4 Free-of-cost tool "SQLite Expert" shows structure (tables on the *left*) and content of one selected table (on the *right*)

a screen dump of "SQLite Expert" one of the mentioned free-of-cost tools. On the right of Fig. 4 you see a table showing the supported variables and their conversion rules to obtain values in physical units from the internally used integer format. All data measured are provided in tables of raw integer format as well as in tables of values converted in physical units.

Flexibility: Implementing new functions and features becomes easier, and progress in AE technology becomes accelerated.

True Energy (E) and Signal Strength (SS) are acquired and can be shown simultaneously. Previously the operator had to select either E or SS prior to starting data acquisition (see Fig. 5).

Variable storage length of waveform data: can be adapted to the length of a hit. Short hits, short waveform length, less memory occupation, long hits, long waveform length, more memory occupation. (Complete realization planned for 2014).

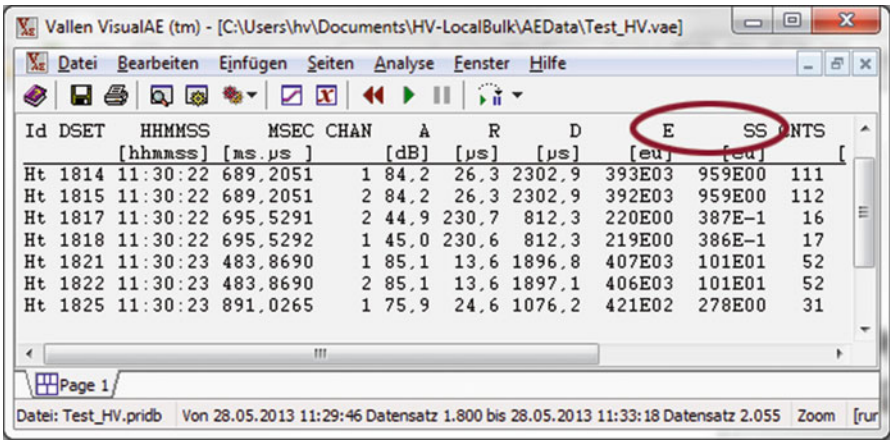

Fig. 5 True Energy (E) and Signal Strength (SS) can be shown simultaneously

Self-describing names for Waveform features extracted by TR feature extractor. Previously, one had to assign one of the names FEx08 to FEx15 to one of 38 offered waveform features in the TR Feature Extractor program in order to get this waveform feature visualized in VisualAE. Now one can select a self-describing name, e.g., "T2_SR5" for "Spectral Ratio of time segment 2 and frequency segment 5" and gets this name offered by VisualAE for data visualizing or filtering.

Any number of external parameters can be supported. The current version supports 16 external parameters (PA0 to PA15, can be expanded to any desired number in near future).

New data integrity check: A manipulation of stored data during or after data acquisition will be discovered and indicated by VisualAE (Fig. 6).

6 Compatibility with Previous Software Releases

Profound changes in software are sometimes met with resentment. We wish to avoid this by making the transition easy and safe. As it can be seen in the sequence of Figs. 1–3, the user realizes the transition just by the modified file extensions PRIDB, TRADB, and TRFDB. The "DB" in the extension gives the hint that each file is a complete and transparent database.

VisualAE, VisualTR, and VisualClass can read the previous as well as the new file format. There is no need to reinstall previous software just for being able to read data acquired in the past. But the client should be aware that data generated by the new software cannot be read by previous software releases.

In Vallen Control Panel (Fig. 7) you find the new tool "PRI2DB." This tool converts any number of PRI and TRA files in one step to PRIDB and TRADB files.

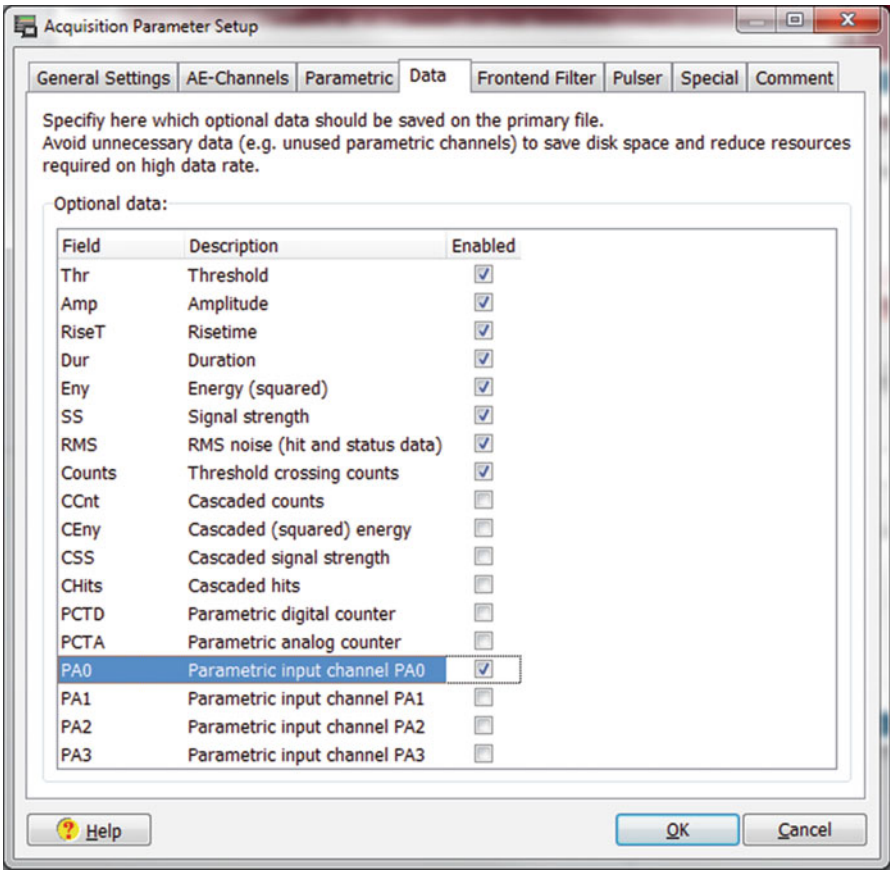

Fig. 6 Parameters not required can now be switched off from data acquisition in order to save space and processing power

7 Prospect

The Implementation of the new data format has been a serious concern for us over the last few years and a challenging task. The new data file format gives us the chance to realize a number of new features addressed by our customers that could not be done in an efficient manner with the previous data file format.

The new format allows read-access of all kind of stored data by third-party software, even during data acquisition. Customers can now, independently of us, develop their own software and perhaps develop new markets for the AE testing method.

Our sincere intention was that the new data file format will contribute to the success of our customers and to further progress of the AE testing technology.

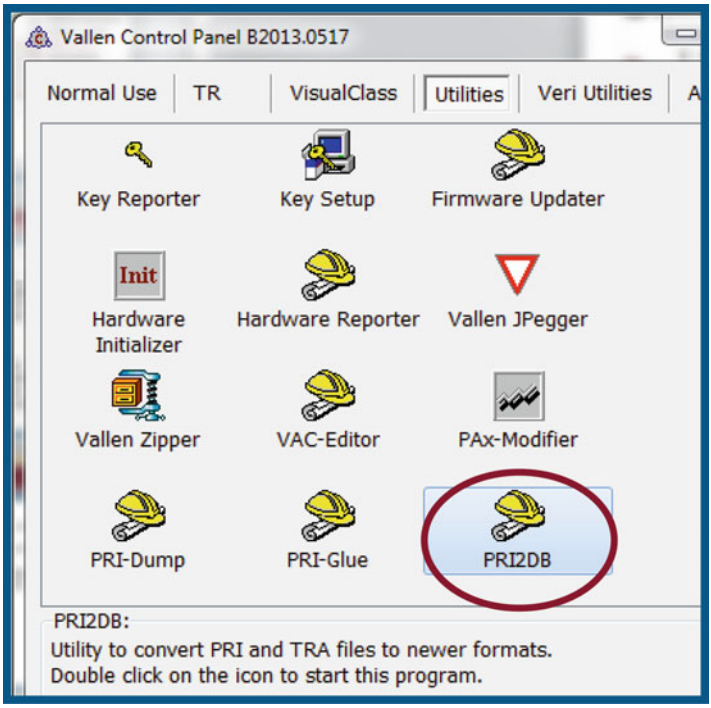

Fig. 7 New Tool "PRI2DB" added, other program names and usage have not been changed remarkably

References

1. Public domain; "Features Of SQLite"; http://www.sqlite.org/features.html
2. The HDF Group, 1800 South Oak Street, Suite 203, Champaign, IL 61820; "What is HDF5", http://www.hdfgroup.org/HDF5/whatishdf5.html

Calibration Principle for Acoustic Emission Sensor Sensitivity

Dingguo Xiao, Zhaona Zhang, Huiling Ren, Bo Yang, Qinxue Pan, and Chunguang Xu

Abstract Acoustic emission sensors are the most important part of an acoustic emission detection system, which directly determines the validity and accuracy of the detection result. In order to improve the reliability of acoustic emission test results, the sensor's sensitivity must be calibrated ahead of time. This chapter investigates the face-to-face secondary calibration method and presents the laser vibrometer primary calibration method for acoustic emission sensor sensitivity. A sensor sensitivity calibration system was built. Calibration experiments have been carried out. Finally, measurement uncertainty was analyzed.

1 Introduction

Acoustic emission (AE) has been defined as the spontaneous release of elastic energy by material when it undergoes deformation [1]. As one of the nondestructive testing methods, AE technique has been widely used in different areas such as petrochemical, aerospace, transportation, metal processing, material testing, and structural health monitoring [2–4].

However, acoustic emission sensors (AE sensors) without calibration cannot ensure results' reliability of the acoustic emission test [5]. With the advance of acoustic emission detection technology, sensitivity calibration of acoustic emission sensor technology has also developed rapidly as an important prerequisite for the former. Sensor sensitivity is the basic information for checking sensor performance, making acoustic emission quantitative detection and tracing quantity.

D. Xiao (✉) • Z. Zhang • H. Ren • B. Yang • Q. Pan • C. Xu
Key Laboratory of Fundamental Science for Advanced Machining, Beijing Institute of Technology, Beijing 100081, China
e-mail: xiaodg@bit.edu.cn

G. Shen et al. (eds.), *Advances in Acoustic Emission Technology: Proceedings of the World Conference on Acoustic Emission-2013*, Springer Proceedings in Physics 158,
DOI 10.1007/978-1-4939-1239-1_4,

The calibration signal should be characteristic of the parameters determined in the time and frequency domains and be as close to the AE signal as possible [2, 6, 7]. So it is necessary to produce a pulse of strictly determined and repeatable AE parameters.

The existing measurement techniques of acoustic emission sensor sensitivity include the reciprocity technique [8], laser vibrometer technique [9, 10], and surface pulse technique [11]. However this chapter develops a method of acoustic emission sensor sensitivity calibration, which takes a broadband ultrasonic transducer as an acoustic emission source and makes acoustic emission sensor face to face coupled to it. One is the standard acoustic emission sensor whose sensitivity has been surveyed, and the other one is a measured acoustic emission sensor. Then it is called face-to-face secondary calibration method.

2 Acoustic Emission Sensor Sensitivity and Its Calibration Method

2.1 The Sensitivity Definition of an Acoustic Emission Sensor

The input of an acoustic emission sensor is force, displacement, or speed, and the output of it is voltage [12]. The sensor can be regarded as a linear system. The sound pressure is often considered as input when sound-transmitting medium is liquid, and the pressure sensitivity is used to describe the characteristics of the sensor:

$$U_p(\omega) = H_p(\omega)P(\omega). \tag{1}$$

When sound-transmitting medium is solid, the particle velocity is used as the input, and the particle velocity sensitivity is used to describe the characteristics of the sensor:

$$U_v(\omega) = H_v(\omega)v(\omega), \tag{2}$$

where $U_p(\omega)$ and $U_v(\omega)$ are output voltage of the sensors, $H_p(\omega)$ and $H_v(\omega)$ are transfer functions of the sensors, $P(\omega)$ is the input sound pressure to the sensor, and $v(\omega)$ is the input particle velocity to the sensor, and the relation between $P(\omega)$ and $v(\omega)$ is

$$P(\omega) = v(\omega)\rho c, \tag{3}$$

where ρ is the density of the sound propagation medium, and c is the sound velocity of the propagation medium. Generally, the amplitude spectra of a sensor transfer function is defined as its sensitivity, namely

$$S_p(\omega) = \left|H_p(\omega)\right| = \frac{\left|U_p(\omega)\right|}{|P(\omega)|} \tag{4}$$

$$S_v(\omega) = |H_v(\omega)| = \frac{|U_v(\omega)|}{|v(\omega)|}, \tag{5}$$

where $S_p(\omega)$ is the sound pressure sensitivity, and $S_v(\omega)$ is the particle velocity sensitivity.

2.2 Primary Calibration and Secondary Calibration

There are two calibration methods of acoustic emission sensor sensitivity, that is, primary calibration and secondary calibration [13–17]. For primary calibration, input and output of the sensor need to be measured directly, and pressure sensitivity or particle velocity sensitivity are worked out by Eq. (4) or (5). For secondary calibration, a standard sensor with its sensitivity calibrated is used. Under the same acoustic emission source, output voltage of the standard sensor and that of the sensor to be tested are measured; sensitivity of the sensor to be tested is calculated based on the sensitivity of the standard transducer and output signals of the two sensors.

The reciprocity method and the surface pulse method can be used for primary calibration, but it is not suitable to use in the industry due to its complexity. Therefore, the secondary calibration method is mostly used in the industry. There are industrial standards to guide the sensitivity calibration of acoustic emission sensor.

GB/T 19800-2005/ISO 12713:1998 nondestructive testing—First calibration of acoustic emission testing transducer [12] provides a primary calibration method for the acoustic emission sensors, which takes the impact force produced by capillary glass tube rupture as a sound source to measure the impact and acoustic emission sensor output voltage and then calculate particle velocity sensitivity. This standard applies to the calibration of the standard sensor used for secondary calibration and high-performance sensors used for detection.

GB/T 19801-2005/ISO 12714:1999 nondestructive testing—Secondary calibration of acoustic emission testing transducer [13] provides a secondary calibration method for acoustic emission sensors; a standard sensor and a tested sensor are placed in the symmetry location from the sound source in a measurement device, which receives solid medium surface elastic waves. The output signals are processed to calculate sensitivity of the tested sensor. This standard applies to the calibration of the sensors used for detection.

This chapter investigates a secondary calibration method to measure acoustic emission sensor sensitivity, where a broadband ultrasonic transducer is taken as a sound source and couples to the acoustic emission sensors face to face. The method has the features of low cost, simplicity of operation, and suitability for industry. Meanwhile, the laser vibrometer primary calibration method is also used to measure the sensitivity, and then, it is compared with the face-to-face secondary calibration method. Finally, the secondary calibration method is confirmed to be correct and feasible.

3 The Calibration Method

3.1 The Laser Vibrometer Primary Calibration Method

In the primary calibration method, a broadband ultrasonic transducer is used as sound source. A laser vibrometer is used to measure the vibration velocity $v(t)$ of the source transducer. As shown in Fig. 1, the output voltage $u_1(t)$ of the vibrometer represents the vibration of the source transducer. If an AE sensor to be calibrated is coupled to the source transducer and its output voltage $u_2(t)$ is measured. Suppose the sensitivity of the laser vibrometer is $S_l(\omega)$ and the Fourier transforms of $u_1(t)$ and $u_2(t)$ are $U_1(\omega)$ and $U_2(\omega)$, the sensitivity of the AE sensor can be obtained as

$$S_t(\omega) = \frac{U_2(\omega)}{U_1(\omega)} S_l(\omega). \tag{6}$$

Take 1 V/(m/s) as reference sensitivity; the sensitivity of the AE sensor to be calibrated can be expressed by decibel as

$$S_t(\omega) = 20\lg\left|\frac{U_2(\omega)}{U_1(\omega)}\right| S_l(\omega) = 20\lg\left|\frac{U_2(\omega)}{U_1(\omega)}\right| + 20\lg S_l(\omega). \tag{7}$$

3.2 The Face-to-Face Secondary Calibration Method

In this method, a broadband ultrasonic transducer is also used as sound source. The acoustic emission sensor is face to face coupled to the source transducer, as shown in Fig. 2.

Broadband ultrasonic transducer would generate sound vibration of good reproducibility with velocity $v(t)$ on its surface under the excitation of repetitive electric signals, and then make the standard sensor with known sensitivity and the sensor to

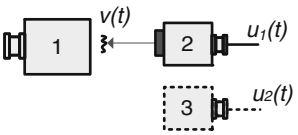

Fig. 1 The primary calibration method. *1*—Sound source transducer, *2*—laser vibration sensor head, *3*—Acoustic emission sensors

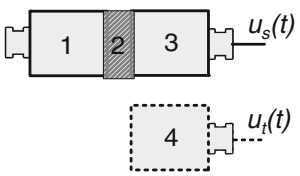

Fig. 2 Transducer coupling. *1*—Sound source transducer, *2*—coupling agent, *3*—standard sensor, *4*—tested sensors

be calibrated by face to face coupled to the source transducer, respectively; the output voltage signals $u_s(t)$ and $u_t(t)$ are measured.

Set the sound source signal spectrum as $V(\omega)$, the spectrum of acoustic emission sensor output signals $u_s(t)$ and $u_t(t)$ as $U_s(\omega)$ and $U_t(\omega)$, respectively, and the transfer function of the standard sensor and the tested sensor as $H_S(\omega)$ and $H_t(\omega)$, according to linear system theory:

$$H_s(\omega) = \frac{U_S(\omega)}{V(\omega)} \tag{8}$$

$$H_t(\omega) = \frac{U_t(\omega)}{V(\omega)}. \tag{9}$$

Combining Eqs. (8) and (9),

$$H_t(\omega) = \frac{U_t(\omega)H_s(\omega)}{U_s(\omega)} \tag{10}$$

$$|H_t(\omega)| = \left|\frac{U_t(\omega)}{U_s(\omega)}\right||H_s(\omega)|. \tag{11}$$

According to the definition of sensitivity, the sensitivity of the standard sensor is $S_s(\omega) = |H_s(\omega)|$, the sensitivity of the sensor to be calibrated is $S_t(\omega) = |H_t(\omega)|$, and then $S_t(\omega) = \left|\frac{U_t(\omega)}{U_s(\omega)}\right|S_s(\omega)$. Take 1 V/(m/s) as reference sensitivity; the sensitivity of the sensor to be calibrated can be expressed by decibel as

$$S_t(\omega) = 20\lg\left|\frac{U_t(\omega)}{U_s(\omega)}\right|S_s(\omega) = 20\lg|U_t(\omega)/U_S(\omega)| + 20\lg S_s(\omega). \tag{12}$$

By measuring output signals of the standard sensor and the tested sensor under the action of broadband ultrasonic transducer sound source, the sensitivity $S_t(\omega)$ of the tested sensor can be calculated by the means of time-frequency domain transform and the known sensitivity of the standard sensor.

For the above two methods, the time-domain signal collected should undergo process of de-noising, windowing, and DC removing. The narrowest main lobe width and larger side lobe attenuation can be obtained as much as possible by windowing, Blackman window is chosen to reduce leakage. Being the DC component, Fourier transforming has the characteristics of low frequency and harmonicity, whose leakage will affect the low-frequency part of the spectrum curve; the signal needs to be DC-removed. As discrete data sampling leads to spectrum leakage and aliasing, and windowing does not ensure side-lobe disappearance completely, a low-pass filter must be used to reduce the error.

4 The Calibration System of AE Sensor Sensitivity

As shown in Fig. 3, the calibration system of AE sensor sensitivity is based on the platform of an industrial computer, which consists of ultrasonic transducer excitation device, sensor coupling device, laser vibrometer, and signal acquisition device. The signal generated by arbitrary waveform generator card will motivate source ultrasonic transducer. The amplified output signals from standard AE sensors and tested AE sensors, which couple to source ultrasonic transducer, will be sampled and quantified into digital signals by the signal acquisition card, by which the computer software will work out the sensitivity by face-to-face calibration. For the primary calibration, the laser vibrometer is used to measure the vibration signal of the sound source transducer. Then output signal of the evaluated sensor is surveyed by secondary calibration. Finally, the sensitivity based on the primary calibration method is calculated by the software.

To make the sound source signal stable, the calibration system uses arbitrary waveform generator card to produce sweep frequency signal, which is a stable and repetitive signal, and can ensure the consistency of the multiple excitation signals.

The standard sensor sensitivity has been calibrated by the US National Institute of Standards and Technology, which can meet the requirements of the secondary calibration and is appropriate to the secondary calibration system.

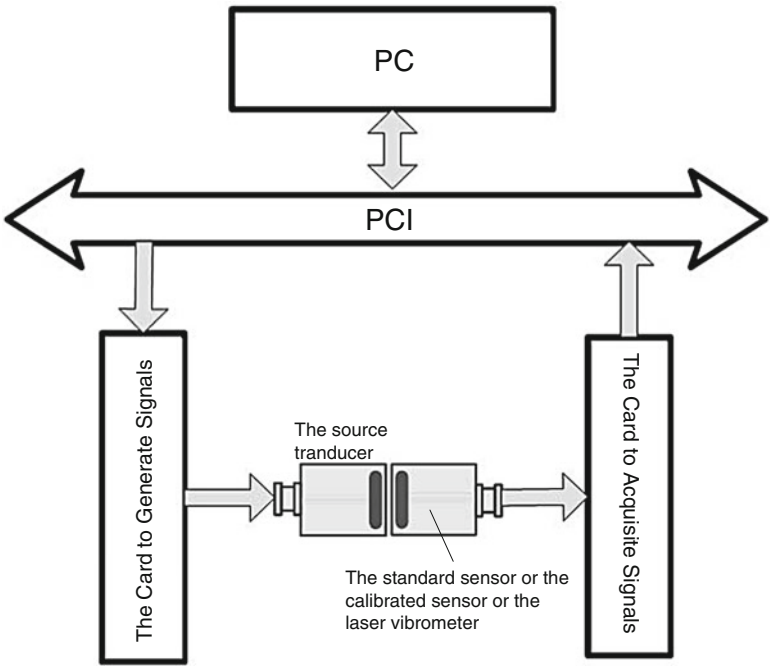

Fig. 3 The calibration system block diagram

Laser vibrometer is manufactured by Polytec GmbH. It consists of a laser sensing head and a vibrometer controller. It can measure the velocity or the displacement of the source ultrasonic transducer.

The acquisition card is a high-speed, low-noise card, with variable gain amplifier and filter; its sampling rate is up to 40 MHz. The card has four high-pass and six low-pass filter selections totally under software control.

5 Calibration Experiments and Result Analysis

5.1 AE Sensor Sensitivity Measuring Experiment

The source transducer employed in the devices is a wideband ultrasonic transducer. Its resonant frequency is 500 kHz. Therefore, the transducer can produce sound wave with frequencies in the range of 0–1 MHz. The standard sensor is an NIST-calibrated R15-type AE sensor made by Physical Acoustic Corporation (PAC).

Firstly, the standard sensor is tested by the primary calibration method with laser vibrometer in order to validate this primary calibration method. The result comparison is shown in Fig. 4.

From Fig. 4, the result of the laser vibrometer primary calibration method is basically consistent with that given by NIST. In the resonance frequency, the difference of sensitivity between two methods is 0.8 dB. In the low and high frequency, the sensitivity tested by the laser is higher than that given by NIST.

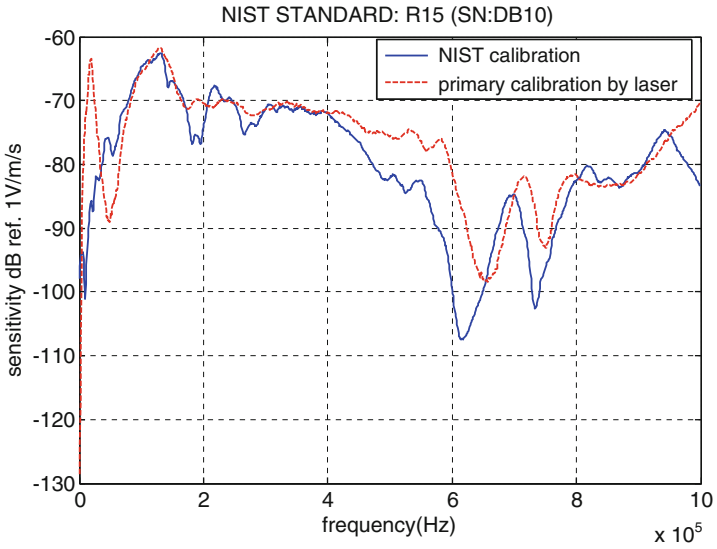

Fig. 4 Comparison of sensitivity of the standard sensor

Given unknown method by NIST, the fact that the laser vibrometer has very high sensitivity is the prime reason to cause errors. Therefore, the laser vibrometer primary calibration is feasible.

Many sensitivity measurement tests are conducted with face-to-face secondary calibration method and the laser vibrometer primary calibration method for various AE sensors, including R15 (SN:DB05), R15 (SN:DB19), R30 (SN:410), and R50 (SN:568) made by PAC company. The sampling frequency is set to 10 MHz that is significantly greater than 1 MHz; the resonant frequency of these sensors ranges from 0 to 1 MHz. The results of the two calibration methods are compared in Fig. 5.

From the figures, it can be seen that the variation trends of the two sensitivity curves achieved by the two methods are extremely consistent. The resonant frequency and its sensitivity value from two methods are listed in Table 1.

According to relevant standard [16], 95 % of the calibration frequency response data must agree with the primary calibration data within an error band defined by $\pm(U + 1.5)$. From these figures and the table, the face-to-face calibration method is very practical.

5.2 Measurement Uncertainty Analysis

The identification of uncertainty causations should embark on the analysis of the measurement process, which means to start a detailed study on the measurement method, measurement system, and measurement procedure.

There are several uncertainty sources in face-to-face calibration, including the inherent random causations, uncertainty of repeated measurements, uncertainty of the standard sensor sensitivity, uncertainty introduced by the preamplifier, and uncertainty caused by signal acquisition.

From these sensors, R15 (SN:DB05) is chosen to calculate its measurement uncertainty. It is measured ten times and the results are shown in Table 2.

According to Table 2, the mean value and standard deviation of sensitivity measurement used in face-to-face calibration method can be calculated, and the results are shown in Eq. (13):

$$\begin{cases} S = -61.36 \text{ dB} \\ \sigma = 0.006 \text{ dB}. \end{cases} \tag{13}$$

Uncertainty of repeated measurements is computed by Eq. (14):

$$\sigma_v = \frac{\sigma}{\sqrt{10}} = \frac{0.006V}{\sqrt{10}} = 0.0019 \text{ dB}. \tag{14}$$

Table 3 lists all uncertainty components analyzed. Uncertainty causations are independent of each other and thus, the combined uncertainty is obtained by Eq. (15):

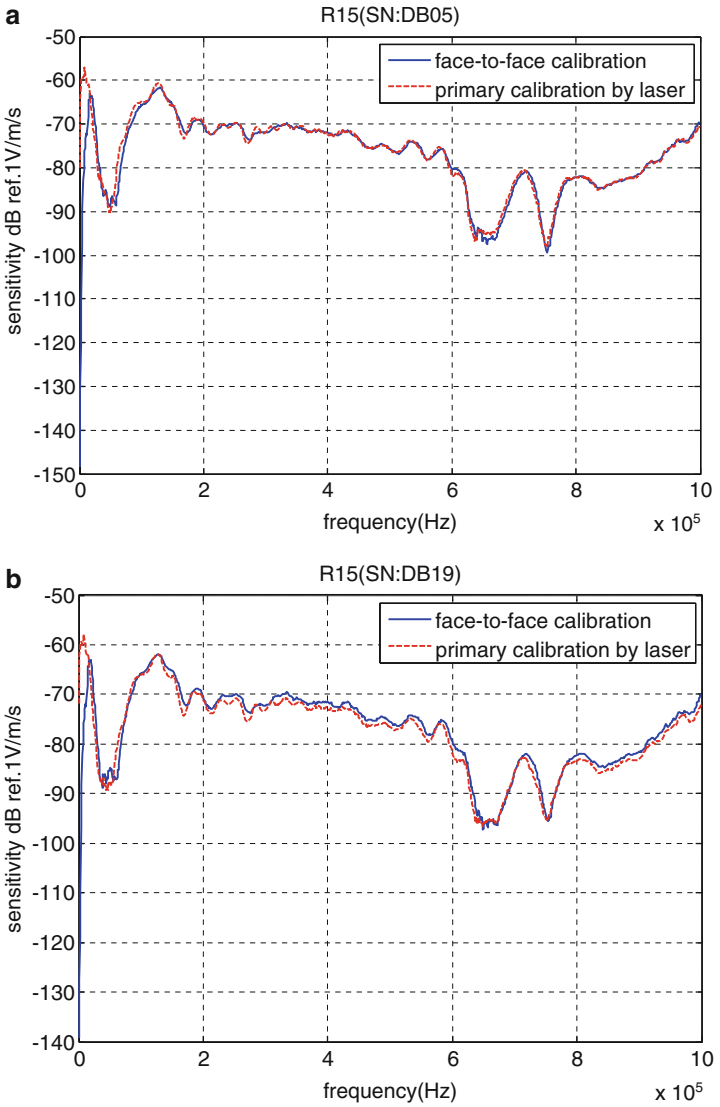

Fig. 5 The comparison of sensitivity of sensors. (**a**) R15(SN:DB05), (**b**) R15(SN:DB19), (**c**) R30 (SN:410), (**d**) R50(SN:568)

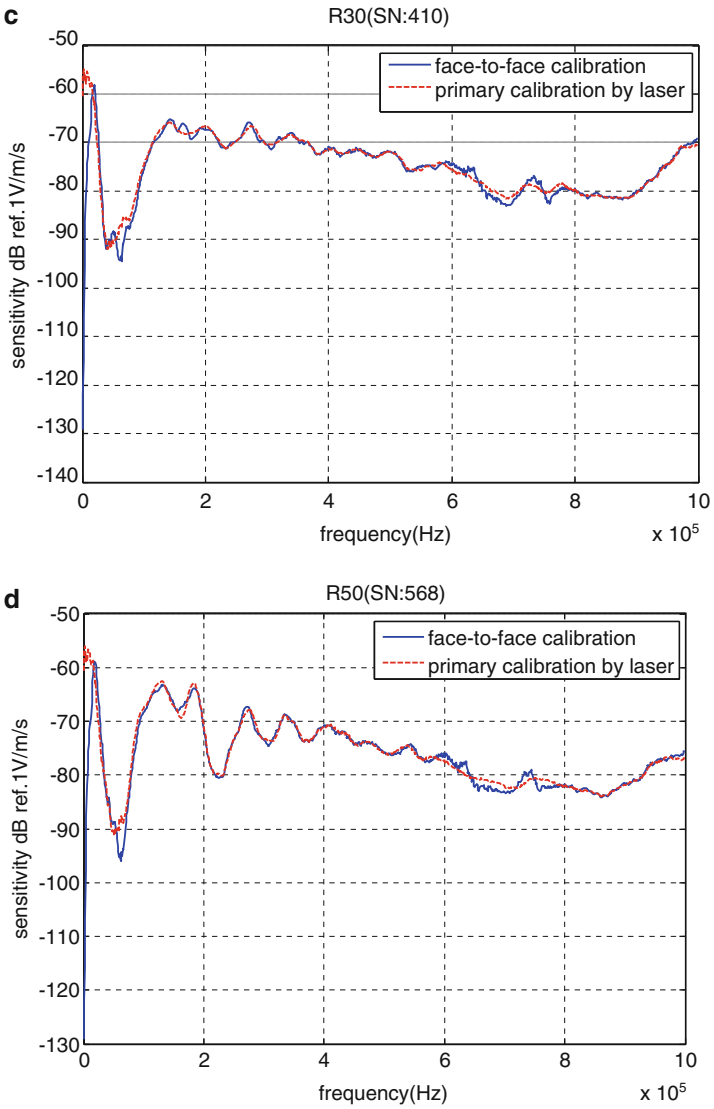

Fig. 5 (continued)

Table 1 Sensitivity value and resonant frequency from two methods

Sensors	Item	Face to face	Laser	Difference (%)
R15 (SN:DB05)	Value (dB)	–61.69	–60.7	1.63
	Frequency (kHz)	130	128	1.56
R15 (SN:DB19)	Value (dB)	–61.89	–61.88	0.02
	Frequency (kHz)	130	127	2.36
R30 (SN:410)	Value (dB)	–67.53	–68.18	0.95
	Frequency (kHz)	272	275	1.09
R50 (SN:568)	Value (dB)	–63.77	–62.97	1.27
	Frequency (kHz)	183	184	0.54

Table 2 Repeatability measurements of R15 (SN:DB05)

No.	Frequency (kHz)	Sensitivity (dB)
1	131	–61.40
2	130	–61.37
3	131	–61.34
4	130	–61.35
5	131	–61.35
6	131	–61.35
7	130	–61.37
8	130	–61.34
9	131	–61.35
10	130	–61.34

Table 3 Uncertainty component list

Components	Evaluation method	Distribution	Uncertainty (dB)
Repeated measurements	A	Normal	0.0019
Standard sensor sensitivity	B	Normal	0.275
Preamplifier	B	Normal	0.1
Acquisition card	B	Uniform	0.289

$$\begin{aligned} u &= \sqrt{u^2(x) + u^2(S) + u^2(S) + u^2(P)} \\ &= \sqrt{0.0019^2 + 0.275^2 + 0.1^2 + 0.289^2} = 0.41 \text{ dB}. \end{aligned} \tag{15}$$

Taking confidence probability $P = 95$ % [17], coverage factor $k = 2$; thus, the expanded uncertainty of sensitivity calibration is

$$U = ku = 2 \times 0.41 \text{ dB} = 0.82 \text{ dB}. \tag{16}$$

6 Conclusion

This chapter proposes a face-to-face secondary calibration method and a laser vibrometer primary calibration method for acoustic emission sensor sensitivity measurement. In this secondary calibration method, a broadband ultrasonic transducer is taken as a sound source and couples to acoustic emission sensors face to face. The standard sensor is calibrated by the primary calibration method, and then its sensitivity is almost the same to that of NIST. The primary calibration is extremely practicable. After that, the two calibration methods are compared, and they are very consistent. Given the popular use and price, the face-to-face calibration method is more cost effective than the laser vibrometer primary calibration. The calibration system has been constructed that adapts to these two methods. It has stable performance and is easy to operate. And this technology for the sensitivity calibration of acoustic emission sensor can be popularized.

References

1. Jiri Keprt, Determination of uncertainty in calibration of acoustic emission sensors, *4th International Conference on NDT*, **10** (2007)
2. J. Kaiser, Messung von geräuschen bei zugbeanspruchung von metallischen werkstoffen. Arch. f. Eisenhüttenwesen. **25**, 43 (1953)
3. Tomasz Boczar, Marcin Lorenc, Determining the repeatability of acoustic emission generated by the hsu-nielsen calibration source. Mol. Quantum. Acoust. **25** (2004)
4. Dai Guang, Acoustic emission technique in China. Non-Destruct. Test. **30**, 7 (2008)
5. Yang Ruifeng, Ma Tiehua, Acoustic emission technology research and application. Acad. J. N. Univ. China. **27**, 5 (2006)
6. Y. Berlinsky, M. Rosen, J. Simmons, H.N.G. Wadley, A calibration approach to acoustic emission energy measurement. J. Nondestruct. Eval. **10**, 1 (1991)
7. Hao Yongmei, Xing Zhixiang, Shao Hui, Gu Xiaohui, Experimental analysis of acoustic emission detection sensitivity calibration source. China. Safety. Sci. Technol. **6**, 5 (2010)
8. H. Hatano, T. Chaya, S. Watanabe, K. Jinbo, Reciprocity calibration of impulse responses of acoustic emission transducers. IEEE. Transact. UFFC. **45**(5), 1221–1228 (1998)
9. Xu Jianping, Li Mingxuan, The calibration and performance measurement for detection ultrasonic transducer. Appl. Acoust. **B**, 6 (1989)
10. Li Guanghai, Liu Shifeng, Geng Rongsheng, Shen Gongtian, The latest method of the acoustic emission source feature identification. Non-Destruct. Test. **12**, 24 (2002)
11. R.K. Miller, P. McIntre, *Acoustic emission testing*. In Nondestructive Testing Handbook, vol. 5. (American Society for Nondestructive Testing, 1987)
12. GB/T 19800-2005/ISO 12713:1998 non-destructive testing—First calibration of acoustic emission testing transducer
13. GB/T 19801-2005/ISO 12714:1999 non-destructive testing—Secondary calibration of acoustic emission testing transducer
14. ASTM Standard E1106-86, Standard method for primary calibration of acoustic emission sensors (ASTM, Philadelphia, 1986)

15. ASTM Standard E750-88, Standard practice for characterizing acoustic emission instrumentation (ASTM, Philadelphia, 1988)
16. ASTM Standard E1781-96, Standard practice for secondary calibration of acoustic emission sensors (ASTM, Philadelphia, 1996)
17. ASTM Standard E976-84, Standard guide for determining the reproducibility of acoustic emission sensor response (ASTM, Philadelphia, 1984)

Development of a Pipeline Leakage Location Instrument Based on Acoustic Waves

Gongtian Shen, Shifeng Liu, and Zhenlong Hu

Abstract A pipeline leakage location instrument based on acoustic method and correlation location of continuous signals was developed. This instrument uses a lot of advanced electronic techniques such as low-frequency acoustic emission sensor, high-speed acquisition of waveform of leakage signals, wireless data communication based on Internet, data high-speed communication-based USB, and time control based on GPS positioning. The real-time leakage location test and remote wireless leakage location test are realized for different kinds of pipelines with different medium leak. The testing result proves that this instrument can detect the leakage of 1 mm hole far from 50 m and 2 mm hole far from 100 m for steel pipeline under 0.4 MPa compressed air.

1 Introduction

Underground pipelines are widely used for water and gas supply in the world. The leakage accidents continually happen due to the corrosion for the steel pipeline. It is very important quickly to test and accurately to locate the leakage point for the disposal of leakage accident. Several models of the leakage location testing instruments based on acoustic waves for water pipeline have been developed and sold in the market. But these instruments are not applicable to test and locate the leakage point of gas [1]. This chapter introduces the development of a new gas pipeline

G. Shen (✉) • Z. Hu
China Special Equipment Inspection and Research Institute, Beijing 100013, China
e-mail: shengongtian@csei.org.cn

S. Liu
Beijing Soundwel Technology Co., Ltd, Beijing 100012, China
e-mail: sliu@soundwel.cn

G. Shen et al. (eds.), *Advances in Acoustic Emission Technology: Proceedings of the World Conference on Acoustic Emission-2013*, Springer Proceedings in Physics 158,
DOI 10.1007/978-1-4939-1239-1_5,

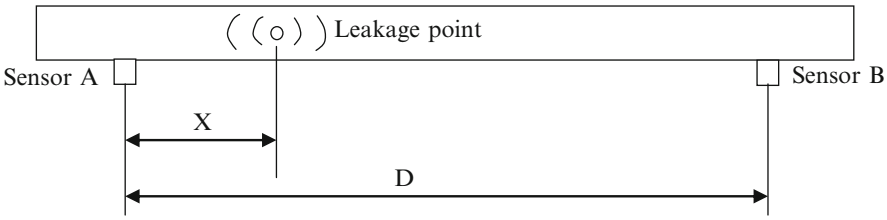

Fig. 1 Principle of leakage point location for pipeline

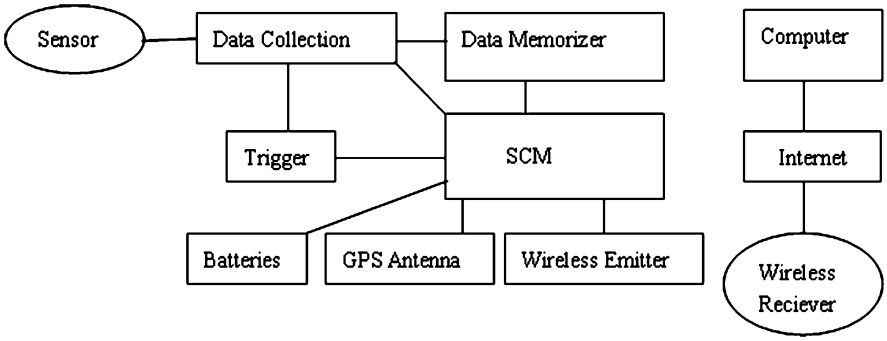

Fig. 2 The configurable chart of the instrument

leakage location testing instrument based on correlation of acoustic waves produced by gas leakage.

Figure 1 is the principle of the gas pipeline leakage location testing. The signals produced by gas leakage are continuous signals for pipeline. The main frequency range is within 5–60 kHz for gas leakage of pipeline. Through performing correlation between waveforms of sensor A and sensor B, the time difference Δt between sensor A and sensor B can be obtained [2, 3]. The coordinate X of leakage point could be calculated as follows:

$$X = [D - (V * \Delta t)]/2. \tag{1}$$

2 Design of the Pipeline Leakage Testing Instrument

Figure 2 is the designed configurable chart of the gas pipeline leakage testing instrument. Low-frequency acoustic emission sensors detect the leakage signals. Data acquisition modules collect the waveforms of leakage signals. After testing, all data of the waveforms collected by data acquisition modules are transmitted to a computer. The correlation analysis and location calculation are performed for the waveforms of two adjacent sensors by the use of the software in the computer.

The acquisition module of leakage signals is controlled by a Single Chip Micyoco (SCM). It includes in A/D cell, data memorizer cells, trigger cell, batteries, time-receiving cell from GPS, USB communication cell, and wireless emitter control circuit. The trigger is responsible for activating the acquisition module according to preestablished time. A/D cell transforms the analog signals to digital data. The digital data are saved in data memorizer. There are three ways for data transmission from acquisition module to computer. The first method is to use USB cable directly. The second method is to use wireless digital transmitter–receiver. The third method is to use wireless CDMA to send the data to Internet, the computer go to internet to download the data.

In order to realize the location of leakage point, it is very important to get the accurate time difference between two sensors. But the clock of different acquisition modules are very difficult to be synchronous. In order to solve this issue, the common accurate clocks are obtained through GPS antenna for different acquisition modules.

3 The Development of the Instrument

In order to develop the gas pipeline leakage testing instrument, the following key techniques have been solved:

1. Design and fabrication of low-frequency and high-sensitive sensors
2. The collection and disposal of the waveforms of leakage signals
3. The acquisition of accurate synchronous clock for different data acquisition modules
4. The transmission techniques of data of waveforms
5. The correlation techniques for continuous signals

Figure 3 shows the picture of one set of the developed new gas pipeline leakage testing instruments. There are two acquisition modules of acoustic waves and one

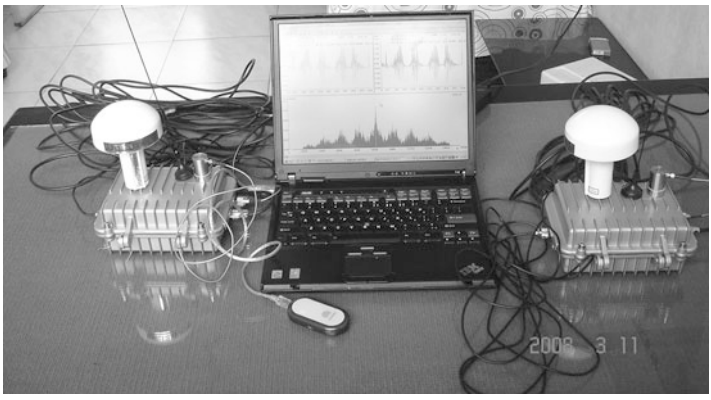

Fig. 3 The developed gas leakage testing instrument

computer in this picture. There are one sensor, one GPS antenna, and one transmitter antenna for each acquisition module.

One set of software was developed for the correlation analysis and location calculation of the leakage signals. The main functions of the software are as follows:

1. Viewing of the original waveforms
2. Analyzing of frequency spectrum of the waveforms by use of Fourier transform
3. Correlation analysis between waveforms from two acquisition modules
4. Calculating and showing the location of the leakage point
5. Giving the intensity of leakage with RMS

The time difference of two adjacent sensors can be obtained through correlation analysis of waveforms from two acquisition modules. The coordinate of the leakage point can be calculated by Eq. (1). The sensitivity of leakage detection can be heightened by the use of wavelet analysis based on waveforms of leakage signals.

4 The Experimental Results by the Use of the Developed Instrument

After developing the testing instrument, a series of experiments have been done for several kinds of under steel pipeline. Since attenuation is the main factor influencing sensitivity and testing distance, the attenuation character of gas leakage signals was tested for an underground steel pipeline. Because the propagation velocity of acoustic waves is the key factor for calculating the location of the gas leakage point, it was tested for different sizes of underground pipeline.

4.1 The Attenuation Testing of Gas Leakage Signals

One underground steel pipeline with size of Φ159 mm × 6 mm × 65 m was used to test the attenuation of gas leakage signals. The buried depth is 500 mm for the pipeline. The compressed air with 0.4 MPa pressure was put inside of the pipeline. The attenuations of leakage signals for 1 mm diameter hole and 2 mm diameter hole were separately tested.

Figure 4 is the RMS attenuation curve of gas leakage for 1 mm diameter hole and Fig. 5 is the RMS attenuation curve of gas leakage for 2 mm diameter hole. The RMS value at 25 m is clearly higher than back noise for 1 mm hole. The RMS value at 45 m is also clearly higher than back noise for 2 mm hole.

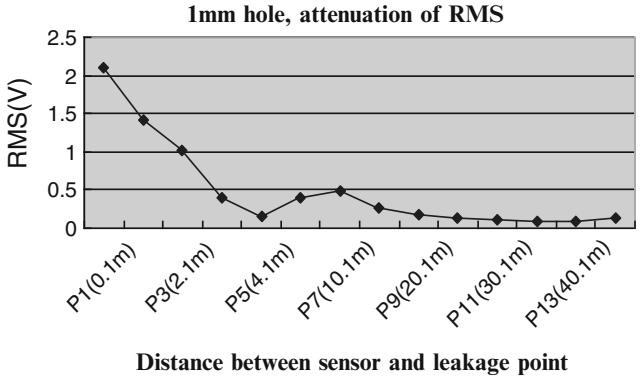

Fig. 4 Attenuation curve of 1 mm hole leakage for steel pipe

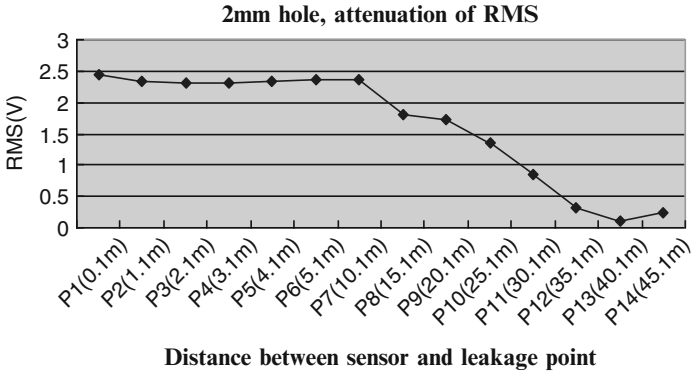

Fig. 5 Attenuation curve of 2 mm hole leakage for steel pipe

4.2 Propagation Velocity Testing of Acoustic Waves

The noise signals produced by leakage will propagate with air inside the pipeline and with the wall of the pipeline. The signals detected by sensors are the mix signals of these two propagation models. The propagation speed of leakage signals should be between the velocity of the sound in air (340 m/s) and the velocity of the transverse wave in the wall of pipe (3,200 m/s). The actual propagation velocities were tested for two kinds of underground steel pipelines and one type of underground cast iron pipeline.

For the underground steel pipeline of size Φ159 mm × 6 mm × 65 m with buried depth of 0.5 m and pressure air of 0.4 MPa, the tested average velocity is 950 m/s. For the underground steel pipeline of size Φ89 mm × 3 mm × 39 m + Φ273 mm × 8 mm × 73.6 m + Φ133 mm × 5 mm × 31 m with buried depth of 1–5 m and pressure air of 0.4 MPa, the tested average velocity is 880 m/s. For the

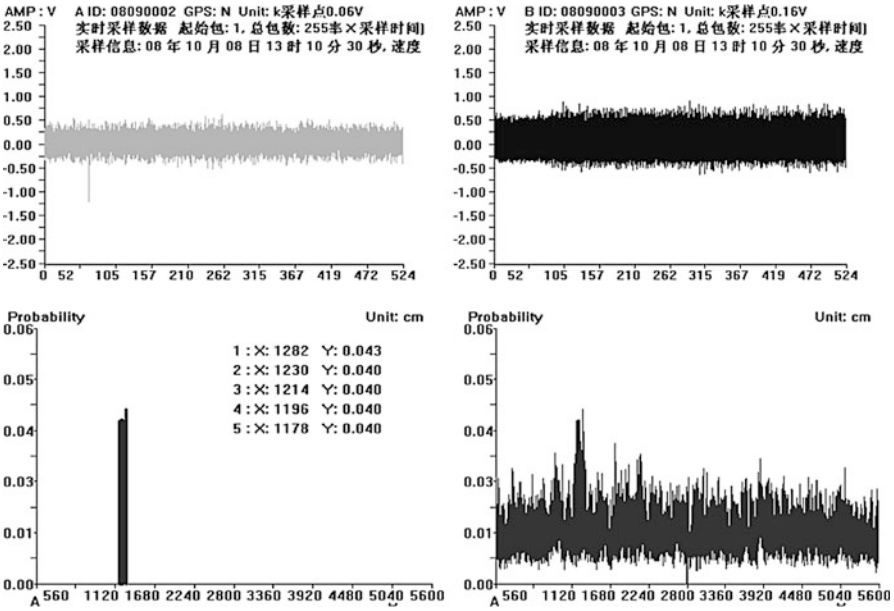

Fig. 6 The correlation located result for Φ1 mm hole leakage

underground cast iron pipeline of size Φ300 mm × 10 mm × 43.5 m with buried depth of about 1 m and pressure natural gas of 0.04 MPa inside, the tested average velocity is 650 m/s.

4.3 Location Testing of Leakage Point

The location testing experiment of leakage point was performed for two kinds of underground pipeline. For the underground steel pipeline of size Φ159 mm × 6 mm × 65 m with buried depth of 0.5 m and pressure air of 0.4 MPa, 1 mm diameter hole leakage could be located for 50 m distance between leakage point and the sensor. The location error was smaller than 0.5 m. Figure 6 shows the waveforms from two sensors and the location result for 1 mm hole.

For the underground steel pipeline of size Φ89 mm × 3 mm × 39 m + Φ273 mm × 8 mm × 73.6 m + Φ133 mm × 5 mm × 31 m with buried depth of 1–5 m and pressure air of 0.4 MPa, 2 mm diameter hole leakage could be located for 100 m distance between leakage point and the sensor. The location error was smaller than 1 m. Figure 7 shows the waveforms from two sensors and the location result for 2 mm hole.

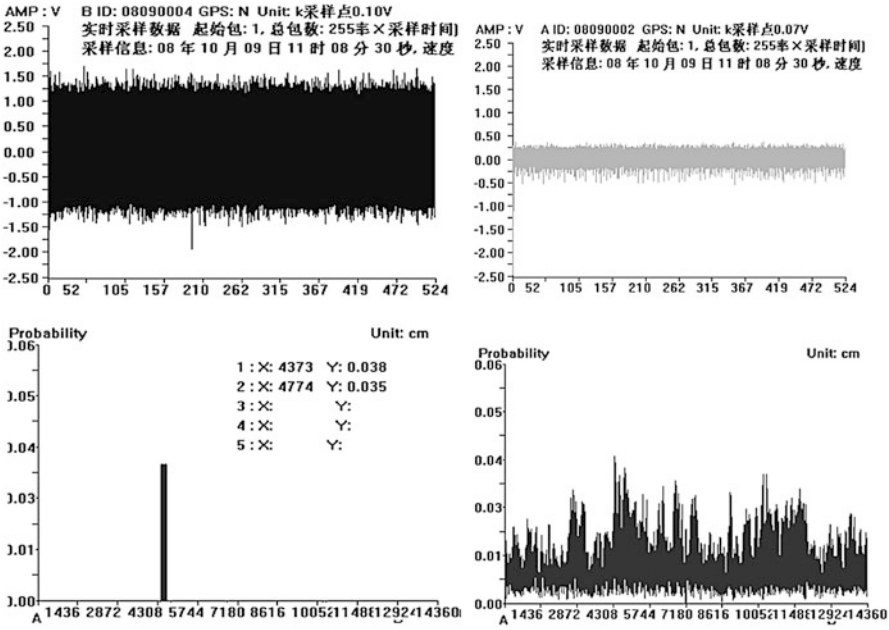

Fig. 7 The correlation located result for Φ2 mm hole leakage

5 Conclusion

According to the testing results, we can get the conclusion as follows:

1. A new testing instrument for leakage point location of pipeline was developed and successfully used. This instrument can detect the leakage of 1 mm hole far from 50 m and 2 mm hole far from 100 m for steel pipeline under 0.4 MPa compressed air.
2. Correlation analysis is an effective location method for leakage point of pressure pipeline.
3. The wavelet analysis based on waveforms of leakage signals can heighten the sensitivity of leakage detection.
4. The main frequency range applied for leakage point location of pipeline is 5–60 kHz.
5. The acoustic waves produced by leakage spread through the wall of pipe and the medium inside pipe. The integrated wave speed is in the range of 880–950 m/s for steel pipeline.
6. If the pressure is steady-going, the intensity of the leakage signals enhances with the increasing of the size of the leakage hole.
7. For the same leakage hole, the intensity of the leakage signals increases with the increasing of the pressure.

Acknowledgment This study was financially supported by Chinese 12th five-year science and technology supporting project 2011BAK06B01.

References

1. G. Shen (ed.), *Nondestructive Testing*, **28** (2006) 261–265
2. R.K. Miller, P. Mclntire (eds.), *Acoustic emission testing*, in *Nondestructive Testing Handbook* (American Society for Nondestructive, 1987)
3. J.S. Bendat, A.G. Piersol, *Engineering Applications of Correlation and Spectral Analysis* (Wiley, New York, 1980)

Part II
Signal Processing and Analysis

On Assessing the Influence of Intermittent Acquisition and Moving Window on the Results of AE Measurements

Ming Fan, Yan Gong, Yuxin Qi, and Gang Qi

Abstract In this chapter, to address dilemma in the stage of data collection, we establish the archetype of observation window ($i-w$, δ diagram), and the intermittent and continuous acquisition can be represented using such a window function. Also, the multiscale analysis and entropy are employed as measurements to evaluate the intermittent acquisition in time domain. Our data showed that the intermittent acquisition and measurement only depends on the history within the moving window, and it can be sampling from ones with minimum moving step, $\delta_{\min}$, and the relative entropy was effective to assess the distance between adjacent windows.

1 Introduction

Measurements of acoustic emission (AE) acquisition were widely used to characterize the behavior and performance of material, mechanical, and civil infrastructural health monitoring. These measurements are in assisting crucial decision-making matters such as life saving and cost reduction [1, 2]. They, often, involve the acquisition of a massive volume of data that demands, consequently, high-performance hardware and strong robust software configuration, particularly in

M. Fan • Y. Gong • Y. Qi
University of Memphis, Memphis, TN 38152, USA
e-mail: mfan@memphis.edu

G. Qi (✉)
University of Memphis, Memphis, TN 38152, USA

Tianjin University of Science and Technology, Tianjin 300222, China
e-mail: gangqi@memphis.edu

G. Shen et al. (eds.), *Advances in Acoustic Emission Technology: Proceedings of the World Conference on Acoustic Emission-2013*, Springer Proceedings in Physics 158,
DOI 10.1007/978-1-4939-1239-1_6,

the circumstances where online monitoring is required. The dilemmas, faced by we engineers, are the following:

1. In the stage of data collection, the acquisition of AE signals can be executed continuously, which may be limited by various reasons. The acquisition can also be obtained intermittently, which may be dependent on the establishment of criteria of the intermittent measurements.
2. In the stage of data processing, the features of the acquired can be extracted either in the time-domain analysis, i.e., analyses of amplitude, relevant domain analysis, waveform, and other parameters [3–6], or in the frequency domain analysis, i.e., power spectrum, maximum entropy spectrum, and envelope spectrum [7–9]. The analyses can be done also in the time–frequency analysis, i.e., STFT (short-time Fourier transform), wavelet transform, and Wigner–Ville distribution [10–12], specifically, however.
3. In the stage of data analysis, AE signals may be processed by multiscale scheme, referring to heterogeneous responses of material mechanical behavior to the applied stress. These responses are particularly important in integrating the microdamage into the evaluation of material behavior that promotes the predictive models.

There have been no established approaches to address such dilemmas. In this work, we shall focus on the understanding of the first dilemma; the main goal is to assess the influence of the acquisition scheme on the results of ultimate measurements. Presently, the measurements are not capable of accurately quantifying non-stationary features and statistics of AE acquisition.

The objectives of this chapter are to (a) establish an archetype of intermittent and continuous acquisition, (b) study the variation of parameters in the archetype and their influence on the measurements when the multiscale analysis in time domain were employed, and (c) determine a quantitative criterion to assess the mentioned influence.

2 Materials and Experiments

The sample material of VersaBond™ bone cement (Smith & Nephew, Inc., Memphis, TN, USA) consists of the powder, polymethyl methacrylate (PMMA), and liquid monomer, methyl methacrylate (MMA). The liquid contains also small particles of $BaSO_4$ to make the material opaque to X-rays. The PMMA powder and MMA liquid are mixed to polymerize. Eighteen specimens were subject to uniaxial quasi-static tension. They were loaded continuously to rupture at a crosshead displacement rate of 1 mm/min using a materials testing machine as shown in Fig. 1.

Three AE sensors (Nano 30, Physical Acoustics, Inc., Princeton, NJ) were attached to the specimen surface. The sensor's resonant and the operating frequency ranges are 140 kHz and 125–750 kHz, respectively. The acoustic signals were preamplified at 40 dB using an AEP4 preamplifier (Vallen-Systeme GmbH, Germany) with a band-pass filter of 2.5 kHz to 3.8 MHz. The signals were then fed to an AE system (ASMY-5, Vallen-Systeme GmbH, Germany).

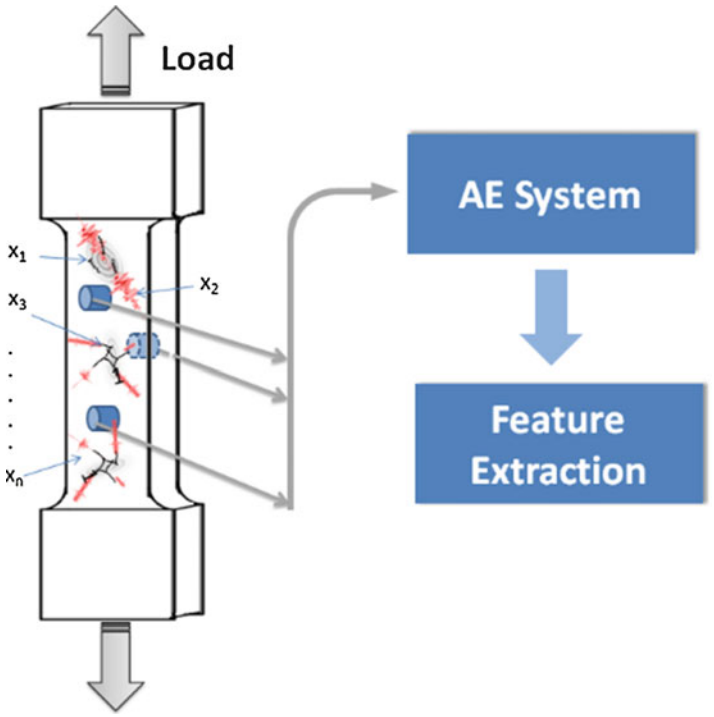

Fig. 1 Quasi-static tension tests (each x_i represents an AE event, and it was captured by AE system)

3 Methods

3.1 *Observation Window and* i−w, δ *Diagram*

Let the observation window be

$$W(i;w,\delta) = \left\{\Delta(i)\middle|(i-1)\delta \le \Delta(i) < w + (i-1)\delta\right\}, \quad i = 1,2,\ldots,M, \quad w > 0, \delta \ge 0 \text{ and } w,\delta \in \mathbb{R}^+, \tag{1}$$

where i is the index of observation window, i increases to represent the window moving, and M is the total number of observation windows. w is the width of window. δ is the moving step, which is the distance between two adjacent windows. Δ is a specific testing variable such as load, time, or other related variables, and Δ determines the physics unit of w and δ.

Hence each window, $W(i, w, \delta)$, is an interval of the endpoints of $[(i-1)\delta, w+(i-1)\delta]$. The diagram of observation window ($i-w$, δ diagram) is shown in Fig. 2.

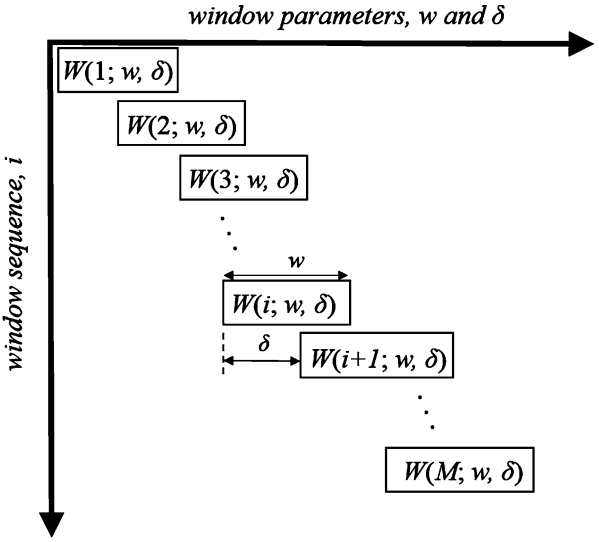

Fig. 2 $i - w, \delta$ diagram

In the practical process of data collection, each acquisition was obtained in each $W(i, w, \delta)$, and there are two typical acquisitions:

1. Intermittent acquisition, which is obtained within a window with fixed w and $\delta > 0$, and the window is denoted as W_I. Especially, if $\delta < w$, we say that the acquisition is intermittent and dependent, and the adjacent acquisitions are overlapped. If $\delta \geq w$, we say that the acquisition is intermittent and independent. For instance, Δ is stress (MPa), and gives rise to $w = 4$ MPa and $\delta = 1$ MPa; hence, window sequences are

$$W(1;4,1) = \{\Delta(1) | 0 \leq \Delta(1) < 4\},$$
$$W(2;4,1) = \{\Delta(2) | 1 \leq \Delta(2) < 5\},$$
$$W(3;4,1) = \{\Delta(3) | 2 \leq \Delta(3) < 6\}, \quad \ldots.$$

2. Continuous acquisition is within a window with an incremental w and $\delta = 0$, and such a window is denoted as W_C. Especially, when w is expansible by fixed increments $w'(w = iw')$ Eq. (1) can be simplified as

$$W_C(i;w) = \left\{\Delta(i) \middle| 0 \leq \Delta(i) < i \cdot w^{'}\right\}, i = 1, 2, \ldots, M, \tag{2}$$

where w' is the incremental width between neighboring window. Obviously, the acquisitions are mutually dependent.

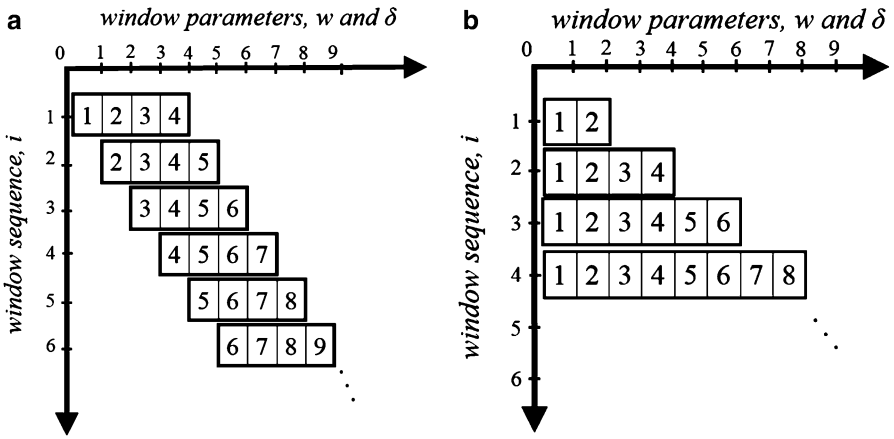

Fig. 3 $i-w$, δ diagram of intermittent and continuous acquisition. (**a**) Intermittent acquisition, $w=4$ MPa and $\delta=1$ MPa, (**b**) continuous acquisition, $w'=2$ MPa

For instance, $w=2$ MPa, and the window sequences are

$$W(1;2)=\{\Delta(1)|0\le\Delta(1)<2\},$$
$$W(2;4)=\{\Delta(2)|0\le\Delta(2)<4\},$$
$$W(3;6)=\{\Delta(3)|0\le\Delta(3)<6\},\quad \ldots.$$

The above mentioned two instances and the corresponding schematic diagram of intermittent and continuous observation window are shown in Fig. 3.

3.2 Multiscale Analysis in Intermittent and Continuous Acquisition

In our previous work, we introduced the concept of multiscale analysis and probabilistic entropy as the measurement of acquisitions in time domain analysis [13–16]. In this chapter, the concept was employed to assess the impact of the above mentioned acquisition.

An AE event, x, in the AE acquisition, can be represented in multiscales with respect to its amplitude. Meanwhile, it can be expressed as $x\in W(i)$ when it is observed in specified observation window $W(i)$. In Fig. 4, the intermittent and continuous acquisitions with multiscale are demonstrated.

In the intermittent acquisition of AE, all events within $W_I(i)$ can be categorized as N different scales depending on their characteristic parameters, for instance, the amplitude. Such an intermittent acquisition is expressed as

$$Y_i := \left(\alpha_{i1}\ \alpha_{i2}\ldots\alpha_{ij}\ldots\alpha_{iN}\right), \tag{3}$$

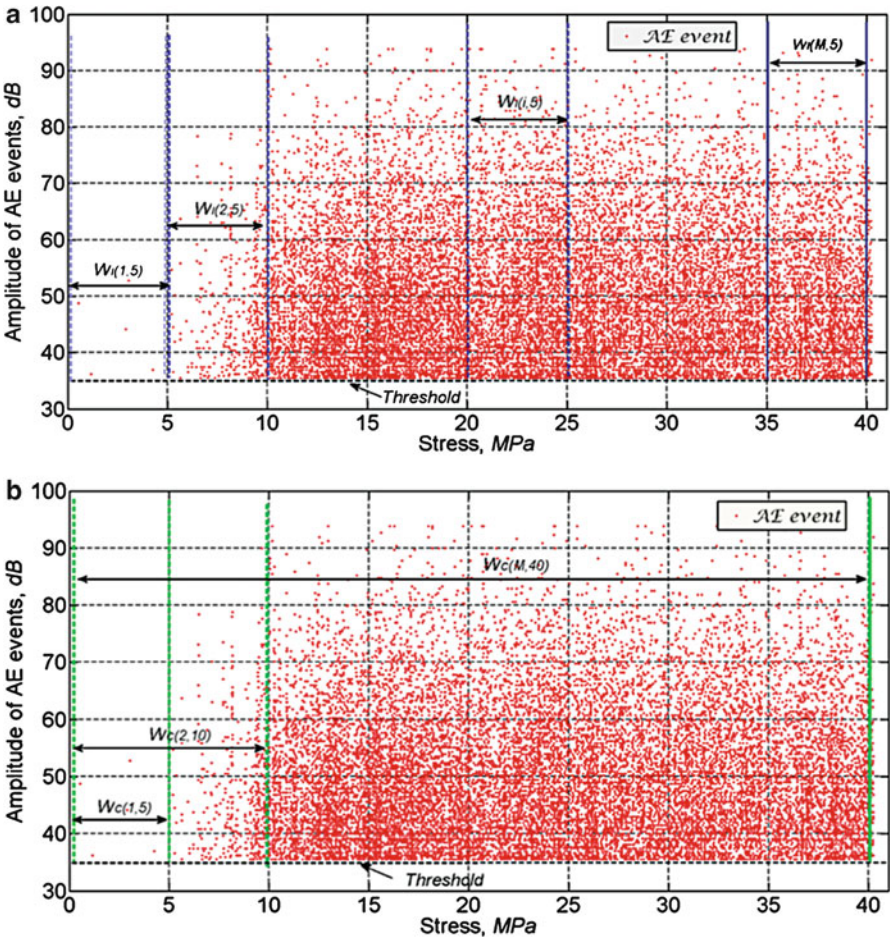

Fig. 4 Intermittent and continuous acquisition with multiscale. (**a**) Intermittent acquisition, $w = 5$ MPa and $\delta = 5$ MPa, (**b**) continuous acquisition, $w' = 5$ MPa

where N is the number of multiscale subintervals, the index of window, i, is the order of $W_I(i)$, and the index of subintervals, j, is the order of subintervals that divides the AE amplitude bandwidth.

The element α_{ij} in Eq. (3) is determined by an index function of x as follows:

$$\alpha_{ij} := \text{Index}\{x\}_{ij}, \text{where} \, x_{ij} \in W_I(i), \tag{4}$$

where function index $\{.\}$ counts for the number of the acquired events, x, in $W_I(i)$, and places it according to its amplitude scale. Thus, α_{ij} is a numerical collection of individually detected x of specified amplitude scale, j, within an observation window, $W_I(i)$. It may be normalized by the volume of the gauge section to eliminate the size effects of the specimen.

With the observation window moving (i is increasing), Eq. (3) evolved into a D_A matrix as

$$D_A := \left[\alpha_{ij}\right]_{M\times N} = \begin{pmatrix} \alpha_{11} & \cdots & \alpha_{1N} \\ \vdots & \ddots & \vdots \\ \alpha_{M1} & \cdots & \alpha_{MN} \end{pmatrix}. \tag{5}$$

D_A is, hence, an intermittent collection of intensive AE data. Its columns are vectors of the scaled acquisitions according to the amplitude of AE events, whereas the rows are vectors of the spectrum of AE events observed in intermittent observation window. Hence, we define D_A to be multiscale and spectrum matrix of random damage.

By the same token, we construct continuous matrix as

$$D_B := \left[\beta_{ij}\right]_{M\times N} = \begin{pmatrix} \beta_{11} & \cdots & \beta_{1N} \\ \vdots & \ddots & \vdots \\ \beta_{M1} & \cdots & \beta_{MN} \end{pmatrix}, \tag{6}$$

where β_{ij} counts the number of AE events in subinterval, j, and within incremental window, $W_C(i; w)$. If $w = iw'$ and $\beta_{ij} = \sum_{i=1}^{i} \alpha_{kj}$ the corresponding probabilities are estimated by

$$p_{ij}^{A} := \frac{\alpha_{ij}}{L_i}, \tag{7}$$

where $L_i := \sum_{j=1}^{N} \alpha_{ij}$. Replacing α_{ij} by p_{ij} in Eq. (5), the corresponding probability space of D_A will be

$$\overline{D}_A = \left[p_{ij}^{A}\right]_{M\times N} = \begin{pmatrix} p_{11}^{A} & \cdots & p_{N1}^{A} \\ \vdots & \ddots & \vdots \\ p_{M1}^{A} & \cdots & p_{MN}^{A} \end{pmatrix}. \tag{8}$$

By the same token, we can also construct continuous probability space of $\overline{D}_B$.

3.3 Entropy Measurement

Since both D_A and D_B ($\overline{D}_A$ and $\overline{D}_B$) are two-dimensional data matrices, a quantitative assessment is demanded to determine the statistical significance that may be used to evaluate the state of random damage of specimen from the spectrum or the probability distribution of random damage. In our previous work, the concept of probabilistic entropy of a statistical ensemble was introduced to summarize the

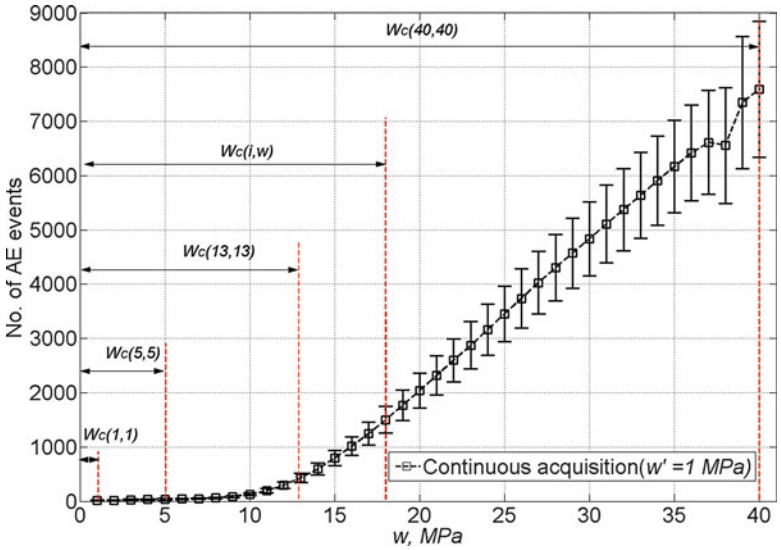

Fig. 5 The conventional measurements of continuous AE acquisition

damage spectrum and probability space. Thus, we recall here only the salient features and the probabilistic entropy is

$$s_i = \sum_{j=1}^{N} p_{ij} \ln\left(\frac{1}{p_{ij}}\right) - \ln N. \tag{9}$$

Each s_i is used to evaluate the acquisition in $W(i)$.

4 Results

4.1 Continuous Acquisition and Measurements

The accumulative measurement of AE acquisition, which counts the number of AE events continuously and accumulatively, is widely used in AE applications. Figure 5 illustrates such a measurement based on the continuous acquisition, and the measurement can be expressed as the function of w (w is incremental by $w' = 1$ MPa). In each observation window, the number of AE events is counted and the measurements increased with the observation window expanding. Results according to Fig. 5 point out that the increasing of AE events is slow when $w < \sim 12$ MPa; however, the increase rate became faster when w exceeded ~12 MPa.

4.2 Multiscale Measurements

Figure 6 shows the surface plot of intermittent D_A matrices of multiscale measurements of AE acquisition ($N = 10$). These plots were with the identical window width ($w = 4$ MPa) and different moving steps. It can be seen that the distribution of AE events maintained the same in each individual scale, just possessed a high resolution when the moving step was small.

4.3 Entropy Measurements

The entropy, which was used to assess the multiscale matrix in Fig. 6, was presented in Fig. 7.

The case of intermittent measurements ($w = 4$ MPa, $\delta = 5$ MPa) was added to demonstrate the tendency when $\delta \geq w$, and the results showed that the value of entropy maintained the same.

5 Discussion

5.1 Sampling of Observation Window

Assuming that $\delta_{\min}$ is the minimum moving step, and the corresponding observation window is $W'(i; w, \delta_{\min})$. In other cases, δ is an integral multiple of $\delta_{\min}$; let μ be the multiple and $\delta = \mu\delta_{\min}$, and the observation window is $W(i; w, \mu\delta_{\min})$. The relationship between W and W' is

$$W(i; w, \mu\delta_{\min}) = W^{'}(\mu i - \mu + 1; w, \delta_{\min}). \tag{10}$$

$W(i; w, \mu\delta_{\min})$ is concerned with the selection of a subset of $W'(i; w, \delta_{\min})$; this results in the acquisition obtained in W, and is the sampling of the acquisition in W'. Therefore, the measurements of multiscale matrix (Eq. (5)), probability space (Eq. (7)), and entropy (Eq. (8)) with δ are the sampling of corresponding measurements with $\delta_{\min}$.

5.2 Distance Between Adjacent Windows

Although acquisitions and measurements can be sampling from the obtained value within W', the distance between adjacent windows is different with respect to δ.

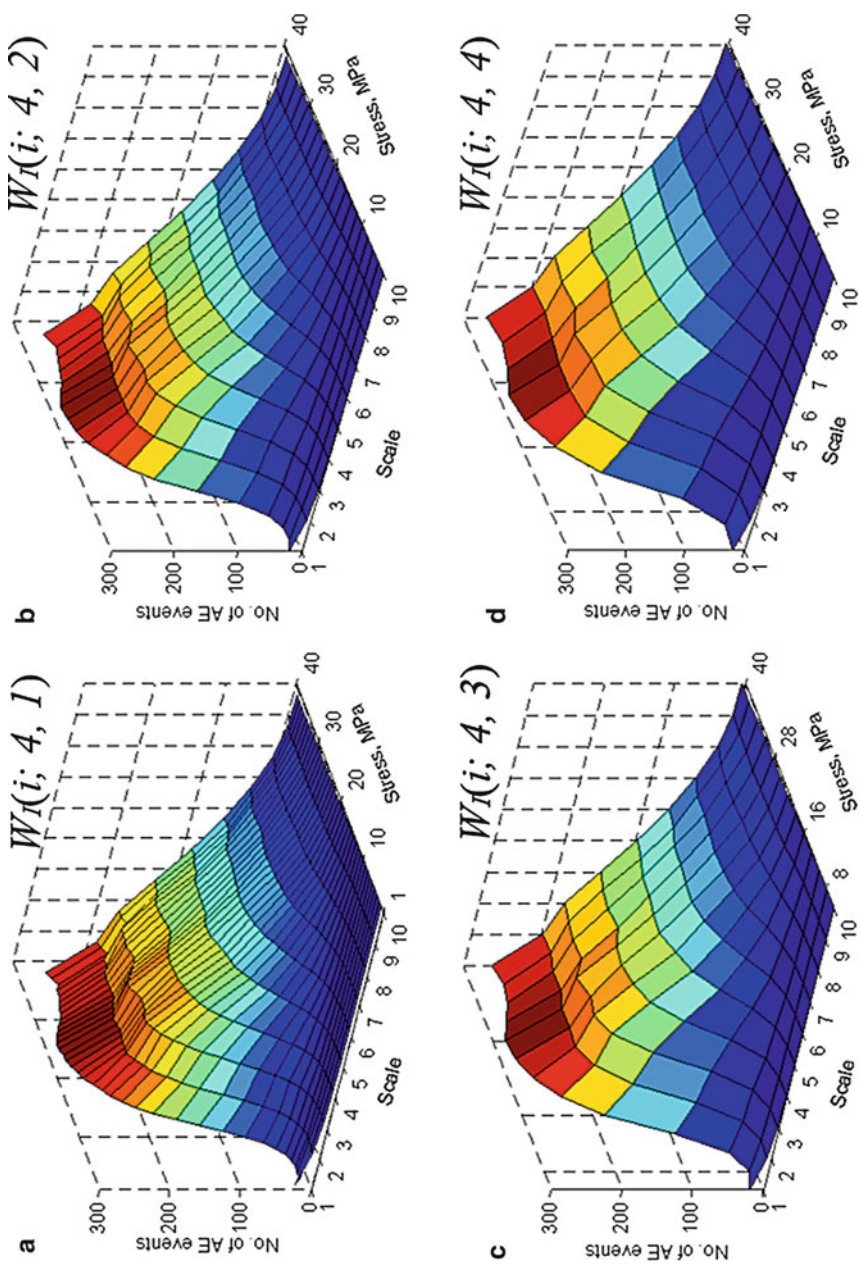

Fig. 6 The intermittent multiscale matrix under various measurements ($N = 10$), with the identical window width ($w = 4$ MPa) and different moving steps. (**a**) $\delta = 1$ MPa, (**b**) $\delta = 2$ MPa, (**c**) $\delta = 3$ MPa, (**d**) $\delta = 4$ MPa

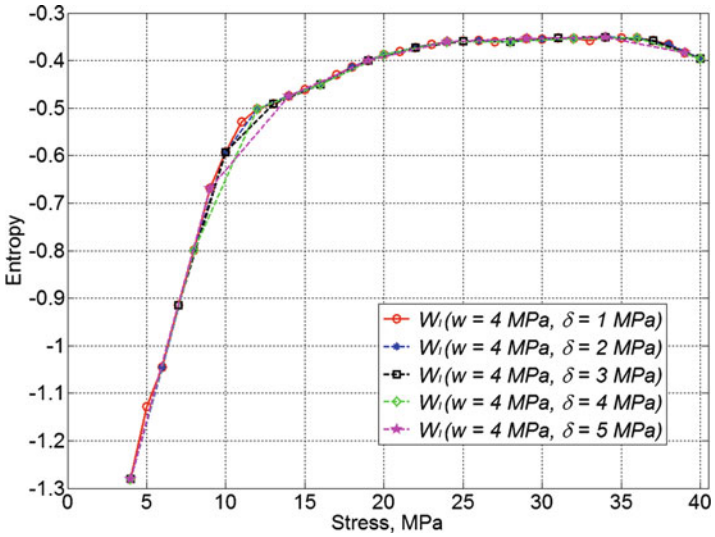

Fig. 7 The entropy of intermittent measurements ($w = 4$ MPa and $\delta = 1$ MPa, $\delta = 2$ MPa, $\delta = 3$ MPa, $\delta = 4$ MPa, and $\delta = 5$ MPa, respectively)

In order to verify whether δ is reasonable to use in practical process, the relative entropy is employed to evaluate the distance between adjacent windows as follows:

$$R(i,k) = \sum_{j=1}^{N} p_{ij}^{A} \ln \frac{p_{ij}^{A}}{p_{kj}^{A}}, \tag{11}$$

where $R(i,k)$ is the relative entropy between adjacent observation window i and k. For the reason of $R\ (i,k) \neq R\ (k,i)$ and considering the practical purpose, which attaches more importance to the impact of a priori observation on the posteriori one, only $k-i=1$ is considered in the following.

Figure 8 shows the relative entropy between adjacent windows when the w was fixed at 4 MPa and δ was increased. As we can see when entropy s significantly increased ($\sigma < \sim$12 MPa in Fig. 7), R value increased with large δ; this is because with the larger value of moving step, the more "new" damage information was included in the adjacent observation window. Whereas when s was almost invariable ($\sigma > \sim$12 MPa in Fig. 7), R remained unchanged at ~0 value, which means that no "new" damage information can be extracted from a posteriori observation and measurements based on our multiscale method are independent to δ. We also infer that the choice of the δ is highly depended on the loading type and characteristic of materials, and a lot more work will go into and release as well.

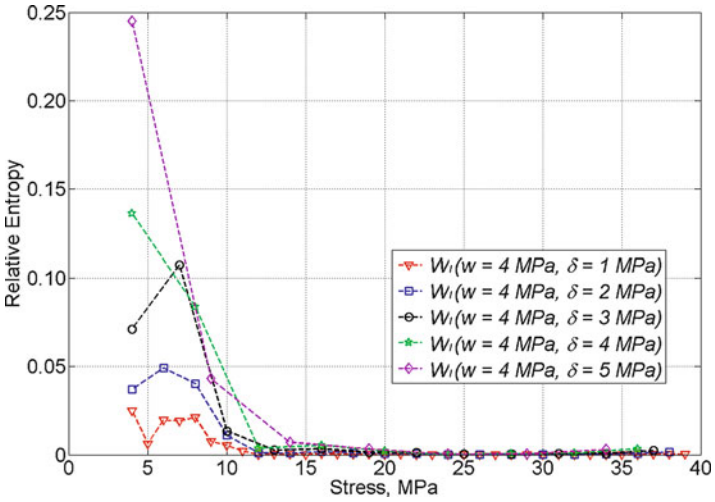

Fig. 8 Relative entropy between adjacent windows with $w = 4$ MPa, and δ increased from 1 to 5 MPa

6 Conclusion

In this work, we established the archetype of observation window and the intermittent and continuous acquisition can be represented using such a window function. Also, the multiscale analysis and entropy were employed as measurements to evaluate the intermittent acquisition in time domain. Our data showed that the intermittent acquisition and measurement only depend on the history within the moving window, and it can be sampling from ones with $\delta_{\min}$, and the relative entropy was effective to assess the distance between adjacent windows.

Acknowledgment Gang Qi wishes to thank for the partial financial support provided by a grant, 11272234, of the Chinese National Natural Science Foundation and an endowed visiting chair-professorship at Tianjin University of Science and Technology by the municipal government of Tianjin, China.

References

1. S. Friker, T. Vogel, Site installation and testing of a continuous acoustic monitoring. Construct. Build Mater. **21**(3), 501–510 (2007)
2. A. Carpinteri, G. Lacidogna, Damage monitoring of an historical masonry building by the acoustic emission technique. Mater. Struct. **39**(2), 161–167 (2007)
3. E. Govekar, J. Gradisek, I. Grabec, Analysis of acoustic emission signals and monitoring of machining processes. Ultrasonics **38**(1–8), 598–603 (2000)
4. J. Bohse, Acoustic emission characteristics of micro-failure processes in polymer blends and composites. Compos. Sci. Tech. **60**(8), 1213–1226 (2000)

5. A. Marec, J.-H. Thomas, R. El Guerjouma, Damage characterization of polymer-based composite materials: multivariable analysis and wavelet transform for clustering acoustic emission data. Mech. Syst. Signal. Process. **22**(6), 1441–1464 (2008)
6. P. Beck, T.P. Bradshaw, R.J. Lark, K.M. Holford, A quantitative study of the relationship between concrete crack parameters and acoustic emission energy released during failure. Key Eng. Mater. **245–246**, 461–466 (2003)
7. M. Giordano, A. Calabro, C. Esposito, A. D'Amore, L. Nicolais, An acoustic-emission characterization of the failure modes in polymer-composite materials. Compos. Sci. Tech. **58**(12), 1923–1928 (1998)
8. C.R. Ramirez-Jimenez, N. Papadakis, N. Reynolds, T.H. Gan, P. Purnell, M. Pharaoh, Identification of failure modes in glass/polypropylene composites by means of the primary frequency content of the acoustic emission event. Compos. Sci. Tech. **64**(12), 1819–1827 (2004)
9. R. Gutkin, C.J. Green, S. Vangrattanachai, S.T. Pinho, P. Robinson, P.T. Curtis, On acoustic emission for failure investigation in CFRP: pattern recognition and peak frequency analyses. Mech. Syst. Signal. Process. **25**(4), 1393–1407 (2011)
10. W.H. Prosser, M.D. Seale, Time-frequency analysis of the dispersion of lamb modes. J. Acoust. Soc. Am. **105**(5), 2669–2676 (1999)
11. T.H. Loutas, V. Kostopoulos, C. Ramirez-Jimenez, M. Pharaoh, Damage evolution in center-holed glass/polyester composites under quasi-static loading using time/frequency analysis of acoustic emission monitored waveforms. Compos. Sci. Tech. **66**(10), 1366–1375 (2006)
12. I. Marinescu, D. Axinte, A time–frequency acoustic emission-based monitoring technique to identify workpiece surface malfunctions in milling with multiple teeth cutting simultaneously. Int. J. Mach. Tool Manuf. **49**(1), 53–65 (2009)
13. G. Qi, J. Li, M. Fan, S. Wayne, Assessment of statistical responses of multi-scale damage events in an acrylic polymeric composite to the applied stress. Probabilist. Eng. Mech. **33**, 103–115 (2013)
14. M. Fan, G. Qi, On evaluating lossy acquisitions of the responses of material hierarchical structures to the applied stress. Mech. Syst. Signal. Process. **37**(1–2), 455–466 (2013)
15. G. Qi, M. Fan, S.F. Wayne, Measurements of a multi-component variate in assessing evolving damage states using a polymeric material. IEEE Trans. Instrum. Meas **60**, 206–213 (2011)
16. G. Qi, M. Fan, G. Lewis, S.F. Wayne, An innovative multi-component variate that reveals hierarchy and evolution of structural damage in a solid: application to acrylic bone cement. J. Mater. Sci. Mater. Med. **23**, 217–228 (2012)

Robust Broadband Adaptive Beamforming Based on Probability Constraint

Yan Wang, Wenfeng Wu, and Guolong Liang

Abstract Broadband adaptive beamformers suffer from severe performance degradation in the presence of array imperfections. To solve this problem, a robust broadband beamforming algorithm based on probability constraint is proposed. Firstly, steering vector error model is established under the hypothesis that array steering errors follow the Gaussian distribution. Secondly, the cost function is constructed by minimizing the array output power while guaranteeing the array response undistorted with sufficiently high probability, which could assure the robustness and ability of suppressing interference. Lastly, we show that the design problem can be formulated as the second-order cone programming (SOCP), which could be solved efficiently via the well-established interior point method. Compared with the worst-case optimization algorithm, the parameters in the proposed algorithm can be better specified by chi-square distribution table, which led to higher performance. Theoretical analysis and simulation results show the effectiveness of the proposed method.

1 Introduction

Adaptive beamformers have better resolution and much better interference rejection capability than the data-independent beamformers [1]. Like narrowband adaptive beamformer, the performance of broadband adaptive beamformers degrades sharply due to the inevitable mismatch between the presumed and actual signal steering vectors [2, 3]. Therefore, the need for robust broadband beamformer arises in many practical applications.

Y. Wang (✉) • W. Wu • G. Liang
Harbin Engineering University, Harbin 150001, China
e-mail: wangyan@hrbeu.edu.cn

G. Shen et al. (eds.), *Advances in Acoustic Emission Technology: Proceedings of the World Conference on Acoustic Emission-2013*, Springer Proceedings in Physics 158,
DOI 10.1007/978-1-4939-1239-1_7,

In recent years, many algorithms have been proposed to improve the robustness of the broadband beamformer against the steering vector error. Among these approaches, diagonal loading is the most popular approach, which is extended from narrowband beamformer [4]. However, selecting the loading factor remains a crucial problem. A diagonal loading approach using spectral averaging in the presence of correlated interferences and look direction uncertainties for broadband beamformer is proposed in [5]. In this method, loading factor is calculated using array steering uncertainty. The beamformer of [6] proposed by Yan She-feng improves the robustness of the beamformer by constraining the norm of its weight vector, which works effectively in the case of pre-delayed error. The robust presteered broadband beamforming based on worst-case performance optimization using convex optimization techniques has been proposed in [7, 8]. However, the constraints in this method are so rigorous that the performance of the algorithm deteriorates in the practical applications.

In this chapter, we propose a robust broadband beamformer based on probability constraint. Probability constraint used in robust beamforming is firstly proposed in [9]; the derivation process of this idea is advanced in this chapter, and then extended to broadband adaptive beamformer. Similarly, we assume that the mismatch vector is drawn from Gaussian distribution. This chapter is organized as follows. Section 2 discuses the problem formulation. The robust broadband beamformer against steering vector error is proposed in Sect. 3. Simulation results are provided in Sect. 4. Section 5 concludes the chapter.

2 Background

A broadband element antenna array processor is shown in Fig. 1, which comprises N sensors followed by an L-order finite impulse response (FIR) filter. The common tap delay is chosen as $T_s = 1/f_s$, where the sampling frequency f_s is chosen to avoid aliasing. A group of pre-delays $T_m = -\tau_m(\theta_0)$ and $m = 1, \ldots, M$ are attached after the sensors, where $\tau_m(\theta_0)$ is the propagation delay between the mth sensor and the reference point associated with look direction θ_0. Here, the pre-steering delays are used to align the signals to the look direction [10].

Let $\mathbf{a}(f, \theta)$ denote the array manifold vector and the adjustable weights of the FIR filter following behind the mth sensor be

$$\mathbf{h}_m = [h_{m1}, h_{m2}, \ldots, h_{mL}]^{\mathrm{T}}, \quad m = 1, 2, \ldots, M \tag{1}$$

The array response (frequency-wavenumber response) of the broadband beamformer can be written as follows:

$$p(f, \theta) = \mathbf{h}^{\mathrm{T}}\mathbf{u}(f, \theta) \tag{2}$$

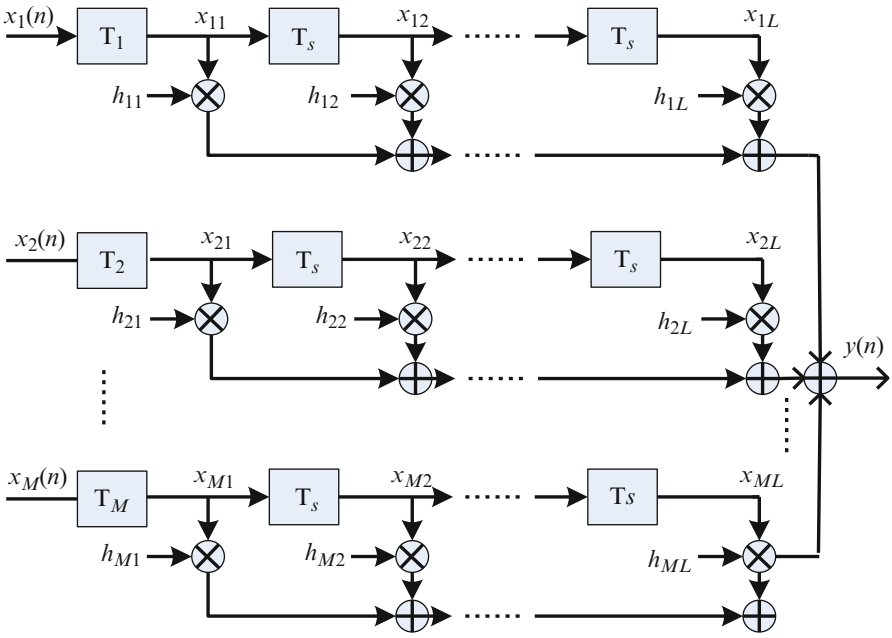

Fig. 1 Structure of Frost beamforming

where $\boldsymbol{h} = [\boldsymbol{h}_1^{\mathrm{T}}, \boldsymbol{h}_2^{\mathrm{T}}, \ldots, \boldsymbol{h}_M^{\mathrm{T}}]^{\mathrm{T}}$ stacks the weight vectors of FIR filters on top of each other. We define $\boldsymbol{u}(f,\theta)$ as the array manifold vector corresponding to the stacked vector $\boldsymbol{h}$, which is different from $\boldsymbol{a}(f,\theta)$. $\otimes$ denotes the Kronecker product and $\circ$ denotes the Hadamard (i.e., element-wise) product of two vectors. It has been assumed in [11] that

$$\mathbf{u}(f,\theta) = \mathbf{e}(f) \otimes [\mathbf{a}(f,\theta) \circ \boldsymbol{\kappa}] \tag{3}$$

$$\mathbf{e}(f) = [1, \exp(-j2\pi f T_s), \ldots, \exp(-j2\pi f (L-1) T_s)] \tag{4}$$

$$\boldsymbol{\kappa} = [\exp(-j2\pi f T_1), \ldots, \exp(-j2\pi f T_M)] \tag{5}$$

Assume that $D+1$ broadband plane waves impinge on the array from directions $[\theta_0, \theta_1, \ldots, \theta_D]$. Suppose the signal of interest (SOI) comes from θ_0. The time series received at the mth sensor can be modeled as

$$x_m(t) = s_0(t - \tau_m(\theta_0)) + \sum_{d=1}^{D} s_d(t - \tau_m(\theta_d)) + n_m(t) \tag{6}$$

where $\{s_d(t)\}_{d=0}^{D}$ is the waveform of the $D+1$ source signals, $n_m(t)$ is the additive noise at the mth sensor, and $\tau_m(\theta_d)$ is the propagation delay between the mth sensor and the reference one point associated with the dth source.

The input of the lth($l = 1, \ldots, L$) tap following behind the mth sensor is given by

$$x_{ml} = x_m(t - T_m - (l-1)T_s) \tag{7}$$

Let $\boldsymbol{x}_m = [x_{m1}, x_{m2}, \ldots, x_{mL}]^{\mathrm{T}}$, $\boldsymbol{x} = [\boldsymbol{x}_1^{\mathrm{T}}, \boldsymbol{x}_2^{\mathrm{T}}, \ldots, \boldsymbol{x}_M^{\mathrm{T}}]^{\mathrm{T}}$, and $\hat{\mathbf{R}}$ denote the $ML \times ML$ data covariance matrix. The frequency spectrum of the received data is limited to $[f_l, f_u]$. Then the optimization problem of Frost beamformer can be written as

$$\min_{\mathbf{h}} \mathbf{h}^{\mathrm{T}} \hat{\mathbf{R}} \mathbf{h}^* \quad \text{s.t. } \mathbf{u}^{\mathrm{T}}(f, \theta_0)\mathbf{h} = 1, \ \forall f \in [f_l, f_u] \tag{8}$$

where $(\cdot)^*$ denotes the conjugate, and $(\cdot)^{\mathrm{T}}$ denotes the transpose. The Frost beamformer is very sensitive to array steering vector errors. To solve this problem, a new robust broadband adaptive beamforming based on probability constraint is proposed.

3 Proposed Beamformer

In the presence of array perturbations and/or calibrated errors, the actual steering vector $\overline{\mathbf{a}}(f, \theta_0)$ differs from the ideal one $\boldsymbol{a}(f, \theta_0)$ by an error vector $\Delta \boldsymbol{a}(f)$

$$\overline{\mathbf{a}}(f, \theta_0) = \mathbf{a}(f, \theta_0) + \Delta \mathbf{a}(f) \tag{9}$$

We assume that $\Delta \boldsymbol{a}(f)$ has circularly symmetric complex Gaussian distribution with mean vector $\boldsymbol{0}$ and covariance matrix $\boldsymbol{C}_\delta$, i.e., $\Delta a(f) \sim N_c(\boldsymbol{0}, \boldsymbol{C}_\delta)$. The actual array manifold vector of the desired signal has been explicitly modeled as

$$\overline{\mathbf{u}}(f, \theta_0) = \mathbf{u}(f, \theta_0) + \mathbf{e}(f) \otimes (\Delta \mathbf{a}(f) \circ \boldsymbol{\kappa}) \tag{10}$$

Since $\Delta \mathbf{a}(f)$ is drawn from a complex Gaussian distribution, $\Delta \mathbf{a}(f) \circ \boldsymbol{\kappa}$ is drawn from the same distribution. Eq. (10) can be written as

$$\overline{\mathbf{u}}(f, \theta_0) = \mathbf{u}(f, \theta_0) + \mathbf{V}(f) \Delta \boldsymbol{\delta}(f) \tag{11}$$

where $\mathbf{V}(f) = \mathbf{e}(f) \otimes \mathbf{I}_M$, $\mathbf{I}_M$ is the $M \times M$ identity matrix, and $\Delta \delta(f) = \Delta \mathbf{a}(f) \circ \boldsymbol{\kappa}$.

The essence of probability constraint is to maintain the beamformer distortionless response only for the incidents with high probability; in other words, ignore the incidents with small probability. This constraint can be written as

$$\Pr\left\{ \left| \mathbf{h}^{\mathrm{T}} (\mathbf{u}(f, \theta_0) + \mathbf{V}(f) \Delta \boldsymbol{\delta}(f)) \right| \geq 1 \right\} \geq p, \ \ \forall f \in [f_l, f_u] \tag{12}$$

where $\Pr\{\cdot\}$ stands for the probability operator, and p is a probability value set by the user. The frequency range $[f_l, f_u]$ is usually discredited into finite frequencies $f_k (k = 1, \ldots, K)$. Under the probability constraint, Frost beamformer Eq. (8) can be rewritten as

$$\min_{\mathbf{h}} \mathbf{h}^{\mathrm{T}} \hat{\mathbf{R}} \mathbf{h}^{*} \quad s.t. \quad \Pr\left\{\left|\mathbf{h}^{\mathrm{T}}(\mathbf{u}(f,\theta_0) + \mathbf{V}(f)\Delta\boldsymbol{\delta}(f))\right| \geq 1\right\} \geq p, \quad \forall f \in [f_l, f_u] \tag{13}$$

Considering the frequency f_k, it is easy to verify that

$$\Pr\left\{\left|\mathbf{h}^{\mathrm{T}}(\mathbf{u} + \mathbf{V}\Delta\boldsymbol{\delta})\right| \geq 1\right\} \geq \Pr\left\{\left|\mathbf{h}^{\mathrm{T}}\mathbf{u}\right| - \left|\mathbf{h}^{\mathrm{T}}\mathbf{V}\Delta\boldsymbol{\delta}\right| \geq 1\right\} \tag{14}$$

If $\|\Delta\delta(f_k)\|$ is small enough (i.e., if $|\mathbf{h}^{\mathrm{T}}\mathbf{u}| \geq |\mathbf{h}^{\mathrm{T}}\mathbf{V}\Delta\boldsymbol{\delta}|$), Signs θ_0 and f_k are omitted for the sake of brevity. An important observation is that the cost function in Eq. (12) is unchanged when $\mathbf{h}$ undergoes an arbitrary-phase rotation. Thus, we can, without loss of generality, choose $\mathbf{h}$ such that

$$\mathrm{Re}\left\{\mathbf{h}^{\mathrm{T}}\mathbf{u}\right\} \geq 0 \tag{15}$$

$$\mathrm{Im}\left\{\mathbf{h}^{\mathrm{T}}\mathbf{u}\right\} = 0 \tag{16}$$

Combining Eqs. (14) and (15), the constraint for the frequency point f_k is inverted to

$$\Pr\left\{\left|\mathbf{h}^{\mathrm{T}}\mathbf{V}\Delta\boldsymbol{\delta}\right| \leq \mathbf{h}^{\mathrm{T}}\mathbf{u} - 1\right\} \geq p \tag{17}$$

Since $\Delta\boldsymbol{\delta}$ is a Gaussian variable vector, the real and imaginary parts of $\mathbf{h}^{T}\mathbf{V}\Delta\boldsymbol{\delta}$ are real Gaussian distributed, that is

$$\mathrm{Re}\left\{\mathbf{h}^{\mathrm{T}}\mathbf{V}\Delta\boldsymbol{\delta}\right\} \sim N_r\left(0, \left\|\mathbf{C}_{\delta}^{1/2}\mathbf{V}^{\mathrm{T}}\mathbf{h}\right\|^2 \Big/ 2\right) \tag{18}$$

$$\mathrm{Im}\left\{\mathbf{h}^{\mathrm{T}}\mathbf{V}\Delta\boldsymbol{\delta}\right\} \sim N_r\left(0, \left\|\mathbf{C}_{\delta}^{1/2}\mathbf{V}^{\mathrm{T}}\mathbf{h}\right\|^2 \Big/ 2\right) \tag{19}$$

where $N_r\{\cdot\}$ stands for real Gaussian distribution. We observe that

$$\frac{\left|\mathbf{h}^{\mathrm{T}}\mathbf{V}\Delta\boldsymbol{\delta}\right|^2}{\left\|\mathbf{C}_{\delta}^{1/2}\mathbf{V}^{\mathrm{T}}\mathbf{h}\right\|^2 \Big/ 2} = \frac{\mathrm{Re}\left\{\mathbf{h}^{\mathrm{T}}\mathbf{V}\Delta\boldsymbol{\delta}\right\}^2}{\left\|\mathbf{C}_{\delta}^{1/2}\mathbf{V}^{\mathrm{T}}\mathbf{h}\right\|^2 \Big/ 2} + \frac{\mathrm{Im}\left\{\mathbf{h}^{\mathrm{T}}\mathbf{V}\Delta\boldsymbol{\delta}\right\}^2}{\left\|\mathbf{C}_{\delta}^{1/2}\mathbf{V}^{\mathrm{T}}\mathbf{h}\right\|^2 \Big/ 2} \tag{20}$$

Obviously, each one of the polynomial on the right side of the equation obeys standard normal distribution, i.e., $N_r(0, 1)$. Therefore, the left side of the equation obeys chi-squared distribution with 2 degrees of freedom, i.e., $\boldsymbol{\chi}^2(2)$.

Let $\mathbf{h}^{\mathrm{T}}\mathbf{u} - 1 = b$, we can replace Eq. (15) by

$$\Pr\left\{\frac{\left|\mathbf{h}^{\mathrm{T}}\mathbf{V}\Delta\boldsymbol{\delta}\right|^2}{\left\|\mathbf{C}_{\delta}^{1/2}\mathbf{V}^{\mathrm{T}}\mathbf{h}\right\|^2/2} \geq \frac{b^2}{\left\|\mathbf{C}_{\delta}^{1/2}\mathbf{V}^{\mathrm{T}}\mathbf{h}\right\|^2/2}\right\} \geq 1 - p \tag{21}$$

For given constant p, the χ^2 value of $\chi^2(2)$ can be found using chi-square distribution table. Let C denote this χ^2 value; the constraint in Eq. (21) can be written in the following form:

$$\sqrt{c/2}\left\|\mathbf{C}_{\delta}^{1/2}\mathbf{V}^{\mathrm{T}}\mathbf{h}\right\| \leq \mathbf{h}^{\mathrm{T}}\mathbf{u} - 1 \tag{22}$$

Using Eq. (22), the problem Eq. (12) can be expressed as

$$\min_{h} \ \mathbf{h}^{\mathrm{T}}\hat{\mathbf{R}}\,\mathbf{h}^{*} \quad \text{s.t. } \sqrt{c/2}\left\|\mathbf{C}_{\delta}^{1/2}\mathbf{V}^{\mathrm{T}}(f_k)\mathbf{h}\right\| \leq \mathbf{h}^{\mathrm{T}}\mathbf{u}(f_k,\theta_0) - 1,\ k = 1,\ldots,K \tag{23}$$

Note that if $\mathbf{h}_0$ is the optimal solution of Eq. (21), the constraints in Eq. (16) are automatically met with appropriate rotation of $\mathbf{h}_0$. Therefore, there is no need to add them to Eq. (23). Let $\hat{\mathbf{R}} = \mathbf{U}\mathbf{U}$ be Cholesky factorization. Then

$$\mathbf{h}^{\mathrm{T}}\hat{\mathbf{R}}\,\mathbf{h}^{*} = \left\|\mathbf{U}^{*}\mathbf{h}\right\|^2 \tag{24}$$

We can rewrite Eq. (22) as

$$\begin{aligned} \min_{\mathbf{h}} \tau \quad & \text{s.t. } \left\|\mathbf{U}^{*}\mathbf{h}\right\| \leq \tau \\ & \sqrt{c/2}\left\|\mathbf{C}_{\delta}^{1/2}\mathbf{V}^{\mathrm{T}}(f_k)\mathbf{h}\right\| \leq \mathbf{h}^{\mathrm{T}}\mathbf{u}(f_k,\theta_0) - 1 \\ & k = 1,\ldots,K \end{aligned} \tag{25}$$

Eq. (25) is the standard second-core program problem (SOCP), which can be solved using highly efficient interior-point method [12]. The MATLAB toolbox such as Sedumi or CVX is available for Eq. (25). It can be seem from Eq. (25) that the expression of the probability constraint method is almost same as the worst-case optimization, except some parameters. Under the assumption of Gaussian mismatch, the parameter values in the proposed method are more suitable than the worst-case optimization in most cases. This will improve the statistical performance of the proposed method.

3.1 Excess Illustrate

The robust broadband beamforming proposed in [13] uses a common upper bound on the 2-norm of the mismatch vector for all frequency values. This method leads to

a better performance as compared to the use of multiple frequency-dependent parameters. Similarly, we use sole $\mathbf{C}_\delta$ for all frequency values. We assume [14]

$$\Delta\mathbf{a} \sim N_c\left(\mathbf{0}, \delta^2\mathbf{I}_M\right) \tag{26}$$

where δ^2 denotes the maximal variance of the steering vector mismatches for all frequency values.

Unlike the process in [9], the chi-squared distribution is adopted to obtain the upper bound on the norm of the steering vector mismatch. The χ^2 value can be found from the table of χ^2 value versus p-value, where p-value is given by subtracting the specified probability P from 1.

4 Simulation Results

Consider a uniform linear array of 12 sensors with $L = 8$ delay sections in each FIR filter. The normalized design band is $[0.16f_s, 0.32f_s]$, where f_s is the sampling frequency. The interval between sensors is half-wavelength spacing at the upper frequency. We assume a far-field signal and a single far-field interference. The signal and interference impinge on the array from the directions 10° and -40°. The interference-to-noise ratio (INR) is set to 30 dB. The background noise of the array is spatially white Gaussian noise. We test the performance of the following methods with the theoretical array covariance matrix as same as [10]. For obtaining each point in the curves, 100 independent runs are used. However, the beampatterns are obtained from one Monte-Carlo realization only. The proposed beamformer is compared with the following methods: (1) the Frost beamformer, (2) the diagonally loaded beamformer (RB-DL), and (3) the worst-case-based beamformer (RB-WC) [13]. Diagonal loading factor of the RB-DL is selected as 20 times of the noise power; the value $\varepsilon = 3$ is used for the worst-case beamformer. The probability value used in our algorithm is set as 0.9.

4.1 Beam Pattern

The assumed steering vector $\mathbf{a}(f)$ is perturbed by white Gaussian noise such that the actual steering vectors are $\mathbf{a}(f) + \Delta\mathbf{a}$, where $\Delta\mathbf{a} \sim N_c(\mathbf{0}, \delta^2\mathbf{I}_M)$. We set $\delta = 0.1$ (i.e., the standard deviation of the error corresponds to 10 % of the complex gain of each array element). The signal-to-noise ratio (SNR) is set to 10 dB. We consider the case when the direction of interesting signal is known exactly. Figures 2 and 3 display the beampatterns of the Frost and the proposed beamformer. Figure 4 illustrates the resultant beam pattern of the proposed algorithm. We note from Fig. 2 that even a relatively small perturbation can cause a significant degradation

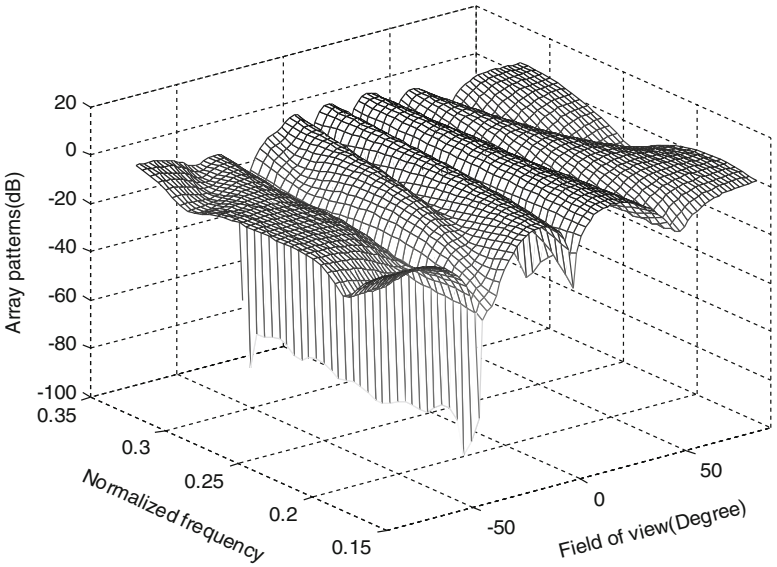

Fig. 2 Array patterns of the Frost beamformer in the presence of random steering vector error

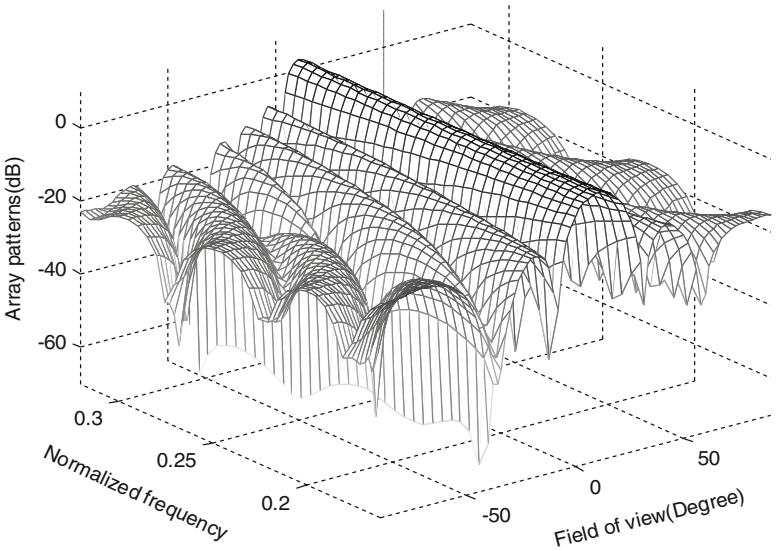

Fig. 3 Array patterns of the proposed algorithm in the presence of random error of random error

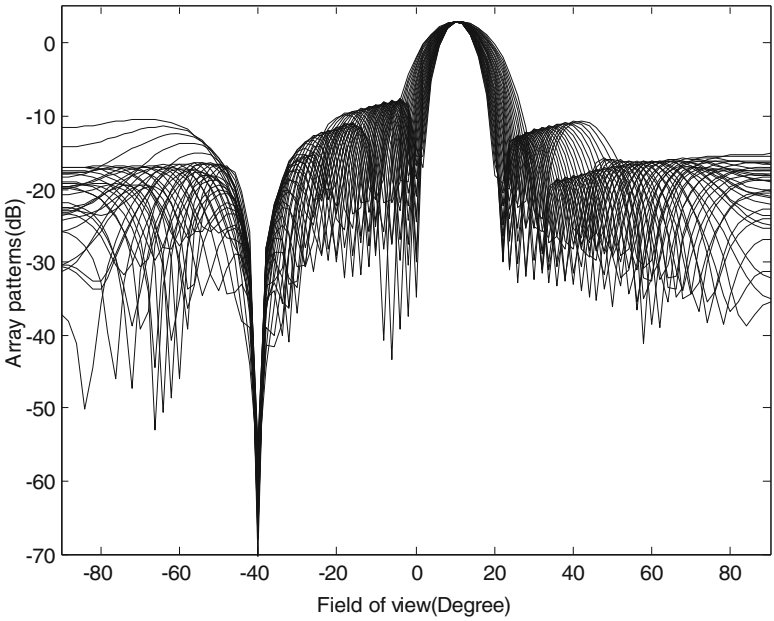

Fig. 4 The resultant beam pattern of the proposed algorithm

of the Frost performance. The SOI is considered to be interference by Frost and hence it is suppressed. As can be seen from Figs. 3 and 4, the proposed algorithm does not have null at the direction of arrival of the interference as deep as the Frost. However, the main lobe of the proposed algorithm point at the direction of SOI and the side lobe level is lower than that of the Frost.

4.2 Comparison of Output SINR

Next, we consider the statistical performance of all beamformers. The simulation condition is same as 3.1. The desired signal SNR is changed from −10 to 20 dB. Figure 5 shows the average output signal-to-interference-plus-noise ratio (SINR) for different algorithms versus SNR of the desired signal. It can be seen from Fig. 5 that the proposed method has better performance in output signal to interference and noise ratio. These performance improvements are especially significant at high SNRs. Although the essence of the proposed algorithm is same as worst-case optimization, the choice of steering vector uncertainty set in our algorithm is more advisable than the latter algorithm.

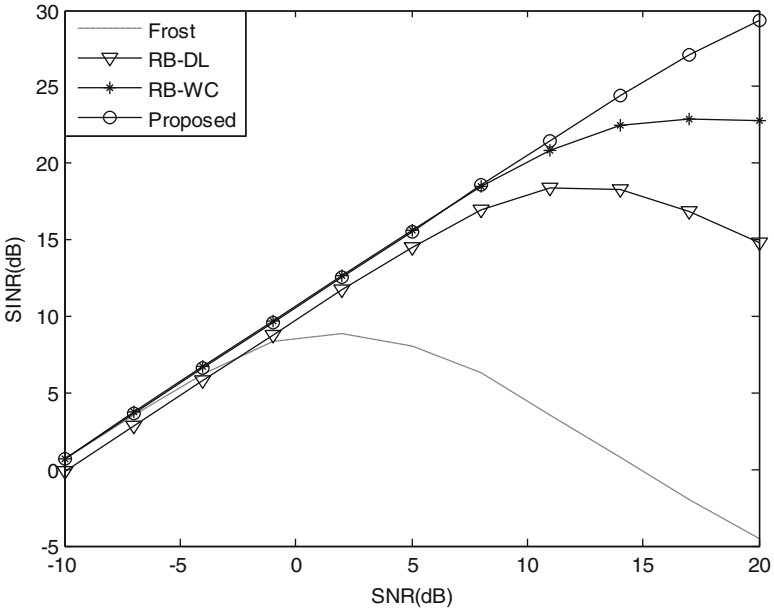

Fig. 5 Output SINR versus SNR

5 Conclusion

In this chapter, a robust broadband beamforming based on the probability constraint is proposed. With the prior information of the distribution of the steering vector mismatch, the radius of the steering vector uncertainty set can be better specified by chi-square distribution table. As a result, the proposed algorithm achieves higher output SINR compared with the worst-case optimization algorithm. Also, the proposed algorithm can be formulated as the SOCP problem and solved using the well-established toolbox. Simulation results show the improved performance of the proposed algorithm as compared to several robust broadband beamformers. This chapter is based on the hypothesis that the mismatch vector has Gaussian distribution; the cases of other distributions need to be researched further.

Acknowledgment This work was supported in part by the Natural Science Foundation of China under Grant No. 51279043, No. 61201411, No. 51209059, the Program for University Young Core of Disciplines from Heilongjiang Province under Grant No. 1253G019, the National High Technique Research and Development Program of China under Grant No. 2013AA09A503, and the Pre-research Program for Naval Equipment of China under Grant No. 1011204030104.

References

1. Y.R. Zhang, R.A. Goubran, Robust near-field adaptive beamforming with distance discrimination. IEEE Trans. Speech Audio Process. **12**(5), 478–488 (2004)
2. K. Slavakis, I. Yamada, Robust wideband beamforming by the hybrid steepest descent method. IEEE Trans. Signal Process. **55**(9), 4511–4522 (2007)
3. M.S. Hossain, L.C. Godara et al., Efficient robust broadband beamforming algorithms using variable loading. Rerista IEEE America Latina **10**(3), 1697–1702 (2012)
4. W. Zhang, B.D. Rao, Robust broadband beamformer with diagonally loading constraint matrix and its application to speech recognition. IEEE International Conference on Acoustics Speech and Signal Processing, Toulouse, 2006, pp. 14–19
5. J.R. Lin, Q. Peng, H. Shao, Broadband robust adaptive beamforming in the presence of correlated interferences and DOA uncertainties. 7th International Symposium on Antennas, Propagation & EM Theory, ISAPE 06, 2006, pp. 1–4
6. S. Yan, M.A. Yuan-liang, *Sensor Array Beampattern Optimization: Theory with Applications [M]* (Science, Beijing, 2009)
7. M. Rubsamen, A.B. Gershman, Robust presteered broadband beamforming based on worst-case performance optimization. Sensor Array and Multichannel Signal Processing Workshop, Darmstadt, 2008, pp. 339–344
8. A. El-keyi, T. Kirubarjan, Wideband robust beamforming based on worst-case performance optimization. Proceedings of IEEE Workshop on Statistical Signal Processing, Bordeaux, 2005, pp.265–270
9. S.A. Vorobyov, Y. Rong, A.B. Gershman, Robust adaptive beamforming using probability-constrained optimization. IEEE Workshop on Statistical Signal Processing, Bordeaux, France, 2005, pp. 934–939
10. S. Yan, C. Hou, Convex optimization based time-domain broadband beamforming with side lobe control. J. Acoust. Soc. Am. **121**(1), 46–49 (2007)
11. S. Yan, C. Hou, Convex optimization based adaptive broadband FIR beamforming with side lobe control. ACTA Acostica **32**(1), 5–9 (2007)
12. A.B. Gershman, Z.-Q. Luo et al., Robust adaptive beamforming using worst-case performance optimization: a solution to the signal mismatch problem. IEEE Ttrans. Signal Process. **52**(2), 313–324 (2003)
13. A. El-keyi, T. Kirubarajan, A.B. Gershman, Wideband robust beamforming based on worst-case performance optimization. 2005 IEEE/SP 13th Workshop on Statistical Signal Processing, Bordeaux, 2005, pp. 265–270
14. D.S. Samuel, Wideband robust capon beamforming for passive sonar. IEEE J. Oceanic Eng. **38** (2), 308–322 (2013)

Near-Field Noise Source Localization in the Presence of Interference

Guolong Liang and Bo Han

Abstract In order to suppress the influence of interference sources on the noise source localization in the near field, the near-field broadband source localization in the presence of interference is studied. Oblique projection is constructed with the array measurements and the steering manifold of interference sources, which is used to filter the interference signals out. 2D-MUSIC algorithm is utilized to deal with the data in each frequency, and then the results of each frequency are averaged to achieve the positioning of the broadband noise sources. The simulations show that this method suppresses the interference sources effectively and is capable of locating the source which is in the same direction with the interference source.

1 Introduction

Interference suppression was one of the central problems in array signal processing [1–3]. There were some interference sources with prior knowledge, whose positions were available. Chen and Su [4] presented jamming jam method (JJM) to filter out the far-field interference whose information was known. In [5], a method called null-forming weights based on Bartlett beamforming was developed to suppress interference. However, these methods only applied to the far-field interference sources. For flank array sonar, the interference sources in the moving platform were within near field, and the prior knowledge could be obtained easily. Such interferences would have an adverse impact on near-field source localization, which

G. Liang (✉) • B. Han
Science and Technology on Underwater Acoustic Laboratory, Harbin Engineering University, Harbin 150001, China
e-mail: liangguolong@hrbeu.edu.cn

G. Shen et al. (eds.), *Advances in Acoustic Emission Technology: Proceedings of the World Conference on Acoustic Emission-2013*, Springer Proceedings in Physics 158,
DOI 10.1007/978-1-4939-1239-1_8,

needed to be suppressed by some methods. In [6], the null-forming weights method based on Bartlett beamforming was extended to the application of near-field underwater acoustic image measurement. The method, in its essence, used the orthogonal projection of the interference array manifold to form directivity zero point. Because the method was based on Bartlett beamforming, the resolution was coarse and the zero point resulted in the nearby side lobe-level rising. The oblique projection was a branch of projection theory. Behrens and Scharf [7] presented the application of oblique projection in signal processing, and deduced the formula of oblique projection to the column space. Tian [8] applied the oblique projection operator to compressive sensing to complete compressive-domain filtering. Some algorithms combining oblique projection with MUSIC were presented to estimate the DOAs of sources [9, 10].

In this chapter, we present a new method used to localize near-field broadband sources in the presence of near-field interference sources. Oblique projection is constructed to eliminate the interference. After projecting, 2D-MUSIC is used to deal with each frequency component, and then the results of all frequency components are averaged to achieve near-field broadband source localization. The proposed method can suppress interferences effectively. When the signal and interference are in same direction, this method is still capable of locating the near-field source. Finally, the effectiveness of the proposed method is proved by computer simulations.

2 Signal Model

Consider that K near-field signal sources and P near-field interference sources impinge onto a uniform linear array (ULA) of $2N+1$ omnidirectional sensors, the distance between adjacent elements is d, and all the sound sources are uncorrelated with each other, as shown in Fig. 1.

Compute DFT of the array data to divide the concerned band into M sub-bands, so the m th sub-band component is given by

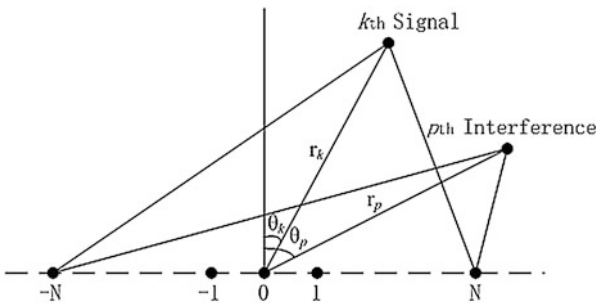

Fig. 1 The geometric schematic diagram of signal and interference sources in the near field

$$\boldsymbol{X}(f_m) = \mathrm{A}_K(f_m)\boldsymbol{s}_K(f_m) + \mathrm{A}_P(f_m)\boldsymbol{s}_P(f_m) + \boldsymbol{n}(f_m) \tag{1}$$

$$\boldsymbol{A}_K(f_m) = [\boldsymbol{a}(f_m, \theta_1, r_1), \cdots, \boldsymbol{a}(f_m, \theta_k, r_k), \cdots, \boldsymbol{a}(f_m, \theta_K, r_K)] \tag{2}$$

$$\boldsymbol{a}(f_m, \theta_k, r_k) = \left[e^{(f_m\beta_{-Nk})}, \cdots, e^{(f_m\beta_{nk})}, \cdots, e^{(f_m\beta_{Nk})}\right]^{\mathrm{T}} \tag{3}$$

$$\beta_{nk} = -j\frac{2\pi}{c}\left(\sqrt{r_k^2 + (id)^2 - 2r_k id\sin\theta_k} - r_k\right) \tag{4}$$

$$\boldsymbol{s}_K(f_m) = [s_1(f_m), \cdots, s_k(f_m), \cdots, s_K(f_m)]^{\mathrm{T}} \tag{5}$$

$$\boldsymbol{n}_K(f_m) = [n_{-N}(f_m), \cdots, n_n(f_m), \cdots, n_N(f_m)]^{\mathrm{T}} \tag{6}$$

In the equations above, $\boldsymbol{A}_K(f_m)$ is the array manifold matrix, whose k th is the array steering vector $\boldsymbol{a}(f_m, \theta_k, r_k)$, and $\boldsymbol{s}_K(f_m)$ and $\boldsymbol{n}_K(f_m)$ are the $K \times 1$ signal vector and the $(2N+1) \times 1$ noise vector, respectively. In Eq. (1), what $\boldsymbol{A}_P(f_m)$ and $\boldsymbol{s}_P(f_m)$ denote are similar to Eqs. (2) and (5), and need not be repeated here.

3 Near-Field Noise Source Localization Based on Oblique Projection

3.1 Oblique Projection Operator

Oblique projection operator is an extension of orthogonal projection operator. Like orthogonal projection operator, it is idempotent, but the difference is that it is not symmetric. Consider two full column rank matrix $\boldsymbol{H}$ and $\boldsymbol{S}$ with the same number of rows, and oblique projection operator $\boldsymbol{E}_{\boldsymbol{HS}}$ is given by [7]

$$\boldsymbol{E}_{\boldsymbol{HS}} = \boldsymbol{H}\left(\boldsymbol{H}^{\mathrm{H}}\boldsymbol{P}_{\boldsymbol{S}}^{\perp}\boldsymbol{H}\right)^{-1}\boldsymbol{H}^{\mathrm{H}}\boldsymbol{P}_{\boldsymbol{S}}^{\perp} \tag{7}$$

where $\boldsymbol{P}_{\mathrm{S}}^{\perp}$ is the orthogonal projection of $\boldsymbol{S}$, and $(\bullet)^{-1}$ and $[\ ]^{\mathrm{H}}$ denote inverse operation and conjugate transpose; we can obtain the following properties by Eq. (7):

$$\boldsymbol{E}_{\boldsymbol{HS}}\boldsymbol{H} = \boldsymbol{H} \quad \boldsymbol{E}_{\boldsymbol{HS}}\boldsymbol{S} = \mathrm{O} \tag{8}$$

So, by oblique projection, we can retain the desired subspace and remove the undesired subspace.

3.2 Proposed Method

For ease in writing, we omit the symbol f_m in the derivation process below. Construct the oblique projection $\boldsymbol{E}_{\mathrm{A}_P\mathrm{A}_K}$ with steering manifolds of signal sources and interference sources:

$$\boldsymbol{E}_{\mathrm{A}_P\mathrm{A}_K} = \mathrm{A}_P\left(\mathrm{A}_P{}^{\mathrm{H}}\boldsymbol{P}^{\perp}_{\mathrm{A}_K}\mathrm{A}_P\right)^{-1}\mathrm{A}_P{}^{\mathrm{H}}\boldsymbol{P}^{\perp}_{\mathrm{A}_K} \tag{9}$$

With the constructed $\boldsymbol{E}_{\mathrm{A}_P\mathrm{A}_K}$, we can obtain

$$\boldsymbol{Y} = \boldsymbol{E}_{\mathrm{A}_P\mathrm{A}_K}\boldsymbol{X} = \mathrm{A}_P\boldsymbol{S}_P + \boldsymbol{E}_{\mathrm{A}_P\mathrm{A}_K}\boldsymbol{n} \tag{10}$$

Then, signal components are filtered out, and interference components are invariable. Subtracting Eqs. (1) and (10), $\boldsymbol{Z}$ can be obtained:

$$\boldsymbol{Z} = \boldsymbol{X} - \boldsymbol{Y} = \mathrm{A}_K\boldsymbol{S}_K + (\boldsymbol{I} - \boldsymbol{E}_{\mathrm{A}_P\mathrm{A}_K})\boldsymbol{n} \tag{11}$$

So, we apply the oblique projection to $\boldsymbol{R}$ as follows:

$$\boldsymbol{R}_{\mathbf{Z}} = E\left[\boldsymbol{Z}\boldsymbol{Z}^{\mathrm{H}}\right] = (\boldsymbol{I} - \boldsymbol{E}_{\mathrm{A}_P\mathrm{A}_K})\boldsymbol{R}(\boldsymbol{I} - \boldsymbol{E}_{\mathrm{A}_P\mathrm{A}_K})^{\mathrm{H}} \tag{12}$$

where $\boldsymbol{R}$ is the original data covariance matrix. Using the eigenvalue decomposition (EVD) to $\boldsymbol{R}_{\mathbf{Z}}$, signal sources can be localized by some subspace methods. However, we can see that there is a difficulty in obtaining $\boldsymbol{E}_{\mathrm{A}_I\mathrm{A}_S}$ by Eq. (9), because the array manifold matrix $\boldsymbol{A}_S$ is unknown. In practice, the oblique projection operator $\boldsymbol{E}_{\mathrm{A}_P\mathrm{A}_K}$ can be estimated by [9]

$$\boldsymbol{E}_{\mathrm{A}_P\mathrm{A}_K} = \mathrm{A}_P\left(\mathrm{A}_P{}^{\mathrm{H}}\boldsymbol{R}^{+}_{\mathrm{A}}\mathrm{A}_P\right)^{-1}\mathrm{A}_P{}^{\mathrm{H}}\boldsymbol{R}^{+}_{\mathrm{A}} \tag{13}$$

where $\boldsymbol{R}_{\boldsymbol{A}} = \boldsymbol{R} - \sigma_n^2\boldsymbol{I} = \boldsymbol{U}_{\boldsymbol{A}}\boldsymbol{\Lambda}_{\boldsymbol{A}}\boldsymbol{U}_{\boldsymbol{A}}{}^{\mathrm{H}}$, $\boldsymbol{U}_{\boldsymbol{A}}$, is the signal subspace, $\boldsymbol{\Lambda}_{\boldsymbol{A}}$ is a diagonal matrix whose diagonal elements are the large eigenvalues of $\boldsymbol{R}$, and $(\bullet)^{+}$ denotes the operator of pseudoinverse. Replace $\boldsymbol{E}_{\mathrm{A}_P\mathrm{A}_K}$ in Eq. (12) by the estimated oblique projection in Eq. (13), and using EVD to $\boldsymbol{R}_{\boldsymbol{Z}}$, the MUSIC spectrum can be obtained:

$$P(f_m, \theta, r) = \frac{1}{\boldsymbol{a}(f_m, \theta, r)^{\mathrm{H}}\boldsymbol{U}_n(f_m)\boldsymbol{U}_n(f_m)^{\mathrm{H}}\boldsymbol{a}(f_m, \theta, r)} \tag{14}$$

where $\boldsymbol{U}_n(f_m)$ is the noise subspace of $\boldsymbol{R}_{\boldsymbol{Z}}$. Because it is difficult to obtain the ideal value of $\boldsymbol{R}^{+}_{\mathrm{A}}$, to ensure that $\boldsymbol{E}_{\mathrm{A}_P\mathrm{A}_K}$ does not make the array manifold vector distort Eq. (14) should be modified as

$$P(f_m,\theta,r)=\frac{\boldsymbol{b}(f_m,\theta,r)^{\mathrm{H}}\boldsymbol{b}(f_m,\theta,r)}{\boldsymbol{b}(f_m,\theta,r)^{\mathrm{H}}\boldsymbol{U}_n(f_m)\boldsymbol{U}_n(f_m)^{\mathrm{H}}\boldsymbol{b}(f_m,\theta,r)} \tag{15}$$

where $\boldsymbol{b}(f_m,\theta,r)=(\boldsymbol{I}-\boldsymbol{E}_{\mathrm{A}_P\mathrm{A}_K})\boldsymbol{a}(f_m,\theta,r)$. Averaging all results of each frequency component, we can obtain the bearing-range spectrum of near-field broadband sources:

$$P(\theta,r)=\frac{1}{M}\sum_{m=1}^{M}P(f_m,\theta,r) \tag{16}$$

Now, the following steps summarize the proposed method.

1. Compute the temporal DFT of the array data to divide all bands of signal into M sub-bands.
2. Use EVD to the array covariance matrix of m th sub-band component, compute $\boldsymbol{R}_{\mathrm{A}}^{+}(f_m)$, and then construct the oblique matrix by Eq. (13).
3. Obtain $\boldsymbol{R}_{\boldsymbol{Z}}$ by applying the oblique projection to the original data covariance matrix.
4. Estimate the noise subspace $\boldsymbol{U}_n(f_m)$ and compute 2D-MUSIC spectrum using Eq. (15).
5. Average all results of each frequency component and estimate $\hat{\theta}$ and $\hat{r}$ by Eq. (16).

4 Simulation Results

In this section, we present simulation results to illustrate the performance of the proposed method. Considering a ULA of 11 sensors ($N=5$), and all the near-field signal sources and interference sources radiate Gaussian white noise, the frequency range is $f_l \sim f_h = 1,000 \sim 3,000$ Hz, the space noise is additive Gaussian noise, and the speed of sound is $c=1,480$ m/s. Broadband incoherent processing methods have some ability to avoid ambiguity, so the distance between adjacent elements is $d=2\lambda_h$, where λ_h denotes the corresponding wavelength of f_h. The number of snapshots is 500, and the length of sliding window and sliding step are 300 and 4, respectively; in other words, the number of frequency-domain snapshots is 50. The positions of the two interference sources are set as (30 m, 18°) and (30 m, 20°). INR is 30 dB.

Simulation 1. Consider two near-field broadband signal sources with SNR = 20 dB impinge onto the array, and they are placed at (60 m, 10°) and (45 m, 8°). Figure 2 shows the localization result using the null-forming weights method based on Bartlett beamforming (hereafter referred to as NWMBB). We can see that the interferences are suppressed, whereas the two signal sources are merged. Figure 3 shows the localization result using the proposed method. It can be seen that our method not only suppresses the interferences but also resolves the two sources.

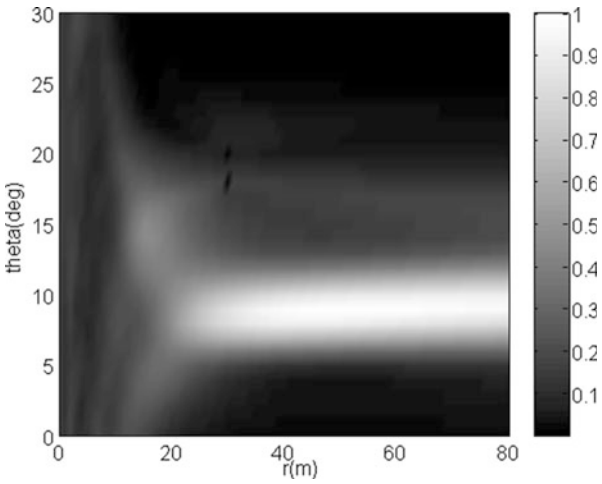

Fig. 2 Source localization in the presence of near-field interference sources by NWMBB

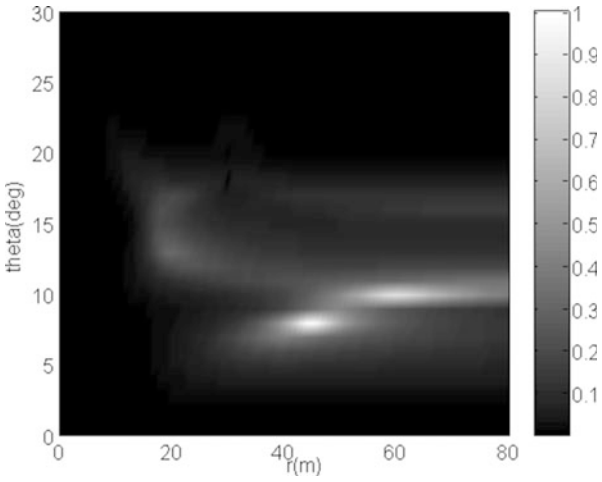

Fig. 3 Source localization in the presence of near-field interference sources by the proposed method

Simulation 2. The other conditions are the same except that the position of source 2 is set as (45 m, 18°), that is, to say source 2 and one of interferences are set in the same direction. The results are showed in Figs. 4 and 5. NWMBB and the proposed method are both able to localize source 1, but only our method is capable of achieving the localization of source 2. Figure 6 shows the spatial spectrum slice at 18°. We can see that both of the methods can form null at the interference position. However, for localizing source 2 which is in the same direction to the interference source, NWMBB loses efficacy and generates a fake peak at (17 m, 18°), while the proposed method has an excellent performance.

Simulation 3. Under the condition of Simulation 2, we perform 200 independent Monte-Carlo simulations. For source 2, only the performance of proposed method

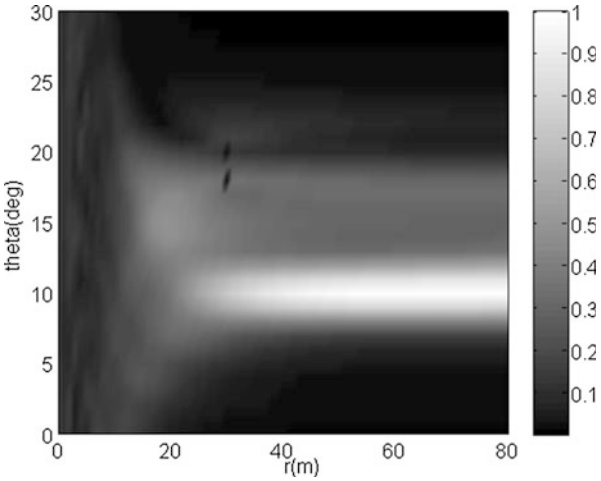

Fig. 4 Source localization in the same direction with interference sources by NWMBB

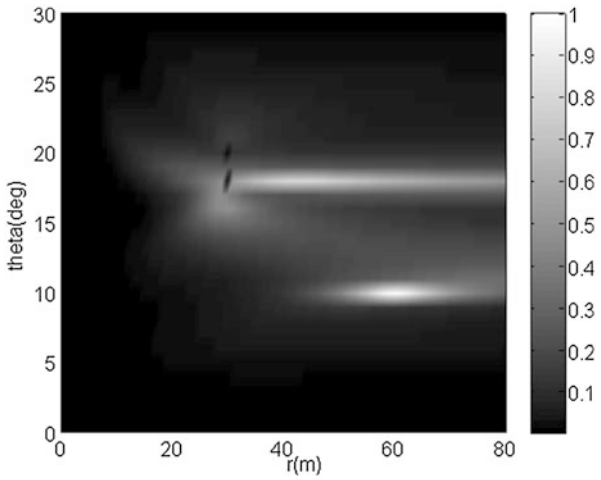

Fig. 5 Source localization in the same direction with interference sources by the proposed method

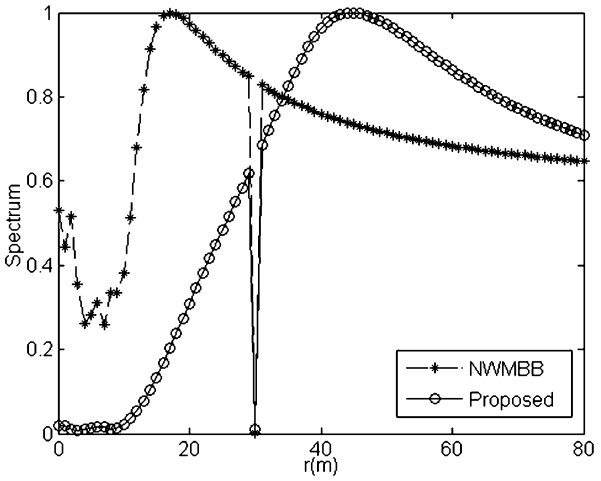

Fig. 6 The spatial spectrum slice at 18°

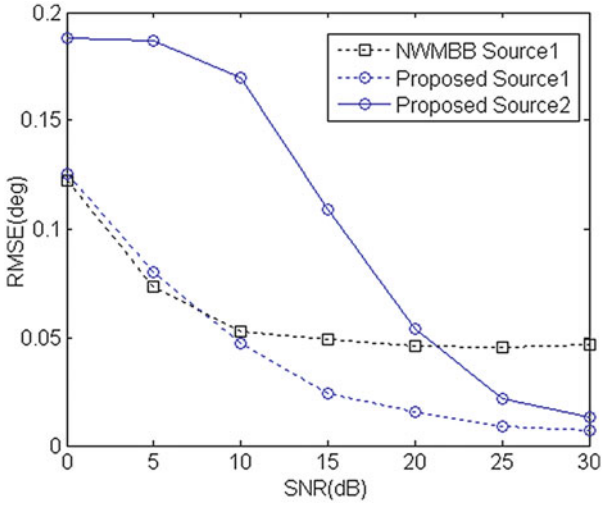

Fig. 7 RMSE of bearing angle versus SNR

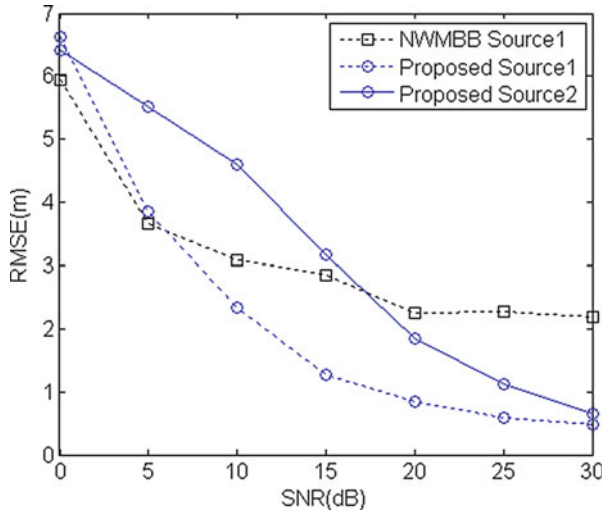

Fig. 8 RMSE of range versus SNR

is showed. Figure 7 shows the RMSE of bearing angle versus SNR. For source 1, NWMBB performs slightly better than the proposed method in low SNR, while our method has advantage over NWMBB in high SNR; the RMSE is less than 0.03° for SNR $>$ 15 dB. For source 2, the RMSE is less than 0.2° by our method. Figure 8 shows the RMSE of range versus SNR. For source 1, the performance of the proposed method is better than the one of NWMBB when SNR is over 5 dB, and the RMSE is less than 1.5 m for SNR $>$ 15 dB. For source 2, the result is acceptable; the RMSE is less than 2 m for SNR $>$ 20 dB.

5 Conclusion

In this chapter, a new near-field source localization method in the presence of interference is presented. This method suppresses near-field interferences by oblique projection, and improves the localization performance. Simulation results confirm that the proposed method is capable of filtering the near-field interferences out and estimating the source position reliably. It is noting that our method can localize the source which is the same direction with interference.

Acknowledgment This work was supported by the National Natural Science Foundation of China under Grant No. 51279043, and the National Natural Science Foundation of China under Grant No. 61201411.

References

1. S.A. Stotts, A robust spatial filtering technique for multisource localization and geoacoustic inversion. J. Acoust. Soc. Am. **118**(1), 139–162 (2005)
2. E. Habets, J. Benesty, P.A. Naylor, A speech distortion and interference rejection constraint beamformer. IEEE Trans. Audio Speech Lang. Process. **20**(3), 854–867 (2012)
3. J. Landon, B.D. Jeffs, K.F. Warnick, Model-based subspace projection beamforming for deep interference nulling. IEEE Trans. Signal Process. **60**(3), 1215–1228 (2012)
4. H. Chen, H. Su, A new approach to estimate DOA in presence of strong jamming/signal suppression. Acta. Electron. Sinica. **34**(3), 530–534 (2006)
5. J. Mei, J. Hui, Y. Wang, Y. Yu, W. Zhou, Designing null- forming weights based on Bartlett beamforming. J. Harbin Eng. Univ. **29**(12), 1315–1318 (2008)
6. J.-d. Mei, X. Sheng, Y. Zhang, L. Guo, M. Jiang, Research on the near field focus null-forming weight interference sound sources suppression technology of the underwater acoustic image measurement. J. Harbin Eng. Univ. **33**(5), 1–6 (2012)
7. R.T. Behrens, L.L. Scharf, Signal processing application of oblique projection operators. IEEE Trans. Signal Process. **42**(6), 1413–1424 (1994)
8. P. Tian, R. Kang, H. Yu, A compressive -domain filtering method based on oblique projector. J. Beijing Univ. Post. Telecommun. **35**(3), 108–111 (2012)
9. M.L. McCloud, L.L. Scharf, A new subspace identification algorithm for high-resolution DOA estimation. IEEE Trans. Antennas Propag. **50**(10), 1382–1390 (2002)
10. J. He, M.N.S. Swamy, M. Omair Ahmad, Efficient application of MUSIC algorithm under the coexistence of far-field and near-field sources. IEEE Trans. Signal Process. **60**(4), 2066–2070 (2012)

Noise Diagnostics at AE Monitoring of Hazardous Industrial Assets

T.B. Petersen, V.V. Shemyakin, and V.Y. Chernigovsky

Abstract This chapter considers the acoustic emission (AE) signal-noise discrimination problem that arises at AE monitoring of polymerization reactor. Different kinds of AE data including AE hit sequences, waveform set, and noise RMS (root mean square) samples were recorded and processed both in time and frequency domains to solve the problem. It was found that at a signal-to-noise ratio exceeding 6–10 dB most of the operation noises can be discriminated from AE data by means of AE parameter prefilters and rather simple post-processing recognition procedures. It was shown, however, that in the case of distant AE sources, when the characteristics of true and noise signals are similar, additional information can be successfully extracted from RMS data, particularly when a random wideband noise is modulated by the low frequencies related to the working equipment. Such RMS-based information not only helps to interpret results but also can be used for the purposes of diagnostics of asset-operating condition. Alternative method is proposed, in which the correlation analysis of AE hit sequences is used to determine the operating noise resonances responsible for the formation of false AE hits; that is, in this case relevant information is extracted directly from AE hit data.

T.B. Petersen (✉)
National Research Centre "Kurchatov Institute", DIAPAC Ltd.,
1, Kurchatov sq., Moscow 123182, Russia
e-mail: Tpetersen@diapac.ru

V.V. Shemyakin • V.Y. Chernigovsky
DIAPAC Ltd., 1-st Pechotny per.6, bld.1, Moscow 123182, Russia
e-mail: VShemyakin@diapac.ru

G. Shen et al. (eds.), *Advances in Acoustic Emission Technology: Proceedings of the World Conference on Acoustic Emission-2013*, Springer Proceedings in Physics 158,
DOI 10.1007/978-1-4939-1239-1_9,

1 Introduction

Application of acoustic emission (AE) method for integrity condition monitoring of hazardous facilities faces some more problems than in the case of traditional short-time AE testing. Without considering technical aspects of the problem, the main challenges of continues AE monitoring of pressure vessels/components during the operation are the presence of high operating noise and the difficulties or even inability to verify the obtained results by complementary testing methods as appropriate.

Generally background noise at the operation of pressure vessels represents complex interrelated thermal, acoustics, and mechanics processes. Mechanical noise signals are often hardly distinguished from true AE signals by traditional discrimination methods; particularly it concerns the distant AE sources. Besides, it was shown earlier that even uncorrelated spatially not localized noise can create clusters of events in the centers of symmetry of sensor arrays, which can be mistaken for genuine AE sources [1]. All this requires a new comprehensive approach for AE data analysis.

The objective of the study was to choose optimal acquisition parameters to obtain appropriate signal-to-noise ratio and to develop the processing procedures of both AE and noise data analysis in order to improve the assessment and interpretation of AE monitoring results, and thus to enhance the confidence of monitoring.

2 Reactor of Polypropylene Production: Technology

Study concerns the initial stage of AE monitoring of polymerization reactor of polypropylene production. Reactor block includes two reactors and the corresponding main and auxiliary equipment.

Polymerization occurs at a temperature of about 60 °C and a pressure of about 2.0 MPa. At a normal working reactor temperature and pressure propylene in the reactor exists in the two states of aggregation (gas, liquid). The reaction of propylene in the gas phase and a catalytic agent produces solid particles of polypropylene powder (PP), which then is discharged from the reactor. In normal operation, each reactor is filled halfway by polypropylene powder, that is, 25–30 t. PP powder is continuously mixed by means of a rotating stirrer that is shown in Fig. 1.

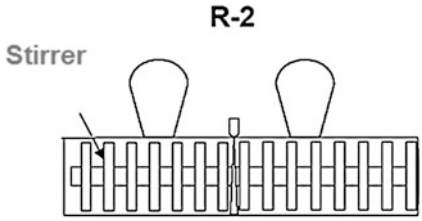

Fig. 1 Reactor stirrer

The reactor itself is a static asset, which comprises dynamic equipment, namely the stirrer and a compressor pump. These apparatus produce high-level audible noise extending also to the ultrasonic range, perceived by AE device. Characteristics of reactor dynamic equipment are the following: reactor stirrer: height—3,029 mm, length—19,481 mm, weight—35,000 kg, constant rotor speed 15 rpm (0.25 Hz); the recycle gas compressor pump has a rotational speed of 1,500 rpm (25 Hz).

A horizontal stirrer comprises the sets of blade pairs (four in a set) arranged on a rotor, which extends along the entire length of the reactor and rotates at a rate of 0.25 Hz (15 rpm—revolutions/min). Each pair of blades rotates at a rate of 0.5 Hz, and the whole set of blades (eight blades) at a rate of 2 Hz.

Possible failures of the equipment are the following:

- Failure of the pump P
- Failure of the recycle gas compressor K
- Propylene leak from the system separator S
- Formation of agglomerates in the layer of polypropylene powder in the reactor R*
- Formation of agglomerates in the domes of the reactor R*

Note that the starred types of faults are the most likely to occur meaning that they have to be controlled with a special attention.

3 Data Acquisition and Processing Methods

AE data were collected using the Sensor Highway II System™, which is a multichannel AE-monitoring system produced by MISTRAS Group, Inc. AE sensors were mounted on the reactor surface at a distance of 3–4 m from each other, forming a regular AE array.

Three types of acoustic data were recorded by each of the multiple AE channels during the acquisition stage: AE hit and waveform sequences, and noise RMS (root mean square) sample. 150–500 kHz filters were used, sampling rate was set up to 1 MHz, and noise RMS subsampling was provided by 10 ms discretization that basically allows analyzing noise frequencies up to 50 Hz. Taking into account the characteristic frequencies of the auxiliary mechanisms, such noise discretization is considered to be acceptable when attempting to extract and study these particular frequencies.

Data-processing methods used in the study include spectral and correlation methods [2], digital filtering, and digital simulation.

4 Principal Problems of Data Processing and Interpretation at a Continuous AE Monitoring

Main problems at AE monitoring are known to be the following:

1. Numerous but incomplete data and a lack of sufficient computing time for thorough data processing
2. Difficulties in verification of the obtained results by complementary NDT methods
3. Presence of high operating noise, causing:
   - High threshold level reducing the likelihood of low-amplitude signal detection
   - Erroneous interpretation of the results obtained
   - Principal difficulties at the rejection of mechanical noise, having the same physical nature as true AE
   - In particular, difficult discrimination of true AE and mechanical interference waveforms in the frequency domain at a distance from the sources

The presence of high-level noise at AE monitoring is considered to be a main factor leading to decrease in the quality and the validity of the control. The mentioned difficulties at data processing are the mechanical nature of true sources and acoustic interferences as well as signal distortion at wave acquisition and propagation.

In fact, true AE signal, e.g., from rapid cracking or PLB (pencil lead break) imitator, is known to have rather wide spectrum, up to frequencies of ~1/T, where T equals to input duration. However, as high frequencies attenuate more than low ones at wave propagation the spectrums tend to shift left in frequency direction for the distant sources.

As an example, the typical patterns of signals obtained nearby and at a distance of 10 m from AE source are shown in Fig. 2a, b, correspondingly. Signals were produced by PLB on a 700 mm diameter and 10 mm width empty steel tube. Signal spectrums are given in Fig. 2c, curves 1 and 2, correspondingly.

Again, though some types of interferences can be discriminated rather easily by standard recognition methods (e.g., electrical, EMI) however, both the localized mechanical noise and genuine AE are produced by a material deformation. Basically these sources can be recognized by the use of informative frequency features when the sources are placed close to the sensors because mechanical interferences have lower frequency range due to larger duration of the effect; however, signal differences reduce at a distance.

Coming around to the reactor noise, which is produced by collisions of bulks of numerous solid particles of PP against a reactor surface during a stirring of the product, let us consider impacts as mechanical interferences and compare typical patterns of a pencil lead break and an impact of a steel sphere against a steel plate,

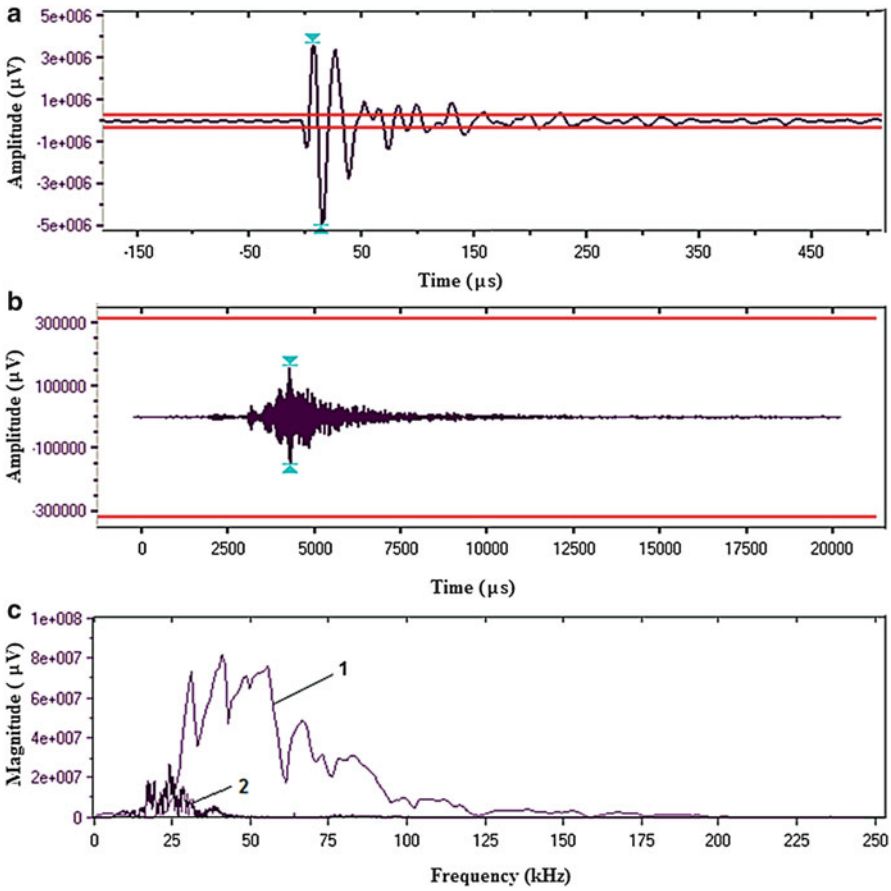

Fig. 2 PLB waveforms and spectrums recorded by R6 sensor: (**a**) PLB waveform recorded near the source, (**b**) PLB waveform recorded at a distance of 10 m from the source, (**c**) spectrums of (**a**) curve *1* and of (**b**) curve *2*

given in Fig. 3a, b, correspondingly. Acquisition parameters were set as follows: sampling rate $Fs = 2$ MHz; filters: HPF and LPF 1–1,000 kHz; and resonance-type sensor—R15 (resonance frequency 150 kHz).

One can see that the impact produces rather high-frequency signals, which, however, can be rather easily distinguished from PLB both in time and frequency domains.

In fact, as it was shown in [3] high-frequency tract of acoustic emission apparatus transforms initial impact perturbance into two separate signals, arriving with delay exactly equal to impact duration that can be calculated using Hertz theory of elastic impacts [4]. AE signals are generated at the moments corresponding to derivative discontinuities of surface displacement function of

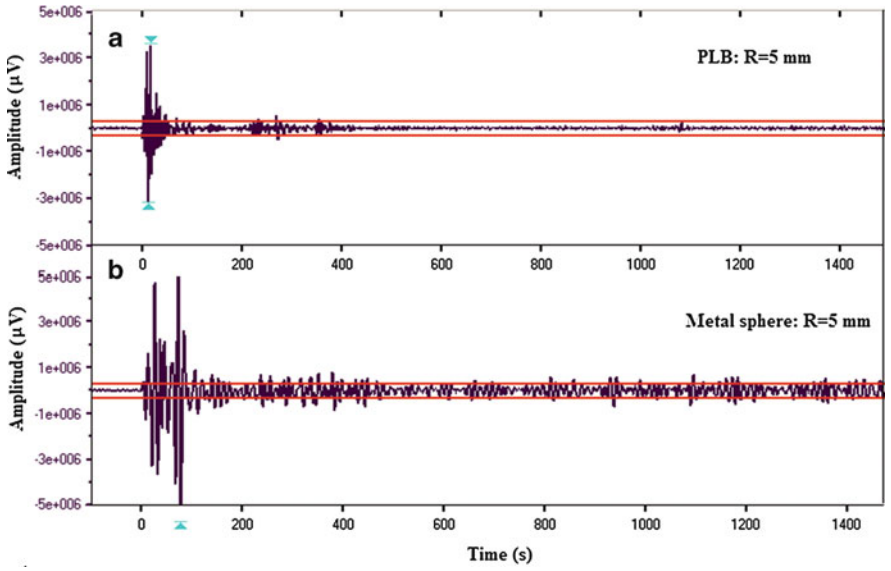

Fig. 3 Waveforms recorded at a distance $R = 5$ mm. (**a**) Source is PLB, (**b**) source is the impact of 8 mm steel sphere against vertical steel plate

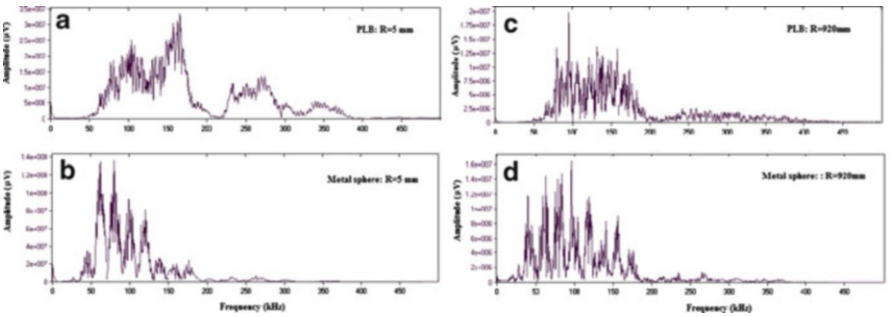

Fig. 4 Frequency spectrums of PLB and impact of steel sphere (**a**, **b**) near the sources, (**c**, **d**) at a distance of 920 mm from the sources

colliding bodies, i.e., at the initial moment of loading and the final moment of contact. Typical signals from PLB and collision of steel 8 mm sphere against a steel 10 mm width plate are given in Fig. 3.

The perceptible difference between PLB and sphere impact spectrums obtained near the sources can be observed in Fig. 4. However, e.g., at the distance of 920 mm these spectrums become rather similar, which results from attenuation of high frequencies at wave propagation. In time domain the difference neglects in a case

of inelastic impact, when a colliding body does not recoil, thus producing a single signal very similar to PLB. It was found out that the less is a weight of a colliding body and the more is a distance from source the less is the difference between PLB and impact signals.

Above considerations confirm that discrimination of random noise fluctuations is a complex problem at AE testing, which has to be solved by thorough analysis of noise waveform/spectral features and further reduction of signal-to-noise ratio.

5 Noise Assessment

Preliminary analysis of noise waveforms recorded with the help of wideband sensor showed that in the examined high frequency band noise can be considered as the so-called colored noise giving a power dependence of PSD (power spectral density) on frequency and decreasing rather abruptly, by about 25 dB per octave.

Such frequency dependence of sensitivity of background noise was used at the determination of system acquisition parameters that provided reduction of amplitude threshold by more than 10 dB.

It was found taking into account the frequency response of the sensor that the observed noise does not have particularities in the examined frequency band, as well as genuine AE, which is broadband on its nature, and also do not have specific features. It means that these two kinds of sources are unlikely to be distinguished in the frequency domain in the chosen frequency range without making phase analysis. Noise streaming study shows that the described colored noise is a high-frequency noise, modulated by the low frequencies; see Fig. 5a. As the low frequencies were filtered from the waveforms at HP filtration during data acquisition (150 kHz high-pass filter cutoff), it means that they do not exist separately from high-frequency wideband noise, which serves as a carrier to them. To extract low frequencies a detection procedure, e.g., squaring, has to be applied to the sampling data. Time-driven RMS data, which is provided by subsampling of initial digitized data, include all the features required for extraction of low modulation frequencies from the high-frequency data. Really, its sample length is large enough to include several periods of low harmonics and besides, RMS is obtained by squaring (and subsequent rooting) of the decimated data.

6 Discussion of the Results

It was found that at an appropriate signal-to-noise ratio, when AE peak amplitude exceeds a threshold by more than 6–10 dB, most of background noise can be discriminated from AE data by means of prefilters and simple post-processing recognition procedures.

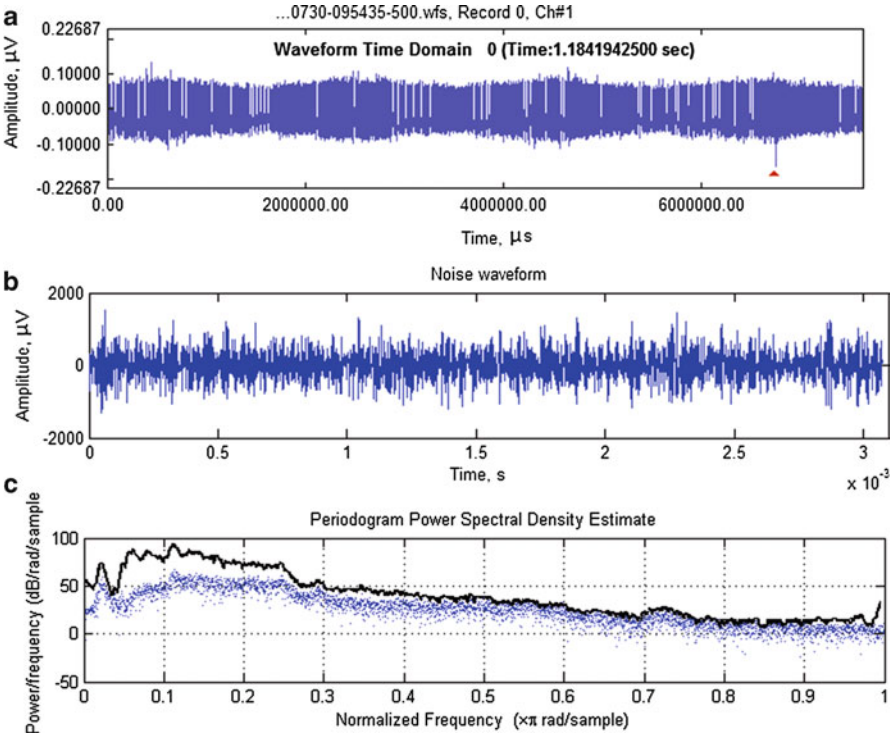

Fig. 5 Noise characteristics: (**a**) Noise streaming, $Fs = 1$ MHz, $t \sim 6$ s; (**b**) noise waveform: $Fs = 2$ MHz, N point $= 6 \times 1{,}024$; (**c**) power spectral density—original (given by *points*) and recovered (*curve*)

However, the periodically recorded noise, which generally serves just as accompanying information at AE testing practically, carries relevant data, so it can be analyzed together with AE hits and waveforms and used for diagnostic purposes.

At the study of RMS recorded during AE monitoring of reactor it was found out that in spite of high-frequency filtering (150 kHz cutoff frequency) applied at data acquisition, RMS samples show the presence of low frequencies (0.5, 2, and 25 Hz); see Fig. 6.

Such an effect can be explained considering that the observed AE hits are formed by random wideband noise modulated by low-frequency external forces, here rotation of mechanisms and pump vibrations. Modulations apparently result from nonlinear interaction of the physical processes, which take place during the operation of reactor, namely collisions of PP powder during its mixing and vibrations.

To obtain the characteristic operating frequencies directly from AE data quasi-autocorrelation function of hit sequences was estimated. The pattern of this function

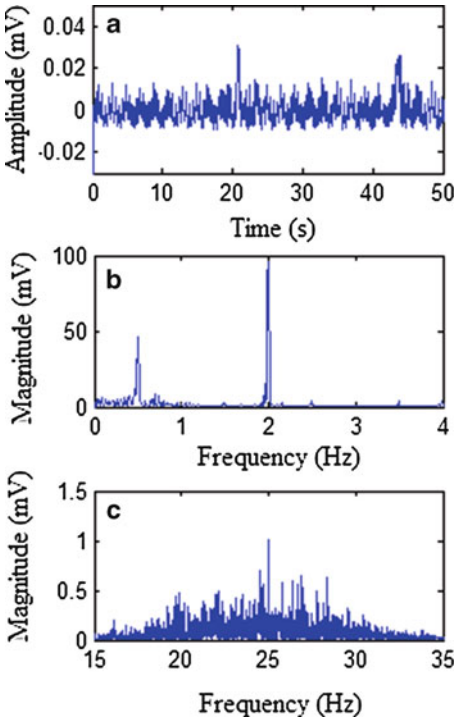

Fig. 6 (**a**) Noise RMS, (**b**) noise spectrum in 0–4 Hz frequency band, (**c**) filtered noise spectrum in 15–35 Hz band

presented in Fig. 7 shows the periods specific to rotation of blade pairs (0.5 Hz) and a set of eight blades (2 Hz). The obtained autocorrelation curve shows that the recorded hits/waveforms correspond to nothing else but to the background noise produced by dynamic mechanisms.

7 Conclusions

To avoid false interpretation of AE data the periodically recorded noise data, e.g., RMS, can be analyzed together with AE hits and AE waveforms, both in time and frequency domains, indicating whether a signal or, what is more important, a cluster of signals relates to genuine emission or noise/interference source.

The obtained resonances of low-frequency noise can serve as the monitoring diagnostic features.

Some harmonics of operating noise responsible for AE hit formation can be obtained directly on the base of correlation analysis of AE hit sequences.

Simultaneous noise diagnostics and AE control using the same data acquisition channel can be a useful practice increasing the confidence level of the correct assessment of asset-operating condition during AE monitoring.

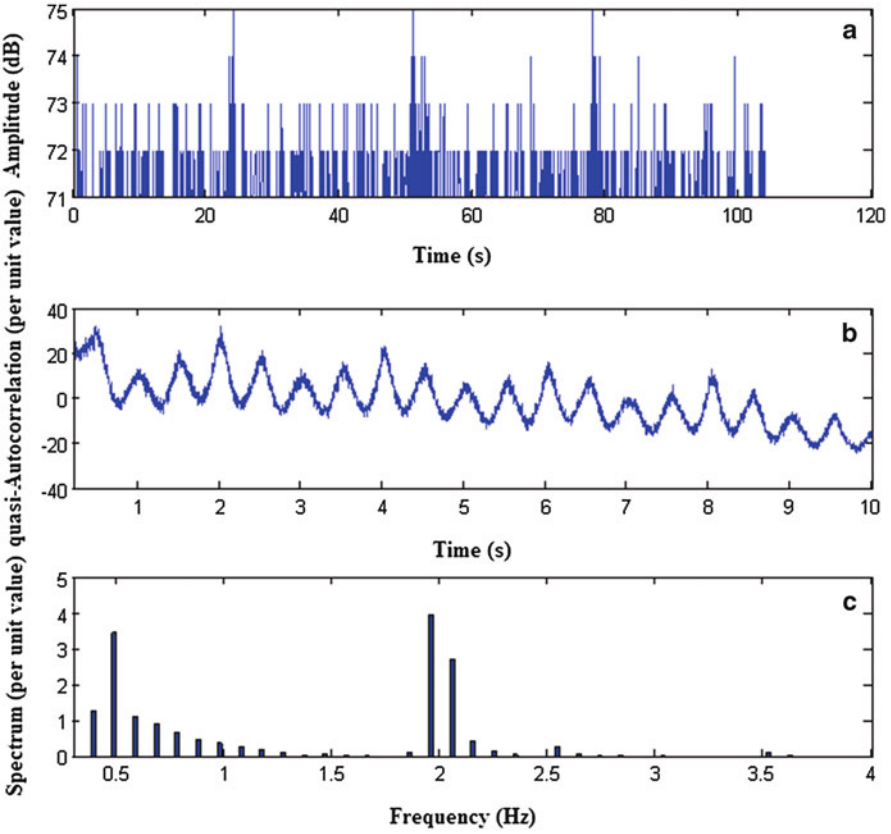

Fig. 7 Quasi-autocorrelation function obtained from AE hit sequence recorded at reactor monitoring: (**a**) Hit sequence, (**b**) quasi-autocorrelation function, (**c**) Fourier transform of quasi-autocorrelation giving the characteristic frequencies of stirrer blade rotation

References

1. T.B. Petersen, The errors of acoustic emission source location at high activity of noise. J. Diagnostics. Control **1**, 23–27 (2007)
2. S. Lawrence Marple Jr., *Digital Spectral Analysis: with Applications* (Prentice-Hall, Englewood Cliffs, NJ, 1987)
3. T.B. Petersen, Acoustic emission from impact of rigid bodies. JAE (USA) **27**, 98 (2009)
4. W. Goldsmith, *Impact* (Edward Arnold Ltd., London, 1960)

AE Source Location on Irregular-Shaped Objects Using 3D Grid Method

Alexey B. Samokhvalov

Abstract The 3D model based on regular cubic cell grid is presented, allowing to perform AE source location on irregular-shaped objects with arbitrary complex geometry.

1 Introduction

Location of AE sources is usually based on simple geometric models: plane, cylinder, sphere, and cone. However, in practice this approach does not always give good results for the following reasons:

1. In many cases irregular and complicated geometry of an object cannot be reduced to simple shapes.
2. The presence of internal medium or devices.
3. The inhomogeneity of material.
4. The complex character of acoustic wave propagation.

Therefore the simple location schema on irregular-shaped objects often results in chaotically placed AE sources ("star sky").

To enhance AE source identification on real objects, besides simple schemata, three-dimensional grid (mesh) models are used. They allow to take into account different details of geometry and design of the object as well as its operation conditions.

There are different approaches to build 3D location models, e.g., surface fragment-based models [1, 2, 3].

A.B. Samokhvalov (✉)
DIAPAC Ltd., 1st Pekhotniy Lane, bld. 6/2, Moscow 123128, Russia
e-mail: asamokhvalov@diapac.ru

G. Shen et al. (eds.), *Advances in Acoustic Emission Technology: Proceedings of the World Conference on Acoustic Emission-2013*, Springer Proceedings in Physics 158,
DOI 10.1007/978-1-4939-1239-1_10,

Nevertheless such models are not widely used yet in practice of AE data analysis. That is why the goal was set to develop special location methodic which would be practical enough and appropriate for complex industrial structures with irregular shapes—the area where the application of grid models is most promising.

2 Requirements to the Model

While defining requirements to the model the following considerations were put forward.

The model should reflect modern knowledge about the nature of sound waves and the character of their propagation.

The ability should be provided to model object components with different conditions of sound propagation; the model should be able to combine together parts made from solid materials, like vessel walls, and internal volumes filled with fluid; parts of object can differentiate one from another by attenuation characteristics and sound speed.

There should be no restriction for the representation of arbitrary object shape; both thin-wall and massive elements could be modeled; the same refers as well to rectilinear and curved shapes.

The model should be reasonably simple from technological point of view, easy to use, and user friendly. Since complex forms often consist of parts with simple regular forms combined together, there should be opportunity to quickly build the model from such parts, wherein the ability to conveniently define the characteristics of joint between parts should be provided.

The model should offer the convenient way to enter the positions of sensors and other characteristic points.

Thus, taking into account these requirements, the 3D grid model based on regular cubic cells was offered.

3 Model Principles

The model is based on the following principles.

The entire space is divided by cubic cells of the same size. Thus, for any point in the space with (X, Y, Z) coordinates the relevant cell is immediately found. Cell can be either empty or belonging to the object. If cell belongs to the object, it can transduce sound impulse to neighbor cells.

In the model the sound impulse propagates by centers of cells, from one point to another; in other words, for sound propagation the 3D grid of cells' center points is used.

In Fig. 1 the schema of propagation of sound from the cell to its neighbors is shown. This is flat representation of the model, but the same principles are easily extended for 3D grid. The cell (x2, y2) is the current source of sound impulse.

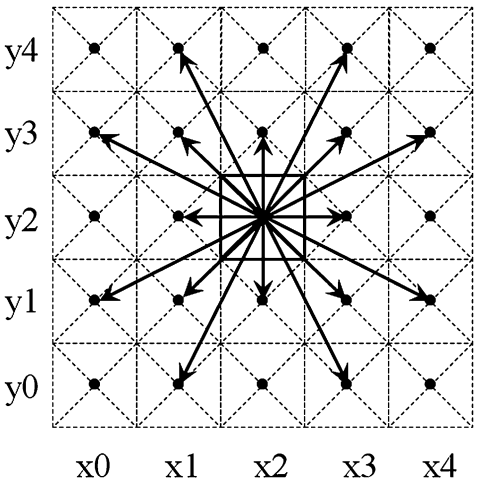

Fig. 1 Propagation of sound in 3D grid model

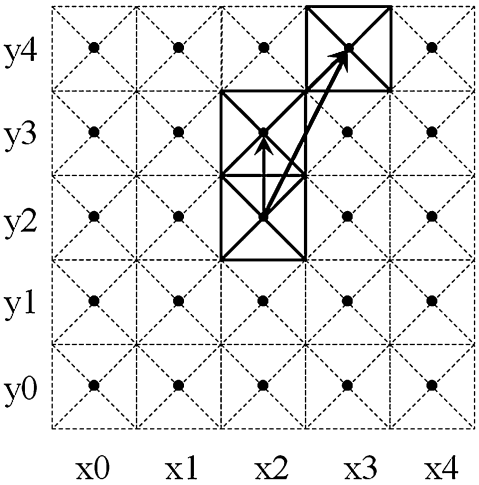

Fig. 2 Propagation shortcut

It can reach, first, its immediate neighbors (first layer)—cells (x1, y1), (x2, y1), (x3, y1), (x1, y2), (x3, y2), (x1, y3), (x2, y3), and (x3, y3). Of course, the sound would go there only if that cell belongs to object, i.e., is not void. The check of the cell—if it belongs to object or not—is quickly done by its (x, y, z) index. The distance between source cell and neighbor is also immediately determined by their relative position, which depends, in its turn, on their indices.

Meanwhile, it could be easily noticed that this rule yet would give significant error in distance for propagation in direction lying between directions to immediate neighbors. For example, if sound propagates from cell (x2, y2) to cell (x3, y4) through cell (x2, y3), it passes 1.08 times more distance than direct pass from (x2, y2) to (x3, y4)—see Fig. 2. To reduce this effect these

shortcuts were included in the model: The rule was applied that if cell from second layer from source cell touches filled cell in the first layer, it is reached by direct shortcut.

4 Building of the Model

Building the model means to define which cells are filled and what sound speed and attenuation they have. This could be done by different ways. The good practical approach which was used in application of the model consists in the following: first split original object by simple parts, then represent each part by cells, and then combine parts together.

Simple parts that compose the object are the following: cylinder, sphere and demisphere, demi-ellipsoid (commonly used for representing vessel head), cone, frustum, and box. Flat fragments, if necessary, are derived from these: plane is flat box, and disc is demisphere with zero height (disc could be used as flat vessel head).

Each simple part could be considered as (1) hollow inside (filled with gas), (2) massive, or (3) hollow, but filled with fluid.

Joints between parts could be of two types: (1) "Nozzle": The smaller part enters another and they have common internal space inside, like nozzle entering the shell of vessel or one pipe composing T-joint with another. (2) "Adjacent volume": This type of joint leaves the wall separating internal spaces of two parts.

When building the model the following algorithm is applied: (1) the appropriate step is selected which is smaller than the size of cell; (2) the surface of component is represented as the set of points in such a way that the distances between neighbor points are less than step; (3) for each point the corresponding cell is found; the set of these cells composes the representation of the surface in 3D grid model. Thus the original surface is wrapped by cells, composing regular grid. This is illustrated by Fig. 3.

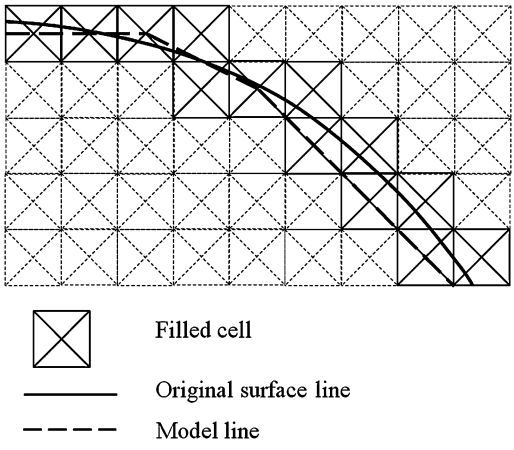

Fig. 3 Presentation of original curved surface in the model

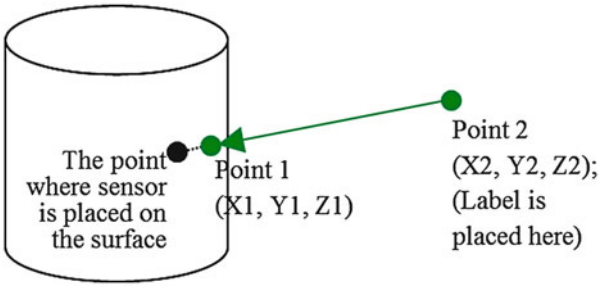

Fig. 4 The placement of sensor (characteristic point) on the surface

After the shape of the object is wrapped by cells, the next task in building the model is to determine the positions of sensors and other characteristic points. This could be done analytically, of course, but on curved surfaces like ellipsoids the true position of sensors often could be defined only approximately; also usually the labels with lines are drawn as well for better visualization and understanding of 3D drawing. So for the purpose of convenience the following supplementary technique was used (see Fig. 4): two points were analytically defined which served as the beginning (Point 2) and the end of line (Point 1). The label was placed near Point 2, and the Point 1 is closer to the surface. To determine the cell where sensor (or other characteristic points) is placed the program starts to move probing point along the ray from Point 2 to Point 1 and stops, when first cell of the surface is hit.

The surface in the cell model, unlike original surface, is not smooth. Nevertheless, the essential assumption of the model is that the distances, calculated between original points of the object and between corresponding cells, do not differentiate too much for the purpose of AE source location. The research was carried out to evaluate the precision of the model and to define recommendations on the selection of its best parameters, namely the size of cell.

5 Evaluation of the Model

In Fig. 5 two variants of cell model are shown for the same spherical vessel with 14.0 m diameter; the first is built with cell side 1.0 m, and second—0.2 m. It is obvious that decreasing of the cell side makes the model more realistic looking and potentially more precise.

We have investigated the preciseness of model by the following procedure: the precise theoretic distances from the points on the surface of ideal shape (sphere, cylinder), corresponding to known cells, to sensors were compared with distances calculated solely by cell model. The result for the same sphere as in Fig. 5b is shown in Fig. 6. The error of the distance evaluated by the model foreseeably is greater at small distances, and it is derived from the roughness of cell model. The maximum error is determined by the size of cell. At the distance more than 2.0 m relative errors are less than 20 %, and at more than 3.0 m—less than 10 %.

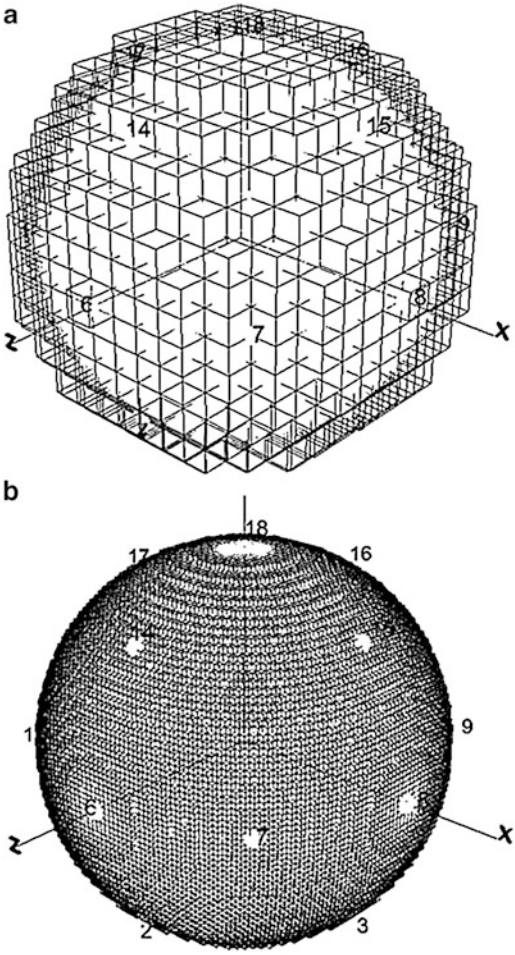

Fig. 5 The representation of the sphere vessel with $D = 14.0$ m in the model: (**a**) Cell side is 1.0 m, 786 cells in the model; (**b**) cell side is 0.2 m, 21,288 cells in the model

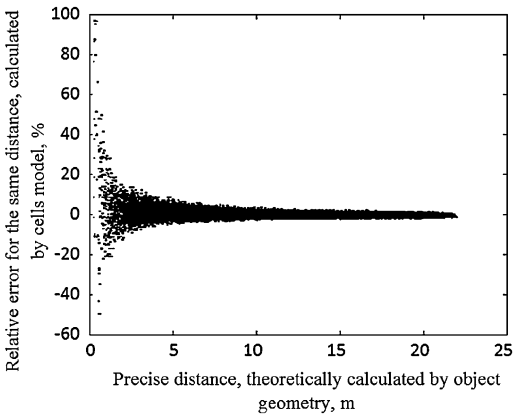

Fig. 6 Relative error of distance from surface points to sensors on sphere ($D = 14.0$, cell side is 0.2 m)

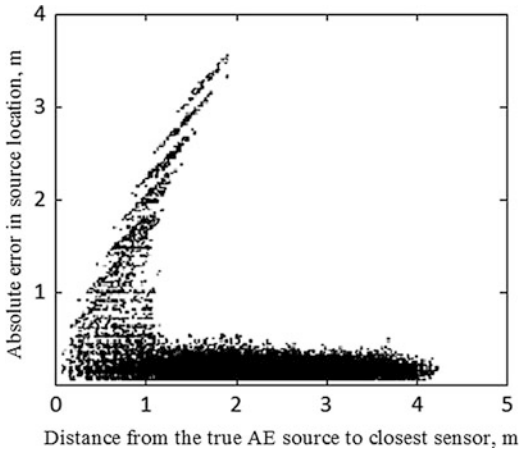

Fig. 7 Location error, calculated using AE event simulation

Meanwhile, the error in distance evaluation is not the same as the error in source location, since location algorithm takes into account several hits on different sensors and thus counterbalances individual distance errors. To evaluate the preciseness of model for location, we have simulated AE events by software model, located them by cell model using pattern recognition algorithm, and compared the result with original event source location. The plot of location error (in absolute distance from original source) against the distance from source to closest sensor is shown in Fig. 7. This plot shows results for the same sphere and model as in Fig. 5b; the number of simulated events is 30,883 (each of them is presented as point on this plot).

From this plot we see that absolute majority of errors is less than 0.5 m, which is quite acceptable for such a structure. At the same time we see the characteristic outburst of large errors rising from the beginning of the plot with right slope. Investigation has shown that this burst of errors belongs to specific zones near sensors, oriented inside triangles built between adjacent sensors (Fig. 8). The zones of high location errors are thus likely connected with "equal delay" hyperboles, so they derive more from the nature of location algorithm than from the model itself.

The statistic characteristics of location preciseness, evaluated by simulation for the same sphere with 14.0 m diameter for two cell sizes—0.2 and 0.4 m—are shown in Table 1.

It is interesting to note that median absolute error in location for cell size 0.2 m is 0.19 m, which is near the cell size itself, and for cell size 0.4 m it is 0.29 m, which is even less than cell size: thus the effect of counterbalancing of location algorithm becomes apparent.

The natural testing of the model was performed on vertical cylindrical vessel ($H = 1.5$ m) with nozzles. AE sources were simulated by signal generator, placed on the inner surface of the shell. 3D view of vessel with located sources is shown in Fig. 9; the envelop view of the shell is presented in Fig. 10.

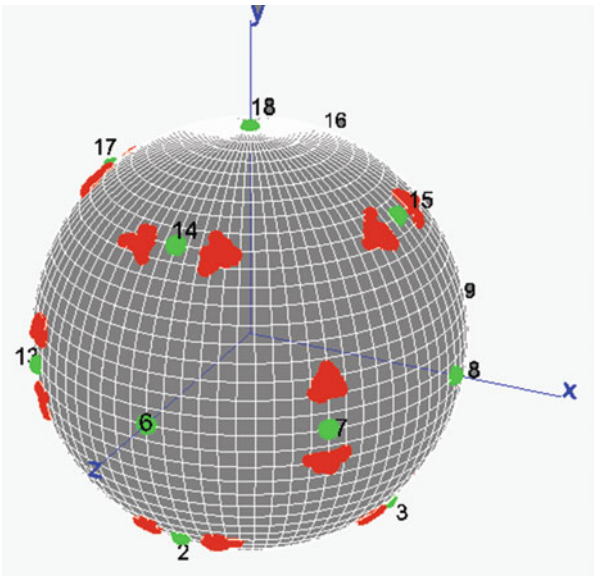

Fig. 8 Zones of location error concentration

Table 1 Statistic of location precision

Characteristic	Cell size (0.2 m)	(0.4 m)
Number of cells in the model	21,288	5,239
Number of events simulated	30,883	15,530
Number of sources located	30,770	15,467
Minimum absolute error, m	0.0005	0.0012
Maximum absolute error, *m*	3.65	3.79
Median absolute error, *m*	0.19	0.29
95 % of errors less, *m*	0.4	0.6

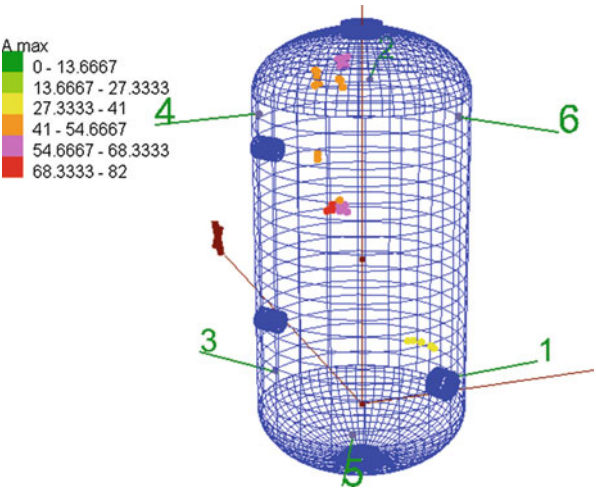

Fig. 9 Cylindrical vessel with located sources, colored by amplitude

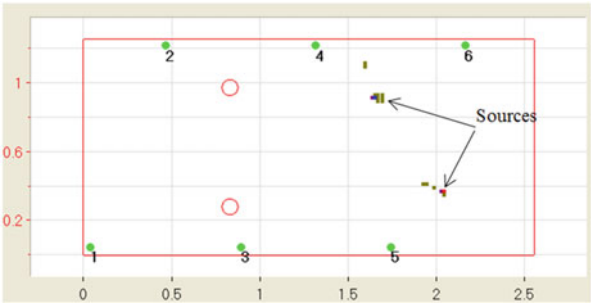

Fig. 10 Envelop view of shell with located sources

6 Application Details

The method produces geometrical model that could be used in different ways.

The appropriate grid is formed after the comprehensive evaluation of the object. The decision is made about the degree of shape simplification and grid roughness. By means of event simulation in every node, the calculations are carried out to determine which pattern of hit parameters is expected at each sensor. Then test data is processed in order to search the correspondence between actually recorded signals and theoretically simulated events prototypes.

The main stages of application of 3D grid method are the following.

6.1 Preparatory Stage

1. Preliminary analysis of the object.
2. Determination of sound speed and attenuation (possibly with differentiation by directions and object's parts).
3. Sensor positioning (if not predetermined).
4. The building of geometrical model: partition of the surface by fragments, determination of coordinates for vertices.
5. Calculation of the model: building of the shortest path map; here well-known search "in breadth" algorithm could be used.
6. Determination of the discrete set of characteristic events for each source.
7. Determination of expected signal image on sensors for each characteristic event.

6.2 Actual Data Processing Stage

1. Determination of possible groups of hits as potentially belonging to one event: All possible hit groups are considered in the scope of event determination time.
2. Distribution of hit groups by event groups: Similar hit groups are assigned to one event group.

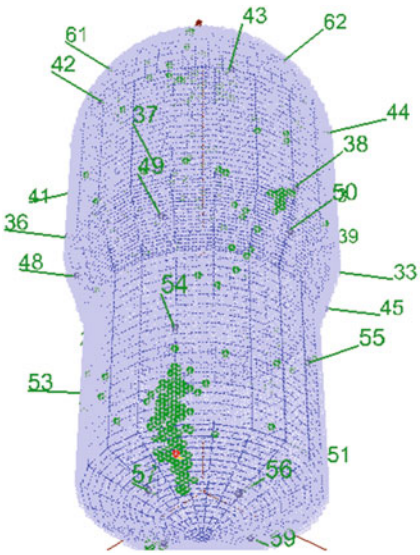

Fig. 11 AE location results (located sources are shown as *green*, *yellow*, and *red*, according to the source amplitude; *lines with numbers* show position of sensors)

3. Analysis of event group statistics and selection of event groups which are of interest for further consideration (by intensity or trend).
4. Assigning of selected event groups to supposed sources (vertices on the grid model): Here the matching of actual and theoretic hit images is done. The event group is linked with the source by similarity criterion.
5. Considering of the event groups for which characteristic sources were not found: To resolve this uncertainty the following can be done: (1) refine the model, e.g., change cell size and orientation; (2) change supposed hit images, e.g., increase the number of considered wave modes and consider obstacles; (3) make similarity criterion less strict.

The sample model, built for real industrial structure (regenerator on oil refinery plant) with location results, is shown in Fig. 11.

7 Conclusions

AE source location on industrial structures using the modeling of design component geometry by means of 3D grid is considered.

The 3D model based on regular cubic cell was developed to perform AE source location on different structures with arbitrary complex form.

This technique allows not only locating AE sources on thin-wall shapes filled with gas, but also in massive 3D structures, in multilayer constructions with different characteristics of layers and/or structural parts, and in objects filled with liquid (tanks, oil reservoirs).

The results, obtained using this methodic, essentially supplement results obtained by traditional location techniques.

The methodic was applied for AE diagnostic of complex structures in oil refinery and chemical industry.

References

1. M.G. Zhang, B.J. Cheng, X.F. Li, M.Y. Wang, A fast algorithm of the shortest path ray tracing. Chin. J. Geophys. **49**(5), 1315–1323 (2006)
2. P. Pechac, Electromagnetic wave propagation modeling using the ant colony optimization algorithm. Radioengineering **11**(3), 1–6 (2002)
3. B. Zhou, S.A. Greenhalgh, 'Shortest path' ray tracing for most general 2D/3D anisotropic media. J. Geophys. Eng. **2**, 54–63 (2005)

Numerical Simulation of Wave-Guiding Properties and Optimization Design for Wave-Guiding Rod

Junpeng Zhou, Ying Zhang, Guang Dai, and Meiping Song

Abstract Wave-guiding rod is an auxiliary detection tool of acoustic emission (AE) testing under special conditions and plays the role of transmitting AE signals. But the AE signals propagating in the wave-guiding rod will produce attenuation, which will affect the test result. In response to this problem, according to the theory of stress wave propagation in the wave-guiding rod, we adopted the ABAQUS software and set up a numerical model of wave-guiding properties to simulate the influences of wave-guiding rod to stress characteristics. The wave-guiding rods are designed in different lengths, diameters, and boss types. By comparing the simulation results, we draw the conclusion that wave-guiding rods of 6 mm in diameter, no more than 0.5 m in length with a plate-shaped boss type, will have the minimum attenuation and basically have no impact on the strength of AE signals.

1 Introduction

Acoustic emission testing technology has widespread applications, but restricted by factors like high temperature, extremely low temperature, radiation, ground-bury and sensor conditions, etc.; the technology can't be effectively employed. In order to achieve the desired result, the wave-guiding rod is often used as an auxiliary tool for acoustic emission detection [1]. One end of the wave-guiding rod is fixed on the surface of the object to be measured either through welding or the connecting mechanism; the other end is connected to a sensor. In the process of detection, stress wave travels through the waveguide rod and is later received by the sensor. Influenced by the geometry size of the wave-guiding rod, the stress wave will

J. Zhou (✉) • Y. Zhang • G. Dai • M. Song
Northeast Petroleum University, Daqing 168813, China
e-mail: jpzhou0844@139.com

G. Shen et al. (eds.), *Advances in Acoustic Emission Technology: Proceedings of the World Conference on Acoustic Emission-2013*, Springer Proceedings in Physics 158,
DOI 10.1007/978-1-4939-1239-1_11,

produce attenuation and finally affect the testing result. Therefore, wave-guiding properties of the wave-guiding rod are the main factors which will affect its design [2].

In this paper, finite element method and ABAQUS software are introduced to simulate the stress wave propagation in the wave-guiding rods. The paper analyzes the influence factors like different lengths, diameters, and boss structure types to stress wave propagation. According to the simulation results, it also optimizes the design of wave-guiding rod so as to suggest the appropriate geometry and size of wave-guiding rod.

2 The Basic Theory on Wave-Guiding Properties of Wave-Guiding Rod

Under a transient load, stress waves are produced at the end of the wave-guiding rod. The propagation of stress wave in wave-guiding rod is shown in Fig. 1. When a uniformly distributed compressive stress σ is suddenly imposed on the left end of the rod, even compression will be produced in the finite layer on the left end, and the compression will be passed on to the adjacent layer in turn.

After time interval dt, part of the length on the left end of wave-guiding rod will be compressed, while the rest of the part where the stress wave does not reach is still in the static stress-free state [3]. According to Newton's second law, the wave equation of stress wave propagation in the uniform diameter wave-guiding rod is as follows

$$\frac{\partial^2 u}{\partial x^2} = \frac{1}{C_0^2}\frac{\partial^2 u}{\partial t^2}. \tag{1}$$

When the stress wave propagates in the wave-guiding rod with a variable cross section, the wave equation is

$$\frac{\partial^2 u}{\partial x^2} + \frac{1}{A}\frac{\mathrm{d}A}{\mathrm{d}x}\frac{\partial u}{\partial x} = \frac{1}{C_0^2}\frac{\partial^2 u}{\partial t^2}. \tag{2}$$

In Eq. (2): u—displacement of particle, x—displacement of wave propagation, C_0—velocity of stress wave, E—modulus of elasticity, ρ—density, t—propagation time of the stress wave, A—cross-sectional area of the wave-guiding rod.

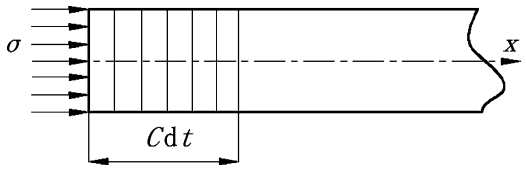

Fig. 1 The impact compression of the wave-guiding rod

3 Model of Numerical Simulation on Wave-Guiding Properties of Wave-Guiding Rod

ABAQUS software is used to carry out numerical simulation of wave-guiding properties of wave-guiding rod. This software is suitable for analyzing complex solid mechanic system [4]. Unidiameter round bar is usually used in acoustic emission testing. Figure 2 is the geometry model of wave-guiding rod without boss structure. C3D8R is selected as a unit type to realize mesh generation of the whole wave-guiding rod.

Stress wave is generated by a plurality of point acoustic sources of elastic wave, and in the simulation the initial acoustic source is a point source. Through the analysis of point acoustic source, we can get stress wave propagation characteristics of the wave-guiding rod. The signal frequency of AE sources ranges widely. The frequency selected in this simulation is 100 kHz. Select half sine type as initial source, as shown in Fig. 3, maximum intensity of the acoustic source for 1×10^5 Pa. The longitudinal wave propagation velocity is 5,064 m/s in the wave-guiding rod and transverse wave velocity is 3,230 m/s. Since the particle displacement caused by longitudinal wave is much greater than by transverse wave, ignoring the influence of transverse wave, this paper only studies the propagation laws of stress wave in wave-guiding rod along the *Y* direction.

Take a wave-guiding rod (length of 0.5 m, diameter of 6 mm) as an example. By the action of acoustic source, we analyze the stress waveform at point A, the circle point of the other end, in the *X* axis, *Y* axis, and *Z* axis direction, as shown in Fig. 4. The stress wave propagation time in the wave-guiding rod is 0.01 s.

As shown in Fig. 2 the initial acoustic source direction parallels to the *Y* axis. As the stress wave will produce waveform transformation in the process of propagation, the stress wave shifts are produced in all the axial direction of wave-guiding rod: stress wave caused by the load in the *Y* direction is the longitudinal wave, while in the *X* and *Z* direction is transverse wave, as shown in Fig. 4. Since the particle

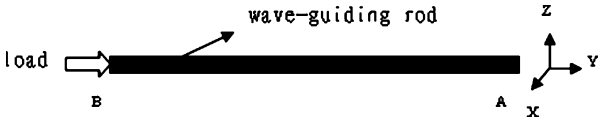

Fig. 2 The wave-guiding rod model of numerical simulation

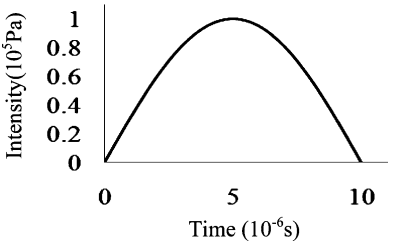

Fig. 3 Type of load applied on the wave-guiding rod

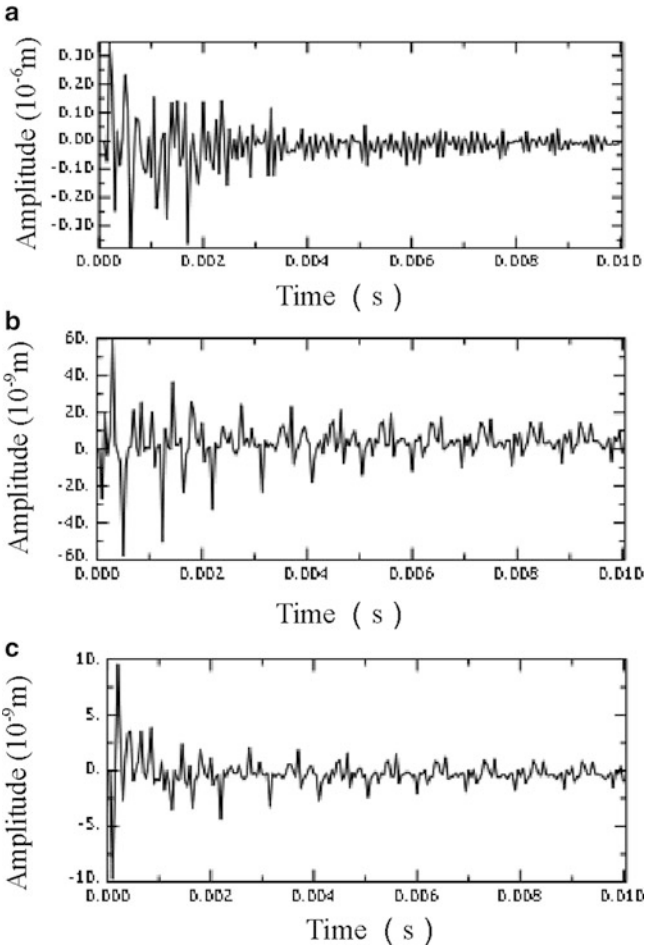

Fig. 4 Waveform diagram of point A at the end of wave-guiding rod (**a**) *Y* axis direction, (**b**) *X* axis direction, (**c**) *Z* axis direction

displacement caused by longitudinal wave is much greater than by transverse wave, ignoring the influence of transverse wave, this paper only studies the propagation laws of stress wave in wave-guiding rod along the *Y* direction.

4 The Numerical Simulation Analysis of Stress Wave Propagates in the Boss Structure

For cylindrical wave-guiding rod, the diameter and length are the main factors that affect the propagation and attenuation of the stress wave, wave-guiding rod without boss structure as the research object. This paper stimulates the wave-guiding

rod with the different lengths and diameters and analyzes their impacts on the waveguide. Combined with actual using requirement of wave-guiding rod, try to find the optimal diameter and length of wave-guiding rod.

4.1 The Impact Analysis of Diameter on Wave-Guiding Properties of Wave-Guiding Rod

Under the condition of same length, wave-guiding rods of diameter 6 mm, 8 mm, 10 mm, 12 mm, and 14 mm, respectively are chosen to analyze the impact of diameter on wave-guiding properties. When the length is 0.5 m, the maximum intensity of the acoustic source is 1×10^5 Pa, propagation time is 0.01 s, and the waveform of the center point A at the end of wave-guiding rod is shown in Fig. 5. Waveforms at the end of the wave-guiding rod with same length and different diameters are roughly the same; after multiple reflection the displacement error approaches to zero gradually. The relationship between the diameter and the initial time magnitude of displacement of stress wave obtained at the center particle of point A at the end of the wave-guiding rod is shown in Fig. 6.

As the graph shows, after receiving p-wave, the displacement magnitude of the center particle of surface A increases with the diameter of wave-guiding rod, but not too much.

In view of material-saving, portability, and stability of the wave-guiding rod, it is better to choose a wave-guiding rod with a diameter of 6 or 8 mm.

4.2 Impact of Length on Wave-Guiding Properties of Wave-Guiding Rod Without Boss

The stress wave will be attenuated with propagation in the wave-guiding rod, so selected a diameter of 6 mm and long of 10 m wave-guiding rod model, to analysis the attenuation situation of stress wave propagation. According to wave propagation theory, the maximum axis Y displacement of the central particle at distances 0 m, 0.25 m, 0.5 m, 1 m, 1.5 m, 2 m ... 10 m from end B is obtained and its relationship with distance is shown in Fig. 7.

Figure 7 shows that the maximum amplitude of particle vibration reduces as the propagation distance increases when the stress wave propagating in the wave-guiding rod, which shows there exists attenuation in the wave propagation, and the farther it spreads the more it attenuates. There is an index relationship between the maximum amplitude of the stress wave and the propagation distance, fitting equation:

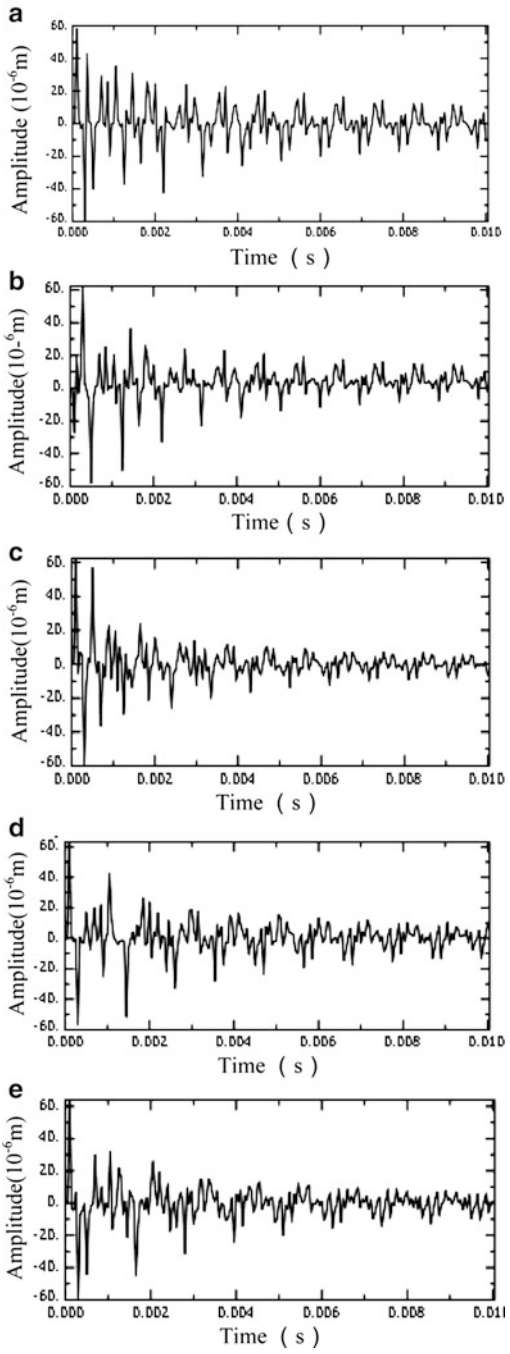

Fig. 5 The relationship between displacement and time of wave-guiding rod with different diameters in the *Y*-axis direction (**a**) Φ6 mm, (**b**) Φ8 mm, (**c**) Φ10 mm, (**d**) Φ12 mm, (**e**) Φ14 mm

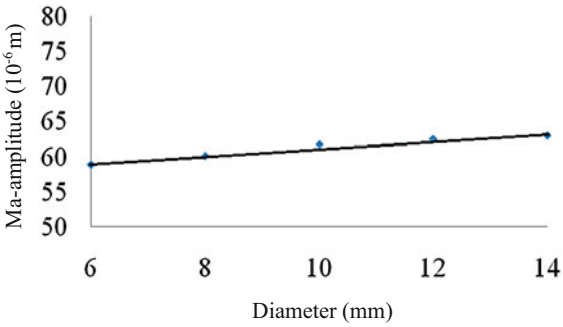

Fig. 6 Max-amplitude of different diameters

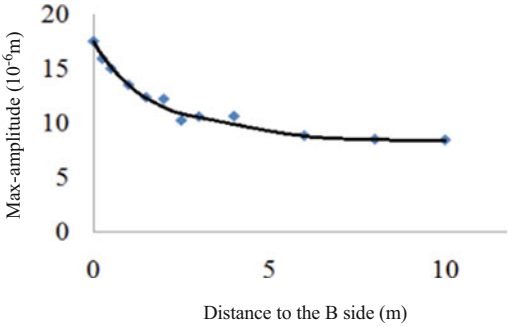

Fig. 7 Max-amplitude in the communication process

$$y = 8.53\mathrm{e}^{(-x/2)} + 8.57. \tag{3}$$

Stress wave propagation in the wave-guiding rod attenuates exponentially, which is consistent with the theory of stress wave attenuation. So the shorter the length of the wave-guiding rod is, the smaller the stress wave attenuation effect is. According to the testing conditions, shorter wave-guiding rods are preferred when choosing wave-guiding rod.

5 The Impact and Selection of Different Boss Structures on Wave-Guiding Properties of Wave-Guiding Rod

The diameter of commonly used acoustic emission sensor is 16 or more, if using the diameter of wave-guiding rod for Φ6 or Φ8, which will influence the coupling between the sensor and the wave-guiding rod and is not easy to install. To solve the problem, we can design the starting end of wave-guiding rod as a boss type and change the cross-sectional area. The wave equation (2) is applicable when the stress wave propagates in the wave-guiding rod with a boss structure.

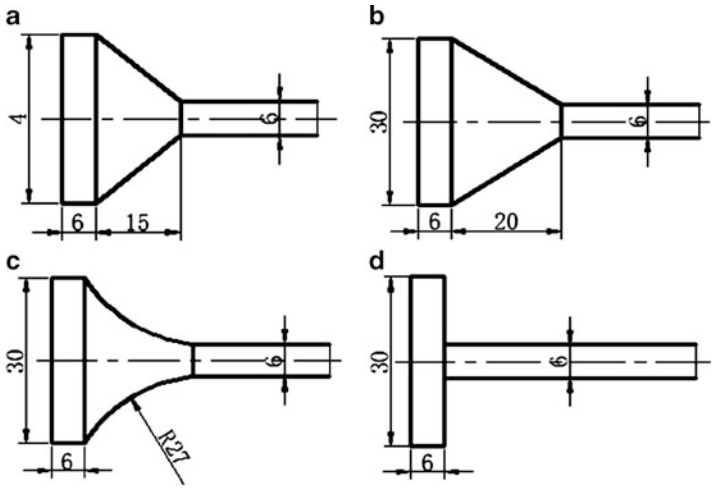

Fig. 8 Models of wave-guiding rod with boss structures (**a**) Short cone boss structure, (**b**) Long cone boss structure, (**c**) Arc boss structure, (**d**) Flat boss structure

5.1 Types of Boss Structure and the Simulation of the Initial Conditions

Boss structure of wave-guiding rod can be designed into four types as shown in Fig. 8 [5]. The wave-guiding rods with the length of 0.5 m and diameter of 6 mm are chosen; the initial acoustic sources imposed on the end of the wave-guiding rod are 1×10^5 Pa, and the wave propagating time is 0.01 s, as shown in Fig. 2.

5.2 Analysis of Simulation Result

Using the finite element method to simulate the stress wave propagation by four forms of wave-guiding rod with boss types, the relationship between the end displacement and time changes can be obtained. Compare it with the curve of wave-guiding rod without boss type, as shown in Fig. 9. As can be seen from Fig. 9, amplitude of stress wave signal received by wave-guiding rods with or without a boss structure is basically the same; wave-guiding rod with boss structure has certain impact of attenuation. For different wave-guiding rods, those with short boss structure are recommended, such as the plate-type boss structure.

Attenuation of non-fixed emission frequency is smaller than that of fixed emission frequency, because acoustic waves of non-fixed emission frequency are composed of high frequency and low frequency components; high frequency

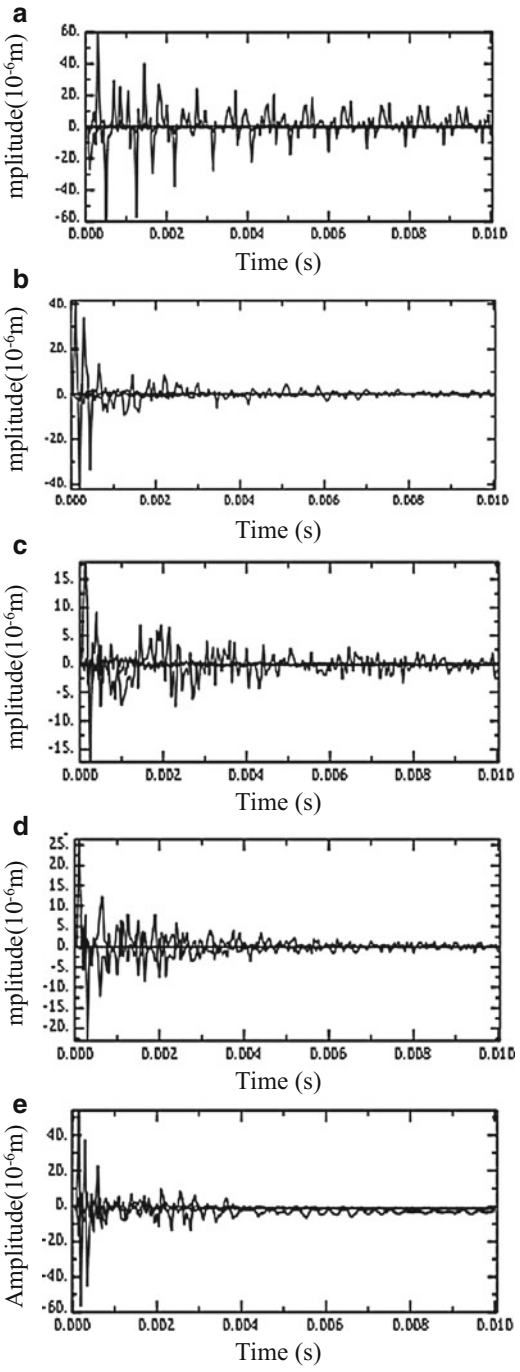

Fig. 9 Comparison chart of waveform of wave-guiding rod with or without boss structure (**a**) Without boss structure, (**b**) Short cone boss structure, (**c**) Long cone boss structure, (**d**) Arc boss structure, (**e**) Flat boss structure

components attenuate faster, low frequency components attenuate slower, and spread farther.

The relative error between theory and experiment of fixed emission frequency is smaller than that of non-fixed emission frequency, but both of them can provide basis for sensor layout scheme and the acoustic source judgment of composite cylinder state detection.

The higher the fixed emission frequency of acoustic wave is, the faster the attenuation is. When an attenuation experiment with fixed emission frequency dummy source is conducted, the proper frequency should be chosen, and the frequencies of no higher than 0.15 MHz are recommended.

6 Conclusion

By using the finite element method to simulate and analyze the wave-guiding properties of wave-guiding rods with different diameters, lengths, and boss structure types, the conclusions are as follows:

Amplitudes of the stress waves received by the wave-guiding rods with same length, different diameter, and no-boss structure are basically the same. This means that the diameter of the rod has little impact on acoustic emission signal. To save material, it is recommended for AE signals with frequency of the order of 100 kHz that the wave-guiding rod diameter should be 6 mm.

Amplitudes of the stress waves received by the wave-guiding rods with same diameter, different length, and no-boss structure vary greatly. The stress wave produces attenuation when travels in the rod and the longer the length of the wave-guiding rod is, the greater the attenuation will be. So wave-guiding rod with short length is recommended in the process of detection.

Boss structure has little impact on the amplitude of stress wave signal. Amplitude of stress wave signal received by wave-guiding rods with or without a boss structure is basically the same, but different types of boss structure will lead to certain attenuation, so wave-guiding rod with short boss structure is recommended, such as the plate-type boss structure.

In this paper, the simulation results and experimental results are in good consistency [4]. In practice, it is suggested to use wave-guiding rod of 6 mm in diameter, less than 0.5 m in length, and with a plate-type boss structure to carry on acoustic emission (AE) testing.

Acknowledgments This work was financially supported by the Heilongjiang Province Natural Science Foundation (E201239) and by the key laboratory's open project, Northeast Petroleum University (HJ201302).

References

1. Y. Zhang, Application of high pressure reactor leak acoustic emission technology. Chem. Mach. **37**(5), 622–625 (2010)
2. C. He, Numerical simulation of guided ultrasonic wave transmitted in pipe. J. Beijing Univ. Tech **30**(2), 129–133 (2004)
3. Y. Xu, X. Wang, Practical wave-guide methods for AE testing of high/low-temperature vessels using ordinary sensors. Nondestr. Test. **33**(12), 93–95 (2011)
4. W. Li, F. Guo, An experimental investigation on the transmission characteristics of the sound emission source in the wave guide rods. Chem. Mach. **34**(4), 179–183 (2007)
5. Y. Zhang, M. Song, G. Dai. "A method for acoustic emission testing length adjustable wave-guiding rod". China Patent, China ZL, 2012, 2 0114924, Dec 2012

Near-Field Beamforming Performance Analysis for Acoustic Emission Source Localization Based on Finite Element Simulation

Haisheng Yu, Tian He, and Denghong Xiao

Abstract This paper attempts to study the localization performance of a near-field acoustic emission (AE) beamforming method by changing some parameters, such as beamforming array types, localization velocity, and the sensors spacing. To investigate how those factors affect AE source localization accuracy, it's necessary to get the AE signals with high signal-noise ratio. The finite element method (FEM) is introduced to model the propagation of AE signal in a steel plate structure. The influences of some parameters on the resolution of AE source localization are discussed. The results provide a reference for the selection of parameters when the beamforming is used to identify AE source.

1 Introduction

Acoustic Emission (AE) is a phenomenon of stress wave radiation caused by a dynamic reconstruction of material's structure that accompanies processes of deformation and fracture. AE signals usually arise from internal changes of a structure, such as propagation of crack, twinning, slip, dislocation movements [1]. Material deformation under stress and crack propagation is an important mechanism of structural failure. The source directly associated with deformation and fracture mechanisms is known as AE source [2]. Modern AE technique, in the early 1950s, starts with Kaiser's research done in Germany. And in the following decades, AE technique has developed rapidly. Now, AE technique is used as a nondestructive testing tool to evaluate structural damage and has its potential advantages in dynamic damage monitoring and source localization, such as fatigue

H. Yu (✉) • T. He • D. Xiao
School of Transportation Science and Engineering, Beihang University, Beijing 100191, China
e-mail: yuhaisheng@dae.buaa.edu.cn

G. Shen et al. (eds.), *Advances in Acoustic Emission Technology: Proceedings of the World Conference on Acoustic Emission-2013*, Springer Proceedings in Physics 158,
DOI 10.1007/978-1-4939-1239-1_12,

crack growth [3, 4]. Due to its potential advantages in kinematic damage monitoring and source localization, AE technique has led to many applications in a variety of fields such as petrochemical industry, aerospace industry, and detection of metal processing [5, 6].

The ability to localize the AE source is an important step in whole damage identification process, by which the accurate AE source location can indicate information about the characteristic of the damage and even the size of the crack with relatively few sensors on large and complex structures. Current localization of AE sources is normally performed by using the time difference of arrival (TDOA) technique which uses the propagation velocity in a material to derive the source location in one, two, or three dimensions from the arrival delay between sensors based on first threshold crossing. However, when the AE wave propagates in the solid medium, the signals may be significantly affected by multi-mode, dispersion, energy attenuation, and other factors, which make it difficult to accurately determine the arrival time. Besides, when there is more than one AE source, the arrival time information may be confused, which is also one key problem of TDOA [7, 8]. To make the localization simple but effective, AE beamforming method is introduced to localize AE source in structure [9]. Although beamforming has been successfully used in damage localization by many scholars, its performance has not been studied in depth. Because the propagation mode of AE signal is different from noise signal and the receiving signal method of AE beamforming is also different from noise beamforming, the array parameters of AE beamforming play a very important role in localization result. However, this work has not been reported so far. This article will discuss how beamforming with different array types affects localization accuracy and algorithms. In order to study AE beamforming localization performance, FEM is applied to get pure AE signal and analyze the propagation mode of AE signal.

2 Methods

2.1 Description of AE Signal Simulation Model

The model is simulated by FE analysis in the general three-dimensional domain implement using the commercial package ABAQUS. The respective AE signals are obtained from the surface displacements at the positions marked by sensors. The rectangular plate is assumed to be a specimen with 1,000 mm $\times$ 800 mm edge length and 5 mm thickness.

The AE waves in plates are generated passively using a mechanical pencil lead break input, and actively using a surface bonded piezoelectric actuator [10]. To model impact, delamination, or crack propagation, a transient excitation such as a delta or step function is needed. In order to excite an AE signal, in the following a triangular forcing function $f(t)$ is applied (Fig. 1). In the present configuration, the

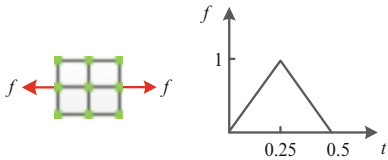

Fig. 1 The acting forces and time function of applied load

total distance of the two points acting as buried dipole source is 1 mm with 1 N force magnitude [11, 12].

The FE simulation model is a homogeneous plate with properties of steel and specifically elasticity modulus, and parameters are set as follows: $E = 209 \times 10^9$ N/m^2; Poisson's ratio $\upsilon = 0.3$; density $\rho = 7{,}800$ kg/m^3. These values lead to longitudinal and shear wave velocities (c_L and c_s) of 5,940 m/s and 3,230 m/s respectively.

In the frequency range of interest, only the zero-order symmetric mode, S_0, and anti-symmetric mode, A_0, are present. These two modes are selectively excited in the model by applying appropriate nodal loads. For a maximum frequency of 200 kHz, the minimum wavelength is for A_0 and it is given by $\lambda_{min} = c_s/f_{max} = 15.7$ mm, considering a theoretical phase velocity of $c_s = 3{,}230$ m/s. In the present study the value of λ_{min} is assigned as 20 mm.

To avoid numerical instability, ABAQUS/EXPLICIT recommends a stability limit for the integration time step Δ_t equal to

$$\Delta_t = \lambda_{min}/c_L. \tag{1}$$

The maximum frequency of the dynamic problem, f_{max}, limits both the integration time step and the element size. A good rule is to use a minimum of 20 points per cycle at the highest frequency, that is:

$$\Delta_t = 1/(20 f_{max}). \tag{2}$$

The size of the finite element, l_e, is typically derived from the smallest wavelength to be analyzed, λ_{min}. For a good spatial resolution 20 nodes per wavelength are normally required:

$$l_e = \lambda_{min}/20. \tag{3}$$

From Eq. (3), the corresponding limit on the element size is $l_e = 1$ mm. According to Eq. (2), this transient problem is solved with an integration time step, $\Delta_t = 0.25$ μs. The chosen excitation time is 5 μs, so the time domain of 5 MHz is sufficient to resolve the observed signals frequency content in the range up to a maximal frequency of 0.2 MHz [13]. Simulation results are shown in Fig. 2.

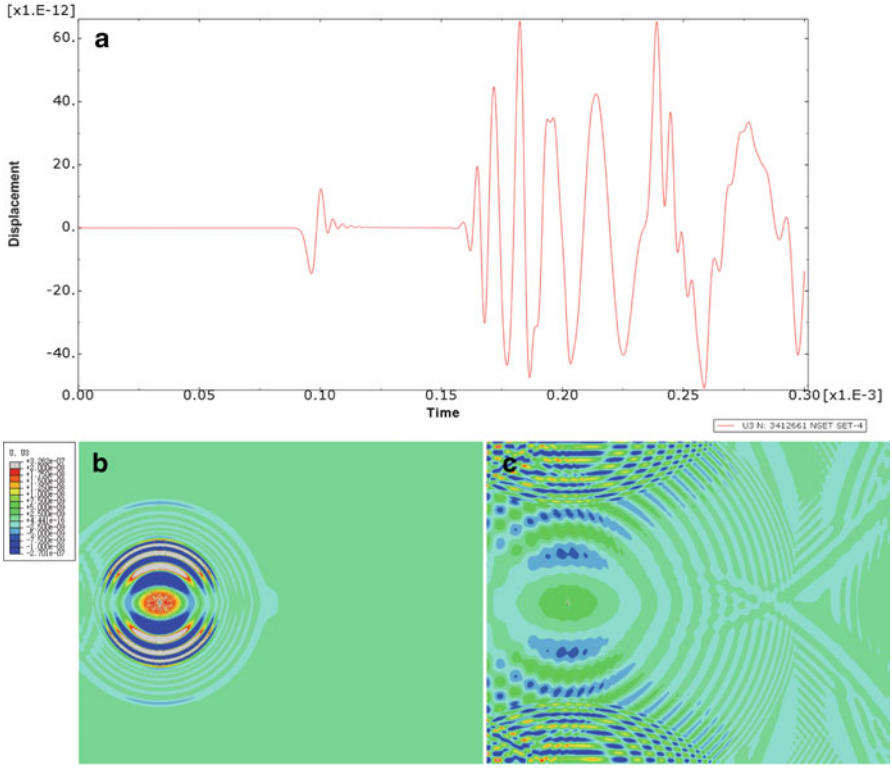

Fig. 2 FE simulation results of AE signal: (**a**) Wave packets received by one sensor; (**b**) Wave propagation scenes at 50 μs; (**c**) Wave propagation scenes at 400 μs

2.2 Delay-and-Sum Beamforming

Delay-and-sum is a simple and effective array signal processing algorithm utilized in beamforming techniques [14].

Considering the distance between AE source and array of sensors, the analysis schemes based on beamforming techniques can be divided into near-field and far-field methods. A common rule of thumb is that the near-field sources are located at a distance of

$$r \leq 2L^2/\lambda, \tag{4}$$

where r is the radial distance from an arbitrary array origin, L is the largest array dimension, and λ is the operating wavelength [15]. The acquired wavefront from the sound source, in such conditions, is assumed spherical due to the transmission characteristics of waves. The far-field sources refer to those at locations r larger than $2L^2/\lambda$, of which the wavefront is usually assumed planar.

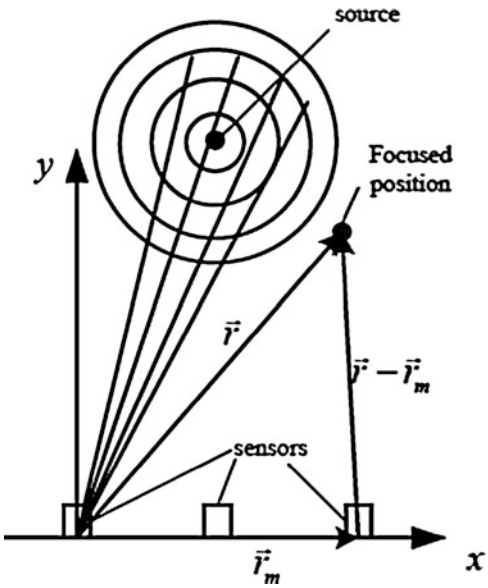

Fig. 3 Illustration of delay-and-sum beamforming

The goal of present study is to estimate the source location of thin plates or shells in aviation fields. The beamforming analysis for such structures is usually categorized into near-field, based on the aforementioned rule. The basic principle of near-field beamforming based on the delay-and-sum algorithm is illustrated in Fig. 3. The incident waves are spherical and thus the array output of these waves can be expressed by

$$b\left(\vec{r}, t\right) = \frac{1}{M}\sum\nolimits_{m-1}^{M} w_m x_m\left(t - \Delta_m\left(\vec{r}\right)\right), \tag{5}$$

where $\vec{r}$ represents the distance of the focus to the reference point. The reference point may be arbitrary and it is the first sensor point on the left side in Fig. 3. M is the number of the sensors and w_m is the weighting coefficient applied to the channel of sensor m. The variable $x_m(t)$ represents the signal acquired from the No. m sensor and $\Delta_m\left(\vec{r}\right)$ indicates the individual time delay of No. m sensor to the reference point. Though different w_m are adopted in the formula to control the beamwidth and sidelobes of the sensor array, a constant $w_m \equiv 1$ is used in this work. And the time delay $\Delta_m\left(\vec{r}\right)$ is adjusted in delay-and-sum beamforming in such a way that signals associated with a spherical wave, incident from the real source, are aligned in time before they are summed when the focus is located at the real source [16]. Conversely, signals are not able to be aligned before summation if positions of the focus and real source are not coincident. As shown in Fig. 3, the time delay $\Delta_m\left(\vec{r}\right)$ is obtained by

$$\Delta_m\left(\vec{r}\right) = \frac{\left|\vec{r}\right| - \left|\vec{r} - \vec{r}_m\right|}{c} \tag{6}$$

where $\vec{r}_m$ represent the distances of reference point to No. m sensor, and c is the propagation velocity of sound.

3 Results

The sampling frequency in FE simulation is 5 MHz. The steel plate specimen has the dimensions of 1,000 mm length, 800 mm width, and 5 mm height. Figure 4 shows the different arrays of sensors with spacing of 30 mm. Coordinate system is established with x and y, and origin of coordinate is on the center of the leftmost sensor. The AE sources are respectively marked with 1# (30 mm, 300 mm), 2# (90 mm, 600 mm), and 3# (380 mm, 300 mm).

The propagation velocity of the AE signals recorded by TDOA method is 5,300 m/s. The waveforms and frequency spectrum of one signal acquired by FE simulation are shown in Fig. 5. It can be seen that in the frequency domain most signal energy is concentrated in the range of 0∼0.4 MHz. Consequently, it has been known that most waves transmitted in a thin steel plate are A_0 and S_0 waves. Figure 6 shows the relation between frequency and group propagation velocities of S_0 and A_0 waves.

This article employs delay-and-sum beamforming to localize the source of AE only with S_0 wave which can be obtained by setting a small threshold. And beamforming localization performance is discussed from the following three aspects.

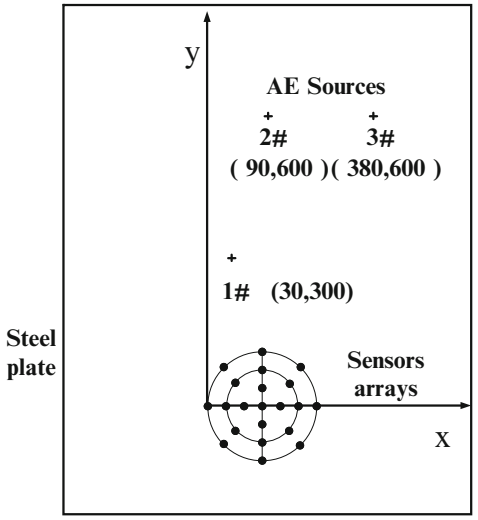

Fig. 4 Arrangements of sensor and positions of AE source

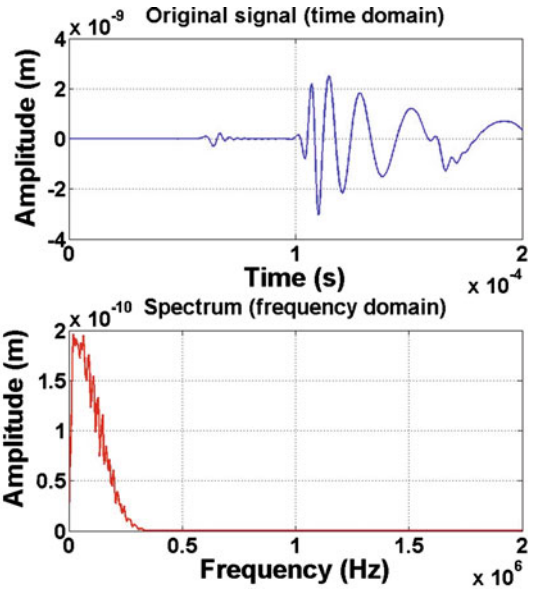

Fig. 5 The waveforms and frequency spectrum of AE signal received by one sensor

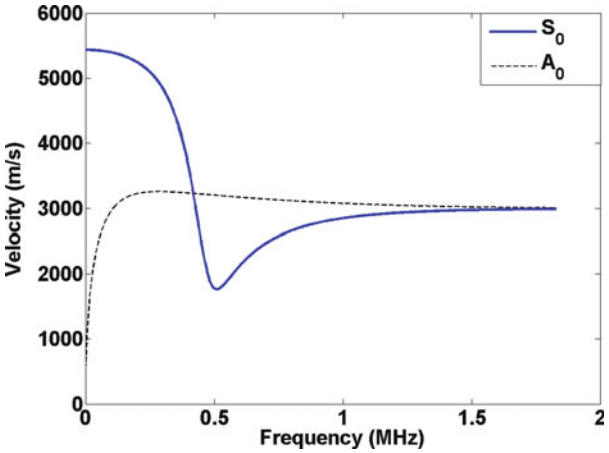

Fig. 6 Dispersion curves of S_0 and A_0 waves in 5 mm steel plate

3.1 Beamforming Array Types

Conventional beamforming has the following basic array types: linear array, circular array, cross array, and rectangular array. This paper mainly studies localization performance of the first three array types in the condition of only one AE source. The parameters of different array types are given in Table 1. Using the proposed delay-and-sum beamforming method for AE source identification, the localization

Table 1 The parameters of different array types

Array types	Number of sensors	Maximum diameter (mm)
Linear array (large)	7	180
Linear array (small)	5	120
Cross array (large)	13	180
Cross array (small)	9	120
Circular array (large)	8	180
Circular array (small)	8	120

Table 2 The localization results of different array types

Array types	AE source location	Identification result (x, y) (mm)
Linear array (large)	1#	(20, 300)
	2#	(90, 580)
	3#	(390, 620)
Cross array (large)	1#	(25, 300)
	2#	(90, 590)
	3#	(390, 610)
Circular array (large)	1#	(20, 300)
	2#	(90, 580)
	3#	(390, 620)

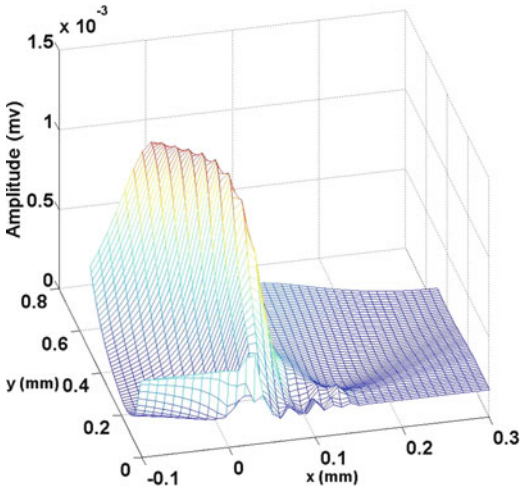

Fig. 7 Energy output contour of linear array on AE source 1#

results of three AE sources identified by different array types are given in Table 2. The localization results of AE source 1# with linear array are given in Figs. 7 and 8. The contour plots in figures represent the outputs of AE beamforming based analysis and the maximal output regions denoted by the dark line are the identified AE source regions, in which the focused position with maximum energy output is the AE source.

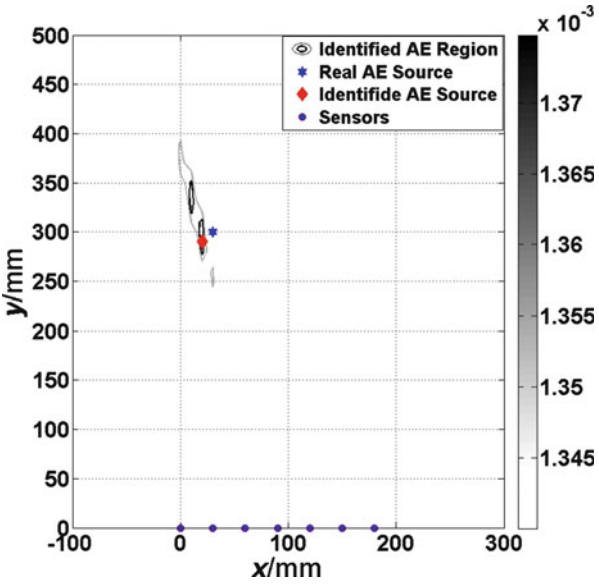

Fig. 8 Comparison between identified and real AE source 1# of linear array (big)

It is clearly seen from Table 2, that in the same array diameter, and the parameters of the same case, all three types of the array can more accurately localize the true AE sources. The cross and circular array types have better localization performance. However, the linear array with a minimum number of sensors and good performance has more advantages than the circular array and cross array in practical engineering applications.

3.2 The Impact of Selected Velocity on the Localization Results

In this paper, the AE signal is obtained by finite element simulation, in which the velocity of main frequency components can be calculated exactly, but in practical engineering applications, the velocity of calculation sometimes is not very accurate. From Eq. (6), $\Delta_m\left(\vec{r}\right)$ is effected by velocity, c. Therefore, it is necessary to know how velocity selection affect the localization accuracy. Figure 9 shows the localization results of linear array at AE source 2# with different velocities. It can be seen from the figure that the x-direction is almost unaffected (of course, to take into account AE source 2# is on the centerline of the array, the accuracy of x-direction is excellent, so we compared the localization results of AE sources 1# and 3#, then got the similar conclusion). However, the accuracy of y-direction is greatly affected. For cross array and circular arrays, the localization accuracy is also affected by selected velocity, but is weaker than the linear array.

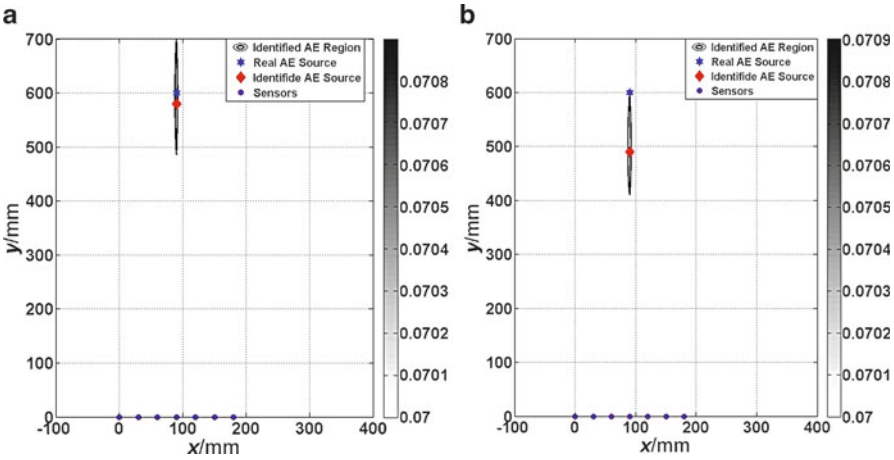

Fig. 9 Comparison between different localization velocities: (**a**) localization with accurate velocity; (**b**) Deviation from accurate velocity with 500 m/s

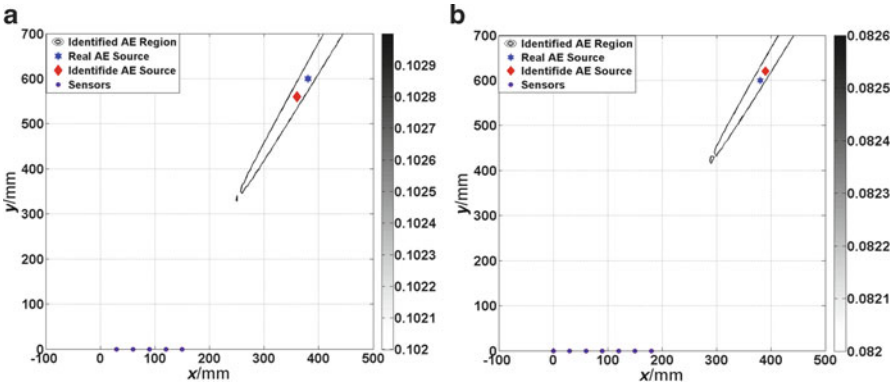

Fig. 10 Localization results comparison between large and small size of linear array: (**a**) Localization results of linear array (*small*) is (360 mm, 570 mm); (**b**) Localization results of linear array (*large*) is (390 mm, 620 mm)

3.3 The Maximum Diameter of the Sensors Spacing

The maximum diameter of the sensor spacing is an important parameter affecting the localization accuracy. Figures 10, 11, and 12 show that localization results of different array types with big and small sizes in the condition of AE source 3#. It is seen clearly that, for these three array types, the larger maximum dimension of the array form is, the better localization accuracy will be. However, large size means to increase the number of sensors, so these factors should be considered in practical engineering applications.

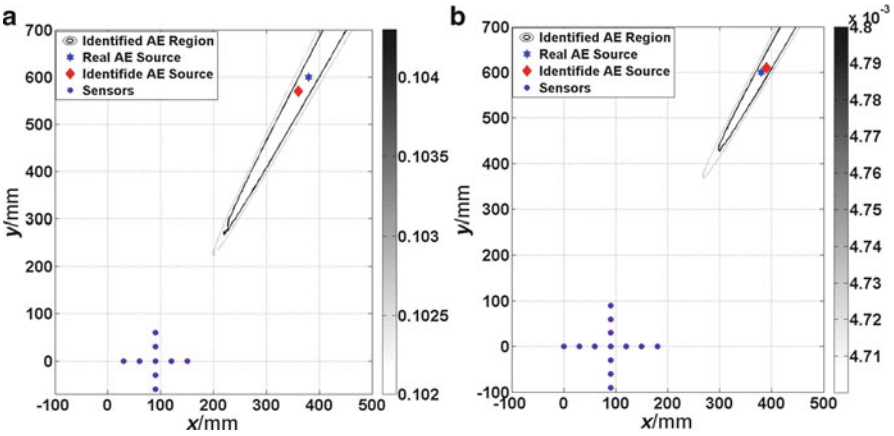

Fig. 11 Localization results comparison between large and small size of cross array: (**a**) Localization results of cross array (*small*) is (360 mm, 570 mm); (**b**) Localization results of cross array (*large*) is (390 mm, 610 mm)

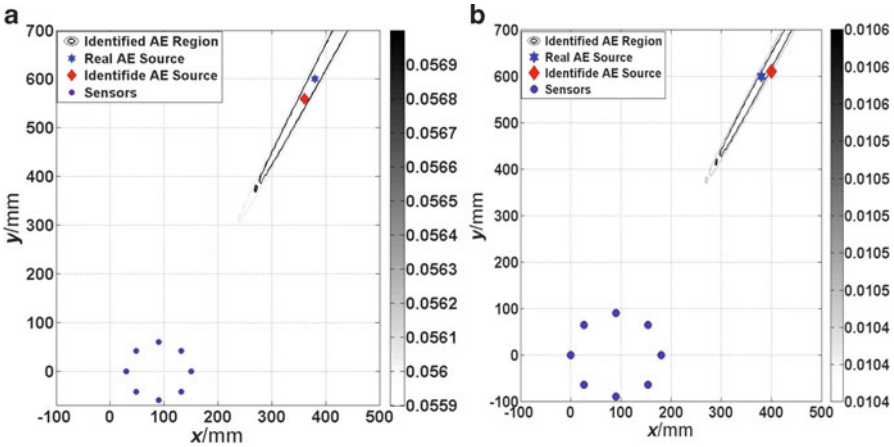

Fig. 12 Localization results comparison between large and small size of cross array: (**a**) Localization results of round array (*small*) is (350 mm, 570 mm); (**b**) Localization results of round array (*large*) is (390 mm, 620 mm)

4 Discussion

According to the above simulation results, the following conclusions can be obtained:

1. When there is only a single AE source, all three kinds of array forms can get a better accuracy. The linear array with a minimum number of sensors and good

performance has more advantages than the circular array and cross array in practical engineering applications.
2. When using the linear array localization, especially AE source is farther away from the array center, selected velocity have some influences on the localization results.
3. For these three array types, the larger maximum dimension of the array type is, the better localization accuracy will be.

So, by establishing the finite element model of AE signal propagation in the plate, the AE propagation characteristics are analyzed. On this basis, the influences of some parameters on the resolution of AE source localization are discussed through simulation of AE signals, such as the type of the AE sensor array, the distance from array center to AE source, and the maximum diameter of the AE sensor array. The results can provide a theoretical foundation for the selection of parameters when using beamforming to do AE source localization.

Acknowledgements This work was finically supported by the National Science Foundation of China (Grant No 51105018) and the Innovation Foundation of BUAA for Ph.D. Graduates.

References

1. S.N. Omkar, U. Raghavendra Karanth, Rule extraction for classification of acoustic emission signals using ant colony optimisation. Eng. Appl. Artif. Intell. **21**, 1381–1388 (2008)
2. V. Salinasa, Y. Vargasa, J. Ruzzanteb, L. Gaetea, Localization algorithm for acoustic emission. Phys. Procedia **3**, 863–871 (2010)
3. T. Kundu, S. Das, S.A. Martin, K.V. Jata, Locating point of impact in anisotropic fiber reinforced composite plates. Ultrasonics **48**, 193–201 (2008)
4. E. Papamichos, J. Tronvoll, A. Skjærstein, T.E. Unander, Hole stability of red wildmoor sandstone under anisotropic stresses and sand production criterion. J. Petrol. Sci. Eng. **72**, 78–92 (2010)
5. J. Hensman, R. Mills, S.G. Pierce, K. Worden, M. Eaton, Locating acoustic emission sources in complex structures using Gaussian processes. Mech. Syst. Signal Pr. **24**, 211–223 (2010)
6. N. Choi, T. Kim, K.Y. Rhee, Kaiser effects in acoustic emission from composites during thermal cyclic-loading. NDT E Int. **38**, 268–274 (2005)
7. D.E. Leea, I. Hwanga, C.M.O. Valenteb, J.F.G. Oliveirab, D.A. Dornfeld, Precision manufacturing process monitoring with acoustic emission. Int. J. Mach. Tool Manufact. **46**, 176–188 (2006)
8. P. Kundu, N.K. Kishore, A.K. Sinha, A non-iterative partial discharge source location method for transformers employing acoustic emission techniques. Appl. Acoust. **70**, 1378–1383 (2009)
9. J. Jiao, C. He, B. Wu, R. Fei, X. Wang, Application of wavelet transform on modal acoustic emission source location in thin plates with one sensor. Int. J. Pres. Ves. Pip. **81**, 427–431 (2004)
10. J.P. Berenger, Simulation of asymmetric Lamb waves for sensing and actuation in plates. J. Shock Vib. **12**, 243–271 (2005)
11. F. Moser, L.J. Jacobs, J. Qu, Modeling elastic wave propagation in waveguides with the finite element method. NDT&E Int. **32**(4), 225–234 (1999)
12. M.G.R. Sause, Simulation of acoustic emission in planar carbon fiber reinforced plastic specimens. J. Nondestr Eval. **29**(2), 123–142 (2010)

13. Xiao Denghong, He Tian, Liu Xiandong, Yu Haisheng. Efficient simulation of acoustic emission with reflections removal based on infinite element and Rayleigh damping, 2013 ASME International Mechanical Engineering Congress Exposition (IMECE), 2013, San Diego, California
14. J. Yang, W.S. Gan, K.S. Tan, M.H. Er, Acoustic beamforming of a parametric speaker comprising ultrasonic transducers. Sens. Actuat. A Phys. **125**, 91–99 (2005)
15. D.H. Johnson, D.E. Dudgeon, *Array Signal Processing: Concepts and Techniques* (Prentice Hall, Englewood Cliffs, NJ, 1993)
16. J.J. Christensen, J. Hald, Beamforming. Brüel & Kjær Tech. Rev. **1**, 1–48 (2004)

Intelligent Evaluation Method of Tank Bottom Corrosion Status Based on Improved BP Artificial Neural Network

Feng Qiu, Guang Dai, and Ying Zhang

Abstract According to the acoustic emission information and the appearance inspection information of tank bottom online testing, the external factors associated with tank bottom corrosion status are confirmed. Applying artificial neural network intelligent evaluation method, three tank bottom corrosion status evaluation models based on appearance inspection information, acoustic emission information, and online testing information are established. Comparing with the result of acoustic emission online testing through the evaluation of test sample, the accuracy of the evaluation model based on online testing information is 94 %. The evaluation model can evaluate tank bottom corrosion accurately and realize acoustic emission online testing intelligent evaluation of tank bottom.

1 Introduction

The condition of tank bottom corrosion is the main indicator to guide the maintenance of tank; however, the special operating environment of tank bottom makes it difficult to detect. At present, the acoustic emission testing is used as the major testing technology to detect the tank bottom corrosion international [1]. The technology has a history of nearly a decade in China; it is widely used in the testing of tank bottom corrosion in the petrochemical industry. But the current application of acoustic emission online testing technique to evaluate the tank bottom corrosion mainly depends on the experience of inspectors [2].

According to the tank bottom online detection of acoustic emission technology, combining the experience, confirming related characterization factors of tank

F. Qiu (✉) • G. Dai • Y. Zhang
Northeast Petroleum University, Daqing 168813, China
e-mail: qiufeng1a2b3c@163.com

G. Shen et al. (eds.), *Advances in Acoustic Emission Technology: Proceedings of the World Conference on Acoustic Emission-2013*, Springer Proceedings in Physics 158,
DOI 10.1007/978-1-4939-1239-1_13,

bottom corrosion, three kinds of BP artificial neural network models on intelligent evaluation, artificial neural network prediction, and evaluation methods of tank bottom corrosion status based on online detection information are established to guide the assessment of tank bottom corrosion. Comparing with the result of acoustic emission online testing through the evaluation of test samples, the model can evaluate tank bottom corrosion accurately and realize acoustic emission online testing intelligent evaluation of tank bottom.

2 Basic Theory of Artificial Neural Networks

Artificial neural network is the human brain function in the computer. Artificial neuron is the basic processing unit of the neural network; it is a mathematical model of approximate biological neurons, and it receives information through the connected other neurons. Neural network is a wide parallel interconnection network which is composed of many simple units; its organizations can simulate biological neural system and make interactive response to real-world objects, and is a large-scale continuous time dynamic system which is highly nonlinear; it plays a network of global role, and has the ability of massive parallel distributed processing and associative learning.

Neural networks can simulate almost any complex nonlinear system; it can approximate any nonlinear mapping function with any accuracy [3]. So it is considered that neural network can be applied to implement tank bottom corrosion status intelligent evaluation. In many neural network models, BP network is the most widely used and successful. BP network is a kind of multilayer feed-forward network accorded to the error back propagation algorithm training [4], without prior reveal described the mathematical equations of the mapping relationship. Its learning rule is to use the steepest descent method, and it adjusts the network weights and threshold constantly by error back propagation, and minimizes the network error sum of squares. BP networks can have several layers; three-layer structure is shown in Fig. 1.

Weights change of input layer, the output weight from the *j* input of hidden layer to the *k* output of output layer is

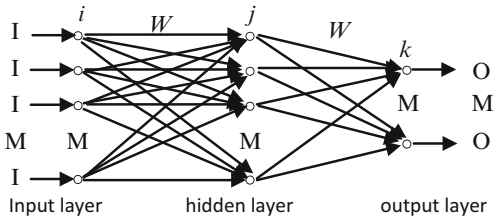

Fig. 1 The structure of three-layer BP neural network

$$\Delta\omega_{kj} = -\eta\frac{\partial E}{\partial\omega_{kj}} = \eta(D_k - X_k)f'_2(s)\cdot S_j \tag{1}$$

Weights change of hidden layer, the output weight from the *i* input of input layer to the *j* output of hidden layer is

$$\Delta\omega_{ji} = -\eta\frac{\partial E}{\partial\omega_{ji}} = \eta\cdot X_i\sum_k (D_k - X_k)f'_1(s) \tag{2}$$

In Eqs. (1) and (2), E—cost function of error, ω—connection weight coefficient, η—learning rate, X_i—input of input layer, D_k—expected output, X_k—actual output, $f(s)$—activation function, and S_j—output of hidden layer [5].

3 Artificial Neural Network Intelligent Evaluation Method of Tank Bottom Corrosion Status

3.1 Definition Standards of Models

According to "Nondestructive testing—Acoustic emission testing and evaluation of atmospheric pressure metal storage tanks," tank bottom corrosion status evaluation hierarchy standards are confirmed [6]. This standard makes tank bottom corrosion status hierarchy for very little, little, medium, dynamic, and high dynamic V grades. Considering the actual maintenance of the tank, selecting the method of more security, combining high-risk level (IV and V grade level) in consideration, the tank bottom corrosion evaluation of neural network is divided into four levels. Table 1 shows the specific classification.

3.2 Data Selection and Preprocessing

180 tank testing data with different characteristic grades from the tank testing database founded by laboratory are selected to establish the original data samples. The database includes acoustic emission testing data, open tank testing data, and experience ranks. 130 pieces of data are selected as training samples randomly;

Table 1 The artificial neural network evaluation classification grades of tank bottom corrosion

Tank bottom corrosion status	Very little	Little	Middle	Dynamic	High dynamic
Acoustic emission evaluation level	I	II	III	IV	V
Artificial neural network evaluation grade	1	2	3	4	4

the remaining 50 are the test samples. Because the orders of magnitudes in some variable data which are defined and selected have great difference in this chapter, and data characteristics influence the effect of artificial neural network classification model, data are normalized, so that the effects on the model have the same scale.

3.3 Establish Artificial Neural Network Intelligent Evaluation Model of Tank Bottom Corrosion Status

(a) Intelligent evaluation model based on appearance inspection information
Through the exploration of tank bottom corrosion damage form and mechanism and expert experience information, the related factors which influence the AE level of storage tank bottom corrosion detection are medium type (X1), serve time (X2), temperature (X3), condition of foundation (X4), surface corrosion (X5), structure type (X6), and insulation construction (X7). Input variables are constituted of seven factors; the neural network discrimination level (Z) is as the output target, according to the established data samples; intelligent evaluation model based on appearance inspection information (model I) is established.

The output presents that training achieves the best effect when it goes six steps; mse (mean square error) value is 0.17427. The mse can be close to 0.01 when training steps are 12, and average result is ideal. But the test result is unsatisfied; it is hard to ensure the accuracy.

Through the improved BP neural network and many experiments, the network has a faster convergence speed and higher accuracy when the number of hidden layer neurons is 18. So it can be confirmed that the network structure of model is $7 \times 18 \times 4$.

(b) Intelligent evaluation model based on AE information.
The factors of Y1, Y2, Y3, Y4, and Y5 five acoustic emission standard factors are confirmed according to the standard and location method. The factors of Y6, Y7, Y8, and Y9 four acoustic emission signal characteristic factors are chosen according to the acoustic emission signal analysis theory. Their definitions are shown in Table 2. Input variables are constituted of the nine factors, and the output target which is tank bottom corrosion status (Z) is acoustic emission testing evaluation result. According to related data samples which have been established, applying approved neural network programming and tank bottom corrosion status evaluation model based on standard acoustic emission factors is established, and the network structure is $9 \times 18 \times 4$.

(c) Intelligent evaluation model based on online testing information
According to appearance inspection information and acoustic emission information, Y1, Y2, Y3, Y4, Y5, Y6, Y7, Y8, Y9, X1, X2, X3, X4, X5, X6, and X7 are confirmed as input variables, and Z is the output target of artificial neural

Table 2 The selection and definition of acoustic emission factors

Tank bottom corrosion status	Definition
Y1	The quotient of the total hits and the number of channels in unit time
Y2	The standard deviation of each channel hits in unit time
Y3	The quotient of the number of the hits which are larger than the average and the number of the channels in unit time
Y4	Positioning event concentration, draw the circle evaluation region of tank bottom with the length not longer than 10 % of the diameter, the number of positioning incidents occurring in unit time in the evaluation region
Y5	Positioning event density, the quotient of the number of positioning events in unit time and tank bottom area (unit: m^2)
Y6	The average count for each channel in unit time
Y7	The standard deviation of the channel counts in unit time
Y8	The average energy of each channel in unit time
Y9	The standard deviation of the channel energy in unit time

Table 3 Evaluation results

Model	Grade (Y)	Accuracy (%)
Model I	1	75
	2	81
	3	77
	4	67
Model II	1	86
	2	85
	3	77
	4	100
Model III	1	100
	2	92
	3	85
	4	100

networks. Combining the data samples of appearance inspection factor and acoustic emission factor, tank bottom corrosion status evaluation model based on online testing information (model III), the network structure is $16 \times 18 \times 4$.

3.4 The Evaluation Capability Analysis of Models

With the established three BP artificial neural network models which are based on appearance inspection information, acoustic emission information, and online testing information, 50 testing samples are evaluated, compared with the evaluation results of acoustic emission testing experts; test sample evaluation results are shown in Table 3.

Tank bottom corrosion status evaluation model based on appearance inspection information (model I) and tank bottom corrosion status evaluation model based on AE information (model II) are established; the evaluation capabilities of models are obtained through evaluating the test samples. The evaluation capability of model II whose accuracy is 87 % is higher than that of model I whose accuracy is 75 % by contrastive analysis; this illustrates that acoustic emission information is an important considered factor. The prediction accuracy of grade 1 is lower than that of grade 2 and grade 3 with model I; some tanks of grade 1 are predicted as grade 2 and grade 3. So the prediction of model I is too reserved; redundant testing will be promoted. The prediction accuracy of grade 3 is lower with model II, and the prediction accuracy of grade 1 is exact; it is illustrated that the analysis of tank bottom corrosion status is reasonable through AE information.

Combining appearance inspection factors and acoustic emission factors, tank bottom corrosion status evaluation model based on online testing information (model III) is established. Applying prediction samples, the evaluation capability of prediction model is analyzed; the accuracy is 94 %; the evaluation of tank bottom corrosion status can be realized with this model.

4 Conclusions

According to acoustic emission technology of tank bottom, combining expertise, extracting the appearance inspection factors and acoustic emission factors related to tank bottom corrosion status, using intelligent evaluation method of improved BP artificial neural network artificial neural network intelligent evaluation model of tank bottom corrosion status based on online testing information is established. Through the evaluation of testing samples, comparing evaluation results of acoustic emission testing, the accuracy of the evaluation model is 94 %. Comparing with the other evaluation models, the accuracy of model III is higher. And the application of artificial neural network intelligent evaluation method compared with Bayesian network and other intelligent evaluation methods also can get tank bottom corrosion status grade accurately. So this intelligence evaluation model can be used to realize corrosion status evaluation of tank bottom, reduce the dependence of testing technology for practitioners' experience, and realize intelligence evaluation of the tank bottom acoustic emission online test.

Acknowledgment This work was supported in part by China national petroleum corporation science and technology development projects under Grant No. 2011D-4603-0101.

References

1. P. Sosoon, K. Shigeo, K. Kenji et al., AE source and relation between AE activity and rate of corrosion of oil tank bottom plate on acidic soils. Mater. Trans. **46**(11), 2490–2496 (2005)
2. E 1930-02, Standard Test Method for Examination of Liquid-Filled Atmospheric and Low-Pressure Metal Storage Tanks Using Acoustic Emission
3. W. Xinyi, S. Huang, W. Zhao, Characterizing magnetic flux leakage signal of cracks based on improved BP neural network. Nondestr. Test. **31**(8), 603–605 (2009)
4. B. Wei, X. Yang, G. Quan, The application of the fuzzy risk evaluation based on neural network technology. Oil Gas Storage Transport. **28**(2), 20–23 (2009)
5. X. Chen, L. Congda, Z. Liao, The improvement of BP algorithm and its implementation in Matlab. Contr.. Eng. **12**(5), 96–98 (2005)
6. JB/T 10764-2007, Non-destructive testing—acoustic emission testing and evaluation of atmospheric pressure metal storage tanks

The Research of Backward Deducing the Peak Frequency of Acoustic Emission Signals in Different Array

Feifei Long, Yang Song, Qiong Wang, Ruilong Dai, and Jianzeng Wang

Abstract This chapter puts forward the formula to calculate the deducing frequency of acoustic emission source, and combines the theory of multi-agent multiple sensors with the acoustic emission technique. Through the linear and circular array AE experiments, it is shown that the mathematical algorithm is suitable for deducing peak frequency of acoustic emission source and has a certain application value.

1 Introduction

Acoustic emission refers to the phenomenon that material's locals rapidly release energy and produce a transient elastic wave; acoustic emission technology belongs to the ultrasonic testing technical field, and is a dynamic nondestructive testing technology [1]. One of the methods that analyze and evaluate acoustic emission signals is characteristic parameters; among them peak frequency refers to the largest amplitude corresponding to the frequency of spectrum distribution curve, as shown in Fig. 1. Through the analysis of the acoustic emission signals' distribution features of the frequency domain, we can effectively test and analyze targeted signal processing [2].

The system of multi-agent is the collection of many agents; each agent is independent; the purpose of the system is to make a large and complicated system to be a small, coordinating, and easy-to-manage system [3, 4]. When testing the equipment, the different distances of each sensor from the source means that the received signals

F. Long (✉) • Y. Song • Q. Wang • R. Dai • J. Wang
College of Mechanical Science and Engineering of Northeast Petroleum University, Daqing 163318, China
e-mail: dqpilf@126.com

G. Shen et al. (eds.), *Advances in Acoustic Emission Technology: Proceedings of the World Conference on Acoustic Emission-2013*, Springer Proceedings in Physics 158,
DOI 10.1007/978-1-4939-1239-1_14,

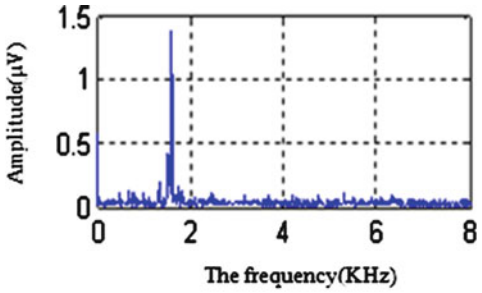

Fig. 1 The signal's frequency spectrum

represent different acoustic emission source information. When evaluating acoustic emission source, we can select the optimal combination of sensor evaluation, in order to more accurately evaluate acoustic emission source [5].

2 The Frequency Attenuation of the Acoustic Emission Wave

Acoustic emission wave speed in the process of wave propagation in the medium is not always constant; with the increasing wave propagation distance, the energy of the signal will be weakened, and the phenomenon of wave velocity attenuation can also appear. Velocity dispersion refers to the phenomenon that the speed of acoustic emission wave travels in the actual medium changing with frequency and it is often accompanied by the characteristics of the amplitude attenuation with the increasing propagation distance [6]. Generally speaking, the phenomenon of velocity dispersion and attenuation in internal particles arranged evenly in non-flawed medium is not obvious. Acoustic emission waves cross the gap and the particles may make friction and energy loss that causes amplitude attenuation. Another important reason is the wave-scattering, acoustic emission wave in the transmission process; the original acoustic emission wave with the one-way transmission spreads out in all directions, and the phenomenon is called scattering [7].

3 Calculating the Attenuation Value of Peak Frequency

In the characteristics study of rock on acoustic velocity dispersion and frequency attenuation, upper limit and floor level velocities are often used as control parameters. And based on them, the last velocity loss formula is established as below [6]:

$$\Delta V = \frac{V_\infty - V_0}{\sqrt{V_\infty \cdot V_0}}. \tag{1}$$

With known characteristic frequency f_c and the actual frequency of sound waves f, frequency attenuation values could be obtained by the type [6]:

$$\Delta f = \frac{V_\infty - V_0}{\sqrt{V_\infty \cdot V_0}} \frac{f/f_c}{1 + (f/f_c)^2}. \tag{2}$$

Acoustic emission wave spreads in metal construction, while the energy of the wave attenuation, wave velocity, and peak frequency decreases, by the type (Eq. 2) to calculate the peak frequency variation, comparing the numerical value with real peak frequency varying widely. Combination of acoustic emission wave propagation theory research and large numbers of experiments, the following formula is performed and is suitable for metal artifact sonic peak frequency variation:

$$\Delta f = \sqrt[K]{\frac{V_\infty \cdot V_0}{V_\infty - V_0}} \frac{f_\infty / f_0}{1 + f_\infty / f_0}. \tag{3}$$

V_∞ is the speed that wave spreads from the first sensor to the second sensor in the selected sensor analysis array, V_0 is the maximum transmission speed, f_∞ is the maximum peak frequency of the sensor analysis array, and f_0 is the minimum peak frequency. K is the valued based on the sensor array; the value of K is 2 when the sensors are linear array, and the value of K is 1.75 when the sensor array is nonlinear.

The peak frequency of acoustic emission source could be known after calculating the peak frequency variation:

$$f = f_{\not\Phi} + \Delta f. \tag{4}$$

f is the peak frequency of acoustic emission, and $f_{\not\Phi}$ is the middle peak frequency of the selected sensor array.

4 Experimental Research and Validation

4.1 Experiment Device

The experiment is done in the steel plate; the length, width, and thickness of the steel plate are 3,000, 2,000, and 10; the sensor model is R15, and the model of preamplifier is 2/4/6, Acoustic emission data acquisition system is MICRO-II made by American PAC company; the part that the sensor contacts with the steel plate should be polished, using vacuum grease as couplant and using magnetic to compact each sensor. Using the method of pencil lead fracture to detect system and the sensor sensitivity correction, ensure that the system meets the requirements.

4.2 Experimental Scheme

4.2.1 Linear Array Test

To avoid edge effect, six sensors are arranged in the middle of the plate along a straight line. Sensor spacing is 500 mm, as shown in Fig. 2, marking as 1–6 from left to right as in the figure. Using lead fracture as acoustic emission source, the lead fracture position is in the root of sensor 1, so regard the acoustic emission source peak frequency measured by sensor 1 as acoustic emission source peak frequency.

The experimental peak frequency of sensor 1 is 164 kHz, and other channel data are shown in Table 1.

1. Selecting 2, 3, and 4 sensors to make analysis array, the average speed that the wave spreads from 2 sensor to 3 sensor is

$$V_{2-3} = \frac{L_{2-3}}{T_3 - T_2} = \frac{0.5}{0.7907173 - 0.7906180} = 5035 \text{ m/s}.$$

$$V_{2-4} = \frac{L_{2-4}}{T_4 - T_2} = \frac{1}{0.7908630 - 0.7906180} = 4081 \text{ m/s}.$$

$$\Delta f_{2-3-4} = \sqrt{\frac{V_\infty \cdot V_0}{V_\infty - V_0}} \frac{f_\infty / f_0}{1 + f_\infty / f_0} = \sqrt{\frac{5035 \times 4081}{5035 - 4081}} \times \frac{157/17}{1 + 157/17} = 132 \text{ kHz}.$$

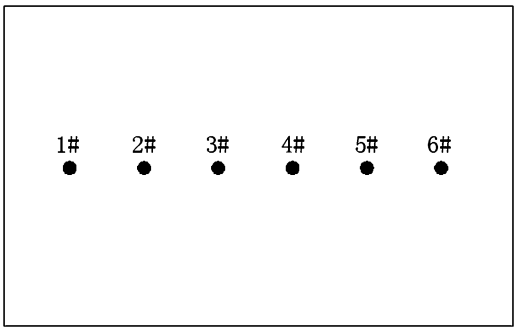

Fig. 2 Sensor is a linear arrangement

Table 1 The signal parameters received by each sensor

Sensor number	The time receiving signal (μs)	Peak frequency (kHz)
2	0.7906180	157
3	0.7907173	17
4	0.7908630	18
5	0.7910423	36
6	0.7910787	32

Table 2 The calculated peak frequency and broken lead peak frequency

Experimental number frequency (kHz)	The calculated peak of broken lead (kHz)	The peak frequency
1	163	164
2	156	160
3	160	163
4	161	166
5	159	165
6	162	166

The middle value measured by the selected sensor analysis array is 18 kHz, so the backward deducing peak frequency of acoustic emission source is $132 + 18 = 150$ kHz.

2. Selecting 2, 3, and 5 sensors to make analysis array, the attenuation value of peak frequency Δf_{2-3-5} calculated as (1) is 98 kHz, and the backward deducing peak frequency is $98 + 36 = 134$ kHz.
3. Selecting 2, 3, and 6 sensors to make analysis array, the attenuation value of peak frequency Δf_{2-3-6} calculated is 160 kHz, and the backward deducing peak frequency is $160 + 32 = 192$ kHz.
4. Taking the average value of maximum and minimum peak frequency calculated by (1), (2), and (3) $f = \frac{134+192}{2} = 163$ kHz, the value conforms to the peak frequency of broken lead of 164 kHz.

If selecting other array analyses, sometimes it may appear in the phenomenon that the value is very small or even negative, eventually leading to the calculated peak frequency of the acoustic emission source varying widely with broken lead values. Aiming at the condition of the linear array sensor, first, selecting two sensors closest to the source as a benchmark, making analysis array with other sensors, and taking the average value of maximum and minimum peak frequency calculated by each analysis array, the average value is the peak frequency of acoustic emission source. Table 2 lists the six groups of experiment backward deducing the peak frequency of acoustic emission source and the peak frequency of broken lead in each group.

Comparing the calculated peak frequency of the six experimental groups with the broken lead peak frequency, the minimum error is 1 kHz.

5 Circular Array Test

This experiment uses six sensors arranged in a circular detecting array. The angle of each sensor is 60°, the diameter of the circle is 1 m, and 7 sensor is in the circular array, as shown in Fig. 3.

Pencil is broken beside no.1 sensor, the acoustic parameters received by the other sensors in the array are listed in Table 3.

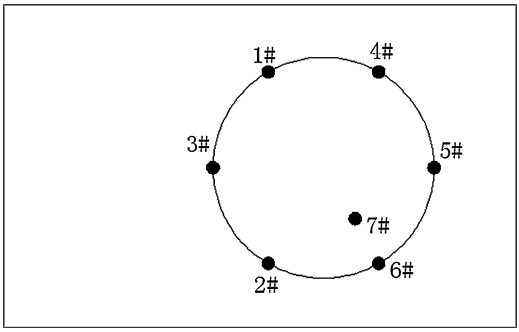

Fig. 3 Sensors in circular permutation

Table 3 The signal parameters received by each sensor

Sensor number	The time receiving signal (μs)	Peak frequency (kHz)
2	0.8644035	35
3	0.8641505	90
4	0.8640169	86
5	0.8645045	40
6	0.8647373	19
7	0.8646095	35

To calculate the peak frequency, select the three closest sensors to the acoustic emission source to make analysis array. Because the signal received by sensors travels in different directions, the wave velocity between two sensors can only be approximately calculated.

When the PLB test is at the base of sensor 1, the three sensors closest to the source are 2, 3, and 4, and 3, 4, and 5. The distance of sensors 2 and 5 to the source is the same; when this happens, adding the peak frequency is done by taking the average value from each analysis array.

1. The distances of 2, 3, and 4 sensor to the source are $L_{1-2} = 0.86$ m, $L_{1-3} = 0.5$ m, and $L_{1-4} = 0.5$ m, on the basis of 2 sensors, similarly to take, $V_{2-3} = \dfrac{L_{1-2} - L_{1-3}}{T_{2-3}} = 1423$ m/s, $V_{2-4} = \dfrac{L_{1-2} - L_{1-4}}{T_{2-4}} = 1016$ m/s

$$\Delta f_{2-3-4} = \sqrt[0.57]{\frac{V_\infty \cdot V_0}{V_\infty - V_0}} \frac{f_\infty / f_0}{1 + f_\infty / f_0} = \sqrt{\frac{1423 \times 1016}{1423 - 1016}} \times \frac{90/35}{1 + 90/35} = 75 \text{ kHz}.$$

   The calculated peak frequency is $75 + 86 = 161$ kHz.
2. In the same way, the peak frequency calculated by sensors 3, 4, and 5 is 148 kHZ.

Table 4 The calculated peak frequency and broken lead peak frequency

The breaking lead sensor	The calculated peak frequency (kHz)	The peak frequency of breaking lead (kHz)
1	162	164
2	156	160
3	160	163
4	161	166
5	159	165
6	162	166

Table 5 The calculated peak frequency and broken lead peak frequency

The experiment number	The calculated peak frequency (kHz)	The peak frequency of breaking lead (kHz)
1	160	164
2	156	160
3	160	163
4	161	166
5	159	165
6	162	166

3. The peak frequency getting from the two groups of analysis array is $f = \frac{161 + 148}{2} = 155$ kHz.

PLB in the root of sensors 2, 3, 4, 5, and 6 in turn, the peak frequency calculated by each experiment, and the peak frequency of PLB are shown in Table 4.

As shown in Table 4, the minimum error that compares the calculating peak frequency with the PLB test is 2 kHz.

PLB test at the base of sensor 7, backward deducing the peak frequency by the sensors 2, 5, and 6 furthest to the sensor 7, and the experimental results are shown in Table 5:

As shown in Table 5, the minimum error that compares the calculating peak frequency with the PLB test is 3 kHz.

Comparing the minimum error of Tables 4 and 5 with Table 2, the data of Table 2 is more accurate; this is because when the sensors test acoustic emission source as the complex array, the signals received by each sensor are transmitted along different directions, so when backward deducing the peak frequency of acoustic emission source, it has certain error. Comparing the minimum error of Table 4 with Table 5, the minimum error of Table 4 is lower than Table 5; because the experimental data in Table 4 refers to the evaluated results of two sets of sensor array, it can better reflect the information of sound source.

6 Conclusion

In this chapter, using the theory of multi-agent and combining the theory and experimental research with the acoustic attenuation problem in metal material, the conclusions are as follows:

1. Through the linear array and circular array experiment on steel, the calculated minimum error of peak frequency is 1 kHz; it means that the algorithm is accurate.
2. The accuracy of backward deducing peak frequency of circular array is lower than linear array, but it does not affect the judgment of source characteristics.
3. When using multi-agent theory and using the different sensor array to backward deduce peak frequency, it can improve the accuracy of the results.

References

1. Hu Chang-yang, Yang Gangfeng, Acoustic emission technology and application in detection. Calculation and Measurement Technology. **35**(6) 1–2 (2008)
2. Geng Rongsheng, Yang Mingwei, *Acoustic Emission Testing*. (China Machine Press, 2010), pp. 41–46
3. B. Pieter, M. Adrian, Y. Jeroen et al., Coordinating self–interested planning agent. Auton. Agent. Multi. Agent. Syst. **12**, 199–218 (2006)
4. Xiao Zheng, Wu Chengrong, Summarize of multi-agent system cooperation and coordination mechanism. Comput. Sci. **34**(5), 139–142 (2007)
5. L. Xiaoning, Ascertaining weight factors of multi-sensor data fusion. Journal of Aircraft Control **24**(1), 64–66 (2005)
6. W. Haiyang, S. Zandong, The frequency scattering and attenuation about acoustic waving spreading in rock. J. Oil. **33**(2), 332–336 (2012)
7. Ying Chongfu, Zhang Shouyu, *Research About Supersonic Wave Spreading and Scattering in Solidity*. (The Chinese Academy of Sciences, 1990) pp. 56–59

Analysis and Research of Acoustic Emission Signal of Rolling Element Bearing Fatigue

Hualong Jia, Xing Wu, Xiaoqin Liu, Chang Liu, and Zhihai Wang

Abstract Surface contact fatigue is one of the most common failures of rolling element bearings. The initialization and propagation of subsurface cracks during early fatigue damages produce acoustic emission (AE) signals. Hence it has the advantage to detect early faults by acoustic emission monitoring technology. In this chapter, acoustic emission signal and vibration signal were collected during fatigue damage experiment of rolling element bearing in a self-made test rig. A number of data-processing methods were used here, such as kurtosis, RMS, and information entropy, to analyze the signal. The experiment indicated that the fault characteristic frequency of AE signal is more significant than that of vibration signal, and AE signal has a higher signal-to-noise ratio than vibration signal, so it is much earlier and more sensitive in detecting the degradation of surface contact fatigue.

1 Introduction

Rolling element bearings are widely used as support components in many rotating machines. They are very easy to be damaged in abominable industry environment [1].

The main failure mode is fatigue damage in rolling contact surface which could grow to pitting or spalling. The deformation or the crack propagation of bearing material by periodic load in the early stage of fatigue releases strain energy by elastic waves [2]. The elastic wave can be collected by acoustic emission sensors. Vibration signal is too weak to detect the possible failure efficiently [3]. As acoustic emission signal is high-frequency stress wave which comes from structure defect, it

H. Jia • X. Wu • X. Liu (✉) • C. Liu • Z. Wang
Kunming University of Science and Technology, Kunming 650500, China
e-mail: dovehuazai@gmail.com

G. Shen et al. (eds.), *Advances in Acoustic Emission Technology: Proceedings of the World Conference on Acoustic Emission-2013*, Springer Proceedings in Physics 158,
DOI 10.1007/978-1-4939-1239-1_15,

has a wider spectrum than vibration signal. The high-frequency property could help avoid the interference of low-frequency vibration noise and promote the accuracy of condition monitoring and diagnosis.

A lot of studies have been done in detecting rolling element bearing fault by acoustic emission by international and domestic academics. Schoess [4] concluded that acoustic emission detection has better ability in detecting train bearing failure compared with other methods such as temperature, acceleration, Hall effect, and stress measurement. Tondon [5] discovered that peak has great advantage than ringing counts in detecting bearing failure of different conditions. Choudhury [6] has analyzed the inner race and roller fault in different working conditions by the distribution of ring down counts events and peak amplitude events. The result shows that ring down counts was an effective parameter in detecting early fault. The development tendency of bearing fault could be diagnosed and predicted by events distribution. Abdullah's [7] research shows that acoustic emission could not only diagnose and recognize early fault but also provide information of the degree of damage compared with vibration signal which was collected simultaneously. Al-Ghamdi [8] further studied the kurtosis of acoustic emission signal and vibration signal of outer race fault. He concluded that the variance of kurtosis of acoustic emission signal could indicate the existence and size of the fault. Acoustic emission signal has a higher anti-interference ability and it could diagnose fault earlier than vibration signal [9]. Rujiang Hao [10] studies the acoustic emission signal and vibration signal in different working conditions and different fault by the parametric analysis method such as evens, amplitude, RMS, and kurtosis. Acoustic emission signal is more obvious and accurate in revealing the feature of fault signal in different testing environments compared with vibration signal.

Most academics studied on artificial defects which could not reflect the advantages of AE in diagnosing the generation and propagation of cracks.

Health bearing (without artificial defects) has been run to failure by D. Mba [11]. He has proved that acoustic emission signal could diagnose the generation and propagation of cracks. This chapter adds vibration signal for comparison analysis and investigates the development of both signals in bearing fatigue wear.

In this chapter, acoustic emission and vibration signals were collected during fatigue damage experiments of rolling element bearing in a self-made test rig. Several data-processing methods were used to study the development of fatigue signal, such as kurtosis, RMS, and information entropy. The result indicated that acoustic emission signal was much effective and sensitive than vibration signal in detecting the degradation of surface contact fatigue.

2 Fatigue Test

Thrust ball bearing (SKF 51207) fatigue test rig was built, as shown in Fig. 1. The bearing is driven by an adjustable-speed motor. A torque sensor is applied to the output side of the motor to monitor load torque. The rotation speed is 600 rpm, and the rotational frequency is 10 Hz.

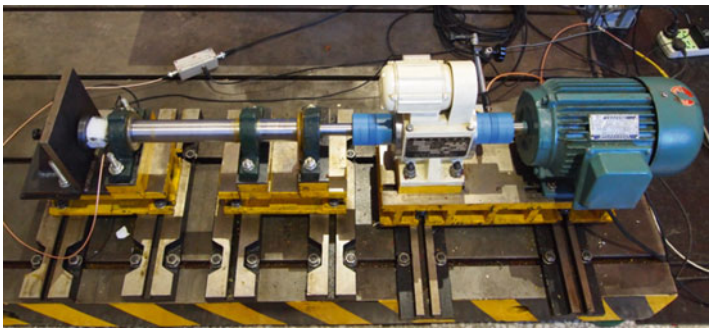

Fig. 1 The rolling bearing fatigue test bed by self-design

The fatigue wear of a conventional bearing is quite slowly, so the out race is replaced by a round steel plate (1045, 080M46) to accelerate bearing wear. Steel plate is different from conventional bearing. A raceway will appear in the operation, while it will not happen to the bearing. Still the signal law has great reference value for the conventional bearing as the fatigue damage mechanisms are similar.

Acoustic emission sensor (US, PAC, aR15) and vibration sensor (US, PCB, 333B30) were mounted at the back of the steel plate. Acoustic emission signals were collected by high-speed data acquisition card (Taiwan, ADLINK, PCI9846H), with sampling frequency of 1,000 kHz. Vibration signal is collected by dynamic signal acquisition card (US, NI, USB9234), with sampling frequency of 25.6 kHz.

The data acquisition system recorded 5-s data at every 5 min. Visual check was done for each hour. There were a lot of pittings in the raceway after 6-h operation.

3 Law of Signal Development

Four parameters were used including kurtosis, RMS, peak, and information entropy to make trend analysis both of acoustic emission signals and vibration signals.

1. Kurtosis is a dimensionless parameter to demonstrate the deviation of probability density of a signal from normal distribution. Kurtosis rises as the initiation and propagation of fault which could increase the probability density of high amplitude and the signal distribution deviates from the normal distribution. Computational formula of kurtosis is

$$\mathrm{KU} = \frac{1}{N}\sum_{i=1}^{N}\left(\frac{\chi_i - \mu}{\sigma}\right)^4 \tag{1}$$

χ_i is the signal sampling value; μ is the average value of signal; N is the sampling length; σ is the standard deviation.

2. RMS (root mean square) demonstrates the average power and strength. Computational formula is

$$\mathrm{RMS} = \sqrt{\frac{\sum \left(\chi_i{}^2\right)}{N}} \tag{2}$$

χ_i is the signal sampling value; N is the sampling length.

3. Peak indicates the maximum amplitude within certain time range. The variation range of peak may be quite large, so it is not very stable [12].

$$P = \max\left(\chi_i\right) \tag{3}$$

χ_i is the signal sampling value; P is the peak.

4. Information entropy (IE) is usually defined as an indicator of instability [13, 14]. The increase of frequency components in acoustic emission signal caused by the deterioration of mechanical system and the initiation and propagation of fault would reduce the regularity and increase the corresponding IE value. Divide all data into n parts of the whole range. P is equal to the data number of each part divide all data number N. With knowledge of the number of events (N) and the probability distribution (P_i) of each event in a given AE signal, IE can be calculated for a set of events using equation (5)

$$P_i = \frac{n_i}{N} \tag{5}$$

$$\mathrm{IE} = -\sum_{i=1}^{N} P_i \times \log(P_i) \tag{6}$$

The tendencies of kurtosis, RMS, peak, and IE both of AE signal and vibration signal are shown in Figs. 2 and 3, respectively. The value of kurtosis, peak, and IE value of both AE signal and vibration signal are quite large at the first 60 min. This may be generated by the plastic deformation of steel plate at the beginning of the test. Kurtosis and peak decreased quickly after 60 min, while the IE value still stayed at a high level. This can be explained that IE value is more sensitive for the plastic deformation of AE signal and vibration signal than the other indicators. All the indicators show a rising trend, although they have fluctuation.

Kurtosis and RMS of AE signal stay a steady state within the 60th–120th minute. The peak of AE signal has a big fluctuation. It falls back to the formal value at 120th minute. It can be explained that the peak is easy to disturb by the impact of rolling element and cage.

Within 120th–180th minute, the kurtosis of AE signal has a big fluctuation in the beginning to 140th minute. RMS value of AE signal in 180th minute is bigger than that in 120th minute and the peak has a small increase too. Within 140th–160th minute, the IE, RMS, and peak of AE signal have an increasing tendency.

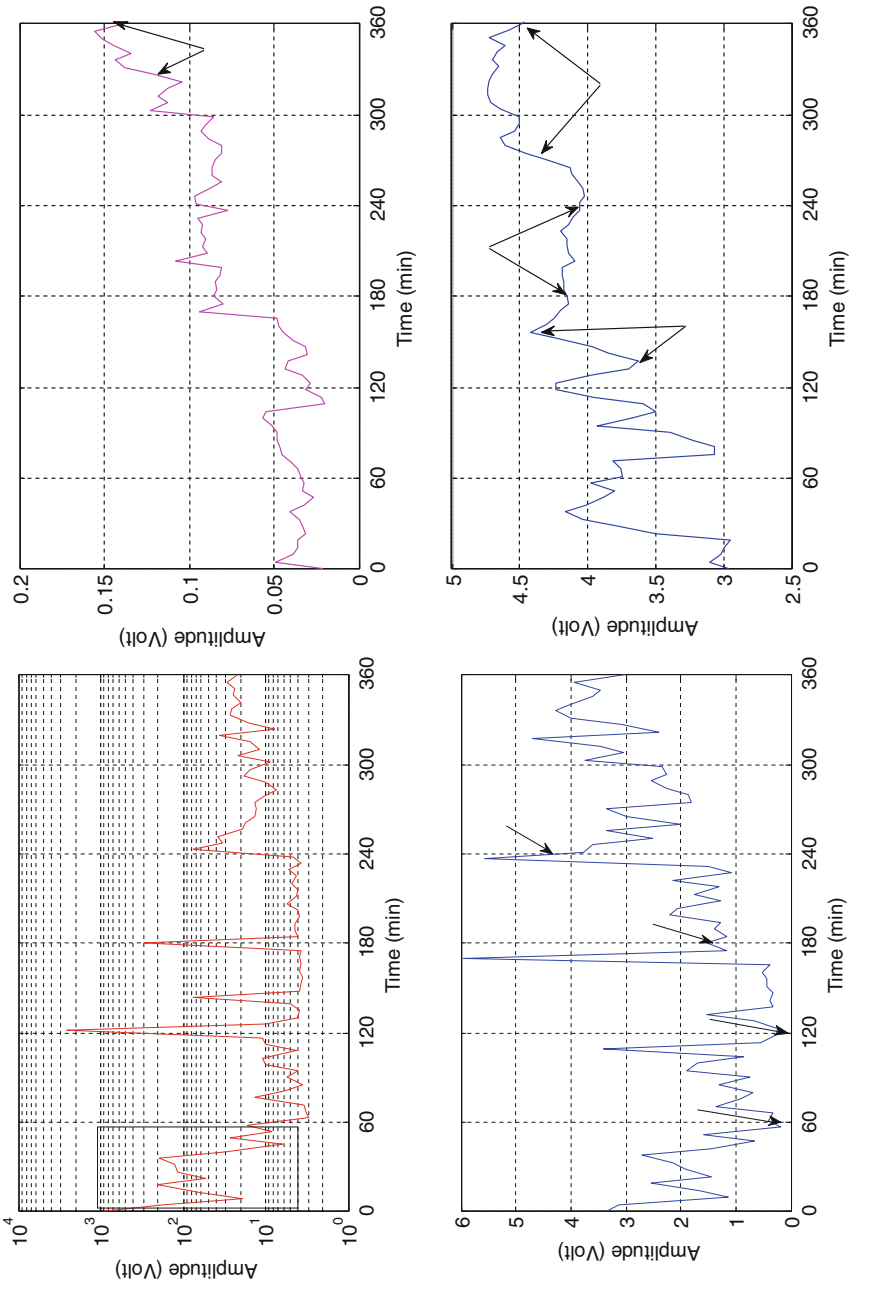

Fig. 2 The trend graph of indicators by AE signal. (**a**) Kurtosis, (**b**) RMS, (**c**) peak, (**d**) IE

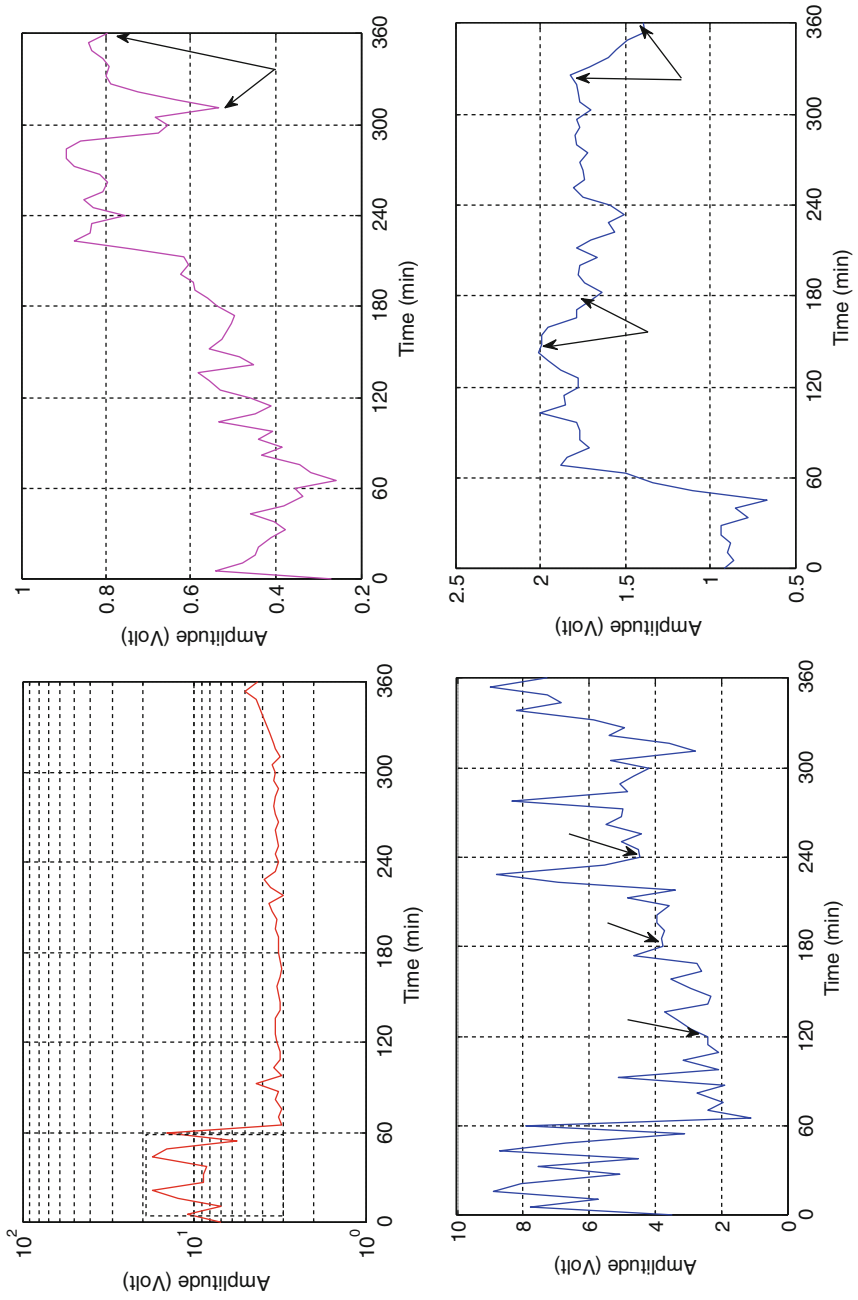

Fig. 3 The trend graph of indicators by AE signal. (**a**) Kurtosis, (**b**) RMS, (**c**) peak, (**d**) IE

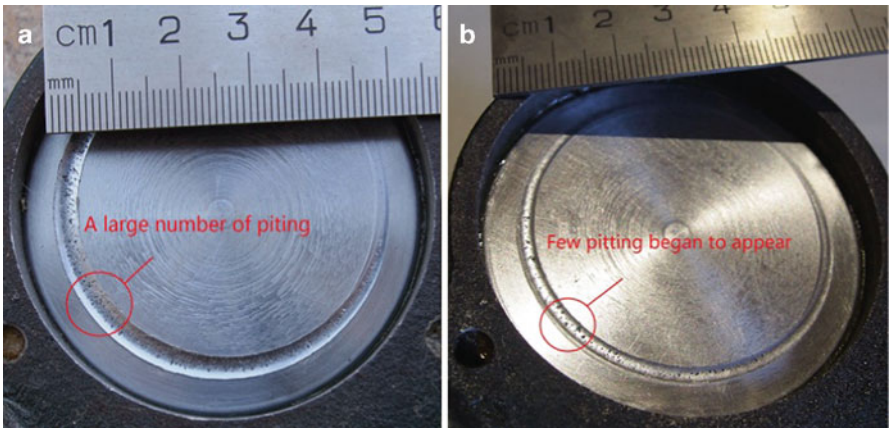

Fig. 4 Wear pattern. (**a**) Wear pattern at 4 h of operation. (**b**) Wear pattern at 6 h of operation

It demonstrates that the AE activity is quite strong and it can be speculated that the fatigue has been appeared at this period. However the kurtosis and RMS of vibration signal remain stable. Peak shows a small increasing tendency while IE decreases conversely. The vibration signal is less sensitive than AE signal, so it has no response to the activity of bearing fault.

Within 180th–240th minute, kurtosis and peak of AE signal have a big fluctuation and then ascend. RMS and IE of AE signal have little decrease. It was proved that the AE activity is quite stable. It can be speculated as the fast propagation of fault; this could be proved in Fig. 4a. The kurtosis, RMS, and peak of vibration signal have a fluctuation at 220th minute. Kurtosis and peak have small increase, RMS has a big increase, and IE decreased quickly in 220th–240th minute. It can be inferred that vibration signal could detect the defect weekly after the appearance of pitting.

Within 240th–300th minute, the kurtosis and peak of AE signal decreased quickly, RMS has little increase, and IE has large increase. The kurtosis, peak, and IE of vibration signal nearly stay constant, and RMS decreased quickly. It can be inferred that the propagation of fault is relatively stable. This can be interpreted as that the kurtosis, RMS, and peak are very sensitive as the presence of the defects is pronounced; their values may decrease when the damage is quite critical.

The kurtosis, RMS, and peak of both AE signal and vibration signal increase sharply at the period of 320th minute to the end of the test, while the IE of vibration signal decreases. The final values of kurtosis, RMS, and peak of both AE signal and vibration signal are quite big. RMS and IE of AE signal reach their maximum value at the end of the test. Serious fault appears at the end of the test; see Fig. 4b.

It can be concluded that AE signal could indicate the initiation of fault, while vibration signal has no effect on this situation by analyzing kurtosis, RMS, peak, and IE of both AE and vibration signal. AE signal could detect the propagation of

fault, while vibration signal hardly detects small pitting that appears in the steel plate. Both AE signal and vibration signal could detect the fault when large pitting appears, but AE signal is more sensitive and obvious than vibration signal.

4 Spectrum Analysis

Rolling element bearing is constituted of inner ring, outer ring, cage, and rollers. Repeat impacting from the fault such as cracks, pitting, and indentation in these parts would produce periodical AE signal; in other words, as the characteristic frequency of bearing fault would "knock" the AE sensor, different parts have their unique characteristic frequency in operation [15].

The frequency of rolling element passing the fault which happens in inner and outer raceway is

$$f_0 = f_1 = \frac{z}{2} f_s = 70\,\text{Hz}$$

Z is the number of rolling element, $z = 14$.

For further comparison of the ability of fault source location of AE and vibration, the AE and vibration signals of 325th minute are analyzed by envelop spectrum. The peaks are at 137.8, 344.5, and 620.2 Hz in the envelope spectrum of vibration signal; see in Fig. 5a. They are two times, five times, and seven times of characteristic frequency, respectively. The peak of 334.5 Hz is most significant, while the others are quite low and close to noise frequency. The peaks are at 69.0, 137.8, 206.8, 275.6, 344.6, 413.4, 482.4, 551.2, and 620.2 Hz in the envelope spectrum analysis of AE signal. The number of peaks is more than that in vibration signal, and the values stand out of the noise frequency. The AE signal has a higher signal-to-noise ratio than vibration signal, so it could be more efficient in fault diagnosing.

5 Conclusion

The thrust ball bearing fatigue test was operated on a self-made test rig until the bearing runs to failure. The result shows that the AE signal could detect fault more quickly and effectively than vibration signal. Vibration signal has no response at the initiation of bearing fault until pitting appears. The fault characteristic frequency of AE signal is more significant than that of vibration signal, and AE signal has a higher signal-to-noise ratio than vibration signal, so it could be more efficient in fault diagnosing than vibration signal.

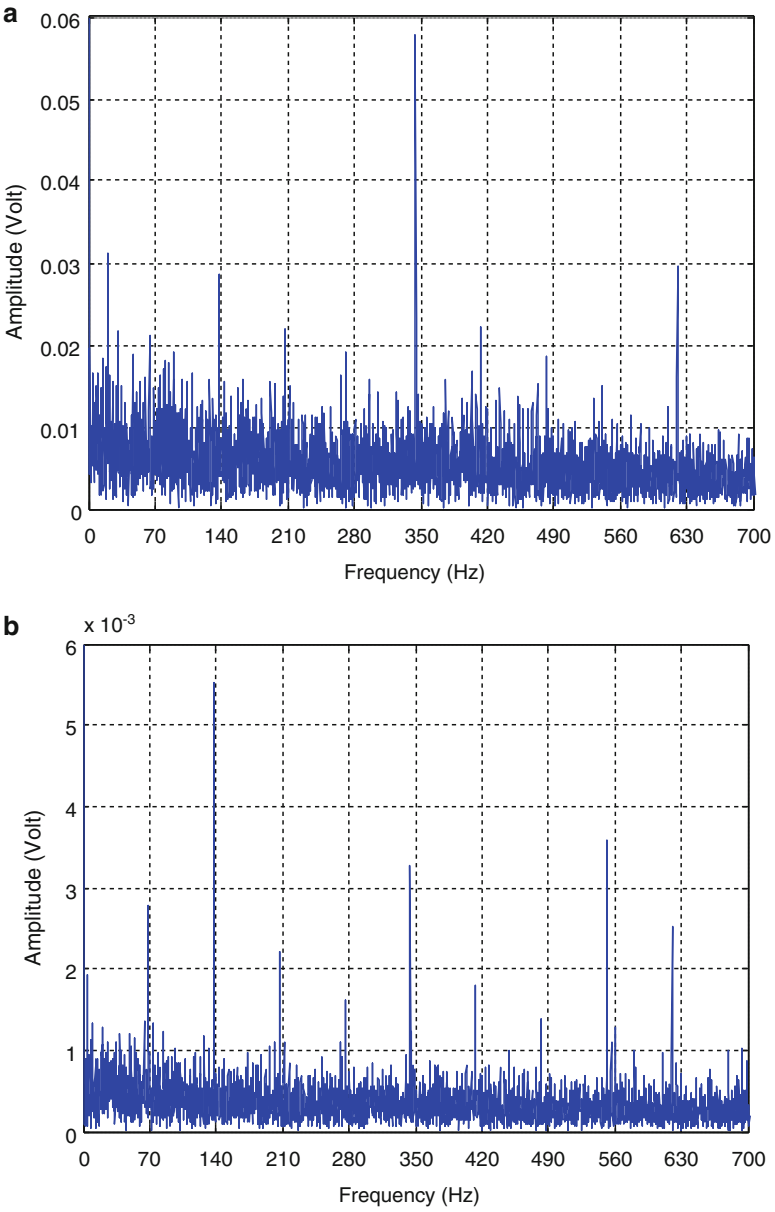

Fig. 5 Envelope spectrum analysis. (**a**) Envelope spectrum analysis of vibration signal. (**b**) Envelope spectrum analysis of AE signal

Acknowledgment This research was supported in part by the National Science Foundation Project of Yunnan Province under Grant No. 2011FZ017. We thank Yunhai Yan (Kunming University of Science and Technology) and Xiaolin Xue (Kunming University of Science and Technology) for generous help of fatigue test rig.

References

1. C. Baozhen, Study and application of fault diagnosis of rolling bearings based one the wavelet analysis. The Master Degree Dissertation of North University, 1–7, 2005
2. B.K.N. Rao Raj, D. Mba, Development of acoustic emission technology for condition monitoring and diagnosis of rotating machines: bearings, pumps, gearboxes, engines, and rotating structures. Shock Vib. Dig. **38**, 3–16 (2006)
3. M.W. Hawman, W.S. Galinaitis, Acoustic emission monitoring of rolling element bearings. Ultrason. Symp. **2**, 885–889 (1988)
4. J.N. Schoess, Development and application of stress-wave acoustic emission diagnosis for roller bearings. Proc. SPIE **3986**, 58–70 (2000)
5. N. Tandon, B.C. Nakra, Defect detection of rolling element bearings by acoustic emission method[J]. JAEMA **9**(1), 25–28 (1990)
6. A. Choudhury, N. Tandon, Application of acoustic emission technique for the detection of defects in rolling element bearings[J]. Tribol. Int. **33**, 39–45 (2000)
7. A.M. Al-Ghamdi, D. Zhechkov, D. Mba, The use of acoustic emission for bearing defect identification and estimation of defect size. EWGAE 2004 Lecture. **38**, 397–406 (2004)
8. A.M. Al-Ghamdi, D. Mba, A comparative experimental study on the use of acoustic emission and vibration analysis for bearing defect identification and estimation of defect size [J]. Mech. Syst. Signal Process. **20**(7), 1537–1571 (2006)
9. L. Fengying, S. Yudi, X. Jun, Acoustic emission technique for fault diagnosis of rolling bearing [J]. NDT **27**(11), 583–586 (2005)
10. H.A.O. Rujiang, L.U. Wenxiu, C.H.U. Fulei, Morphology filter for analyzing roller bearing fault using acoustic emission signal processing [J]. Tsinghua Univ(Sci & Tech), **48**(5), 812–815 (2008)
11. M. Elforjani, D. Mba, Accelerated natural fault diagnosis in slow speed bearings with acoustic emission [J]. Eng. Fract. Mech. **77**, 112–127 (2010)
12. C. Xing, The application of time-domain parameters in bearing fault diagnosing [J]. Eng. Tech. **24**, 35 (2010)
13. J.P. Sethna, *Statistical Mechanics: Entropy, Order Parameter and Complexity* (Oxford University Press, USA, 2006)
14. A. Papoulis, *Probability, Random Variables and Stochastic Processes* (McGraw-Hill, New York, NY, 1991)
15. L. Mengyuan, S. Zhendong, C. Haichao, *Acoustic emission detection and signal processing [M]* (Sciences Press, Beijing, 2010)

Research on Compression Method of Acoustic Emission Signal Based on Wavelet Transform

Zhihai Wang, Xing Wu, Xiaoqin Liu, Chang Liu, and Hualong Jia

Abstract Long-term operation of the mechanical equipment leads to structural fatigue damages. The damages always come with internal crack initiation and propagation, which radiate acoustic emission (AE) signal. It is possible to monitor the whole damage development process of mechanical equipment by AE technology. AE signal is usually collected at a high sampling rate which leads to large data sets, and occupying huge storage space. This goes against long-term online monitoring. This research uses different threshold-level settings of wavelet transform to compress raw AE signal. Compared with the original signal, the compressed signal could retain key features including energy, rms, kurtosis, etc. The signal-to-noise ratio (SNR) of the reconstruction signal also has been improved. This algorithm was confirmed by AE signal of rolling bearing in a fatigue damage test.

1 Introduction

The transient elastic waves which are generated from the power of the local stress concentration by the rapid release in the material are called acoustic emission (AE). In the 1950s, Kaiser, the German scholar, discovered and named Kaiser effect, wherein AE signal coming from a material is not generated when it is reloaded before the stress value reaches the maximum of the last load stress. Thus, Kaiser created the modern AE technique by his discovery. AE technique has been applied to the petrochemical industry, power industry, material testing, civil engineering, aerospace and aviation industry, metal processing, transportation, etc. constantly by using this nature in materials in the past. There are many advantages compared with

Z. Wang • X. Wu (✉) • X. Liu • C. Liu • H. Jia
Kunming University of Science and Technology, Kunming 650500, China
e-mail: wzh_kmust@163.com; xwu@kmust.edu.cn

G. Shen et al. (eds.), *Advances in Acoustic Emission Technology: Proceedings of the World Conference on Acoustic Emission-2013*, Springer Proceedings in Physics 158,
DOI 10.1007/978-1-4939-1239-1_16,

the traditional means of nondestructive testing, such as AE can detect energy from the measured object itself, is sensitive to the linear defects, generally evaluates the status of the structural defects, and warns the premature failure. There are elastic waves (i.e., AE signal) due to the injury inside the material. Then the elastic waves transmit to the surface of the material and begin to reflex against the sensor. The collected AE signal is the mixture of the elastic waves which overlay each other and accompanied with a lot of noise [1, 2]. Since AE signal sampling rate is extremely high, it could be acceptable in short-term monitoring. But in long-term monitoring, AE signal will take a lot of storage space. It is necessary to remove redundant signal in the collected AE signal and retain a valid signal. Then we could reach for the purpose of AE signal compression and improved SNR and then it could save large amounts of hard disk space. Compression of AE signal makes the long-term monitoring to be true.

Since Burt and Adelson proposed multiresolution pyramid decomposition algorithm [3] successfully instead of discrete cosine transform (DCT) [4–6], Mallat proposed multiresolution signal decomposition technique based on wavelet transform soon afterwards [7]. Their work drove wavelet multiresolution technique maturity gradually. I. Daubechies [8], A.N. Akansu [9] and C.K. Chui [10] introduced the signal processing method of multiresolution analysis which was based on wavelet transformation respectively. And since the 1980s, the innovative work of J. Morlet, the French engineer; A. Grossman, the physicist; and Y. Meyer, the mathematician, etc., made wavelet a worldwide research hotspot quickly. Wavelet compression technology has become a powerful tool for signal processing, which is widely used in image processing and signal processing. It is possible to introduce the idea of wavelet compression into AE field for a mount of experiences and methods of wavelet compression technology were accumulated by the foregoing scholars.

This study attempts to combine probabilistic method with wavelet compression technology to compress AE signal of the rolling bearing and proposes a method of layered secondary-threshold compression based on 3σ criterion combined with the method of self-adaptive threshold. In the end, the effectiveness of the method in AE signal compression processing is confirmed by contrasting with the characteristic parameters of the signal.

2 Wavelet Compression

2.1 Wavelet Transform

Since 1910, Alfred Harr firstly proposed to make use of the telescopic and the translation idea to construct the first orthonormal wavelet basis, after a large number of scholars worked on wavelet theory, which led wavelet theory into many application fields, such as signal analysis, image processing, quantum

mechanics, the physical theory, military electronic warfare, computer classification and identification, synthetic music and language, medical imaging and diagnostics, seismic exploration, and mechanical fault diagnosis.

In wavelet theory, it introduces the elements which need wavelet transform into Hilbert space, and then wavelet transform could be obtained by the inner product. Gradually it developed continuous wavelet transform, discrete wavelet transform, and multiresolution analysis algorithm, involving contents of functions of real variable and functional analysis.

According to the theory of multiresolution wavelet analysis algorithm, no matter how complex the signal is, no matter they are in the time domain or the frequency domain, it can be decomposed as the combination of approximate signal and detail signal. During the reconstruction of orthogonal wavelet transform, the character of the general picture and the outline of the signal is enhanced step by step while the details are reducing; the leading role is the basic characteristic if the scale is over a certain level m0 (i.e., m is greater than m0), or above it which is the scale for the basic feature extraction. Conversely, each scale below m0 is as the approximation of the detail characteristics. The following form can be obtained from the basic formula of wavelet transform:

$$P_{m-1}x(t) = P_m x(t) + Q_m x(t) \tag{1}$$

where:

m—index of decomposition layer
$P_{m-1}x(t)$—approximation part of the signal at $m-1$ layer
$P_m x(t)$—approximation part of the signal at m layer
$Q_m x(t)$—details part of the signal at m layer

which leads to Mallat algorithm:

$$a_{m+1}(n) = \sum\nolimits_{l=-\infty}^{+\infty} a_m(l)h(l-2n) = \left(a_m^* \overline{g}\right) \cdot (2n) \tag{2}$$

$$d_{m+1}(n) = \sum\nolimits_{l=-\infty}^{+\infty} a_m(l)g(l-2n) = \left(a_m^* \overline{g}\right) \cdot (2n) \tag{3}$$

where $a_m(n)$ is the signal that needs to be decomposed; $a_{m+1}(n)$ and $d_{m+1}(n)$ are the approximate part and the detail part after $a_m(n)$ was decomposed; h and g are the filters of the two scale differential equations, $\overline{h} = h(-n)$, $\overline{g} = g(-n)$.

The reconstruction formula is

$$a_m(n) = \sum\nolimits_{l=-\infty}^{+\infty} a_{m+1}(l)h(n-2l) + \sum\nolimits_{l=-\infty}^{+\infty} d_{m+1}(l)g(n-2l) \tag{4}$$

2.2 The Principle of Wavelet Compression

In wavelet compression techniques, wavelet function, layers of wavelet decomposition, threshold selection criteria, threshold level, etc. are always the subjects of

research. Among them, research of threshold is always the focus of wavelet compression technology.

According to the non-stationary AE raw data, the desired wavelet function is selected. For non-stationary signal, it is good to choose a wavelet function with a strong character of compact support; and it should choose the wavelet function with strong regularity for stationary signal or regular periodic signal.

In this study, *db4* wavelet is considered which has a strong comprehensiveness as the mother wavelet of the wavelet compression arithmetic.

In the technology of wavelet analysis, it is very important to determine the maximum decomposition level. The max number of the decomposing layer is decided by the length of the raw signal data. The decomposition layer is denoted as l, and the length of the raw data is denoted as N; l is less than or equal to $\log_2(N)$. A large number of experimental studies have shown that when the decomposition level is greater than 4, the effect of wavelet compression for the signal is tending towards stability [11]; it will set 4 as the maximum decomposition level.

2.3 Typical Threshold Selection Criteria and Selection Method

For the signal with white noise, four kinds of threshold selection rules mostly used are as follows:

1. Adaptive threshold based on the principle of Stein's unbiased likelihood estimate (quadratic equation). If for a given threshold value, we can get its likelihood estimate, then minimize the non-likelihood, and we could get the threshold. F. Luisier, etc. used SURE method to decide an appropriate threshold by using soft threshold method [12].
2. Use the form of a fixed value; the resulting threshold is $\sqrt{2\log(\text{length}(X))}$ (where X is a signal, *length* means the length of X).
3. Method of heuristic is optimal for low SNR signal with high SURE estimate noise.
4. Use the method of the minimax principle to choose the threshold; it generates an extreme value of the minimum of the mean square error; this extreme value estimator can minimize the maximum of mean square error for a given function in a focus set.

The threshold method includes the selection of soft or hard threshold and global threshold or layered threshold method.

Soft threshold method compares the amplitude of the signal with the given threshold. It is retained if the value of the signal amplitude is equal or greater than it, while the rest parts are replaced as the value of the signal amplitude minus the given threshold. Hard threshold method is similar to the soft threshold method; it is also retained if the amplitude value of the signal is equal to or greater than the

given threshold, while the rest parts of it are set to zero. Global threshold compression method takes the same threshold to process each layer of the wavelet compression. Layered threshold compression method takes a different threshold to process each layer of the wavelet compression.

Hard threshold method is common for data compression. The final nonzero value is the valid data. The raw data is compressed. The selection of global threshold method or layered threshold method is decided by the specific case of the original data. Because of the different threshold from the same computing method for each layer of wavelet coefficients of AE signal, this chapter uses layered threshold method to compress AE signal data.

3 Wavelet Threshold Compression for AE Signal

The collected AE signal consisted of the effective AE signal and the noise. For this research, the work of collecting AE signal was done in the lab, so the noise of the collected AE signal is just made up of background noise in the lab. And environmental noise is always present as the form of zero mean white noise throughout the whole signal time domain; the case of AE signal in the time domain is shown in Fig. 1 where V is the unit of voltage. Compared with the effective AE signal in the mixed signal, the noise signal in the time domain is distributed relatively even. We can also see from the power spectrum of the original signal that AE energy is concentrated on certain frequency bands while the noise energy is uniformly distributed in a broad band. The case of the raw signal power spectrum is shown in Fig. 2. It is possible to conclude that the collected signal is a uniform distribution in both time domain and frequency domain. The larger wavelet coefficients are generally represented as the actual signal, while the smaller coefficients are

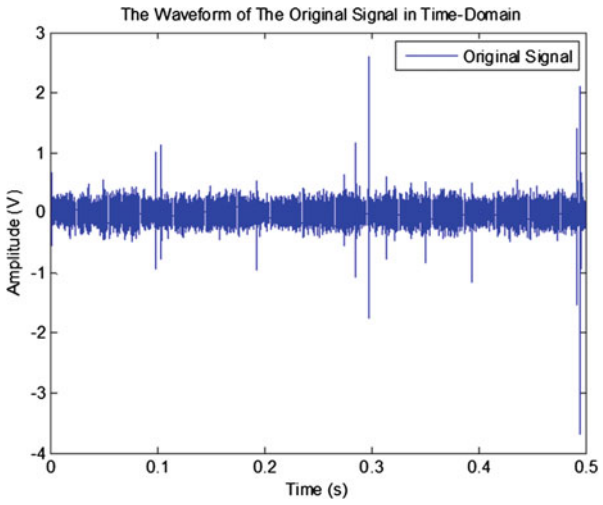

Fig. 1 The waveform of the original signal in the time domain

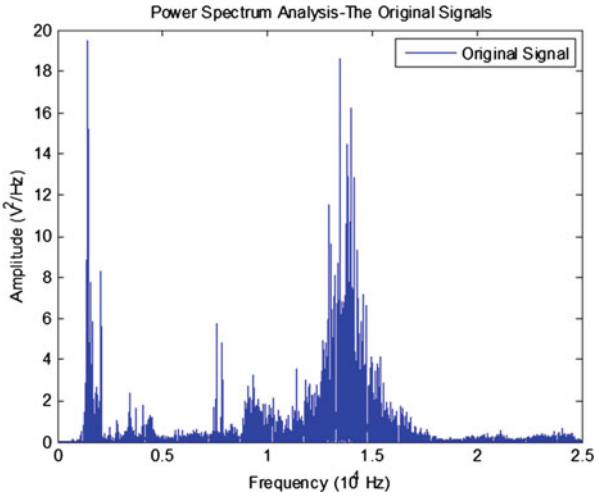

Fig. 2 The power spectrum analysis of the original signal

generally from the noise signal greatly [13]; if the noise signal which distribution is wide in each layer could be rejected by setting the threshold and retaining the effective AE signal, the purpose of compressing AE signal and increasing signal-to-noise ratio will come true. Taking into account this characteristic, it provides us an idea of using the principle of probability of AE signal to choose the threshold rule: firstly, to determine the maximum decomposition level and the selection of wavelet, then using the probabilistic methods combined with self-adaptive threshold to determine the secondary threshold for each level of the wavelet coefficient, and lastly, using the hard threshold method to process wavelet coefficients in each level and reconstruct the compressed signal.

3.1 The Situation of Wavelet Decomposition

In this research AE signal is collected from rolling bearing according to the character of AE signal structure to decide the signal compression method by using wavelet. The collected AE signal is taken from a rolling bearing fatigue test bed by self-design; the case of the test bed is shown in Fig. 3. And firstly to take a part of the data which was in the stage of pitting as the original signal, the case of the original signal is shown in Fig. 1. In the end, the author takes some other kinds of rolling bearing fatigue test AE signal to confirm the universality of this compression algorithm. Then, a conclusion is made.

This research takes *db4* wavelet as the mother wavelet. The case of four-layer decomposition is shown in Fig. 4.

From the graph of wavelet decomposition (Fig. 4) we can see that the whole graph is divided into five levels; in order to contract easily, the top layer of the graphs (row a in Fig. 4) is time domain waveforms of AE signal of the original

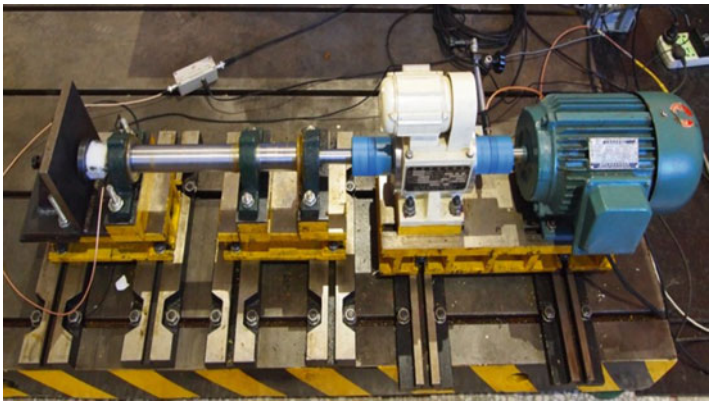

Fig. 3 The rolling bearing fatigue test bed by self-design

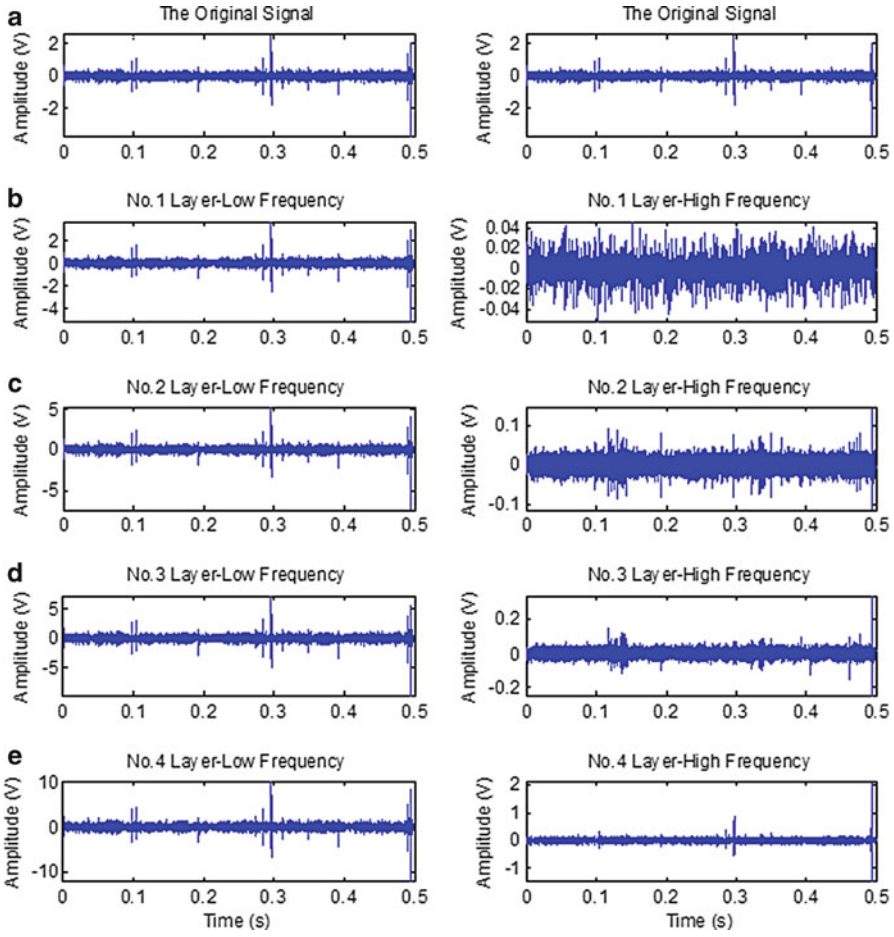

Fig. 4 Four layers of the approximation (*left column*) and the detail waveform (*right column*) of wavelet decomposition of the original signal

collection. Below this figure is the diagram of the fourth layer of wavelet decomposition from the first layer to the fourth layer sequentially; the left side are the parts of the approximation of each decomposed layer, and the right side are the parts of the details of each decomposed layer. From the left side of the exploded view of each layer, compared with the original signal, we could see that, after every time of the decomposition, the approximate parts have little changes, while from the right side of the exploded view of each layer, the details parts change obviously. Thus, during later threshold processing, approximation parts should be reserved, so the final reconstructed signal could be mostly identical to the original signal.

3.2 A Combined Method to Determine the Threshold

From the probability theory, if σ is standard deviation of a function, the probability of the function in the interval of $[-3\sigma, 3\sigma]$ is 99.74 % [14, 15]. And the collected AE signal just consists of the effective AE signal and zero mean white noise. This could make a judgment by autocorrelation of each layer of the high-frequency detail coefficients of wavelet decomposition. If the autocorrelation function gets the maximum only at the zero position, it can say that the function has a great similarity with zero mean white noise; then the threshold can be set to 3σ in this layer [13]. Then use hard threshold method to compress each layer. Because the effective AE signal has the characteristics of period more or less, the autocorrelation function of AE signal has the characteristics of approximate period; then the effective AE signal needs to be completely retained.

Using 3σ criterion to do the autocorrelation analysis for the four levels of the detail parts of wavelet decomposition is shown in Fig. 5.

By 3σ criterion, the noise can be reduced and SNR of AE is greatly improved. The noise exists in the collected AE signal from beginning to end and distributes over a wide frequency range. Effective AE signal, often as short-time pulses, distributes more discretely in waveform. So we could decide the secondary threshold by using self-adaptive threshold method. The wavelet coefficient of noise has a large number and a smaller amplitude while the effective AE signal of it is small in number and greater in amplitude. If there is noise signal, in the case of the threshold value grown at a fixed value every time, each time the growth of the number of zero value will be large and similar to each other. As the threshold value increases, if there is little noise signal, the number of the zero value will become smaller each time and there is a big gap between the growth in the number compared with the signal with noise [16]; thus a critical value will be obtained to determine to stop or continue to increase the threshold for the compression processing. The selected fixed incremental value should be appropriate; if the incremental value is too large, the threshold process will wipe off the effective signal of AE signal partially, while if the increment value is too small, the threshold process will increase the computation time; thus a comprehensive measure should be taken. On this basis, in order to explore the effective signal more and remove the noise more, this study considers

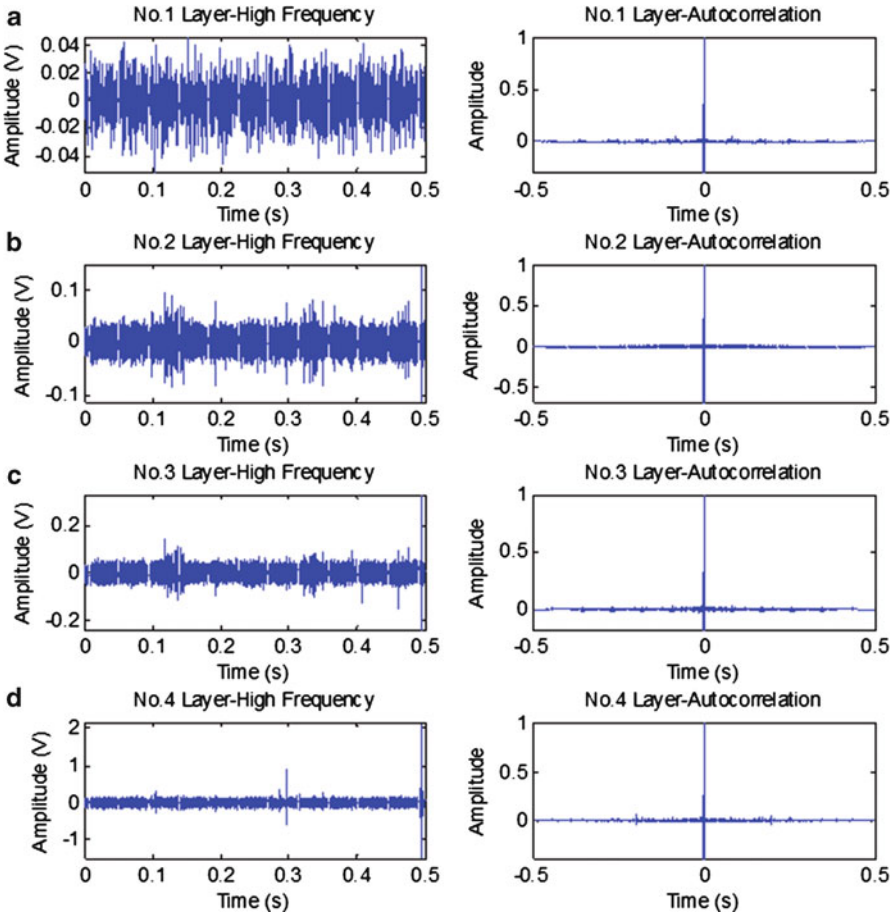

Fig. 5 Four level of the high-frequency part of the wavelet decomposition (*left column*) and its autocorrelation (*right column*)

the threshold which is calculated with 3σ criterion as the initial threshold based on the characterization of the distribution of the noise signal and AE signal, and then appropriately selects the threshold value increment and the termination conditions to get the final threshold and to reach the purpose of increasing SNR of the compressed signal greatly.

In order to be conservative, make one percent of the number level (that is 0.01) of the original threshold (3σ threshold) as the fixed increment value; 0.0001 is the fixed increment value for each namely, and take the half number of the first growth of zero of the signal as the termination conditions of the threshold growth; the calculations of each level are the same, and then take four calculated thresholds as the final threshold for the detail coefficients of the original AE signal decomposition at each level and according to hard threshold compression method. Finally,

compare with the compressed signal to evaluate comprehensively in the compression ratio and the compression effect.

4 The Effect Evaluation of the Measured AE Signal Data Compression of the Rolling Bearing

4.1 Compression Ratio Analysis

It can measure the power ability to compression of this arithmetic by calculating the compression ratio. The compression ratio is the ratio of the original signal to the compressed signal. The formula is shown as follows:

$$\mathrm{CR} = \mathrm{Sig}/\mathrm{Sig\_}C \tag{5}$$

where:

CR—Compression ratio
Sig—The original signal
Sig _ *C*—The compressed signal

After the calculation, the final compression ratio is 14.33, and it is 8.22 by using the common compression software; it achieves a satisfactory compression ratio which increased nearly two times.

4.2 Compression Effect Analysis

The case of contrasting the characteristic parameters of the compressed signal and the original signal is shown in Table 1.

The mean of the compressed signal changes 0.064 %, mean square value changes 1.53 %, and variance changes 1.53 % by being compared to the original signal. The compression of the two signals in the frequency domain is as shown in Fig. 6. Kurtosis changes 2.89 %. The mean of the amplitude error changes 0.0681 %.

Table 1 The characteristic parameters of the two signal

Parameters	Original signal	Compressed signal	Unit
Mean	0.00022008	0.00022022	V
Mean square value	0.01679	0.016533	V^2/s
Variance	0.01679	0.016533	V^2
Index of the power spectrum peak	1420	1420	N/A
Value of the power spectrum peak	19.507	19.507	V^2/Hz
Kurtosis	30.7282	31.6149	N/A

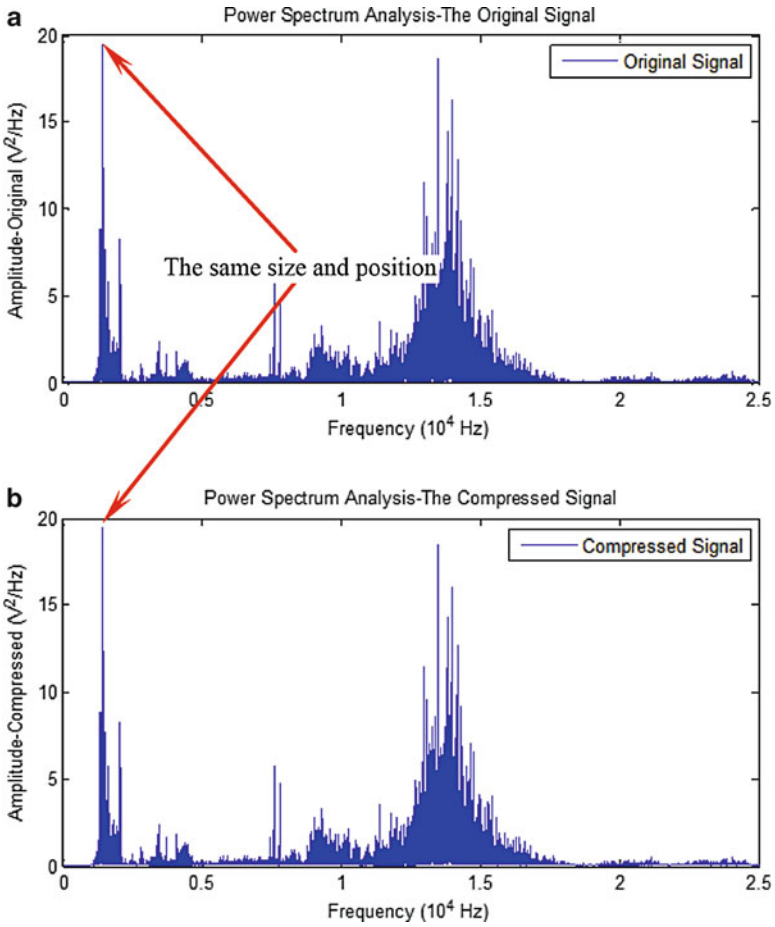

Fig. 6 (**a**) The power spectrum of the original signal. (**b**) The power spectrum of the compressed signal

It can be seen from Fig. 6 that the power spectrum of the compressed signal is nearly the same as the original signal. The position and the size of the peak in the power spectrum have no change. Then, we calculate the error value of the compression algorithm by using the original signal minus the compressed signal, which is shown in the last row of Fig. 7.

From Fig. 7, the waveform display of the compressed signal and the original signal is almost the same.

In the end, the author takes some extra different stages of rolling bearing fatigue test AE signal to calculate compression ratio by using the same algorithm and get satisfactory results as the previous one. For example, at first, to select a part of no-damage AE signal, the result of compression ratio is 14.16. Then, to select a more serious damage part of AE signal, the result of compression ratio is 14.89.

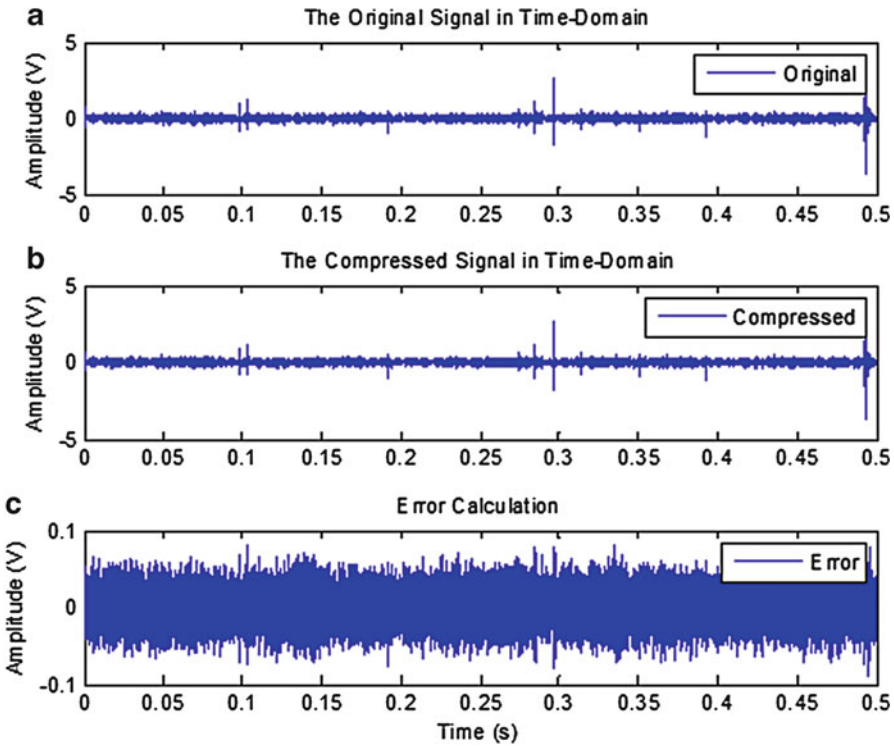

Fig. 7 (**a**) The original signal. (**b**) The compressed signal. (**c**) Error value of the compression algorithm

And the mean of the compressed signal, mean square value, variance, kurtosis, etc. changes nearly the same as the aforementioned experimental verification by being compared to the original signal.

5 Conclusion

According to the character of AE signal, this chapter presents a compression method of wavelet decomposition combined with probabilistic. The method gets the final threshold of wavelet coefficient by calculating the threshold twice to each layer of wavelet decomposition. And it is used to compress AE signal of rolling bearing in a layered threshold way. It can achieve a nearly two times larger compression ratios than the common compression software by using this method. Finally, it is concluded that the compressed signal could be used instead of the original AE signal to make a further analysis with the subsequent step by comparing the characteristic parameters in both time domain and the frequency domain of the two signals and evaluating the compression effect. This study does not research in

compressing the approximate wavelet coefficient which represents the general picture and the outline character of the original signal in the last decomposition layer. This allows AE signal compression technology to still have a certain research space with this arithmetic; it can make a greater compression ratio by a supplementary study.

Acknowledgment This research was supported in part by Science and Technology Department Foundation Project of Yunnan Province under Grant No. 2011FZ017 and Education Department Foundation Project of Yunnan Province under Grant No. 2013J060. We thank all of our dear teammates in MCVN for their support for this work.

References

1. T. Jin, Z. Sun, L. Sun, Modeling of acoustic emission due to crack growth with finite element method and time-frequency analysis of the signal, J. Vib. Meas. Diagn. **27**(4) Shanghai, P. R. China. 288–291 (2007)
2. R. Hao, W. Lu, F. Chu, Review of diagnosis of rolling element bearings defaults by means of acoustic emission technique, J. Vib. Shock. **27**(3) Peking, P. R. China. 75–79 (2008)
3. P.J. Burt, E.H. Adelson, The Laplacian pyramid as a compact image code, IEEE Trans. Commun. **31**(4) Troy, NY, USA. 532–540 (1983)
4. M.J.T. Smith, T.P. Barnwell III, A procedure for designing exact Reconstruction filter banks for tree-structured sub-band coders, in *Proc. IEEE ICASSP*. (Atlanta, GA, USA, 1984), pp. 421–424
5. F. Mintzer, Filters for distortion-free two-band multirate filter banks. IEEE Trans. ASSP. **33** (3), 626–630 (1985)
6. P.P. Vaidyanathan, Quadrature mirror filter banks, M-band extensions and perfect reconstruction techniques. IEEE Signal Process. Mag. **4**(3), 4–20 (1987)
7. S. Mallat, Multiresolution Representations and Wavelets, Ph.D. Thesis, University of Pennsylvania, 1988
8. I. Daubechies, Ten Lectures on Wavelets, SIAM. Conference Board in Mathematical Science. New Jersey, USA. (1992)
9. A.N. Akansu, R.A. Haddad, Multiresolution Signal Decomposition: Transforms, Subbands, and Wavelets, Academic Press. A Harcourt Science and Technology Company. New Jersey, USA. (1992)
10. C.K. Chui, *An Introduction to Wavelets*, Academic Press. St. Louis, USA. (1992)
11. P. Jiang, *Study on Wavelet Application in Signal Denoise and Data Compression* (Institute of Modern Control Engineering, College of Info Science and Engineering, ZheJiang University, Hangzhou, P.R.China, 2004)
12. F. Luisier, T. Blu, M. Unser, A new SURE approach to image denoising: interscale orthonormal wavelet thresholding. IEEE Trans Image Process **16**(3), 593–606 (2007)
13. Y. Zang, D. Zhang, W. Wang, Per-level threshold de-noising method using wavelet and its application in engine vibration analysis. J. Vib. Shock. **28**(8) Changchun, Jilin, P. R. China. 57–60 (2009)
14. B. Li, Y. Zhang, Z. Yang, Long-term extreme estimation method to determine maximum buffet design loads. J. Vib. Shock. **31**(14) Xi'an, Shanxi, P. R. China, 1–6 (2012)
15. J. Li, S. Teng, H. Lin, J. Wang, Design of weighing module of moisture analyzer based on CS5532. Transduc. Microsyst. Technol. **31**(10) Changsha, Hunan, P. R. China. 106–108 (2012)
16. C. Huang, S. Han, Research on self-adaptive threshold algorithm based on wavelet transform. Ship Electron. Eng. **31**(3) Wuhan, Hubei, P. R. China. 59–63 (2011)

Feature Extraction of Corrosion Acoustic Emission Signals Based on Genetic-Matching Pursuit Algorithm

Yang Yu, Nan Zhang, Ping Yang, Bo Liu, and Yuan Fu

Abstract The acoustic emission (AE) detecting is an effective online tank bottom corrosion monitoring method. It is easy to discover early corrosion. Aiming at random unstable features of AE signals from tank bottom corrosion, genetic-matching pursuit arithmetic was presented to extract features of tank bottom corrosion AE signal. The main characteristics of the signals are given by the acoustic emission detector. The characteristics include count, energy, amplitude, and average frequency. Matching Pursuit (MP) arithmetic is used to extract characteristic parameters. The AE signals can be well reconfigured. The genetic algorithm (GA) was used to optimize MP algorithm. The projection on the atom of the signal or its residue in MP arithmetic was served as the GA fitness function, and the best matching atomic parameter was confirmed. The experimental results show that the best pursuit atomic parameters are extracted and the amount of calculation is reduced substantially by this method. In the reconstructed signal process, signal noise can be effectively removed by this method, so as to achieve a certain de-noising effect. It has much practical value and theoretical application value.

1 Introduction

Metal corrosion causes huge losses, in which different types of corrosion, pitting, and erosion are the most harmful. Although pitting corrosion appears pitting or pits in a few concentrated points, but with the passage of time, pits continue to develop depth, and corrosion pits will be formed like holes [1]. This is a kind of devastating

Y. Yu (✉) • N. Zhang • P. Yang • B. Liu • Y. Fu
Shenyang University of Technology, Shenyang 110870, China
e-mail: yuy@sut.edu.cn

G. Shen et al. (eds.), *Advances in Acoustic Emission Technology: Proceedings of the World Conference on Acoustic Emission-2013*, Springer Proceedings in Physics 158,
DOI 10.1007/978-1-4939-1239-1_17,

localized corrosion, but appearance is subtle. If left unchecked, it will lead to perforated metal until the entire structure is destroyed [2].

In the actual detection process of storage tank, how to effectively de-noise the signals and extract feature of the corrosion AE signals are the key points of the AE signals detection after the collection of corrosion signal information.

In the past, such as Fourier transform, Winger transform, and Wavelet transform are commonly used in acoustic emission signal processing methods. The basic functions are used to expand the signals by these methods. Researches show that, whether Wavelet basis or Fourier basis, using only one or a few basic functions to reconstruct the signal, the linear expansion of single basic function as a substrate is a certain lack of flexibility. The resolution of the two methods is not very high.

For some signals, such expansion coefficients may be difficult to clearly reflect the contents and features of the signals. For example, since Fourier transform has no ability to distinguish time domain, the Fourier expansion coefficients which will be used are difficult to find the clear correspondence. Common de-noising methods are optimal estimation method and threshold method based on Wavelet transform and spectral subtraction method, etc. These methods are implemented in a certain range of the signal de-noising, but they are dependent on the statistics of signal or noise, which is often priori unknown in practical application; the applications of these methods are limited. This problem is solved by MP effectively. It makes the signal decompose into the best match for the linear summation of signal structure time-frequency atoms. So the signal can be reconstructed well.

Signal sparse decomposition based on MP algorithm is an adaptive method of signal decomposition and representation. Noise can be de-noised effectively. The significant wave will not be damaged through this method. A priori access to the statistical characteristics of signal and noise is not required, so it can be applied to a variety of different signal feature extraction and de-noising. A wide range of applications will be gotten.

The Matching Pursuit algorithm (MP) applies to corrosion studies of acoustic emission signals. Signal noise can be removed effectively and feature extraction will be well obtained. This method contributes to a better analysis of the characteristics of acoustic emission signals corrosion. The diagnostic validity and reliability are improved. The biggest limitation of MP algorithm is a large computer memory, and the operation amount is too large. It is very time-consuming. Only a certain optimization is performed. This method could be better applied to AE detection. Genetic algorithm will be used in this chapter to reduce the matching pursuit algorithm (MP) in calculated amount of acoustic emission signals feature extraction. The same results are obtained while the computational efficiency is significantly improving.

2 The Analysis of GA-MP Signal Sparse Decomposition Method

2.1 Signal Sparse Decomposition Based on MP

In the early 1990s, the MP algorithm was put forward by Mallat and Zhang [3]. MP sparse representation is a wavelet analysis method. It is mainly considered that the main signals feature can be retained. Based on that how to reconstruct signals and filter out the noise are discussed. The matching part of the signal and the atomic structure characteristic are decomposed and reconstructed by MP. Noise is random and irrelevant, so it has no structural characteristics. Therefore AE signals that are reconstructed by the sparse decomposition could eliminate the influence of noise. The signal will be expressed with fewer atoms. It is possible to keep the signal having main structures. The cost of the signal processing is reduced as well. Algorithm has no specific requirements for atom and almost any function can be used as atomic. Great flexibility for application is provided by the method. It has been widely applied to different types of environmental signal de-noising [4], sounds recognition [5], pattern recognition [6], etc.

The signal to be decomposed $f \in H$ is assumed, the length is N, H is the Hilbert space, $D = (g_{\gamma k})_{\gamma k \in \Gamma}$ is for signal sparse decomposition over-complete dictionary atoms. Atoms are normalized, each atom has a unit of energy $\|g_{\gamma k}\| = 1$, $g_{\gamma k}$ is the atom which is defined by the parameter set γ_k, and Γ is the set of the parameter set γ_k. In the over-complete atoms, the number of atoms in the dictionary should be much greater than the signal length. The process of the MP method that decomposes a signal is as follows:

Step 1. From the over-complete atoms dictionary D we select the best match (similar) atoms with the decomposed signal f. It is satisfied:

$$\left| < f g_{\gamma 0} > \right| = \sup_{\gamma \in \Gamma} < f, g_{\gamma} > \left| . \right. \tag{1}$$

The signal can be decomposed into the component of the best matching atom $g_{\gamma 0}$ and the residual signal. That is:

$$f = < f g_{\gamma 0} > + R^1 f. \tag{2}$$

Step 2. Go on decomposing the remains:

$$R^k f = < R^k f, g_{\gamma k} > g_{\gamma k} + R^k f. \tag{3}$$

$R^k f$ is the residual signal of using the best matching atom to match the original signal, $g_{\gamma k}$ is satisfied:

$$\left| < R^k f, g_{\gamma k} > \right| = \sup_{\gamma \in \Gamma} < R^k f, g_\gamma > \left| . \right. \tag{4}$$

Step3. Judging $\|R^k f\| < \varepsilon(\varepsilon > 0)$, ε is the residual signal threshold setting, if $\|R^k f\| < \varepsilon$ is up, then turn to Step 4; otherwise, let $f = R^k f$, $k = k + 1$, turn to Step 1.

Step 4. Export the Lth approximate expansion:

$$f \approx \sum_{k=0}^{L} \langle R^k f, g_k \rangle g_k. \tag{5}$$

L is the total number of iterations $L \ll N$, it is also the number of the reconfiguration signal. The signal sparse representation idea is reflected by formula (5) and $L \ll N$. As decomposition progresses, it means K is increasing. Residual signal $R^k f$ is decreasing, converges to 0.

2.2 *Signal Sparse Decomposition Based on Genetic Algorithms and Structural Properties of Atomic Dictionary*

2.2.1 The Structural Properties of Atomic Over-Complete Dictionary

The key to achieving the signal sparse decomposition is lying on using an over-complete atomic library. The following is the forming method of over-complete dictionary [7]:

$D = (g_\gamma)_{\gamma \in \Gamma}$ is formed by Gabor atoms. One Gabor atom is formed by the modulated Gaussian window function:

$$g_\gamma(t) = \frac{1}{\sqrt{s}} g\left(\frac{t-u}{s}\right) \cos(vt + w) \tag{6}$$

$g(t) = e^{-\pi t^2}$ is the Gaussian window function; Time-frequency parameters are $\gamma = (s, u, v, w)$, the discrete time-frequency parameters are: $\gamma = (s, u, v, w) = (a^j, pa^j \Delta u, ka^{-j} \Delta v, i\Delta w)$, $0 \le i \le 12$, $0 < i \le \log_2 N$, $0 \le p \le 2^{-j+1}$, $a = 2$, $\Delta u = 1/2$, $\Delta v = \pi$, $\Delta w = \pi/6$.

In the over-complete dictionary $D = (g_\gamma)_{\gamma \in \Gamma}$, an atom is determined by time-frequency parameters $\gamma = (s, u, v, w)$, the wave of g_γ is determined by parameters s, v, and w, the central location of an atom is determined by the parameter u, s is the scale, u is the translation, v is the frequency, w is the phase [8].

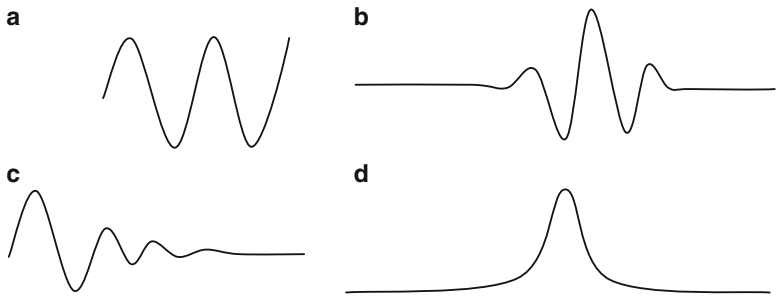

Fig. 1 Concentrated typical schematic diagram of primitive function waveform. (**a**) Fourier primitive functions, (**b**) Wavelet primitive functions, (**c**) Impulse response primitive functions, (**d**) Shock response spectrum

In theory, the over-complete atom dictionary which has a good structure should contain the quantities and species of atoms as much as possible, so that a better effect can be obtained [9]. From a practical computing point of view, the dictionary as far as possible should not contain similar atoms, so as to meet the storage and computation requirements. Therefore, from the perspective of the actual calculation, the parameter u should be constant, $u = N/2$, so the size of atomic dictionary will be greatly reduced, and the amount of computation will meet the computer memory requirements. In each step of MP sparse decomposition [10], the atom: (s_i, v_i, w_i), $(u = N/2)$ is taken from the atomic dictionary, and then by translating. The atom $\gamma_i = (s_i, u_i, v_i, w_i)$ $(u \neq N/2)$ will be obtained. Figure 1 shows the signal sparse decomposition process concentrated typical schematic diagram of primitive function waveform.

2.2.2 Finding of the Best Optimized Matching Atom

In the signal MP sparse decomposition, the key to every arithmetic iteration step is to find the maximal projection of the signal or the residual signal in the over-complete atom dictionary, the most calculated amount is spent on searching the best matching atom, each search step is necessary to match the atomic signal one time, and then making the product operation, so the maximum result of the operation will be selected. The searching of the atom is a question of optimization, so the GA can be used to solve this problem.

Genetic algorithm for solving the optimal solution to the problem is through the searching process for a chromosome. The searching space of a problem is made up of all the chromosomes. The characteristics of genetic algorithm have been listed below: that is, handling object is not a parameter itself, instead, it is the parameter set after encoding; the GA has implicit parallelism. GA is capable of handling groups of multiple individuals; it estimates the individual based on fitness function; algorithm is not constraint by the function continuity and differentiability; the searching process is guided by probabilistic.

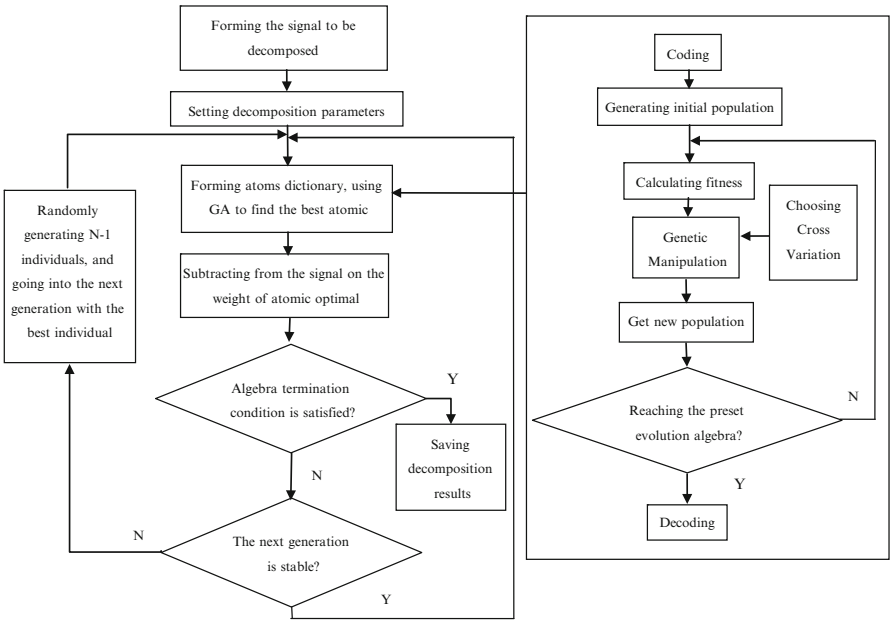

Fig. 2 Signal sparse decomposition based on GA-MP algorithm

GA relies on regeneration to remain the outstanding populations, and relies on crossover and mutation operations to change the search space, in order to continue to be the best solution. The probability of mutation and crossover operation is large. There will be a greater damage possibility of optimal solution.

Therefore, when the GA is used, people are constantly changing to adjust these two probabilities in order to expand the search space, but the best solution which has gotten will not be destroyed. Because the current optimal solution does not participate in crossover and mutation, so the best individual of the offspring population is no more than the parent's best individual. In the next generation, the obtained optimal solution better than the current one is to retain it. And the worst solution using retention method directly participates for variability. Invalid genes of inferior solutions which participate in the cross will be avoided, and the condition of effective genes being deleted also will be avoided. It is helpful to regulate the local minimum. Therefore, GA using elitist strategy can speed up the search rate. The optimal solution will be approximated well. Figure 2 shows a signal based on GA-MP sparse decomposition algorithm flow. The GA is used to optimize the MP, in order to increase the speed of progress.

2.2.3 Determining Optimum Atoms of MP

Genetic algorithm to solve optimization problems is an ideal algorithm. Each atom in the over-complete atomic library is as a chromosome of GA, chromosomes

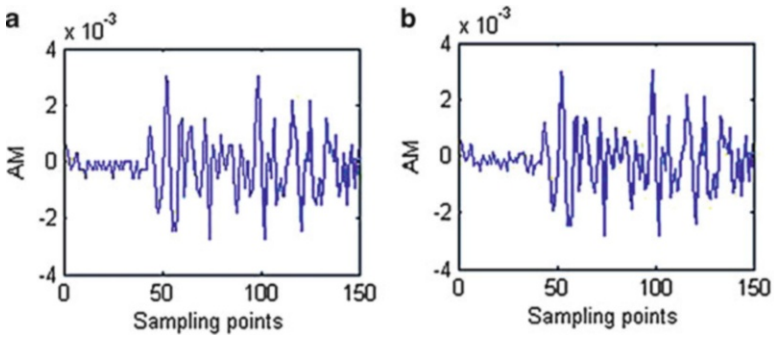

Fig. 3 (**a**) Original pitting acoustic emission sampling signal (**b**) Extracted signal based on MP

randomly generate an initial population, and then four temporal frequency parameters are set as $\gamma_i = (s_i, u_i, v_i, w_i)$, the four temporal frequency parameters once are determined, and the atom function should be uniquely corresponded. The absolute value of the signal or its residual signal projection $|R^k f, g_\gamma|$ is used as the fitness function of GA, and the value is used for evaluating the pros and cons of atom; the bigger the fitness function, the better would be the atom. Genetic algorithm is to find the optimal chromosome, and the use of signal sparse decomposition is to find the optimal atom.

In this chapter, tank bottom corrosion acoustic emission signals are used to test the algorithm and the results are compared before and after the extraction process. It is shown as Fig. 3. Interception length of pitting acoustic emission signals sampling points is 150.

Figure 3a shows the original pitting acoustic emission sampling signal, and Fig. 3b shows the extracted signal based on MP.

The process of genetic algorithm using elitist strategy to select the best matching atom in the over-complete atoms library is as follow [11]:

Initialization

1. The population size is designed as N, crossover probability Pc, mutation probability Pm, increasing multiples k, and evolution algebra, $N = 400$, $Pc = 0.7$, $Pm = 0.01$, $k = 12$, the evolution algebra is 80.
2. The initial population is randomly generated; the number of individuals is N.
3. The population fitness value of each individual is calculated. The individuals are ranked in ascending order according to the individual fitness value; fitness function is the absolute value of signal inner product or the residual signal and atom, i.e., $<f, g_{\gamma 0}>$ or $<R^k f, g_{\gamma k}>$.

Population evolutionary

1. A largest fitness value of an individual and a minimum is selected; other $N-2$ individuals according to the relative adaptive value, the probability of each

individual which is selected will be calculated, and selection procedure will be done next.

2. From the above selected population, in addition to the best, the worst individuals, sets of two, compete for survival, the $(N-2)/2$ surviving competition winners then hybridize by crossover probability Pc, the individual of hybrid formation enters into the next generation; in addition to the best and the worst individuals, randomly select a chromosome, the chromosome does the gene mutation by mutation probability Pm; for the worst individual, the chromosome does the gene mutation by the increased mutation probability kPm; the best individual directly enters into the next generation.

Termination inspection

If it reaches the preset evolution algebra, Algorithm stops; otherwise, determine whether the next generation is steady, if it is steady, then produces $N-1$ individuals randomly, enter into the next generation with the best individual, then turn to 2); if it is unsteady, turn to 2). For structural characteristics of the signal, the best atom has a strong expression, therefore, we can use minority of atoms to reconfigure the major structures of the signal.

2.2.4 The De-noising of Algorithm

In this chapter, genetic-matching pursuit algorithm is used for signal reconstruction. It can improve the computational speed, also can play de-noising effect. Matching Pursuit is a greedy algorithm, decomposition iteration is to select the largest projection atom, and the convergence speed is fast. The noise is removed by traditional de-noising methods from the signal, unlike this signal de-noising method based on sparse decomposition; it starts with the sparse component that is extracted from the signal. Then the signal is reconstructed by the sparse component. The signal will be the reconstructed signal whose noise is removed. In this chapter, signal de-noising is based on the sparse decomposition method; it has no matter with the type of signal and noise levels. It does not need to be informed about the statistical characteristics of the signal and noise in advance. An adaptive de-noising method is provided for the signal and the well de-noising effect can be achieved.

2.3 The Advantage and Disadvantage of the GA-MP Algorithm

Of course, the algorithm also has its limitations. De-noising is successful or not, sometimes it is dependent on the similarity between the signal and noise. If a noise is very similar to the signal, then MP for de-noising effect of this noise is not very good. In addition, when the problem size is small, the optimal solution of this

problem can be gotten; when the problem size is large, only the approximate solution can be gotten, then the population size and the maximum number of generations will be increased to approximate the optimal solution. However, in this chapter for acoustic emission signals, there is a significant difference between the noise and the signal characteristic, so it is possible to obtain a good extraction. In this chapter, using GA to optimize the MP, the signal can be matched very well simultaneously, it can be able to meet the large amount of calculations needs and every step of the inner product of the maximum can be quickly searched, and then the global optimal solution can be obtained to achieve the purpose of speed.

3 Results

The result of feature extraction based on Genetic-Matching Pursuit algorithm is shown in Fig. 4.

As Fig. 4 shows, (a) is the original signals, (b) is one of the matching atoms, (c) is the residual signals after matching, and (d) is the reconstructed signals. It can be seen that the GA-MP matched AE signal waveform well and the reconstructed signal had the best similarity with original corrosion AE signal from the comparison of Fig. 4a, d. This approach effectively filters out glitch information. It has a good de-noising ability.

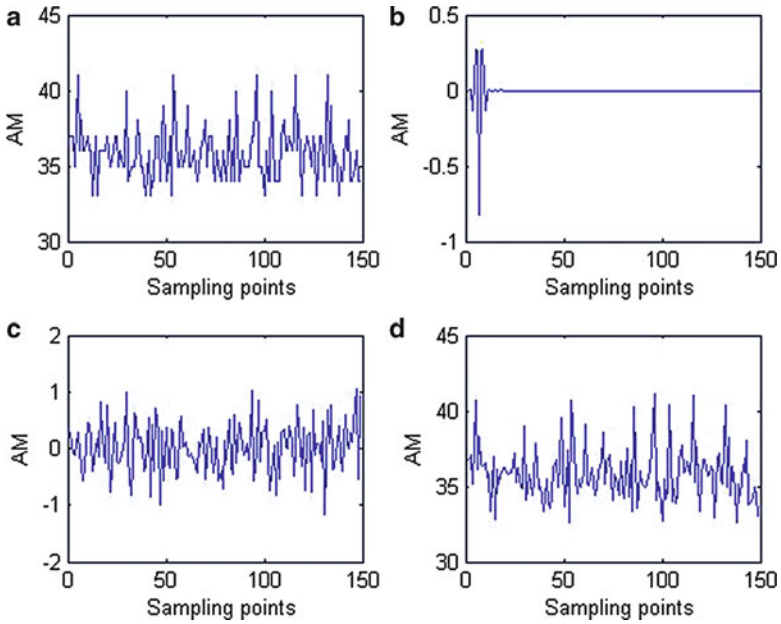

Fig. 4 (**a**) Original signals (**b**) A matching atom (**c**) Residual signals (**d**) Reconstructed signals

Table 1 Run time comparison

	MP (s)	GA-MP (s)
Running time	184.302029	4.962305

The length of sampling data is 150 points. The running time of MP and GA-MP process given in Table 1.

4 Conclusion

Corrosion condition of tank bottom is simulated in a lab environment. The signals are collected by the AE sensor. The characteristic is the voltage amplitude of acoustic emission corrosion signals.

On the basis of Fig. 3a, b, the two methods have the same result of waveform, and from the view of Fig. 4, the signals can be de-noised effectively.

The runtime comparison of Table 1 clearly indicates that the speed is increased significantly by using GA-MP.

GA-MP has strong adaptability and good stability, and primitive orthogonal functions are not required. Its accuracy is higher than other methods. The signals are reconstructed by atoms though GA-MP. Running speed has improved significantly than the MP. The signals can be de-noised very well through this method.

Acknowledgment This work is supported by the Creative Team Project Foundation of the Education Department of Liaoning Province, China (Grant No. LT2010082).

References

1. R.S. Geng, Pitting corrosion mechanism of acoustic emission sources. J. Acoust **27**(4), 369–372 (2002)
2. H. Fan, Q.F. Meng, Y.Y. Zhang, W.W. Feng, Q. Gao, Feature extraction and its application based on improved matching pursuit algorithm. Mech. Eng. J. **43**(7), 115–119 (2007)
3. S. Mallat, Z. Zhang, Matching pursuits with time-frequency dictionaries. IEEE Trans. Signal Process. **41**(12), 3397–3415 (1993)
4. S. Qian, D. Chen, Signal representation using adaptive normalized gaussian function. Signal Process. **36**(1), 1–11 (1994)
5. J.C. Xie, D.L. Zhang, W.L. Xu, Wavelet image de-noising review. Chin. J. Image. Graphics. **7**(3), 209–217 (2002)
6. S. Chu, S. Narayanan, C.-C.J. Kuo, Environmental sound recognition with time-frequency audio features. Proc. Audio. Speech. Lang. Process. **17**(6), 1142–1158 (2009)
7. P.L. Arthur, C.L. Philipos, *Voiced/unvoiced speech discrimination in noise using gabor atomic decomposition*. Proceedings of IEEE ICASSP, vol. 1 (IEEE Press, Hong Kong, 2003), pp. 820–828

8. K.Z. Yin, J.Y. Wang, J. Shao, Signal sparse decomposition based on structural properties of atom. Southwest Jiaotong Univ. J. **40**(2), 173–178 (2005)
9. P.J. Huber, Projection pursuit. Ann. Stat. **13**(2), 435–475 (1985)
10. J.Y. Zhao, Z.J. He et al., Generalized adaptive wavelet diagnosis in internal combustion engines. Vib. Meas. Diagn. **17**(3), 30–36 (1997)
11. G.L. Chen, X.F. Wang, Z.Q. Zhuang et al., *Genetic algorithm and application* (People's Posts and Telecommunications Press, Beijing, 1996)

Part III
Material Characteristics

Damage Evaluation in Consideration of Distance Decay and Frequency Characteristics of Elastic Wave

T. Shiotani, Y. Takada, H. Ohtsu, and T. Watanabe

Abstract Such parameters in the conventional elastic wave method, as frequency and velocity, connected to the damage so far, did not take the influence of the attenuation of propagation distance into consideration so that they were not able to directly connect to the index of degradation. This research studies the quantitative damage evaluation of heterogeneous materials by using frequency response characteristics of elastic waves according to the propagation distance for the purpose of establishment of the elastic wave degradation index which is not influenced by the propagation distance and frequency. Several mortar specimens, which were given by two types of styrene material simulating false cavity, were prepared for examination, and elastic waves were excited and propagated through the specimen. As a result, it was clarified that the quantitative damage evaluation of heterogeneous materials could be performed by comparing two detected waveforms in combination with the ratio of a frequency response.

1 Introduction

When evaluating the degree of damage of inhomogeneous materials such as concrete quantitatively by elastic wave methods, some parameters, such as elastic wave velocity, an attenuation slope of amplitude, and frequency, have been used as

T. Shiotani (✉) • Y. Takada • H. Ohtsu
Department of Urban Management, Kyoto University, Kyoto 6158530, Japan
e-mail: shiotani.tomoki2v@kyoto-u.ac.jp

T. Watanabe
Institute of Technology and Science, The University of Tokushima,
Tokushima 7708560, Japan
e-mail: watanabe@ce.tokushima-u.ac.jp

G. Shen et al. (eds.), *Advances in Acoustic Emission Technology: Proceedings of the World Conference on Acoustic Emission-2013*, Springer Proceedings in Physics 158,
DOI 10.1007/978-1-4939-1239-1_18,

indices of the evaluation so far [1]. However, as parameters such as velocity and amplitude depend on frequency, the former shows dispersion (a characteristic in which velocity changes depending on the frequency) [2–4], and the latter differs in a damping characteristic by the propagation distance as well as the frequency. Therefore, when associating such elastic wave parameters with deterioration, it is necessary to evaluate also paying attention to the frequency. Besides, high-frequency component of an elastic wave decreases not only by advance of deterioration of a propagation medium but also by the increase in propagation distance [5]. That is, even if we detect an elastic wave on the intact specimens, the frequency of the detected wave is different in the propagation distance. Therefore we cannot always represent the degree of damage with frequency features of the waveform. This research thus studies a quantitative damage evaluation index of heterogeneous materials which does not depend on the propagation distance and the frequency by utilizing frequency response characteristics of the elastic waves.

2 Methods

In case of discussing a feature of a detected wave by analyzing the spectrum of it, the spectrum does not coincide with the frequency component at the source. That is, AE signals are subjected to many different influences caused by the materials' properties along the wave ray path and the recording system (coupling condition, sensor characteristic, amplifier, and so forth). According to the concept of Fourier analysis, the outline can be shown as in Fig. 1.

AE waveforms are obtained as the convolution of functions of source, propagation media, sensor, and acquisition system in the frequency domain, and those frequency responses can be formulated by a simple multiple equation:

$$X(f) = U(f)T(f)D(f)S(f) \tag{1}$$

Here, $X(f), S(f), D(f), T(f), U(f)$ are Fourier transforms of the detected AE waveforms, AE source, propagation media, AE sensor, and acquisition system, respectively. $D(f)$ in Eq. (1) is a target to quantify the damage; however, as $S(f)$ is not readily obtained in AE technique, an approach to identify $D(f)$ irrespective to source time function is crucial. On the other hand, when $D(f)$ is dependent on propagation attenuation, $D(f)$ can be defined by Eq. (2) as well, where f is a

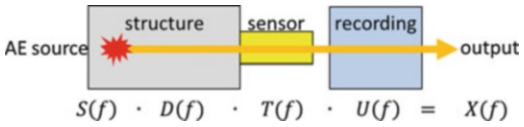

Fig. 1 An elastic wave detection route in AE testing

frequency (Hz), V is a P-wave velocity (m/s), and Q is a normalized value demonstrating attenuation rate:

$$D(f) = \exp\left(-\frac{\pi f}{VQ}d\right) \tag{2}$$

When the wave with energy level, E, is attenuated by ΔE over one wavelength propagation, Q is defined as

$$Q = \frac{2\pi E}{\Delta E} \tag{3}$$

The larger the Q value is, the lower the attenuation is, and Q value becomes larger than 1,000 for general metals, while Q value becomes lower than 100 for the case of concrete [6].

In AE application, multiple sensors are commonly employed to locate the AE source in 2D or 3D, and therefore the comparison of waveforms detected among different sensors for an AE source could suffice this requirement as shown in Eq. (4) assuming that the frequency responses of all the sensors employed are compatible:

$$\frac{X_2(f)}{X_1(f)} = \frac{T_2(f)}{T_1(f)} \cdot \frac{D_2(f)}{D_1(f)} \cong \frac{D_2(f)}{D_1(f)} \tag{4}$$

Furthermore, Eq. (5) is obtained by combining Eqs. (2) and (4):

$$\frac{X_i(f)}{X_1(f)} \cong \frac{D_i(f)}{D_1(f)} = \exp\left(-\frac{\pi f}{VQ}\Delta d_i\right) \tag{5}$$
$$\Delta d_i = d_i - d_1\,(d_i \geq d), (i = 2, \ldots, n)$$

Equation (5) shows that a function of the ratio of frequency responses can be expressed by an exponential function composed from the difference of distance, Δd, and frequency, f. In this regard, using the waveform with a smaller propagation distance for the denominator of the ratio of a frequency response, it is fixed that $\Delta d > 0$.

3 Experiment

In this study, as a preliminary phase to verify whether the above theory of the ratio of the frequency responses is applicable to the concrete, an inhomogeneous material, standard mortar was used as test specimens. The mix proportions of mortar specimens are shown in Table 1. Mortar prism specimens were prepared as seen in Fig. 2. All the sections were 150 × 150 mm with different heights of about 100, 200,

Table 1 Mix proportions of mortar specimens

Sand (kg)	Cement (kg)	Water (kg)	W /C (%)
1,475	491	270	55

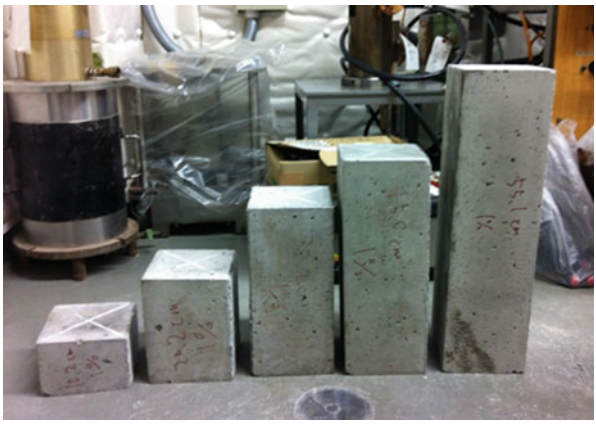

Fig. 2 Mortar test specimens (ϕ 6 mm, damage content of 1 %)

300, 400, and 500 mm to simulate different propagation distances. In order to reproduce damage, two types of spherical styrene balls (6 mm and 3 mm in diameter) were employed as a false cavity, and four kinds of the mix rate of 0, 1, 5, and 10 % by the volume were prepared. The reason why we adapted those two types of different diameter balls is that it has been reported that the attenuation characteristic of elastic wave was different in the size of inclusions even in the same mixing rate [2]. Elastic wave excitation was made by pencil lead break, and piezoelectric sensor of 60 kHz resonant was employed for the receiver. The signals were amplified by 40 dB, and processed and recorded by AE monitoring system (SAMOS, PAC) with 1 MHz sampling and 1 k samples. The elastic wave was excited in the center on the upper surface of a test specimen, and the receiving sensor was installed in the opposite side. In all the measurements, exactly the same receiving sensor was used, so that $T_2(f)/T_1(f)$ in Eq. (4) will perfectly become 1 in all frequency bands by removing the effect of the sensitivity error of the sensors.

4 Results and Discussion

The result of the case of ϕ 6 mm and damage content of 10 % is shown in Figs. 3, 4, and 5 as an example among two types of spherical styrene balls and four kinds of mix rates. As shown in Fig. 3 showing the frequency distribution, spectral content decreases according to the increase in propagation distance, and the amount of attenuation becomes larger as frequency becomes higher. So it can be suggested that this result well conformed to Eq. (2) which shows the attenuation by the distance. Since the frequency component of a detection waveform is changed this much by

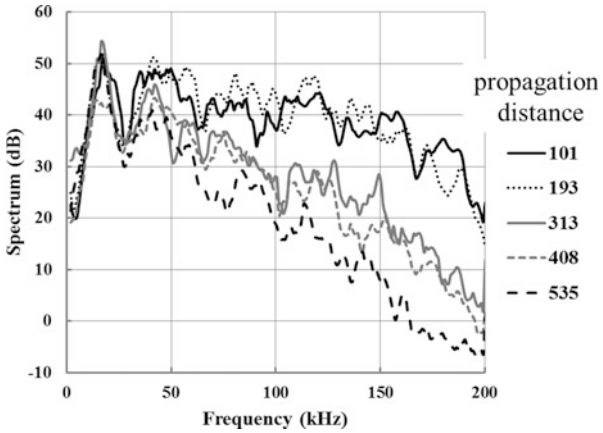

Fig. 3 Frequency distribution (ϕ 6 mm, 10 %)

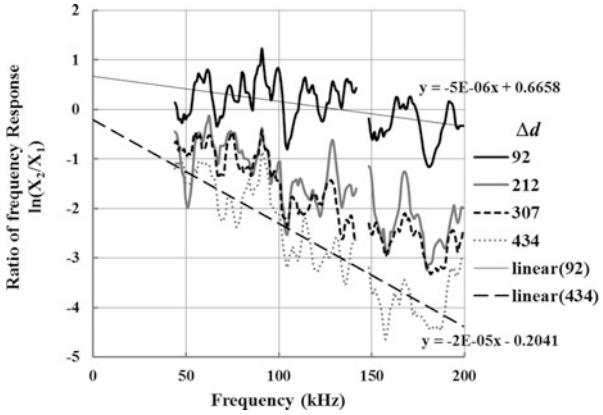

Fig. 4 Ratio of frequency responses (ϕ 6 mm, 10 %)

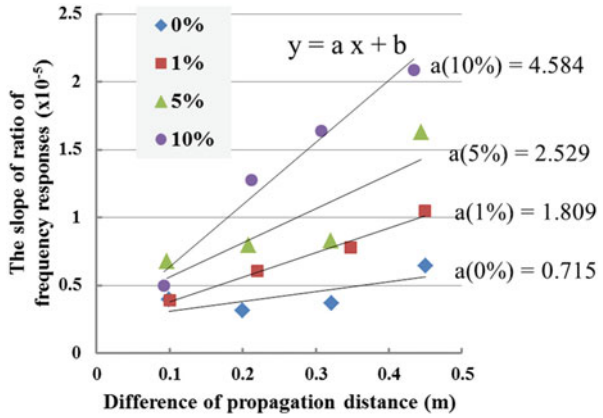

Fig. 5 Relation between slope of ratio of frequency responses and difference of propagation distance (ϕ 6 mm)

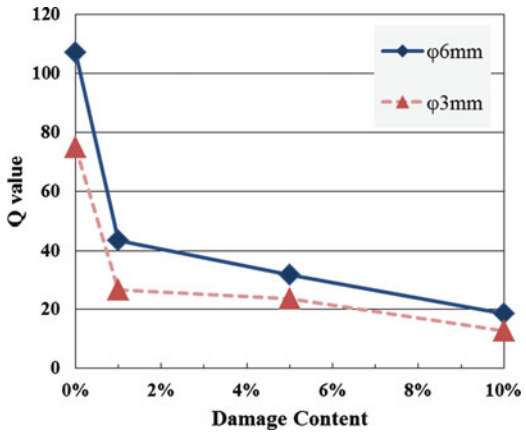

Fig. 6 Q value as a function of damage contents

propagation distance even in the same degree of damage, it turns out that it is not easy to evaluate damage only by one parameter, the so-called central frequency and peak frequency, which has been tried to use as indices of damage evaluation so far.

The ratio of frequency responses in case of ϕ 6 mm and damage content of 10 % calculated from detected frequency distributions by Eq. (4) is shown in Fig. 4. As it is expected that a frequency response ratio shows an exponential function, the logarithmic function is used for the vertical axis. The ratios of frequency responses of four kinds of distance differences are, respectively, obtained from the difference between the shortest propagation distance and other propagation distances. Linear approximations have applied to the ratios of Fig. 4 between 43–141 and 148–200 kHz, showing the frequency range of high sensitivity of the sensor employed. The approximation over the sensitive frequency range is crucial because other ranges are considered to be diverged when obtaining the ratio due to the very low sensitivity. Then the average inclination can be calculated by linear approximation of the frequency response ratio.

As seen in Fig. 4, the larger the difference of propagation distance becomes, the larger the slope of the ratio of frequency responses becomes, in harmony with the theoretical formula. The relation between the slope of the ratio of frequency responses and the difference of propagation distance to each damage mix rate in ϕ 6 mm are shown in Fig. 5. As seen, good correlations were obtained in any damage mix rate, and the inclination becomes large with the increase of the mix rate.

As the relations between the distance differences and this slope become linear, in Fig. 5, a can be defined by the following formula with linear approximation lines:

$$a = \frac{\pi}{VQ} \tag{6}$$

Q value can be calculated using this slope, a, and the P-wave velocity, V, which was obtained by another measurement. Figure 6 shows the Q value calculated by a

Table 2 Physical parameters

ϕ 6 mm damage content (%)	0	1	5	10
Density (kg/m^3)	2,236.00	2,213.75	2,124.75	2,013.51
P-wave velocity (m/s)	4,127.88	4,030.03	4,010.43	3,944.54
Young's modulus (GPa)	34.29	32.36	30.76	28.20
Damage parameter Ω	0.000	0.056	0.103	0.178
ϕ 3 mm damage content (%)	0	1	5	10
Density (kg/m^3)	2,236.00	2,213.75	2,124.75	2,013.51
P-wave velocity (m/s)	4,066.29	4,034.16	3,954.55	3,884.21
Young's modulus (GPa)	33.27	32.42	29.91	27.34
Damage parameter Ω	0.000	0.046	0.120	0.196

function of damage content. In case of both ϕ 6 mm and ϕ 3 mm, the Q value becomes smaller with increase of damage content. Comparing the result of ϕ 6 mm and ϕ 3 mm, all Q values of ϕ 3 mm show smaller values than those of ϕ 6 mm. This result exhibits in agreement with the result of past study [2], which is a characteristic that the attenuation becomes high if the size of mixture materials is small, even if a mixture rate is the same. However, it is noted that two results of 0 %, in which specimens have no styrene, namely no damage, show different Q values. This might be attributed to the heterogeneity of the specimen or a slight difference of sensors' setup condition or propagation paths. So, it cannot be concluded that this experiment verifies that the differences of Q value between ϕ 6 mm and ϕ 3 mm are caused by the size of mixture materials. However, it can be resulted that the Q value exhibits the unique value depending on the degree of damage by dimensionless quantity, and this is the very concept to quantify the damage of the materials with the frequency response ratio using AE waveforms.

According to the continuum damage mechanics, the state of damage is represented by the scalar damage parameter, Ω [7]. Young's modulus, E, of a damaged materials is expressed as

$$\Omega = 1 - \frac{E}{E*} \tag{7}$$

where Young's modulus, E^*, is that of an intact material. So, the damage parameter, Ω, depends on the ratio of Young's modulus of the intact state to that in the damage state, and this can be one of the quantitative damage evaluation indices. However, it is not easy to know the Young's modulus in an intact state, so methods to estimate it are intensively studied [8]. Hereafter, it will be verified whether this damage parameter can be associated with Q value, by examining the relation between Q value and Ω value calculated from this experiment.

Table 2 shows some physical parameters in this experiment. The relation between Q value and damage parameter, Ω, is shown in Fig. 7. Here, Young's modulus in the intact state, E^*, being necessary to calculate Ω value is regarded as that of 0 %, so that both Ω values of 0 % in ϕ 6 mm and ϕ 3 mm become 0.

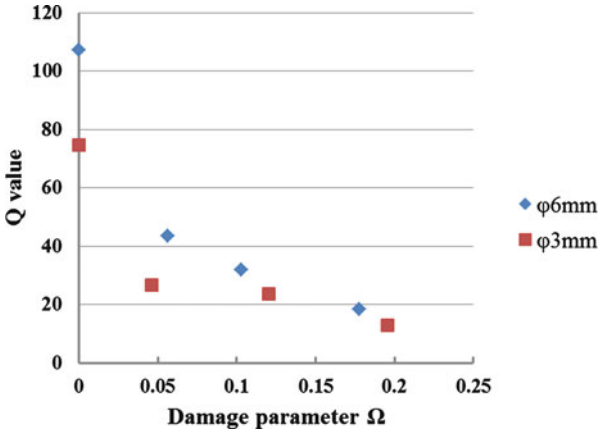

Fig. 7 Q value vs. damage parameter Ω

Comparing the results of ϕ 6 mm and ϕ 3 mm in the same damage content, the Ω values differ slightly by P-wave velocity and Young's modulus changing when the size of mixture materials changes. So, it turns out that the Ω value does not depend on only the quantity of air, but shows the comprehensive damage degree of the material. It will be difficult to evaluate the quantity of air from Q value directly because Q value depends on not only the porosity but also the shape and the size of the cavity, as shown in Fig. 6. However, it will be possible to evaluate the damage degree from Q value because Q value and Ω value have good correlation as shown in Fig. 7. In future, it is necessary to establish enough databases and to continue studying the generality of this relationship.

As shown in Fig. 7, the Q values decrease greatly when the Ω value increases from 0 to 0.05. That is, Q value has good characteristics of not only independence of propagation distance and frequency but also sensitivity to the initial damage stage, so this parameter is useful for screening the structures of which it cannot be evaluated the degree of damage from the surface state.

5 Conclusions

Paying attention to the ratio of the frequency response of detected waveforms, Q value analysis can be conducted by calculating more than one ratio of frequency responses, and thereby the attenuation characteristic of an elastic wave can be obtained. The Q value was discussed that it was the dimensionless quantity independent of the propagation distance and the frequency. Accordingly using the Q value as the damage index, the quantitative deterioration assessment in the initial damage state will be possible. Furthermore, in order to generalize the Q value as a damage index, the Q value should be verified in the ordinal concrete materials.

In practical applications, through the AE monitoring which identifies the emission source with multiple numbers of the same type of sensors, Q value can be

readily obtained, while the Q value with the AE monitoring represents the average of damage for the material of interest so that heterogeneous characteristics of the materials could not be evaluated with the current procedure so far.

References

1. T. Shiotani, D.G. Aggelis, Wave propagation in cementitious material containing artificial distributed damage. Mater. Struct. **42**, 377–384 (2009)
2. D.G. Aggelis, T. Shiotani, Effect of inhomogeneity parameters on wave propagation in cementitious material. ACI Mater. J. **105**, 187–193 (2008)
3. W.I. Futterman, Dispersive body wave. J. Geophys. Res. **67**(13), 5279–5290 (1962)
4. D.G. Aggelis, T. Shiotani, T.P. Philippidis, D. Polyzos, Stress wave scattering: Friend or enemy of non destructive testing of concrete?. J. Solid Mech. Mater. Eng. **2**(4), 397–408 (2008)
5. D. Polyzos, A. Papacharalampopoulos, T. Shiotani, D.G. Aggelis, *Dependence of AE Parameters on the Propagation Distance, Progress in Acoustic Emission XV* (The Japanese society for NDI, 2010), pp. 43–48 (2019)
6. M. Ohtsu, Sensor and instrument. in *Acoustic Emission Testing*, ed. by C.U. Grosse, M. Ohtsu (Springer, 2008), pp. 37–38
7. K.E. Loland, Continuous damage model for load—response estimation of concrete. Cement Concr. Res. **10**, 395–402 (1989)
8. T. Suzuki, M. Ohtsu, M. Shigeishi, Relative damage evaluation of concrete in a road bridge by AE rate-process analysis. Mater. Struct. **22**, 30–38 (2007)

Characteristic Identification of Cracking Acoustic Emission Signals in Concrete Beam Based on Hilbert-Huang Transform

Aijun Gu, Ying Luo, and Baiqiang Xu

Abstract Acoustic emission (AE) technique is a powerful and potential nondestructive testing method in civil engineering. The AE behavior of concrete beams tested under flexural loading was investigated to characterize and identify cracking damages. The AE signal characteristics were analyzed by Hilbert-Huang transform (HHT) which is suitable for analyzing nonlinearity and nonstationarity signals. It decomposes a signal into several intrinsic mode functions (IMF). By means of the digital image correlation (DIC) method, the cracking process was identified. With the theory of elasticity and simulation, the physical mechanisms of IMF were interpreted. The corresponding frequency behavior reasonably reflected the character of damage and wave propagation in different stages, especially in failure stage.

A. Gu
Key Laboratory for Mechanical Structure Damage Detection Technology of China Machinery Industry Federation, Faculty of Civil Engineering and Mechanics, Jiangsu University, Mailbox 84, 212013 Zhenjiang, China

School of Hydraulic, Energy and Power Engineering, Yangzhou University, 225009 Yangzhou, China
e-mail: ajgu@yzu.edu.cn

Y. Luo (✉)
Key Laboratory for Mechanical Structure Damage Detection Technology of China Machinery Industry Federation, Faculty of Civil Engineering and Mechanics, Jiangsu University, Mailbox 84, 212013 Zhenjiang, China
e-mail: luoying@mail.ujs.edu.cn

B. Xu
Faculty of Science, Jiangsu University, 212013 Zhenjiang, China

G. Shen et al. (eds.), *Advances in Acoustic Emission Technology: Proceedings of the World Conference on Acoustic Emission-2013*, Springer Proceedings in Physics 158,
DOI 10.1007/978-1-4939-1239-1_19,

1 Introduction

Acoustic emission technique (AET) is a powerful and potential nondestructive testing method in civil engineering. In the development of AET, the source identification is a cornerstone. AE signals occurring from structural deterioration contain a wealth of damage information. The feature information can be extracted by using suitable processing method to identify the damage. Some methods have been proposed for these purposes, such as Fourier spectrum analysis and time–frequency analysis. The spectral analysis is always used to describe the frequency feature of signals, which reflects some physical mechanisms. But it is not suited to the case when the signal frequency characteristics are varying with time. The time–frequency analysis comprises those techniques that study a signal in both the time and frequency domains simultaneously, using various time–frequency representations, such as short-time Fourier transform, wavelet analysis [1, 2], Wigner-Ville distribution [3], and HHT [4]. The objective of time–frequency analysis in AET is to establish the relationship between damages and AE characteristics. It is important to determine an appropriate signal processing method to investigate the characteristics from a huge number of AE signals. The HHT method which is suitable for dealing with nonlinear and nonstationary signals is used in AET in recent years. It is unique and different from other methods of data analysis, and is truly an adaptive time–frequency analysis [5]. It does not require a priori functional basis. It decomposes a signal into several intrinsic mode functions (IMF) which correspond to some physical mechanisms. Understanding these mechanisms is helpful for identifying AE sources. But in civil engineering, it is difficult to relate a certain IMF of an AE signal to a real physical mechanism.

In this chapter, a four-point bending test was performed on a concrete beam to investigate the characteristics of AE signals in cracking process. The AE signals were analyzed by HHT method. By means of DIC method, the cracking process was identified. With the theory of elasticity and simulation, the physical mechanisms of IMF were interpreted. The instantaneous frequency corresponding to maximum instantaneous energy of a signal was presented to identify the damage states. The variation reasonably reflected the character of damage and wave propagation in different stages, especially in failure stage.

2 Hilbert-Huang Transform

HHT is a new type of signal processing method, which is very suitable for dealing with nonlinear and nonstationary signals. It is composed of two parts [6]. First, the data are decomposed into a set of IMF and a residue through an adaptive method of EMD as

$$x(t) = \sum_{i=1}^{n} c_i + r_n \tag{1}$$

where $x(t)$ is a signal to be analyzed, c_i is the ith IMF component, n is the number of IMF, and r_n is the residue. The decomposition is based on the simple assumption that any data consist of different simple intrinsic modes of oscillations.

Second, applying the Hilbert transform to each IMF component, the following equation is obtained:

$$\hat{c}_i(t) = \frac{1}{\pi} \int_{-\infty}^{\infty} \frac{c_i(\tau)}{t - \tau} d\tau \tag{2}$$

Constructing analytic signal

$$z_i(t) = c_i(t) + j\hat{c}_i(t) = a_i(t) e^{j\phi_i(t)} \tag{3}$$

the amplitude function $a_i(t) = \sqrt{c_i^2(t) + \hat{c}_i^2(t)}$ and the phase function $\phi_i(t) = \arctan \frac{\hat{c}_i(t)}{c_i(t)}$ can be obtained. By computing the instantaneous frequency $\omega_i(t) = \frac{d\phi_i(t)}{d(t)}$, the Hilbert spectrum, which shows the time–frequency distribution of the amplitude, is finally obtained:

$$H(\omega, t) = \mathrm{Re} \sum_{i=1}^{n} a_i(t) e^{j \int \omega_i(t) dt} \tag{4}$$

In the process of EMD, if some IMF shows a characteristic of noise, which usually displays high frequency and undiminished character, it can be eliminated from the original signal. This provides a method of denoising.

3 Experiment

3.1 Specimen Preparation

Opening mode cracking of concrete is a simple and practical damage pattern in civil engineering. A plain concrete beam subjected to four-point bending was studied to investigate the characteristics of AE signals.

The beam was 150 mm wide, 180 mm high, and 1,500 mm long as shown in Fig. 1. It was reinforced with two thin steel wires in pressure side. Stirrups were also used in shear zone. The purpose of using rebar was to maintain the integrality of beam after collapse, and would not influence the fracture process of concrete beam.

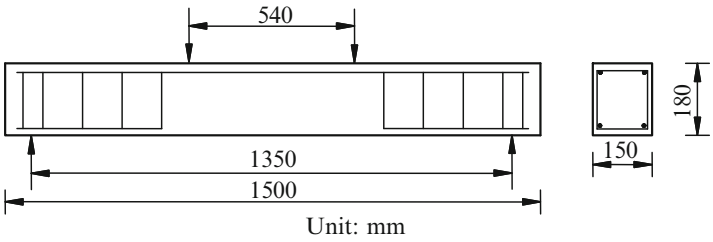

Fig. 1 Specimen setup and dimensions

Fig. 2 Experimental setup

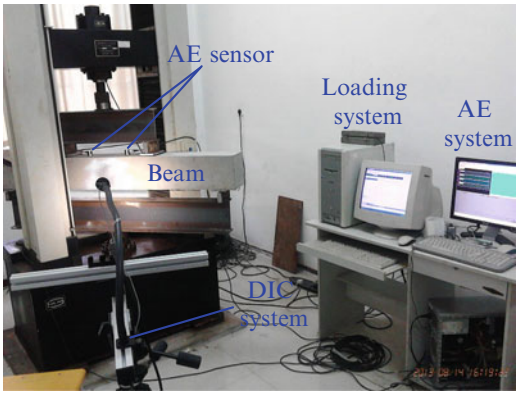

The normal aggregate with about 9 mm maximum diameter was used to satisfy the homogeneous assumption of concrete. Four wide-band AE sensors (PAC WDI-AST) were attached to the beam's surface by couplant to collect AE signals (Fig. 2). The tests were performed on a testing machine. The displacement-controlled loading method was used with the loading velocity of 2 mm per minute.

3.2 Experimental Method

In order to establish the relationship between AE signals and damage mechanism, the location and severity of cracking should be determined. The loading curve recorded by the testing machine can only reflect the accumulation of strain energy and the final collapse. The DIC method was used to calculate variation of strain field, and deduce the cracking process. DIC is an optical method that employs tracking and image registration techniques for accurate 2D and 3D measurements of changes in images. The experimental setup is shown in Fig. 2.

When a damage state is determined, the corresponding AE signals are picked out and analyzed using HHT. This analysis decomposes a signal into several IMF, which

will be analyzed to find the physical mechanism. This mechanism usually dominated by the formation of crack and was influenced by the propagation property of AE wave. Therefore, the geometry and material of the specimen should be considered. To assist the mechanism analysis, a numerical simulation was also performed.

4 Simulation

To better understand the mechanism of AE signals, a 2D finite element simulation was performed using Comsol Multiphysics software. This work focuses to the AE source mechanism and wave propagation in concrete beam. An AE event is simulated with an equivalent force. Considering the micro damage and macro cracking in concrete beam, two kinds of AE sources named point source and line source were modeled. The point source was modeled as a pair of internal forces named dipole, whose two forces were equal and opposite in direction and some distance apart. The line source was modeled as several continuous point sources, which were applied in sequence along the cracking direction.

The source force model of P. Hora [7] was used as

$$f_0(t) = at\exp(-bt) \tag{5}$$

where a and b are parameters controlling duration and amplitude of the source.

In addition, with the proceeding of damage, the stiffness of material between dipole forces was gradually attenuated. This was simulated by the weakening of elasticity modulus (E) to that material. The decay of E was simulated as

$$E(t) = E_0 \cdot S_\alpha(t) \tag{6}$$

where E_0 is elasticity modulus of undamaged material, and $S_\alpha(t)$ is attenuation function of elasticity modulus represented as

$$S_\alpha(t) = \frac{1}{1 + \mathrm{e}^{(t-t_0)/\alpha}} \tag{7}$$

where t_0 is the beginning of attenuation, and α is the parameter controlling attenuation velocity.

The geometric model used for simulating was the same as the experimental beam. The material was assumed as a homogeneous elastic media, which was reasonable in the case that the wavelengths were longer than the sizes of heterogeneous inclusions. Ono et al. [8] have elucidated the fact that the sensor of type WD used in our investigation primarily responds to the surface velocity motion rather than to surface displacement. So the vertical velocity component was collected at the sensor position on the surface [9].

5 Results

5.1 AE Characteristics of Simulated Signals

In simulation, the AE signals show different characteristics in source mechanisms, source location, distance of wave propagation, geometry of model, etc. Figure 3 shows three AE signals stimulated by a point source at bottom edge, a point source within the beam, and a line source. The signal emitted from the point source at bottom edge possesses a simple waveform which can clearly show the pressure

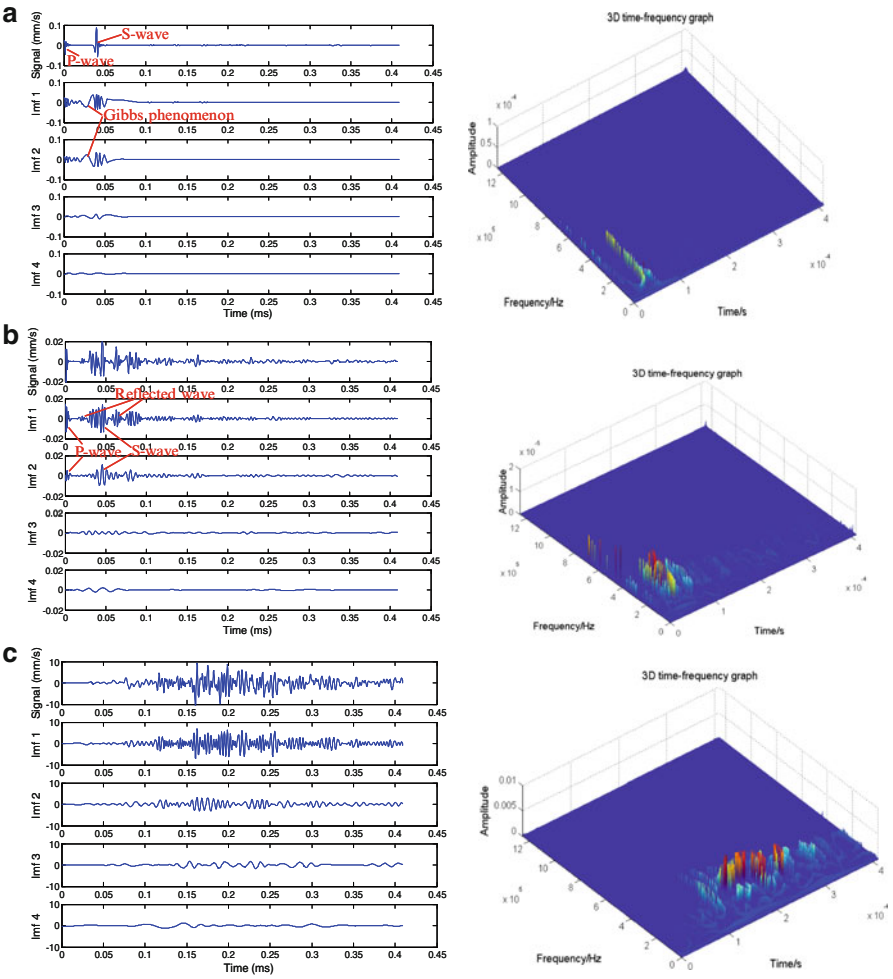

Fig. 3 Three types of AE signals by simulation. (**a**) A signal of point source at bottom edge. (**b**) A signal of point source within the beam. (**c**) A signal of line source

Table 1 Instantaneous frequency in different damages

Damage type	Frequency (kHz)
Point source at bottom edge	281.25
Point source within the beam (5 cm)[a]	312.5
Point source within the beam (10 cm)[a]	340.625
Line source (5 cm)[a]	215.625
Line source (10 cm)[a]	259.375

[a]From bottom edge

wave (P-wave) and shear wave (S-wave). Because it is started from the lower edge, the reflected wave is tiny in amplitude, and is far away from the main wave in time. When EMD method is used to this kind of signal, some pseudo information appears due to the "Gibbs phenomenon" (Fig. 3a). The pseudo information always shows high amplitude and low frequency characteristics, which should be ignored in source identification.

When an AE signal comes from a point source within the beam, the reflected wave emerges, which makes the waveform more complex than that of edge point source. The source is 5 cm above the bottom edge. The 10 cm round trip distance makes the reflected wave to be later than the direct wave for about 25 μs, which can clearly be seen in IMF 1 (Fig. 3b). In IMF 2, the reflected P-wave is not so clear because of attenuation. The P-wave and S-wave can easily be identified.

The line source always corresponds to a severe cracking with a certain length. The simulated cracking is 10 cm long, which is about half the length of the beam depth. Such a severe AE event releases big energy which makes the previous waveform vanishing. Continuous source emission makes various waves to be generated and superposed together, and produces a signal with long duration, large amplitude, and complex waveform (Fig. 3c).

Sometimes, two or more damages occur at different points of the beam simultaneously. The waves emitted from several point sources will interplay and generate complex signals. It is hard to identify the source mechanism by analyzing the complex signals in time domain. So the frequency characteristic was employed in the further analysis. The time–frequency distribution in Fig. 3 reflects the signal feature of different sources. For comparison, the instantaneous frequency corresponding to maximum instantaneous energy in a signal was used. Table 1 gives the change of instantaneous frequency in different damages. It is notable that the pseudo information caused by "Gibbs phenomenon" in the signal of point source at bottom edge was ignored.

It shows that there is a little increase in instantaneous frequency when the point source approaches the receiver (on upper surface). Also, the frequency increases with the growth of line source. But in general, the frequency of line source is lower than that of point source. This is due to the more degradation of concrete (expressed as the decrease of elasticity modulus) which makes the stiffness attenuate.

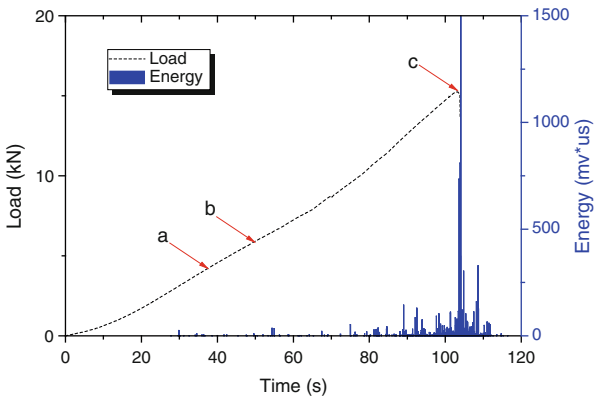

Fig. 4 Loading curve and the corresponding AE energy

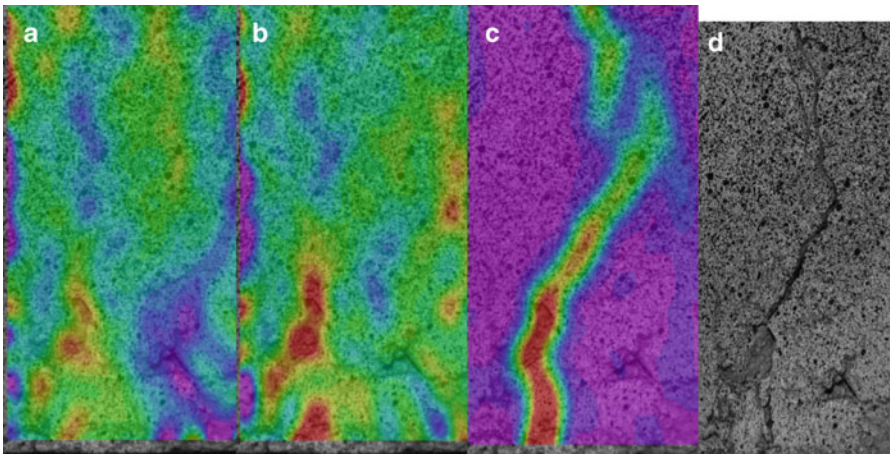

Fig. 5 Evolution of crack. (**a**) 38 s, (**b**) 48 s, (**c**) 103 s, (**d**) 104 s

5.2 Damage Evolution in Experiment

The load-time curve and the synchronous AE energy from one sensor are shown in Fig. 4. The horizontal strain field which indicated the cracking stages could be obtained from DIC method. Figure 5a–c shows the strain field from three typical instants which correspond to some AE active points marked a, b, and c in Fig. 4. From these strain distribution, the damage evolution, e.g., formation (a), development (b, c), and failure (d), can clearly be identified.

5.3 Analysis of Experimental Signals

Some typical AE signals from different crack patterns were picked out to analyze the characteristics. The HHT method was used to help identify the physical mechanisms. It can be seen from Fig. 5a that the initial damage is the degradation of concrete at several points (red zone) in tension side of the beam. Then the developments of damage (Fig. 5b, c) lead to crack nucleation and result in collapse of the beam (Fig. 5d). Figure 6 shows four signals emitted from initial damage (a), development of damage (b), largish development of crack (c), and collapse (d), which are corresponding to four instants in Fig. 5, respectively. The first four IMF and the 3D time–frequency distribution are also shown in the figure.

The signal of Fig. 6a (corresponding to Fig. 5a) was emitted from one or several points within the beam. There are more influences in experiments which make the signals more complex. However the first IMF shows similar characteristics with that of simulation (Fig. 3b, point source within the beam).

The signal from development of damage (Fig. 6b) shows long duration character. In the first IMF, several closer waves indicate the source of multipoint excitation. The high frequency and undiminished signal component is regarded as noise which may be caused by shattering of local concrete. The second IMF is the main component which possesses the biggest energy of the signal. The regular change of wave enveloping indicates that a point source dominates the signal.

The signal from largish development of crack (Fig. 6c) also has a relatively long duration. But the regularity of wave enveloping is not obvious in IMF, which is similar as the signal of line source (Fig. 3b).

The signal of unstable crack propagation (Fig. 6d) is different from other signals. The main character is the long duration which lasted in the sampling time. Also an obvious noise is shown in the first IMF. The second IMF reveals the major characteristic of the signal which is generated by excitation of continuous acoustic source.

Table 2 gives the change of instantaneous frequency of these typical signals. An important change law of instantaneous frequency can be found in the table. In the process of cracking, the frequency of signals generally reduces with the aggravation of damage. While in the instant of collapse, the frequency obviously increases.

The decrease of frequency is mainly due to the degradation of concrete. This shows that the degradation of concrete dominated the damage process before collapse. The true cracking is the last collapse which is regarded as a line source. In addition, it is a long line source which is relatively close to the receiver and makes the frequency of signal higher.

In experiment, the frequency is generally lower than that of simulation because of attenuation. In addition, the simplification to material and geometry and the idealization to calculation all influence the result.

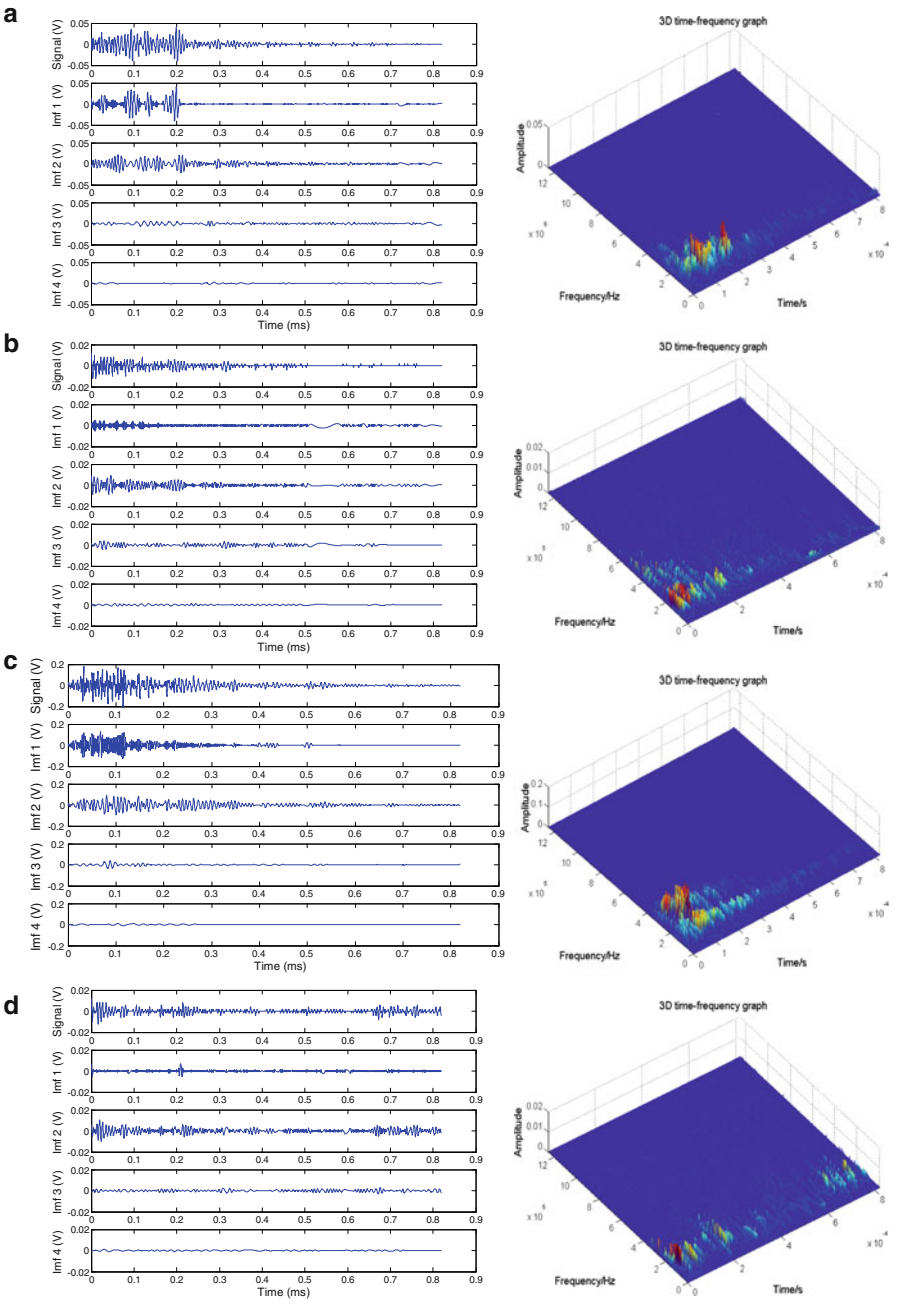

Fig. 6 Typical AE signals and their IMF (*left*), and their time–frequency distribution (*right*). (**a**) Initial damage. (**b**) Development of damage. (**c**) Largish development of crack. (**d**) Unstable crack propagation

Table 2 Instantaneous frequency of typical signals

Damage	Frequency (kHz)
Initial damage (a)	146.875
Development of damage (b)	137.5
Largish development of crack (c)	93.75
Collapse (d)	165.625

6 Conclusions

In this chapter, an experimental study as well as a simulation were performed on a concrete beam to investigate the characteristics of AE signals in cracking process. The AE signals were analyzed by HHT method. The following conclusions are obtained:

1. The signals from different points show different waveforms. The instantaneous frequency is a little increase when the point source approaches the receiver. Also, the frequency increases with the growth of line source. But in general, the frequency of line source is lower than that of point source. The periodicity of wave enveloping reflects the influence of boundary of geometry.
2. In experiment, the deterioration of concrete generally occurs from several points. Also, the main frequency of signals reduces with the aggravation of damage. While in the instant of collapse, the frequency obviously increases. This feature can be used as a warning signal.
3. There are some problems in using HHT method, such as "end effect," as is well known. Besides that, the "Gibbs phenomenon" produced in EMD may cause distortion in IMF, which makes the analysis more difficult.

Acknowledgment The authors are grateful to the Natural Science Foundation of China (No. 11272138 and No. 11172114) for supporting this work.

References

1. D. Yoon, W. Weiss, S. Shah, Assessing damage in corroded reinforced concrete using acoustic emission. J. Eng. Mech. **126**, 273–283 (2000)
2. A. Gu, Y. Luo, in *Proceedings of International Conference on Health Monitoring of Structure, Material and Environment*, ed. by A. Li. Characterization Extraction from Waveform Acoustic Emission Signals in Prestressed Concrete Structures (Southeast University Press, Nanjing, China, 2007), pp. 590–596
3. S. Holland, T. Kosel, R. Weaver, W. Sachse, Determination of plate source, detector separation from one signal. Ultrasonics **38**, 620–623 (2000)
4. C. Lu, P. Ding, Z. Chen, Time-frequency analysis of acoustic emission signals generated by tension damage in CFRP. Procedia Eng. **23**, 210–215 (2011)
5. N.E. Huang, S.S.P. Shen (ed.), *Hilbert-Huang Transform and Its Applications* (World Scientific Publishing, Singapore, 2005), p. 324

6. N.E. Huang, Z. Shen, S.R. Long, M.C. Wu, H.H. Shih, Q. Zheng et al., The empirical mode decomposition and the Hilbert spectrum for nonlinear and non-stationary time series analysis. Proc. R. Soc. Lond. A Math. Phys. Eng. Sci. **454**, 903–995 (1998)
7. P. Hora, O. Červená, Acoustic emission source modeling. Appl. Comput. Mech. **4**, 25–36 (2010)
8. K. Ono, H. Cho, T. Matsuo, Transfer functions of acoustic emission sensors. J. Acoust. Emiss. **26**, 72–90 (2008)
9. M.G.R. Sause, S. Horn, Simulation of acoustic emission in planar carbon fiber reinforced plastic specimens. J. Nondest. Eval. **29**, 123–142 (2010)

Acoustic Emission from Elevator Wire Ropes During Tensile Testing

Wenjie Bai, Mengyu Chai, Lichan Li, Yongquan Li, and Quan Duan

Abstract The acoustic emission (AE) technique was used to monitor the tensile testing process for two kinds of elevator wire ropes in our work. The AE signals from wire breaks were obtained and analyzed by AE parameters and waveforms. The results showed that AE technique can be a useful tool to monitor wire break phenomenon of wire ropes and effectively capture information of wire break signal. The relationship between AE signal characteristics and wire breaks is investigated and it is found that the most effective acoustic signal discriminators are amplitude and absolute energy. Moreover, the wire break signal of two kinds of ropes is a type of burst signal and it is believed that the waveform and spectrum can be applied to analyze the AE wire break signals.

1 Introduction

Wire ropes have been widely applied as a traction and bearing structure in industry such as coal, petroleum, and chemical and transport industries. However, some phenomenon such as wire breaks, fatigue, abrasion, and fracture are liable to occur in long-term use owing to poor working conditions. The damage condition and loading capacity of wire ropes directly related to the normal usage and worker's safety. Therefore, strengthening the research on failure feature extraction of wire ropes and developing new efficient detecting techniques possess a great significance [1, 2].

W. Bai (✉) • M. Chai • L. Li • Y. Li • Q. Duan
School of Chemical Engineering and Technology, Xi'an Jiaotong University,
28 Xianning West Road, Xi'an 710049, China
e-mail: bwj0319@gmail.com

G. Shen et al. (eds.), *Advances in Acoustic Emission Technology: Proceedings of the World Conference on Acoustic Emission-2013*, Springer Proceedings in Physics 158,
DOI 10.1007/978-1-4939-1239-1_20,

The acoustic emission (AE) phenomenon is based on the rapid release of energy within a material generating transient elastic wave propagation. AE technique has a high sensitivity and can detect the dynamic defects and conducts the continuous, online, and nondestructive monitoring [3]. In view of these advantages many researchers at home and abroad have performed related works. AE were firstly applied on nondestructive monitoring of wire ropes by J.F. Taylor and N.F. Casey from the UK. Casey reviewed the AE monitoring of wire rope and confirmed that the most realistic application of the method is in the detection and location of wire breaks. This review also showed that AE technique can be a useful laboratory tool, but application of the technique to ropes in service will probably be limited and specific to certain applications [4]. Shao Yongbo from Northeastern University firstly employed AE technique on defect monitoring of wire ropes at home, researched the failure of wire ropes, fatigue damage, noise elimination, and pattern recognition of wire breaks, and also confirmed the applicability of defect detection on wire ropes by AE technique [5–8]. G. Drummond investigated the relationship between acoustic emission signal characteristics and wire breaks and found that the most effective acoustic signal discriminators are energy and amplitude and the pattern of AE signals during a fatigue test was also studied [9]. Although many achievements have been acquired, to the best of our knowledge, few works or papers concentrated on the waveform and spectrum analysis of wire break signals.

So in this work, a tensile testing process of two kinds of wire ropes is investigated, firstly to find out the characteristic of wire break signals. Then the waveform and spectrum analysis of wire break signals are also discussed in detail.

2 Methods

AE signals generated during two kinds of elevator wire ropes in tensile testing process were collected and recorded by Macro-SAMOS AE monitoring system manufactured by Physical Acoustic Corporation (PAC). The software system applied is AE-win system researched by PAC. The voltage thresholds were set at 26 dB to eliminate noises. Two DP15I-AST sensors (50–350 kHz) with an integral 40 dB preamplifier were used to capture AE signals. Two fixtures were clamped in order that the sensors can be installed firmly. The distance between two sensors was 400 mm. The PDT, HDT, and HLT were set at 300, 600, and 1,000 μs, respectively. The parameters of AE collection are given in Table 1.

Table 1 The parameters of AE collection

AE channel	Threshold		Gain for preamplifier (dB)	Analog filter (kHz)		Waveform parameters		
	Type	dB		Minimum	Maximum	Sampling rate (M s^{-1})	Pre-trigger (μs)	Length (k)
1	Fixed	26	40	100	400	1	256	1
2	Fixed	26	40	100	400	1	256	1

Fig. 1 Platform of wire rope tensile testing

According to GB 8903-2005: *Steel wire ropes for elevators*, the two kinds of ropes we have used were dual tensile rope, $8 \times 19S + FC$ (fiber core) and $8 \times 19S + IWR$ (steel core). The diameter of wire rope specimens was 10 mm and the length was 1,000 mm. The tensile testing machine model is WAW-1000C manufactured by Jinan Test Group Corporation. The largest tensile force is 100 ton, and the minimum and maximum tensile speed is 0.1 and 50 mm/min, respectively. Figure 1 shows the platform of wire rope tensile testing. The method of first quick and then slow tensile speed was employed due to the good tensile strength and plasticity of wire rope. A tensile speed of 10 mm/min was first applied until the tensile force reached 20 kN, and then the tensile speed was changed to 5 mm/min until the tensile force reached 30 kN. The tensile speed was further reduced to 2.5 mm/min until the loading achieved 50 kN. Finally the tensile speed was adjusted to 1 mm/min until the wire rope strands fractured.

3 Results and Discussion

In the process of tensile testing, when we heard a large number of the "bang bang" wire break sound, we could find that some special and distinct wire break signals had been collected and recorded by AE monitoring system. These signals of the two kinds of ropes have the similarity and also have some differences.

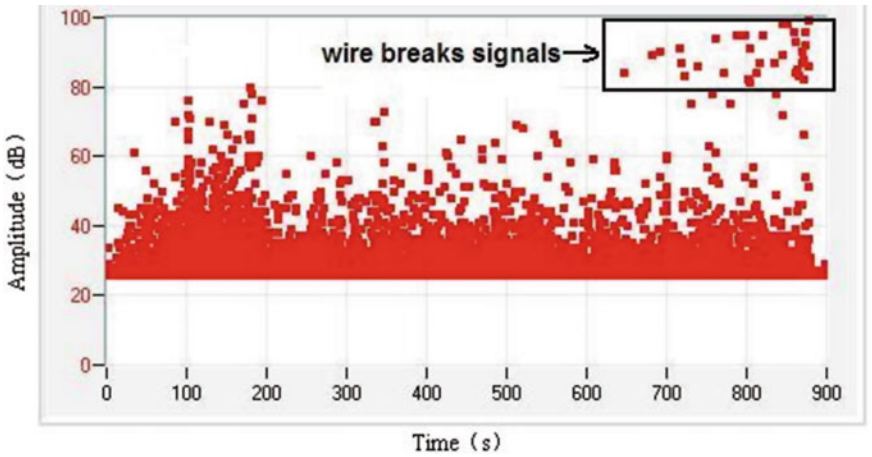

Fig. 2 Amplitude of FC rope wire break signals

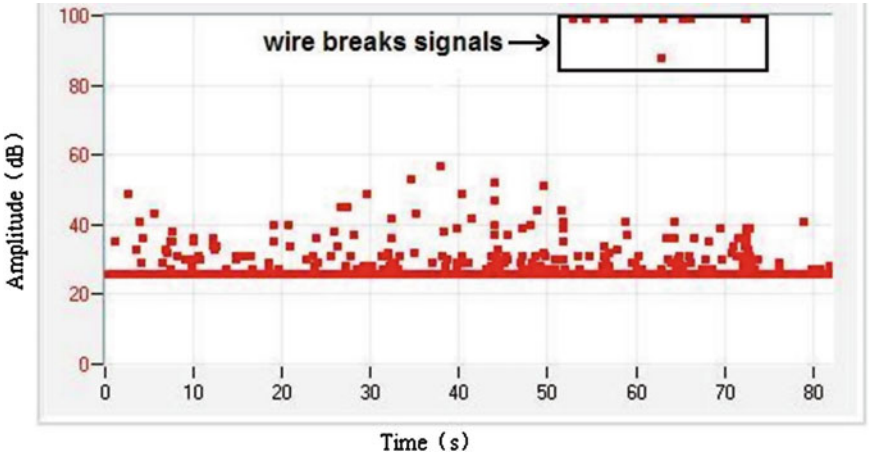

Fig. 3 Amplitude of IWR rope wire break signals

3.1 Amplitude

Figures 2 and 3 display the amplitude of wire break signals of FC ropes and IWR ropes, respectively. From the two figures we can see that the wire break signals of both ropes have higher amplitude than that of other signals and the amplitude mainly ranges from 80 to 100 dB. Therefore, high amplitude can be regarded as a feature to identify the wire break signals, which agrees well with the results of Drummond [9]. In addition, those AE signals with low amplitude may be caused mainly by mutual friction among steel wires or extrusion of fiber core in the rope.

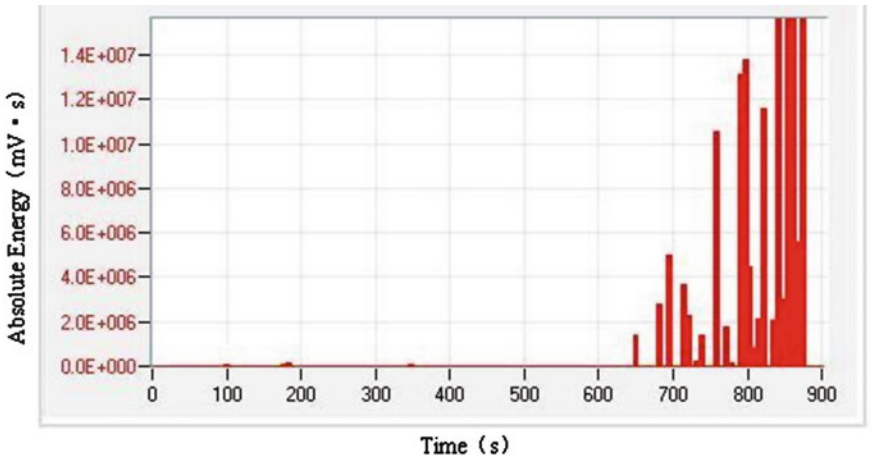

Fig. 4 Absolute energy of FC rope wire break signals

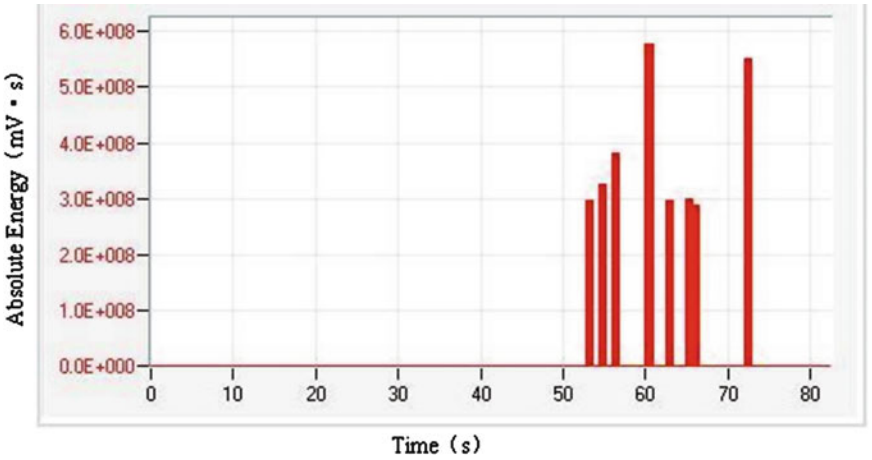

Fig. 5 Absolute energy of IWR rope wire break signals

3.2 Absolute Energy

Figures 4 and 5 show the absolute energy of wire break signals of FC ropes and IWR ropes. It can be seen from the two figures that the absolute energy of wire break signals is far higher than that of other signals when wire breaks occurred. Consequently, high absolute energy can also be used to characterize the wire break signals, which also agrees with Drummond [9]. Moreover, the absolute energy of IWR rope wire break signals is much higher than that of FC rope wire break signals.

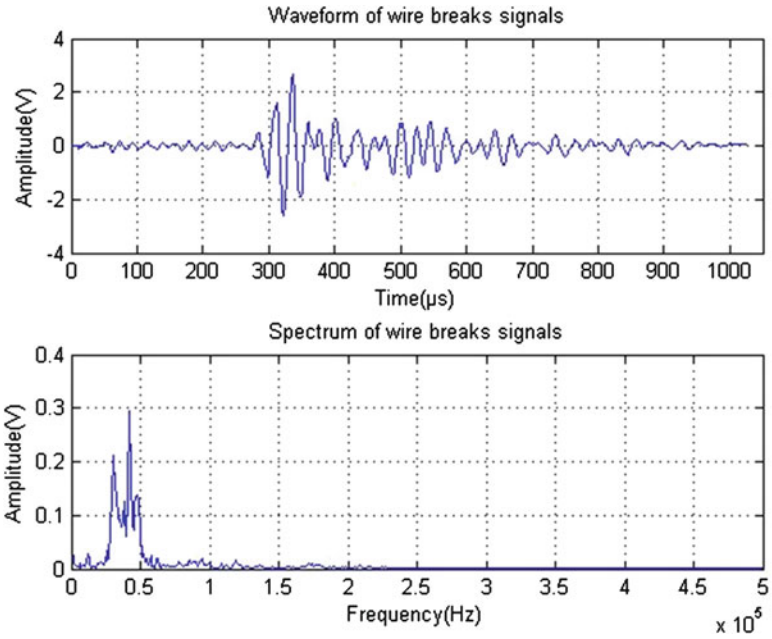

Fig. 6 Spectrum of FC rope wire break signals

The wire break signals can be characterized qualitatively when the absolute energy of FC rope and IWR rope wire break signals reached almost 2×10^6 mV s and 3×10^8 mV s, respectively.

In short, AE characteristics of the two kinds of wire ropes are different and the amplitude and absolute energy of IWR ropes are higher than those of the FC ropes. That is probably due to the difference of stiffness and strength of the two kinds of wire ropes. The most effective AE wire break signal discriminators are energy and amplitude. Therefore, AE technique can be used to identify wire break signals qualitatively very well.

3.3 Waveform and Spectrum Analysis

Parameter analysis of AE signals is a simplified process by which the information of complicated signals can be described by defining some characteristic parameters. Although the method is fast and easy, it cannot fully reflect the features of AE signals. Waveform analysis is an approach to study the primitive information of the AE signals and many professors and scholars try to apply waveform analysis to truly describe information and features of AE signals [10, 11].

Figures 6 and 7 depict the waveform and spectrum of wire break signals of FC ropes and IWR ropes. From Fig. 6 it can be seen that wire break signal of FC ropes

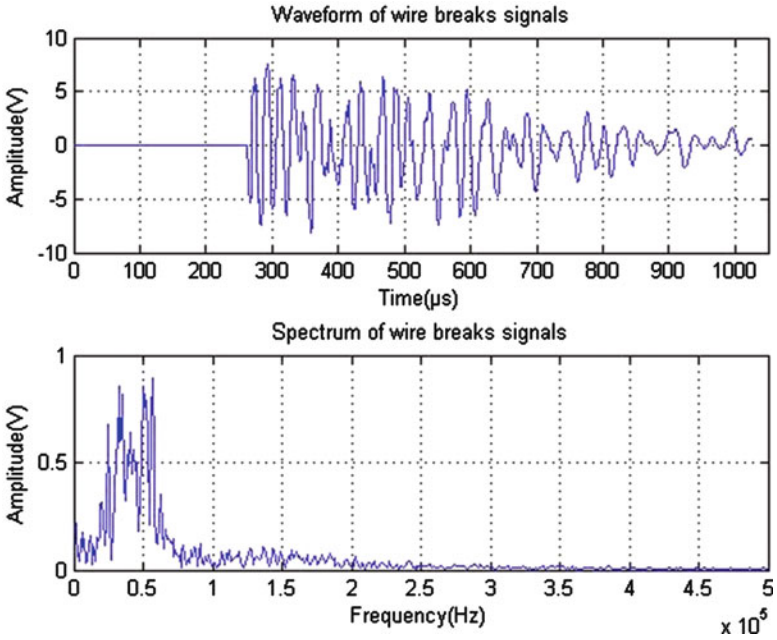

Fig. 7 Spectrum of IWR rope wire break signals

is a type of burst signal. The spectrum was obtained by fast Fourier transform and the frequency mainly ranges from 25 to 50 kHz. However, Fig. 7 presents that the wire break signal of IWR ropes is not a full burst-type signal. This is probably due to some information beyond the capture scope of sensors. It also can be seen from the spectrum that the frequency mainly ranges from 20 to 60 kHz.

Generally the waveform contains much information about the wire break signal. In this work we only analyzed the type and frequency range of the wire break signal. Factually, some modern digital signal processing technologies should be used to explore and analyze more information about the wire break signal. So it is believed that waveform and spectrum analysis can reveal more characters of the wire break signals to some extent.

4 Conclusions

The tensile testing process of the two kinds of wire ropes is investigated to find out the characteristic of wire break signals by parameter analysis and waveform and spectrum analysis. The following conclusions can be drawn.

First, the AE technique can be a useful tool to monitor wire break phenomenon of wire ropes and effectively capture information of wire break signal.

Second, the most effective acoustic signal discriminators are amplitude and absolute energy. The features of wire break signals are high amplitude and high absolute energy.

Third, the wire break signal of the two kinds of ropes is a type of burst signal and it is believed that waveform and spectrum can be applied to analyze some information about AE wire break signals.

Acknowledgment The authors would like to express their appreciation to all personnel involved in this research program for their technical guidelines and comments. The financial support from Shanxi Province industrial research program (No. 2012K06-22) is greatly acknowledged.

References

1. J.W. Tan, *Wire rope safety testing theory and technology* (Science, Beijing, 2009), pp. 3–10
2. F. Yang, B.L. Hu, Z.J. Zhou, An analysis on the research status quo and prospects of defect detection methods of wire ropes. Machinery Design & Manufacture. **2,** 260–262 (2010)
3. M.W. Yang, R.S. Geng, *Acoustic Emission Testing* (Engineering Industry Press, Beijing, 2005), pp. 110–115
4. N.F. Casey, P.A.A. Laura, A review of the acoustic emission monitoring of wire rope. Ocean Eng. **24**(10), 935–947 (1997)
5. Y.B. Shao, D.A. Yu, S. Wang, The method of noise elimination for acoustic emission detection of steel wire during fatigue test. Physics Examination and Testing. **6**, 21–24 (1998)
6. Y.B. Shao, Z. Pei, Z.M. Zhu, Pattern recognition for wire breakage detection of a steel rope by acoustic emission techniques. Appl. Acoust. **18,** 1 (1999)
7. Y.B. Shao, Z. Pei, D.A. Yu, Acoustic emission during fatigue damage of steel wire. Chinese J. Mat. Res. **14**(2), 163–166 (2000)
8. Y.B. Shao, Z.M. Zhu, W.Q. Yin, Fatigue damage of steel wire by acoustic emission monitoring. Iron and Steel **35**(3), 52–55 (2000)
9. G. Drummond, J.F. Watson, Acoustic emission from wire ropes during proof load and fatigue testing. NDT & E. **40**(1), 94–101 (2007)
10. G.T. Shen, R.S. Geng, S.F. Liu, Parameter analysis of acoustic emission signals.NDT. **24**(2), 72–77 (2002)
11. R.S. Geng, G.T. Shen, S.F. Liu, Acoustic emission signal processing technique based on waveform analysis.NDT. **24**(6), 257–361 (2002)

Effect of Specimen Thickness on Fatigue Crack Propagation and Acoustic Emission Behaviors in Q345 Steel

Junrong Li, Hongyun Luo, Zhiyuan Han, and Feixiang Jin

Abstract The effects of specimen thickness on fatigue crack growth rate (FCGR) and acoustic emission (AE) behaviors of Q345 steel were investigated. The four-point bending fatigue tests were carried out with AE monitoring simultaneously. Based on the thickness effect analysis, fatigue behavior studies, and AE investigations, the effects of specimen thickness on AE signal and AE source mechanisms during fatigue crack propagation were proposed. The results show that as specimen thickness increased, the FCGR was accelerated slightly, while the AE count rate was increased significantly, suggesting that AE signal was more sensitive to the changes in thickness. By analyzing the AE signals at the new plastic yielding area and the crack tip micro-fracture process, AE source mechanisms were explained. These results suggest that the effects of thickness must be considered to obtain a more accurate estimation of fatigue crack propagation through AE technique.

1 Introduction

Q345 steel is widely used in ship, building, pressure vessels, bridges, and other fields due to its excellent mechanical properties in China. In many cases, these steel structures are often subjected to alternating load which results in promotion of micro-cracks and crack propagation, causing a decline in strength and stiffness of steel or even fracture failure. Therefore, it is very important to analyze the fatigue crack propagation (FCGR) in Q345 steel.

J. Li • H. Luo (✉) • Z. Han • F. Jin
Key laboratory of aerospace advanced materials and performance (Beihang University), Ministry of Education, School of Materials Science and Engineering, Beihang University, Beijing 100191, China
e-mail: junrong619@163.com; luo7128@163.com

G. Shen et al. (eds.), *Advances in Acoustic Emission Technology: Proceedings of the World Conference on Acoustic Emission-2013*, Springer Proceedings in Physics 158,
DOI 10.1007/978-1-4939-1239-1_21,

The thickness of steel structures varies with different application conditions. So the effects of thickness on FCGR should be investigated. The effects of specimen thickness on FCGR had been investigated, but the explanations were generally conflicting. Some researchers reported that the specimen thickness had little effect [1, 2] whereas others reported FCGR increased [3, 4] or decreased [5] by increasing thickness. The paucity and diverse conclusions of presently available information concerning the effect of material thickness on FCGR provide little engineering guidance for the design of steel structures. Therefore, the effects of thickness on FCGR still need further investigations.

Acoustic emission (AE) is transient elastic waves generated by the rapid release of energy from a localized source within a material under stress. Fatigue crack growth is a well-known source of acoustic emission inside materials. Numerous studies [6–9] show that AE was capable of monitoring the fatigue crack propagation in steels. Thus, AE has been widely used as a nondestructive testing technique to detect the fatigue damage in different materials. An equation is proposed similar to the Paris law used to express the relationship between fatigue crack growth behavior and the AE parameters:

$$\frac{\mathrm{d}C}{\mathrm{d}N} = B(\Delta K)^p, \tag{1}$$

where C is the total AE counts, N is the fatigue cycle, $\mathrm{d}C/\mathrm{d}N$ is the AE counts rate, ΔK is the stress intensity factor range, and B and p are the constants for a particular material and test condition. It will be possible to use the information extracted from the crack-related AE signals to estimate the fatigue crack growth phenomenon. However, in the studies of AE behaviors during fatigue crack propagation, few researchers considered the effects of thickness. There is still lack of knowledge of the effects of thickness on AE behaviors. Therefore, in order to obtain a more accurate estimation of fatigue crack propagation, the effect of specimen thickness on AE behaviors still needs investigations.

In this study it is attempted to investigate the effect of specimen thickness on fatigue crack propagation and acoustic emission behaviors in Q345 steel. The four-point bending fatigue tests were carried out, and AE monitoring was performed simultaneously. Based on the thickness effect analysis, fatigue behavior studies, and AE investigations, the effects of specimen thickness on FCGR, AE signal, and AE source mechanisms during fatigue crack propagation were proposed for better application of AE to monitor the fatigue.

2 Methods

In this chapter, four-point bending fatigue tests are carried out to study the effect of specimen thickness on fatigue crack propagation and acoustic emission behaviors on a British made Instron 8801 servo-hydraulic testing machine at ambient temperature (300 K). The four-point bending specimens of different thickness

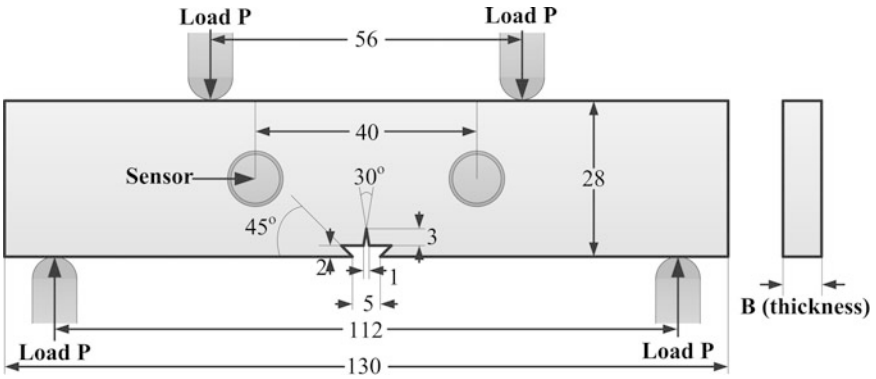

Fig. 1 Details of four-point bending specimen

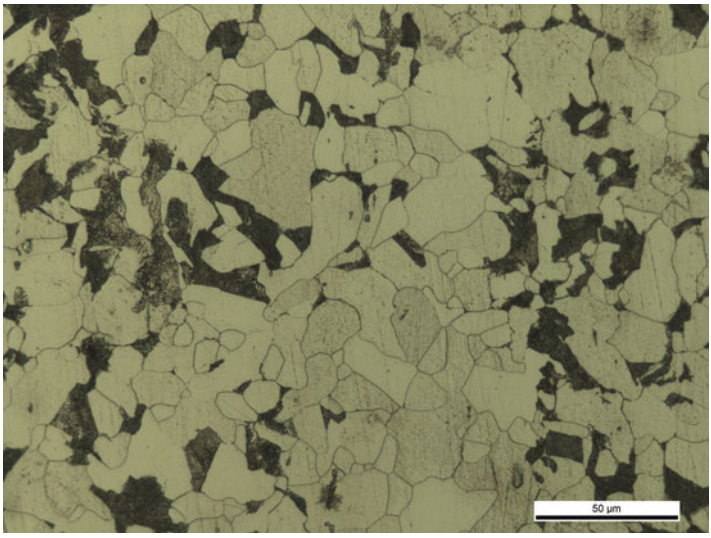

Fig. 2 Microstructures for Q345 steel

(7, 8.95, 13.73, 15.62, 19.01 mm) were processed by commercial Q345 steel along the rolling direction; the shape and dimensions of specimens are shown in Fig. 1. Figure 2 shows that the microstructure of Q345 steel was ferrite and pearlite. All specimens were tested under sinusoidal cyclic loading at a frequency of 8 Hz and load ratio of 0.1. The loading positions are shown in Fig. 1. The fatigue crack length was measured by a standard crack tip opening displacement (CTOD) gage, which had an accuracy of 0.01 mm and was set at the tip of the initial notch. The crack length data was recorded, and the stress intensity factor range was calculated from the crack length simultaneously.

After the fatigue tests, the fracture surfaces were observed using scanning electron microscope (SEM, Model: JSM-5800, JEOL, Japan).

AE signals generated during the fatigue tests were recorded and analyzed by using a DiSP with an AEwin v2.19 AE system (Physical Acoustic Corporation, USA). Two broadband piezoelectric transducers with a band-pass filter from 10 kHz to 2 MHz were used to pick up these AE signals. The sensors were attached to the specimen with a ring-shaped magnet. Vaseline was used at the interface between the sensors and the specimen surface to obtain proper signals. A preamplifier with 40 dB gain and a compatible filter (10 kHz–2 MHz) were used to capture AE signals. The positions of AE sensors are shown in Fig. 1. This position was also used to make a linear source location of the AE signals. The AE energy and average frequency thresholds were set to eliminate noises. The linear AE source location was also used to make sure that the obtained signals were generated from the crack area.

3 Results

The relationships between the FCGR (da/dN) and stress intensity factor ranges ΔK for different thickness specimens are plotted on the double-logarithmic axes in Fig. 3. The da/dN of all specimens was linear with ΔK on logarithmic axis range, which can be described by Paris–Erdogan as follows:

$$\frac{\mathrm{d}a}{\mathrm{d}N} = c(\Delta K)^m \tag{2}$$

where c and m are constants for a particular material. Figure 3 indicates that the FCGRs were increased as specimen thickness increased, but the amount of increase was small. This result was similar to the reference [3].

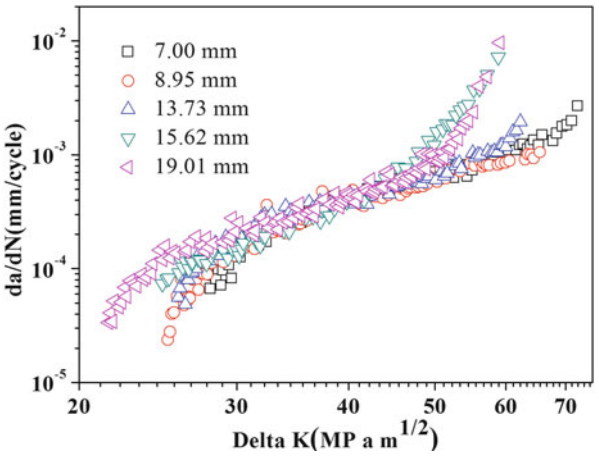

Fig. 3 Relationships between FCGR and ΔK for different thickness specimens

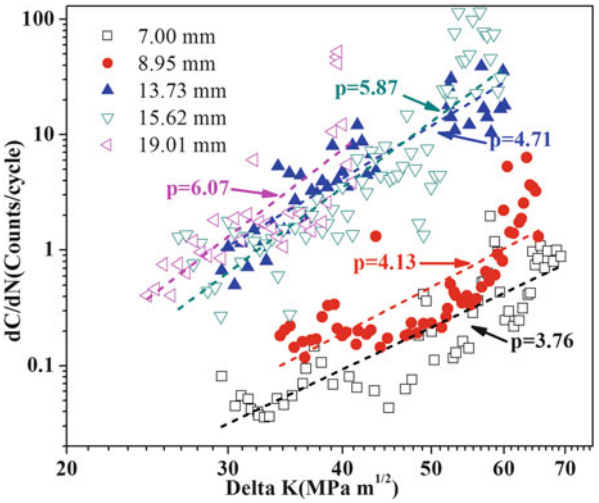

Fig. 4 Relationships between dC/dN and ΔK for different thickness specimens

Figure 4 shows the relationships between the AE count rates (dC/dN) and stress intensity factor ranges (ΔK) for different thickness specimens. The AE count rates increased in a linear relationship with the increase in ΔK on the log–log axes, which was well consistent with Eq. (1). Similar to the results of the crack growth rates, the higher AE count rates were observed in the thick specimens than in the thin specimens. However, in the 7.00 mm specimen and 8.95 mm specimen, the AE count rates were almost in the range of 0–1; in the 13.73, 15.62, and 19.01 mm specimen, the AE count rates were almost in the range of 1–100; there is a big difference in the AE count rates of different thickness specimens. In addition, the slopes of the lines for the thick specimens were higher than thin specimens also suggesting that the thick specimens generated more AE signals during fatigue crack propagation.

The scanning electron micrographs of fracture surfaces for different thickness specimens (8.95, 19.01 mm) in stable crack growth stage are shown in Fig. 5. Figure 5a, c indicates that the micro-morphologies in the edge of fracture surfaces revealed the ductile features of numerous tearing ridges. In the inside of fracture surfaces, there were mainly the flat facets, secondary cracks, and fatigue striations as shown in Fig. 5b, d. It suggested that the fatigue crack growth mechanisms for different thickness specimens were similar. The different micro-morphologies between edge and inside of fracture surfaces could be caused by the stress state. It is well known that the surface of a plate specimen is almost in the state of plane stress, while in its inside is in plane strain due to the constraints of strain in the thickness direction. Comparison of Fig. 6b, d shows that the depth of secondary cracks increased as specimen thickness increased.

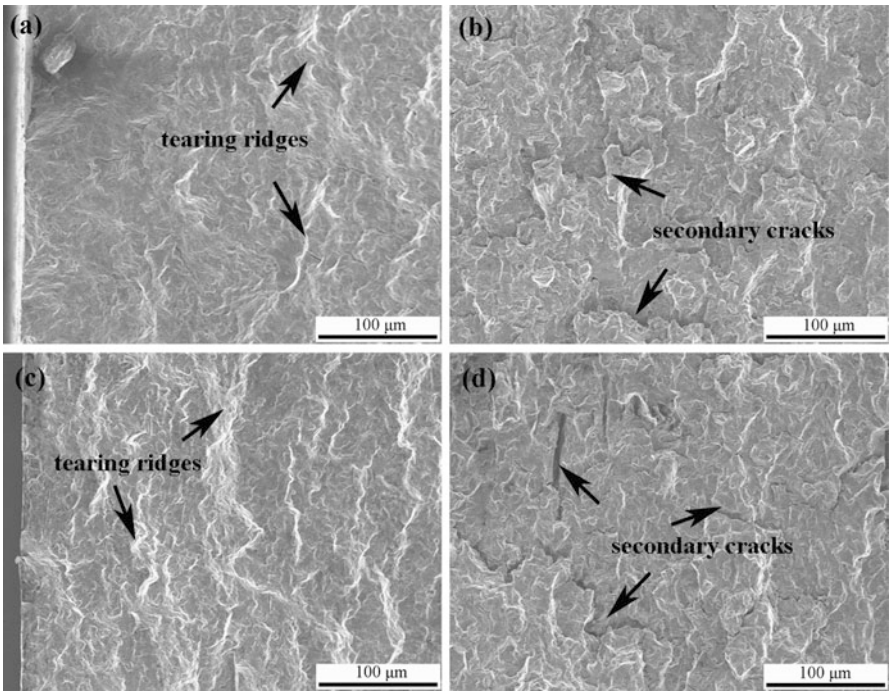

Fig. 5 SEM of fracture surfaces for (**a**)–(**b**) the 8.95 mm specimen and (**c**)–(**d**) the 19.01 mm specimen in *edge* (**a**, **c**) and *inside* (**b**, **d**), when the specimens were in stable crack growth stage

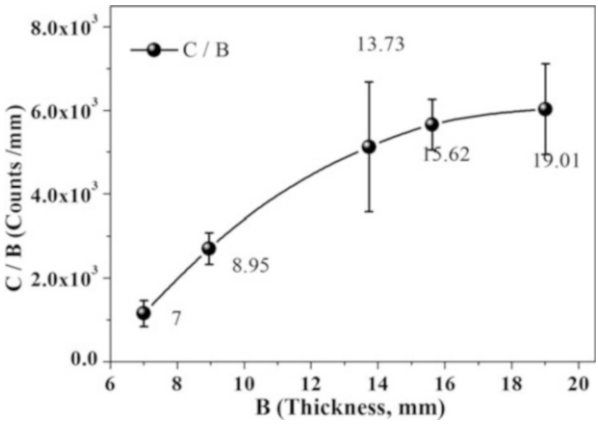

Fig. 6 The C/*B* for different thickness specimens ($a = 10$ mm)

4 Discussion

4.1 Effect of Thickness on Fatigue Crack Propagation

In this chapter, as specimen thickness increased, the FCGR was accelerated slightly (Fig. 3). Generally, thick specimens have more plane strain condition in the crack tip than the thin specimens in which a plane stress condition is dominant. It means that constraints of strain in the thickness direction increase with thicker specimens. Heung–Bae Park [10] concluded that the crack tip plastic deformation caused crack tip bluntness and stress transfer to promote further plastic deformation in the plastic zone and this plastic deformation decreased FCGR. From the above analysis, it is suggested that the less plasticity in thicker specimens leads to the crack growth rates accelerated slightly with the increase of specimen thickness.

4.2 Effect of Thickness on AE Source Mechanisms

Based on the analysis of Fig. 4, it is shown that the AE count rate was increased significantly as the specimen thickness increased. Some researchers [6, 11] proposed that micro-fracture process at the crack tip was an important AE source during fatigue. Therefore, the increase of AE parameters (AE count rate) by increasing thickness can be attributed to the larger cracking area. Assuming that fatigue crack grows a, the cracking area is A. The total AE counts, C, is directly proportional to A [6]. The relationship is described as Eq. (3), where α is constant. The total AE counts in unit thickness can be calculated according to Eq. (4):

$$C = \alpha \times A = \alpha B a. \tag{3}$$

$$C/B = \alpha a. \tag{4}$$

Figure 6 shows the total AE counts in unit thickness (C/B) for different thickness specimens ($a = 10$ mm). If the length of crack growth is same, the C/B is a constant according to Eq. (4). However, the C/B had a higher value in the thick specimen compared to the thin specimen shown in Fig. 6, suggesting that micro-fracture process was not the only AE source, and other AE sources existed which increased the AE signals as specimen thickness increased. The new plastic yielding at the crack tip was also considered as the important AE source during fatigue crack growth in metallic materials especially in a ductile material [6]. The combined contribution of micro-fracture process and new plastic yielding to AE count rate was described as Eq. (5) [11], where the first term in Eq. (5) is the contribution of new plastic yielding and the second is the contribution of micro-fracture process, R is the stress ratio, and C_p, C_s, and m are the constants for a particular material. In this chapter, because of the cracking area increase with increase in the thickness,

the volume created by new plastic yielding which was directly proportional to the total AE counts increases. So new plastic yielding is another AE source which increases the AE signals:

$$\frac{\mathrm{d}C}{\mathrm{d}N} = C_p \Delta K^m \frac{\Delta K^2}{(1-R)^2} + C_s \frac{\Delta K^m}{(1-R)^m}. \tag{5}$$

It can be seen in Eq. (3) that the cracking area in unit thickness is constant at the same crack length. However, as shown in Fig. 5b, d there were some secondary cracks in the inside of fracture surfaces in which a plane strain condition was dominant; the growth and connection of secondary cracks led to the increase of cracking area. Therefore, in thicker specimen, the region which is in plane strain state has more cracking area in unit thickness. It can cause the C/B increase by increasing thickness. The growth and connection of secondary cracks also play as extra AE sources which increase the AE signals. Simultaneously, it is also demonstrated in Fig. 6 that as the thickness increases, the C/B increases rapidly firstly, and then increases slowly. This trend of C/B may be caused by the stress state. In thin specimen such as 7.00 and 8.95 mm, the specimen surface which is almost in plane stress state plays an important role. With the increase in thickness, the proportion of plane strain in the specimen increases, which causes larger cracking area in unit thickness, so the C/B increases. For the thick specimen such as 13.73, 15.62, and 19.01 mm specimen, the plane strain condition is dominant. The difference between different thickness specimens becomes small. So the C/B increases slowly.

The AE signals during fatigue crack growth could be used to assess fatigue damage severity [12], and predict the crack length and remaining fatigue life [7–9]. The key point of applying AE to monitor fatigue is relating the AE signals to fatigue crack growth parameters. Based on the above analysis, the thickness of specimen has a significant effect on AE signals. So the effects of thickness must be considered to obtain a more accurate estimation of fatigue crack propagation through AE method.

5 Conclusions

In this study, the effect of specimen thickness on fatigue crack propagation and acoustic emission behaviors in Q345 steel has been investigated through the four-point bending fatigue tests and AE monitoring. Based on the detailed analysis, several conclusions can be obtained as follows:

As specimen thickness increased, the FCGR was accelerated slightly, while the AE count rate was increased significantly, suggesting that AE was more sensitive to the changes in thickness.

By relating the AE signals to the new plastic yielding, the crack tip micro-fracture process, and the growth and connection of secondary cracks, the major AE

sources are proposed. The inside of specimen which is in plane strain creates more cracking area due to the growth and connection of secondary cracks, and then produces more AE signals.

The thickness of specimen has a significant effect on AE signals. It is suggested that the effects of thickness must be considered to obtain a more accurate estimation of fatigue crack propagation through AE method.

Acknowledgment This work was financially supported by the following funds: (1) National Science and Technology Major Project: Life Management Technology of Nuclear Power Plant (No. 2011ZX06004-002) and (2) National Natural Science Foundation of China (No. 51175023).

References

1. A. Soboyejo, S. Shademan, M. Foster, N. Katsube, W. Soboyejo, A multiparameter approach to the prediction of fatigue crack growth in metallic materials. Fatig. Fract. Eng. Mater. Struct. **24**(4), 225–242 (2001)
2. A. Sullivan, T. Crooker, The effects of specimen thickness and stress relief on fatigue crack growth rate in nickel-chromium-molybdenum-vanadium steel. ASTM. J. Test. Eval **5**(2), 96–101 (1977)
3. H. Bao, A. McEvily, On plane stress-plane strain interactions in fatigue crack growth. Int. J. Fatigue **20**(6), 441–448 (1998)
4. A.A. Korda, Y. Mutoh, Y. Miyashita, T. Sadasue, Effects of pearlite morphology and specimen thickness on fatigue crack growth resistance in ferritic–pearlitic steels. Mater Sci Eng A Struct Mater. **428**(1–2), 262–269 (2006)
5. A. Jack, A. Price, Effects of thickness on fatigue crack initiation and growth in notched mild steel specimens. Acta Metall. **20**(7), 857–866 (1972)
6. A. Sinclair, D. Connors, C. Formby, Acoustic emission analysis during fatigue crack growth in steel. *Mater. Sci. Eng*, **28**(2), 263–273, 1977
7. T. Roberts, M. Talebzadeh, Acoustic emission monitoring of fatigue crack propagation. J. Constr. Steel Res. **59**(6), 695–712 (2003)
8. T. Roberts, M. Talebzadeh, Fatigue life prediction based on crack propagation and acoustic emission count rates. J. Constr. Steel Res. **59**(6), 679–694 (2003)
9. J. Yu, P. Ziehl, B. Zárate, J. Caicedo, Prediction of fatigue crack growth in steel bridge components using acoustic emission. J. Constr. Steel Res. **67**(8), 1254–1260 (2011)
10. H.B. Park, B.W. Lee, Effect of specimen thickness on fatigue crack growth rate. Nucl. Eng. Des. **197**(1–2), 197–203 (2000)
11. F. Hamel, J. Bailon, M. Bassim, Acoustic emission mechanisms during high-cycle fatigue. Eng. Fract. Mech. **14**(4), 853–860 (1981)
12. M. Rabiei, M. Modarres, Quantitative methods for structural health management using in situ acoustic emission monitoring. Int. J. Fatigue **49**, 81–89 (2013)

Acoustic Emission Behavior of Titanium During Tensile Deformation

Gongtian Shen, Lifei Li, Zheng Zhang, and Zhanwen Wu

Abstract Application of the acoustic emission (AE) technique allows investigating collective processes of plastic deformation at different time scales spreading from microseconds up to the duration of the mechanical test. This chapter presents acoustic emission (AE) characteristics of the commercially pure titanium during tensile deformation. The tensile test was carried out with samples of titanium TA2 at 293 K, which was continuously recorded by AE system using two types of AE sensors. The results show that higher AE signals were generated around yielding and fracture of the tensile loading for two types of sensors. The maximum amplitude of AE signals was 80 dB. The frequency distributions of AE signals for resonant sensor and broadband sensor are different. The resonant sensor shows a narrow band (135–160 kHz) of FMAX, while the broadband sensor shows a wide-range FMAX (90–330 kHz). And the FMAX of the broadband sensor with higher frequency (210–330 kHz) occurred around the yield point, and this phenomenon lasted until fracture.

1 Introduction

Acoustic emission (AE) is defined as the pressure or the stress waves generated during dynamic processes in materials [1]. It is well known that crystalline materials deform by specific deformation mechanisms and processes, and that detectable AE may be generated if the deformation processes are accompanied by a sudden stress

G. Shen (✉) • Z. Wu
China Special Equipment Inspection and Research Institute, Beijing 100013, China
e-mail: shengongtian@csei.org.cn

L. Li • Z. Zhang
Beijing University of Aeronautics and Astronautics, Beijing 100191, China
e-mail: tihutihu@163.com

G. Shen et al. (eds.), *Advances in Acoustic Emission Technology: Proceedings of the World Conference on Acoustic Emission-2013*, Springer Proceedings in Physics 158,
DOI 10.1007/978-1-4939-1239-1_22,

relaxation and/or strain accommodation. By this time, AE characteristics of titanium alloys have been studied [2–6]. AE during tensile deformation of Ti-6Al-4V alloy at low strain (<3 %) has been shown to be due to twin formation [2]. AE generated during compressive deformation of two-phase TiAl alloy with near-gamma microstructure has been attributed mainly to the formation of twins [3]. Ti-8A-1Mo-1V alloy was examined by AE wave analysis system during fracture toughness test, and AE source characterization indicated that many AE events correspond to the generation of micro cracks before the final fracture [4]. F. McBagonluri et al. used AE to track damage evolution of dwell fatigue crack growth in Ti-6242, and found similar damage mechanisms in all three microstructures, equiaxed, elongated, and colony [5]. Jalaj Kumar et al. studied AE of smooth and notched specimens of near-alpha titanium alloy [6]. The peak amplitude distribution of AE hits is shifted to lower amplitudes in notched specimens as compared to the smooth specimen. But few information is available about commercially pure titanium, which has been used more widely in the construction of facilities for the chemical industry and power generation [7, 8]. Furthermore, in their study, most researchers employed a narrow-frequency-band AE sensor (usually 100–300 kHz), which is only a fraction of the AE signals' broad spectral range. Therefore, there is still lack of knowledge of the relationship between the deformation and AE in this material.

In this chapter, the AE data generated during tensile test in commercially pure titanium was recorded. And the AE signals from two types of sensors were compared and analyzed, which were resonant type and broadband one. Based on the AE results, the AE source mechanisms and the deformation modes of the material were discussed as well.

2 Materials and Experimental Procedures

Commercially pure titanium TA2 was supplied as annealed plate. The chemical composition is given in Table 1. The specimens are cut out from 0° relative to the rolling direction of thin plate. These specimens had gauge length of 100 mm, width 15 mm, and thickness 4 mm.

The schematic of the experiment is illustrated in Fig. 1. Uniaxial tensile loading performed for specimens was carried out at 293 K (room temperature) using the mechanical testing machine Shimadzu AG-25TA at a strain rate of 1.4×10^{-3} s^{-1}. The AE measurements were realized with the AE system AMSY-6 (Vallen-System, Germany). Two resonant AE sensors with frequency bandwidth of 100–400 kHz (VS150, Vallen) were mounted on the specimen surface. A broadband AE sensor with frequency range from 100 to 900 kHz (VS900, Vallen) was mounted on the other side of the specimen. The output signals are amplified 34 dB by the preamplifiers.

Table 1 Chemical composition of TA2

Fe	C	N	H	O
0.09	0.02	0.01	0.001	0.13

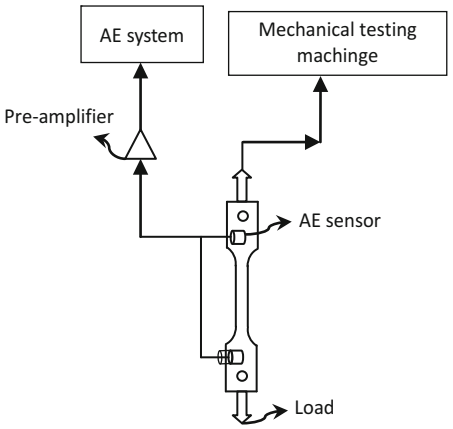

Fig. 1 Schematic of the experimental setup

Table 2 Mechanical property of TA2 plate

Rm	Rp0.2	A
445 MPa	340 MPa	27 %

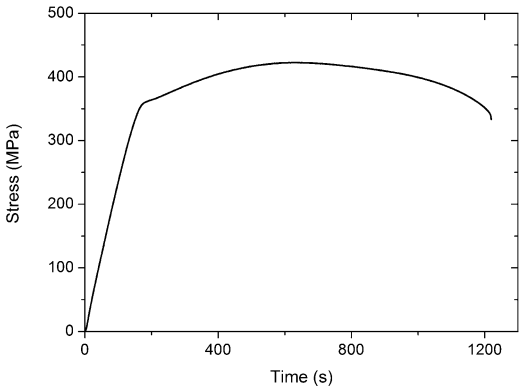

Fig. 2 Stress-test time curve of TA2 plate

The threshold was set as 36.6 dB and 40 dB for the resonant AE sensors and broadband AE sensor, respectively. AE data were recorded at a sampling rate of 5 MHz.

3 Testing Results

3.1 Tensile Properties

The strength and ductility of TA2 are shown in Table 2. The stress-test time curve under monotonic loading is given in Fig. 2. It exhibits smooth yielding at 293 K.

3.2 AE Activities During Tensile Deformation

The variation of load and AE parameters such as amplitude, count rate, and hit versus test time and the correlation diagram of amplitude and rise time for the commercial pure titanium specimen (TA2) are shown in Figs. 3 and 4. In Fig. 3a, just before the stage of yielding, a rapid increase in the AE amplitude is detected, which is from 40 to 80 dB. In Fig. 3b, c, it is obvious that just before the stage of yielding, the amplitude of AE signals increases with a concurrent increase in the AE count rate and hits. After yielding, the amplitude, count rate, and hits descended slowly until 243 s. Then, around the stage of necking, the amplitude, count rate, and hits increased continuously up to 703 s. Followed with a slight decline, AE parameters of amplitude, count rate, and hits raised again until fracture. These changes show that the magnitude and quantity of AE signals reached maximum around the stage of yielding, necking, and fracture. The trend during yielding and fracture is similarly shown in Fig. 4. But for necking in Fig. 4, the amplitude and amount of AE signals decreased sharply. Furthermore, the AE quantity and signal voltage of resonant sensor are higher than the broadband one, with an amazing ascent in the AE count rate and hits. As is shown in Figs. 3d and 4d, the correlation diagrams of amplitude and rise time for two types of sensors are similar.

3.3 AE Waveform Behavior During Tensile Deformation

After the test, the maximum frequency (F_{MAX}) is calculated for all AE wave signals. Figures 5 and 6 give the AE waveform behavior of two types of sensors for the whole processing of tensile loading. As presented in Fig. 5, results show a narrow band of distributing of F_{MAX}, which is mostly between 135 and 160 kHz. And the distribution is almost unvaried along with the test time. But for broadband sensor in Fig. 6, F_{MAX} is in a wider range, which is 90–330 kHz. And it clearly shows that the signals with higher frequency (from 210 to 330 kHz) occurred beginning in the yield point, and this phenomenon lasted until fracture.

Figures 7 and 8 give the AE wave and frequency spectrum of two types of sensors for polycrystalline pure Ti under tensile loading around test time 300 s. The first peak frequency in Fig. 8 is the same as peak frequency in Fig. 7. But for the resonant sensor, the second peak frequency in Fig. 8 is unable to be measured. In Fig. 6, F_{MAX} around 210–330 kHz appeared at the yield region and lasted for the whole test. It indicates that another deformation mechanism different from elastic stage occurred from the stage of yielding and lasted until fracture.

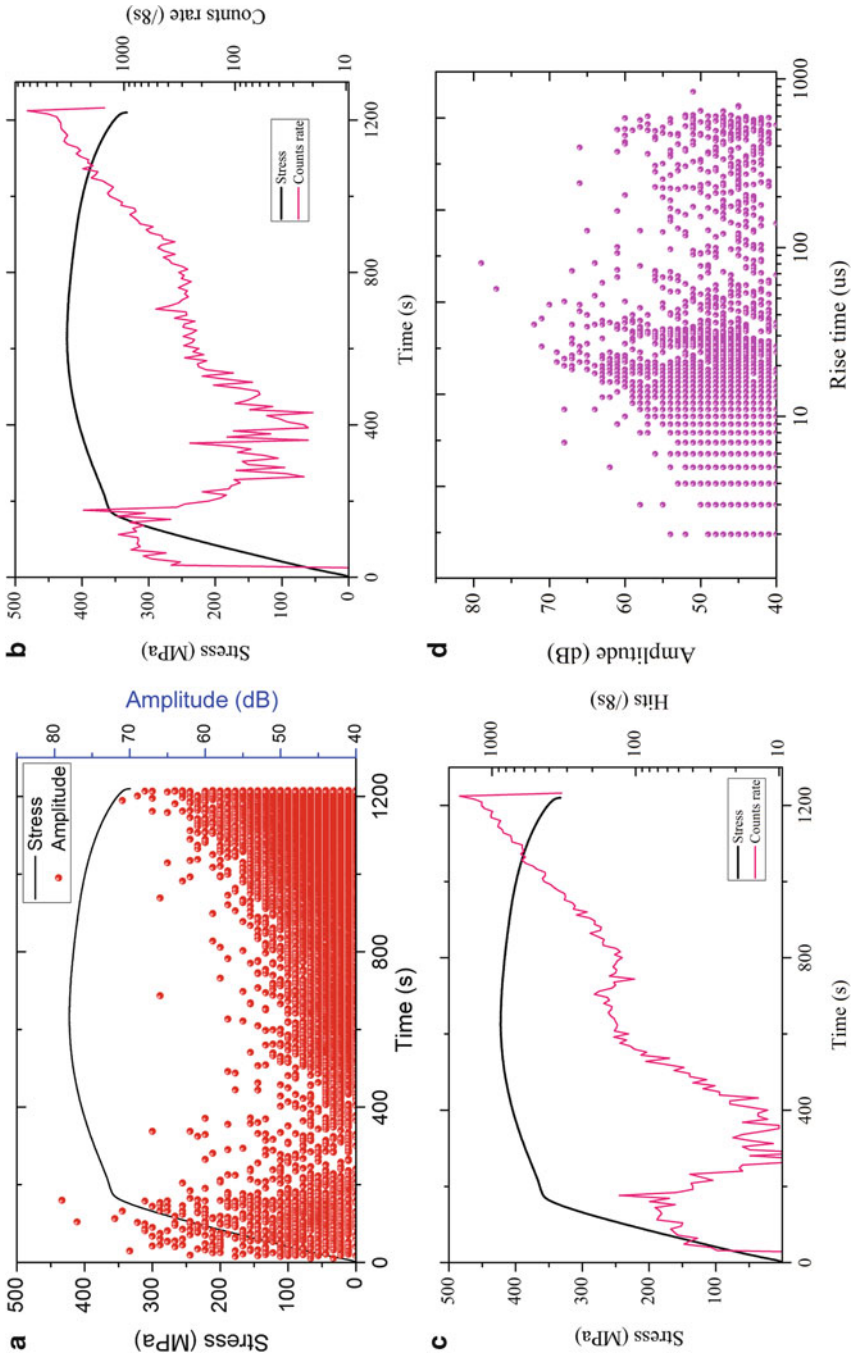

Fig. 3 Load and AE parameters vs. time for resonant sensor

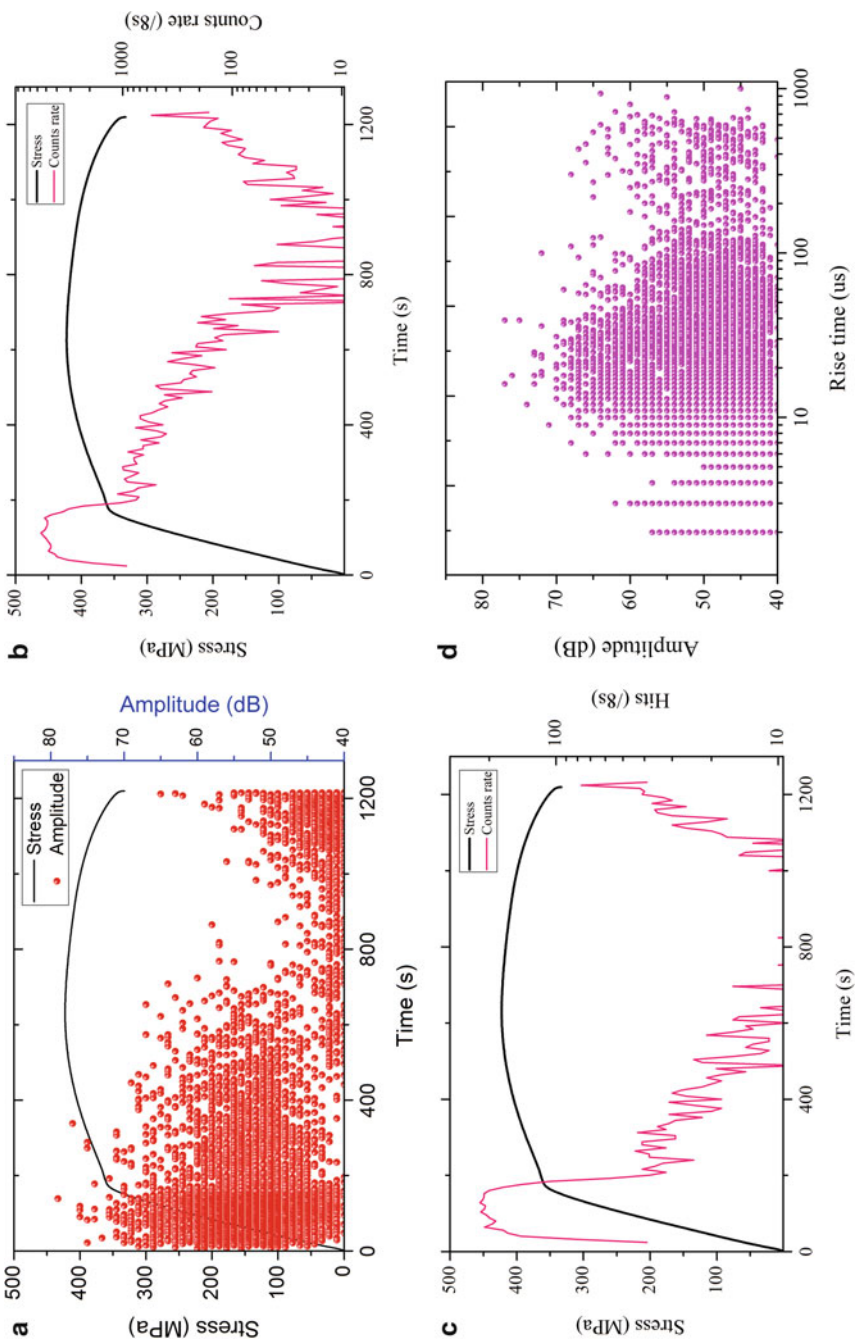

Fig. 4 Load and AE parameters vs. time for broadband sensor

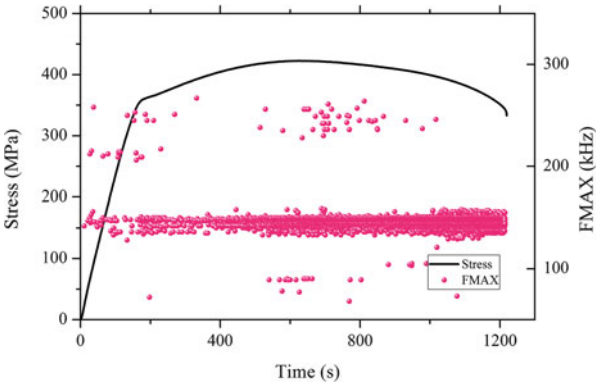

Fig. 5 F_{MAX} vs. time for resonant sensor

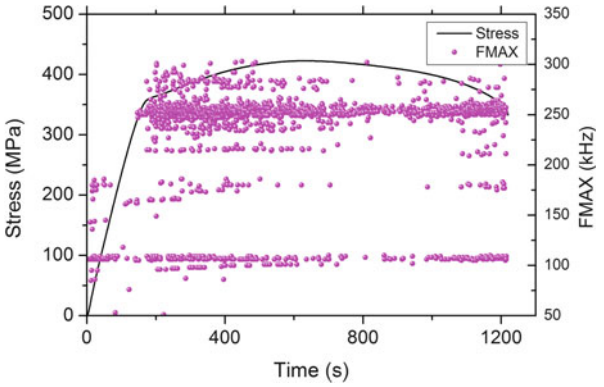

Fig. 6 F_{MAX} vs. time for broadband sensor

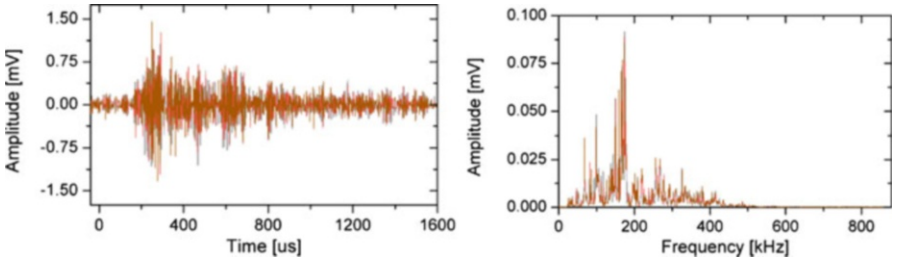

Fig. 7 AE wave and frequency spectrum for resonant sensor

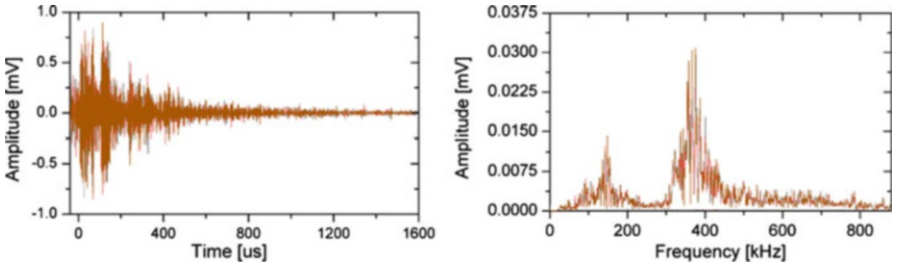

Fig. 8 AE wave and frequency spectrum for broadband sensor

4 Discussion

As mentioned above, the AE measured in tensile test is characterized by a pronounced peak at yield and fracture, and the AE waveforms are continuous in nature. Acoustic emission from dislocation sources generally reaches a maximum near yield [9]. Various researchers have noted prism slip (propagated as Luders bands) to be the primary mechanism at yield in single and polycrystalline alpha titanium. Thus, a relationship between the sources of AE in these regions and the deformation mechanisms responsible could be expected.

In this test, AE peak observed at yield region is primarily due to the initiation of dislocation slip. As well known, titanium is a material of hexagonal close-packed (HCP) structures. Due to the low symmetry of the HCP lattice, the basal slip system provides only two independent slip systems, which are less than five independent systems needed for a uniform deformation. Therefore, this makes the role of <c + a> slip modes and twinning modes, which can accommodate strain along the *c*-axis, important to determine. But after fracture, twinning was not observed in metallographic photo (Fig. 9). It indicates that deformation twinning did not occur while tensile and different dislocation slips took place in our experiment. For different slip systems activated at different conditions, the movements of slip systems are intermittent and last until fracture. Thus, the count rate and hits of AE signals presented a kind of behavior of fluctuation before rupture, other than smooth curves. This trend is already confirmed by the inflection points around yielding in Figs. 3 and 4. And the higher frequency AE signals (F_{MAX}: 210–330 kHz) appeared at the yield region and lasted for the whole test in Fig. 6 further evidencing that the AE sources were due to the movements of slip systems.

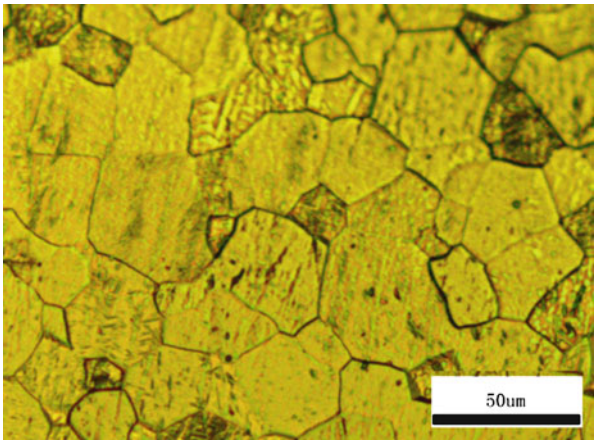

Fig. 9 A metallographic photo near fracture of specimen after tensile

5 Conclusion

According to the testing results, three AE characteristics of TA2 during tensile deformation can be drawn:

(a) The AE activities vs. test time recorded by resonant sensor and broadband sensor are similar for stages of yielding and fracture, that is, AE count rate showing avalanche behavior (first peak) around the early stage of yield point and another peak around the fracture region during tensile loading. But for resonant sensor, AE signals also increased during necking. The maximum amplitude of AE signals was 80 dB.
(b) The frequency distributions of AE signals for resonant sensor and broadband sensor are different. The resonant sensor shows a narrow band (135–160 kHz) of F_{MAX}, while the broadband sensor shows a wide-range F_{MAX} (90–330 kHz). And the F_{MAX} of the broadband sensor with higher frequency (210–330 kHz) occurred around the yield point, and this phenomenon lasted until fracture.
(c) The AE observed at the stage of yield is primarily due to the initiation of dislocation slip, and different systems of dislocation slips took place in the whole test.

Acknowledgment This study was financially supported by Chinese 12th five-year science and technology supporting project 2011BAK06B03.

References

1. R.K. Miller, P. McIntire, Acoustic emission testing, in *Nondestructive Testing Handbook*, ed. by R.K. Miller, P. McIntire, vol. 5 (American Society for Nondestructive Testing, Columbus, OH, 1987)
2. J.R. Kennedy, Acoustic emission during deformation of Ti-6Al-4V. Scr. Metall. **16**(5), 525–530 (1982)
3. F. Kauffmann, T. Bidlingmaier, G. Dehm, A. Wanner, H. Clemens, On the origin of acoustic emission during room temperature compressive deformation of a γ-TiAl based alloy. Intermetallics **8**(7), 823–830 (2000)
4. S. Mashino, Y. Mashimo, T. Horiya, M. Shiwa, T. Kishi, Analysis of microfracture mechanism of titanium alloy by acoustic emission technique. Mat. Sci. Eng. A. Struct. **213**(1–2), 66–70 (1996)
5. F. McBagonluri, E. Akpan, C. Mercer, W. Shen, W.O. Soboyejo, An investigation of the effects of microstructure on dwell fatigue crack growth in Ti-6242, Mat. Sci. Eng. A. Struct. **405**(1–2), 111–134 (2005)
6. J. Kumar, S. Punnose, C.K. Mukhopadhyay, T. Jayakumar, V. Kumar, Acoustic emission during tensile deformation of smooth and notched specimens of near alpha titanium alloy. Res. Nondestruct. Eval. **23**(1), 17–31 (2012)
7. M. Friesel, S. Carpenter, Determination of the sources of acoustic emission generated during the deformation of titanium. Metall. Trans. A. **15**(10), 1849–1853 (1984)
8. G. Murasawa, R. Takahashi, S. Orikasa, Intermittent twin region nucleation measurement using acoustic emission, in *Imaging methods for novel materials and challenging applications*, ed. by H. Jin, C. Sciammarella, C. Furlong, vol. III (Springer, New York, 2013), pp. 269–277
9. C.R. Heiple, S.H. Carpenter, Acoustic emission produced by deformation of metals and alloys – a review: Part I. J. Acoustic. Emission. **6**, 177–204 (1987)

A Study on Characteristics of Acoustic Emission and Position Entropy of Q345R in Tensile Loading at Room Temperature

Wei Li, Xin Jia, and Yu Yang

Abstract The tensile loading of Q345R was monitored in this study through acoustic emission at room temperature. The relationship between the mechanical process and the internal damage situation was established. The hits and accumulated energy of acoustic emission in the tensile loading of the specimen as well as the acoustic emission characteristics of Q345R in the tensile loading were obtained. By calculating the position entropy value of acoustic emission events, the damage to Q345R in the tensile loading was quantitatively described. We conclude that the position entropy value in the tensile loading changes at different stress states.

1 Introduction

Acoustic emission refers to the phenomenon wherein the transient stress wave emerges because of the rapid release of strain when the stress of the material or component exceeds the yield limit and reaches the irreversible plastic deformation stage or the formation, propagation, and fracture of cracks [1]. A corresponding relationship exists between acoustic emission and internal damage in the material. When a metal material is stretched, internal energy would accumulate and acoustic emission would occur when plastic deformation or crack extension is initiated. Acoustic emission signals contain important information on the acoustic emission source. The strained condition and degree of injury can be obtained through the analysis of the acoustic emission signal [2], damage degree, and other characteristics. Position entropy is the measure of system disorder (uniformity). The disordered degree of the system is high (more homogeneous) when the entropy value is large;

W. Li (✉) • X. Jia • Y. Yang
Mechanical Science and Engineering College of Northeast Petroleum University, Daqing 163000, China
e-mail: liweidqpi@163.com

G. Shen et al. (eds.), *Advances in Acoustic Emission Technology: Proceedings of the World Conference on Acoustic Emission-2013*, Springer Proceedings in Physics 158,
DOI 10.1007/978-1-4939-1239-1_23,

otherwise, the ordered degree is high (uneven). Position entropy has been used for the damage evaluation of rock [3]. For a metal structure where it is hard to keep long-time stress monitoring, the method of acoustic emission can be used. The method of position entropy can be checked to estimate the damage degree of metal structure. In this paper, monitoring the acoustic emission of Q345R at room temperature in the tensile loading and investigating the change of its position entropy, quantitative description of internal damage in simple component can be achieved, providing a foundation for the application of this method in complicated practical structural.

2 Acoustic Emission Signal Position Entropy

The concept of position entropy was applied in this study to quantitatively evaluate the order (concentration level) of acoustic emission events in spatial distribution at different stress levels. The definition of position entropy of acoustic emission events in spatial distribution is [4].

$$Q^N = -\sum_{i=1}^{R}\sum_{j=1}^{S}\sum_{k=1}^{T} P_{ijk}^N \times \frac{\log P_{ijk}^N}{\log(R \cdot S \cdot T)}. \tag{1}$$

where N is the total number of acoustic emission events collected. R, S, and T are the unit position areas in the length, width, and height direction of the specimen, respectively. P_{ijk}^N is the probability of the occurrence of acoustic emission events in the small area of (i, j, k), which can be replaced by relative frequency. Q^N is position entropy, which reflects the degree of order. The smaller this value, the higher the degree of order; otherwise, the lower the degree of order.

Problem (1) can be simplified as

$$Q^N = -\sum_{i=1}^{R}\sum_{j=1}^{S} P_{ij}^N \times \frac{\log P_{ij}^N}{\log(R \cdot S)} \tag{2}$$

The one-dimensional problem can be simplified as

$$Q^N = -\sum_{i=1}^{R} P_i^N \times \frac{\log P_i^N}{\log R} \tag{3}$$

In the analysis of the tensile testing of Q345R, the thickness of the specimen is considered much smaller than its length and width. The main problem is the damage in the longitudinal direction. The problem can thus be simplified as a one-dimensional problem, and the position entropy can be calculated by Eq. (3). In the calculation of the acoustic emission signal position entropy of Q345R in the tensile testing, we selected AE (Acoustic Emission) events to reflect the generation

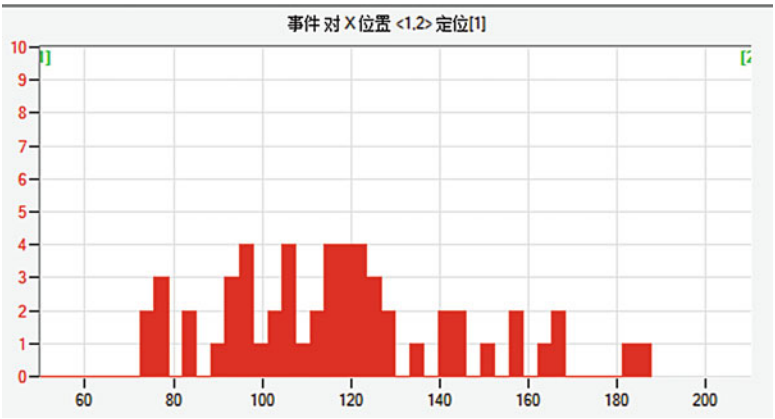

Fig. 1 Location of the acoustic emission event

of the acoustic emission source of specimen in the tensile testing and calculated position entropy, which corresponds to the initiation, expansion, and other microscopic processes of material internal defect.

Select the 23rd minute of tensile testing as an example, calculate the location entropy of Q345R. Evenly divide the tensile area that distanced 60–200 mm from sensor 1 by 20 mm, and count the number of acoustic emission events in each region. Put the number of acoustic emission events in each region and specimen size into Eq. (3); after calculation, the location entropy of tensile specimen at the moment was $Q^N = 0.837$. The location of acoustic emission events is shown in Fig. 1.

The introduction of noise in tensile loading will affect accuracy of the located acoustic emission events, which in turn affect the accurately calculating of position entropy, the pre-tension of specimen was applied before acoustic emission collection to prevent the friction interference in the process of tensile. Set the threshold of acoustic emission instrument to 40 dB to filter out environment noise.

3 Experimental Process

The load device was a 300 kN all-digital microcomputer-controlled electronic universal testing machine. The specimen was normalized at 900 °C, and the grain was refined to improve the toughness of the material for the tensile test. The loading method was uniform loading, and the loading speed was 1,000 N/min. The tensile testing was monitored through acoustic emission. The size and shape of the specimen are shown in Fig. 2. The monitoring system was a PAC PCI-8 digitized acoustic emission monitoring system, as shown in Fig. 3. The tensile test was conducted at 20 °C. The mechanical behavior and chemical component of Q345R are shown in Table 1. The system parameters of the acoustic emission testing system are shown in Table 2.

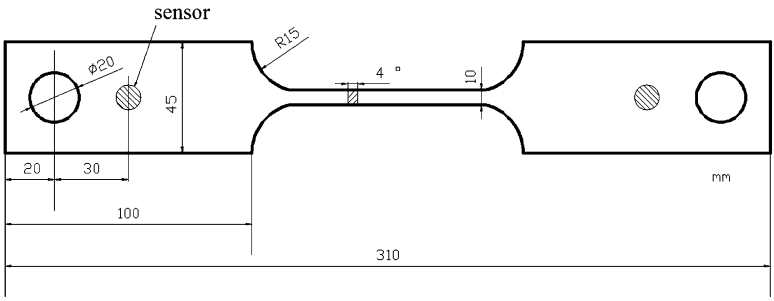

Fig. 2 Specimen shape and size

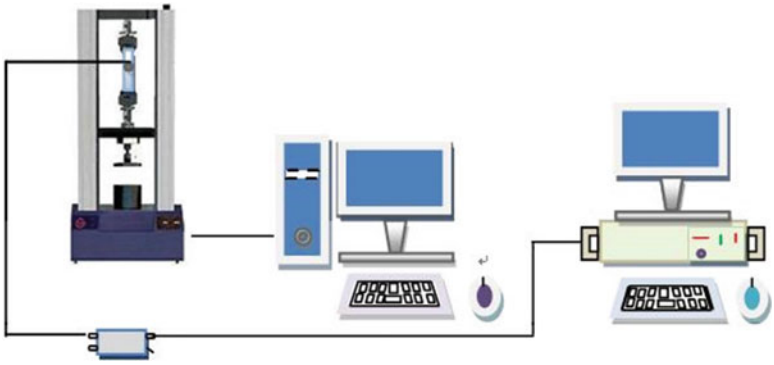

Fig. 3 Schematic of the acoustic emission experiment system

Table 1 Mechanical behavior and chemical component of Q345R

Q345 Mechanical behavior	σ_s	364 MPa
	σ_b	539 MPa
	E	364 GPa
	γ	0.3
	Ψ	4.58 %
	Φ	60.58 %
Q345 Chemical component	C	0.17 %
	Mn	1.42 %
	Si	0.019 %
	P	0.020 %
	S	0.010 %

Table 2 System parameters of the acoustic emission detection system

Parameter	Value
Threshold	40 dB
Sampling rate *C*	1,000 K/s
Peak definition time (PDT)	200 μs
Hits defined time (HDT)	600 μs
Hits lockout time (HLT)	800 μs

4 Analysis and Discussion of Experimental Results

Tensile testing of the first specimen was analyzed detailedly, the second and third specimen were for comparison analysis. The tensile curve is shown in Fig. 4. The points in the figure represent initial stretching point A, specimen yield point B, yield stage end point C, intensity limit point D, and breaking point E. Load displacement is shown in Table 3.

The position entropy in the tensile loading of Q345R was calculated every few minutes. The position entropy diagram of Q345R in the tensile testing was obtained after determining the statistics as shown in Fig. 5.

Position entropy can correctly reflect the concentration of microscopic damage in space and allows the approximate quantification of the evolution process of the interior defects in the tensile testing [5]. This study considered the hit count, accumulated energy, and position entropy of the tensile specimens to describe the change in the damage condition of Q345R at different stages. The energy–time variation diagram and hit count–time relationship of the acoustic emission signal in the damage tensile loading of the specimen are shown in Figs. 6 and 7, respectively.

The tensile damage process of Q345R was divided into four stages, namely, AB, BC, CD, and DE, corresponding to the stages of elastic deformation, yield, strengthening, and local deformation, respectively.

1. Elastic deformation stage (0–877 s, 0–364 MPa). AE hit and accumulated energy steadily increased in this stage, and the value of position entropy was large and

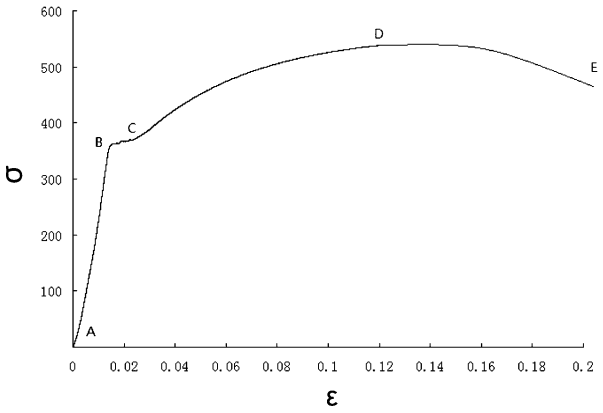

Fig. 4 Tensile curve

Table 3 Load displacement of the shift points of Q345

Transition point	Stress (MPa)	Displacement (mm)	Time (s)
B	364	1.27	877
C	386	2.34	928
D	539	9.66	1,310
E	440	16.40	1,631

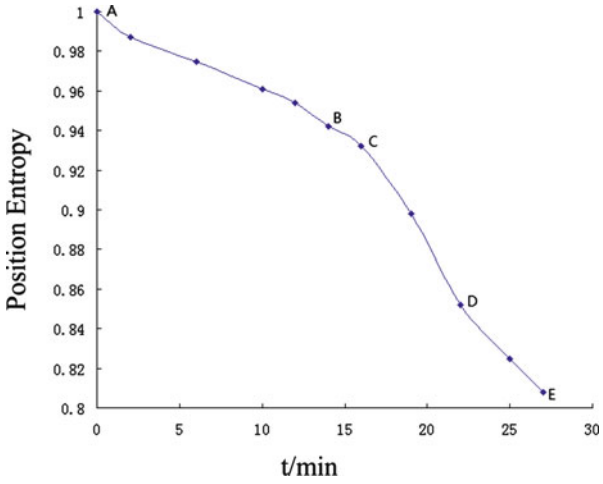

Fig. 5 Position entropy and time curve

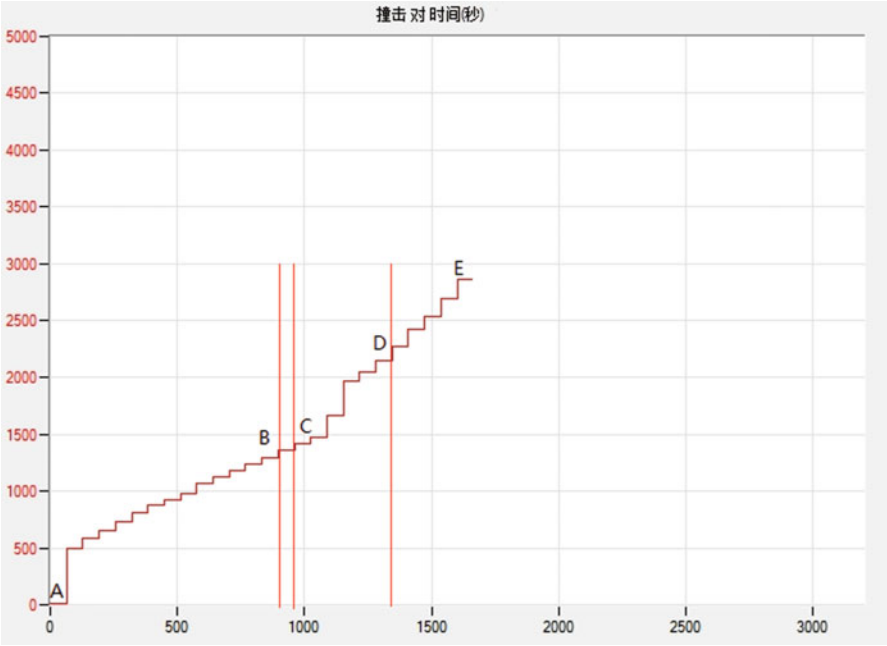

Fig. 6 Hit-to-time curve

decreased gradually. No obvious injury to the material was found in this stage. A small amount of acoustic emission was observed during the phase of loading in which damage from interface friction between inclusions and second phase particles has been documented to occur [5]. The distribution of acoustic emission events in space was dispersed, the degree of order was low, and the entropy value was large.

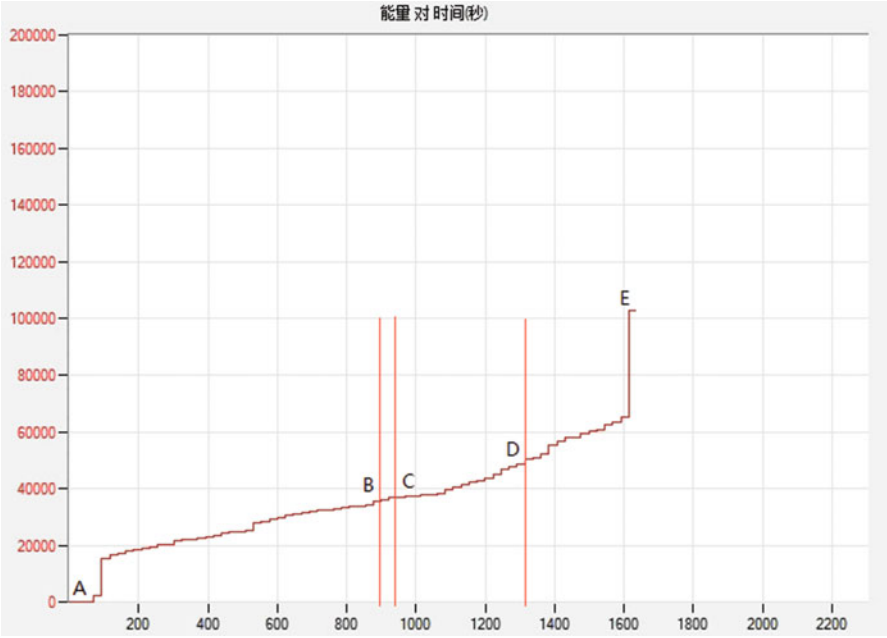

Fig. 7 Energy-to-time curve

2. Yield stage (877–928 s, 364–386 MPa). Strain increased even though stress exhibited no obvious increase in this stage. This condition was the initial stage of damage. AE hit and accumulated energy continued to increase in this stage, whereas the value of position entropy continued to decline steadily. The breaking of microholes between the inclusions and second phase particles and the detachment of inclusions from the substrate interface has been documented to occur. However, the position of the acoustic emission source was dispersed. The degree of distribution concentration of acoustic emission events in the space was low, and the value of position entropy remained large.
3. Strengthening stage (928–1,310 s, 386–539 MPa). The specimen was in a state of homogeneous strain in this stage. The damage developed further, AE hit and accumulated energy increased rapidly, and the value of position entropy decreased sharply. The microholes produced during the yield stage and the newly produced microholes grew under stress; nucleation began to occur along the surface of the grain boundary. The energy of the acoustic emission was high, causing cumulative energy to increase significantly. The spatial concentration of the AE events increased rapidly, and the value of position entropy fell sharply. These occurrences are prewarnings of serious internal injuries.
4. Local deformation stage (1,310–1,631 s, 539–440 MPa). When the stress in the specimen reached ultimate strength point D, the strength increase caused by work hardening was unable to compensate for the section shrinkage effect. Thus, necking occurred and the deformation of the material became uneven. A large

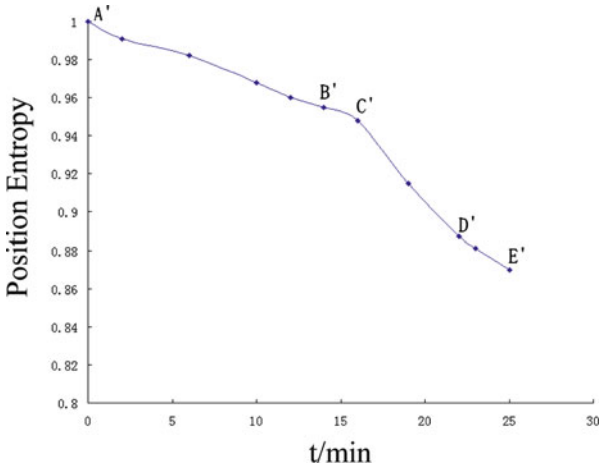

Fig. 8 Position entropy and time curve

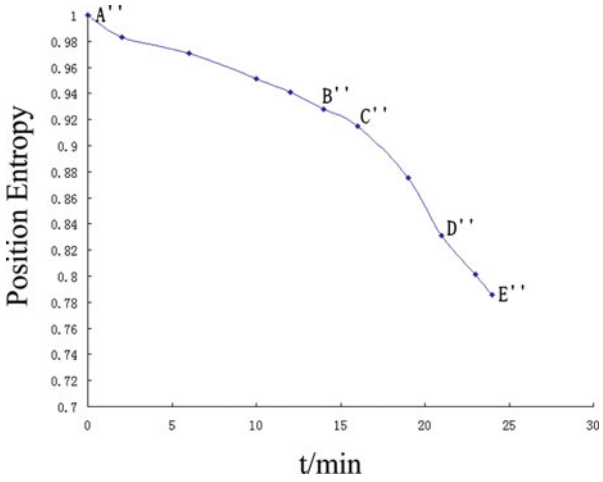

Fig. 9 Position entropy and time curve

number of acoustic emission signals emerged in this stage. AE hit and accumulated energy increased rapidly. The value of position entropy continued to decrease; however, position entropy decreased more slowly in this stage than in the yield stage. The microholes formed in this stage continued to grow rapidly along the grain boundary. The spatial concentration of AE events in space continued to increase, and the value of position entropy continued to decline. The specimen fractured when stretched to point E.

The position entropy diagram of the second and the third specimen is shown in Figs. 8 and 9; the changing trend of location entropy presented the same trend as the first specimen; location entropy fell sharply in the strengthening stage, which can predict internal serious damage.

5 Conclusion

1. A direct correspondence exists between the internal damage process and acoustic emission parameters of Q345R in the ductile fracture stage. The changes in acoustic emission parameter accumulation reflect the internal injury of the material. Thus, acoustic emission can be utilized to monitor the damage.
2. The rapid increase in accumulated acoustic emission energy and the sharp decrease in position entropy in the tensile loading of Q345R indicate that the degree of internal damage to the material increased significantly; thus, serious internal injuries are expected to appear in the material.
3. A close relation exists between the position in space where the acoustic emission events of Q345R occurred and the mechanical and evolutionary processes of the internal structure. Position entropy function can be utilized to quantitatively describe the spatial evolution law. The concentration in the spatial distribution of the acoustic emission events and the sharp decrease in position entropy are important prewarnings of serious injuries in the material.

References

1. Shen Gong-tian, Liu Shi-feng, Dai Guang, *Acoustic Emission Testing*. (China Machine Press, 2004), pp. 5–7
2. Xu Yan-ting, Dai Guang, Zhang Bao-qi, *16MnR Steel Tensile Specimens Experimental Study of Normal and High Temperature Acoustic Emission Characteristics*. (Daqing Petroleum Institute, 1995), **19**(2), pp. 75–77
3. Takayuki Hirata, Fractal structure of spatial distribution of microfracturing in rock. *Geophysics J. R. Austr. Sco*. **90**, 369–374 (1987)
4. Ji Hong-guang, Cai Mei-feng, Concrete materials in the fracture process AE spatial self-organization evolution characteristics and its application in structural instability prediction. *Civil. Eng. J*. **34**(5) 15–19 (2001)
5. A.L. Gurson, Continuum theory of ductile rupture by void nucleation and growth: Part I-yield criteria and flow rules for porous ductile media. *Trans. ASME. J. Eng. Mat. Technol*. **8**(1) 1–15 (1977)

Acoustic Emission Behavior of 12MnNiVR Under Stretching

Jingpin Jiao, Xinjian Wang, and Guanghai Li

Abstract As large atmospheric tank is more and more applied in the petrochemical industry, detection method for it also receives great attention. However, there have been many problems in detection for tank testing: off-line detection method has lots of advantages, but it takes a lot of manpower, and online detection is unable to assess the damage state of tank. In order to achieve the goal of real-time monitoring for large atmospheric tank, in this chapter the characteristic parameters AF and RA are used in analysis. From the signal characteristics of four stages, plastic deformation, yield, strengthening, and necking the regular, can be found. Furthermore the acoustic signals are processed using the methods of Empirical Mode Decomposition (EMD) and Hilbert-Huang Transform (HHT), and the characteristics of acoustic signals in different stages are described in time-frequency domain. The results provide a method to identify the damage state of atmospheric tank steel; meanwhile this laid a solid foundation for AE detection in large atmospheric tank. In this chapter characteristic parameters and waveform analysis method are combined, and characteristic parameters AF and RA are introduced.

1 Introduction

Oil supply security has an important influence on national economic ups and downs, and even relates to national security and social stability. At present, tank rupture is one of the most serious accidents on storage and transportation oil system. So the

J. Jiao (✉) • X. Wang
Beijing University of Technology, Beijing 100022, China
e-mail: jiaojp@bjut.edu.cn

G. Li
China Special Equipment Inspection Institute, Beijing 100013, China
e-mail: liguanghai@csei.org.cn

G. Shen et al. (eds.), *Advances in Acoustic Emission Technology: Proceedings of the World Conference on Acoustic Emission-2013*, Springer Proceedings in Physics 158,
DOI 10.1007/978-1-4939-1239-1_24,

demand of condition monitoring for the tank wall and bottom has become more and more urgent. Main points of this chapter are as follows: in the tensile test the AE signal under static load tensile until breaking is obtained. There are two methods for signal processing: characteristic parameter and waveform analysis. The damage states in each stage of the material under static load tensile state (linear elastic, plastic deformation and plastic yield, strengthening, and necking) can be characterized. This chapter is structured as follows: AE technique will be used to detect material 12MnNiVR that is commonly used in large-scale atmospheric tank as research object with AE testing tensile test system under static load tensile state until the breaking. The signal received from last experiment uses the method of characteristic parameter analysis and waveform analysis. According to these two methods damage states in each stage of this material under static load tensile state (linear elastic, plastic deformation and plastic yield, strengthening, and necking) can be characterized. The result provides method for the future study of 12MnNiVR material damage state representations.

Zhou Meng [1] used AE technology to test nickel plated steel belt in tensile experiment and analyzed the characteristics of AE signals in different tensile conditions. According to the result he proved the correlation between specimen damage status and characteristic parameters of AE signals. Luo Zhigao [2, 3] used genetic algorithm and Mahalanobis distance method to solve AE signals. This method can identify the damage status of micro crack and identify status of metal stretch forming quality. Dimitrios and D. Soulioti [4, 5] describe the AE behavior of concrete under four-point bending. Steel fibers of varying content were used as reinforcement in concrete slabs and their influence on the fracture process and the acoustic activity was investigated. Analysis revealed that particular AE parameters change monotonically with the progress of damage and can be used for the characterization of the failure process. Seif E. Hamdi [6] used the Hilbert–Huang transform for the extraction of new relevant damage descriptor to be adopted for AE pattern recognition in order to help understand the damage process. AE signals collected from unidirectional glass-fiber-reinforced polymer composite samples were studied. First, the frequency content of the recorded signals in each test is analyzed. Secondly, the performance of the Hilbert–Huang transform damage classification approach is evaluated. Li Lin [7, 8] addresses an application of recently developed signal processing tool based on the Hilbert–Huang transform (HHT) to characterize the acoustic emission (AE) signals released from the offshore structure model. The AE signal analysis based on HHT is an effective tool to extract the features and this opens perspectives for crack recognition in offshore structures. Khamedi [9] investigated the application of wavelet-based AE signal processing on micromechanics to identify failure in dual-phase steels (DPSs). The results were verified with microscopic observations and they indicate that wavelet-based signal processing is an efficient tool in the analysis of AE signals to detect micromechanics identifying failure in DPS.

So material performance directly determines the bearing structure stress-strain relationship. In this chapter according to the characteristics of acoustic emission

signal from 12MnNiVR steel material commonly used in large atmospheric tank the damage state of large atmospheric tank is realized.

2 Methods

AE technique (AET) is an advanced nondestructive evaluation (NDE) tool that possesses the ability for understanding deformation and fracture behavior of materials [10–12]. AE signal analysis method has two categories in this chapter; the two methods will be used to process the signals. AE technique (AET) is an advanced nondestructive evaluation (NDE) tool that possesses the ability for understanding deformation and fracture behavior of materials. AE is defined as the class of phenomenon whereby transient elastic waves are generated by rapid release of energy from localized sources in a material like location of transient relaxation of stress and strain fields. An AE sensor coupled to a sample undergoing dynamic changes detects a part of the strain energy that is emitted in the form of elastic waves and gives information about the nature of changes taking place in the sample. AE signal analysis method has two categories: one is parameter analysis method, using characteristic of waveform AE parameters to analyze. As showed in Fig. 1, besides traditional parameters one of the crucial parameters is the average frequency, AF, which is defined by the ratio of threshold crossings over the duration of the signal and is measured. It is one estimate of the basic frequency content of the

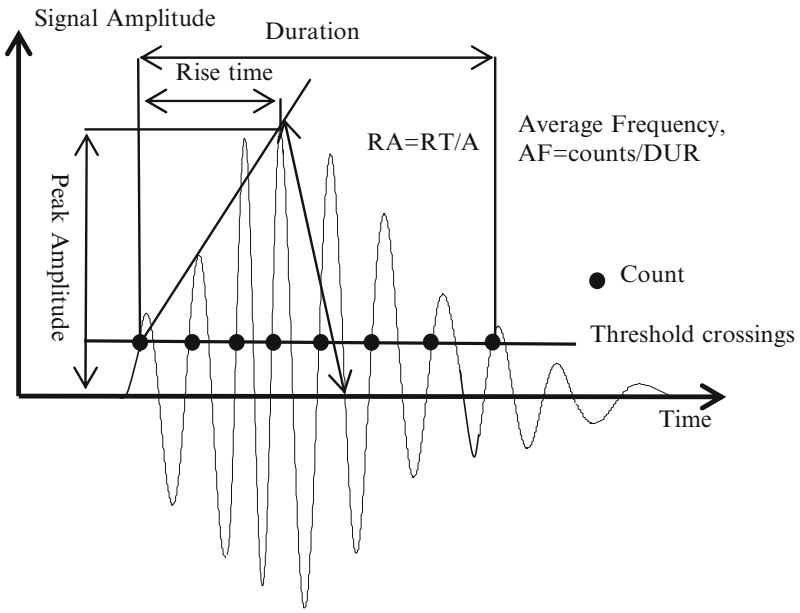

Fig. 1 Characteristic parameter

waveform. Another crucial parameter is the RA value which is the rise time (RT, delay between the onset and the maximum amplitude) over the amplitude; as shown in the formulas (1) and (2), f represents frequency, N represents counts, t_d represents duration, k represents RA, t_r represents rise time, and A represents amplitude. According to this new AE parameters the AE characters can be described more vividly. Another is the waveform analysis method: received waveform is used to take time-frequency analysis. In this chapter, the two methods are used to process the signals:

$$f = \frac{N}{t_d} \tag{1}$$

$$k = \frac{t_r}{A} \tag{2}$$

The Hilbert–Huang transform [16, 17] developed by Huang et al. in late 1990s was specially tailored for treating nonlinear and non-stationary data. The essence of the Hilbert–Huang transform is to identify the intrinsic oscillation modes by their characteristic time scales in the data empirically, and then to decompose the data accordingly. Generally, the finest vibration mode or component of the shortest period at each instant will be identified and decomposed into the first intrinsic mode function (IMF). The components of longer periods will be identified and decomposed into the following IMFs in sequence. The IMF is a counter part to the simple harmonic function, but it is much more general: instead of constant amplitude and frequency, IMF can have both variable amplitude and frequency as functions of time. This frequency time distribution of the amplitude is designated as the Hilbert amplitude spectrum, or simply the Hilbert spectrum. Contrary to the other decomposing methods, the Hilbert–Huang transform is empirical, intuitive, direct, and adaptive.

3 Experiment

This test system is composed of tensile specimen, AE sensors, AE acquisition card, computer (analysis software), and signal cable [13–15]. This system is showed in Fig. 3. AE parameter settings are shown in Table 1.

Because the influence of the AE signals is highly susceptible, how to reduce the noise is an important issue. The noise sources include connection friction between pin and sample, electronic noise from tensile testing machine, etc; there are some methods to reduce the noise level: take rubber pad between pin shaft and sample

Table 1 AE parameter settings

Threshold (dB)	Sample point	Sample frequency (MHz)	PreTrig	Dur.DisT. (μs)
40	1,024	2.5	200	400

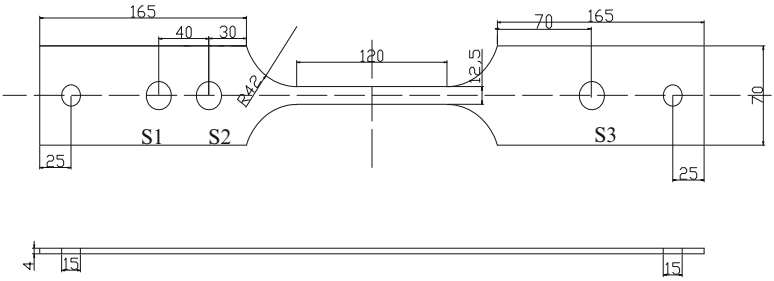

Fig. 2 Specimen size

interface to reduce friction signal transmission. Start tensile testing machine and AE instrument in the same time; connect AE instrument with the material testing machine to eliminate the electronic noise interference. The test start load is 1.5 kN. The loading speed is 3 mm/min and the whole process is continuous.

In this experiment 12MnNiVR specimen that is commonly used in large atmospheric tank was cutting from the tank bottom plate. The specimen size is designed by the national standard GB/T 228.1 2010. The size is shown in Fig. 2. The AMSY-6 digital multichannel AE instrument produced by Vallen was used in the test. The probes VS45-H and VS150-RIC AE sensors are used in data acquisition.

4 Result

4.1 Tensile Experiment Result Analysis

In this part three specimens are used in this experiment; the same regular can be found in the result. So one of the results is chosen to express in this chapter (Table 2). Specimen tensile process of loading force-time history is showed in Fig. 3b. Duration time $t = 107.6$ s, and maximum tension $F_{\max} = 39.150$ kN. Based on the analysis of the loading force and time relationship curve and steel tensile property [13, 17], the whole tensile stage can be divided into the following five stages, as shown in Table 3. The composition of 12MnNiVR and performance of the material using tensile experiment are presented in Tables 4 and 5.

4.2 Parameter Analysis

AE characteristic parameter signal analysis method is an important method in AE signal analysis methods. The AE parametric approaches using AE hit rate,

Table 2 12MnNiVR typical mechanical property parameter table

Yield strength (N/mm^2)	Tensile strength (N/mm^2)	Fracture toughness (kJ/m^2)
>490	>610	95.49

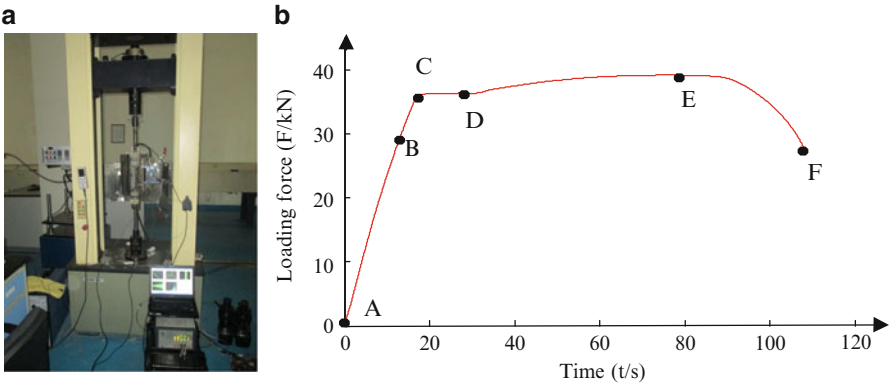

Fig. 3 (**a**) 12MnNiVR specimen tensile test AE detection system. (**b**) Loading force versus time

Table 3 Tensile experimental parameter result table

Sectional area (mm^2)	Elasticity modulus (kN/mm^2)	Yield strength (N/mm^2)	Tensile strength (N/mm^2)	Elongation (%)	Percentage reduction area (%)
61.10	204.7	584.92	643.31	12.78	64.84

Table 4 12MnNiVR composition result table

C (%)	Si (%)	Mn (%)	S (%)	P (%)	Cr (%)	Ni (%)	Al (%)
0.10	0.12	1.52	0.0043	0.0080	0.0050	0.26	0.034

Table 5 Results in different stages

	Linear elastic	Plastic deformation	Yield	Strengthening	Necking
Time (s)	0–12.72	12.72–17.14	17.14–31.64	31.64–76.52	76.52–110.3
Loading (kN)	0–28.85	28.85–36	36–36.39	36.39–39.15	39.15–23.88

amplitude, energy, duration, average frequency, and rise amplitude have been applied to the study of various fracture processes.

As shown in Fig. 5a, before the time is 12.72 s, there is few AE signal; when time is 12.72–17.14 s, signal amplitude is decreased, and the distribution range is 40–45 dB; when time is 17.14–31.64 s, the distribution range of signal amplitude is 40–75 dB; when time is 31.64–76.52 s, the main distribution range is 40–60 dB; this phase is where most of the value has also fallen sharply; when time is 76.52–107.8 s, signal amplitude continues to fall, the distribution range is 40–55 dB,

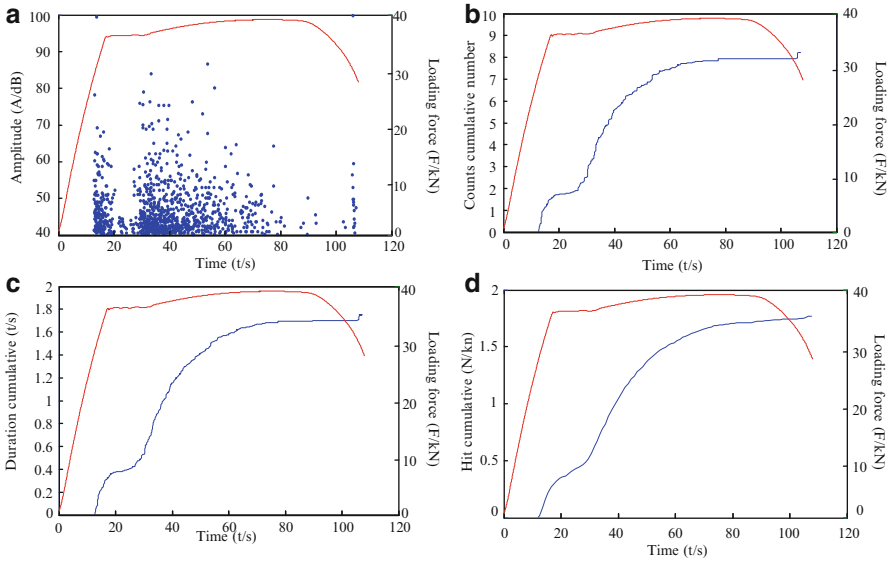

Fig. 4 (**a**) Amplitude versus time. (**b**) Count cumulative versus time. (**c**) Duration cumulative versus time. (**d**) Hit cumulative versus time

before fracture the signal significantly decreases, and the amplitude is about 50 dB; when the specimen starts to break, signal amplitude increases.

In Fig. 4b–d, the three parameters, counts, duration, and hit versus time accumulated figure, are worked out. From these pictures we find some rules: since 12.72 s three parameters to present a very large growth, until 17.14 s, slow down the growth trend; after 31.64 s, three parameters present the relatively fast growth; after 76.52 s growth rate slows again, until the break. According to the variation of parameter duration, in the yield and necking stage, the AE signals are shorter than other stages. The AE signal duration in plastic deformation and strengthening is long. Therefore the AE signals in yield and necking stage are burst AE signal and others are continuous AE signals.

Figure 5 shows us the relation between energy and time. In this whole process, signal energy appears as four peak values which concentrate in 12.72, 31.64, 50.39, and 110.3 s. In these four parts, internal material releases a lot of energy and the four parts are plastic deformation stage, yield stage, strengthening stage, and last of necking stage. In addition, except the last signals which are the specimen fracture voice the others are the AE signals for crack generation and propagation.

The behavior of new AE parameters, AF and RA, for the same experiment is depicted in Fig. 6. In order to make the characterization of these two parameters more clearly, the two parameters in the different stages are compared. AF distributes 20–40 kHz during plastic deformation stage. During the yielding stage AF is below 20 kHz. When the strengthening phase is coming, AF rises again; AF is higher than the previous stage and the peak value is 60 kHz. The AF in necking

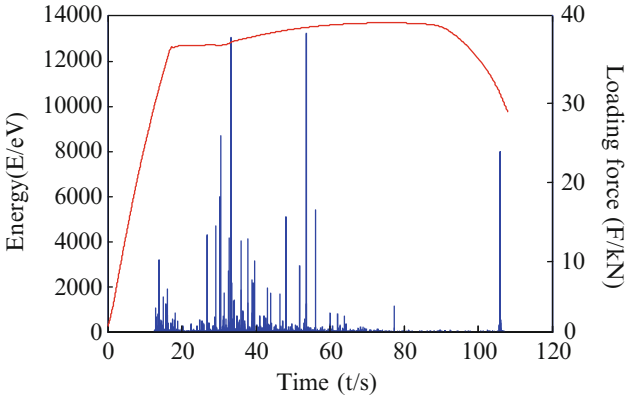

Fig. 5 Energy versus time

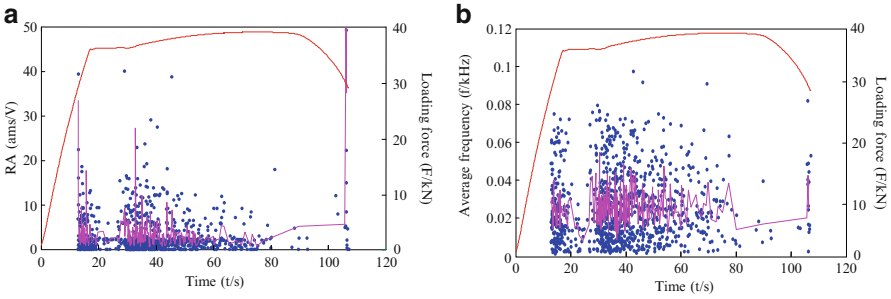

Fig. 6 (**a**) RA versus time. (**b**) AF versus time

stage gradually reduced. The characteristic parameter RA also showed the same trend. Just like the signal amplitude, AE hit rate, amplitude, energy, duration, AF, and RA can match well with the damage process of 12MnNiVR specimen.

How to select a different threshold for the experimental results is an influential threshold. The too low threshold may result in the introduction of excessive noise signal threshold and the too high threshold may result in loss of valid signal, so in signal acquiring process, measuring the background noise is very necessary. Since the noise is mainly center in high frequency and has lower amplitude, the influence of threshold on AF and RA is as following. If the threshold lowers, the AF and RA are larger; if threshold higher, the RA and AF become smaller.

4.3 Waveform Analysis

According to discussion on AE signal analysis using characteristic parameter method in the previous chapter characteristic parameters represent the

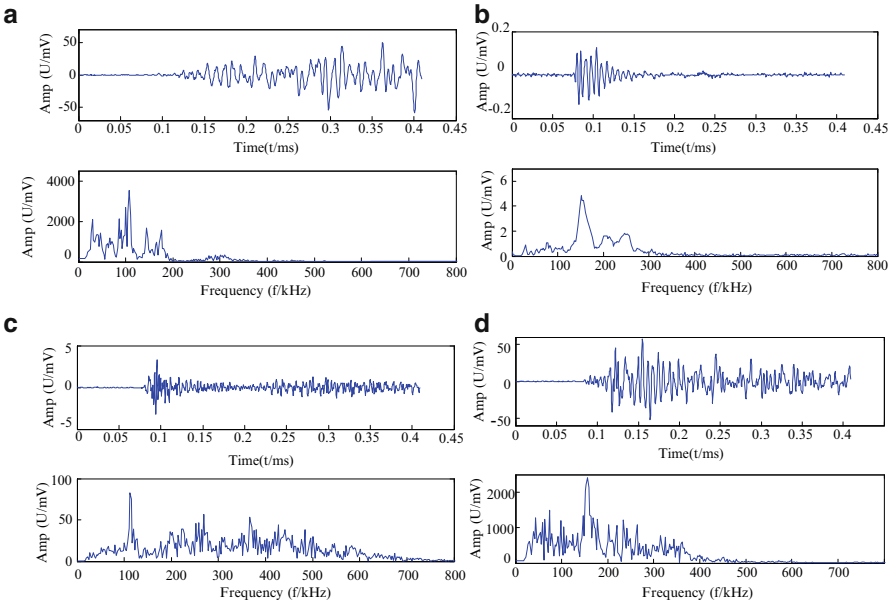

Fig. 7 AE signal and FFT in (**a**) plastic deformation part, (**b**) yield part, (**c**) strengthening part, (**d**) necking part

characteristics of tensile process. In this chapter the HHT and EMD method is used to analyze AE signal in the stages of linear elastic, plastic deformation, plastic yield, strengthening, and necking.

In the part the signal is chosen from the four parts of the process of stretching. Twenty signals are chosen at first; the same regular can be found. So we use one of these to analyze. The signal was received by the wideband probe VS45-M and the sampling rate is 2.5 MHz and sampling point is 1,024. From Fig. 7, we can see the AE signals in time and frequency domain in plastic deformation, plastic yield, strengthening, and necking. As we can see in this picture only the signal in plastic yield stage is burst AE signal, and others are continuous. From the perspective of signal amplitude, the amplitude of plastic deformation and necking stage is bigger than others. It is 50 mV. In strengthening and yielding stages, the amplitude is 5 mV and less than 0.2 mV. From the perspective of signal frequency, the frequency band of plastic deformation and yielding stages is narrow, which is mainly distributed in 20–360 and 100–300 kHz. Signal frequency band of strengthening and necking stages is relatively wide, mainly distributed in 20–700 and 20–360 kHz.

In order to find more characteristic of AE signal, IMFs of four stages are obtained. Based on the energy of these eight-layer decomposition, we can get the proportion of the total energy as shown in Table 6. The result shows that the sum of first four components is more than 99 % of the total energy and the sum of other components is only about 1 %.

Table 6 Energy proportion in different stage

	IMF1 ratio (%)	IMF2 ratio (%)	IMF3 ratio (%)	IMF4 ratio (%)	Other IMF ratio (%)
Plastic deformation	48	31	13	7	1
Yield	75	19	3	1	2
Strengthening	58	26	13	2	1
Necking	60	20	13	4	3

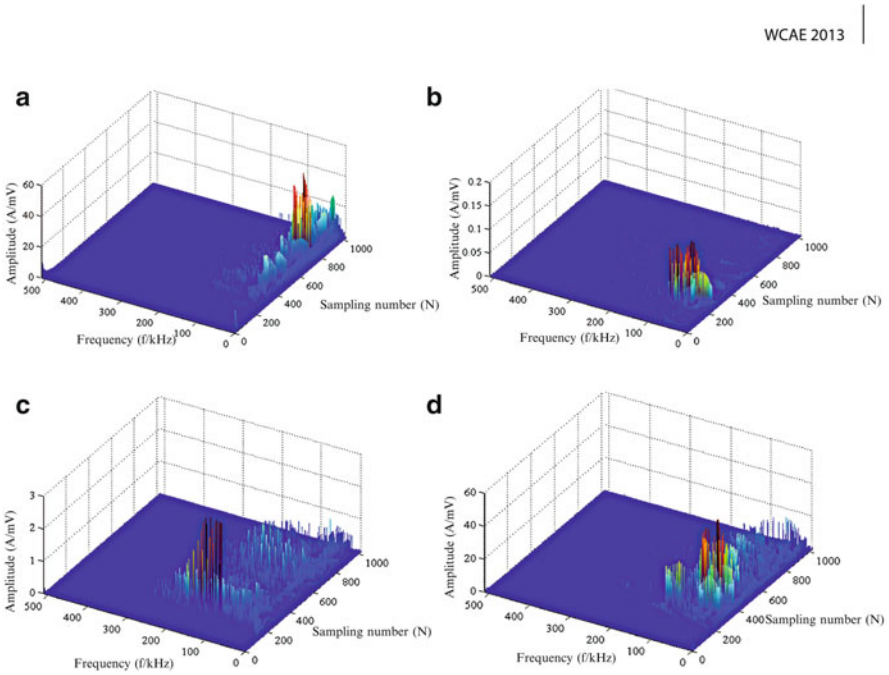

Fig. 8 3D Hilbert spectrum in (**a**) plastic deformation part, (**b**) yield part, (**c**) strengthening part, (**d**) necking part

In order to analyze the AE signal further, 3D Hilbert spectrum which is an excellent time-frequency analysis method is worked out. Three elements, sampling points, frequency, and energy, can be seen in 3D figure. Many time-frequency characteristics can be found from the four figures (Fig. 8): The AE signal frequency of plastic deformation stage is mainly concentrated in the 0–100 kHz, 90 % energy mainly distributed in the range of 800–900 sampling points. The AE signal frequency of yield stage is mainly concentrated in the 0–220 kHz, 90 % energy mainly distributed in the range of 200–300 sampling points. The AE signal frequency of strengthening stage is mainly concentrated in the 0–300 kHz, 90 % energy mainly distributed in the range of 0–1,000 sampling points. Energy is relatively fragmented, distribution of sampling points in a 200–300, and the peak frequency of 100–200 kHz

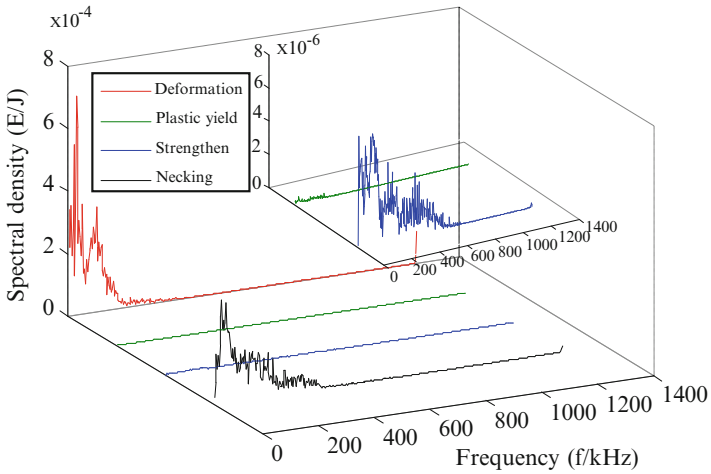

Fig. 9 Marginal spectrum in four stages

range. Necking phase of the signal frequency is mainly concentrated in 0–400 kHz, sampling points within the scope of 200–1,000 peaks concentrated in sampling points to 300–500, and signal frequency in the range of 50–100 kHz.

According to signal frequency and energy distribution in other stages (plastic deformation, plastic yield, and strengthening) it is easy to find differences. Therefore this analysis method is very helpful for us to distinguish four stages of the signal.

Marginal spectrum analysis is carried out, as shown in Fig. 9. The four colors, red, green, blue, and black, represent the four stages of marginal spectrum, respectively. The marginal spectral density from plastic deformation and necking stages is larger than others. The signal frequency distribution of plastic deformation and necking stages is, respectively, 0–200 kHz and 0–400 kHz. Compared with plastic deformation and necking stages, marginal spectral density of plastic yield and strengthening stages is smaller. The frequency distribution of yielding is 0–200 kHz and the strengthening stage is 0–600 kHz. The main energy concentrates in the 0–200 kHz.

5 Conclusion

1. In this chapter, the AE signal characteristic parameters such as amplitude, count, hit, and energy can match well with damage evolution process of 12MnNiVR material. Therefore based on characteristic parameters of AE signal the goal of real-time monitoring for 12MnNiVR steel damage status can be achieved.
2. Based on traditional AE signal characteristic parameters, two new feature parameters are created: average frequency and RA. The analysis of the two new characteristic parameters can also characterize the damage process of 12MnNiVR steel better.

3. The time-frequency characteristics obtained from four stages, plastic deformation, yield, strengthening, and necking, are different and can be used for characterization of the stages; therefore the signal time-frequency analysis can also be used to monitor the damage status of 12MnNiVR steel.

Acknowledgment This study was financially supported by Chinese 12th five-year project 2011BAK06B03-03.

References

1. Zhou Meng, Long Shiguo, Ma Zengsheng. Characteristics of AE signals of nickel planted steel sheet under tensile fracture condition. Piezoelectrics Acoustooptics. **34**(1), 121–124 (2012)
2. Luo Zhigao, Fan Xiangwei, Chen Qiang. AE signal characteristic parametric optimization of initial crack and status identification for metal drawing parts. J. Vib. Shock. **31**(17), 154–158 (2012)
3. Luo Zhigao, Ye Hongying, Xu Aicheng. Extraction of characteristic parameters of AE signals for molded metal drawing parts based on time-series analysis and MATLAB. J. Vib. Shock. **31** (17), 120–123 (2012)
4. D.G. Aggelis, Classification of cracking mode in concrete by AE parameters. Mech. Res. Comm. **11**(38), 153–157 (2011)
5. D. Soulioti, N.M. Barkoula, A. Paipetis, T.E. Matikas, T. Shiotani, D.G. Aggelis, AE behavior of steel fiber reinforced concrete under bending. Construct. Build. Mater. **23**(12), 3532–3536 (2009)
6. S.E. Hamdi, Alain Le Duff, Laurent Simon, Guy Plantier, Anthony Sourice, Mathieu Feuilloy. AE pattern recognition approach based on Hilbert–Huang transform for structural health monitoring in polymer-composite materials. Appl. Acoust. **74**(5), 746–757 (2013)
7. Li Lin, Fu lei Chu. Feature extraction of AE characteristics in offshore structure model using Hilbert–Huang transform. Measurement. **44**(1), 46–54 (2011)
8. Li Lin, Fu lei Chu. HHT-based AE characteristics of natural fatigue cracks in rotating shafts. Mech. Syst. Signal Process. **26**(1), 181–189 (2012)
9. R. Khamedi, A. Fallahi, A. Refahi Oskouei, Effect of martensite phase volume fraction on AE signals using wavelet packet analysis during tensile loading of dual phase steels. Mater. Des. **31**(6), 2752–2759 (2010)
10. Ja-UkGu, Hyun-Sung Yoon, Nak-Sam Choi. AE characterization of a notched aluminum plate repaired with a fiber composite patch. Comp. Part A. **43**, 2211–2220 (2012)
11. C.K. Mukhopadhyay, G. Sasikala, T. Jayakumar, B. Raj, AE during fracture toughness tests of SA333 Gr.6 steel. Eng. Fract. Mech. **96**, 294–306 (2012)
12. Guo Hongbao, Wang Bo, Jiao Guiqiong, Yang Chengpeng, Liu Yongsheng. Tensile properties and failure analysis of 2D-C/SiC composite laminates with circular holes. J. Aeronaut. Mater. **32**(4), 80–86 (2012)
13. Xu Changhang, Liu Liqun, Chen Guoming. Characteristics analysis of AE signals from steel specimens under tensile fracture and fatigue crack condition. J. China University Petroleum. **33**(5), 95–99 (2009)
14. Meng Songhe, Tian Xiaoxiao, Du Shanyi. Mechanical properties testing and failure mechanism analysis of 3D woven carbon/epoxy composites. Acta Materiae Composit. Aesinica. **29** (2), 115–120 (2012)
15. Xu Feng, Liu Yunfei. Feature extraction and pattern recognition of AE signals generated from plywood damage based on EMD and neural network. J. Vib. Shock. **31**(15), 30–35 (2012)
16. Wang Hui. *Research on the HHT Method and Its Applications*. (Hefei University of Technology, Heifei, 2009)
17. Cao Zhengmin. *The Investigations on Lamb Wave Testing Technique and HHT Time-Frequency Analysis Method*. (Dalian University of Technology, Dalian, 2008)

Statistical Analysis of Events of Random Damage in Assessing Fracture Process in Paper Sheets Under Tensile Load

Liang Zhang, Ming Fan, and Jianyu Li

Abstract This investigation presents an experimental, computational, and data-enabled method to study the statistics of these ERD in the evolution of fracture process in paper sheets, which holds the key to making accurate characterization and evaluation of paper material failure. Firstly, an experimental method based on acoustic emission (AE) monitoring was established to accomplish the acquisition of all possible ERD that represent most physics of fracture process originating from the hierarchical microstructure of paper sheets under the influence of uniaxial tensile load. Then the acquired experimental damage data on characteristics of AE signal (such as timing, quantity, amplitude, magnitude, energy) was integrated as a measurable multivariate D_A based observation windows and multi-scale criteria, which was defined in our previous work. Ultimately entropy S, originated from the Gibbs probabilistic entropy, was obtained and applied to assess the evolving damage states in the evolution of fracture process. The significance of this multivariate (D_A) and entropy (S) is the application of multi-scale statistical analysis and data-enabled thoughts to deal with the problem of the nonequilibrium damage evolution to macroscopic failure involving multiple space and time scales in paper material, respectively. Particular attention is given to that trajectory of damage states (TDS), $S-T$ relation (when entropy S is correlated with varying tensile strength), is adequate enough to provide a realistic description of whole fracture process. The results evidenced that the multi-scale statistical analysis of ERD in fracture process is equivalent to build a "bridge" to study the connection between micro- and macro-systems. Furthermore, a spectroscopic technique (scanning electron microscope (SEM)) has also been proved to be a powerful method to study morphology of the fractured paper specimen.

L. Zhang (✉) • J. Li
Tianjin University of Science and Technology, Tianjin 300222, China
e-mail: liangzhangchina@outlook.com; lijianyu@tust.edu.cn

M. Fan
University of Memphis, Memphis, TN 38152, USA
e-mail: mfan@memphis.edu

G. Shen et al. (eds.), *Advances in Acoustic Emission Technology: Proceedings of the World Conference on Acoustic Emission-2013*, Springer Proceedings in Physics 158,
DOI 10.1007/978-1-4939-1239-1_25,

1 Introduction

When strained to certain level or even failure, the paper sheet experiences irreversible random damage states in nature. Due to complexity of physical, chemical, and mechanical properties, randomness and irreversibility of fracture process in this disordered media, and other known or unknown factors, the generation, growth, and accumulation process of these damage during fracture process, seem so complicate that characterizing and evaluating the failure behavior of paper sheets are yet to be well tackled. In recent years, although great efforts have been made to cope with the damage and fracture behavior of paper material using classical mechanical approach [1–4], the description of fracture process involving the multiple space and time scales, in particular the nonequilibrium damage evolution to macroscopic failure, still stays in a "smeared out" sense [5, 6].

Here, we focus on the results of damage evolution, which are revealed by a series of continuous internal structural variations (or random microscopic damage mechanisms) residing in the microstructure of paper sheets under mechanical loading [1], and should therefore be measurable. We terms all irreversible events originating from a multitude of random microscopic damage mechanisms in the fracture process, such as fiber breakage, fiber–fiber bond failure, a systematic combination of multiphase delamination as fiber pullout, nonfibrous component failure, microfracture propagation, and fatigue in dislocation of fibers, to be events of random damage (ERD) [1, 7–11]. These responsive ERD range from the nanoscale to several millimeters in dimension, and often also have a great effect on the reliability and stability of paper structures. Gradually and erratically, the occurrence of ERD releases strain energy rapidly in forms of stress waves, which phenomenon is usually termed as acoustic emission (AE), and then these waves travel volumetrically until captured by resonant-type transducers and become detectable AE signal via AE monitoring system [1, 12]. Inevitably, the propagation of AE waves was influenced by various factors; hence the obtained AE signal is the function of various influencing factors, which is introduced in the next section.

Synthesize those mentioned above, the entire evolution of ERD that represent the most physical essence of fracture process can be acquired by AE measurements and hence statistics of the some parameters on the AE signal characteristics, such as timing, quantity, magnitude, amplitude, energy, and even extrinsic parameters (i.e., applied tensile load), is equivalent to statistical analysis of ERD. The present work is to apply a multi-scale statistical, computational and data-enabled method is to study the statistics of ERD in fracture process of paper sheets under monotonic tensile loading, and the objectives are (1) to establish an experimental approach to acquire ERD of paper sheets in fracture process accurately and correctly and (2) to make realistic characterization and evaluation of fracture process in paper sheets.

2 Methodology

2.1 A Multivariate Approach to Quantify the Evolution of Events of Random Damage

Let Ω be a set of primary variables such as timing, quantity, other AE parameters that may be used to scale the magnitude of the acquired ERD (i.e., amplitude, energy, and intensity), and extrinsic parameters that characterize driving conditions such as applied tensile load. To extract and integrate the valuable variables, a multivariable D_A is given by [13, 14]

$$\begin{aligned} D_A :&= \{X_1, X_2, \cdots, X_j, \cdots, X_N\} = [\alpha_{ij}]_{M\times N} \\ &= \begin{pmatrix} \alpha_{11} & \cdots & \alpha_{1N} \\ \vdots & \ddots & \vdots \\ \alpha_{M1} & \cdots & \alpha_{MN} \end{pmatrix} \quad \text{on } \Omega \\ i &= 1,\ 2,\ 3,\ \ldots, M,\ j = 1,\ 2,\ 3,\ \ldots, N \end{aligned} \tag{1}$$

where X_j ($j = 1, 2, 3, \ldots, N$) is the jth column vector (also a variate), and the number of column vectors, N, indicates the number of multi-scale subinterval of D_A (also the multi-scale criteria), which is dependent on AE characteristic parameters such as amplitude, energy, and intensity. Here, amplitude scale is used to be divided into N subintervals equably from the lowest scale subinterval X_1 to the highest scale subinterval X_N in ascending order. The number of row vectors, M, indicates the total number of the observation window; here intermittent acquisition is in need. If we let the observation window be $W(i, w, \delta)$, where i is the order of window sequence, w represents the width of observation window, and the moving step $\delta = w$ [15]. That i increases when the observation window is moving indicates variation of the driving conditions (or extrinsic parameters, such as applied tensile load), as shown in Fig. 1.

Furthermore, the element α_{ij} of D_A in Eq. (1) is determined as an index function of x as follows:

$$\alpha_{ij} := \text{Index}(x)_{ij} \tag{2}$$

where the function index(·) means accumulation of the number of acquired x that represents an acquired ERD in the form of AE signature according to the specified observation window width and its amplitude scales. Nevertheless, the transformation from ERD to acquired AE signature involves various influencing factors such as time, space, physical characteristics, conditions of instrumentation, physical conditions, and physical characteristics of the solid materials; meanwhile it is not to be neglected that there exists noise, attenuation, and changes when stress propagates; hence we symbolize it as

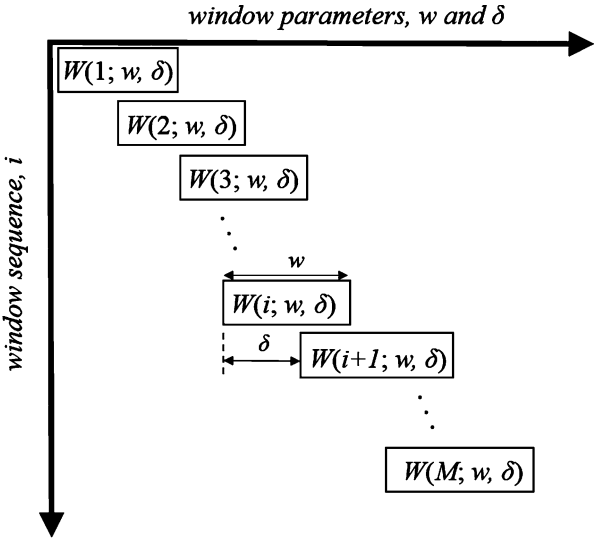

Fig. 1 The intermittent acquisition diagram, $W(i, w, \delta)$, where i is the order of window sequence, w represents the observation window, the moving step $\delta = w$

$$x = f(\text{time, space, physical characteristics, instrumentration and physical conditions, physics of solid materials}) \tag{3}$$

where the physical characteristics include variables such as the amplitude, energy, duration, rise time, and other signal features that may be used to represent the physics of ERD [14, 16].

In series of our previous works, we have reported the applications of D_A to evaluate the state of damage in a polymeric material (bone cement) [13, 14, 16], but have not applied it to study the fracture process of paper material. The establishment of D_A, a variate of multicomponent, by approaches of the multivariate analysis, suggests that damage is not only "physical" but also "statistical," and lays the foundation for further multi-scale analysis of ERD in such sophisticated damage system in the fracture process of paper sheets.

As mentioned above, columns of D_A are vectors of the evolution of scaled ERD acquisitions in specified amplitude subinterval, whereas the rows are vectors of the spectrum of ERD observed in specified observation window. Then corresponding adequate description of the latter is followed:

$$D_A = \begin{pmatrix} {Y_1}^A \\ \vdots \\ {Y_i}^A \\ \vdots \\ {Y_M}^A \end{pmatrix} \quad \text{on } \Omega \quad {Y_i}^A = (\alpha_{i1},\ \alpha_{i2},\ \alpha_{i3}, \ldots, \alpha_{iN}),\ \ i = 1, 2, 3, \ldots, M \tag{4}$$

where ${Y_i}^A$ is the ith row vector, which actually represents one spectrum on distribution of ERD when multi-scale subinterval varies from the minimum α_{i1} to the maximum α_{iN}, and its variation from ${Y_1}^A$ to Y_M^A is dependent on present driving

conditions, that is to say that when the driving conditions vary (or observation window moves), the spectrum evolves and ultimately a multivariate D_A on evolution of ERD is established.

2.2 The Application of Gibbs Probability Entropy to Assess the Evolving Damage States

The Gibbs probabilities of α_{ij} are approximated by

$$p_{ij}^A = \alpha_{ij}/L_{ij}^A \tag{5}$$

where L_{ij}^A is

$$L_{ij}^A = \sum_{j=1}^{N} \alpha_{ij} \tag{6}$$

If we replace α_{ij} by p_{ij}^A in Eq. (1), then the resulting probability space matrices of ERD, $\overline{D}_A$, is to be

$$\overline{D}_A : = \left(p_{ij}^A\right)_{M\times N} = \begin{pmatrix} p_{11}^A & \cdots & p_{1N}^A \\ \vdots & \ddots & \vdots \\ p_{M1}^A & \cdots & p_{MN}^A \end{pmatrix} = \begin{pmatrix} P_1^A \\ \vdots \\ P_i^A \\ \vdots \\ P_M^A \end{pmatrix} \tag{7}$$

where P_i^A is the probability spectrum of ERD, which can reflect the probability distribution of the individual scale subinterval in the certain specified observation window.

An entropy value is employed via Gibbs formula [16, 17]:

$$S = \int_0^1 \rho(x)\ln(1/\rho(x))dx \tag{8}$$

where $\rho(x)$ is the probability density of the Gibbs continuous function. Let x denote the amplitude of ERD, so we divide the scales between the lowest amplitude scale and the highest amplitude scale into the N subintervals in ascending order as follows $(0, 1/N]$, $(1/N, 2/N]$, ..., $((N-1)/N, 1.0]$. In the jth scale subinterval the probability is $p_{ij}(x) = \int_{(1/N)(j-1)}^{(1/N)j} \rho(x)dx$; then we can get $\rho_{ij}(x) = 1/(1/N)) \int_{(1/N)(j-1)}^{(1/N)j} \rho(x)dx = Np_{ij}(x)$; this gives the following approximation [13, 16]:

$$S \approx s = \sum_{j=1}^{N} (1/N)\rho_{ij}(x)\ln\left(1/\rho_{ij}\right) = \sum_{j=1}^{N} p_{ij}(x)\ln\left(1/\left(Np_{ij}(x)\right)\right) \tag{9}$$

where $p_{ij}(x)$ is replaced by p_{ij}^{A} in Eq. (5). Naturally, the absolute value of S also is dependent on various factors: the specified criteria (such number of multi-scale subintervals, N, and number of observation window, M), and other factors that influence ERD. Entropy S means uncertainty of information about the occurrence of ERD. Its minimum value is $\ln(1/N)$, when all acquired ERD fall in the same scale subinterval, and its maximum value is zero when all ERD are distributed evenly in every scale subinterval [13]. Thus, the entropy S, as a macroscopic value defined by Eq. (9), gives a quantified measurement of ERD evolution or fracture process, and can be used to assess the evolving damage states of materials.

3 Experiments

An experimental method is developed to accomplish the acquisition of ERD in laboratories.

3.1 Fabrications of Specimen

Samples of paper sheets were prepared by cutting into the standard metal-specimen-like tension specimens (gauge length is 40 mm, and the width is 20 mm) in using a conventional cutter, as shown in Fig. 2. Adequate and accurate arc transition area is needed to be reserved with a view to give rise to a uniform and unidirectional stress state along cross section. In this experiment, the ivory board (its grammage is 240 g/m^2), a high-quality family of paper sheets and wildly used in cigarette, pharmaceutical, food, and video products in various cassette packaging and in business card invitation card, certificate, etc. in the printing industry, is used to illustrate our novel approach. Here, we prepared one group consisted of 20 specimens in mechanical direction (MD).

3.2 Acquisition of Events of Random Damage in Paper Specimens Subjected to Uniaxial Quasi-Static Tension

Mechanical testing of paper specimens was carried out under identical laboratory conditions (constant humidity and temperature, about 28 °C, 65 % RH) with a view to obtain reproducible results since paper is strongly influenced by moisture [7].

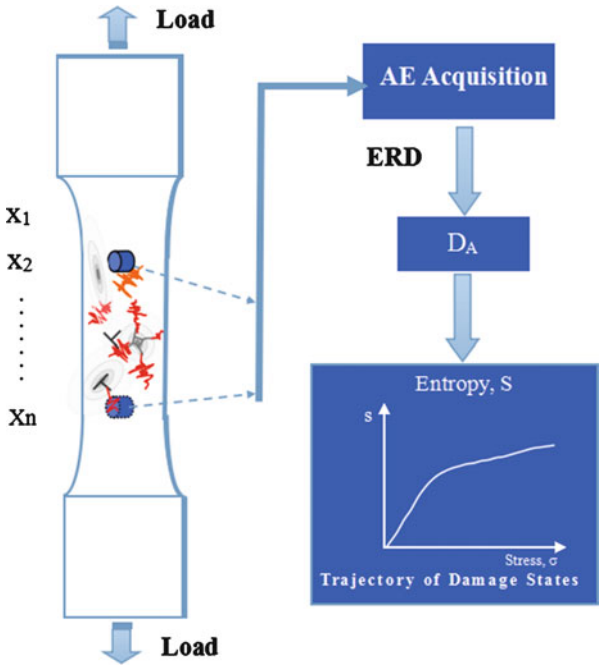

Fig. 2 Experimental data acquisition setup and assessment flow

All specimens were loaded continuously to rupture at a constant displacement rate of 0.75 mm/min using an MTS Universal Tensile Testing Machine (CMT4304). Meanwhile AE tests were carried out simultaneously with the stress tests by using a PAC (Physical Acoustics Co.) data acquisition system (Micro-II AE of PAC). To capture the acoustic emission waves, we bonded the piezoelectric sensor onto the surface of the specimen directly.

Given that paper sheets may be susceptible to binder, two symmetrical sensors were laid out equidistantly beyond the range of fracture location, where they were about 20 mm far from the centerline of the gauge length. To exclude the external noise (mechanical noise mainly) a threshold value 30 dB for the output is defined, which was determined by setting gradient increasing value of PAC AE instrument at zero loading until finding one value below which no detectable AE signals exist. The sensor's name is NANO-30 and the acoustic signals were preamplified by 40 dB using a preamplifier (PAC) with a band-pass filter of 20–1,200 kHz. The signals were then fed into a PAC AE measuring system.

After the experiment is properly started, once load reached certain level and AE amplitude exceeded the predetermined threshold (30 dB), AE data was captured, and meanwhile the corresponding loading parameter was recorded.

Experimental AE data was then extracted, filtered, and integrated and then a measurable multivariate D_A was then established and entropy S can be applied to quantify the evolution of ERD. The assessment of ERD damage state is as follows. All the above is shown in Fig. 2.

4 Results and Discussion

4.1 Scanning Electron Microscope Study of Paper Specimen

The surface characterization of the morphology of microstructure within fracture and non-fracture regions of investigated paper sheets (the ivory board) is examined using SEM, and the obvious white spots or areas are damage regions, as shown in Fig. 3.

It is obvious that the crack line of paper sheet presents nonlinear (it is found to self-affine in some studies) in Fig. 3a. The nonlinearity of paper fracture may relate to the disordered geometry of the fiber network, local mass nonuniformity, localization of existing inherent or newly generated damage inside paper sheet, and other factors those together result in disorder of stress field during fracture, which inevitably implies the randomness and complexity of fracture process. In non-fracture regions (Fig. 3b), the obvious white spots or areas are damage regions, which are developed by the increasing stress, or also in manufacturing and converting process. The fracture region is further amplified in Fig. 3c for detailed view; white fibers were filled out and space information was obvious (the dark grey of surface is the color of clad layer made before SEM procedure). In order to observe the fracture fibers more clearly, the local region is further amplified in Fig. 3d, where every individual fiber is distinguishable and morphology of fiber tip is sickle shaped, which is very close to raw wood fibers.

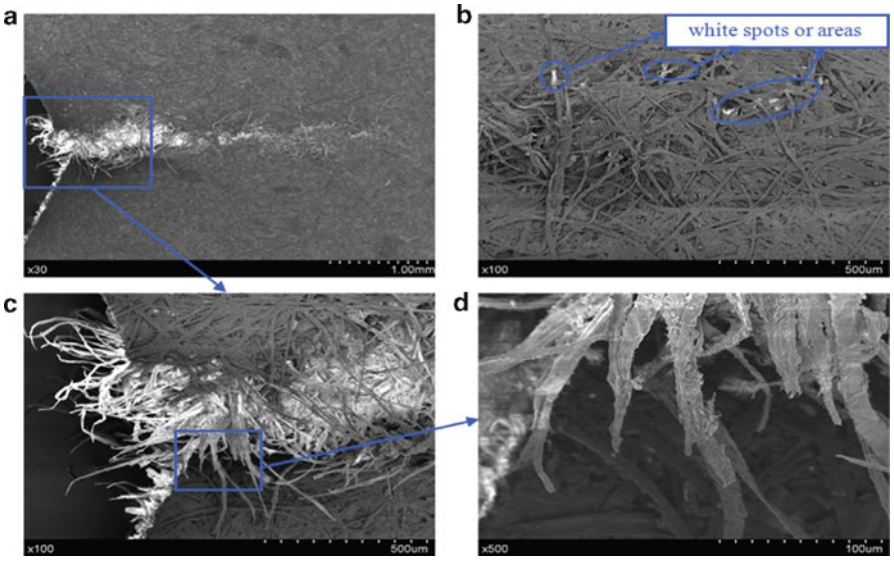

Fig. 3 (**a**) Overview of fracture, (**b**) non-fracture region, (**c**) detailed view of fracture region, (**d**) broken or raw fibers

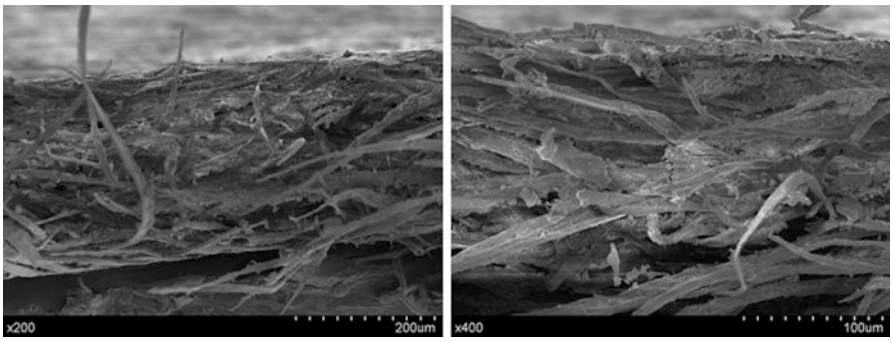

Fig. 4 Cross section of investigated paper material (ivory board)

As mentioned, it is reasonable to describe fracture process as follows: when submitted to mechanical loading to a certain level, the paper sheet enters the initiation of an irreversible random damage state activated from certain defects (e.g., existing damage or newly generated damage in use), which is regarded as weak spots or areas. If overstressed, the specimen ruptured completely, when a nonlinear trace of rupture is behind.

In Fig. 4a, the internal structure of the network in cross section is layered. Most of the failure fibers are observed to be partial and the orientation of the stretched fibers corresponds to the direction of the tensile direction. The shape of fibers is disordered and their surfaces are curved. Besides, closely nonfibrous components (such as fillers and fines) between fibers can be observed. Therefore, we concluded that when fibers were filled out from network body during fracture process, besides fiber breakage and the fiber–fiber bond failure, the damage mechanism in the structure also included delamination between fibers and nonfibrous components, disintegration of nonfibrous components, and "fretting" between different components (that is, the friction in dislocation of fibers).

4.2 The Amplitude Spectrum of $\mathbf{D_A}$ *to Reveal the Evolution of Multi-scale Events of Random Damage*

We first examine the amplitude spectrum of D_A. In this work, the amplitude of acquired ERD was divided into 20 scales ($N = 20$), and the width of observation was 0.25 N/mm ($w = 0.25$ N/mm). In Fig. 5a, every individual amplitude spectrum shows the distribution shape of no. of ERD covering all scales of amplitude at a certain observation window (here tensile strength is used as observation criteria), and also shows the evolution of amplitude spectrum with moving observation window during fracture process. Furthermore Fig. 5b also shows variation of the amplitude spectrum of D_A more obviously in 3D. Then we make the following observations:

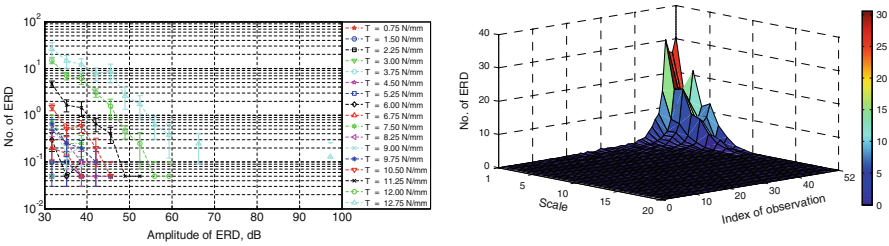

Fig. 5 The amplitude spectrum of D_A distributions in paper specimens in MD. Here, the amplitude of acquired ERD was divided into 20 scales ($N = 20$), and width of observation window was 0.25 N/mm ($w = 0.25$ N/mm). (**a**) 2D, (**b**) 3D

1. Initially, low-amplitude ERD is dominant, as T increases, and higher amplitude ERD emerge and gradually populate more bandwidth of the spectrum during fracture process. Assumption, cited in our previous work, is that, statistically each random damage mode would cover a certain range of ERD amplitudes, here spectrum that presents continuously spreading means changing random damage modes.
2. In the preceding phase (about $T \leq 10.5$ N/mm), the no. of ERD is less (average value is less than one mostly) and nearly all are of low amplitudes (most in 30–40 dB). Thus we make the following analysis: since the amplitudes are proportional to the energy released by the responsive ERD, it is reasonable to infer that in the preceding phase at these tensile-strength levels those ERD releasing lower energy occur in the modes of weak debonding, fibril breakage, and other initiation of low-energy-intensive micro-damage [9]; hence acoustic emission activity is less pronounced and their numerous amplitudes are below the predetermined threshold (30 dB), so it is hard to capture them and exhibits small group of data. As a whole, this phase will remain for a substantial long term all over fracture process. The physical nature of this phenomenon may be determined by rheological nature of paper material causing a long ductile/elastic stage under quasi-static tensile, which is influenced by instrumentation and physical conditions at the same time.
3. After $T > 10.5$ N/mm, ERD (some average no. of ERD > 1) begin to occur noticeably. Appreciable ERD begin to team with increasing T due to the increasing severity degree of damage activities, when higher energy-intensive micro-damage, such as failure of fiber–fiber bonds with high bonding energy and mass fiber–fiber breakages begin to appear.
4. The no. of ERD (Fig. 5a) shows a monotonic decreasing trend with increasing amplitude scale at specified tensile strength level, but no. changes insignificantly in the last subinterval, especially after $T > 10.5$ N/mm. No. of ERD (Fig. 5b) in same scale increases monotonically with increasing T except in the last stage, when the shape of amplitude spectrum of ERD toboggans at about 12.5 N/mm, which becomes a precursor to the failure of paper specimens.

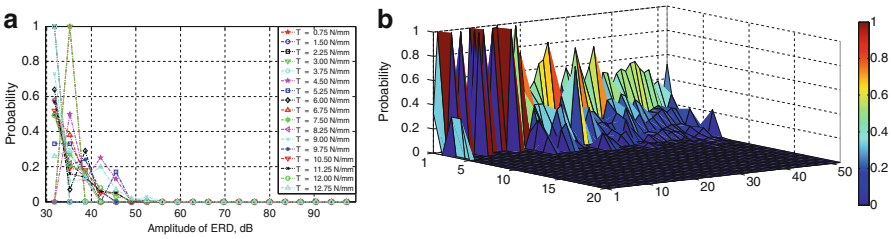

Fig. 6 The probability spectrum space of D_A under tension. (**a**) 2D, (**b**) 3D

5. Last but not the least, we should not overlook one observation that the amplitude of ERD just can reach about 50–65 dB mostly, and ERD whose amplitude is higher than 65 dB is nearly "total blank." Only at high level of stress (T >12.75 N/mm) ERD rarely appears at about 99 dB, when it is thought to be the moment of paper sheets ruptured and audible sounds produced.

4.3 *Probability Spectrum Space of* $\mathbf{D_A}$ *to Reveal the Evolution of Multi-scale Events of Random Damage*

Figure 6 shows the similar results given in Fig. 5, but now presented using probability distribution $\overline{D_A}$. In Fig. 6a, multiple probability spectrum being put together seems to be disordered, but it is obvious that ultimately all the probability spectrums overlap to the same null line after about 65 dB, which means amplitude of ERD rarely goes beyond 65 dB. In Fig. 6b, the shape of probability spectrum appears smoother with the increasing observation levels, which indicates higher amplitude of ERD accounts for less and less proportion in all amplitudes with the ever-increasing T.

4.4 *Trajectory of Damage States to Assess the Fracture Process of Paper Specimens*

When entropy S is correlated with the applied tensile strength, we get trajectory of damage states (TDS), namely $S-T$ curve. As shown, it is difficult to distinguish from different various stages of fracture process in Fig. 7a (the tensile strength vs. entropy curve figure), while more details of fracture process were easily showed in Fig. 7b (tensile strength vs. entropy curve figure).

In Fig. 7b, data fluctuation of S value at certain T value is inevitable due to statistical effects of mass specimen's data, which, however, have been smoothed by using a moving average algorithm. Next we shall show how S can be used to recognize and assess the evolving damage states in fracture process. Overall, the

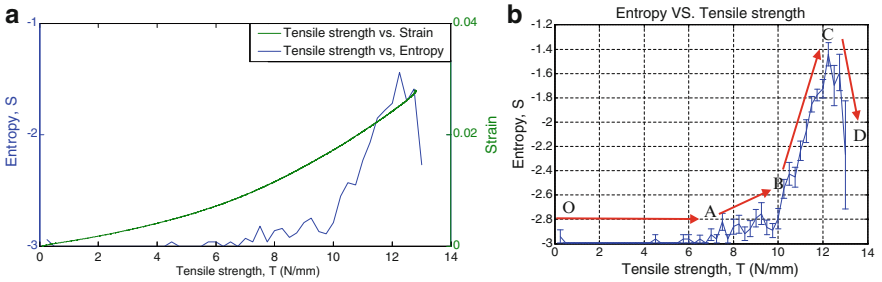

Fig. 7 (**a**) Tensile strength versus strain curve and tensile strength versus entropy. (**b**) Trajectory of damage states (TDS) for paper specimens in MD under tensile loading

$S-T$ curve is clearly distinguished according to the variations of the tendency of S: zero stage (labels O–A), slow growth stage (labels A–B), rapid growth stage (labels B–C), and failure (after point C). The increase of S value demonstrates increase of the uncertainty on damage states. The fracture process can be divided into the following successive stages:

1. Firstly, during zero stage (labels O–A), S remains almost at the least value ($S=-2.9957$), when none of the ERD appears but remarkably the stress has been increasing.
2. Secondly, during slow growth stage (labels A–B, $dS/dT_{A-B}>0$ mostly), from point A the entropy S begins to increase, which implies the initiation of fracture process.

   These above two stages (before at critical point B) correspond to the preceding phase (about $T \leq 10.5$ N/mm) in Fig. 5 when the no. of ERD is less (average is less than one mostly) and nearly all that have low amplitudes (most in 30–40 dB) in weak damage modes (such as feeble debonding, fibril breakage, and other initiation of low-energy-intensive micro-damage) are dominant.
3. Thirdly, the rapid growth stage (labels B–C, $dS/dT_{C-D}>dS/dT_{A-B}$ mostly) illustrates that more and severe ERD such as fiber failure begin to emerge. This stage corresponds to the noticeable occurrence of ERD (after $T>10.5$ N/mm) in Fig. 5, when appreciable ERD begin to team with increasing T due to the increasing severity of damage activities.

   On the whole, entropy S ($dS/dT>0$) keeps increasing with the growth of T (the moving of observation window) until the peak value point C, but consistent S ($\mathrm{d}S/dT=0$) seems not to be existent. Meanwhile, this state corresponds to continuous-spreading spectrum that demonstrates changing random damage modes in Fig. 5, which evidenced the law that evolution of ERD tends to maximize the value of probabilistic entropy. Therefore, this evaluates the conclusion that the more the observed amplitudes will be spread out over the available range, the more the different random damage modes are present, and so the larger will be the entropy.

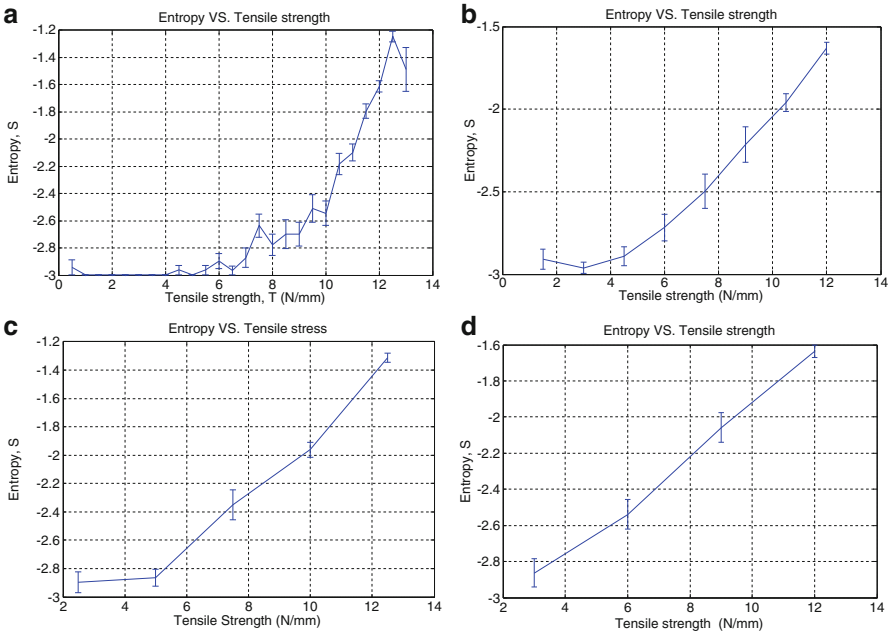

Fig. 8 Trajectory of damage states (TDS) for different widths of observation window. (**a**) $w = 0.5$, (**b**) $w = 1.5$, (**c**) $w = 2$, (**d**) $w = 3$

4. The $S - T$ curve bends downward abruptly as soon as after C point, and then the degree of dispersion is larger and larger. Once this stage is entered, the paper sheets must approach failure.

   Synthesizing those mentioned above, TDS shows an excellent agreement with the abovementioned spectrum in Fig. 5 and provides a realistic description of whole fracture process. Actually, the critical points A, B, C, and D present the transition zone of knee in TDS. The first stage (labels O–A) in TDS corresponds to the viscoelastic behavior of paper material (Fig. 7a), and only after that (in visco-plastic stage) the acoustic activities begin to occur progressively [7, 12]. Presently, it is not yet clear whether the critical phenomenon of TDS is associated with any mechanical significance of paper material.

4.5 The Influence of Width of Observation Window, w, *on Trajectory of Damage States*

Criteria assume that the acquiring ERD were divided into 20 scales and the width of observation window was 0.25 N/mm in the abovementioned TDS ($N = 20$, $w = 0.25$ N/mm). These, and others, may have given a relative adequate characterization and evaluation of the fracture process in paper sheets. If the width of observation window, w, is different, TDS is dissimilar correspondingly. Figure 8

shows transient curves at w ranging from 0.5 to 3 N/mm. The larger the w is set, the more smooth the $S-T$ curve looks due to cumulative effect of observation window. But the apparent advantage of larger observation width is capability of grasping the whole growing trend of S, which, however, may potentially overwhelm useful transient details of fracture process. We call this phenomenon as "fuzzy effect" from the point to surface in observation window. The extremity of max observation width is just a slop line joining several points, and the value of S, on the whole, keeps increasing in a sense. All curves (covering different w value) indicate that an approximate trend of entropy S is increasing, but fluctuates frequently in detailed section.

Presently the influence of width of observation window, w, on TDS is just in a "smeared out" sense in terms of presenting the evolution nature of fracture process, if we must term it, comprehensively termed "multi-width of observation window" provisionally. The idea is that w are "elastic" and can be determined by degrees of truth needed. Practically, the width of the observation window depends on material itself and damage style (such as loading state, loading styles). This finding again deserves further investigations.

Obviously, it is desirable to combine the usage of some or all multi-width of observation window when comprehensive and systematic inquiry is required.

5 Conclusion

This investigation herein presents an experimental, computational, and data-enabled method to study the statistics of ERD in fracture process in paper sheets subjected to tensile load. An experimental means has been developed to make characterization and evaluation of fracture process in paper sheets with view to its difficulties of theoretical study, of which the acquisition of ERD based on AE monitoring in paper specimens subjected to uniaxial quasi-static tension was recorded real timely. A multivariate approach to quantify the evolution of ERD laid the foundation for further multi-scale analysis of ERD in such sophisticated damage system in the fracture process of paper sheets. It was found that the spectrum of multi-scale ERD represented fracture process under a nominal stress field and laid broad merit for studying the physical nature of the actual damage evolution. The trajectory of damage state (TDS), namely $S-T$ relationship, was proposed to provide a realistic description of fracture process on a nonequilibrium damage system involving multiple space and time scales in fracture process, which display the evolution of detailed stages by data-enabled method. Hence the Gibbs probability entropy S was employed to recognize and assess evolving irreversible damage states successfully.

The investigation tells a story about a novel method to study the statistical analysis of damage evolution based on a multicomponent variate in paper material. But, this is not the end of the story. Further efforts are therefore required to make for

better understanding of the fracture process involving its physical and mechanical properties in paper material.

Acknowledgment The authors would like to thank the pioneering work of Gang Qi in this field and thank for the financial support provided by Tianjin University of Science and Technology.

References

1. P. Isaksson, R. Hägglund, P. Gradin, Continuum damage mechanics applied to paper. Int. J. Solid. Struct. **41**, 4731–4755 (2004)
2. C.A. Bronkhorst, Modelling paper as a two-dimensional elastic-plastic stochastic network. Int. J. Solid. Struct. **40**, 5441–5454 (2003)
3. Q.S. Xia, M.C. Boyce, D.M. Parks, A constitutive model for the anisotropic elastic-plastic deformation of paper and paperboard. Int. J. Solid. Struct. **39**, 4053–4071 (2002)
4. M.K. Ramasubramanian, Y. Wang, A computational micromechanics constitutive model for the unloading behavior of paper. Int. J. Solid. Struct. **44**, 7615–7632 (2007)
5. Y.L. Bai, M.F. Xia, F.J. Ke, H.Y. Wang, Statistical mesomechanics of solid, linking coupled multiple space and time scales. Appl. Mech. Rev. **58**, 372–388 (2005)
6. Y.L. Bai, H.Y. Wang, M.F. Xia, F.J. Ke, Trans-scale mechanics: looking for the missing links between continuum and micro/nanoscopic reality. Acta Mech. Sin. **24**, 111–126 (2008)
7. S. Dillon, R. Jones, V. Buzzi, On the mechanical behaviour of aging and recycled paper structures under cyclic humidity. J. Compos. Struct. **47**(1–4), 727–736 (1999)
8. D. Graham, D. Kao, B. Knight, Acoustic emission applied to mechanically loaded paper, *EWGAE, DGZfP-Proceedings BB 90-CD*, Lecture. **41** (2004)
9. T. Yamauchi, S. Okumura, M. Noguchi, Acoustic emission as an aid for investigating the deformation and fracture of paper. Trans. Tech. Sect. Can. Pulp Pap. Assoc. **16**(2), 44–47 (1990)
10. M.P. Sarfarazi, *Acoustic Emission and Damage Constitutive Characteristics of Paper* (The Institute of Paper Science and Technology, Atlanta, GA, 1992)
11. L. Salminen, *Aspects of fracture processes in paper* (Helsinki University of Technology, Espoo, Finland, 2003)
12. T. Yamauchi, S. Okumura, K. Murakami, Measurement of acoustic emission during the tensile straining of paper. J. Pulp Pap Sci. **15**, 23–27 (1989)
13. G. Qi, M. Fan, S.F. Wayne, Measurements of a multicomponent variate in assessing evolving damage states using a polymeric material. IEEE Trans. Instrument. Measure. **60**(1), 206–213 (2011)
14. G. Qi, J.Y. Li, M. Fan, J.H. Li, S.F. Wayne, Assessment of statistical responses of multi-scale damage events in an acrylic polymeric composite to the applied stress. Probabilist. Eng. Mech. **33**, 103–115 (2013)
15. Ming Fan, et al. On assessing the influence of intermittent acquisition and moving window on the results of AE measurements, Advance in Acoustic Emission Technology: Proceedings of the World Conference on Acoustic Emission-2013.
16. G. Qi, S.F. Wayne et al., Probabilistic characteristics of random damage events and their quantification in acrylic bone cement. J. Mater. Sci. Mater. Med. **21**, 2915–2922 (2010)
17. J.W. Gibbs, *Elementary Principles in Statistical Mechanics*, vol. 168 (Dover, New York, 1960), pp. 44–45

The Use of Acoustic Emission for the Construction of a Generalized Fatigue Diagram of Metals and Alloys

O.V. Bashkov, T.I. Bashkova, and A.A. Popkova

Abstract The chapter presents results of acoustic emission (AE) studies of the stages of fatigue fracture of steels and aluminum alloys. Studies were conducted to review the technique of constructing generalized fatigue diagrams of various metals and alloys using the AE method, which greatly reduces the number of tests conducted using fractography. Fatigue stages at tests of sample alloys were identified from the activity of AE signals emitted by various types of AE sources (dislocations, micro- and macrocracks). Separation of the AE source types was made on the basis of an analysis of the distribution of "AE signal energy E_{AE} vs. frequency parameter K_f." Generalized fatigue diagrams of some alloys were built according to the results of fatigue tests with different maximum stress values.

1 Introduction

A wide variety of engineering manufactures and constructions are used under conditions of cyclic strain. A material's properties, which influence the durability of constructions, determined by the resistance variable external stress.

At the present time, the evolution of dislocations and fault structures of metal materials at cyclic loading is considered to be stepwise. In 1928, B. P. Heig [1] revealed the staging of velocity accumulation of heat in fatigue tests. In the works of V. S. Ivanova, V. F. Terentyev, S. Kocanda, et al. [2–4], the process of fatigue fracture was divided into four periods on the basis of the studies of mechanical properties and fractography analysis: (1) incubation; (2) development of microcracks; (3) irreversible damage; and (4) destruction. The first period includes

O.V. Bashkov (✉) • T.I. Bashkova • A.A. Popkova
Komsomolsk-on-Amur State Technical University, Komsomolsk-on-Amur, Russia
e-mail: bashkov_ov@mail.ru

G. Shen et al. (eds.), *Advances in Acoustic Emission Technology: Proceedings of the World Conference on Acoustic Emission-2013*, Springer Proceedings in Physics 158,
DOI 10.1007/978-1-4939-1239-1_26,

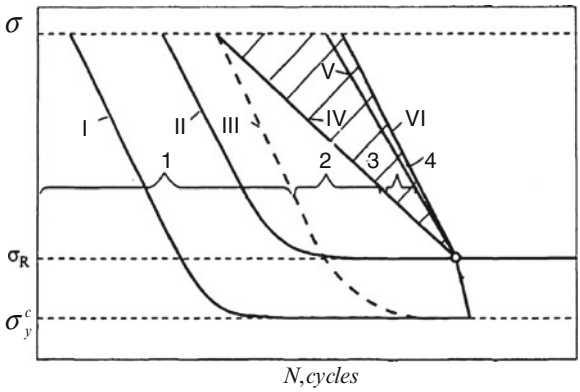

Fig. 1 Schematic representation of the diagrams of fatigue: σ_R—fatigue limit; σ_y^c—cyclic yield stress limit

three stages: I—cyclic microyield; II—cyclic yield; III—cyclic hardening. The second period comprises stage IV—propagation of submicrocracks up to the size of microcracks. The third period includes the step of microcrack propagation up to the size of macrocracks (stage V). The fourth period is the shortest and comprises the step of failure (stage VI). Stages were named by analogy with the static deformation. For different materials, research findings were the basis for generalized fatigue diagram division at the stage of fatigue (Fig. 1). Study of AE stages of fatigue-crack propagation in materials presented in [5, 6].

In this chapter, AE data during cyclic deformation of various alloys (steel, titanium alloy, aluminum alloy) were analyzed in order to construct generalized fatigue diagrams for these alloys.

2 Materials and Methods of Investigation

Studies were carried out on metal alloys that are actively used in industry and aircraft: aluminum alloy 2024, steel 20. Samples were made of sheet material with a thickness of 2 mm by cutting the electrical discharge circuit. Samples were in the form of an isosceles triangle (a beam with equal stress) (Fig. 2). Form samples were chosen to ensure an equal probability of damage accumulation over the entire surface of the sample material.

The authors developed a testing machine to test samples from different alloys on cyclic fatigue.

The test facility ensures the division of contours of constructive metal connections by laying a sound-absorbing material. The testing machine carries out cyclic tests of samples by a console bend. A structural kinematic scheme of the testing machine is shown in Fig. 3.

On the massive passive grip 5, sample 3 is attached to frame 8 through absorbing elements 7. The piezoelectric sensor 4 is mounted on the sample. The movable portion of the sample is also attached through absorbing elements 2 to movable gripper 1. Movable gripper 1 is driven by a crank mechanism 9 through pusher

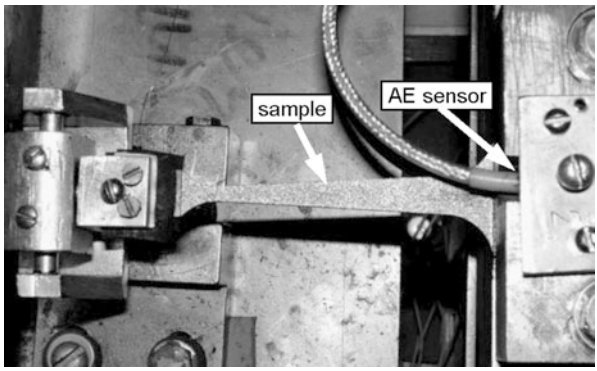

Fig. 2 Sample mounted in the test apparatus for cyclic tests

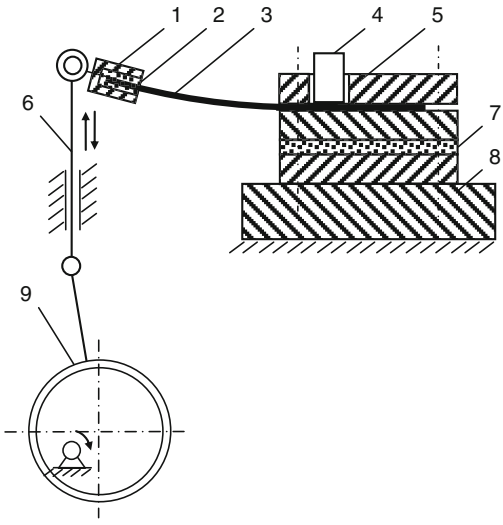

Fig. 3 Structural kinematic scheme of testing machine

6. Cyclic tests were carried out according to the scheme of the cyclic bending samples with fixed end at a frequency of 29 Hz. The piezoelectric sensor has a frequency bandwidth of 50–550 kHz.

Studies were conducted on a given test program: Some of the samples were brought to destruction; the others were adjusted to varying degrees with differing numbers of fatigue load cycles. The maximum stress in the test was set to be less than the yield stress. Each series of tests was carried out for at least two stresses. After reaching a predetermined number of cycles, testing was stopped, and microstructural studies were performed to detect microcracks in the samples. To do this, samples were cut using a cutting spark along the plane dividing them into two equal symmetrical halves. The analysis of AE signals was performed using the AE signal separation technique developed by the authors. AE signals were

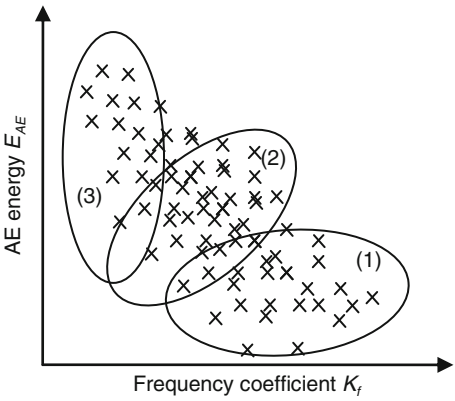

Fig. 4 Two-parameter distribution E_{AE} vs. K_f: (1) dislocations; (2) microcracks; (3) macrocracks

divided into various types of emitted sources [7]: dislocations (the sources of plastic deformation), micro- and macrocracks.

As a result of previous studies, AE signals were classified by source types based on the analysis of the two-parameter distribution AE energy E_{AE} between the frequency coefficient K_f (E_{AE} vs. K_f) (Fig. 4).

The frequency coefficient K_f was determined from the calculated coefficients of the wavelet decomposition of AE signals. K_f is defined as the sum of standard deviations of AE signals' wavelet decomposition coefficients.

The wavelet transform was carried out on the basis of wavelet db8. The frequency coefficient K_f shows the contribution of a frequency component in a signal:

$$stdFQ_j = \sqrt{\frac{1}{n}\sum_{i=1}^{n}\left(x_{ji} - \overline{x}_j\right)^2},$$

$$K_f = \sum_{j=1}^{m}\left(stdFQ_j \cdot (m+1-j)\right) \Big/ \sum_{j=1}^{m}\left(stdFQ_j\right),$$

where $stdFQ_j$ is the standard deviation of the j-th wavelet decomposition coefficient of AE signal, n is the number of discrete samplings of AE signal, m is the number of the wavelet decomposition coefficients, x_{ji} is the value of the i-th discrete sampling of the j-th wavelet decomposition coefficient, and $\overline{x}_j$ is the mean value of the j-th wavelet decomposition coefficient.

The physical sense of frequency coefficient K_f can be defined as the contribution of the frequency component of the wavelet decomposition in the AE signal as a whole.

To establish the membership of AE signals recorded during the deformation and failure of various materials, researchers have conducted numerous tests. The tests were conducted under static tension/compression and cyclic loading conditions.

The distributions affect the geometric factor (sample size) and hardware parameters. The results of the separation of AE signals are not influenced by the type of alloy, as the origin and size of AE sources (microcracks, dislocations) are identical [8–10]. Thus, the same types of samples were prepared by common types of classification parameters for AE sources.

3 Research Results

Analysis of AE signals during the period from the formation of cyclic fatigue until the destruction of the samples showed that the accumulation of damage has a stage character. We found that testing the sample at various maximum tensions maintains the stage character and the number of selected stages. Schematically, the nature of the AE count for AE signals emitted by various AE sources is as follows (Fig. 5).

Based on the total AE diagrams obtained with test alloys of aluminum, titanium, and steel at various maximum tension cycles, stages of cyclic fatigue have been allocated. These stages have been allocated on the basis of the analysis of the nature of the AE count radiated from various AE sources.

From AE signals recorded during the test, there are graphs of the two-parameter distribution $E_{AE} - K_f$. Figure 6 shows diagrams of the two-parameter distribution $E_{AE} - K_f$ AE signals recorded in samples of aluminum alloy 2024, brought to destruction with varying stress amplitudes of the cycle.

The distribution of $E_{AE} - K_f$ AE signals was divided into different groups according to the method developed earlier for materials under the static test. After this procedure, we divided the signals into different types of AE sources: dislocations, microcracks, and macrocracks.

The distribution indicates the separation of AE signals on the types of sources:

1. Dislocations: $(K_f > 3.5) \cap (E_{AE} < 0.5\ \text{mV}^2\ \text{s})$;

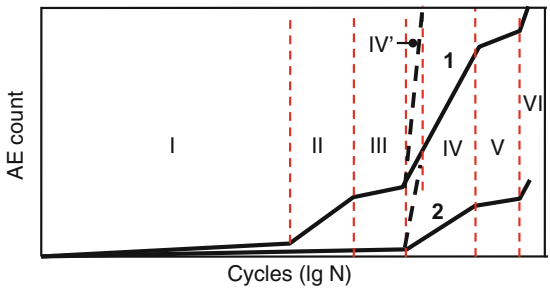

Fig. 5 Schematic representation of AE count $N_{AE} = f(N)$ at the damage accumulation during cyclic fatigue: (1) AE count of dislocation-type AE sources; (2) AE count of AE sources at the formation and development of microcracks

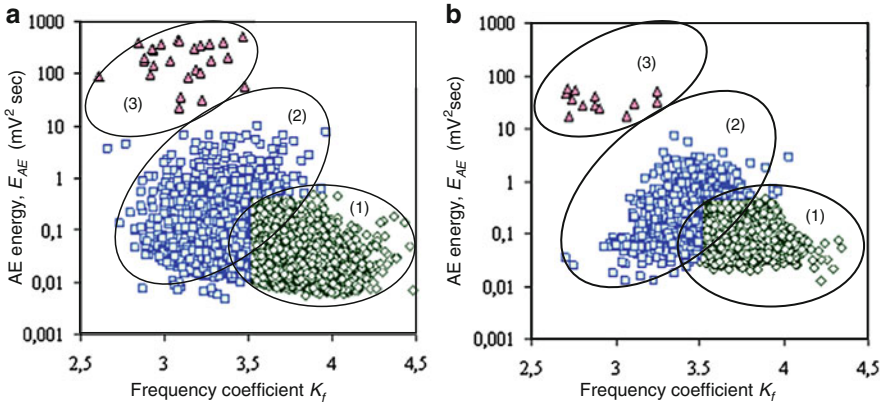

Fig. 6 Two-parameter distribution E_{AE} vs. K_f when testing samples of alloy 2024 [(1) dislocations, (2) microcracks, (3) macrocracks, (the sources of plastic deformation)]: (a) $\sigma_{max} = 218$ MPa; (**b**) $\sigma_{max} = 235$ MPa

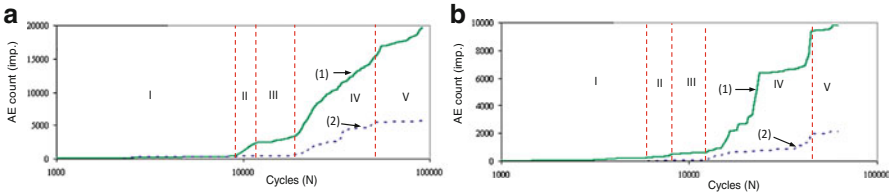

Fig. 7 AE count of different types of AE sources when testing samples of alloy 2024 [(1) dislocation, (2) microcracks]: (**a**) $\sigma_{max} = 218$ MPa; (**b**) $\sigma_{max} = 235$ MPa

2. Microcracks: $[(0.5 < E_{AE} < 20\ \text{mV}^2\ \text{s}) \cap (K_f > 3.5)] \cup [(E_{AE} < 20\ \text{mV}^2\ \text{s}) \cap (K_f < 3.5)]$;
3. Macrocracks: $(K_f < 3.5) \cap (E_{AE} > 20\ \text{mV}^2\ \text{s})$.

Macrocracks differed from microcracks in that the elongation of the crack for one episode of AE signal radiation was greater than 5–10 μm.

After the signals are separated into groups on the same graph plots, separate storage of AE signals is constructed, as shown in Fig. 5. Diagrams of the AE count for samples of aluminum alloy 2024 are presented in Fig. 7.

A graphical account of AE (Fig. 7) allows an indirect assessment of the evolution of defect accumulation at various stages of fatigue. This becomes possible when analyzing the activity of different types of AE sources (dislocations, microcracks, and macrocracks).

Unlike classic endurance tests, studies outlined in the work were carried out on a small number of samples for each test point and do not exceed three. Each of the

samples of the test material has an absolutely distinct structure within which statistical confidence is a major factor determining the endurance of the material at a given stress level. Based on this hypothesis, the evolution of the defect structure of the material under cyclic loading must respect general registration patterns of AE signals in the accumulation of fatigue. Figure 6 contains graphs of AE count for various sources under cyclic loading of 2024 alloy samples with different stress amplitudes σ_{max}. One should note the presence of common trends and patterns of change in the accumulation of AE signals not only in view of the graphs, but also for all of the tests of samples of this alloy.

We can identify many small steps in each of the graphs, causing the change in the slope of curves accounting for AE, considering the unsteady development of the accumulation of fatigue. However, the selection and explanation of cyclic fatigue stages on basis of the AE data was possible only on set graphs of AE count various signal types.

Based on diagrams of AE count obtained when testing aluminum, titanium alloys, and steel for various values of maximum stress, we allocated stages of cyclic fatigue. These stages have been allocated by analyzing patterns of accumulation of AE signals emitted by different AE sources.

4 Discussion

Below is the technique for separation of fatigue stages on the analysis of AE count graphs for AE signals of various types (Fig. 6). Phase I has a minor extent and has relatively low activity of both types of AE signals.

In stage II, there is an increase in the activity of dislocation-type AE signals associated with the general cyclic yield, and the average count rate over the term of the AE stage II peaks in comparison with the other stages. The activity of microcrackstypes AE signals in stage II is minimal.

Stage III, as a rule, is the most prolonged and has a low counting rate of AE signals of all types. During phase III, the basic processes of hardening or softening of the alloy occur.

Stage IV is characterized by an increased activity of the AE signals emitted by the formation of microcracks and dislocation-type AE signals. Is observed typical for microcracks propagation increase the activity of dislocation-type AE signals with subsequent relaxation.

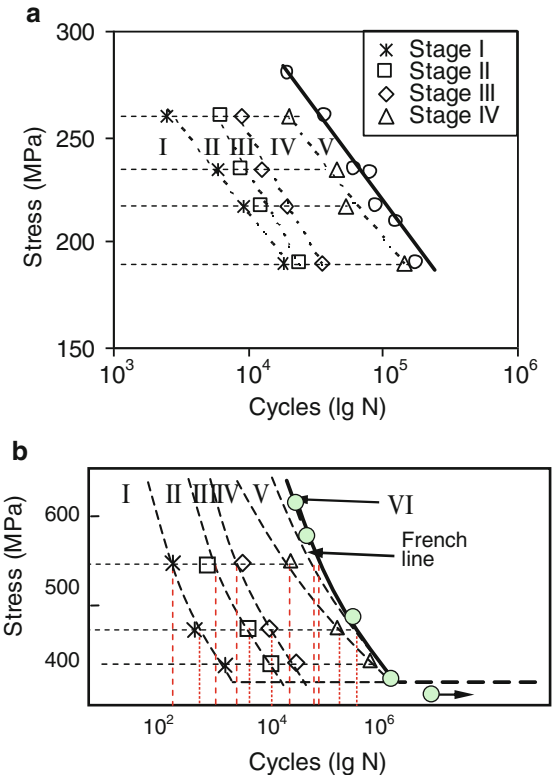

Fig. 8 Generalized fatigue diagram: (**a**) aluminum alloy 2024; (**b**) steel 20

In stage V, the activity of AE signals emitted of the dislocation type and microcracks may decrease due to deformation localization by combining multiple cracks in a small number of macrocracks.

During the short-term stage VI, a fuller sample occurs, accompanied by bursts of activity signals of all types due to the high growth rate of the main crack. A generalized fatigue diagram was built on leased stages for 2024 aluminum alloy and carbon steel 20 (Fig. 8).

References

1. B.P. Haigh, Hysteresis in relation to cohesion and fatigue. Trans. Faraday Soc. **24**, 125–137 (1928)
2. V.S. Ivanova, V.F. Terentyev, *The Nature of Metal Fatigue* (Metallurgy, Moscow, 1975), 456 p
3. V.S. Ivanova, A.A. Shanyavsky, *Quantitative Fractography. Fatigue Failure* (Metallurgy, Chelyabinsk, 1988), 400 p
4. S. Kocanda, *Fatigue Failure of Metals* (Sijthoff and Noordhoff, Alphen aan den Rijn, 1978), 368 p

5. A. Berkovits, D. Fang, Study of fatigue crack characteristics by acoustic emission. Eng. Fracture Mech. **51**(3), 401–416 (1995)
6. D.O. Harris, H.L. Dunegan, Continuous monitoring of fatigue crack growth by acoustic emission techniques. Exp. Mech. **14**(2), 71–91 (1974)
7. O.V. Bashkov, T.I. Bashkova, A.A. Popkova, Stages of bending fatigue of titanium alloys and their identification by acoustic emission, in *30th European Conference on Acoustic Emission Testing, 7th International Conference on Acoustic Emission*, Granada, Spain, 12–15 September 2012, # 76
8. S.V. Panin, A.V. Byakov, V.V. Grenke, I.V. Shakirov, O.V. Bashkov, Developing and testing a laboratory system for recording and analysis of acoustic emission. Optoelectron. Instrument. Data Process. **47**(1), 93–103 (2011)
9. S.V. Panin, A.V. Byakov, P.S. Lyubutin, O.V. Bashkov, Staging of a localized plastic deformation during ex-tension of D16AT alloy specimens based on the data of acoustic emission, mapping of surface deformations, and strain gauging. 1. Specimens with holes of different diameters. Russ. J. Nondestruct. Test. **47**(9), 611–622 (2011)
10. S.V. Panin, A.V. Byakov, P.S. Lyubutin, O.V. Bashkov, Staging of a localized plastic deformation upon the tension of D16AT alloy specimens on the basis of acoustic emission, sur-face deformation mapping, and strain gauging data. II. Specimens with notches of different depths. Russ. J. Nondestruct. Test. **47**(12), 815–823 (2011)

Deflection on Hit-Count Curves in Acoustic Emission Could Reflect the Damage Extent of C/C Composite Material Structure

Haibei Gu, Peng Ge, Kai Zhang, and Guoliang Wang

Abstract Counts of each hit are related to the damage extent of C/C composite material structure. The relative curves of Hit and Count as well as Hit and Energy of AE, attained from static load procedure of C/C composite structure, could reflect the severity of damage extent in a quite noticeable way—the ascending curves of Hit and Count as well as Hit and Energy deviate from their prior linearity and deflection point appears in a sudden when more severe damage occurs; and the ratio of load at this time to the final fracture load is steady for a certain structure. This method could early warn the failure of C/C composite structure effectively and estimate the fracture load. This phenomenon could also provide some suggestion to interpret the evolution of damage field of composite structure.

1 Introduction

Observing the acoustic emission (AE) data of the composite structure in loading process, a general principle would be found: The Counts-cumulative histogram of the channel near to area of final structural damage is prominent comparing with that of the other channels. But the hits-cumulative histogram is not so obvious. In the process of structure destruction from damage occurrence to damage extension under load, what are the growing rules of the Counts and Hits of each channel like? Is there a specific relationship between the correlation of the two parameters and the extent of structural damage?

H. Gu (✉) • P. Ge • K. Zhang
Beijing Institute of Structure and Environment Engineering, Beijing 100076, China
e-mail: moonisland@yeah.net

G. Wang
Key Laboratory of Space Physics, Beijing 100076, China

G. Shen et al. (eds.), *Advances in Acoustic Emission Technology: Proceedings of the World Conference on Acoustic Emission-2013*, Springer Proceedings in Physics 158,
DOI 10.1007/978-1-4939-1239-1_27,

From the definition of AE counts [1] it can be estimated that counts of each AE hit are associated with threshold. In addition, it is also associated with duration, frequency, and amplitude of the signal. In case of a fixed threshold, higher frequency, longer duration, and greater amplitude all lead to more counts. Literature [2] shows that damage mode of the composite material mainly includes matrix cracking, interfacial damage, and fiber breakage. In these types of damage, the two modes of base material macro-cracking and fiber breakage are quite serious and close to the whole damage under different damage mode. Interfacial damage also includes disconnect of the matrix and fiber interface, fiber pull-out, separation between layers etc. Fiber breakage also includes positive off of the fibers, fiber splitting, etc. The research of Meng et al. [3] shows that the damage process at first is the damage of original defects, and then is the interfacial damage and separation of matrix of fiber bundles accompanied by a small amount of monofilament breakage inside the fiber bundles, and at last is the mass of the fiber bundle breakage and pulling out. Interfacial damage and separation of matrix of fiber bundle are corresponding to higher amplitude, longer duration, and greater energy AE signals. So it was preliminary estimated that the prominent character of counts comparing with hits corresponding to structural damage is not an accidental phenomenon. It may be related with feature of AE signals under different damage extents of composite material structure. How does the damage extent of composite material structure become severe in loading process? When does it generate more serious stress wave? Could it be reflected by the relationship between the two parameters?

2 Damage Development Model

Define a specific physical quantity as the material damage field, which can be determined by its existence of a group of parameters in space and time. These parameters are separated as basic parameters and educed parameters. Basic parameters contain time, amounts, size, and so forth of damage which together constitute basic sub-parameters. Educed parameters contain the other ones, including the growth and form of crack, the location of damage, etc., which constitute the educed sub-parameters. From the energy point, damage development is actually a stress energy-releasing procedure. Much research has proven that stress wave and the physical characters are related. For example, amplitude and energy of wave are in direct relation with the extent of damage. Stress wave occurs when the damage starts [4]. In this chapter, we aim to find some parameters of stress wave which could reflect the extent of damage.

There are some initial flaws in composite material structures, which result in amounts of acoustic emission activities during its first loading procedure. However, the trifle flaws such as micro-displacement arouse stress wave with low amplitude and energy. Owing to the randomness of the initial flaw, the location, time, size, and speed of damage are random. But with the development of trifle flaws, the location and extent of damage occurrences become more certain. Specifically, trifle flaws grow and

accumulate to bigger ones, resulting in reduction of mechanical performance and then further development of damage. And then the location of the major damage becomes certain, which evolves into the final failure source. During the evolution of damage, the characteristics of acoustic emission signals change as well.

In this chapter, we aim to find the turning point where trifle flaws grow into severe damage, from analyzing the development principle of Hits and Counts in composite material structure.

3 Experiment and Analysis

In this chapter, C/C composite material is tested and analyzed during the procedure of its steady load to breakup; AE parameters are analyzed.

3.1 AE Monitor of Experiment

To analyze the regular patterns of acoustic emission activities from damage occurrences till its breakup of C/C composite material under load, three groups of composite tubular test specimens were imposed on static load. These three test specimens were of similar form and under the same load of stretching and torsion. Each specimen experienced load twice—in the first process, load was under the safety one, while in the second process, load grew higher until the final specimen failure.

Time—Hits and Time—Counts curve during the first loading process is shown in Fig. 1. The growth trends of the two curves are quite similar in spite of their difference in magnitude. The same type of figure during the second loading process

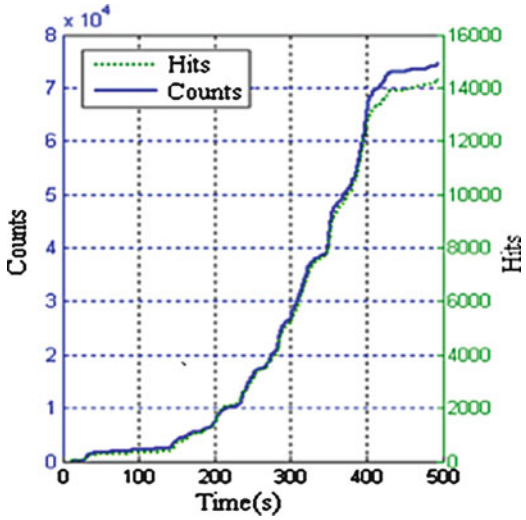

Fig. 1 Curve of AE Hits and Counts with slight damage

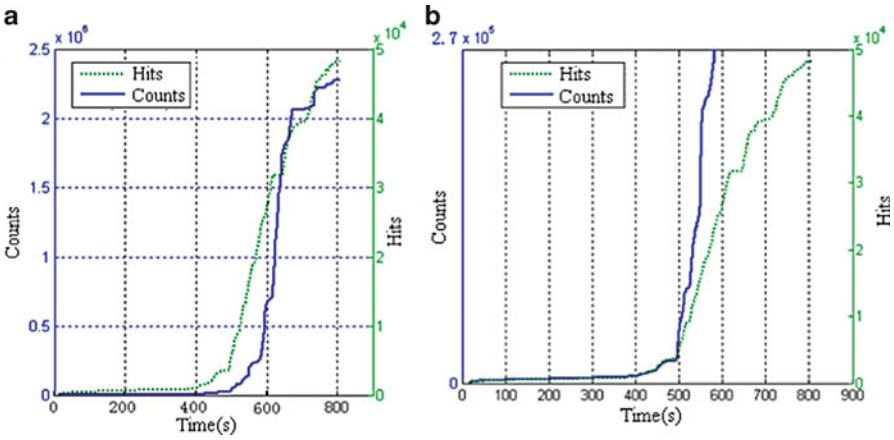

Fig. 2 Separate curves of AE Hits and Counts with severe damage to structure failure. (**a**) Total curves. (**b**) Rescaled curves

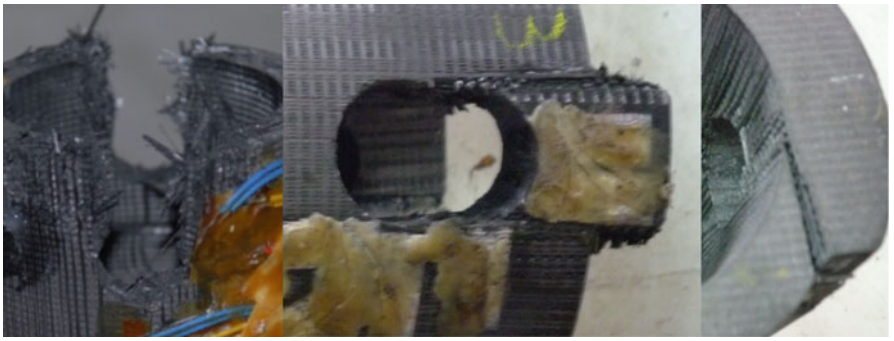

Fig. 3 Photos of specimen failures under static load

is shown in Figs. 2 and 3. It is noticed that the two curves separate from each other after 500 s and the trend of their separation grows until the final breakup (Fig. 4).

In order to elucidate the two parameters' relation during their growth, put them on the two axes of figure. The relation curves of the two load process are presented in Fig. 5. It could be noticed that Hits and Counts grow in similar trend and are in linear relation. This indicates that, though Counts of each Hit are different, each AE event occurs in different position and amplitude, and their average Counts are steady. They are in accordance with the statistical characteristics. This phenomenon keeps with the AE principle of metal fatigue crack propagation test. This period of acoustic emission from damage source could be regarded as a steady stochastic process. Its randomness is clearly shown in Fig. 9. However, when the damage develops to severe state, a deflection point appears on the relation curve, which means that Counts of each Hit increase dramatically. This course may occur several times until the structure fails.

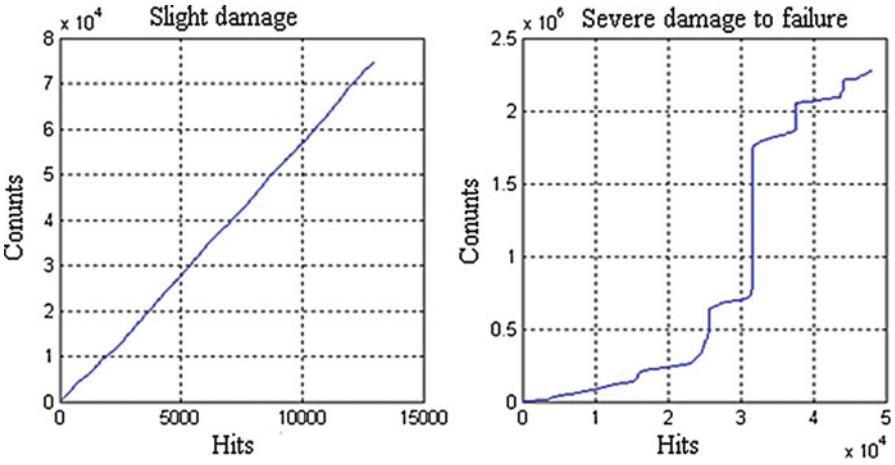

Fig. 4 Relation curve of Hits and Counts with different damage extent

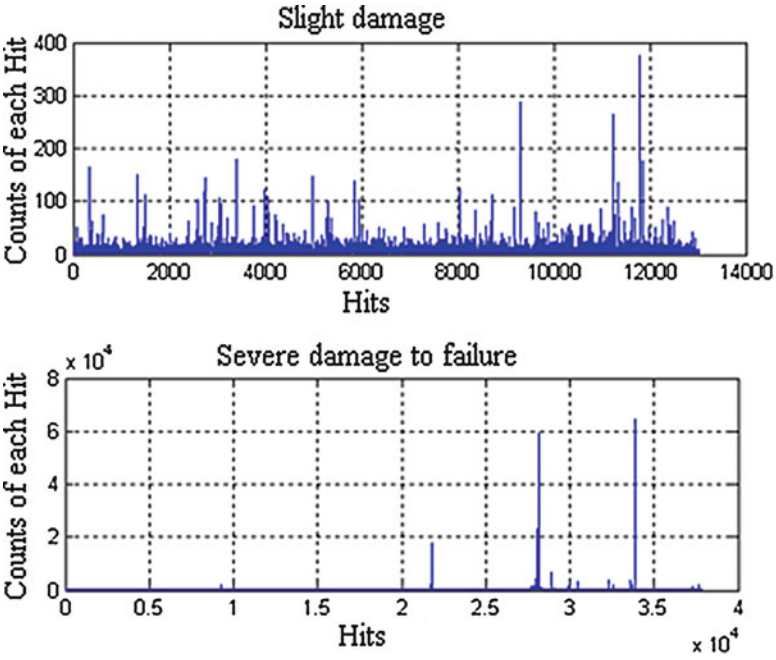

Fig. 5 Counts of each Hit with different damage extent

Every saltation corresponds to a series of Hits with great number of Counts, which is clarified in Fig. 9. Series of Hits with amounts of Counts was considered to relate with the damage mode of macroscopic size of interface delamination and fiber evulsion. This speculation is verified examining the wrecked specimen. The photos of the wrecked specimens are shown in Fig. 3.

3.2 Discussion of the Experiment Results

There are two periods of damage development. One is steady developing period, in which slight damage occurs stochastically both in time and in space; it is defined as period S and damage extent is tiny in this period. The other is directed developing period, in which one or more main damage source is conceived and begins to lead the trend of the whole damage field; it is defined as period D and damage extent becomes severe in this period. We call the Counts of AE K_t, and call Hits of the AE event H_t. Then when T is larger than some constant T_0, if

$$\int_{t}^{t+T} (\kappa_t / H_t) = \text{Const},$$

determine damage fall into period S; else if

$$\int_{t}^{t+T} (\kappa_t / H_t) = \text{Const} \times (1 + x\%),$$

determine period S finishes and damage extent becomes severe.

Besides, the accumulative curve of energy growing with hit presents similar principles in the two different extents of damage. The relation curves are shown in Figs. 6 and 7.

If we define the increase of uncertainty of stress wave from damage as entropy production, in the period S, damage extent is trifle, and entropy production is steady. With the increase of load, tiny damage source merges to greater ones and some main damage source outstands; entropy production process stops. Meanwhile, stress waves from these greater damage sources change greatly as well, of which amplitude, frequency, duration, and so forth are separated from the former ones. This course presented in this chapter is the appearance of a series of Hit with much more Count, or the deflection point on the relative curve of Hit and Count.

There is another interesting phenomenon that the proportion of load at the deflection point to the final breakup load is in some certain range. Take the three experiments mentioned for example; the ratio is listed in Table 1.

3.3 Traditional AE Method to Evaluate the Damage Extent

To confirm and contrast with traditional AE method, Time-Amplitude distribution figures of the two procedure of load are shown is Figs. 8 and 9. It is noticed that the inflection point appears when the AE event with larger amplitude

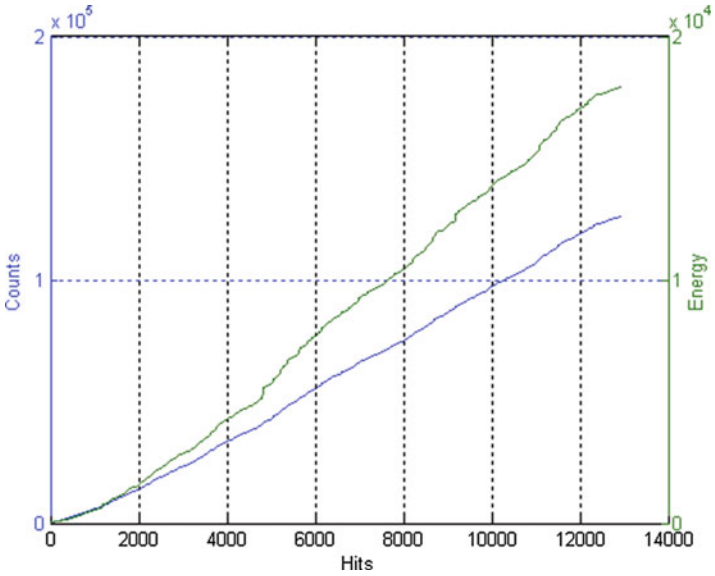

Fig. 6 Relation curves of Hit and Count as well as Energy with slight damage

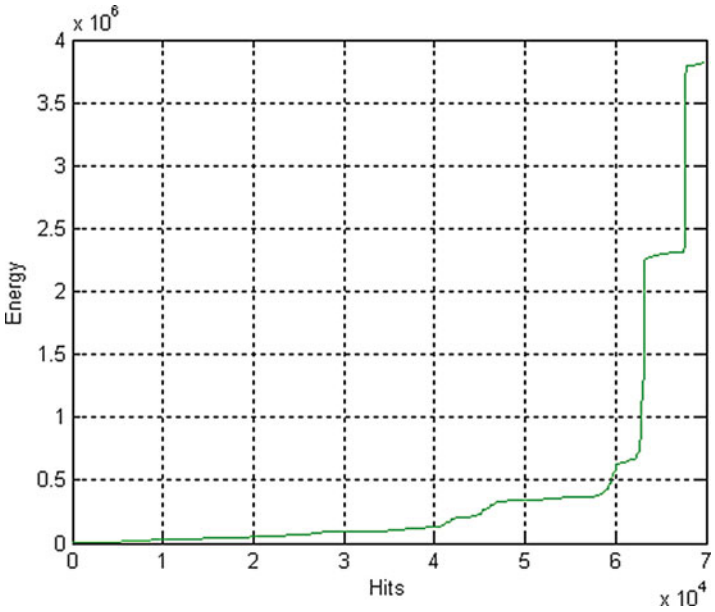

Fig. 7 Relation curves of Hit and Energy with severe damage to failure

Table 1 Deflection point load and breakup load ratio

Test article no.	1	2	3
Deflection point load	38.5	23.8	39.3
Breakup load	44.4	27.4	45.4
Ratio	86.7 %	86.9 %	86.5 %

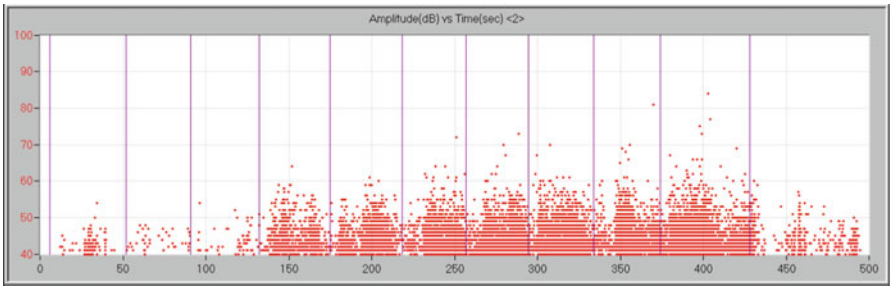

Fig. 8 Time-Amplitude distribution figure with slight damage

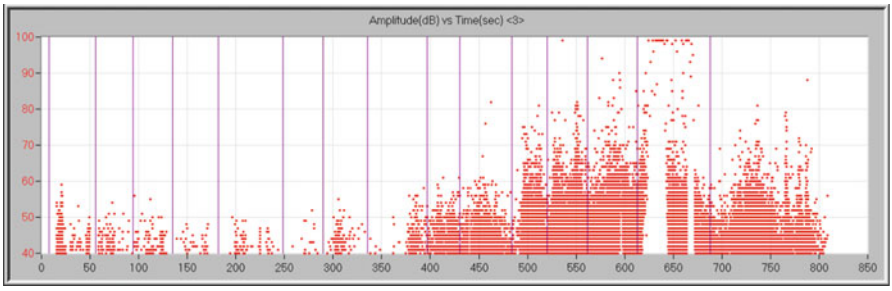

Fig. 9 Time-amplitude distribution figure of AE when loading up to fail

(Amplitude >80 dB) becomes more. These two methods could be verified by each other. Both indicate that the current of the development of damage field changes, damage extent becomes larger, and further load may result in breakup of the structure. But evaluating the damage extent relying on Time-Amplitude distribution figure is a little empirical: the question that how many AE events with large amplitude indicate the change of damage filed is uncertain. This may result in wrong judgment, while the correlation curve of Hits and Counts, with appropriate threshold, could supplement in resolving this problem.

4 Conclusion

Acoustic emission parameters, Hits and Counts as well as Energy of the structure standing under load, could reflect the damage extent of C/C composite material structure, and precaution the breakup of it. The details of the principle could be expressed as follows:

With slight damage, properties of the AE signal from tiny source of damage in composite material structure are under the stationary probability distribution, the rising ratios of the two parameters are equal, and the correlation curve of Hits and Counts is presented as a straight line; when the damage extent becomes severe,

a group of Hits series with large number of Counts occurs, which results in inflection point on the correlation curve; gradient of the enveloping line of the curve becomes larger evidently and then returns back. This procedure may recur several times, until the breakup of the structure.

For some specific C/C composite material structure, the load when the first series of Hits with large Counts occurs, and the first inflection point appears on the correlation line, is of certain proportion of the final breakup load (in this chapter, the proportion is about 85 %). Therefore, these correlation lines could precaution the static load breakup of C/C composite material structures and estimate the final breakup load.

References

1. Y. Mingwei, G. Rongsheng, *Acoustic Emission Detection[M]* (Mechanic Engineering Publishing, Beijing, 2004)
2. Y. Guangsong, *Damage Mechanics and Damage of Composite Materials[M]* (National Defense Publishing, Beijing, 1995)
3. M. Songhe, T. Xiaoxiao, D. Shanyi, Mechanical properties testing and failure mechanism analysis of 3D woven carbon/epoxy composite[J]. Acta Mater. Comp. Sinica. **2**, 115–119 (2012)
4. Q. Gang, F. Ming, The dominance of the antinomy between the inherent structure and irreversible damage in evaluating material's performance[J]. J. Dialectics Nat. **2**, 118–218 (2012)

Acoustic Research on the Damage Mechanism of Carbon Fiber Composite Materials

Bing Wang, Yanlei Liu, and Shuiping Sheng

Abstract This thesis involves the study about different processes including the tensile fracture, inter-layer tear or avulsion, as well as the interlaminar shear or split regarding carbon fiber composite materials with the aid of acoustic emission technique. Also, various acoustic emission signals that are released by composite samples in the process of fracture are analyzed. As is indicated by the test results, different acoustic emissive signals that are released by carbon fiber layers in various stages of damage and fracture bear different characteristics. Acoustic detection can effectively monitor the whole stage of elastic deformation, the damage development, and even the accumulation process while figuring out in an efficient manner about the internal activities of the composites, plus the diverse types of damages. In addition, its fabulous application value lies in its relevant structural evaluation as well as the evaluation of integrity with regard to carbon fiber composite.

1 Introduction

With the gradually increasing application of carbon fiber composite materials in the fields of pressure vessel, aerospace, and likewise [1–3], the analysis of damage modes (breakage, split-level, or opening) of composite materials and overall integrity detection has been done a lot. Due to the rapid release of the energies during the destruction process of material, the phenomenon of acoustic emission (AE) is induced, which causes the acoustic emission to carry a particular sensitivity toward the defect initiation and extension [4–6]. Acoustic emission technology is not only

B. Wang (✉) • Y. Liu • S. Sheng
Hangzhou Special Equipment Inspection and Research Institute, Hangzhou 310003, China
e-mail: victory7179_cn@sina.com

G. Shen et al. (eds.), *Advances in Acoustic Emission Technology: Proceedings of the World Conference on Acoustic Emission-2013*, Springer Proceedings in Physics 158,
DOI 10.1007/978-1-4939-1239-1_28,

the nondestructive testing method of internal defects and damages, but also more and more an essential method in the course of material performance (including fracture properties and mechanical performance) study, strength test, and service life evaluation.

In this chapter, the static tensile test and bending opening test have been carried out with the carbon fiber composite material. At the same time the special acoustic emission equipment imported from the PAC company in the USA has been applied throughout the whole acquisition process of various acoustic emission signals. Also, the counting, energy, and other parameters as well as waveforms are all analyzed. Combined with the mechanical properties of composite materials, this chapter discusses the correspondence of damage behavior of composites and the AE signal characteristics, thus providing reliable reference for the study of the AE techniques in composite material's damage mechanism and relevant safety performance evaluation.

2 Experiments

The tensile test uses the carbon fiber [0/90] 4 s composite material supplied by the Zhejiang University, the sample size being $250 \times 25 \times 1.8$. The mixed-mode sample is of the size of $150 \times 20 \times 3$. The gap at the end of sample had length of 25 mm, where tow layering mode (the opening and shearing) can be formed. At the same time, bury the teflon film of 50 mm long and 0.02 mm in length into the surface of the geometry, and accordingly the prefabricated delamination is completed.

Load the sample with the aid of MTS 810-type material testing machine. Take Samos-48 made in PAC as the AE detector. The defined peak time 50 μs is set as the AE parameter, the definition of impact time as 200 μs, impact lock time 300 μs, threshold value 40 dB, vacuum grease as the coupling agent. The R15I-type sensor is coiled and fixed on the sample. The test units involved are shown in Figs. 1 and 2, respectively.

3 Test Result and Analysis

Tensile stress–strain curve of the sample is shown in Fig. 3. In the initial stretching period, the material shows a linear increase stress with the strain (B-M). This phase is called the elastic deformation stage, as in the phase the material presents a good resistance to the deformation as a whole showing its internal state of stability. With the further increase of load in the Zone M-Y, the stress manifests a nonlinear rise with the increase of strain. The underlying reason is primarily that the high stress causes interface debonding, delamination, and matrix shear failure. Those defects such as remaining gaps in the course of manufacturing encounters with the stresses that has concentrated to a certain extent and eventually arouse partial damages. This process is actually part of the damage development and accumulation stage.

Fig. 1 Tensile test device

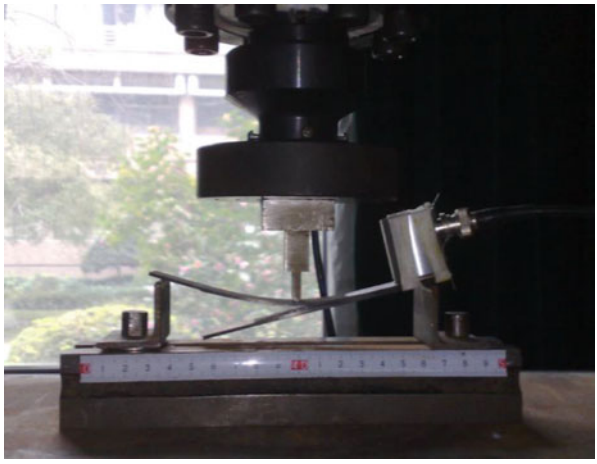

Fig. 2 Bending test device

The main damage forms include interlayer shedding, fiber fracture, and longitudinal splitting.

The mixed-mode displacement-load curve is shown in Fig. 4. At the beginning of loading, the load shows a linear growth with the increase of load displacement, making a good linear loading stage a (0–95 s). It reflects the micro damage accumulation in the interface and interlamination, with the interlaminar shear force being the layering force. When the load exceeds the critical value of interlaminar shear, microcosmic rupture occurs between layers. There shows a weak nonlinear process b (95–160 s), during which period the interlaminar fiber and bonding surface meet continuous tensile force and shearing force that induce fracture in succession. Macroscopic observation at the moment says that there

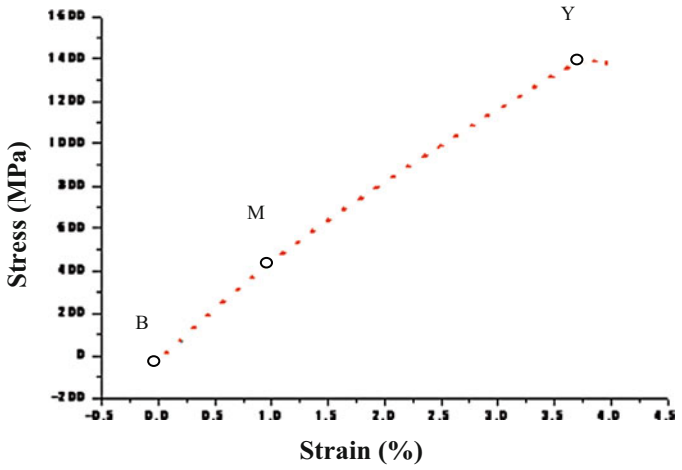

Fig. 3 Stress–strain curve

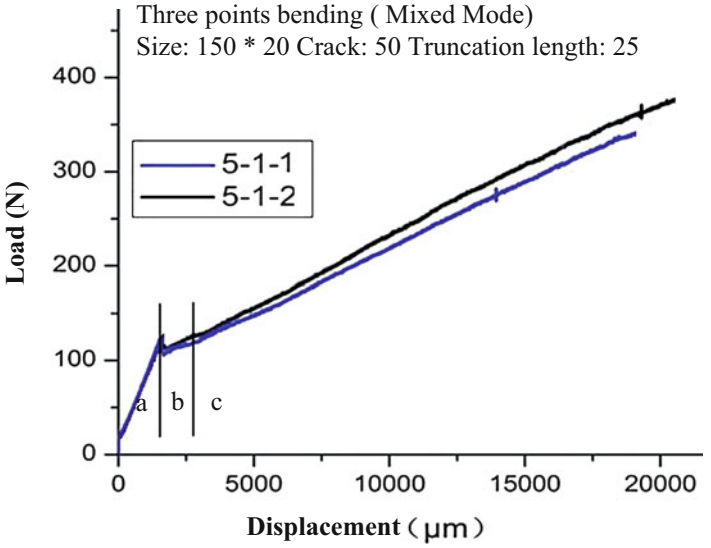

Fig. 4 Displacement versus load

has been relative dislocation between the layers, and the prefabricated film has its layer gradually opening and load slightly descending. What follows is a controllable and stable layer-by-layer extension process, namely in this very process the displacement continues to increase, delamination unfolds smoothly, displacement ceases, and hierarchical opening suspends. As is seen, the lamination gradually opens along the tangent direction of the bending, and the delamination is caused by tensile force.

4 Acoustic Result and Analysis

Figures 5 and 6 show an inflection point of the sample at the 280 s in the process of stretching. All the signals before that show a low amplitude, with the counting slowly growing over time. The corresponding internal stress at the 280 s is 392 MPa, which is pretty close to the 410 MPa of the transformation load at M,

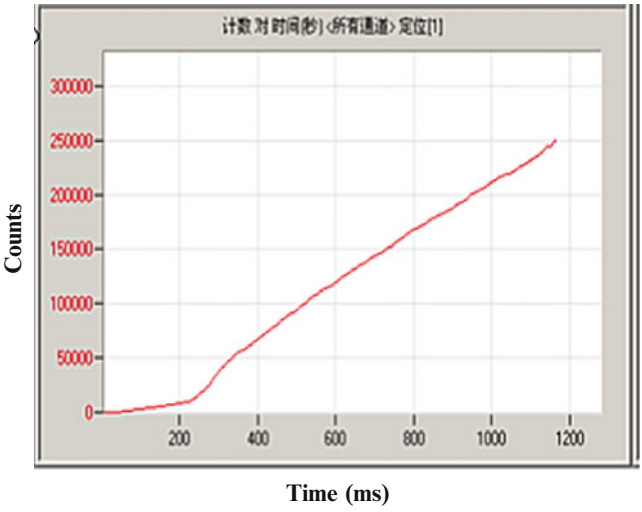

Fig. 5 Count versus time curve (tensile samples)

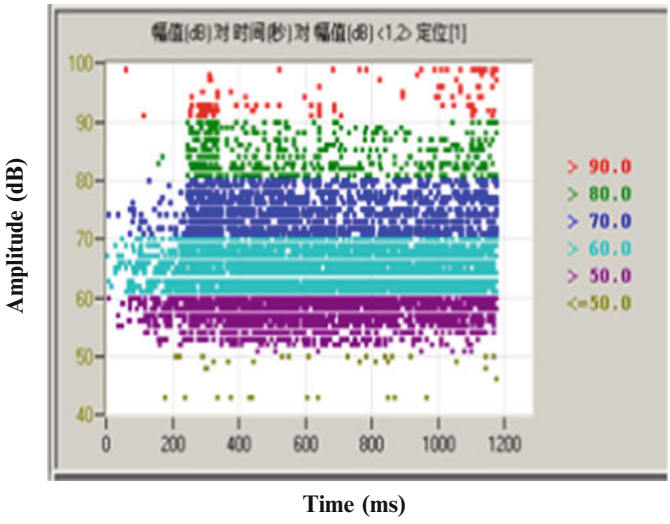

Fig. 6 Amplitude versus time (tensile samples)

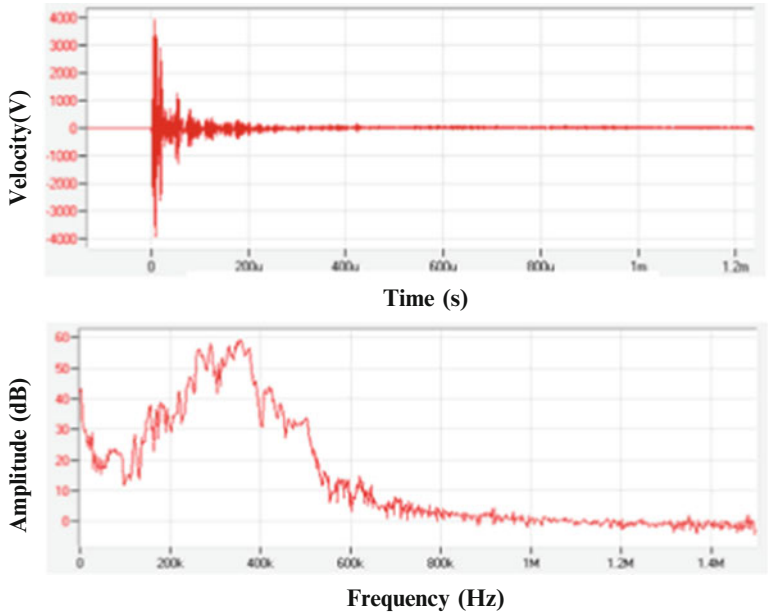

Fig. 7 Waveform, spectrum map (tensile samples)

which illustrates all the previous 280 s belonging to the elastic stage of the aforesaid B-M. After that the technology rapidly rises over time, coupling with the release of plenty of acoustic emission signals that are of a amplitude larger than 90 dB. It is mainly because that part of the fragile 0° fiber bundles gradually fracture after the elastic stage, giving out the high-amplitude signals and the inter-story displacement occurs. Meanwhile, the debonding also releases higher amplitude acoustic emission signals. In the last 200 s there comes the concentrated emergence of the high-amplitude signals, reflecting the internal damage accumulation at the moment. There produces a great number of fiber collective fracture partially, until the final material fracture, showing that AE signals can well reflect the internal damaging process of the material.

Figure 7 is the typical waveform spectrogram of acoustic emission signals generated out of carbon fiber bundles' fracture. It can be seen that the waveform signal is full, with its energy instantly and concentrated released, showing a large amplitude within a short time. Its center frequency is generally concentrated around the high frequency range of 170–220 kHz.

Figure 8 is the energy-time MAP for mixed-mode sample. As is shown in this figure, 0–95 s (Phase a) are filled with low-energy signals with sustainability, accounting for the steady accumulation of the micro damage and the release of weak signals around the matrix and interface between layers in this phase. From 95 to 160 s (Phase b) medium-energy impact is constantly produced, which can be interpreted as the start of rupture of the layered interface after reaching the critical value of interlaminar shear. As is observed, the upper and lower layers gradually

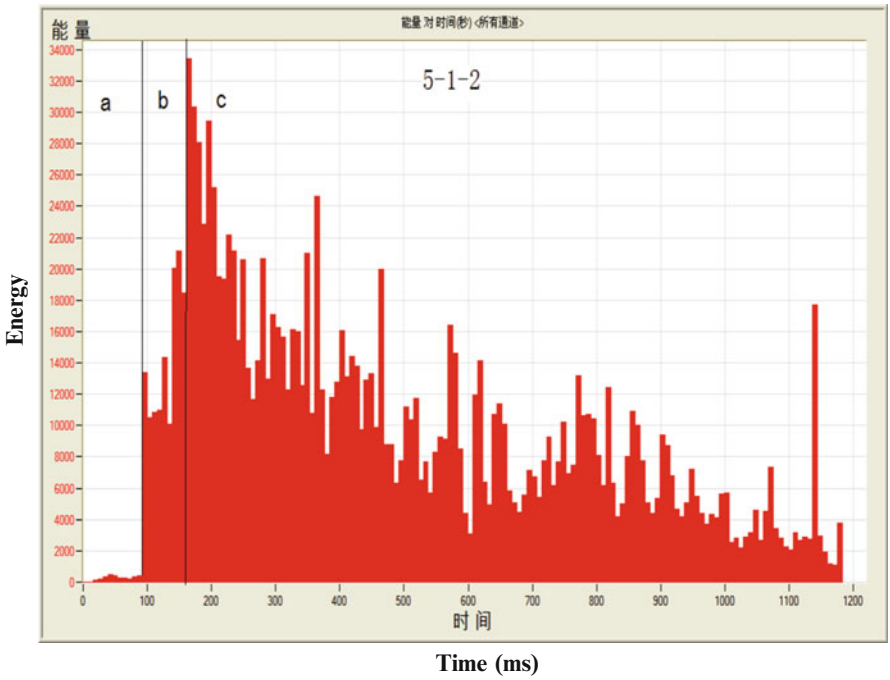

Fig. 8 Energy versus time (mixed-mode sample)

unfold itself along the prefabricated film layer. Also, there involves the release of certain energy from the signals due to the fracture in succession of part of the short fiber bundles and binder due to the exposure of elements such as certain shear stress and tensile force.

With the sample being further bended (Phase c), the leading edge of lamination constantly advances and cracks, and more short fibers are pulled apart. The upper and lower layers gradually delaminate and unfold itself along the prefabricated film layer, and more short fibers are pulled apart. At the 258 s, the delamination cracks all the way to the loading point, where the lower layer is tangent to the bending curve, and overall a large number of high-energy signals are released at this very phase.

The time-count and time-energy relations of the two samples are clearly displayed in Fig. 9. There exist two inflection points (at 95 and 160 s) in this single curve. The three phases correspond with the Phases a, b, and c in Figs. 4 and 8. The stress state of the sample as well as the internal activeness can thus be inferred by merely observing the inflection point.

The acoustic emission sources of the mixed-mode layered composite materials can be simplified as three basic formats: the tensile fracture of fiber, the rupture friction due to interlaminar shear, and the interface debonding.

As can be seen in Fig. 10, the impact signals are divided into two typical zones. The Zone I has the low-rising value and low amplitude (less than 50 dB).

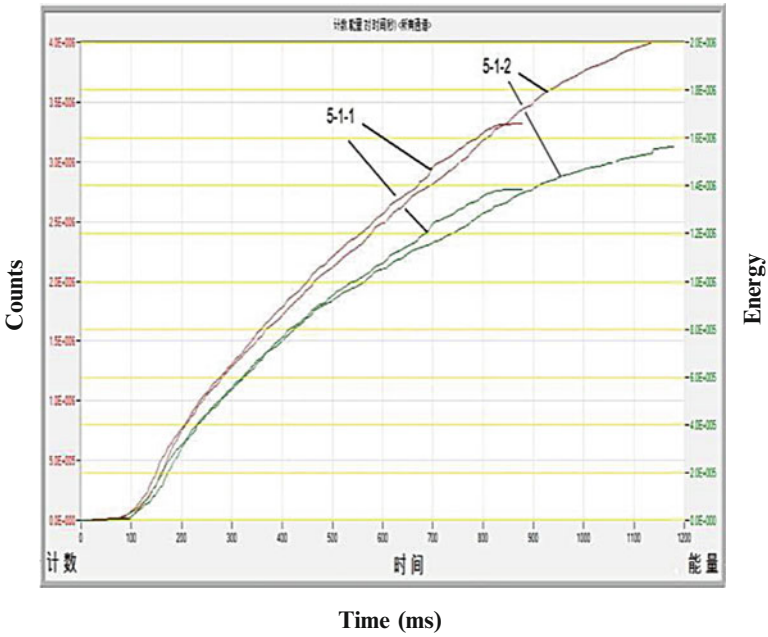

Fig. 9 Energy/counts versus time (mixed-mode sample)

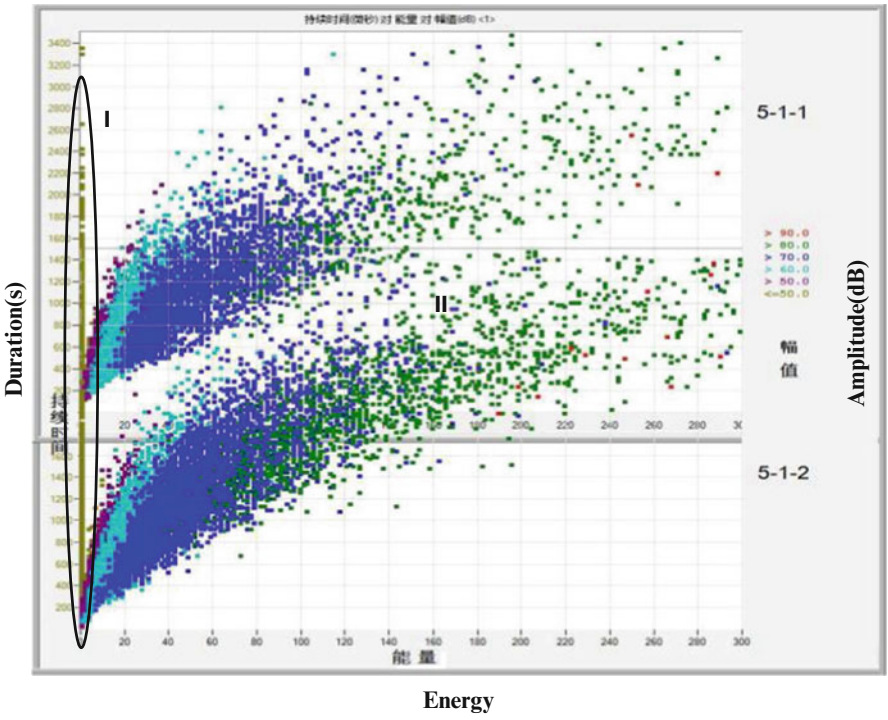

Fig. 10 Duration–energy–amplitude curve

The disproportionate energy of the impact signals to the duration is because of the slight displacement and mutual friction of interlayer shear. The interfacial debonding emits sound waves that are of small energy, low amplitude, and singular signal around the region of the high frequency. The Zone II has the kind of signals whose energy is proportional to the duration, of a high amplitude and wide distribution. These signals can be taken as the release due to fiber breakage and tend to possess relatively conspicuous features.

5 Conclusion

1. The damage and fracture of the material in the tensile bending process can release abundant acoustic emission signals whose measurability is good. The signals show remarkable correspondence with the stress–strain of the material.
2. The inflection point of damage development can be found through the analysis of the emission signal parameters, which signal the essential transformation in the mechanical state of the material to be judged, providing further proof for the prediction as to the limit of the damage deterioration.
3. Signal analysis is a way that enables effective monitoring over the internal activeness. Fiber breakage signals have the characteristics such as a large amplitude and short duration, its center frequency generally concentrating within the high frequency range of 170–220 kHz. Both the energy and amplitude of the signals around the shear layer tend to be low, while in the mixed layer, its signals have a relatively larger amplitude, and the energy proportional to the duration. What shows in the tension stratification period is typical fiber breakage signals with its own feature set.

References

1. N. Sato, T. Kuraychi, O. Kamigaito, Fracture mechanisms of unidirectional carbon reinforced epoxy resin composite [J]. J. Mater. Sci. **21**(3), 1005–1010 (1986)
2. S. Filonenko, T. Nimchenko, A. Kosmach, Model of acoustic emission signal at the prevailing mechanism of composite material mechanical destruction [J]. Aviation **14**(4), 95–103 (2010)
3. H. Fu, S. Wei, The application of carbon fiber composite materials in giant plane [J]. Hi-Tech Fiber Appl. **32**(6), 5–8 (2007) (in Chinese)
4. O.I. Benevolenski, J. Karger-Kocsis, T. Czigdny, Mode I fracture resistance of glass fiber mat-reinforced poly propylene composites at various degree of consolidation [J]. Comp. Part A **34**(3), 267–273 (2003)
5. P.J. De Groot, P.A.M. Wijnen, R.B.F. Janssen, Real-time frequency determination of acoustic emission for different fracture mechanisms in carbon/epoxy composites [J]. Comp. Sci. Technol. **55**(4), 105–412 (1995)
6. M. Giordano, A. Calabro, C. Esposito, An acoustic emission characterization for the failure modes in polymer composite materials [J]. Comp. Sci. Technol. **37**(3), 411–428 (1990)

Damage and Toughening Analysis of Ceramics by AE Location Method

Liang Chu, Huilan Ren, and Jianguo Ning

Abstract The acoustic emission method was employed for investigation of fracture process of the 95 % alumina ceramic and zirconia toughened alumina (ZTA) with a 15 % volume fraction of tetragonal zirconia in the Brazilian split test. Geiger location algorithm was used for location analysis. The results showed that calculated AE locations by Geiger algorithm and ceramics failure process were consistent and the location results could reflect the process of damage. In the initial stage the quantity of AE events is very little, and AE events significantly increase after the initial crack formation. In the unstable stage AE events can hardly be captured due to the sampling frequency constraint. The toughening effect of ZTA can be analyzed through acoustic emission waves, hits, and signal amplitudes.

1 Introduction

Alumina ceramic has received significant attention in machinery manufacturing, biomedicine, aerospace industry, and other fields because of its high hardness, high strength, low density, good corrosive resistance, and excellent high-temperature stability. However, it has the disadvantage of low toughness and inclination to abnormal grain growth (AGG). Zirconia-toughened alumina (ZTA) ceramic has displayed more satisfying mechanical properties than monolithic alumina on account of strengthen and toughen effects of zirconia grains [1]. Crack propagation process and toughening mechanism have always been a hot spot of the research on high-performance ceramics. Alumina and ZTA are widely applied structural

L. Chu • H. Ren (✉) • J. Ning
State Key Laboratory of Explosion Science and Technology, Beijing Institute of Technology, Beijing 100081, China
e-mail: 3120100065@bit.edu.cn; huilanren@bit.edu.cn

G. Shen et al. (eds.), *Advances in Acoustic Emission Technology: Proceedings of the World Conference on Acoustic Emission-2013*, Springer Proceedings in Physics 158,
DOI 10.1007/978-1-4939-1239-1_29,

ceramics, and locating their damage position accurately is very important in researching on crack propagation and toughening mechanism.

Acoustic emission (AE) is a stress wave produced when the materials undergo changes in the mechanical and thermal. AE technique is helpful to research destruction process because it can monitor microcrack nucleation and propagation in brittle materials which has been widely used in researching on fracture mechanism and characterization of rocks, concretes, and ceramics [2–5].

Although a lot of work has been done in the area of AE detection of structural ceramic by scholars at home and abroad, the research mainly focuses on the parameter analysis method [6–8]. In previous work, we have preliminary mastered AE characteristic of alumina ceramics damage process through parameter analysis method [9, 10]. The study of AE source location in structural ceramics is inadequate.

AE location technology has been widely used in the failure process of rocks and concretes. Xingdong Zhao et al. used Geiger location algorithm to study various rock samples failure process in uniaxial compression [11]. C. Grosse et al. implemented a 3D localization and a classification of AE events in concrete [12]. Because of high intensity, ceramic samples cannot be so big as rocks and concretes in order that it can be crushed, which makes AE location very difficult for ceramics. There is an important sense in studying ceramic damage process by AE location technology, because AE location technology can reflect the damage process more intuitively than parameter analysis methods.

In this chapter, acoustic emission (AE) locating technique was applied to studying the fracture process of alumina ceramics (Al_2O_3) and zirconia-toughened alumina ceramics (ZTA) through the Brazilian Split test. The location results of Geiger algorithm were analyzed with the location accuracies comparatively. The toughening effect of ZTA can be analyzed through acoustic emission waveforms, hits, and signal amplitudes.

2 Location Method

The TDOA location method was employed for ceramics damage localization. Assuming that (x_0, y_0, z_0) is the position of the AE source at time t. (x_i, y_i, z_i) is the position of the ith receiver, and t_i is the time when the signal arrived at the ith receiver. We need to calculate the time difference $t_i - t$ and distance difference $\sqrt{(x_i - x_0)^2 + (y_i - y_0)^2 + (z_i - z_0)^2}$ and measure the velocity of P-wave v_p, and then using Geiger location algorithm, make (x_0, y_0, z_0) close to the real value through multiple iterative calculations. That is

$$\sqrt{(x_i - x_0)^2 + (y_i - y_0)^2 + (z_i - z_0)^2} = v_p(t_i - t) \tag{1}$$

The numerical calculation process is as follows:

Through transposition, Eq. (1) can be written as

$$t_i = t + \frac{\sqrt{(x_i - x_0)^2 + (y_i - y_0)^2 + (z_i - z_0)^2}}{v_p} = t + T_i \tag{2}$$

Linearizing Eq. (2) by using a first-order Taylor expansion:

$$t_i = t_0 + \delta t + T_{i0} + \frac{\partial T_i}{\partial x_0}\delta x + \frac{\partial T_i}{\partial y_0}\delta y + \frac{\partial T_i}{\partial z_0}\delta z \tag{3}$$

where t_0 is the moment of AE event occurrence by iteration calculation, and T_{i0} is the travel time which signals arrive at the ith receiver by iteration calculation.

Through transposition, we can obtain:

$$t_i - t_0 - T_{i0} = \delta t + \frac{\partial T_i}{\partial x_0}\delta x + \frac{\partial T_i}{\partial y_0}\delta y + \frac{\partial T_i}{\partial z_0}\delta z \tag{4}$$

For n receivers, we can get n equations which can be written in matrix form:

$$A\delta\varphi = B \tag{5}$$

where

$$A = \begin{bmatrix} 1 & \frac{\partial T_1}{\partial x_0} & \frac{\partial T_1}{\partial y_0} & \frac{\partial T_1}{\partial z_0} \\ \vdots & \vdots & \vdots & \vdots \\ 1 & \frac{\partial T_n}{\partial x_0} & \frac{\partial T_n}{\partial y_0} & \frac{\partial T_n}{\partial z_0} \end{bmatrix}, \quad \delta\varphi = \begin{bmatrix} \delta t \\ \delta x \\ \delta y \\ \delta z \end{bmatrix}, \quad B = \begin{bmatrix} t_1 - t_0 - T_{10} \\ \vdots \\ t_n - t_0 - T_{n0} \end{bmatrix}.$$

Through Eq. (5), the modified vector can be got:

$$\delta\varphi = A^{-1}B \tag{6}$$

Setting $\varphi + \delta\varphi$ as the new trial solution and then continuing iterating until $\delta\varphi$ is small enough.

3 Experimental

Two alumina-containing ceramics were investigated: Al_2O_3 ceramic having a composition 95 vol.% alumina and 5 vol.% calcia, monox, and other impurities and ZTA ceramic containing 15 vol.% zirconia and 2 mol.% yttria (stabilization).

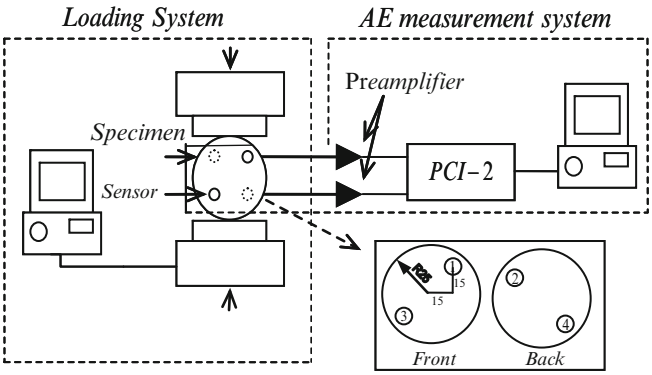

Fig. 1 Experimental setup

All of the specimens were disc shaped having dimensions of ϕ 50 mm × 20 mm (diameter × thickness). Material compression tests were performed on a hydraulic material testing machine at a load rate of 20 kN/min. We added heel blocks between specimen and pressure head because of the high hardness of specimens.

Acoustic emission signals and waves were real time acquired using PCI-2 four-channel AE collection system (PAC, USA). Piezoelectric sensors have resonant frequency at 150 kHz, and broadband is 100–400 kHz. A preamplifier (40 dB gain) and a band-pass filter (100–400 kHz) were used. The threshold was set at 40 dB and sampling frequency was set at 1 MHz. Experimental setup was shown in Fig. 1.

4 Results

4.1 Fracture Process of Al_2O_3 Ceramic

Figure 2 shows the AE location results by Geiger location algorithm and the damage photographs of Al_2O_3 specimen after the completion of Brazilian split tests. The AE location results and the failure process of Al_2O_3 specimen are consistent, and the location results by Geiger location algorithm can reflect the fracture process.

At the initial stage, before the pressure was loaded to 13KN (about 10 % of failure stress), the number of AE events was small. The locating points were mainly distributed on the bottom and machining defects of the sample. The sample was in the stage of pressure consolidation, and the defects did not propagate. With the increase of external load, the latest locating points mainly concentrated at the top and bottom of the sample as a result of the stress concentration. When external load increased to 40 kN (about 30 % of failure stress), the initial microcrack had

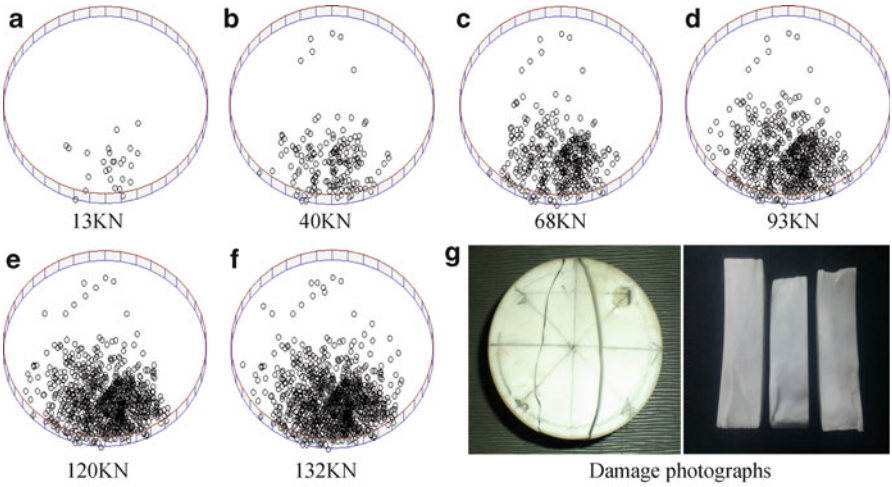

Fig. 2 AE location results of the fracture process of Al_2O_3

extended to the sample center from the bottom of the defect area. Locating point mainly concentrated in the loading axis which was consistent with the actual fracture. As pressure continued increasing, the sample produced a large number of AE locating points around the main crack. When the force reached 132 kN, the main crack propagated quickly and breakthrough the sample along the loading axis, and the sample was fractured at last.

Observing the fracture surface, we found that the bottom was unsmooth, and the top was very smooth. We could infer that there were machining defects at the bottom leading to a number of locating points, and the top was mainly unstable failure resulting in a few locating points. We could draw the conclusion that the location method could reflect the fracture process of alumina.

In the process of loading, a total of 4,176 AE events were recorded, where 1,127 (27 %) locating points were located within the sample. Considering the 7 mm diameter of receivers there were 1,400 (33.5 %) locating points which deviation within 7 mm.

4.2 Fracture Process of ZTA Ceramic

Figure 3 shows the AE location results by Geiger location algorithm and the damage photographs of ZTA specimen after the completion of Brazilian split tests.

At the initial stage, because of the stress concentration, locating points mainly concentrated at the top and bottom of the sample. With the increase of external load, microcrack nucleated at both ends, and then extended to the center along the loading axis. There might be some machining defects, and the sample had been

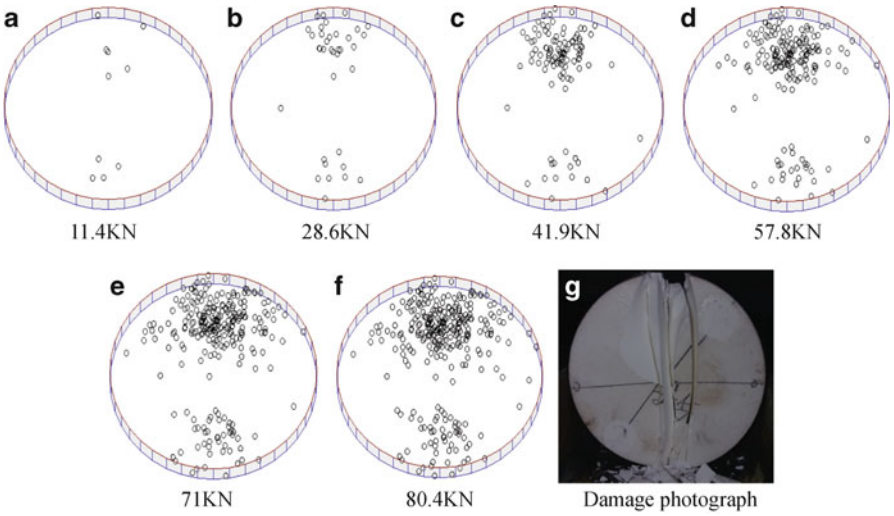

Fig. 3 AE location results on the fracture process of ZTA

fractured before the external load reached expected intensity. A total of 1,253 AE events were recorded, where 399 (31.8 %) locating points were located within the sample. There were 459 (36.6 %) locating points which deviate within 7 mm.

4.3 Toughening Analysis of ZTA Ceramic

AE signal is transient and randomness and it consists of a series of different frequency and mode signals. Figure 3 shows typical AE waveform figures of two kinds of ceramics in the fracture process.

Time domain description cannot reflect all of the AE features, and we still need to analyze the frequency information of signals in order to learn more of their different damage characteristics. In the base of known parameters of time domain, the signals are transformed by FFT algorithm. The spectrogram of Fig. 4 is shown in Fig. 5.

Through the analysis of all spectrograms, we find that high amplitude is mainly distributed in the relative high-frequency region in the failure process of Al_2O_3 ceramics, but the frequency band for ZTA ceramics is relatively low. We believe that the toughening effect of zirconia particles leads to a decrease in the AE frequency.

Figure 6 shows load-time curves and the distributions of AE hit rate with time of Al_2O_3 ceramic and ZTA ceramic. AE Hits are usually used to evaluate the total and frequency of crack activity.

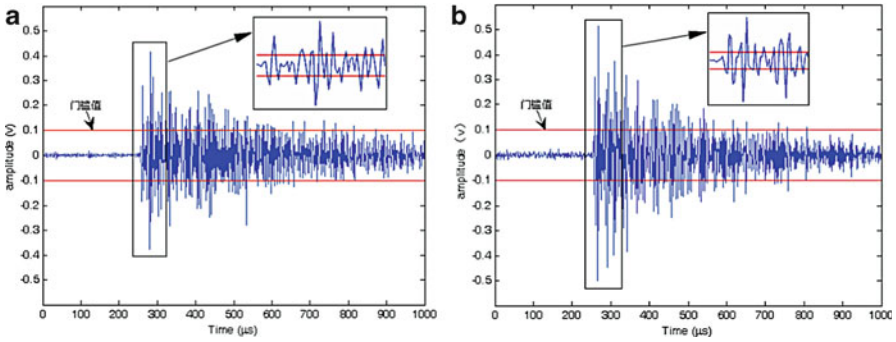

Fig. 4 Typical AE waveforms in the fracture process: (**a**) Al_2O_3. (**b**) ZTA

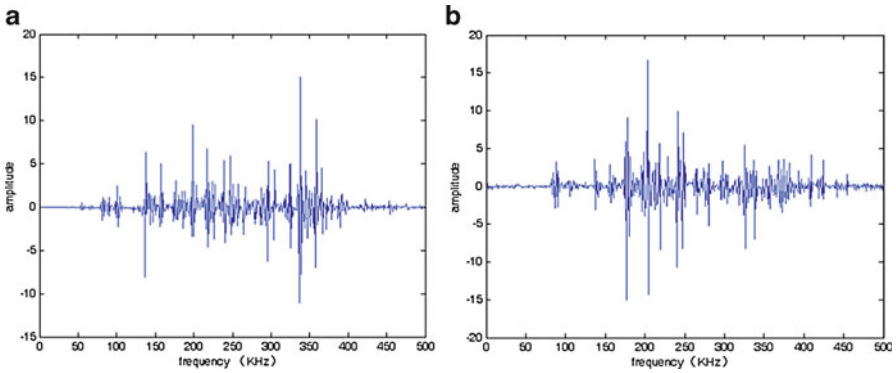

Fig. 5 Typical AE spectrograms in the fracture process: (**a**) Al_2O_3. (**b**) ZTA

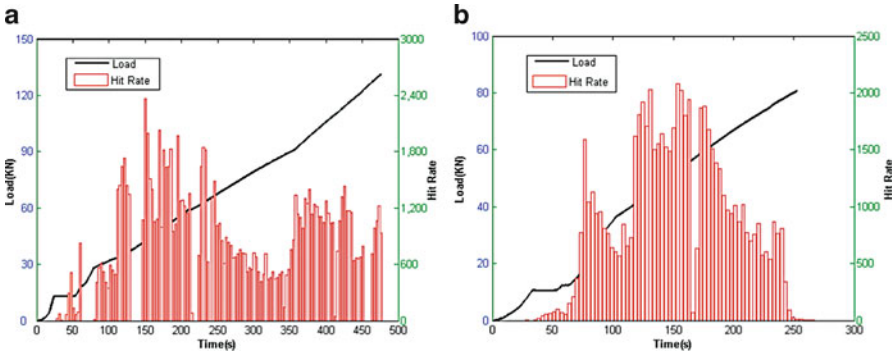

Fig. 6 Load-time curves and distribution of hit rate. (**a**) Al_2O_3. (**b**) ZTA

Table 1 AE hits distribution with amplitude

	Al_2O_3 ceramic	ZTA ceramic
Amplitude (db)	Proportion of AE hits (%)	Proportion of AE hits (%)
0–40	0	0
40–50	34.9	18.06
50–60	53.85	63.97
60–70	10.27	12.23
70–80	0.9	3.31
80–90	0.07	1.25
90–100	0.01	1.18

At the initial stage (0–60 s), the number of AE hits of ZTA ceramic was lower significantly than that of 95 % alumina ceramic. The reason may be that the microcrack or hole was hardly open at low stress in ZTA ceramic as a result of zirconia particles toughening effect.

AE hits distribution with amplitude is shown in Table 1. AE signal amplitude is directly associated with the type and intensity of the crack source.

A proportion of low-amplitude AE hits (below 50 dB) of 95 % Al_2O_3 ceramic was significantly higher than that of the ZTA ceramic, while a proportion of high amplitude (above 70 dB) was less than 1 %, and the proportion in ZTA was higher than 5 %. We believed the reason was complex but the toughening effect of zirconia particles was prominent. Because of the toughening effect of zirconia particles, the alumina matrix endured residual compressive stress, and higher fracture surface energy will be released if microcracks extended.

5 Conclusions

1. Acoustic emission 3D location method with Geiger algorithm can reflect exactly the position of crack initiation and propagation in Al_2O_3 disc and ZTA disc. Initial cracks are usually formed on the top, bottom, or machining defects of the sample in the Brazilian split experiment.
2. Crack propagation is a major cause of AE events. The number of AE events was rare before the cracks initiation. Once cracks form, the number of AE events increases obviously with the increase of external loading. But AE location technology cannot capture penetration of cracks in the instability process.
3. AE technology can intuitively reflect the toughening effect of ZTA ceramic. The toughening effect of zirconia particles leads to a decrease in the AE frequency. ZTA ceramics have less AE events at the initial stage. ZTA ceramics have more high-amplitude signals than Al_2O_3. It shows that cracks in ZTA ceramics are not easy to propagate because of the toughening effect of ZrO_2 particles, but when the cracks extend, higher fracture surface energy will be released.

Acknowledgment This work was supported in part by the National Natural Science Foundation of China under Grant No. 11172045.

References

1. G.W. Liu, Z.P. Xie, Y. Wu, Fabrication and mechanical properties of homogeneous zirconia toughened alumina ceramics via cyclic solution infiltration and in situ precipitation. Mater. Des. **32**(6), 3440–3447 (2011)
2. V.T. Kim, D.B. Nele, L. Frank, U.G. Christian, Acoustic emission analysis for the quantification of autonomous crack healing in concrete. Construct. Build Mater. **28**(1), 333–341 (2012)
3. P. Baud, E. Klein, T.F. Wong, Compaction localization in porous sandstones spatial evolution of damage and acoustic emission activity. J. Struct. Geol. **26**(4), 603–624 (2004)
4. A.G. Evans, M. Linzer, Failure prediction in structural ceramics using acoustic emission. J. Am. Ceram. Soc. **56**(11), 578–581 (1973)
5. A. Bussiba, M. Kupiec, S. Ifergane, R. Piat, T. Bohlke, Damage evolution and fracture events sequence in various composites by acoustic emission technique. Comp. Sci. Technol. **68**(5), 1144–1155 (2008)
6. S. Momon, M. Moevus, N. Godin, M. R'Mili, P. Reynaud, G. Fantozzi, G. Fayolle, Acoustic emission and lifetime prediction during static fatigue tests on ceramic-matrix-composite at high temperature under air. Comp. Part A Appl. Sci. Manuf. **41**(7), 913–918 (2010)
7. E. Maillet, N. Godin, M. R'Mili, P. Reynaud, J. Lamon, G. Fantozzi, Analysis of acoustic emission energy release during static fatigue tests at intermediate temperatures on ceramic matrix composites: towards rupture time prediction. Comp. Sci. Technol. **72**(9), 1001–1007 (2012)
8. H. Mei, Y.Y. Sun, L.D. Zhang, H.Q. Wang, L.F. Cheng, Acoustic emission characterization of fracture toughness for fiber reinforced ceramic matrix composites. Mater. Sci. Eng. A **560**, 372–376 (2013)
9. H.L. Ren, J.G. Ning, Y. Wang, Acoustic emission characterization of ceramic fracture. J. Mater. Eng. **2**, 54–57 (2009)
10. H.L. Ren, M.J. Fang, J.H. He, Experimental study of acoustic emission activity of alumina under compression. J. Mater. Eng. **2**, 30–34 (2012)
11. X.D. Zhao, J.P. Liu, Y.H. Li, J. Tian, W.C. Zhu, Experimental verification of rock locating technique with acoustic emission. Chin. J. Geotech. Eng. **30**(10), 1472–1476 (2008)
12. C. Grosse, H. Reinhardt, T. Dahm, Localization and classification of fracture types in concrete with quantitative acoustic emission measurement techniques. NDT&E Int. **30**(4), 223–230 (1997)

Acoustic Emission Tomography to Improve Source Location in Concrete Material Using SART

Yu Jiang, FeiYun Xu, Antolino Gallego, Francisco Sagata, and Oswaldo Gonçalves dos Santos Filho

Abstract Acoustic emission (AE) source location is one of the most attractive tools for structural health monitoring (SHM). In order to visualize source location from the different views under investigated objects, simultaneous algebraic reconstruction technique (SART) is proposed from new perspectives for AE tomography source location in complication geometric structures. Based on this method, experiments of AE on two concrete specimens (one with reinforcement and the other without reinforcement), using pencil breaking sources, i.e., Hsu–Nielsen sources, are implemented. Collecting signals for its posterior analysis with AE tomography SART algorithm, a successful three-dimension (3D) reconstruction result is obtained, clearly showing the influence of the reinforcement on the AE wave propagation speed and improving the AE event location, giving a better precision to corresponding damaged location inside the structures of objects in terms of a locally varying wave speed distribution (a reduction in location error from 16.26 %, a sample without steel iron, to 13.68 % a sample with steel iron).

Y. Jiang • F. Xu (✉)
School of Mechanical Engineering, Southeast University, Nanjing 211189, China
e-mail: fyxu@seu.edu.cn

A. Gallego • F. Sagata
Department of Applied Physics, University of Granada, Granada 18072, Spain
e-mail: antolino@ugr.es

O.G. dos Santos Filho
Eletrobras Eletronorte, Technology Center, Belem, PA 3257 1966, Brazil
e-mail: Oswaldo.Filho@eletronorte.gov.br

G. Shen et al. (eds.), *Advances in Acoustic Emission Technology: Proceedings of the World Conference on Acoustic Emission-2013*, Springer Proceedings in Physics 158,
DOI 10.1007/978-1-4939-1239-1_30,

1 Introduction

Source location technique is often used acoustic emission (AE) technique, which can reveal how and where failure in the material occurred in theory [1]. AE source location is normally performed using time-of-arrival (TOA) technique which uses the wave propagation velocity in a material in order to derive the source location in one, two, and three dimensions from the arrival delay between sensors based on the first threshold crossing [2, 3]. In this technique, one assumes that the wave propagation path is unobstructed, and that structure is homogenous; that is, waves travel at the same velocity in all directions. However this assumption is unrealistic for heterogeneous materials or complex structures. Relational conclusion about time-of-arrival-based approaches to locate impact-generated wave events in anisotropic composites plates is discussed [4]. In order to overcome this problem, Baxter and collaborators [5] proposed the "Delta T (DT)" AE source location technique. Based on the Delta T approach, Hensman and collaborators used Gaussian processes (GP) to represent the relationship between Δts and the spatial grid to locate AE sources in complex structures, which makes the technique more useful in real engineering situations [6]. However, the information usually obtained with these methods is mostly global. In most cases, it is also desirable to obtain a more local image of the damage location [7]. Tomography is one of the best methods for locating a local damage location [8, 9], which in general employs mathematic theory that reconstructs the internal condition of an object by analyzing multiple sets of projections through the object [10, 11]. The most commonly applied tomography is the so-called travel-time tomography by using transmission compression waves (P-waves) [12, 13]. In this technique, the first arrival times for P-waves transmitted through an object from a source to multiple receivers located on different sides are measured and the observed data are then used for reconstructing a velocity tomogram to characterize the ray-covered region [14]. Research and application have been reported by Aggelis and Shiotani for different types of concrete structures [15]. Especially being an in situ application, this technique was successfully implemented in evaluating repair effect of a crack found on the bridge deck by Shiotani [16, 17].

AE tomography uses AE events as signal sources and combines traditional source location algorithm with the travel-time tomography algorithm to improve AE event location [18]. For the iterative travel-time tomography, the SART is considered to be the trademark of algebraic approaches [19], which can be used to reconstruct 3D internal structure of objects nondestructively, by acquiring projections data from many different viewing angles from 0 to 180°. The SART algorithm is an effective image reconstruction technique especially in irregular geometry samples, incomplete data sets, and limited projection angles. At present, it has been only applied to image reconstruction, not for AE source location yet.

This chapter proposes the application of the SART algorithm to the AE tomography field in concrete material in order to reconstruct 3D internal structure of objects nondestructively from a locally varying wave speed mapping to aid the

analysis of AE source location. Based on this method, experiments of acoustic emission on concrete specimens, using pencil breaking leading sources, i.e., Hsu-Nielsen sources, are implemented. A successful result is obtained to improve the source location in terms of a locally varying wave speed distribution.

2 Methods

AE tomography source location TOA algorithm is [7] a two-dimensional model of the AE tomography for simplification as shown in Fig. 1.

The time of arrival of the AE signal generated in the source to the kth sensor (for $k = 1, \ldots, s$, s being the number of sensors), $T_{\mathrm{K}}^{\mathrm{A}}$ can be stated as

$$T_{\mathrm{K}}^{\mathrm{A}} = T_{\mathrm{K}}^{0} + \sum w_{ij}^{k} s_{ij} \tag{1}$$

Being, (i, j) is the axis indexes of cell defining the position of each tomographic cell ($i = 1, \ldots m; j = 1, \ldots, n$). In Eq. (1), s_{ij} is the slowness of the signal propagation along the tomographic cell (i, j), defined as

$$s_{ij} = {}^{1}/_{c_{ij}}$$

Being, c_{ij}, is the propagation speed in the each cell (i, j). On the other hand, w_{ij}^{k} is the distance travelled by the k-th ray into the cell (i, j). Obviously, most of these elements are zero, since only a relatively small number of cells are crossed by each ray. Finally, T_{k}^{0} is the time of occurrence of the AE event that originates the ray k. Note that in practice, the position of the source, its time of occurrence, and the wave propagation speed are unknown a priori variables. However, time elapsed from the

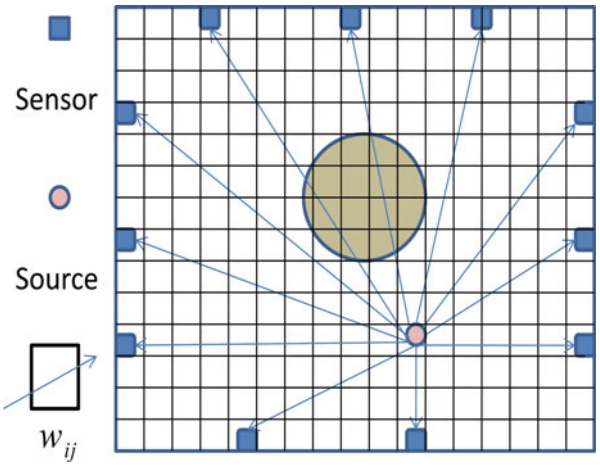

Fig. 1 AE tomography model

AE source occurrence to the arrival of the wave to the sensors can be measured with an appropriate acquisition equipment. For the solution of Eq. (1), the iterative SART algorithm can be used as described below.

The SART uses bilinear elements for the cells in order to represent the ray integrals and gives as outputs a better estimate of the event locations and smooth images; the iterative formula is given by [20]

$$x_j^{(k+1)} = x_j^{(k)} + \lambda_k \frac{\sum_{i=1}^{M} \frac{w_{ij}}{w_{i,+}} \left(b_i - \overline{b}_i \left((x)^k \right) \right)}{w_{+,j}} \tag{2}$$

where $W = (w_{i,j})$ denotes an MxN matrix under interest field, $b = (b_1 \ldots, b_M) \in R^M$ is the projection data, $x = (x_1, \ldots, x_N)^{tr} \in R^N$ shows an underlying image, and tr denotes transpose matrix. The algorithm aims to reconstruct image x from W and b, defining

$$W_{i,+} = \sum_{j=1}^{N} \left| w_{ij} \right|, \quad i = 1, 2, \ldots, M \tag{3}$$

$$W_{+,j} = \sum_{i=1}^{M} \left| w_{ij} \right|, j = 1, 2, \ldots, N \tag{4}$$

$$\overline{b}(x) = Wx \tag{5}$$

For that, the basic six steps of the algorithm are given below:

- An initial guess is defined for the underlying image:

$$\overline{x}_j = \overline{x}_j^{(0)} \quad j = 1, 2, \ldots, N \tag{6}$$

- The estimated value of projection data are calculated as

$$\overline{b}_i(x) = \sum\nolimits_{i=1}^{N} w_{ij} x_j^{(0)} \quad i = 1, 2, \ldots, M \tag{7}$$

- The projection error is calculated as

$$\Delta_i = b_i(x) - \overline{b}_i(x) \tag{8}$$

- The jth tomography cell correction value c_j is calculated as

$$c_j = \frac{1}{w_{+,j}} \sum_{l=1}^{M} \mathrm{l} \Delta_i \frac{w_{\mathrm{l}i}}{w_{i,+}} \tag{9}$$

where l is the summation for all rays through the jth cell.

- Update the value of the *j*th cell crossed by a mean for all rays as

$$\left| x_j = x_j^{(0)} + c_j \right| \tag{10}$$

  Namely, the *j*th cell correction value for all rays is calculated to complete the first iteration.
- The result of the first iteration is selected as the initial value. The process is repeated from step 2 to step 5, getting a final sequence $\overline{x}^{(1)}, \overline{x}^{(1)}, \ldots, \overline{x}^{(k)}$, with the convergence range ζ:

$$\left| x_j^{(k)} - x_j^{(k-1)} \right| < \zeta \; j = 1, 2, \ldots, N \tag{11}$$

3 Experimental

As shown in Figs. 2, 3, 4, and 5, AE source location was performed on two concrete plates of 400 × 400 mm with 100 mm of the thickness and a 60 mm diameter circle in the center of specimens (one with reinforcement and the other without reinforcement) under a planar location test setup using H-N sources. Reinforcements were carried out in order to act as geometric obstacles to the wave propagation, introducing reflections, scattering, and a nonhomogeneous wave propagation speed

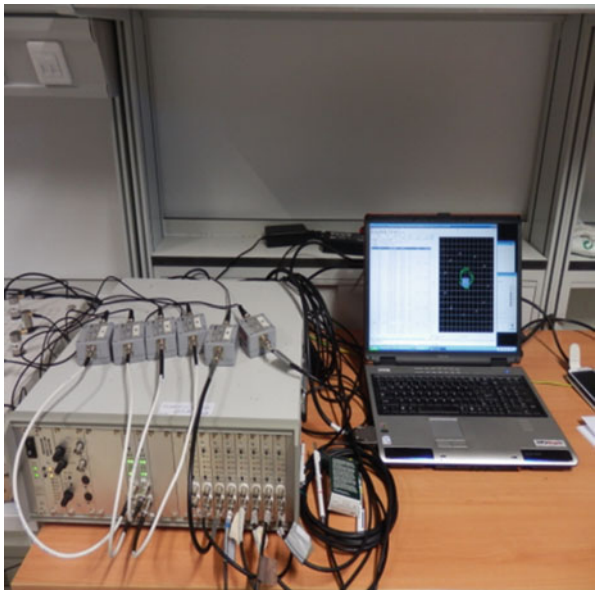

Fig. 2 Vallen system (16 channels)

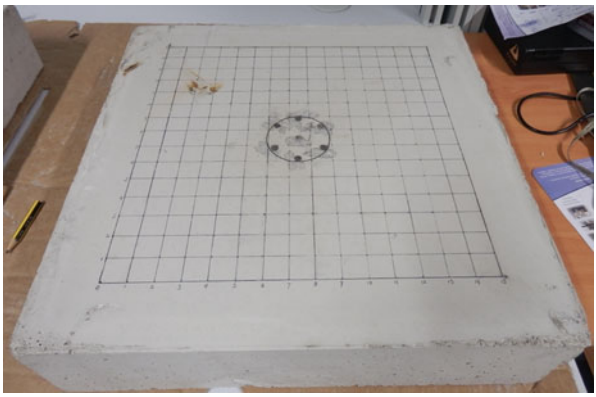

Fig. 3 The location of seven reinforces

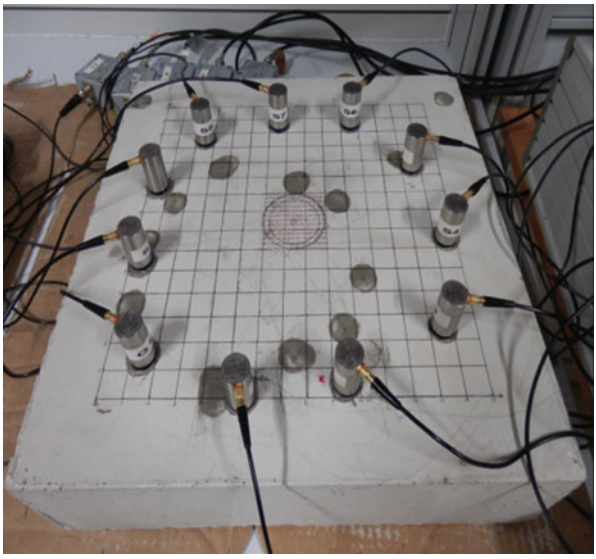

Fig. 4 Concrete sample without steel (sample 1)

distribution along the sample. Distribution of seven steel reinforced positions as shown Fig. 3, the diameter of each steel is 6 mm.

Since the specimen is a small concrete plate, and the density of AE sensors used was relatively high (see Figs. 4 and 5), some factors such as wave attenuation were ignored. Nonetheless, reinforcement in the sample produced a lot of problems into the source location algorithm (waves can be reflected, different wave modes can be formed and travelled around the circle at different speeds, and some sensors are blind to some areas of the steel plate), making it a significant challenge.

Eleven low-frequency sensors resonant at 25–80 kHz (VS-30) were coupled directly to the sample using an acoustic couplant layer of silicone grease. Sensor sensitivity and calibration were evaluated using the classical PLB (pencil

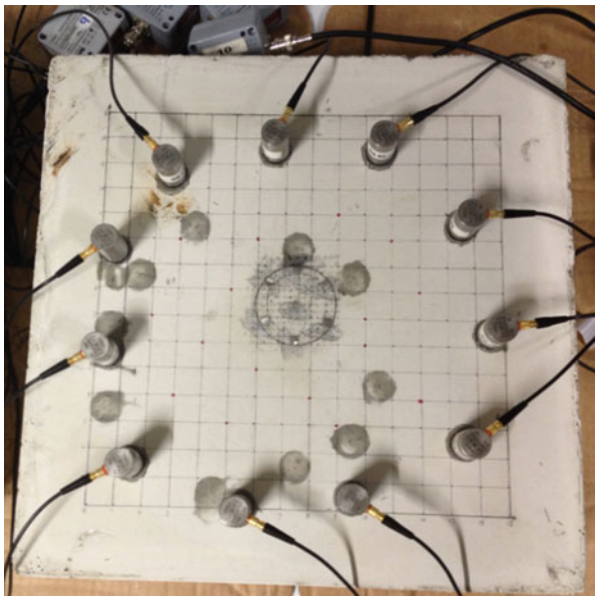

Fig. 5 Concrete sample with steel (sample 2)

lead break) technique, i.e., by means of Hsu-Nielsen artificial sources. Sixteen-channel Vallen AMSY-5 System equipment (Vallen, Europe AE team) was used as signal acquisition system in order to collect AE waveforms and data. For that, the following acquisition configuration was used: sample rate of 5 MHz, waveform data length of 4,096, retrigger rate of 600, 30.6 dB of threshold level (P-waves), preamplifier gain of 34 dB, and digital filtering range from 25 to 180 kHz (experiment system and sample as shown in Figs. 2–5).

After configuration, an AE source location test using PLB as AE artificial sources was implemented on the sample, and the sample area was divided into a matrix with $n \times m = 40 \times 40$ tomography cells, 2×2 cm each [5]. A five of Hsu-Nielson (H-N) sources was conducted on each cell node around each sensor. Response of all sensors to the H-N source was above 98 dB amplitude, demonstrating that all sensors were correctly mounted and coupled. After this mandatory calibration testing, the time of arrival of each PLB event to each sensor and the arrival sensor sequence order were recorded with the equipment and software. Time of arrival was considered as the classical first threshold crossing (FTC). Note that this is the only AE signal parameter needed for the AET algorithm (variable $T_{\mathrm{K}}^{\mathrm{A}}$ in Eq. (1)).

4 Results and Discussion

In AE tomography SART algorithm, the initial estimation of propagation speed of the concrete plate was 3.3 km/s. Projection data from 0 to 180° view ranges are available, the sampling interval is 0.02, iteration initial value was defined as zero,

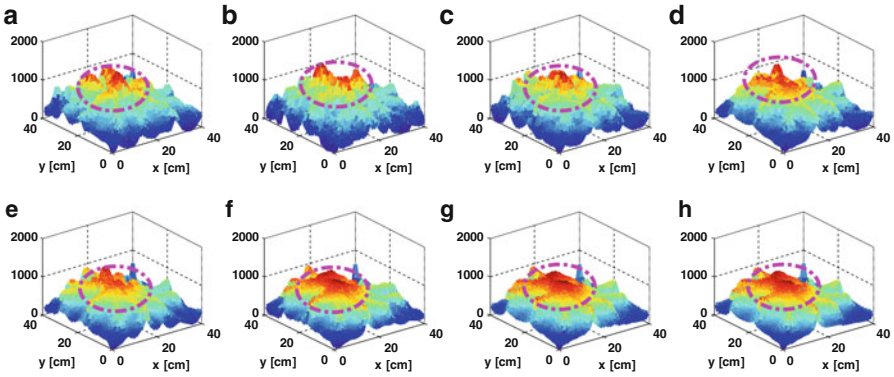

Fig. 6 The SART result without reinforcement (sample 1). (Three-dimensional (3D) reconstruction images after 0–180° by the SART, iterations are 3, 4, 6, 9, 15, 23, 36, and 72 from (**a**) to (**h**))

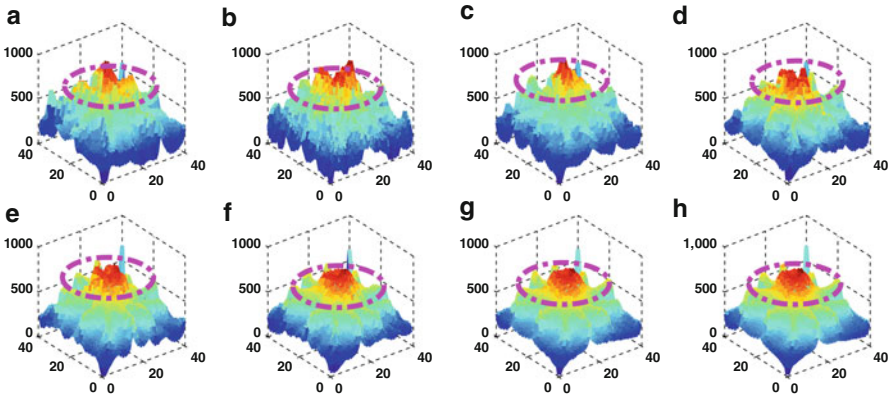

Fig. 7 The SART result with reinforcement (sample 2). (Three-dimensional (3D) reconstruction images after 0–180° by the SART, iteration are 3, 4, 6, 9, 15, 23, 36, and 72 from (**a**) to (**h**))

λ was 0.07, ζ was 0.0100001, and data vector $N = [60, 45, 30, 20, 12, 11.25, 5, 2.5]$ was input to the AET-SART routine that performs on Matlab 7.8 platform. Three hundred and fifty-three AE events are typical chosen for the reconstruction imaging results in two samples.

After 3, 4, 6, 9, 15, 23, 36, and 72 iterations, a mapping of AE tomography was constructed using the SART, 353 AE events were recorded, and the results of source location in two concrete sample were shown such as in Figs. 6 and 7; some interesting characters are as follows:

- One big region in the concrete plate is observed from different view ranges from 0 to 180°, where the propagation speed was higher than in its surroundings as in

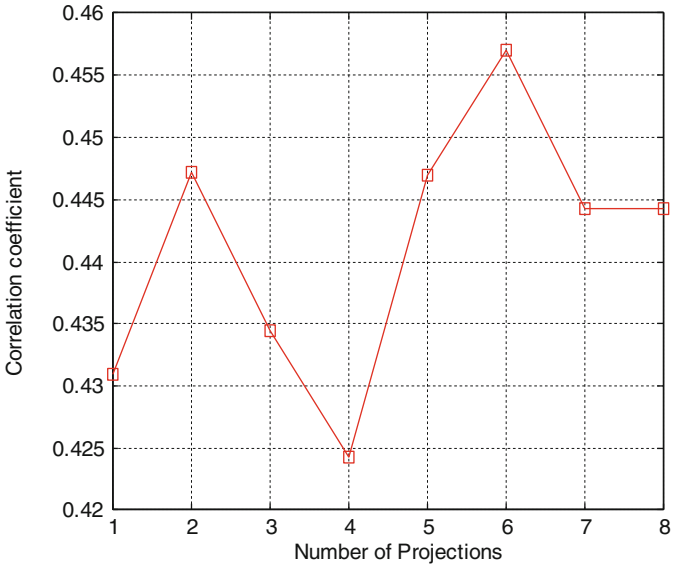

Fig. 8 CC (sample 1)

Figs. 6 and 7, which corresponds to big circle area (diameter: 60 mm) in the center of concrete specimen.

- The results of AE tomography using the SART show the influence of the reinforcement on the AE wave propagation speed clearly; the slowness values of sample 2 with steel iron are obviously getting smaller.
- The same original data available in conventional AE testing equipment is used in AE tomography. No specific hardware is required to develop.

To further effectively evaluate reconstructed 3D image quality using the SART, correlation coefficient (CC) and mean absolute error (MAE) are typically considered as evaluate indexes:

$$\mathrm{CC} = \sqrt{\sum \left(\hat{b}_i(x) - \overline{b}(x)\right)^2 / \sum \left(\hat{b}_i(x) - \overline{b}(x)\right)^2} \tag{7}$$

$$\mathrm{MAE} = \frac{1}{n} \sum_{i=1}^{n} \left| b_i(x) - \overline{b(x)} \right| \tag{8}$$

$b_i(x)$: is the ith projection data, $\overline{b}(x)$ is aver projection data, and $\hat{b}_i(x) - \overline{b}(x)$ is the residual error.

According to the indexes, the reconstructed 3D image quality is analyzed using the SART and evaluation indexes, from Figs. 8 and 9, the results of CC show the smaller correlation in the Number 4 of sample 1, i.e., 23 iterations (42.5 %); the Number 1 of sample 2, i.e., three iterations (50.03 %) and larger MAE is presented in 4 iteration of the sample 1 (28.7 %), In the sample 2, larger MAE is shown in

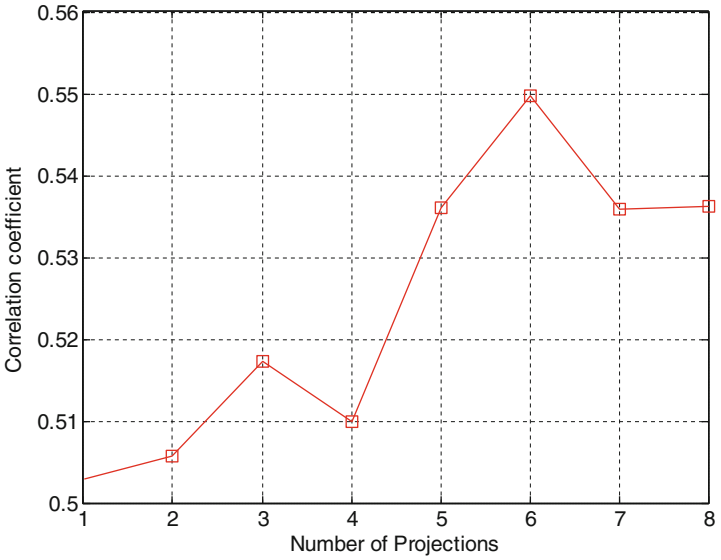

Fig. 9 CC (sample 2)

Table 1 Error estimation for AE source location

	MAE		CC	
Iteration	Sample 1	Sample 2	Sample 1	Sample 2
3	0.2818	0.1542	0.4310	0.5020
4	0.2862	0.1558	0.4470	0.5060
6	0.2800	0.1522	0.4350	0.5180
9	0.2782	0.1518	0.4250	0.5100
15	0.2716	0.1468	0.4470	0.5360
23	0.2681	0.1459	0.4460	0.5500
36	0.2689	0.1461	0.4450	0.5380
72	0.2689	0.1461	0.4450	0.5380
Average	0.2754	0.1498	0.4410	0.5250

4 iteration of the sample 1 (15.6 %), i.e. the two Number of projections. An improvement can be seen in 23 iteration in sample 1 (26.8 %) and sample 2 (14.9 %), i.e., the six Number of projections. Moreover, after 36 and 72 times iteration, a saturation behavior can be observed in terms of image quality; detail analysis results by estimated indexes are shown in Table 1. Compared with the AE source location results between sample 1 and sample 2, average errors (MAE) were decanted from 27.5 to 14.98 %. CC is improved from 44.1 to 52.5 %. It is shown that reinforcements have a great influence on AE wave propagation and AE source location (Figs. 10 and 11).

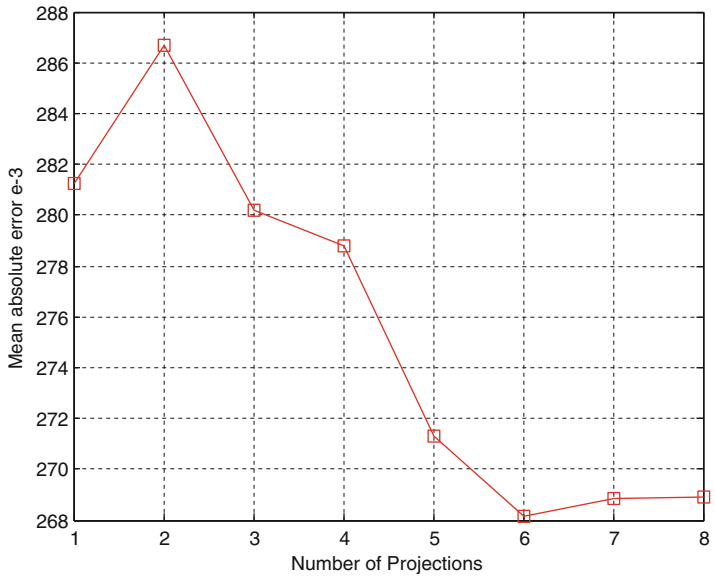

Fig. 10 MAE (sample 1)

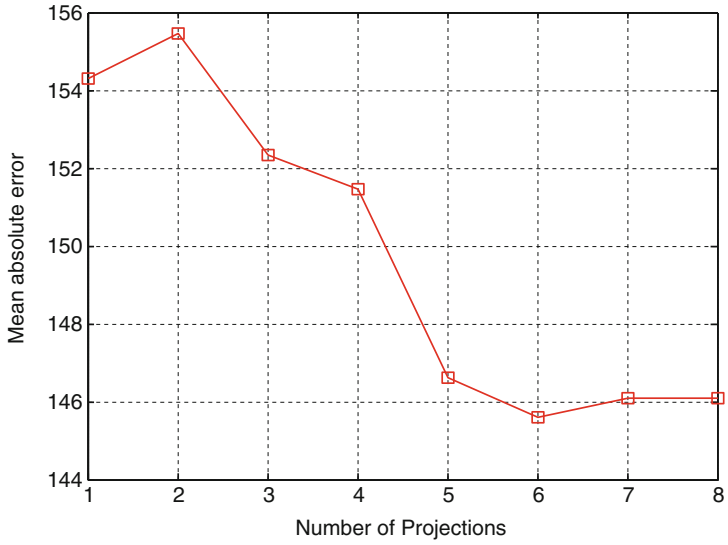

Fig. 11 MAE (sample 2)

5 Conclusions

AE tomography methodology using the SART is proposed and used in AE test on concrete specimen (one with reinforcement, i.e., sample 1, and the other without reinforcement, i.e., sample 2), wherein the performance proves to be very good. A successful three-dimension (3D) reconstruction result is obtained, which clearly shows the influence of the reinforcement on the AE wave propagation speed and improves the AE event location, giving a better precision to corresponding damaged location inside the structures of objects in terms of a locally varying wave speed distribution. Average errors are improved from 27.5 to 14.98 %.

The SART combined with tomography is also first applied to concrete material to construct 3D internal structure of objects nondestructively from AE incomplete data sets, by acquiring projections data from many different viewing angles from 0 to 180°. In terms of a locally varying wave speed distribution, the new technique proposed here can reveal the details of internal concrete structure and obtain a better source event location, which would be considered as a great potential for future engineering applications in AE fields.

Acknowledgment This work is supported by the National Natural Science Foundation of China (No. 51175079, No. 51305176), the Fundamental Research Funds for the Central Universities (CXLX12_0079), SNADS group of University of Granada, and the Ministry of Education in Spain for faculty (FPU).

References

1. ASTM, *Standard Terminology for Nondestructive Testing*, E1316, ASTM Book of Standards, vol 303 (ASTM, published annually)
2. K.M. Holford, D.C. Carter, Acoustic emission source location. Key. Eng. Mat. **167–168,** 162–171 (1999)
3. Y. Cheng, R. Mitra, P. Hagn, Development and future aspect of acoustic emission data processing methods, in: *The 30th European Conference on Acoustic Emission Testing & 7th International Conference on Acoustic Emission University of Granada*, 12–15 September 2012
4. F. Ciampa, M. Meo, A new algorithm for acoustic emission localization and flexural group velocity determination in anisotropic structures. Compos. Part A **41**, 1777–1786 (2010)
5. M.G. Baxter, R. Pullin, K.M. Holford, *Detla T Source Location for Acoustic Emission, Mechanical System and Signal Processing*, vol 21. (2007) pp. 1512–1520
6. J. Hensman, R. Mills, S.G. Pierce, Locating acoustic emission sources in complex structures using Gaussian processes. Mech. Syst. Signal Process. **24**, 211–233 (2010)
7. E. Maire, V. Carmona, J. Courbon, W. Ludwig, Fast X-ray tomography and acoustic emission study of damage in metals during continuous tensile tests. Acta Mater. **55**, 6806–6815 (2007)
8. A.C. Kak, Tomographic Imaging with Diffracting and Non-diffracting Sources, in *Array Signal Processing*, ed. by S. Haykin (Prentice-Hall, Engle-wood Cliffs, NJ, 1985), pp. 203–272
9. F. Schubert, Basic principles of acoustic emission tomography. In *26th European Conference on Acoustic Emission Testing*, (2004), pp. 693–708, http://www.ndt.net, July 25, 2011

10. Oswaldo G dos Santos Filho, Acoustic emission tomography to improve event locations and diagnostics of inhomogeneous equipments and structures. In *Proceeding of Word Conference on Acoustic Emission-2011,* Beijing, August 2011, pp. 310–314
11. Yu. Jiang, F.Y. Xu, Research on source location from acoustic emission tomography. In: *The 30th European Conference on Acoustic Emission Testing & 7th International Conference on Acoustic Emission* University of Granada, 12–15 September 2012
12. D.G. Aggelis, T. Shiotani, Repair evaluation of concrete cracks using surface and through-transmission wave measurements. Cem. Concr. Compos. **29**, 700–711 (2007)
13. T. Shiotani, S. Momoki, H.K. Chai, D.G. Aggelis, Elastic wave validation of large concrete structures repaired by means of cement grouting. Constr. Build. Mater. **23**(7), 2647–2552 (2009)
14. T. Shiotani, D.G. Aggelis, O. Makishima, Global monitoring of large concrete structures using acoustic emission and ultrasonic techniques: Case study. J. Bridg. Eng. **14**, 188–192 (2009)
15. H.K. Chai, D.G. Aggelis, S. Momoki, Y. Kobayashi, T. Shiotani, Single-side access tomography for evaluating interior defect of concrete. Constr. Build. Mater. **24**(12), 2411–2418 (2010)
16. H. Chai, S. Momoki, Y. Kobayashi, D. Aggelis, T. Shiotani, Tomographic reconstruction for concrete using attenuation of ultrasound. NDT. E. Int. **44**, 206–215 (2011)
17. D.G. Aggelis, T. Shiotani, S. Momoki, A. Hirama, Acoustic emission and ultrasound for damage characterization of concrete elements. ACI Mater. J. **106**, 509 (2009)
18. F. Schubert, Tomography techniques for acoustic emission monitoring. In: *28th European Conference on NDT*-September 2006, (Berlin Germany, ECNDT, 2006), http://www.ndt.net, Accessed July 25, 2011
19. A.H. Andersen, A.C. Kak, Simultaneous algebraic reconstruction technique (SART): A superior implementation of the ART algorithm. Ultrason. Imaging **6**, 81–94 (1984)
20. M. Jiang, G. Wang, Convergence studies on iterative algorithms for image reconstruction. IEEE. Trans. Image. Proces. **22**, 569–579 (2003)

Experimental Research on Tensile Process of Carbon Fiber Composite Materials Basing on Acoustic Emission

Yanlei Liu, Bing Wang, Weizhong Li, Bing Yu, and Fuyong Xia

Abstract With the extensive application of carbon fiber composite materials in the region of high-pressure vessel and aerospace, the related material damage mechanism analysis and integrality detecting is also massively being carried out which is more complex than the sole material. Acoustic emission technique can monitor the tensile process of carbon fiber composite laminate. And the acoustic emission signals by tensile specimens of different winding angles were investigated. Different angles in specimen's layers of carbon fiber had different mechanical properties and failure mechanisms. The results show that there were different signal characteristics from carbon fiber in different stages. Analysis on experimental data showed that acoustic emission testing technique can determine the process of different internal activities in carbon fiber composite laminate.

1 Introduction

Along with the extensive application of carbon fiber composite materials in the region of high-pressure vessel and aerospace, the related material damage mechanism analysis and integrality detecting is also massively being carried out which is more complex than the sole material [1, 2]. Its damage process is usually divided as substrate dehiscence, contact surface dehiscence, fiber breakage, interlayer debonding, and so on [3–6]. Thus, there is no nondestructive inspection method to examine these complex flaws so far. And in the practical application, different complementary methods are adopted according to the composite material component's shape, type, operation requirements and flaw type, size, position, orientation,

Y. Liu (✉) • B. Wang • W. Li • B. Yu • F. Xia
Hangzhou Special Equipment Inspection Institute, Hangzhou 310008, China
e-mail: liuyanlei@zju.edu.cn

G. Shen et al. (eds.), *Advances in Acoustic Emission Technology: Proceedings of the World Conference on Acoustic Emission-2013*, Springer Proceedings in Physics 158,
DOI 10.1007/978-1-4939-1239-1_31,

examination ability, and so on. However, the aims of nondestructive testing of composite components are to obtain its structural integrity, strength, and carrying capacity, assessing its service life and safety.

Acoustic emission (AE) refers to the generation of transient elastic waves produced by a sudden redistribution of stress in a material. When a structure is subjected to an external stimulus, localized sources trigger the release of energy, in the form of stress waves, which propagate to the surface and are recorded by sensors. AE is different with most other nondestructive testing techniques in two regards. The first difference pertains to the origin of the signal. The second difference is that acoustic emission testing (AET) deals with dynamic processes in a material. With the right equipment and setup, motions can be identified. In composites, substrate dehiscence, contact surface dehiscence, fiber breakage, and interlayer debonding contribute to acoustic emissions [7]. In this chapter, the process of composite tensile test was monitored by AE method. And the acoustic emission signals by tensile specimens of different winding angles were analyzed.

2 Methods

The specimen was made by carbon fiber composite laminate composed by eight layers, sized as 250 mm × 25 mm × 1.8 mm with a 0.5 cm diameter hole in the middle location. And four angles in specimen's layers of carbon fiber were considered, as shown in Fig. 1. There were two specimens of each type.

The equipment we used were PAC samos-48 and tensile testing machine MTS 810. Two AE transducers (R15I) with frequency between 5 and 400 kHz were used to collect AE waveforms. To hold the two sensors in place, gummed fabric tape was used. The two AE sensors were coupled to the specimen using a couplant. The difference in arrival times of the AE signal received by the two sensors was used to establish event source location. Peak value definition time, hit definition time, and hit latching time were settled as 20 μs, 20050 μs, and 300 μs. The testing site was shown in Fig. 2.

3 Results and Discussion

3.1 Mechanical Property

The peak stress of four pieces of carbon fiber composite laminate is shown in Table 1. We can find that there was different peak stress with different layer angle. And there was a highest value with type 2. Its strain rate is the highest since the 90° layer can bear the highest pulling stress. There is a lowest value with type 1. However, its strain rate is higher than type 3 and type 4. The stress–strain curve of four types is shown in Fig. 3.

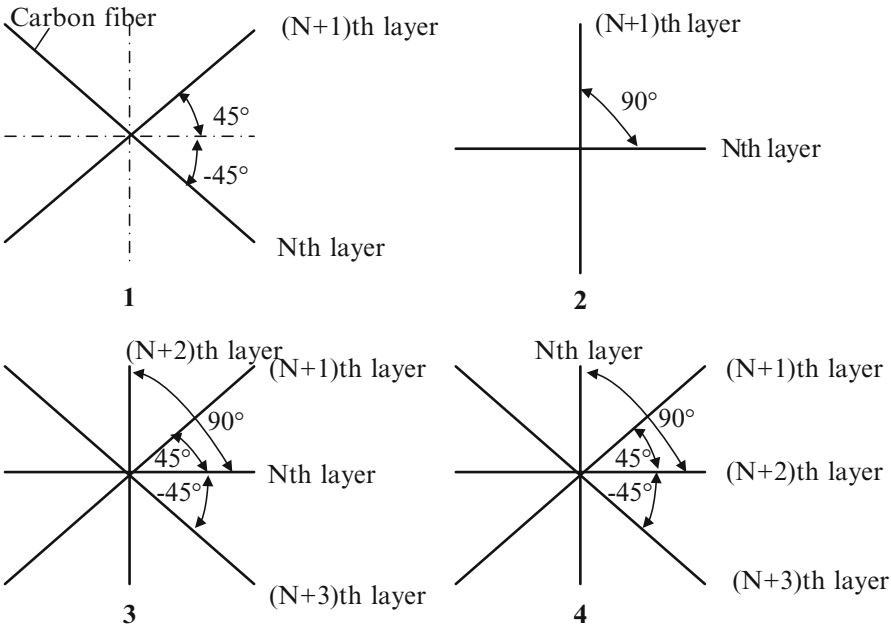

Fig. 1 Specimen with four different layers

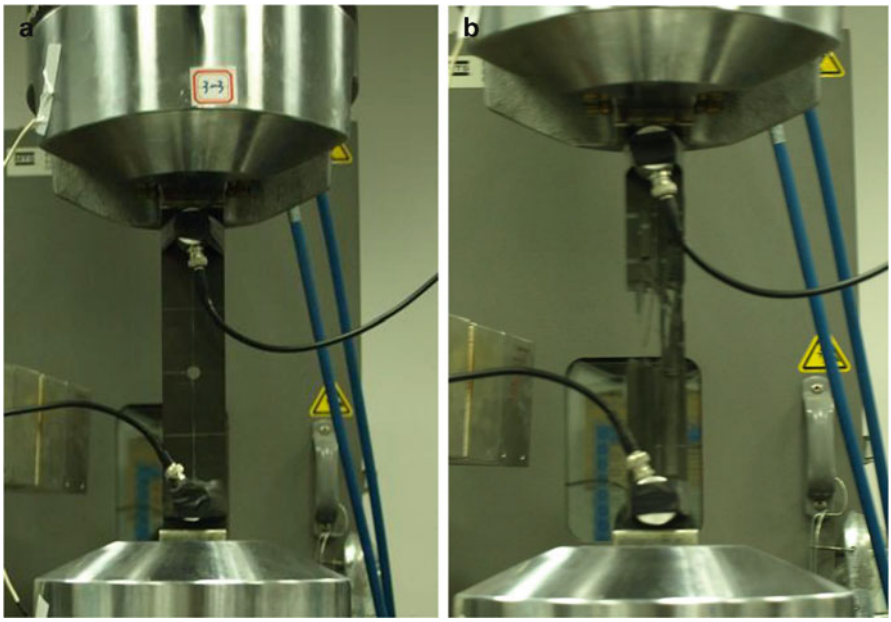

Fig. 2 Experimental equipment (**a**—before tensile, **b**—after tensile)

Table 1 Experimental data of peak stress of four types of specimens

Specimens	Layer angles (°)	Strain rate (%)	Peak stress (MPa)
1	45/−45	3.81	153.7
2	0/90	3.99	1,377
3	0/45/90/−45	3.20	749.1
4	90/45/0/−45	3.52	893.5

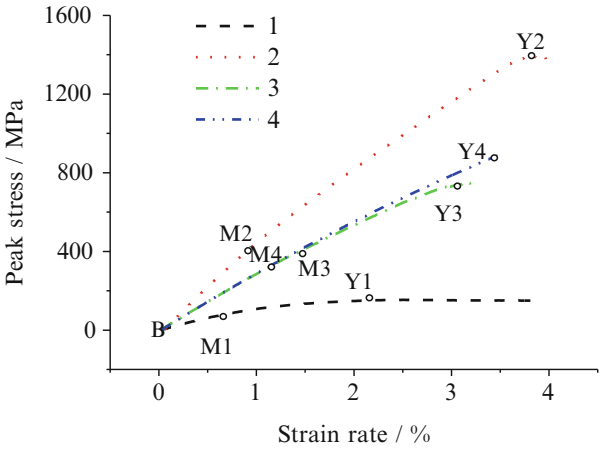

Fig. 3 Stress strain curve of four types (M—yield stress; Y—tensile strength)

We can see from Fig. 1 that the stress increases linearly with increasing strain in the stretch initial stage (B-M) which is called the elastic deformation stage,. Along with the increasing load (M-Y), the stress increases not linearly as in B-M stage in which the damage is developed and accumulated due to the contact surface debonding, the lamination and the substrate shearing failure, and residual gap in the matrix partial failure.

In theoretical analysis, there is a highest peak stress with 45/−45° layer. But there was a lowest peak stress due to the small width of the laminate which is just 25 mm. So, the ability of high bearing pulling stress was not performed. As there are similar layer distributions, type 3 and type 4 have a near-mechanical property.

3.2 Acoustic Emission Signal and Analysis

The frequency and waveform character of low-amplitude AE signal is shown in Figs. 4 and 5. From the figure, we find that there is a quick rising time, a short endurance time (<300 μm), and low counts. And highest frequency value is between 170 and 220 Hz. Low-amplitude AE signal is created by substrate dehiscence, contact surface dehiscence, and interlayer debonding.

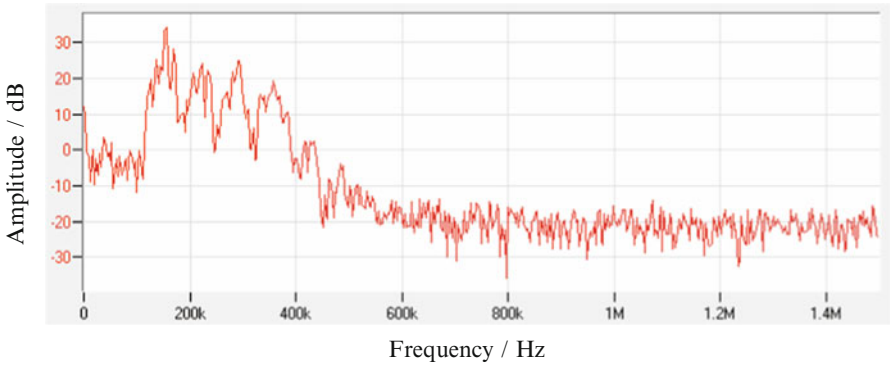

Fig. 4 Frequency character of low-amplitude AE signal

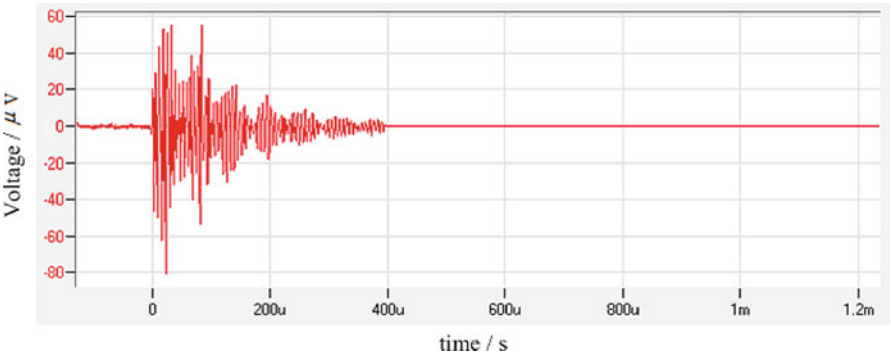

Fig. 5 Waveform of low-amplitude AE signal

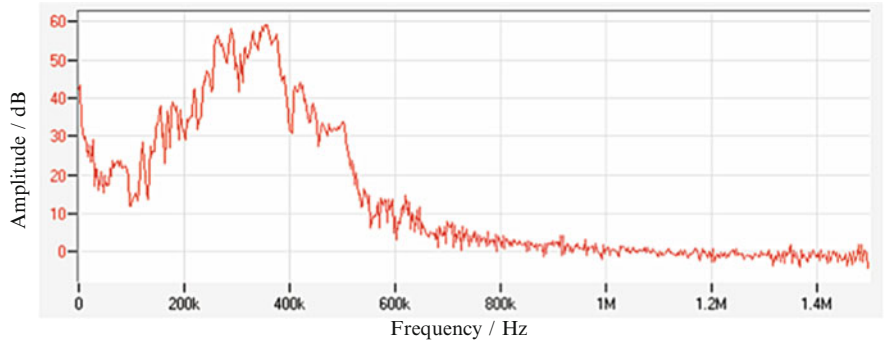

Fig. 6 Frequency characteristic of high-amplitude AE signal

The frequency and waveform character of high-amplitude AE signal is shown in Figs. 6 and 7. From the figure, we find that there is a slower rising time, a longer endurance time (>600 μm), and higher amplitude value than the low-amplitude AE

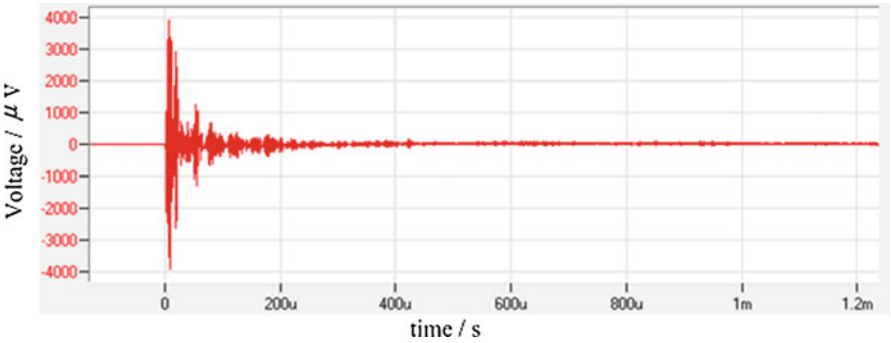

Fig. 7 Waveform of high-amplitude signal

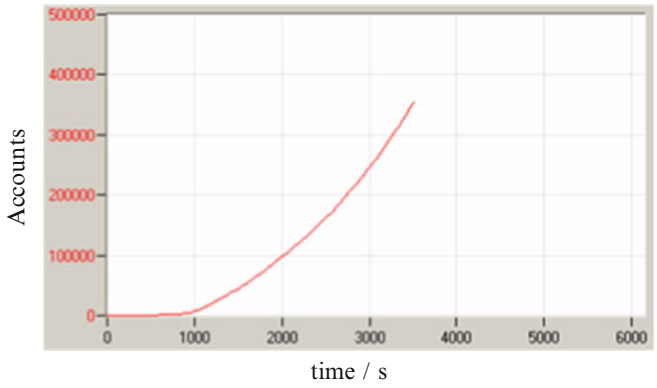

Fig. 8 Accounts with increasing time of type 1

signal as shown in Fig. 4. And highest frequency value is between 290 and 350 Hz. High-amplitude AE signal is created by carbon fiber breakage.

3.3 Acoustic Emission Results and Analysis

From Figs. 8 and 9 we can see that there are few AE signals in previous 910 s (B-M1 in Fig. 3) with low-amplitude value and fewer accounts. It is to say that, in this period, interior activity is quiet. A few signals only occur for the better coordinated distortion, and minor mounts of brittle contact surface dehiscence are carried out. Otherwise, the energy is very low which showed that this stage has no obvious damage. The strain is 82 MPa at 910 s, which is quite close with M1 transformation load of 89 MPa. After 910 s, counts of the AE signal which is higher than 70 dB occur and increase with the time. And the amplitude of AE signal higher than 80 dB

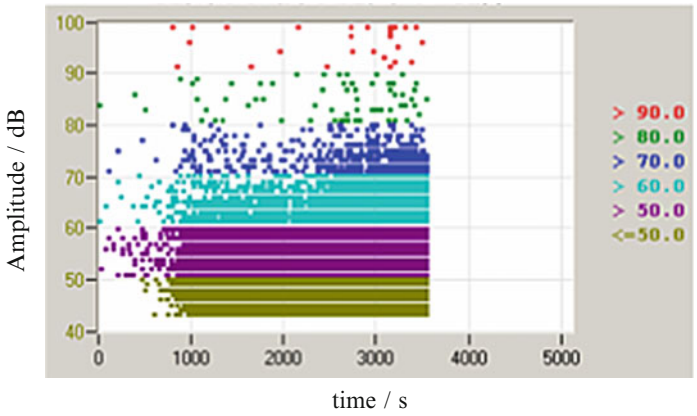

Fig. 9 Signal amplitude with time of type 1

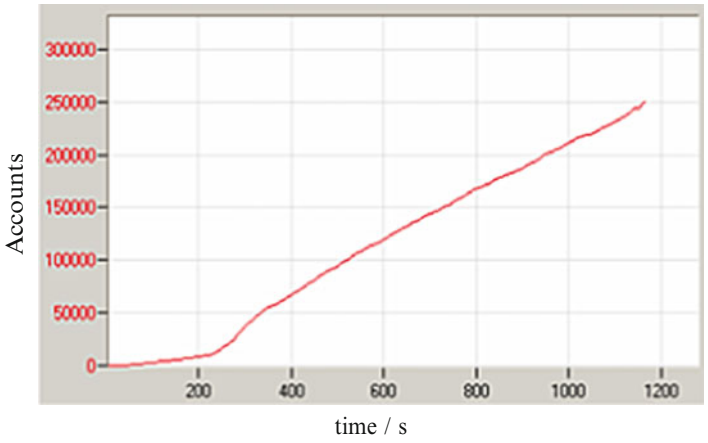

Fig. 10 Accounts with increasing time of type 2

appeared. At this moment the damage inside the laminate was accumulated to a certain extent, which led to finally breakage.

From Figs. 10 and 11 we can see that there are few AE signals in previous 280 s (B-M2 in Fig. 3) with low-amplitude value and fewer accounts. It is to say that, in this period, interior activity is quiet. A few signals only occur for the better coordinated distortion, and minor mounts of brittle contact surface dehiscence are carried out. Otherwise, the energy is very low which showed that this stage has no obvious damage. The strain is 392 MPa at 280 s, which is quite close with M2 transformation load of 410 MPa. After 280 s, counts of the AE signal which is higher than 90 dB occur and increase with the time. In this period, 0° layer goes to breakage. In the last 200 s before fracture, the high-amplitude signal occurs

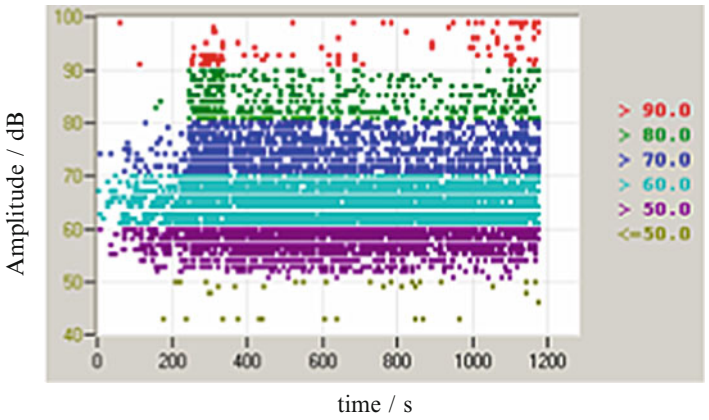

Fig. 11 Signal amplitude with time of type 2

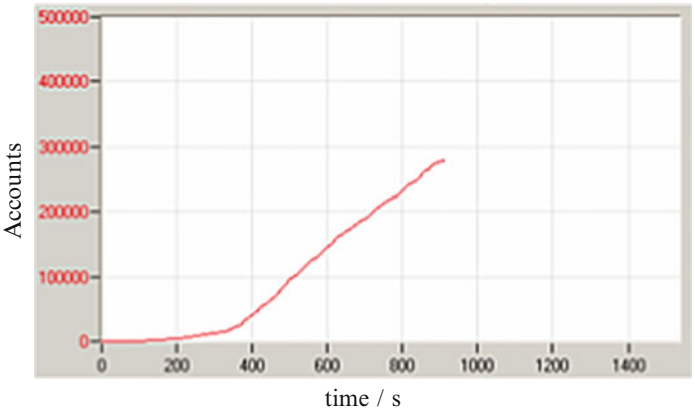

Fig. 12 Accounts with increasing time of type 3

concentratively because 90° layer goes to failure. It shows that the damage inside the laminate was accumulated which led to finally breakage of the laminate.

From Figs. 12 and 13 we can see that there are few AE signals in previous 350 s (B-M3 in Fig. 3) with low-amplitude value and fewer accounts. The strain at the time of 350 s is 342 MPa, which is quite close with M3 transformation load of 350 MPa. After 350 s, counts of the AE signal which is higher than 90 dB occur because 90° layer goes to failure. It shows that the damage inside the laminate was accumulated which led to finally breakage of the laminate. These are similar with Figs. 14 and 15.

From Figs. 9, 11, 13, and 15, we can find that there are some signals whose amplitude value is above 90 dB in the initial stage. By analysis, we find that these are originated by friction of clamp and laminate as its location is near that area.

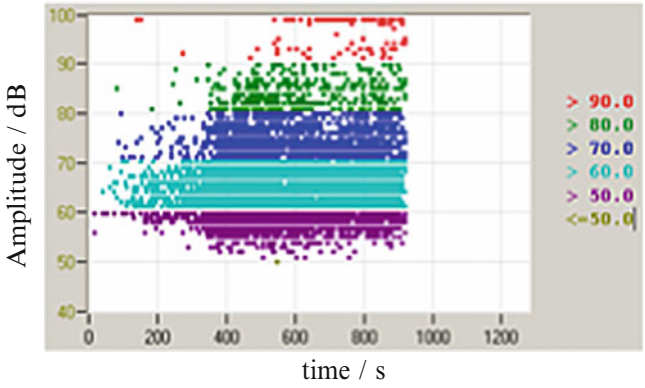

Fig. 13 Signal amplitude with time of type 3

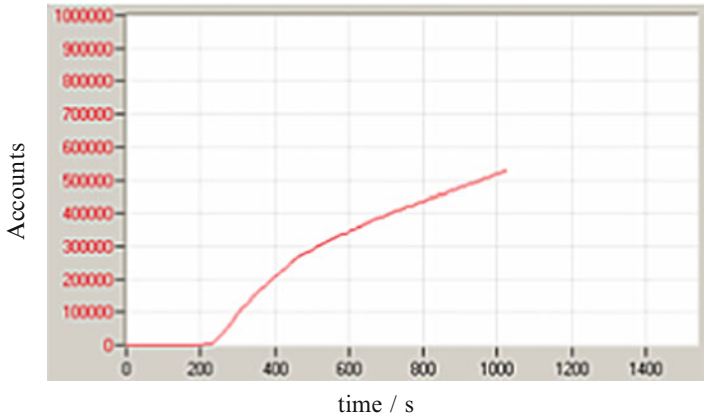

Fig. 14 Accounts with increasing time of type 4

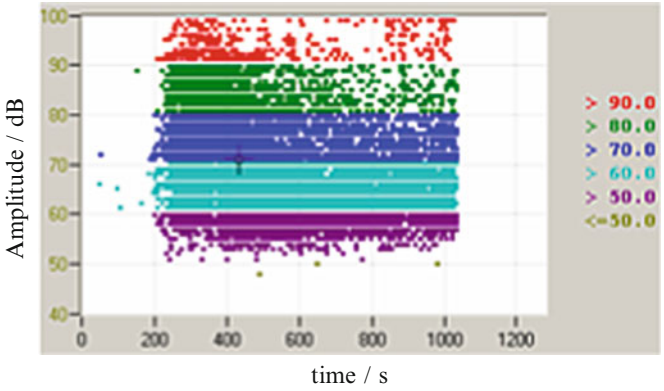

Fig. 15 Signal amplitude with time of type 4

4 Results

Tensile process of carbon fiber composite laminate was monitored by acoustic emission technique. By analysis we find the following:

1. Frequency value of AE signals generated by carbon breakage is between 290 and 350 Hz. And different angles in specimen's layers of carbon fiber had different mechanical properties and failure mechanisms.
2. Acoustic emission testing technique can determine the process of different internal activities in carbon fiber composite laminate. Therefore, it can be used in the integrity evaluation for carbon fiber composite materials.

Acknowledgment This work was supported in part by the Zhejiang Province science and technology innovation team project under Grant No. 2010R50001.

References

1. N. Sato, T. Kuraychi, O. Kamigaito, Fracture mechanisms of unidirectional carbon reinforced epoxy resin composite. J. Mater. Sci. **21**(3), 1005–1010 (1986)
2. F. Sergey, N. Tatiana, K. Alexandr, Model of acoustic emission signal at the prevailing mechanism of composite material mechanical destruction. Aviation **14**(4), 95–103 (2010)
3. F. He, W. Sun, The application of carbon fiber composite materials in giant plane. Hi-Tech Fiber Appl. **32**(6), 5–8 (2007)
4. O.I. Benevolenski, J. Karger-Kocsis, T. Czigdny, Mode I fracture resistance of glass fiber mat-reinforced poly propylene composites at various degree of consolidation. Comp. Part A **34**(3), 267–273 (2003)
5. P.J. De Groot, P.A.M. Wijnen, R.B.F. Janssen, Real-time frequency determination of acoustic emission for different fracture mechanisms in carbon/epoxy composites. Comp. Sci. Technol. **55**(4), 405–412 (1995)
6. M. Giordano, A. Calabro, C. Esposito, An acoustic emission characterization for the failure modes in polymer composite materials. Comp. Sci. Technol. **37**(3), 411–428 (1990)
7. D.J. Collins, *Damage Detection in Composite Materials Using Acoustic Emission and Self-Sensing Fibers* (University of Birmingham, Birmingham, 2010)

Concrete Crack Damage Location Based on Piezoelectric Composite Acoustic Emission Sensor

Yuesheng Xu, Dongyu Xu, Jiao Qu, Xin Cheng, Hudong Jiao, and Shifeng Huang

Abstract It is significant to use acoustic emission technology to study crack damage location of concrete. In order to study concrete crack damage of linear positioning, pencil lead broken method was used to simulate crack initiation in concrete with affixed and embedded acoustic emission sensors manufactured by 1–3-type piezoelectric composite material. The results show that the accuracy of embedded sensors can reach above 95 %, which is higher than that of the affixed sensors. Moreover, it is easier to operate and suitable for special environment monitoring of buildings using embedded sensors to monitor the random crack of the concrete. This research provides a theoretical basis for concrete crack damage monitoring with acoustic emission technology.

1 Introduction

Many engineering examples [1] show that numerous buildings which have caused great economic losses did not reach their working life. In recent years, more and more attention is drawn to use all kinds of intelligent materials and technology for health monitoring of concrete structure [2]. Researchers are interested in acoustic emission technology because it is a new online monitoring method. An important aim is to judge the damage degree of material based on the knowledge of acoustic emission signal [3–5]. It is vital to study the acoustic emission characteristics of defect source because the location of the acoustic emission source is the most intuitive way for researchers to know the damage of the concrete structure. Pencil lead broken method was simulated as acoustic emission phenomena. According to

Y. Xu • D. Xu • J. Qu • X. Cheng • H. Jiao • S. Huang (✉)
Shandong Provincial Key Laboratory of Preparation and Measurement of Building Materials, University of Jinan, Jinan 250022, China
e-mail: mse_huangsf@ujn.edu.cn

G. Shen et al. (eds.), *Advances in Acoustic Emission Technology: Proceedings of the World Conference on Acoustic Emission-2013*, Springer Proceedings in Physics 158,
DOI 10.1007/978-1-4939-1239-1_32,

the analysis of AE signal sensors received, the location of concrete crack and accuracy of linear positioning can be obtained, which will provide a theoretical basis for concrete crack damage monitoring with acoustic emission technology.

2 Experiment

2.1 Test Principle

The sensors were affixed to the surface of the material to detect mechanical transient waves generated from the defect in a structure. AE signals are acquired and stored in the acquisition system. The testing principle is shown in Fig. 1.

Linear location of crack damage is based on wave velocity and time of acoustic emission signals [6]. In the test, it is assumed that the distance between two sensors is L, and the distance between defect source and sensor 1 is X. $T1$ is the time the wave needs to propagate from source to sensor 1, and $T2$ is the time the wave needs to propagate from source to sensor 2. The velocity V can be calculated from $T1$ and $T2$ of an artificial event stimulated at one sensor. The crack position is calculated as

$$X = \frac{L - \Delta T \cdot \mathrm{V}}{2} \tag{1}$$

where ΔT is the time difference between $T1$ and $T2$.

2.2 Experimental Procedures

Concrete composition is shown in Table 1. There are two concrete beams and four sensors were prepared: (1) two beam specimens of 100 mm × 100 mm × 400 mm

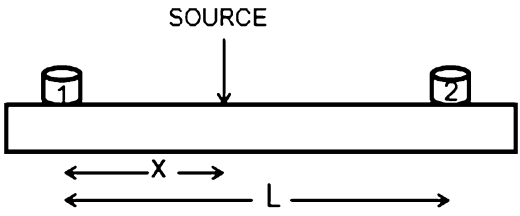

Fig. 1 Linear location principle

Table 1 Concrete composition

Materials	Cement	Water	Sand	Stone	Unit weight (kg/m^3)
Weight (kg)	427	187	712	1,074	2,400

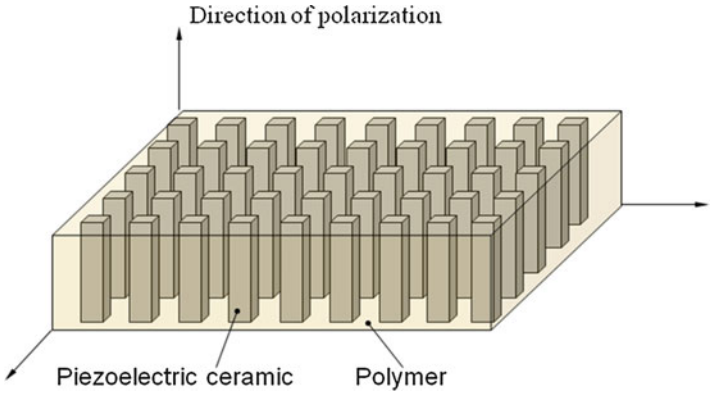

Fig. 2 Structure of 1–3-type piezoelectric composite

Fig. 3 Schematic of concrete structure with sensors inside

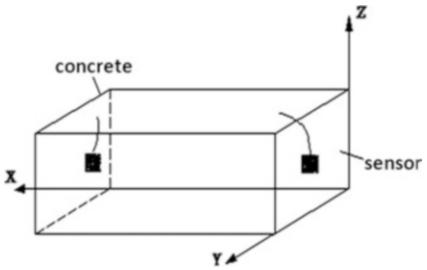

(thickness × depth × span) with a smooth boundary; (2) four sensors of 10 mm × 10 mm × 10 mm by using 1–3-type piezoelectric composite were designed of the PZT-5 piezoelectric ceramic [7] as the piezoelectric element (shown in Fig. 2 [8]). Cement and epoxy resin were used as encapsulation materials of acoustic emission sensor [9]. Two sensors were located in the ends of concrete beam along the center line. The position of embedded sensors is shown in Fig. 3. At the same time, two sensors were affixed on another concrete specimen surface for contrast. Acoustic emission acquisition device was used to acquire AE signal and measure the threshold lower than 40 dB before conducting the experiment. Meanwhile, front gain was set to 40 dB, and filter was set to 20–400 kHz.

The AE system manufactured by the Physical Acoustic Corporation (PAC) was used for acquiring the signal in process of pencil lead broken. It needs ten times of pencil lead in the center of the specimen surface with broken lead position coordinates of (200 mm, 50 mm). The experiment setting is shown in Figs. 4 and 5.

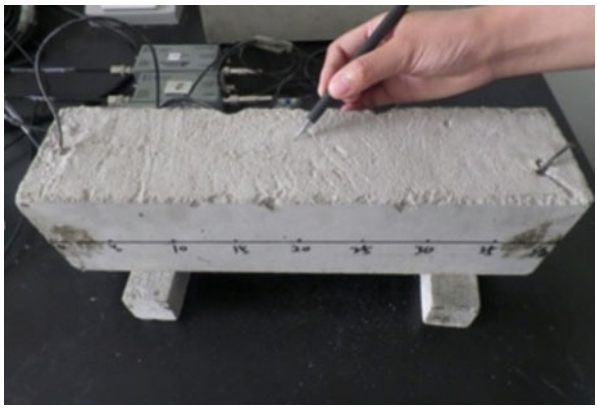

Fig. 4 Pencil lead broken at the concrete with embedded sensors

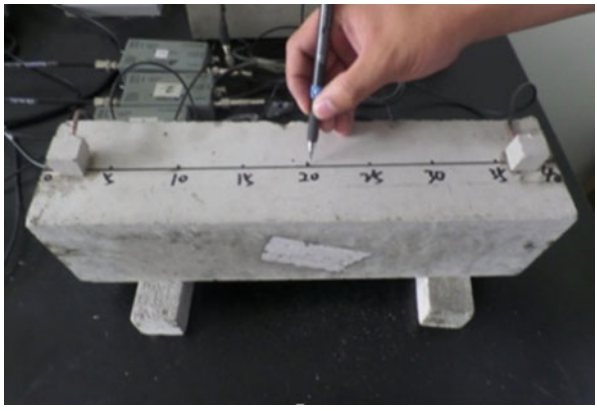

Fig. 5 Pencil lead broken at the concrete with affixed sensors

2.3 Results and Analysis

Figures 6 and 7 show the amplitude response of signals received by the sensors, and the signals are typical AE signals. The results show that embedded and affixed 1–3-type piezoelectric composite sensors possess good signal response and can be used in concrete monitoring.

As shown in Figs. 6 and 7, there are different response amplitudes between affixed sensors and embedded sensors. It is due to the energy decrement that embedded sensors receive a lower signal. According to the energy decrement phenomenon, different amplitudes can be analyzed and the position of the defect source can also be accurately found. From Figs. 8 and 9, it can be found that signals for each time can be acquired by the sensors, which indicates that the 1–3-type piezoelectric composite sensors possess a high sensitivity.

From Tables 2 and 3, it could be seen that the accuracy of affixed sensors is 95.26 % and 96.02 % for the embedded.

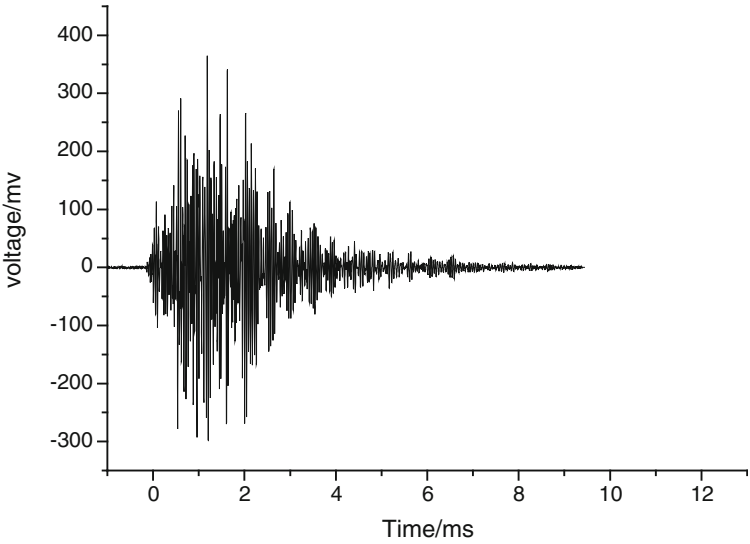

Fig. 6 Response of affixed sensors

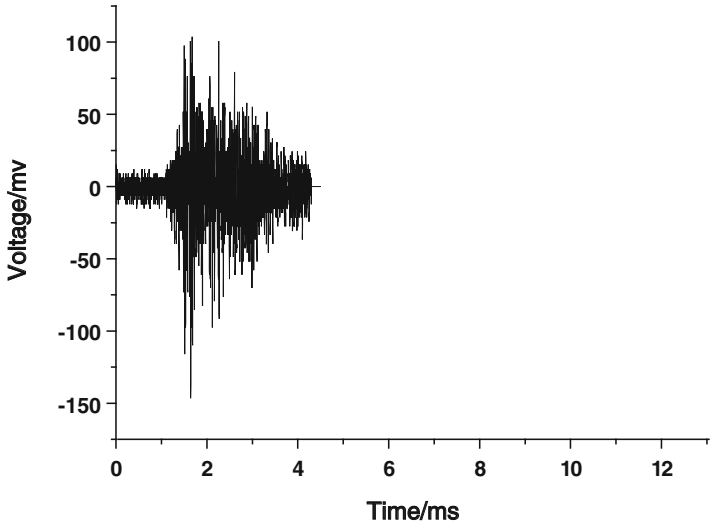

Fig. 7 Response of embedded sensors

As shown in Tables 2 and 3, it can be found that embedded sensors have a higher accuracy than the affixed sensors. However, some large precision error may occur, and the reason may be that the frequency is different when the lead was broken.

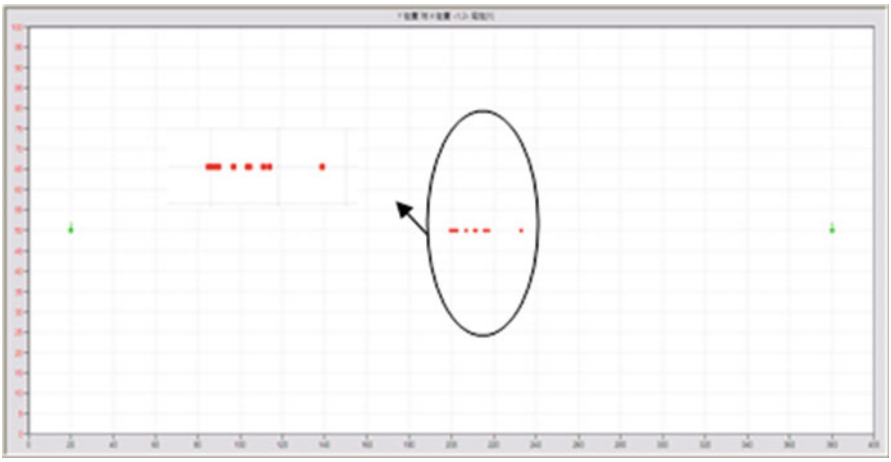

Fig. 8 Linear location of affixed sensors

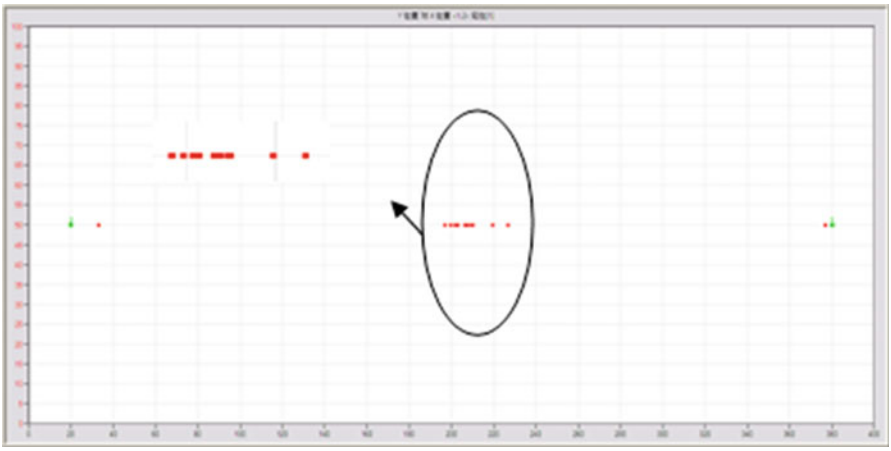

Fig. 9 Linear location of embedded sensors

Table 2 Detect source location accuracy of fixed sensors

Ordinal	Theoretical coordinates (mm)	Actual coordinates (mm)	*X*-axis error (%)	*Y*-axis error (%)	Total error (%)
1	(200, 50)	(233.1, 50)	16.55	0	16.55
2	(200, 50)	(211.0, 50)	5.50	0	5.50
3	(200, 50)	(199.5, 50)	0.25	0	0.25
4	(200, 50)	(217.3, 50)	8.65	0	8.65
5	(200, 50)	(201.0, 50)	0.50	0	0.50
6	(200, 50)	(215.7, 50)	7.85	0	7.85
7	(200, 50)	(202.6, 50)	1.30	0	1.30
8	(200, 50)	(201.0, 50)	0.50	0	0.50
9	(200, 50)	(211.5, 50)	5.75	0	5.75
10	(200, 50)	(201.0, 50)	0.50	0	0.50

Table 3 Detect source location accuracy of embedded sensors

Ordinal	Theoretical coordinates (mm)	Actual coordinates (mm)	*X*-axis error (%)	*Y*-axis error (%)	Total error (%)
1	(200, 50)	(226.8, 50)	13.4	0	13.4
2	(200, 50)	(203.1, 50)	1.55	0	1.55
3	(200, 50)	(206.3, 50)	0.25	0	0.25
4	(200, 50)	(209.4, 50)	4.70	0	4.70
5	(200, 50)	(219.4, 50)	9.70	0	9.70
6	(200, 50)	(201.6, 50)	0.80	0	0.80
7	(200, 50)	(207.3, 50)	3.65	0	3.65
8	(200, 50)	(207.9, 50)	3.95	0	3.95
9	(200, 50)	(196.9, 50)	1.55	0	1.55
10	(200, 50)	(199.5, 50)	0.25	0	0.25

3 Conclusions

In the process of linear location, the embedded 1–3-type piezoelectric composite sensors possess good sensitivity and high accuracy that can reach above 95 %. Meanwhile, the response amplitude can reflect the distance between sensors and defect source, so the defect source can be accurately located. The research of this chapter also provides a theoretical basis for concrete crack damage monitoring with acoustic emission technology.

Acknowledgment This study was financially supported by the National Natural Science Foundation (Grants Nos. 51272090, 51202089) and A Project of Shandong Province Higher Educational Science and Technology Program (Grant No. J12LA05).

References

1. D.G. Childer, *Modern Spectrum Analysis* (IEEE Press, Piscataway, NJ, 1978)
2. C.Z. Chen, G. Luo, B.S. Bai, *Structure Damage Monitor and Intelligent Diagnosis* (Science Press, Beijing, 2000a), pp. 1–3
3. G.T. Shen, R.S. Geng, S.H. Liu, Acoustic emission source location [J]. NDT **24**(3), 114–117 (2002)
4. H.D. Pang, X.M. Zheng, F.X. Jiang, The spectrum analysis of acoustic emission signal in rock materials [J]. J. China Coal Soc. **29**(5), 540–544 (2004)
5. A. Gallego, J.F. Gil, J.M. Vico et al., Coating adherence in galvanized steel assessed by acoustic emission wavelet analysis [J]. Scripta Mater. **2**(10), 1069–1074 (2005)
6. B. Chen, L.X. Zhang, J.Y. Liu, Study on the acoustic emis-characteristics of the concrete beams under three-point bending load [J]. Nondestruct. Technol. **22**(3), 109–111 (2000b)
7. S.F. Huang, Z.M. Ye, S.D. Wang et al., Fabrication and properties of 1–3 cement based piezoelectric composites [J]. Acta Mater. Compos. Sinica **24**(1), 122–126 (2007)
8. M. Sun, D.Y. Xu, S.F. Huang, Analysis of the 1–3 piezoelectric composites and transducer [J]. Mater. Sci. Forum **687**, 339–342 (2011)
9. D.Y. Xu, X. Cheng, S.F. Huang et al., Non destructive evaluation based on impedance method using embedded PZT sensor [J]. Adv. Mater. Res. **79–82**, 35–38 (2009)

Part IV
Structure

Visualization of Damage in RC Bridge Deck for Bullet Trains with AE Tomography

Tomoki Shiotani, Satoshi Osawa, Shohei Momoki, and Hiroyasu Ohtsu

Abstract In recent years, a lot of accidents associated with infrastructures occur in Japan because of the remarkable deterioration of the infrastructures. Considering the expected reduction of construction investment year after year, it is important to repair and reinforce those structures with the limited budget as well as to extend their service life in the future. From the viewpoint of management and maintenance for those ageing infrastructures, preventive maintenance shall be taken rather than the reactive maintenance. In the preventive maintenance, repairing and reinforcing structures shall be implemented before any fatal deterioration to the structures. However, the reasonable diagnostic method for preventive maintenance has not been established so far. NDT approaches to diagnose the early internal damage of structures is thus in high demand. To solve these issues, the authors had proposed "AE tomography" which executes both AE monitoring and elastic wave tomography. The AE tomography enables to provide accurate AE source locations as well as velocity distribution with the tomography simultaneously. In this paper, in order to verify this proposed AE tomography for in situ infrastructures, deteriorated RC bridge deck for bullet trains was investigated.

T. Shiotani (✉) • S. Osawa • H. Ohtsu
Department of Urban Management, Graduate School of Engineering,
Kyoto University, Kyoto 615-8540, Japan
e-mail: shiotani.tomoki.2v@kyoto-u.ac.jp

S. Momoki
Research Institute of Technology, Tobishima Corporation,
Tobishima 270-0222, Japan
e-mail: shouhei_momoki@tobishima.co.jp

G. Shen et al. (eds.), *Advances in Acoustic Emission Technology: Proceedings of the World Conference on Acoustic Emission-2013*, Springer Proceedings in Physics 158,
DOI 10.1007/978-1-4939-1239-1_33,

1 Introduction

In recent years, a lot of accidents occur due to deterioration of infrastructures such as RC bridge and tunnels. This makes it more important to maintain and reinforce those deteriorated structures in a proper manner. In action plans for maintaining and managing the structures, there are two maintenance strategies, namely corrective maintenance and preventive maintenance. The former is the action plan for repairing and reinforcing structures when it becomes the fatal deterioration, while the latter is the action plan of which those shall be executed thereby preventing a remarkable damage. As the preventive maintenance is known as the best maintenance strategy because it enables to extend the life of structures with reasonable cost, the techniques to diagnose early internal damage of the structures are in high demand. NDT such as ultrasonic testing has so far been applied for the evaluation of early internal damage; however, as it was a spot assessment requiring a lot of time to test, the author's group has proposed "AE tomography" consisting AE monitoring and elastic wave tomography. The AE tomography allows implementing AE source location and tomography simultaneously. The AE tomography can evaluate the wide range of damage scale such as microscopic to macroscopic damage as to adapt sensors being suitable or corresponding to be frequency range to the damage scale. The AE tomography has been applied to some actual structures so far [1]; however, the number of application has been insufficient and the applicability for actual structures hasn't been verified. In this paper, in order to verify the AE tomography for in situ infrastructures, it was applied to the deteriorated RC bridge deck for bullet trains.

2 AE Tomography

AE tomography consists of AE monitoring and elastic wave tomography. Figure 1 shows the configurations of AE monitoring. AE (acoustic emission) occurs in association with the occurrence or progress of the crack. AE monitoring is the method to identify the detail of the AE source such as location by using arrival time differences among AE sensors, where AE sources were generated due to the crack occurrence by load applications. The conventional AE source locations are conducted assuming elastic wave velocity of the structure being homogeneous; however, in civil engineering materials or failure-progressed materials, the velocity was not distributed uniformly due to materials' heterogeneity. Therefore the AE source locations are not always accurate in actual structures or materials in which the velocity does not exhibit homogeneous or the failure evolves successively. Then elastic wave tomography is well used together with AE monitoring in many cases. Figure 2 shows the configuration of elastic wave tomography.

Elastic wave tomography is the method to evaluate the distribution of elastic wave velocity over the structures. In the principle procedure, elastic wave is excited

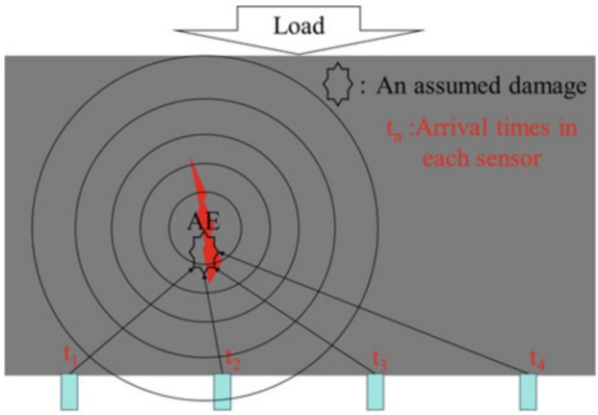

Fig. 1 AE monitoring

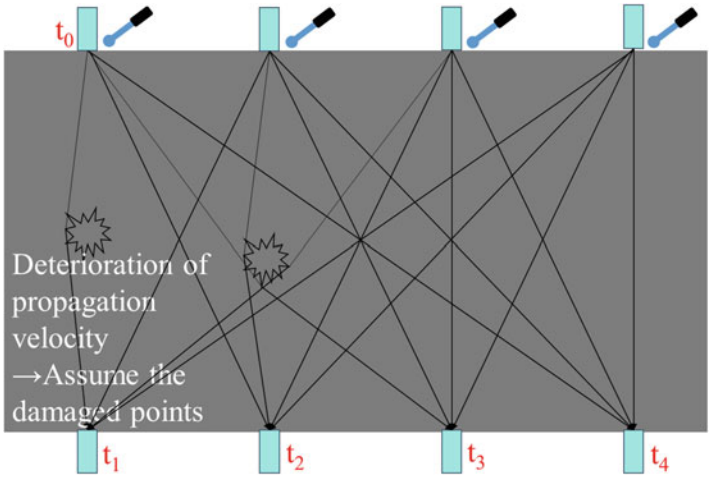

Fig. 2 Elastic wave tomography

at the specific location near the sensor as to provide the excitation time for the first, and the excited elastic waves were to be received by all sensors in the opposite surface. In this way, both the excitation time and the time of arrivals in all of the sensors can be obtained. In order to obtain the individual velocity over the structures, the structures are divided into some cells. Initially, elastic wave velocity is assumed to be the same in each cell. Then it can be possible to calculate the elastic wave velocity of each cell by using both excitation time and the time of arrivals in all of the sensors.

As shown above, it has been necessary for examining internal damages with high accuracy to use both AE monitoring and elastic wave tomography so far, leading to take a lot of time and cost to assess the structures. In order to solve this issue, author's group has proposed "AE tomography" which implements AE monitoring

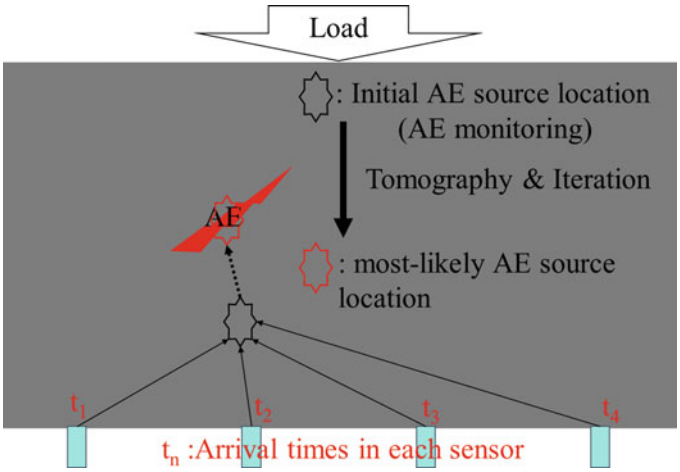

Fig. 3 AE tomography

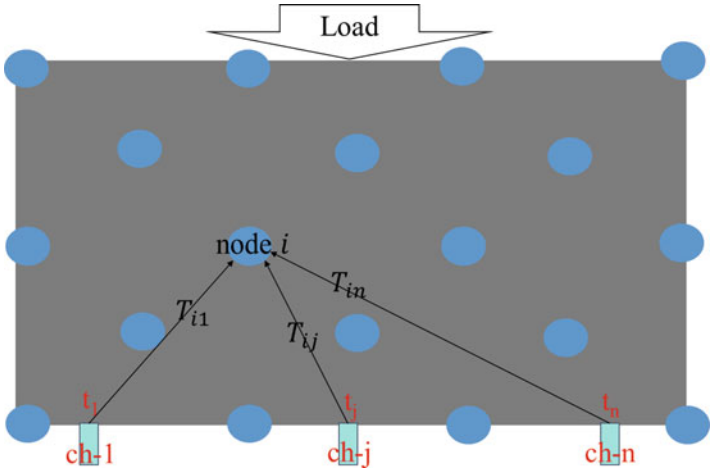

Fig. 4 Overview of ray-trace technique

and elastic wave tomography simultaneously. Figure 3 shows the configuration of AE tomography. AE tomography does not use elastic wave excited actively, but the AE wave generated within structures. It is possible to obtain the exact excitation time in elastic wave tomography; however, it is impossible to get the generation time of AE wave in AE tomography, so that the way of estimation of generation time of all AE waves is crucially important.

As shown in Figs. 4 and 5, in AE tomography, the area of interest is divided into some elements consisting of three cell nodes forming triangular shape. In addition, each side with two nodes is divided into smaller parts to increase source location

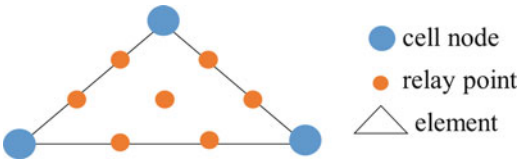

Fig. 5 Composition of an element

candidates by adapting relay points as shown in Fig. 5. Again, both of cell nodes and relay points can be the candidate for AE sources. Figure 4 shows the configuration of ray-trace technique. As shown in Fig. 4, firstly, theoretical propagation time: T_{ij} is calculated from receiver point: j to all cell nodes: i and relay points. Then, T_j which defines the difference between the obtained time of arrivals and theoretical propagation time: T_{ij} in receiver point: j is calculated. Subsequently, above process is conducted in each location of receiver (from receiver 1 to receiver n). And, by using the Eqs. (1) and (2), source locations giving the smallest variance are identified. Here T_{im} is average of estimated occurrence time and σ_i is the variance of estimated occurrence time in the case of nodal point: i.

$$T_{im} = \frac{\Sigma_j \left(T_j - T_{ij}\right)}{N} \tag{1}$$

$$\sigma_i = \frac{\Sigma_j \left(T_j - T_{ij} - T_{im}\right)^2}{N} \tag{2}$$

Based on the renewed AE source locations, the elastic wave velocity of each element is updated. This process is the one cycle for getting renewed both of AE source locations and elastic wave velocity. Finally it is possible to obtain the most likely AE source locations and elastic wave velocity of each cell by iterating this process. This is the principle of ray-trace technique. In this way, unlike the conventional AE monitoring, the AE source location in consideration of the heterogeneity of the elastic wave velocity in the structures is successfully identified.

3 Application of AE Tomography in RC Bridge Deck for Bullet Train

In our past studies, the AE tomography has been applied for the concrete specimens in the laboratory and the applicability of AE tomography for the specimen has been verified [2]. In this study, as one of the actual structures, the RC bridge deck for bullet train was assessed by the AE tomography. In the RC deck of the investigation site, some exfoliations are estimated in the shallow areas by impact acoustic test as shown in Fig. 6. It is noted that the only damage near the surface doesn't always reflect the situation of the internal damage. Accordingly Rayleigh wave tomography, which could examine more internal damage than the impact acoustic test, was also carried out for the verification of the AE tomography.

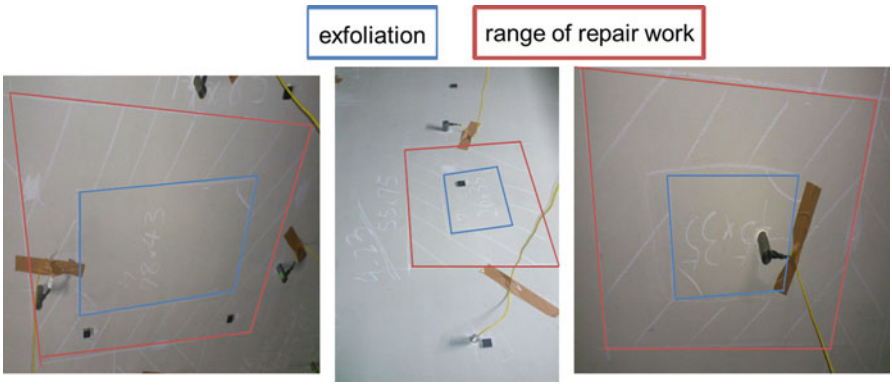

Fig. 6 Exfoliations and range of repair work in the surface of RC bridge deck

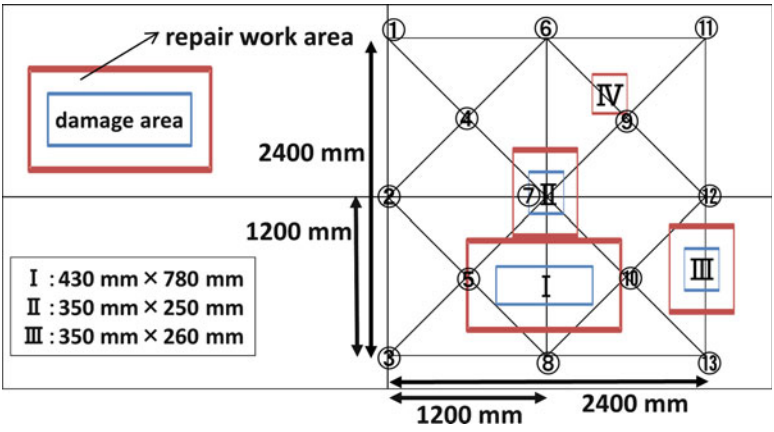

Fig. 7 Sensor array of AE tomography

3.1 Experimental Setup

This experiment was held in the repair work site near H Station. The objective area of the investigation was 2,400 × 2,400 mm on the surface of RC bridge deck for bullet train. In Fig. 7, 13 AE sensors are arranged, and an array of 16 accelerometers can be found in Fig. 8 for the Rayleigh wave tomography.

3.2 Rayleigh Wave Tomography

There are several wave modes such as P-wave, S-wave, and Rayleigh wave in the elastic wave propagation. Rayleigh waves propagate along the surface of materials

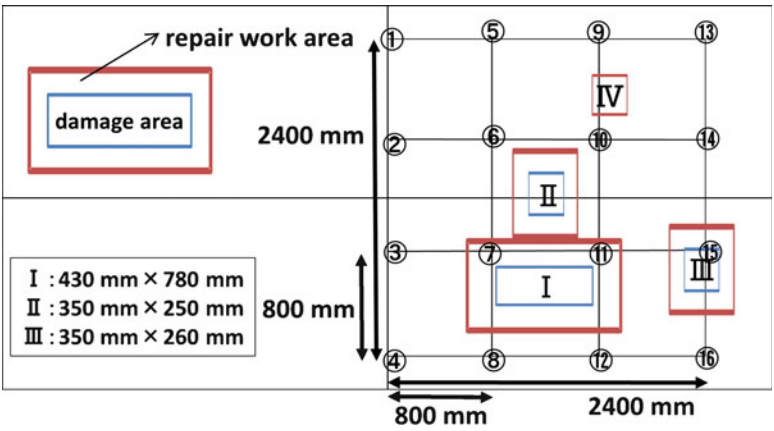

Fig. 8 Sensor array of Rayleigh wave tomography

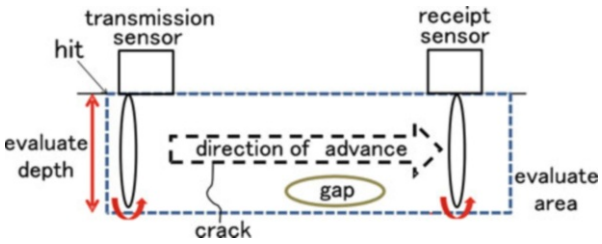

Fig. 9 Rayleigh wave tomography

with rotation in an elliptical orbit manner. Among those wave modes, Rayleigh wave exhibits the largest energy which accounts for 70 % of the whole energy, with lower attenuation rate than those of other wave modes. Based on these characteristics, Rayleigh wave tomography has been proposed which can diagnose the inner part of structures from the surface [3, 4]. Figure 9 shows the overview of the Rayleigh wave tomography. Firstly, Rayleigh waves have been excited on the surface with hammering. Then when internal damages such as cracks and voids exist in the shallow layer, reflection and dispersions of Rayleigh wave are generated, resulting in the longer propagation distance than the shortest propagation path. As shown in the figure, as it takes more time to reach the sensor, the resulted propagation velocity shows smaller than that of intact. Accordingly it is possible to evaluate the inner damage widely by calculating the propagated velocity corresponding to the dominant frequency of Rayleigh wave adapting the tomography procedure. In this technique, the effective maximum depth of Rayleigh wave corresponds to the wavelength calculated by the dominant frequency. Specifically the diameter of hammer edge changes the frequency, enabling to adjust the measurement depth. It is noted, however, that the evaluation depth is limited to the half of thickness at most.

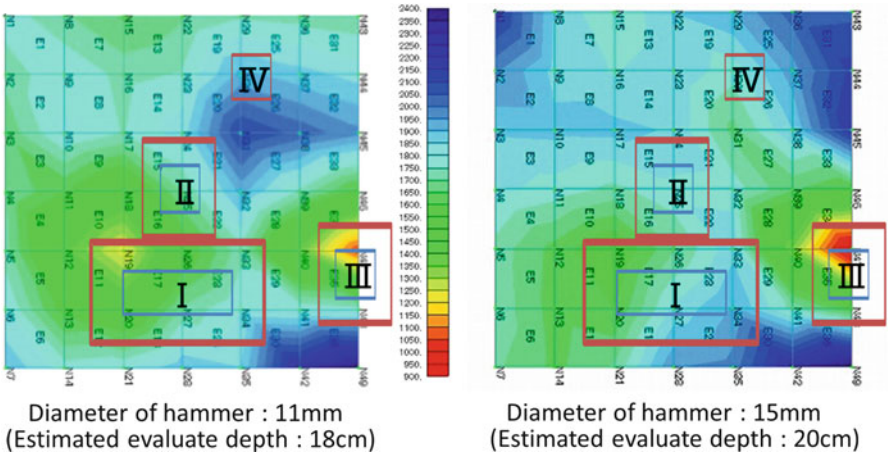

Fig. 10 The result of Rayleigh wave tomography

3.3 Result of Rayleigh Wave Tomography

Figure 10 shows the result of Rayleigh wave tomography, where the result of impact acoustic test is overlaid additionally. The damage areas from I to IV were highlighted in advance, specifically from I to III were evaluated by impact acoustic test; however, no information could be obtained for the IV damage. With the result of the two methods, it is confirmed that there are several damages located near the lower right, III and the center area, I and II in the measurement area. However, as explained the two methods can evaluate only the shallow layer, and it is impossible to evaluate the deeper area. In other words, the damage areas shown in Fig. 10 exhibit the damage area located shallower than the evaluation depth.

3.4 AE Measurement

AE wave monitoring was conducted repeatedly corresponding to 10 times passage of bullet trains. As the AE waves obtained from the measurement consisted of background noises, mechanical vibrations caused by trains passage, and secondary AE activity, it was important to extract only the secondary AE activity generated from existing damages, where only the secondary AE activity can serve as AE data to AE tomography analysis. It has been already reported that the AE activity induced by the background noises has small energy, so that the noise-related AE activity was eliminated by filtering the AE waves having small energy. After that filtering, the secondary AE waves were eliminated from those due to the vibrations. Figure 11 shows the AE wave due to vibration of the train, while in Fig. 12, the AE wave generated from the existent damage, namely secondary AE activity is

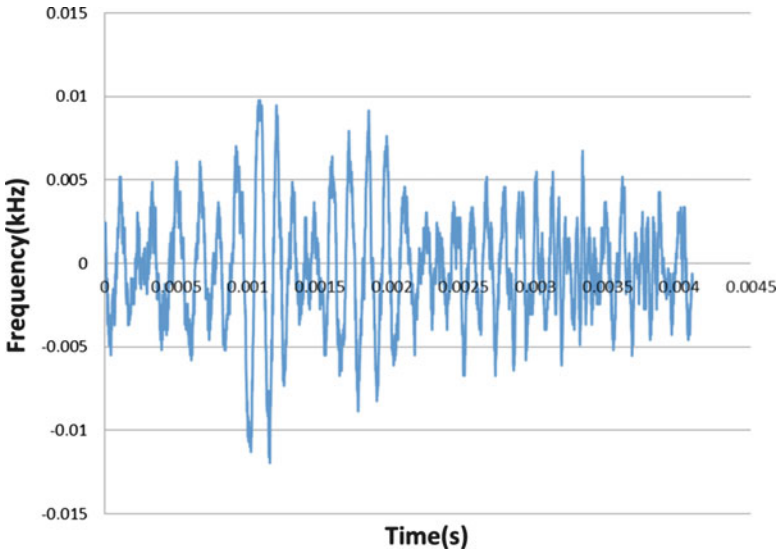

Fig. 11 Vibration-related AE wave

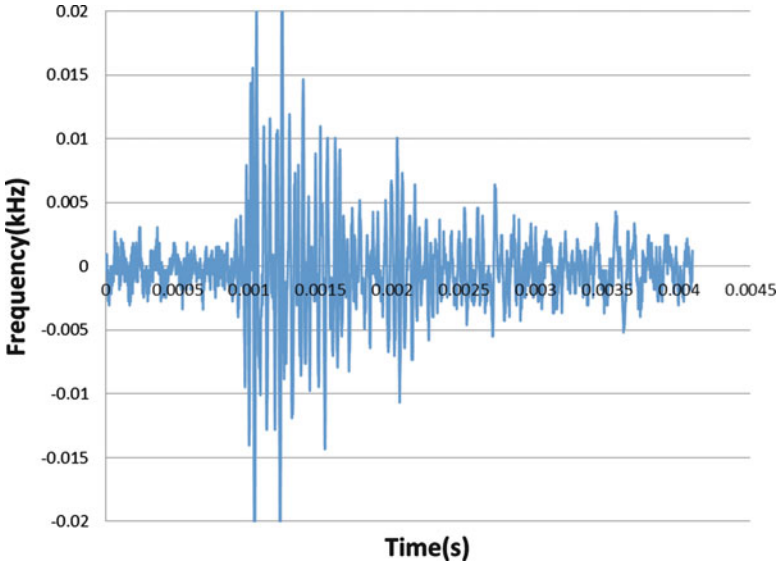

Fig. 12 AE wave generated from existing damages

exhibited. As shown in these figures, the AE wave from the existent damage has short rise time and exponential attenuation behavior over the time, whereas vibration-induced AE activity has longer rise time and lower frequency in comparison to the secondary AE wave [5, 6].

Table 1 The result of two AE parameters

Passage		Energy	Average FRQ	Center FRQ	Peak FRQ
First	AE wave	30.6	14.3	32.8	18.4
	Vibration wave	54.123	6.875	33	6.75
Second	AE wave	101	13.75	28.91667	21.66667
	Vibration wave	95	10	29.36364	7.181818
Third	AE wave	117.1667	11.83333	31.66667	21.83333
	Vibration wave	100.2	9.9	30.8	7

Based on these qualitative characteristics of waveform features, ten typical two types of AE waves were extracted and averaged for each parameter as shown in Table 1. This process was carried out with regard to three times passages of bullet trains respectively.

As shown in Table 1, obvious differences between two types of AE activity were verified with peak frequency, and therefore the peak frequency was used for classifying the two types of AE waves. Specifically AE waveforms with higher peak frequency were extracted as the secondary AE waves, and these were used for the AE tomography.

3.5 The Result of AE Tomography

Figure 13 shows the result of AE tomography. The blue dots in the figure show the original source locations based on the conventional source location algorithm, while the red exhibits the improved source locations with proposed AE tomography. In the figure, the damage areas estimated by AE tomography correspond well with the damage areas I, II, and III confirmed by the impact acoustic test and the Rayleigh wave tomography. The AE tomography can also estimate the damage area IV, presumably located in the deeper area which is difficult to be detected by both of the impact acoustic test and the Rayleigh wave tomography. That's because the damage area IV wasn't verified by the two methods, but estimated by AE tomography enabling to diagnose the deeper area in comparison to the two methods. Thus it is clarified that the AE tomography can evaluate not only the damages near the surface but also the damages lurked in the deeper areas. As a result, it is clarified that AE tomography can evaluate the internal damage which cannot be confirmed by the acoustic impact test, and this will effectively contribute to the proactive maintenance which needs to identify the early damage evolving inside of the materials.

3.6 Future Works

Issues to be settled in the future are listed below.

1. It is necessary to accumulate more data when applying AE tomography to more in situ structures.

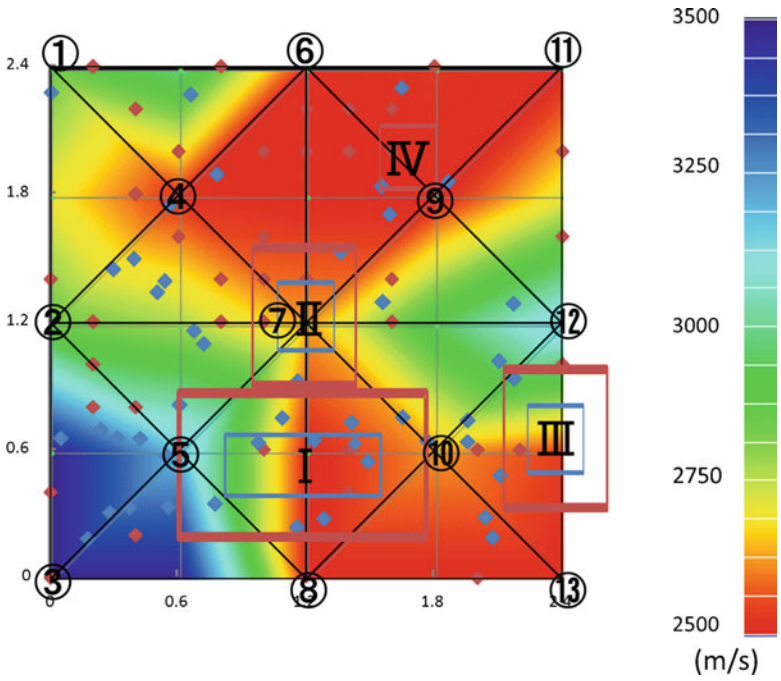

Fig. 13 The result of AE tomography

2. The internal damages can be evaluated by using AE tomography, namely velocity distribution; however, in order to contribute more on proactive maintenance program, the velocity shall be quantified with damage. The study of the elastic wave parameters relating to the damage can be found in our paper [7].

4 Conclusions

In this study, we investigated the deterioration of RC bridge deck for bullet trains with the proposed AE tomography. The result can be summarized as follow:

1. Only AE waves were extracted from three types of waves: background noises, mechanical vibrations, and secondary AE waves in order to enhance the accuracy of AE tomography. AE tomography was applied to the in situ structure with only AE waves. In addition, to verify application of AE tomography, investigation with impact acoustic test and Rayleigh wave tomography was carried out. The two methods exhibited the damages in shallow area. As a result, the compatible result was obtained by AE tomography, so that it was clear that AE tomography could identify the damages in shallow area.

2. AE tomography could examine the damage in the area where the damage was not examined by both impact acoustic test and Rayleigh wave tomography; however, the two methods could evaluate only the damages in the shallow layer. Accordingly using AE tomography, it might be possible to examine damages in deeper area beyond the evaluation depth of impact acoustic test or Rayleigh wave tomography.
3. Identification of the internal damages in RC bridge deck for bullet train was possible with AE tomography, extracting only the secondary.
4. AE waves occurred in the deck and utilizing the data into AE tomography, AE tomography could evaluate the internal damage which could not be confirmed by conventional methods. Accordingly AE tomography will effectively contribute to the proactive maintenance which needs to identify the early damage evolving inside of the materials.

References

1. T. Shiotani, N. Okude, S. Momoki, and Y. Kobayashi, Proposal of AE tomography technique for the assessment of infrastructures, *Japanese Soc. for Non Destructive Inspection, 18th National Conference on Acoustic Emission* (2011), pp. 39–42
2. N. Okude, T. Shiotani, Y. Kobayashi, S. Momoki, The trial of the new damage evaluation technique of the concrete structure with AE technique. JSNDI Acoust. Emission Sect. **AE-00018**, 13–20 (2012)
3. H.K. Chai, D.G. Aggelis, S. Momoki, Y. Kobayashi, T. Shiotani, Single-side access tomography for evaluating interior defect of concrete, Elsevier Science. Construct. Build Mater. **24**, 2411–2418 (2010)
4. S. Momoki, K. Hwa, M. Yorikawa, Y. Mochizuki, T. Shiotani, Y. Kobayashi, Development of one side placement model-elastic tomography by characteristic of surface wave. Tobishima Tech. Rep. **61**, 41–46 (2012)
5. T. Shinomiya, H. Morishima, Y. Nakanishi, T. Shiotani, Damage diagnosis technique for brick structures using acoustic emission, *6th World Congress on Railway Record*, Edinburgh, 2003.
6. T. Shiotani, Y. Nakanishi, X. Luo, H. Haya, T. Inaba, Damage evaluation for railway structures by means of acoustic emission. Trans. Tech. Pub. Key Eng. Mater. **270–273**, 1622–1630 (2004)
7. T. Shiotani, Y. Takada, T. Watanabe, H. Ohtsu, Damage evaluation of heterogeneous materials by Q-value analysis of AE waveforms. JSNDI Prog. Acoust. Emission **16**, 1–6 (2012)

Acoustic Emission for Structural Integrity Assessment of Wind Turbine Blades

Nikolaos K. Tsopelas, Dimitrios G. Papasalouros, Athanasios A. Anastasopoulos, Dimitrios A. Kourousis, and Jason W. Dong

Abstract Over the last 16 years, pioneering research work has resulted in significant progress in the area of acoustic emission condition monitoring of wind turbine blades. From laboratory static tests on small blades to laboratory full-scale fatigue tests, then to static field tests on actual wind turbines, we are now in the position to instrument and monitor in real time the structural integrity of rotating blades on operating machines with multichannel acoustic emission systems, via the Internet.

This chapter provides an overview of the research conducted, the various types of tests carried out, and the milestones in developing the application, and summarizes the recent developments on in-service monitoring of wind turbine blades during operation. Emphasis is given to the difficulties faced, the means these were overcome, the challenges that still need to be dealt with, and propositions for future work and research. Apart from summary results from the initial and subsequent laboratory experiments, characteristic results from recent long-term health monitoring of the blades of an operating machine with acoustic emission are presented. The importance of fusion of acoustic emission data with operational data from the wind turbine (wind speed, torque, RPM, etc.), for the proper assessment of the blade's condition, is also demonstrated.

N.K. Tsopelas (✉) • D.G. Papasalouros • A.A. Anastasopoulos • D.A. Kourousis
Mistras Group Hellas A.B.E.E., Athens, Greece
e-mail: nikolaos.tsopelas@mistrasgroup.gr

J.W. Dong
Physical Acoustics Corporation, Princeton, NJ, USA
e-mail: Jason.Dong@mistrasgroup.com

G. Shen et al. (eds.), *Advances in Acoustic Emission Technology: Proceedings of the World Conference on Acoustic Emission-2013*, Springer Proceedings in Physics 158,
DOI 10.1007/978-1-4939-1239-1_34,

1 Introduction

Over the last three decades, significant research has been carried out in the area of acoustic emission (AE) testing of wind turbine blades. Research initiated in laboratories performing static and fatigue tests on small- or full-scale blades progressed to static field tests on actual wind turbines, while, currently, it is achievable to instrument and monitor in real time the structural integrity of rotating blades on operating machines with multichannel acoustic emission systems, via the Internet.

2 Development of the Method

Already in 1994, Sutherland et al. [1] conducted static and fatigue tests in Sandia laboratories in the USA. The results demonstrated the potential of the technique to detect and locate damage in FRP blades. In 1998 and 1999, CRES and Envirocoustics (now Mistras Group Hellas) performed, to the authors' knowledge, the first in Europe static and biaxial fatigue tests on full-scale blade while monitoring with multichannel AE equipment (Fig. 1). Conventional analysis by Anastasopoulos et al. [2–4] revealed that AE managed to detect damage initiation and pinpointed weak areas of the blade at early stages, before any damage became visible. Specifically, already from the first loading of the blade, concentrated AE sources were located using arbitrary planar location on the maximum chord area.

Eventually, the blade failed after several thousands of fatigue cycles, while follow-up inspection revealed a visible crack on the trailing edge of the blade, at the maximum chord area. At a second stage, the same authors [5] performed the novel unsupervised pattern recognition on the received AE data of the static test which revealed AE classes of data attributed to critical damage. Subsequently, supervised pattern recognition was applied to the fatigue data and enhanced the understanding of the damage process within the fatigue cycle and in time.

In 1998, within the scopes of an EC-funded R&D project, a consortium of several partners was formed and conducted extensive research in the field of AE testing of

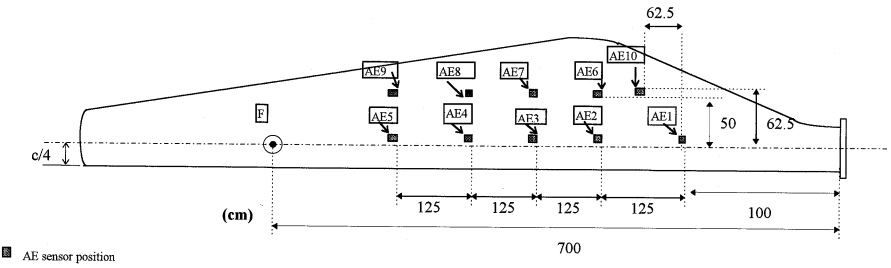

Fig. 1 AE sensors' positions and load application point for the static test of a wind turbine blade [3]

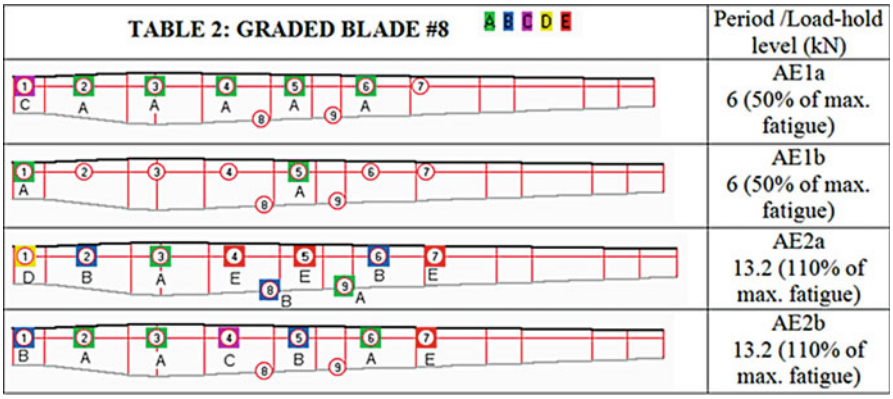

Fig. 2 Color-grading results (from A—"Good" to E—"Bad") of a proof-tested blade indicating weak zones [7]

wind turbine blades, and produced an abundance of publications (e.g., [6–11]). Ten small and two large blades were tested to failure while monitored with AE under static or fatigue loads in lab conditions. AE data was analyzed by traditional and advanced techniques and very useful conclusions were drawn regarding the AE behavior of the blades during loading and close to failure, as well as about damage assessment using AE. As a result, wind turbine blade testing procedures were developed, as well as a special "blade condition grading" system through dedicated software for AE testing during "proof" loading of blades (Fig. 2). Grading evaluates zones around each AE sensor and is based on the amount and the characteristics of the AE activity. Grading may be applied for different load levels, applying special loading sequence with load holds, evaluating the capability of the blade to undertake the specific load.

Subsequently, the consortium attempted the first ever AE test on an installed blade on a stationary turbine with pulleys used for loading. Finally, a semipermanent AE installation (sensors attached on outer surface) and monitoring were attempted on a rotating blade using radio telemetry system and an AE data logger on the ground at RAL's facilities [11]. Since then, attempts for continuous health monitoring of in-service wind turbine blades had been limited due to several technical difficulties, although there had been some experience in condition monitoring of other wind turbine parts in-service [12].

From 2009 to 2012, within the scopes of EC-funded R&D project "NIMO" [13], significant research was carried out by the project consortium, aiming towards the development of an integrated condition monitoring system for wind turbines, including an acoustic emission module for monitoring of the blades. The innovation introduced was a permanent installation for real-time, online AE monitoring of rotating blades in combination/integration with other diagnostic techniques [14–16]. The work resulted in the first successful efforts, to the authors' knowledge, for long-term AE monitoring of full-scale in-service wind turbine blades.

Data analysis revealed promising results, based on the direct comparison and dissimilarities between simulated AE sources acquired off-line and located AE signal families on the monitored areas acquired during operation.

3 AE Instrumentation During NIMO Project

AE monitoring of wind turbine blades during operation poses several challenges and difficulties to be met by the condition monitoring system, not only due to the (inherent in composites) complex nature of the blade's defects aimed to be detected but also for a number of application-specific factors such as the harsh environment and the conditions under which such a system will operate, accessibility reasons for system installation in the hub and sensor mounting (e.g., on the inside surface of the blades), power issues for the system residing in the hub, and, most important, the necessity for wireless data communication or telemetry posed by the rotation of the blades.

Based on current state-of-the-art AE components, a modular eight-channel online AE system was implemented, meeting all the requirements mentioned above. An illustration of the complete AE system installation is presented in Fig. 3. The system

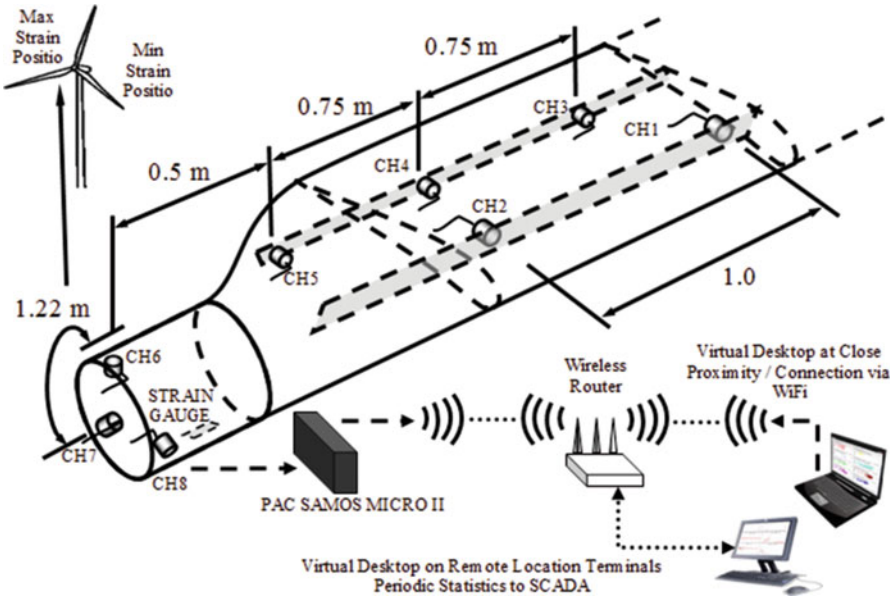

Fig. 3 Schematic illustration of the AE system implemented for online monitoring of the blades. The system is composed by five 60 kHz resonant frequency AE sensors mounted on the internal spar of the blade (CH1–CH2) and on the inner surface of the trailing side of the blade (CH3–CH5) and three 150 kHz resonant frequency AE sensors mounted near blade's root (CH6–CH8) driven by a compact 8-channel AE system implemented inside an industrial compact case (PAC SAMOS MICRO II) [16]

Fig. 4 Mounting of two AE sensors on the internal spar of a blade and one sensor on the inner surface of the trailing side of a blade [16]

was composed by five sensors with resonant frequency of 60 kHz (PAC R6I-AST) mounted on the internal spar of the blade and on the inner surface of the trailing side of the blade (Fig. 4) and three sensors with resonant frequency of 150 kHz (PAC R15-AST) mounted near blade's root (Fig. 4). Both types of sensors incorporate integral amplifiers allowing them to drive long cables without the need for a separate preamplifier, minimizing the weight of the system and also the RFI/EMI interference. In addition they feature an auto sensor test (AST) capability allowing them to act as pulsers and receivers simultaneously, enabling automated verification of each sensor coupling and performance at any time desired by the operator. AE sensors' mounting was performed on the inner surface of one of the three blades (with the blades on the wind turbine) using epoxy-based couplant and special hold-down devices developed for the long-term attachment of the sensors while sensor cables were connected and securely routed to the rotor's hub.

The AE sensors were driven by a compact modular eight-channel AE system implemented inside a waterproof industrial case mounted inside the wind turbine's hub (Fig. 5). The system was designed to be relatively lightweight to minimize unbalancing forces due to its incorporation inside the hub, to be of low power consumption (below 100 W) and versatile to be powered by AC or DC input. In this project the system was powered by a 12 V DC input provided through a special design slip ring fitted in the wind turbine by the wind farm operator. Finally, for the purposes of enhanced data interpretation and correlation the system was designed to accept additional external inputs such as wind velocity, rotation speed, torque, and yaw angle from existing wind turbine instrumentation. For the scopes of this project a strain gauge was attached on the outer surface of the leading edge of the blade and was connected as external input to the acquisition unit. This would provide an accurate synchronization between the acoustic emission data and wind turbine

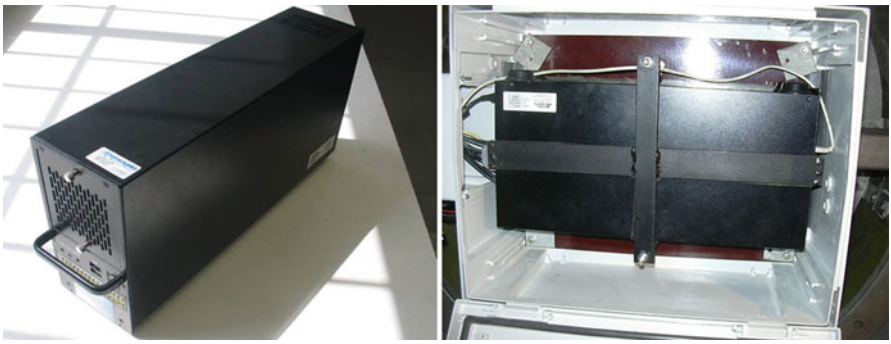

Fig. 5 Acquisition unit of AE system (PAC MICRO II AE) (*left photo*) and same unit installed inside the wind turbine hub (*right photo*)

operating conditions, a good approximation of the blade's position, and finally a good estimation of the average power produced by the wind turbine.

Data transmission, as well as remote control of the system, was performed through a wireless connection established between the AE system and an access point positioned in the base of the wind turbine tower. The latter was connected to the internal network of the wind farm operator and, through this network, to the Internet. This way the system was monitored and controlled from any place with Internet access and was also able to transmit in real time the full AE data set acquired and/or only the processed data and alarms to the central monitoring system of the wind farm operator. In addition, the AE system was able to send automated e-mails notifying about detected events and threshold crossings and/or send e-mails with the status of the system and any faults occurred. A system upgrade could also enable notifications and alerts to be sent automatically through SMS.

4 Continuous Monitoring Results During NIMO Project

System was successfully installed and operated via the connected networks for more than 6 months under real-time conditions. Statistically, this time period should be long enough to capture a large variation of the wind turbine operating conditions which may have different impact upon the generated AE of the monitored areas. Real-time data analysis was performed using the advanced AE analysis software NOESIS [17] installed in the same system, while the system was also acquiring AE signals. The system's behavior was found to be very reliable and stable in all cases, even during prolonged periods of power loss or technical difficulties, in which cases the system always rebooted and resumed operation and acquisition when the power was restored.

An illustration of 10-min average statistics of wind speed, wind turbine-generated power, and wind direction during a period of 69 days of continuous blade monitoring is shown in Fig. 6. The additional color dimension in Fig. 6 represents the 10-min average rotational speed of the wind turbine rotor. The green

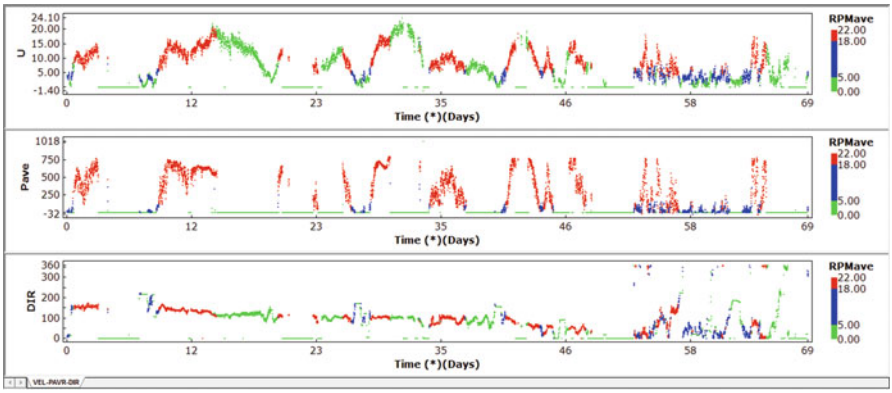

Fig. 6 From *top* to *bottom*: Wind speed (m/s), average generated power (kW) of wind turbine, and wind direction (degrees) versus time (days), during a period of 69 days of continuous monitoring. The color ranges of the data correspond to the average RMP of the wind turbine (0–22 RPM) [16]

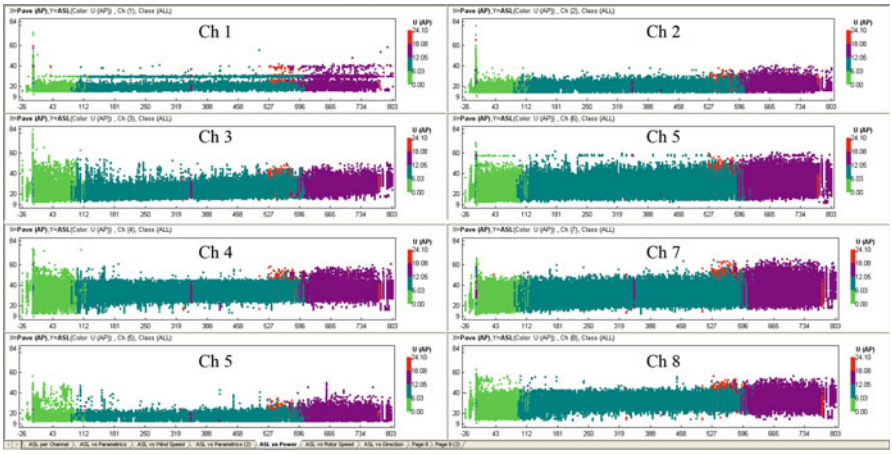

Fig. 7 Time-driven ASL (dBae) of each channel versus average generated power (kW), for a period of 69 days of continuous monitoring, colored by wind velocity (m/s) [16]

color indicates periods where the rotor was stopped from a lack of wind, maintenance, or other reasons. The blue color indicates periods where the rotor was operating at low speed (15 RPM) as well as the transitional values of the rotor's speed during the transitional stages from zero to low speed (5–15 RPM) and low to high speed (15–18 RPM). Finally, the red color represents the periods that the rotor was operating in high speed (22 RPM). It is worth noting that even when the rotor was at stop position there was still AE emission from the blade due to the wind loading indicating the stochastic nature of loading and thus of the AE data.

The distribution of the time-driven average signal level (ASL) in correlation with average generated power of the wind turbine (Fig. 7) and wind velocity (Fig. 8)

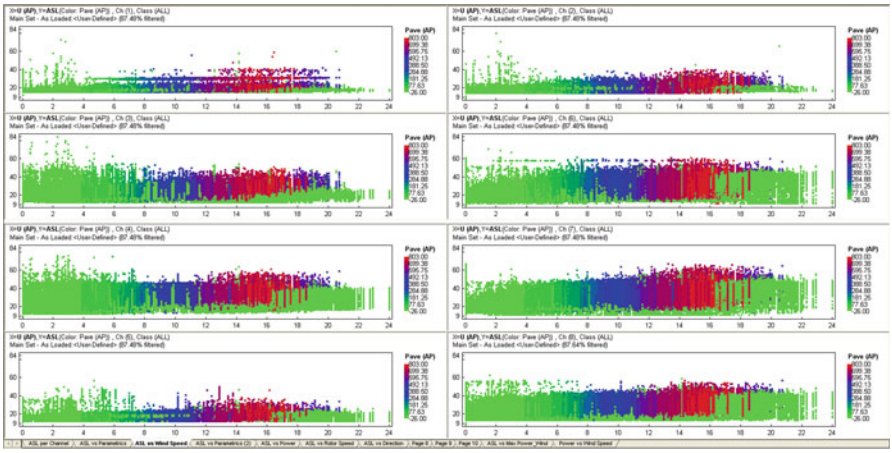

Fig. 8 Time-driven ASL (dBae) of each channel versus wind velocity (m/s), for a period of 69 days of continuous monitoring, colored by average generated power of wind turbine (kW). Channel order is identical to Fig. 6 [16]

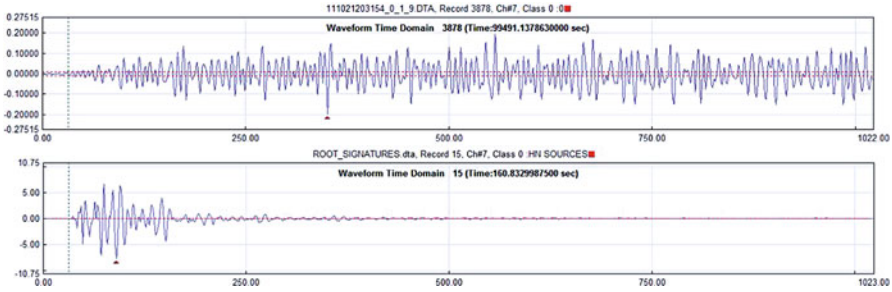

Fig. 9 *Top*: Example waveform of the majority of signals as received from channel 7, mounted on root area, during normal operation. *Bottom*: Example waveform of a simulated AE source as received from same channel

for the same period of 69 days of continuous monitoring does not directly reveal a clear correlation pattern between the AE and the generated power or velocity.

A simplified analysis based on time-driven data alone is not feasible as there are a great number of parameters not related to blade structural integrity that may influence the acoustic emission hit rate such as mechanical noise generated from moving parts, cables, and other mechanical equipment placed inside the blade as well as from parts outside the blade such as mechanical noise generated from main bearings, the gearbox, the generator, the yaw drives, and auxiliary mechanical equipment and which is transmitted to the root area and the blade itself through the rotor shaft and the rotor hub. In Fig. 9 an example of a typical AE waveform acquired from channel 7 mounted on root area is displayed in comparison with

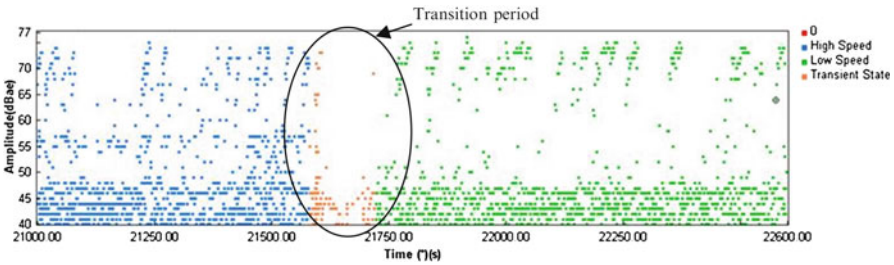

Fig. 10 AE activity recorded by R15 sensor mounted near root area during a rotor transition from high speed (22 RPM) to low speed (15 RPM). Absence of high-amplitude AE hits is obvious during the transitional state [14]

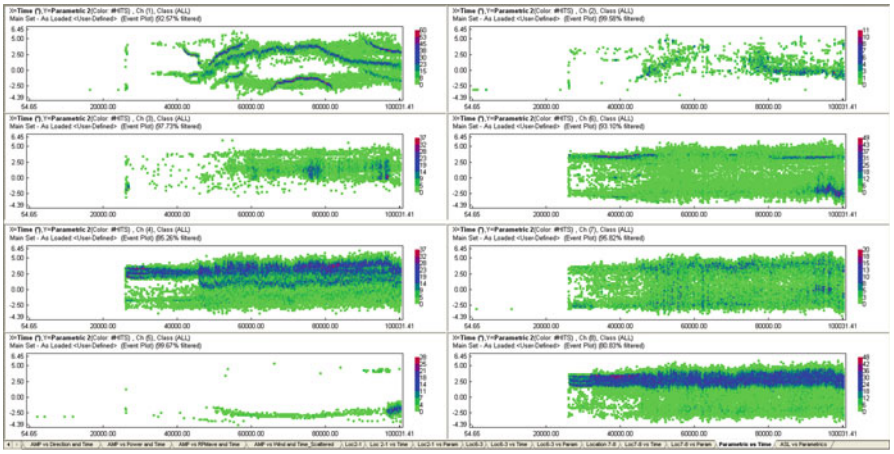

Fig. 11 AE hit density in time versus strain gauge value for each channel during a period of 28 h of continuous monitoring. Channel order is identical to Fig. 6

a simulated Hsu-Nielsen AE hit acquired from the same sensor. The difference of the two signals is more than obvious and, while the second presents a genuine burst-type AE hit, the first signal presents a low-amplitude continuous signal that is mostly related to mechanical, frictional, or some other continuous type of noise.

The influence of mechanical noise on an operating wind turbine can also be seen in Fig. 10 where the AE activity recorded by R15 sensor mounted near to the root area during a rotor transition from high speed (22 RPM) to low speed (15 RPM) is presented. The absence of high-amplitude AE hits during the transition period which lasts for almost 100 s is obvious and may be related to the disengagement of gearbox or the absence of other kind of mechanical noise during this operation.

Plotting the acquired AE hit density in time, over a period of 28 h of continuous monitoring, versus strain gauge value (Fig. 11) per channel allows the correlation of AE generation with a very good approximation of blade's position, enabling us to

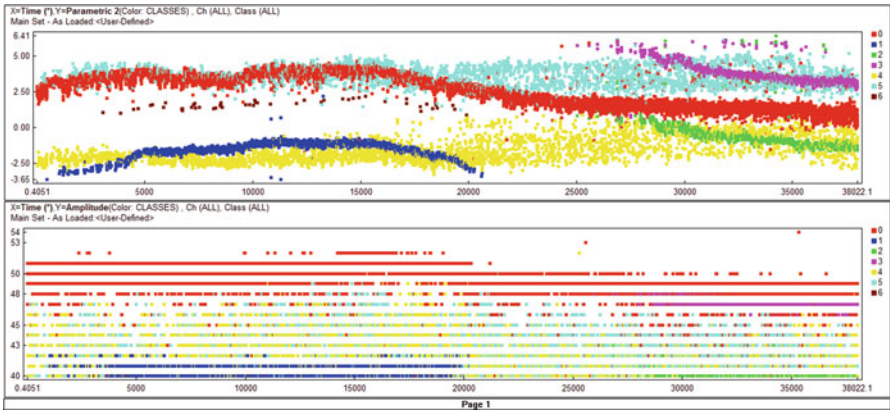

Fig. 12 AE hits in time versus strain gauge value for channel 1 (zoomed period of channel 1 of Fig. 11), colored by class color

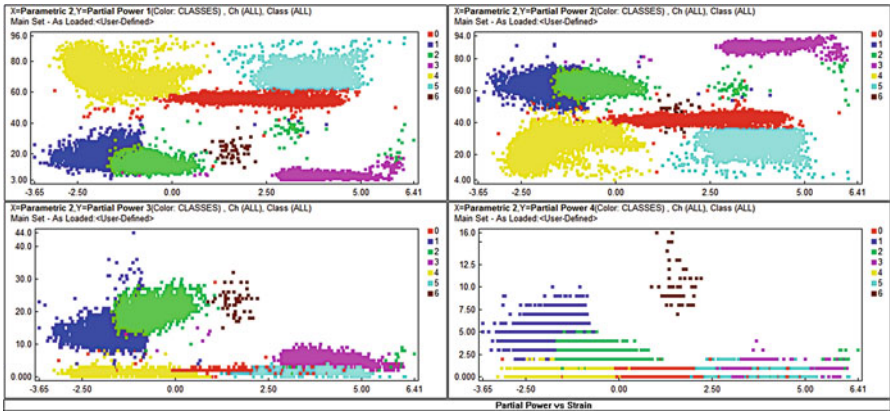

Fig. 13 Discrimination of seven different well-defined classes, through a multi-frequency power separation technique. From *top* to *bottom* and *left* to *right*: Partial power frequency range 1–4

get a feeling of when AE hits are generated and investigate the reason and the mechanism producing these AE hits. It is obvious by the density plot that the generated AE hits are not evenly distributed indicating specific positions of the blade where the maximum activity per each channel is recorded. This is more or less the case for most channels. However, as there may be a lot of mechanical noise present in the data advanced AE analysis and pattern recognition techniques should be applied to filter the acquired mechanical noise and overcome the limitations imposed from the simplified time-driven data analysis.

An example of possible discrimination—classification of mechanisms generating AE through advanced AE analysis is presented in Figs. 12 and 13 for the data acquired by channel 1, during a 10-h segment of the previously presented 28-h time

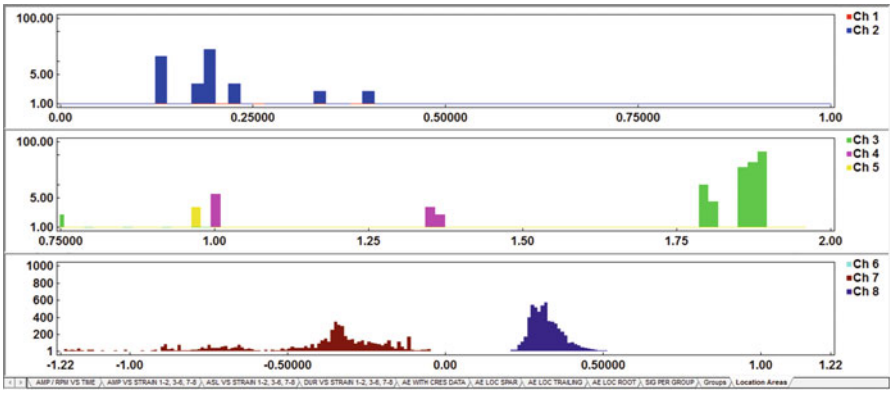

Fig. 14 Located events versus event's location (m). From *top* to *bottom*: Linear location of channels 1–2 (spar area), channels 3–5 (trailing edge area), and channels 6–8 (root area) is presented [16]

period of Fig. 11. Fusion of blade position information (strain gauge value) with the information acquired from manual multi-frequency separation of AE signal's power defined seven (7) well-separated classes as presented in Figs. 12 and 13. The mechanisms producing these classes are unknown and further investigation is needed for a more effective characterization/classification. However, as shown below, there is no clear evidence of correlation with blade's incipient damage.

In Fig. 14 the results of linear located events on three different areas of the blade are presented. The three groups are defined from sensor 1 and 2 mounted on spar, sensors 3–5 mounted on trailing edge, and sensors 6–8 mounted on root (see Fig. 3). It is obvious that there are a few areas in the blade where a significant number of events are located, especially in third group (root area); however without a comparison of the signatures of these events and genuine acoustic emission it cannot be confirmed whether these are or are not related with blade's structural integrity.

In Fig. 15 a comparison of the signatures of these located events and genuine AE events produced from simulated Hsu-Nielsen sources in the same area is presented for each channel group. In blue are presented the first hits of the located AE events on each monitored area while in red are overlapped the simulated Hsu-Nielsen sources. The red dataset (simulated sources) corresponds to the expected AE events that could be present in the case of actual damage in this monitored area.

The direct comparison of both data sets reveals separation of the respective data clusters. The located AE events when compared with the simulated sources applied on the same areas appear to have similar durations and counts however appear to have significantly less amplitude. Therefore the mechanisms producing the located events seem to be different from the mechanisms that are related to the structural integrity of the blade.

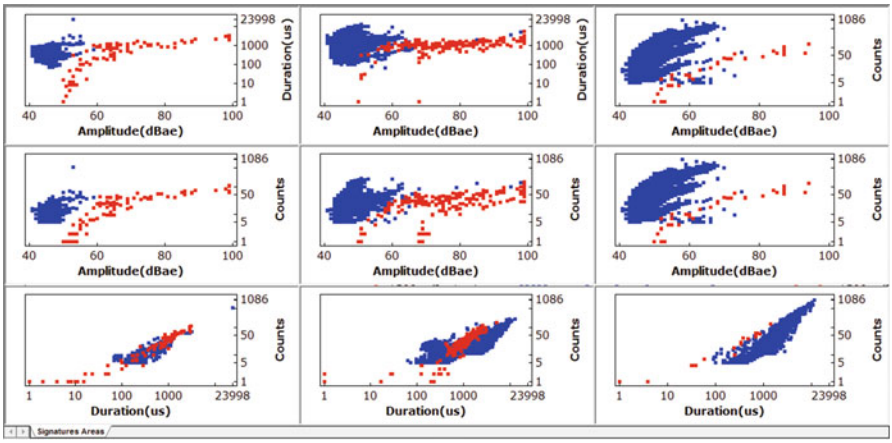

Fig. 15 Signature graphs of AE features, in *blue* are the located AE events and in *red* the simulated Hsu-Nielsen sources. From *left* to *right columns* are the signatures of the spar, trailing edge, and root area [16]

Also, it is obvious that the AE signature for each area has a different and rather unique 2D cluster shape. Therefore the AE system should be trained for each specific area that it is monitored based on the extracted AE signatures of a healthy blade, creating effective pattern recognition techniques. The latter could also be enriched with AE data acquired during full-scale blade testing improving considerably the effectiveness of the automated pattern recognition and the classification of the blade's in-service accumulated damage in real time.

5 Discussion

After years of advanced research, long-term monitoring of the structural integrity of wind turbine blades with acoustic emission is now perfectly feasible, technically. Future work should be focused in the management of the huge volume of data obtained, as well as fusion of the acoustic emission data with real-time operational data acquired from the wind turbine (wind speed, torque, RPM, etc.) for the proper assessment of the blade's condition. Development of effective pattern recognition techniques based on the extracted AE signatures of a healthy blade under normal operating conditions of the wind turbine will allow the system to focus mainly to feature space areas that have a higher likelihood to correlate with incipient damage while discarding all other (non-relevant) data, ensuring a more compact data set, thus greatly minimizing the data storage needs. In addition, due to the more compact data set, streaming of data will be more efficient as well.

Acknowledgment Most of the research leading to the results presented herein has received funding from the European Community's Non-Nuclear energy program under contract number JOR3-CT98-0283 and Seventh Framework Programme (FP7/2009-2013) under grant agreement no. 239462.

References

1. H. Sutherland, A. Beattie, B. Hansche et al., The application of non-destructive techniques to the testing of a wind turbine blade. Sand. Natl. Lab. Rep., Ref: SAND93-1380.UC-261, New Mexico, USA, June 1994
2. A.A. Anastasopoulos, D.A. Kourousis, P. Vionis, V. Kolovos, Acoustic emission NDE of a wind turbine blade during full scale testing. Insight **41**(6), 3 (1999)
3. P.S. Vionis, A.A. Anastasopoulos, V.K. Kolovos, D.A. Kouroussis, Non-destructive testing of full scale wind turbine blade by means of acoustic emission monitoring during controlled static loading, in *Wind Energy for the Next Millennium, Proceedings of 1999 European Wind Energy Conference*, Acropolis Convention Centre, Nice, France, 1–5 March, 1999, pp. 691–694
4. D. Kouroussis, A. Anastasopoulos, P. Vionis, V. Kolovos, Acoustic emission monitoring of a 12m wind turbine FRP blade during static and fatigue loading, in *Emerging Technologies in NDT*, Proceedings of the 2nd International Conference on Emerging Technologies in NDT, Athens, Greece, 24–26 May, 1999, eds. by D. Van Hemelrijck, A.A. Anastasopoulos and T. Philippidis, © 2000 Balkema, Rotterdam, ISBN 90 5809 127 9, pp. 59–66
5. D. Kouroussis, A. Anastasopoulos, P. Vionis, V. Kolovos, Unsupervised pattern recognition of acoustic emission from full scale testing of a wind turbine blade. J. Acoust. Emission **18**, 217–223 (2000)
6. A.G. Dutton, M. Blanch, P. Vionis, V. Kolovos, D.R. Van Delft, P. Joosse, A. Anastasopoulos, D. Kouroussis, T. Kossivas, J. ter Laak, T. Philippidis, Y. Kolaxis, G. Fernando, G. Zheng, T. Liu, A. Proust, Acoustic emission monitoring from wind turbine blades undergoing static and dynamic fatigue testing. Br. J. NDT Insight **42**(12), 805–808 (2000)
7. A.A. Anastasopoulos, D.A. Kouroussis, V.N. Nikolaidis, A. Proust, A.G. Dutton, M. Blanch, L.E. Jones, P. Vionis, D.J. Lekou, D.R.V. van Delft, P.A. Joosse, T.P. Philippidis, T. Kossivas, G. Fernando, Structural integrity evaluation of wind turbine blades using pattern recognition analysis on acoustic emission data. J. Acoust. Emission **20**, 229–237 (2002)
8. A.A. Anastasopoulos, D.A. Kouroussis, A.G. Dutton, M.J. Blanch, P. Vionis, D.J. Lekou, D.R.V. van Delft, P.A. Joosse, A. Proust, T.P. Philippidis, T. Kossivas, G. Fernando, Real-time evaluation of wind turbine blades with acoustic emission monitoring during certification tests. NDT.net. **7**, 9, http://www.ndt.net/v07n09.htm
9. M.J. Blanch, D.A. Kouroussis, A.A. Anastasopoulos, V.N. Nikolaidis, A. Proust, A.G. Dutton, L.E. Jones, P. Vionis, D.J. Lekou, D.R.V. van Delft, P.A. Joosse, T.P. Philippidis, T. Kossivas, G. Fernando, Analysis of acoustic emission, acousto-ultrasonic and infra red thermography data from ten small wind turbine blade tests. *Global Windpower*. Paris, France, 2002
10. D.J. Lekou, P. Vionis, P.A. Joosse, D.R.V. van Delft, D. Kouroussis, A. Anastasopoulos, M.J. Blanch, A.G. Dutton, A. Proust, Full-scale blade testing enhanced by acoustic emission monitoring. *EWEC 2003 Proceedings, European Wind Energy Conference and Exhibition*, Madrid, Spain, 16–19 June 2003
11. M.J. Blanch, A.G. Dutton, Acoustic emission monitoring of field tests of an operating wind turbine, damage assessment of structures, *Proceedings of the 5th International Conference on Damage Assessment of Structures (DAMAS 2003)*, Southampton , UK, 1–3 July 2003
12. D. Lekou, F. Mouzakis, A. Anastasopoulos, D. Kourousis, Fused acoustic emission & vibration techniques for health monitoring of wind turbine gearboxes and bearings. *Scientific Proceedings of European Wind Energy Conference*, Marseille, France, pp. 78–82

13. Development and Demonstration of a Novel Integrated Condition Monitoring System for Wind Turbines – NIMO, Seventh Framework Programme of the European Community (2007–2013), Theme: 7, Energy, Activity Code: ENERGY-2007-2.3-04 Demonstration of large scale systems for on-and off-shore wind farms, http://www.nimoproject.eu/
14. D. Kourousis, D. Lekou, N. Tsopelas, D. Papasalouros, Fr. Mouzakis, A. Anastasopoulos, Health monitoring of wind turbine blades with acoustic emission (in Greek), *Proceedings of the 7th* N*ational Conference of the Hellenic Society of Non-Destructive Testing (HSNT)*, entitled: *The Contribution of Non Destructive Testing for the Safe of Small and Big Works and Constructions*, NTUA, Athens, Greece, 15–17 October 2010
15. N. Tsopelas, D. Kourousis, I. Ladis, A. Anastasopoulos, D.J. Lekou, F. Mouzakis, Health monitoring of operating wind turbine blades with acoustic emission. *Proceedings of the 5th International Conference on Emerging Technologies in Non Destructive Testing*, UOI, Ioannina, Greece, 19–21 September 2011, pp. 347–352
16. D. Papasalouros, N. Tsopelas, I. Ladis, D. Kourousis, A. Anastasopoulos, D.J. Lekou, F. Mouzakis, Health monitoring of a NEG-MICON NM48/750 wind turbine blade with acoustic emission. *Proceedings of the 30th European Conference on Acoustic Emission (EWGAE) & 7th International Conference on Acoustic Emission*, Granada, Spain, 12–15 September 2012, pp. 67–80
17. NOESIS Ver.5.2, *Envirocoustics, User's Manual*

Analysis of Acoustic Emission Parameters from Corrosion of AST Bottom Plate in Field Testing

C. Jomdecha, C. Jirarungsatian, and W. Suwansin

Abstract Field testing of aboveground storage tank (AST) to monitor corrosion of the bottom plate is presented in this chapter. AE testing data of the ten AST with different sizes, materials, and products were employed to monitor the bottom plate condition. AE sensors of 30 and 150 kHz were used to monitor the corrosion activity of up to 24 channels including guard sensors. Acoustic emission (AE) parameters were analyzed to explore the AE parameter patterns of occurring corrosion compared to the laboratory results. Amplitude, count, duration, and energy were main parameters of analysis. Pattern recognition technique with statistical was implemented to eliminate the electrical and environmental noises. The results showed the specific AE patterns of corrosion activities related to the empirical results. In addition, plane algorithm was utilized to locate the significant AE events from corrosion. Both results of parameter patterns and AE event locations can be used to interpret and locate the corrosion activities. Finally, basic statistical grading technique was used to evaluate the bottom plate condition of the AST.

C. Jomdecha (✉) • C. Jirarungsatian
Maintenance Technology Center, King Mongkut's University of Technology, Thonburi 10140, Thailand
e-mail: axlrosez13@hotmail.com

W. Suwansin
Thai NDT Public Company Limited, Bangkok 10240, Thailand
e-mail: electronics-engineer@hotmail.com

G. Shen et al. (eds.), *Advances in Acoustic Emission Technology: Proceedings of the World Conference on Acoustic Emission-2013*, Springer Proceedings in Physics 158,
DOI 10.1007/978-1-4939-1239-1_35,

1 Introduction

Development of acoustic emission (AE) for corrosion monitoring is under researches to improve accuracy and reliability of result interpretation and evaluation. AE can be demonstrated that it is the suitable method for corrosion detection [1, 2]. The AE detection of corrosion was established using appropriated AE sensors and instruments. AE parameters such as amplitude, count, and energy can be utilized to analyze severity levels of corrosion under control environment. In addition, types of different corrosion such as uniform, pitting, and stress corrosion cracking (SCC) were classified by AE signals and parameter analysis in some researches in laboratory [3, 4]. However, the results from lab scale are difficult to implement in the field testing. There are many factors affecting AE testing for corrosion monitoring of the AST bottom plate. Differences of tank condition, product media, corrosion rate, and environment are the difficult factors for setting up AE parameters during testing. The problem is complicated signals and parameter to distinguish. Since the AE researches related to AST field testing, the classification of the tank floor condition has been the aim of testing to reduce maintenance cost of industries.

Nowadays, the AE analysis of tank floor monitoring and grading is embedded to AE analysis software. Most of them apply classification and grading techniques using neural network and pattern recognition. However, AE personnel have to process and analyze to make their own specific grading by themselves from obtained testing data. The results of testing had been reported by various techniques such as statistical and classification methods [5, 6]. The AE testing results are used to evaluate the tank floor conditions and the period of future testing.

To improve the accuracy of AE for corrosion monitoring in this chapter, an analysis of AE parameters in the field testing was accomplished related to the laboratory results of pattern recognition technique. Then, the statistical operation was done to grade the condition of the AST bottom plate. The example of the MFL testing result during empty tank was shown for the bottom plate condition compared to the analyzed AE result.

2 AE Testing in Field vs. Laboratory

2.1 Field Testing Setup for AST

More than ten above-ground storage tanks with different media were done to monitor corrosion of bottom plates. The bottom plate materials were carbon steel and stainless steel grade 304 (SS304). The AE system used in the testing was the 24-channel Vallen ASMY-5 for all of the testing tanks. Sensor frequency of 30 kHz was mainly used to detect the corrosion of the bottom plate. In addition, sensor

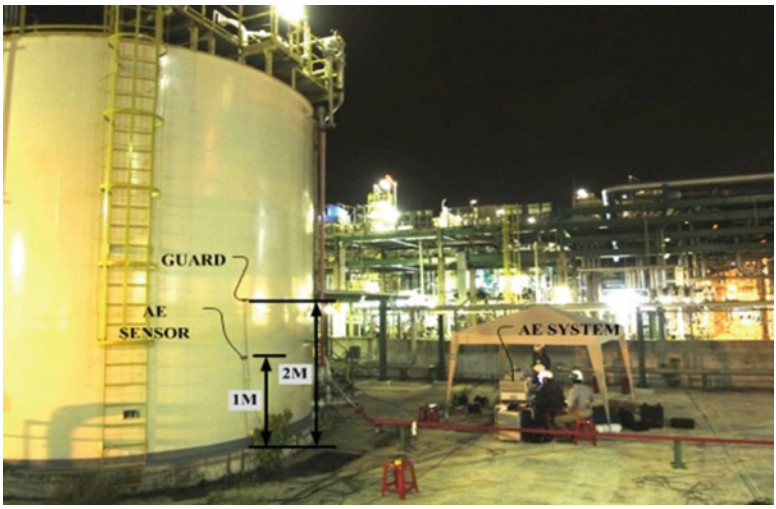

Fig. 1 AE setting up for monitoring of corrosion on an AST bottom plate

frequency of 150 kHz was used to be guard sensors in application of float-roof storage tanks to eliminate AE from mechanical signals.

The levels of media product were constantly stressed from 50 to 70 % and isolated for 12 h before AE testing. The AE testing for corrosion on the AST bottom plate was shown in Fig. 1. Setting parameters were generally the following:

- Average sensor sensitivity more than 80 dB and less than 4 dB varying
- Type of used coolant: Normal ultrasonic type or high-temperature type of hot surface up to 65 °C
- Sensor number and spacing
- Preamplifier gain
- Power/signal cable length which is less than 150 m to avoid the signal drop and standing waves
- Background noise/detection/evaluation threshold
- Signal processor filter 25–45 kHz band-pass
- Hit definition time calculated by the sensor spacing and medium velocity

Before testing, calibration by pencil lead break was done for all of the mounted sensors including guards to check the sensor sensitivity, signal losses, and noises. Background noise prior to testing was identified, minimized, and recorded after setup of the AE system for 15 min to 1 h to verify parameter setting. If background noise is too high above evaluation threshold, the source of the noise was eliminated. The AE monitoring period was 1–2 h. The AE activities were monitored and recorded gathering with AE event location. The AE parameter relation including amp, hit, count, duration, and energy was collected in real-time function. After testing, system verification was performed again. The sensor sensitivity should not be lower than 70 dB.

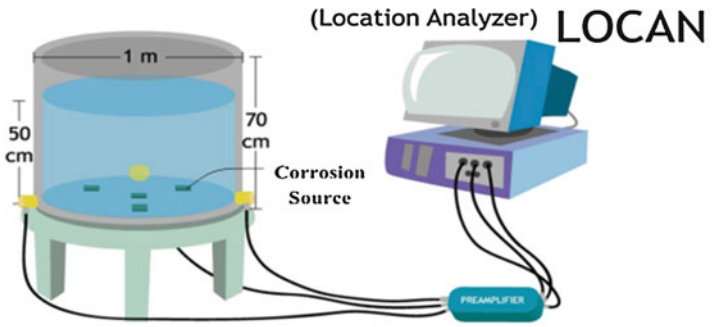

Fig. 2 Experiment setup for corrosion monitoring

2.2 Laboratory Experiment Setup

In the experiments, the tank dimension of 1×0.7 m ($D \times H$) was employed as shown in Fig. 2. Producing uniform and pitting corrosions was conducted on carbon steel and SS304 plates inside the experimental tank, respectively. For uniform corrosion producing, a corrosive environment was 30 % NaCl solution with pH of 1. The solution was stored in the tank with a level of 50 cm. The carbon steel shims which were polished using wet sand paper grade 1200 were placed on the tank bottom plate to accelerate the corrosion. For pitting corrosion, an electrochemical environment was organized using 3 % NaCl solution with a pH of 2 controlled by HCL and a potentiostat (Solartron 1284) gathering with a voltage-to-current converter. The electric current density constantly of 0.2 mA/cm^2 was generated to the solution using a specific electrode. The pitting potential was controlled electrochemically by the potentiostat for accelerating the pitting corrosion mechanism. The location of producing pitting was on the prepared SS304 plate which was placed on the bottom of the tank as in Fig. 2. A LOCAN L320 AE analyzer was used to monitor the corrosion activities via broadband AE sensors mounted on the bottom shell of the tank. The AE signals were 60 dB amplified by preamplifier sets. The monitoring time was 24 h per condition. The signal was then sent to the AE analyzer to process and store AE parameters which were amp, count, energy, rise time, duration, and event locations. Vallen Visual AE program was used to analyze AE data obtained from AE analyzer.

3 AE Source Clustering and Classification

3.1 Cluster Analysis of AE Parameters

As our previous works, pitting and uniform corrosion sources had been identified using corrosion mechanisms [2]. The AE source was divided into three groups of

Table 1 Correlation between AE parameters

Correlation coefficient	Amp	Count	Energy	Duration
Amp	1.00	0.77	0.84	0.83
Count	0.77	1.00	0.78	0.95
Energy	0.84	0.78	1.00	0.92
Duration	0.83	0.95	0.92	1.00

bubble occurring, passive film breakage, and pitting propagation. These AE features were done by observation and filtering techniques. However, AE data obtained from the field testing are complicated due to several sources of noises. So, the pattern of corrosion sources is needed to recognize and compare with the field testing results.

The AE data collected from controlled conditions in the laboratory were employed to recognize the pattern of uniform and pitting corrosions. As of the AE data are categorized by parameters. They are unsupervised data in which there are no predefined learning or classes. The relation between AE parameters from laboratory was done by correlation analysis following Pearson coefficient (r) as in Eq. (1). The coefficient correlations are presented in Table 1 where the Z score is the standard value of data X and Y for population of N:

$$r = \sum \frac{(Z_x Z_y)}{N} \tag{1}$$

From the correlation of AE parameters, it can be implied that the four parameters including amp, count energy, and duration were in good relation. However, count related to energy and duration almost linearly. This correlation may not contain the different characters. Hence, amp, count, and energy were employed for cluster analysis.

For clustering the AE data, statistic cluster analysis, K-means, has been utilized to group the corrosion the sources of corrosion mechanism by finding similarities between data according to the characteristics found in the data and grouping similar data objects into clusters. The K-means clustering is one of the partitioning methods of database x_j objects into a set of k clusters, where E is the sum square of minimized distance d as Eq. (2), where c_i is the centroid of cluster Ci:

$$E = \sum_{i=1}^{k} \sum_{x_j \in \mathrm{Ci}} \left(d\left(x_j, c_i\right)\right)^2 \tag{2}$$

To give the group of cluster, k, clustering algorithm was used to calculate a silhouette value for each observation. The silhouette value is the parameter to define the minimum data associated with the assigned cluster and maximum dissimilar from other clusters. Each data point has a silhouette value and the mean silhouette value over all points summarizes the overall quality of the clustering. The possible

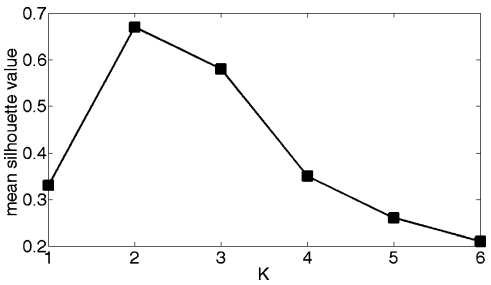

Fig. 3 The mean silhouette values for clustering to two groups

Table 2 Grading of tank floor condition

Floor condition	Event/h · m^2(E_R)
Minor	≤10
Medium	>10 and ≤34
High	>34 and ≤55
Very high	>55

Table 3 Recommendation of inspection plan

Floor condition	Next inspection (years)
Minor	4
Medium	1–2
High	0.5–1
Very high	Require internal inspection

cluster after repeating analysis is shown in Fig. 3. The line has a peak at 2, which indicates that the mean silhouette values of the AE data distribution can be partitioned into two groups.

3.2 Classification of Bottom Tank Condition

To classify the bottom plate condition of AST, AE data obtained from field testing were statistic filtered and tested based on the feather database of laboratory-clustered results. Selected AE parameters including amp, count, energy, and event hits were mainly used to classify the corrosion grading. In addition the factors affecting the grading results are tank size, stored product, product level, and tank age. Their data were used to compensate the AE data from field tests.

At present, number of events per period time from any of 1 m^2, which is considered as event rate, was calculated from processed tested data. Total AE event rate/h · m^2 (E_R) was employed in our grading of tank floor according to Table 2.

The tank floor condition grading in Table 2 is based on an empirical data from the research work of corrosion severity study which is related to an AE activity of field testing. The ranking is considered for recommendation of an inspection planning which is shown in Table 3.

4 Results and Discussion

4.1 Laboratory Results

In Fig. 4, the previous results of AE parameters (amp vs. count) were analyzed to explore the AE parameter patterns of occurring corrosion from uniform and pitting, respectively, using Vallen Visual AE [2]. AE activities generated from uniform corrosion grouped around the actual position of the corrosion source. The activities showed amount data of amp between 45 and 65 dB and counts less than 1,000. But some amp had high level (up to 75 dB) with fewer counts as in Fig. 4a. The similarity pattern of AE obtained from pitting corrosion is shown in Fig. 4b. Sum of AE data was less than uniform corrosion; however, both amplitude and counts were similar. From observation of corrosion mechanisms, AE were generated from several of hydrogen bubble breaking caused by the destroyed passive films of the material surface to produce uniform corrosion and pitting corrosion. The high amplitude and count AE data probably came from passive film breakage at the beginning of both types of corrosion processes. However, these results were filtered, during which some important data were lost and could not be interpreted.

To group the AE data features, cluster analysis was implemented to recognize the AE data both from uniform and pitting corrosions. The results of clustering of raw data obtained from an experimental tank in Fig. 2 by repeating *K*-means with two groups were done. The AE data relation between amp vs. count and energy vs. count can be clustered into two groups which were corrosion sources and noise sources. The results are shown in Fig. 5. These clusters can be confirmed with the previous work results. Corrosion sources can be partitioned higher than noise sources clearly. The patterns of both uniform and pitting corrosion were rising to about 1,000 counts. On the other hand, Noise sources which could be occurred from electrical signals and environments are near the ground. Corrosions can be distinguished from noises when count higher than 200 for both relates to amp and energy. Especially, corrosion patterns of uniform and pitting corrosion are nearly matched. Therefore, AE parameter clusters of both corrosions were similar in this study.

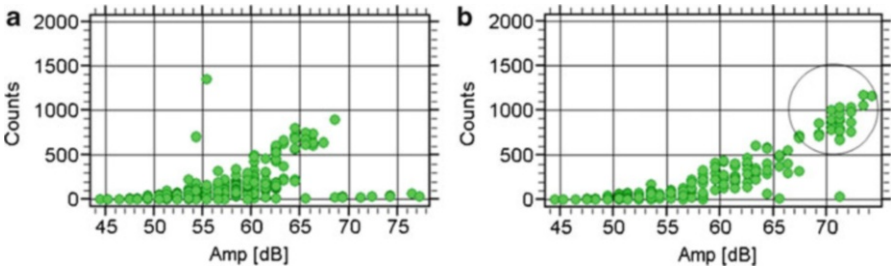

Fig. 4 Amp vs. count of laboratory experiments: (**a**) uniform corrosion, (**b**) pitting corrosion

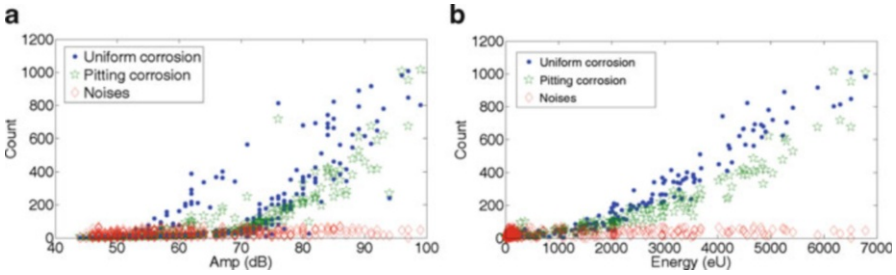

Fig. 5 Clustering results of corrosion sources: (**a**) Amp vs. count, (**b**) energy vs. count

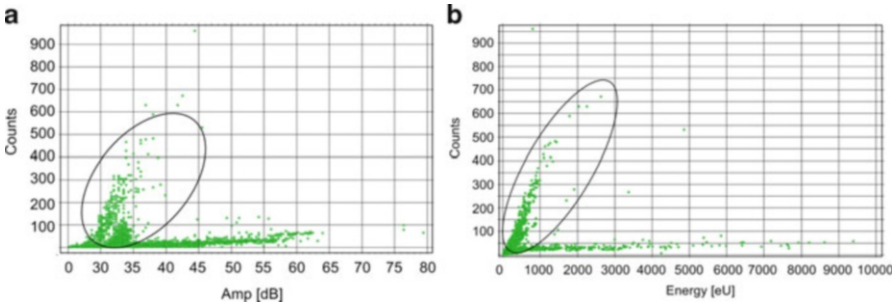

Fig. 6 AE parameter relation obtained from field testing: (**a**) Amp vs. count, (**b**) energy vs. count

4.2 Field Testing Results

Twelve AST with different media were tested to monitor corrosion of bottom plates. Compared to the laboratory results, amp, count, and energy were main parameters of analysis. The results of field testing showed the specific AE patterns of corrosion activities analyzed by Vallen Visual AE software. AE parameter relation obtained from tank no. TK1 was shown in the example. To clearly distinguish corrosion sources, amp vs. count, there were two groups of AE counts with different amplitudes, which were low count and high count as shown in Fig. 6a. Corrosion activities were grouped into high counts up to about 1,000 with low amplitude between 30 and 50 dB as shown in the circle. In the same way, there were two groups of AE counts related to energy as shown in Fig. 6b. The group of high counts showed data between energy of 0 and 3,000 eU. Another group showed less than 100 counts related with high energy.

To test the pattern recognition, analyzed corrosion clusters from Sect. 3 were implemented to recognize the correlation with all of the testing tanks. The trained data sets were repeated and tested before use to identify the data of field testing. Target of the output was the cluster of corrosion. The average accuracy of training set was 92.4 %. The results of classification were done by pattern recognition process and resulted in Table 4. The accuracy of pattern recognition can show the

Table 4 Accuracy of corrosion pattern recognition on AE field testing

Tank no.	Average accuracy (%)
TK1	78.4
TK2	65.3
TK3	67.6
TK4	74.4
TK5	73.9
TK6	62.5
TK7	70.8
TK8	71.4
TK9	73.1
TK10	66.2
TK11	68.8
TK12	71.4

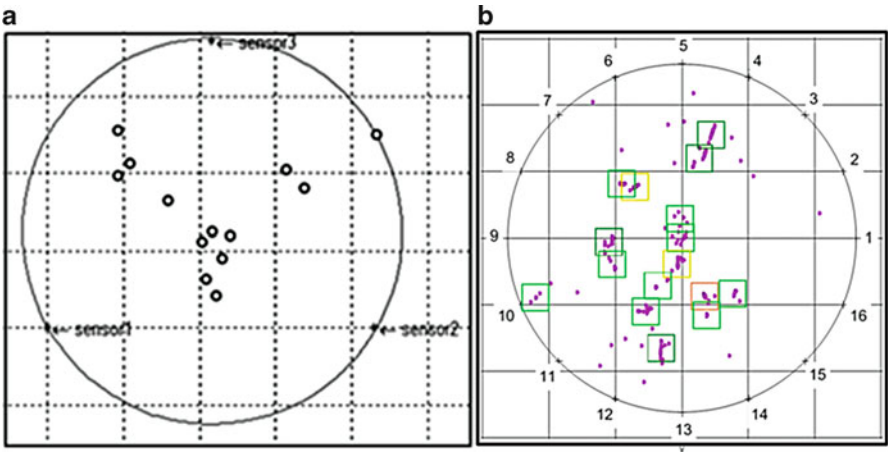

Fig. 7 AE event locations of (**a**) experiment tank, (**b**) field testing tank no. TK1

fair relationship with the percentage of average accuracy more than 60 % from 12 AST. The different output performances compared to the training set can occur due to the AE parameter range and shape of corrosion patterns. The data should be more compensated with the accuracy results. Specific tank history factors including tank size, stored product, product level, and tank age will be employed to improve the results in the future.

To classify AST bottom plate condition, results of AE event locations of the field testing were processed according to the clustered data of corrosion. The statistic clustering algorithm following experimental data was utilized to grade the severity of AE activity area. As for the issues of location events from the experimental tank (uniform corrosion), the locations were clearly shown; the location on the same produced corrosion sources as in Fig. 7a. For field testing tank no. TK1 (example), after filtering noise signals from original testing data, the outcome data were shown

Table 5 AE monitoring results of AST bottom plate

Tank no.	Floor condition	Next testing (year)
TK1	High activity	1
TK2	Minor activity	3–4
TK3	Minor activity	3–4
TK4	Medium activity	2–3
TK5	Minor activity	3–4
TK6	Medium activity	2–3
TK7	Minor activity	3–4
TK8	Minor activity	3–4
TK9	High activity	1
TK10	Minor activity	3–4
TK11	Minor activity	3–4
TK12	Minor activity	3–4

as corrosion source location in Fig. 7b. The result shows that the events number of AE activities produced the low amplitude with high count, duration, and energy. They can be referred to the bottom plate activities. The cluster of AE events spread on the floor. Referred to our grading program, the tank floor was ranked to high activity grade which should be tested again in 1 year. The off-line inspection by MFL of empty tank was used to inspect the bottom plate condition after AE testing. The results showed the corrosion pit spread on the floor. The deepest wall lost was about 60–70 % of plate thickness around the middle of the floor.

5 Conclusion

AE data obtained from corrosion sources on field testing of the above ground storage tank (AST) were identified and clustered by comparing to the lab results. Corrosion sources from the controlled environment in the laboratory were analyzed and identified from the pattern of AE parameter correlation using cluster analysis. The relation of amp, count, and energy was the main parameter to recognize the corrosion patterns. The clustering results can be shown for the similarity between uniform and pitting corrosions which are the main type of corrosion on AST bottom plates. Field testing data were tested using the pattern recognition technique to validate the accuracy of corrosion cluster. The results were shown for the relation with more than 60 % of accuracy. Therefore, AE parameter correlations of both testing field and experiment were similar. In addition, analyzed AE event rate occurring from corrosion sources was used to classify the condition of AST bottom plate. The summary grading of field tank testing is presented in Table 5.

Acknowledgements This project is under the program "Co-operation between industry and university 2012-2014." We would like to thank PTT Groups, SCG Groups, and Thai Tank Terminal Co., Ltd. for supporting on-field testing. We would like to thank Thai NDT Co., Ltd (Public) for co-operation and support of AE equipment.

References

1. C. Jirarungsatean, A. Prateepasen, P. Kaewtrakulpong, *Pitting Corrosion Monitoring of Stainless Steels by Acoustic Emission* (Corrosion Control & NDT, Melbourne, 2003)
2. C. Jirarungsatian, A. Prateepasen, Pitting and uniform corrosion source recognition using acoustic emission parameters. Corros. Sci. **52**, 187–197 (2010)
3. C. Jomdecha, A. Prateepasen, P. Kaewtrakulpong, P. Thungsuk, *Corrosion-Source Location by an FPGA-PC Based Acoustic-Emission System* (IEEE TENCON, Chiangmai, 2004)
4. C. Jomdecha, A. Prateepasen, P. Kaewtrakulpong, A study on source location using an acoustic emission system on various types of corrosion in industry. NDT&E Int. **40**, 584–593 (2007)
5. P. Cole, J. Watson, Acoustic emission for corrosion detection, *3rd Middle East Nondestructive Testing Conference & Exhibition* (27–30 Nov 2005), Bahrain
6. S. Liying, L. Yibo, Investigation on sensor array in large vertical storage tank bottom inspection using AE methods, *Chinese Control and Decision Conference (CCDC)*, 2011

Identification of Acoustic Emission Signal of Tank Bottom Corrosion Based on Weighted Fuzzy Clustering

Yang Yu, Hui Cao, Ping Yang, Yuan Fu, and Ling Jun

Abstract The identification of corrosion acoustic emission signal of tank bottom is the basis of improving detection accuracy. However, under some circumstances, the types of corrosion acoustic emission signal of the tank bottom are unknown, and a weighted fuzzy clustering recognition method was proposed to solve this problem. The main characteristics of the signal were given by acoustic emission detector; the characteristics included rise time, count, energy, duration, amplitude, and average frequency. Aiming at the randomness of clustering initialization, nearest neighbor method was used for optimizing initial clustering. For improving the accuracy of edge data, a weighted fuzzy clustering method was proposed to increase the difference of various acoustic emission signals. The data redistribution method of fuzzy clustering is adjusted with the weighted distance between the gravity and center to substitute the traditional distance and then allocated data to the set which had the minimum weighted distance. This study shows that the veracity of weighted fuzzy clustering increases by about 9 %.

1 Introduction

Storage tank is the main tools to conserve liquid petroleum. For storing the huge amount of oil, storage tanks usually have a large size. However, in most situations, the large size has made cleaning and inspection of a tank a hard work. To solve this

Y. Yu (✉) • H. Cao • P. Yang • Y. Fu
Shenyang University of Technology, Shenyang 110870, China
e-mail: yuy@sut.edu.cn

L. Jun
Drilling and Production Technology, Institute of Liaohe Oilfield, PetroChina, Panjin 124010, China

G. Shen et al. (eds.), *Advances in Acoustic Emission Technology: Proceedings of the World Conference on Acoustic Emission-2013*, Springer Proceedings in Physics 158,
DOI 10.1007/978-1-4939-1239-1_36,

problem, acoustic emission inspection has been proposed. This method allowed us to detect the damage of oil tank jar bottom without surface cleaning. Nowadays the identification of corrosion acoustic emission signal of tank bottom becomes the basis of improving detection accuracy.

However, under some circumstances, the types of corrosion acoustic emission signal of the tank bottom are unknown. In fact, reasons such as the excessive pressure, oil soaking, and poor working conditions made the bottom the most easily to be hurt of all parts of a tank, and one of the biggest damage was corrosion problems. The major reason of the corrosion was that the dynamic force was generated when filling and discharge brings stress corrosion cracking and electrochemical corrosion cracking on the corrosion layer with water plash [1]. An open circuit can be caused by oxidation, excessive charring, or insulating deposits on the contacts. At potentials above a critical potential that is well below the pitting potential measured from the surface covered with oxide film, corrosion pit would occur on the freshly generated surface [2]. Electrochemical corrosion cracking often manifest as corrosive pitting while stress corrosion cracking often manifest as crack propagation and oxide spalling. Of all the corrosive injuries, pitting is the main one. In this chapter, three different kinds of corrosion could be distinguished with others by using the weighted fuzzy clustering algorithm [3].

In the following, the study was arranged as this order: Sect. 2.1 presents the sense of our study in the identification of acoustic emission signal of tank bottom corrosion; Sect. 2.2 gives the improved weighted fuzzy clustering algorithm. In contrast to the classical fuzzy clustering algorithm, this method performs a higher precision. In Sect. 2.3 we effectively extracted classified signals and provided reliable single characteristic analysis for each set of data. The result of analysis was used to identify the corrosion type.

2 Methods

In this section, we elaborate on the weighted fuzzy clustering in the following paragraphs. First of all, due to the initialization dependence of acoustic emission data structure, a nearest neighbor method was proposed and applied to confirm the cluster number and the center directly. Second, aiming at the similar in dataset structure problem which exists in different types of AE signal parameters, this chapter proposes a relative membership-grade weighted method. Then, by studying the change disciplinarian of different corrosion types and AE parameter, change relation between corrosion and AE parameter has been achieved [4]. Finally, an experiment shows that theoretical analysis results match to the experimental results [5].

Here, we briefly introduce the classical fuzzy clustering method here. In 1973, Dunn proposed the hard clustering means (HCM) to fuzzy situation. Then Bezdek spread it to a more general situation and gave a general description of fuzzy

clustering [6]. The fuzzy clustering problem can be formulated as the following mathematical programming problem:

$$\begin{aligned} J_{\min}(u,v) &= \sum_{i=1}^{c}\sum_{j=1}^{n} u_{ij}^{m} {d_{ij}}^2 \\ \sum_{i=1}^{c} u_{ij} &= 1 \end{aligned} \tag{1}$$

An iterative algorithm was given by Bezdek to get the optimal solution of the above mathematical programming problem. The iterative formula in the algorithm is

$$\begin{aligned} u_{ij}^{(k)} &= \frac{1}{\sum_{r=1}^{c}\left(\frac{d_{ij}^{(k)}}{d_{rj}^{(k)}}\right)^{\frac{2}{m-1}}} \\ v_i^{(k+1)} &= \frac{\sum_{j=1}^{n}\left(u_{ij}^{(k)}\right)^{m} x_j}{\sum_{j=1}^{n}\left(u_{ij}^{(k)}\right)^{m}} \end{aligned} \tag{2}$$

The algorithm is convergent and at the solution point the objective function achieves its local minimum.

The clustering algorithms based on the objective function are almost all using Euclidean distance. In 1987, Gustafson added covariance into the expression of the distance and proposed covariance fuzzy clustering algorithm. Then Bezdek promoted the application range of the fuzzy C-means clustering algorithm by improving the clustering criterion with the distance of data point to the center of cluster set [7]. Based on fuzzy clustering algorithm, we studied the objective function of the traditional fuzzy C-means algorithm and proposed a modified objective function for FCM. The weighted fuzzy clustering problem can be formulated as the following mathematical programming problem:

$$\begin{aligned} J_{\min}(u,v) &= \sum_{i=1}^{c}\sum_{j=1}^{n} w u_{ij}^{m} {d_{ij}}^2 \\ \sum_{i=1}^{c} u_{ij} &= 1, 1 \le j \le n \end{aligned} \tag{3}$$

where c is the number of clusters, n is the number of dataset X, m ($m > 1$) is the fuzzy weighting exponent and its best value is between 1.5 and 2.5 in experience, w is the weighting coefficient, $w = 1/|v_r - g_r|$ is the weight coefficient, and $d_{ij} = \|x_i - v_j\|$ is the Euclidean distance between clustering center and sample point.

2.1 Initialization

The fuzzy clustering method algorithm overly depends on the initial points but the right value of c is unknown and selecting the initial points effectively is also difficult [8]. In theory, clustering algorithm needs transcendental knowledge about the data set to be clustered in general, and so do fuzzy clustering. So this chapter gives a nearest neighbor algorithm to confirm the cluster number and center directly.

The nearest neighbor method is one of the simplest search algorithms. This method regarded the first data as the center of first group. If distance between a data and the center of the set is less than the expected value, then the data would be put into this set. In other words, the optimal center of this set must be nearly to this data; otherwise the data was the new center.

Initialization steps:

1. Begin with the first data x_0, regard this data as a center x_c^1, and set up a radius d.
2. Calculate the distance between the k-th data and centers $(x_c^1, x_c^2, \ldots, x_c^M)$ $|x_0^k - x_c^l|$ $(l = 1, 2, \ldots, M)$. Assume that the minimum distance was $\left|x_0^k - x_c^{l_k}\right|$, and $x_c^{l_k}$ was the nearest neighbor rule.
3. If $\left|x_0^k - x_c^{l_k}\right| < d$, x_0^k was the new center; otherwise if $\left|x_0^k - x_c^{l_k}\right| > d$, then continue to iterate.

2.2 Weighting

The fuzzy clustering method is a dynamic process in which clustering center and membership degree matrix are continuously being modified during clustering [9]. Starting from the random initial center the fuzzy clustering method converged to local minimum of the objective function after several iterations. So the algorithm performance depended on the initial clustering center. In view of the problem above, the nearest neighbor algorithm was used to selecting the clustering center with high reliability [10].

For the similar structure of acoustic emission signal, a weighted fuzzy clustering method was proposed to increase the difference of various acoustic emission signals. This method adjusted traditional data redistribution method instead of the distance of fuzzy clustering method of the weighted distance between the gravity and center and then allocated data to the set which had the minimum weighted distance. The results show that the chance that data farther from center belonged to the big and sloppy set allocated to the wrong set had been decreased by this algorithm.

The main characteristics of the signal were given by acoustic emission detector; the characteristics included rise time, count, energy, duration, and average frequency. In this method, a weighted fuzzy clustering algorithm is presented to solve classification problem. Initial cluster centers had been selected then through the

Table 1 Accuracy comparing

Algorithm	FCM	K-means	WFCM
Accuracy	84.00 %	89.33 %	93.33 %

nearest neighbor algorithm. And the optimal cluster center can be found. The initialed data can offer necessary knowledge and information of classification; furthermore, they are a row vector which contains the entire eigenvalue of AE parameters. Each type of the parameter has its own center of gravity. The weight of each type of characteristic parameter can be achieved by calculating the distance of the center of gravity and the cluster center. This way, the external distance can be increased while the internal distance can be reduced. And finally, the accuracy rate of fuzzy clustering can be increased.

Compared with general fuzzy clustering method, the classification credibility of weighted fuzzy clustering is improved effectively. Then, a traditional clustering algorithm carries on the optimization, improved as weight cluster algorithm.

Steps:

1. Fuzzy indicators $m = 2$, and cluster number $c = 3$. Calculate the random initial cluster centers v_j.
2. Calculate the highly reliable clustering center by nearest neighbor algorithm.
3. Calculate the weight, clustering with the weighted clustering criterion.

To reflect the optimization discussed above, Table 1 listed the comparison of three kinds of algorithms. The methods were fuzzy clustering method K-means method and weighted fuzzy clustering method.

Accuracy comparison for fuzzy clustering algorithms:

Table 1 shows that the veracity of weighted fuzzy clustering increases by about 9 % than fuzzy clustering, and 4 % than K-means.

2.3 Identification (Laboratory and Field)

Characteristic parameter played an important role in the source recognition during the corrosion process. So the different signals can be set apart from others stereotypically [11].

Different acoustic emission signals had different characteristics [12]. Basic information of the class to which those objects belong could be represented by the classified data. Tests are conducted under laboratory conditions; those characters below had an obvious differentiation; they were sufficient to meet the demand [13].

In the sort module, multicolor was assigned to different clustering based on the value of c, so the colors are assigned randomly. Result of optimization can also be seen by those figures (lab).

From Figs. 1, 2, 3, and 4, by contrasting (a) and (b), it can be seen that clustering result of the figures below has a striking optimization. Figures 1, 2, 3, and 4 show

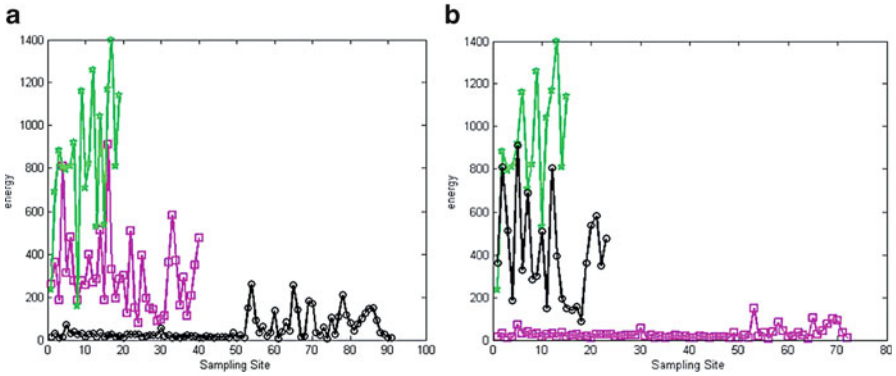

Fig. 1 The energy distribution of experimental data. (**a**) Energy distribution of the FCM, (**b**) energy distribution of the WFCM

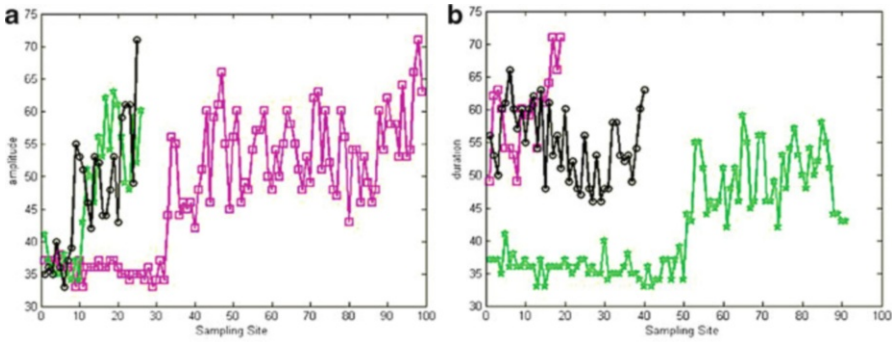

Fig. 2 The amplitude distribution of experimental data. (**a**) Amplitude distribution of the FCM, (**b**) amplitude distribution of the WFCM

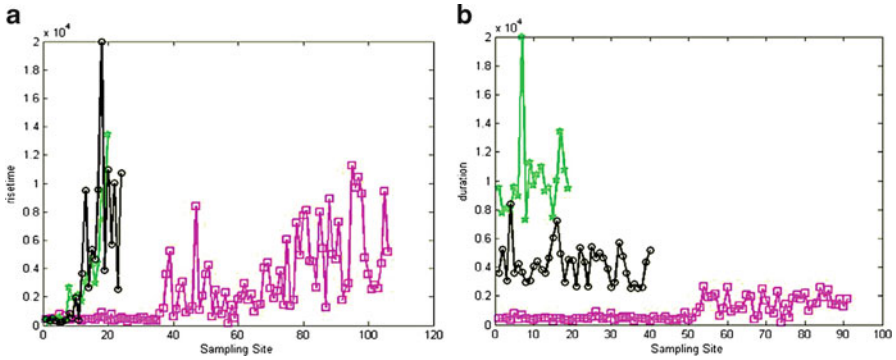

Fig. 3 The duration distribution of experimental data. (**a**) Rise time distribution of the FCM, (**b**) rise time distribution of the WFCM

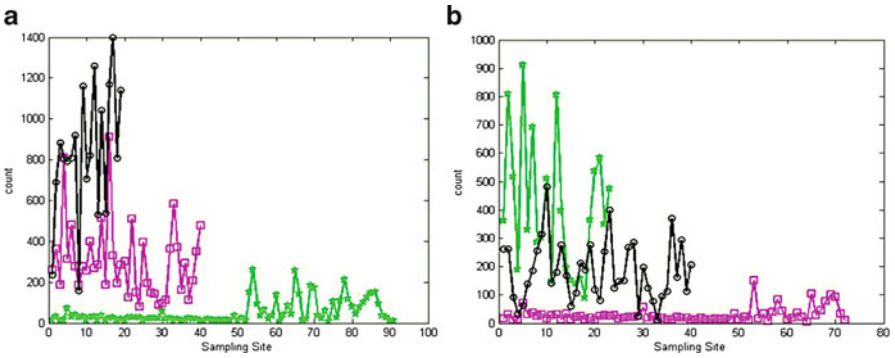

Fig. 4 The count distribution of experimental data. (**a**) Count distribution of the FCM, (**b**) count distribution of the WFCM

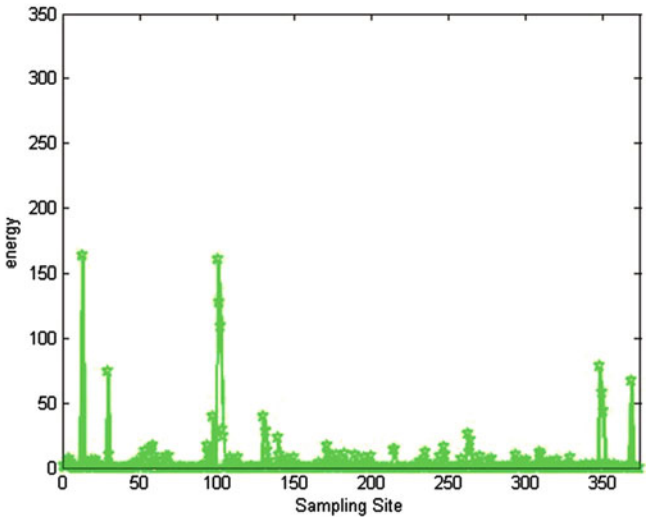

Fig. 5 The energy distribution of field data

the experimental result while Figs. 5, 6, 7, and 8 show the analysis result. After each figure, comparison of classical value range is given.

From Fig. 1 it can be seen that corrosion energy has the following characteristics. Energy of crack and oxide film appeared to undergo a sudden and random increase while pitting has a low energy.

Figure 2 shows that amplitude of pitting characteristic has little change over time, generally in the range of 30–40.

Figures 1 and 2 show that pitting acoustic emission signals could be clearly discriminated by energy and amplitude. And recognition effect of amplitude was superior to energy.

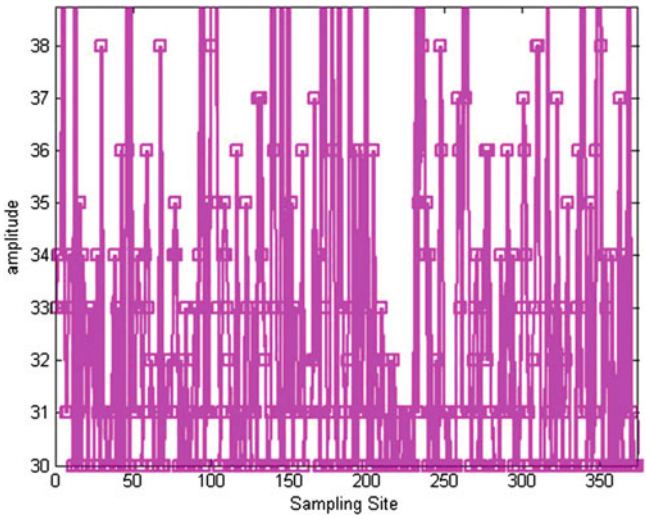

Fig. 6 The amplitude distribution of field data

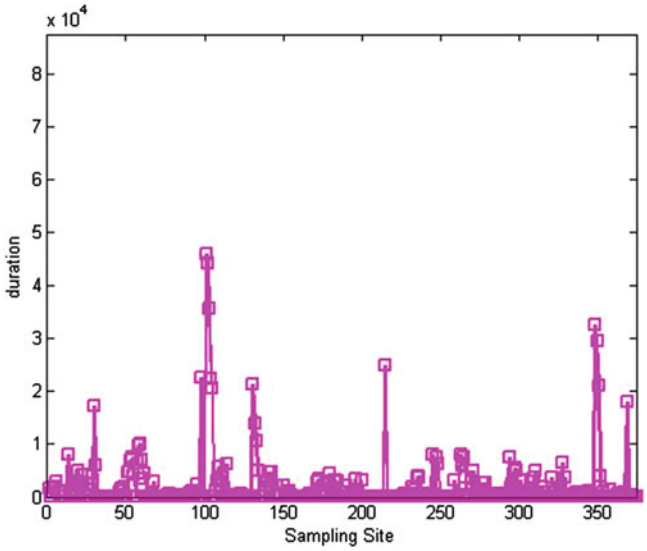

Fig. 7 The duration distribution of field data

From Fig. 3 it can be seen that corrosion duration has the following characteristics. Duration of oxide film changed greatly in the range of 0.8–2 while crack around 0.4.

Figure 4 shows that corrosion energy had the following characteristics. Crack initiation and propagation were associated with spalling behavior of the oxide film

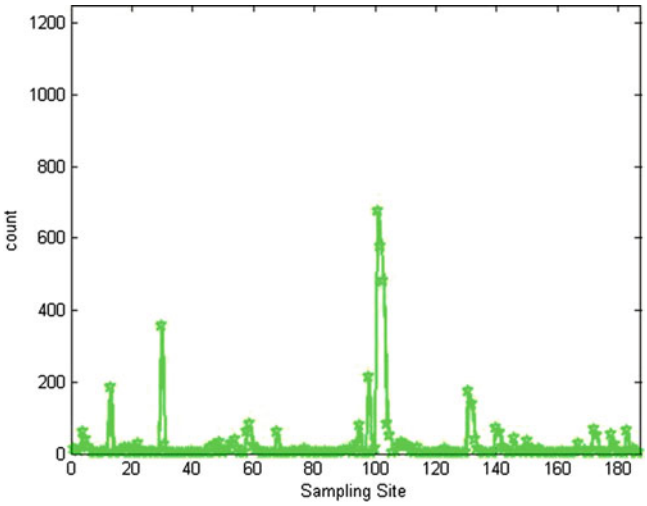

Fig. 8 The count distribution of field data

under applied stress. Count of crack characteristic was generally in the range of 3–500 while oxide film was much higher.

Figures 3 and 4 show the relationship between crack and oxide film acoustic emission signals, and they could also be discriminated from the other one.

The weighted fuzzy clustering method is employed for real-time online monitoring of tank bottom plate. The tank has been used for more than 25 consecutive years and has a 50,000 m^3. The monitoring provided real-time data and analytics below (field):

From Fig. 5, the energy of part sample value was at a relatively low range. Comparing with others, pitting may exist at the bottom of the storage tanks corresponding to laboratory findings.

From Fig. 6, the amplitude of part sample value was at a range of 30–50. Comparing with others, pitting may exist at the bottom of the storage tanks corresponding to laboratory findings.

From Fig. 7, the duration of part sample value was at a range of 1–2.2. Comparing with others, oxide film may exist at the bottom of the storage tanks corresponding to laboratory findings.

From Fig. 8, the count of part sample value was at a range of 3–500. Comparing with others, crack may exist at the bottom of the storage tanks corresponding to laboratory findings.

Consider the complexity of site data, in those figures (field); only the character that had a useful effect for the identification was drawn up here.

3 Results

Based on the fuzzy clustering algorithm, this chapter proposed an improved partition coefficient method of clustering initialization to confirm the cluster number c, and a weighted fuzzy clustering method to decrease the wrong allocation of the data farther from center. By feature analysis of corrosion acoustic emission signal, the types of corrosion source can be successfully identified.

Acknowledgment This work is supported by the Creative Team Project Foundation of the Education Department of Liaoning Province, China (Grant No. LT2010082).

References

1. S. Ramadan, L. Gaillet, C. Tessier, Detection of stress corrosion cracking of high-strength steel used in prestressed concrete structures by acoustic emission technique [J]. Appl. Surf. Sci. **254**, 2255 (2008)
2. A. Cakir, S. Tuncell, A. Alptekin, AE response of 316LSS during SSR test under potentiostatic control [J]. Corros. Sci. **41**, 1175 (1999)
3. M.J. Bennett, D.J. Buttle, P.D. Colledge, Spallation of oxide scales from 20 % Cr-25 N-i-Nb stainless steel [J]. Mater. Sci. Eng. **A120**, 199 (1989)
4. W. Jin, C.Z. Chen, Z.H. Jin, B. Gong, B.C. Wen, The three-ratio method of acoustic emission source recognition [J]. Chin. J. Sci. Instrum. **29**(3), 530 (2008)
5. G.Y. Gong, Study of FCM algorithms on parameters and its applications. Xi'an University of electronic science and technology [D] (2004)
6. J.C. Bezdek, *Pattern Recognition with Fuzzy Objective Function Algorithms* (Plenum, New York, NY, 1981), pp. 95–107
7. N.R. Pal, J.C. Bezdek, On cluster validity for the fuzzy for the fuzzy C-means model. IEEE Trans. Fuzzy. Syst. **3**(3), 370–379 (1995)
8. X. Zhang, G. Zhang, P. Liu, Based on the clustering criterion function improved K-means algorithm. Comput. Eng. Appl. **47**(11), 123 (2011)
9. S. Nittel, T.L. Kelvin, A. Braverman, Scaling clustering algorithms for massive data sets using data streams [C]. Proceedings of the 20th International Conference on Data Engineering, ICDE'04, 2004, p. 830
10. P.S. Bradley, U. Fayyad, C. Reina, Scaling clustering algorithms to large databases [C]. Proceedings of the 4th ACM SIGKDD, New York, 1998, pp. 9–15
11. H. Shaikh, R. Amirthalingam, T. Anita, Evaluation of stress corrosion cracking phenomenon in an AISI type 316LN stainless steel using acoustic emission technique [J]. Corros. Sci. **49**, 740 (2007)
12. W.K. Wang, Z.M. Zeng, G. Du, Y.J. Wei, S.Z. Song, Clustering analysis of acoustic emission signals during stress corrosion of 304 stainless steel [J]. CIESC Journal. **62**(4), 1027 (2011)
13. W.K. Wang, Y.B. Li, G. Du, T. Zhang, S.J. Jin, Based on cluster analysis of acoustic emission signal fusion method at the tank bottom. J. Vibr. Shock. **31**(17), 181 (2012)

The Present Status of Using Natural Gas Cylinders and Acoustic Emission in Thailand

C. Jomdecha, C. Jirarungsatian, W. Methong, and B. Poopat

Abstract This chapter presents the status of using natural gas cylinders (CNG/NGV) and acoustic emission (AE) in Thailand. During the period from 2006 to 2013, more than 600,000 CNG cylinder units for vehicles were installed and used for transportation, cars, and trucks in Thailand. The number of cylinder units will be tentatively increased in the future due to the increase in gasoline price. Due to the use of high-pressurization equipment in public, the issue of a risk to public safety has been raised. As of this writing, in 2013, the testing standard from the Thai Department of Energy Business recommends inspection every 5 years using effective inspection methods in order to guarantee safe usage of gas cylinders, including the AE method, following ISO 16148. Normally in Thailand, AE is used in research and petrochemical plants as a special technique. The main applications are testing of pressure vessels, aboveground storage tanks, and university research. Few companies are available to conduct AE for testing natural gas cylinders due to the limited safety of the high-pressure operation and AE equipment and a lack of qualified AE personnel. To develop AE techniques, equipment, procedures, and acceptance criteria of natural gas cylinders are the main focus of AE personnel in Thailand. A desired achievement for current development is for natural gas cylinder testing, which can be applied in field tests and supported by a national testing standard.

C. Jomdecha (✉) • C. Jirarungsatian • W. Methong
Maintenance Technology Center, King Mongkut's University of Technology, Thonburi 10140, Thailand
e-mail: axlrosez13@hotmail.com

B. Poopat
King's Welding Research and Consultant Center, King Mongkut's University of Technology, Thonburi 10140, Thailand
e-mail: bpoopat@yahoo.com

G. Shen et al. (eds.), *Advances in Acoustic Emission Technology: Proceedings of the World Conference on Acoustic Emission-2013*, Springer Proceedings in Physics 158,
DOI 10.1007/978-1-4939-1239-1_37,

1 Introduction

At present, natural gas is one form of alternative energy for vehicles in Thailand. The demands for natural gas have tentatively grown since 2006, especially in the transportation sector. As of July 2013, more than 600,000 vehicles, including passenger cars, public vehicles, and industrial and transport trucks, have installed natural gas (CNG/NGV) cylinders. More than 250,000 t/month of natural gas is dispensed in this sector [1]. The main motivations for this trend are increasing gasoline prices and support from both the Thai government and Thailand's national energy company, PTT Public Company Ltd. The price of natural gas is only 30 % that of gasoline and 40 % that of diesel. Due to the rapidly increasing use of CNG cylinders, the issue of risk to public safety has been raised because of accidents from natural gas cylinders at load pressures of more than 200 bar. Therefore, inspection and testing of in-service CNG cylinders are highly important for public safety.

Acoustic emission (AE) is the proven method to test a CNG cylinder as a pressure vessel. The advantages of AE testing include decreased test pressure compared to a hydrostatic test and a much greater benefit than only leak detection; additionally, the AE testing result can be evaluated to grade the cylinder condition.

In this chapter, the status of using CNG cylinders and acoustic emission in Thailand is reported. The chapter is organized into three sections: the type of CNG cylinders used in Thailand; the CNG cylinder inspection/testing methods; and the status of AE testing in Thailand.

2 Type of CNG Cylinders Used in Vehicles

As of 2013, two groups of transportation had installed CNG cylinders in Thailand. The first group includes passenger cars, vans, and trucks, which use natural gas as fuel for their vehicles. Pursuant to ISO 11439 standard, "Gas cylinders: High pressure cylinders for the on-board storage of natural gas as a fuel for automotive vehicles" [1, 2], Fig. 1 shows the types of CNG cylinders installed in automotive vehicles in Thailand. The four types of CNG cylinders used include

1. CNG-1 Metal,
2. CNG-2 Metal liner reinforced with resin impregnated continuous filament (hoop wrapped),
3. CNG-3 Metal liner reinforced with resin impregnated continuous filament (fully wrapped),
4. CNG-4 Resin impregnated continuous filament with a nonmetallic liner (all composite).

The second group is transport trucks. They use CNG cylinders to transport natural gas from main stations to the more than 450 substations placed throughout the country [1]. There are six types of CNG cylinders installed in transport trucks:

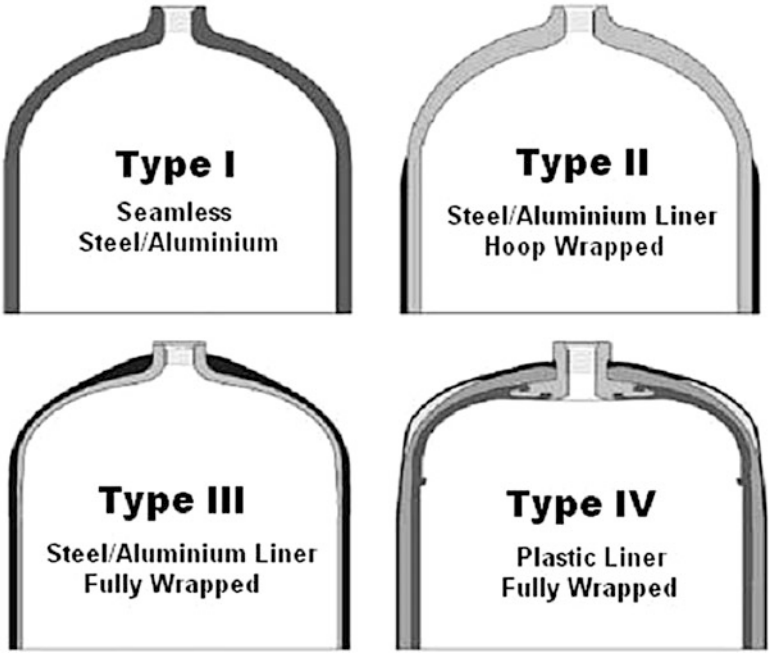

Fig. 1 Types of CNG cylinders according to ISO 11439

1. Steel type following ISO 9809 type 1–3: refillable seamless steel gas cylinders;
2. Steel type following ISO 11120: refillable seamless steel tubes for compressed gas transport;
3. Metal with composites, or all composites type following ISO 11119: refillable composite gas cylinders and tubes;
4. Metal, metal with composites, or all composites type ISO 11439: high-pressure cylinders for the on-board storage of natural gas as a fuel for automotive vehicles;
5. Jumbo tube: design and construct following ASME Sec. VIII DIV. 3 and ISO 11119-1;
6. TATAN tank: metal with high-density polyethylene (HDPE) liner.

All of these cylinder types are installed in the transport trucks that carry natural gas for Thailand's national energy company, PTT Public Company Ltd. Today, more than 1,600 PTT transport trucks are used to transport natural gas from main stations to substations. The specific type of transport truck is classified in seven models according to the types and sizes of installed cylinders:

1. Mini transport truck: six wheels that contain 35 CNG cylinders. They have a capacity of 6,825 L (water). Net weight of natural gas is 1.65 T.
2. Semi-trailer 20-ft transport truck that contains 80 CNG cylinders. They have a capacity of 11,760 L (water). Net weight of natural gas is 2.86 T.

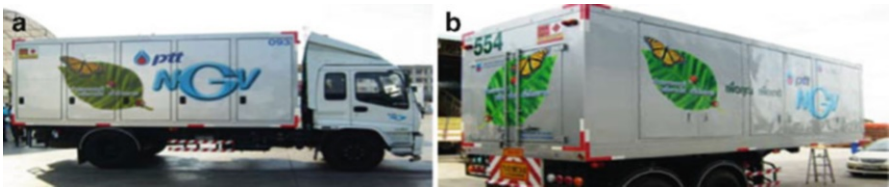

Fig. 2 City transportation trucks: (**a**) mini transport truck; (**b**) semi-trailer

Fig. 3 Semi-trailer transport trucks

Both of these transport trucks, as illustrated in Fig. 2, are used for city transportation due to size, weight, and city traffic.

3. Semi-trailer 40-ft transport truck that contains 92 CNG cylinders. They have a capacity of 17,940 L (water) as shown in Fig. 3. Net weight of natural gas is 4.3 T.
4. Tube trailer or long tube transport truck that contains eight CNG cylinders. They have a capacity of 17,920 L (water), as shown in Fig. 4. Net weight of natural gas is 4.34 T.
5. Neo gas 2 shafts that contain eight CNG cylinders. They have a capacity of 17,680 L (water). Net weight of natural gas is 4.28 T.
6. Neo gas 3 shafts that contain nine CNG cylinders. They have a capacity of 19,890 L (water). Net weight of natural gas is 4.82 T.

Fig. 4 Tube-trailer transport trucks

Fig. 5 Neo gas transport truck

Both types of transport trucks are illustrated in Fig. 5. Natural gas is transferred to the receiving station via hydraulic principle. The advantage is that natural gas can be supplied to the station more than other types using hydraulic oil pressurization. Today, the Neo gas truck is also used to contain the TATAN tank, which is metal with a high-density polyethylene (HDPE) liner. The capacity of natural gas can be increased to 5 T.

7. Jumbo-tube transport truck that contains three CNG cylinders. They have a capacity of 28,000 L (water). Net weight of natural gas is 6.79 T (Fig. 6).

3 CNG Cylinder Inspection and Testing

There are many types of discontinuity among in-service CNG cylinders. Normally, external damage to a CNG cylinder can be classified as two types, as described in Table 1. They must be inspected and evaluated for the level of damage by nondestructive testing (NDT) methods. In most inspections today, visual inspection of the surface of the outside cylinder wall is the means of detecting cylinder damage.

Fig. 6 Jumbo-tube transport truck

Table 1 Type of CNG cylinder damage

General damage	Corrosion damage
Bulge	General corrosion
Dent	Local corrosion
Cut or gauge	Isolated pit
Fire damage or burn	Chain pit
Crack, scratch, or fracture	Corrosion line
Plug or neck threads	Crevice corrosion

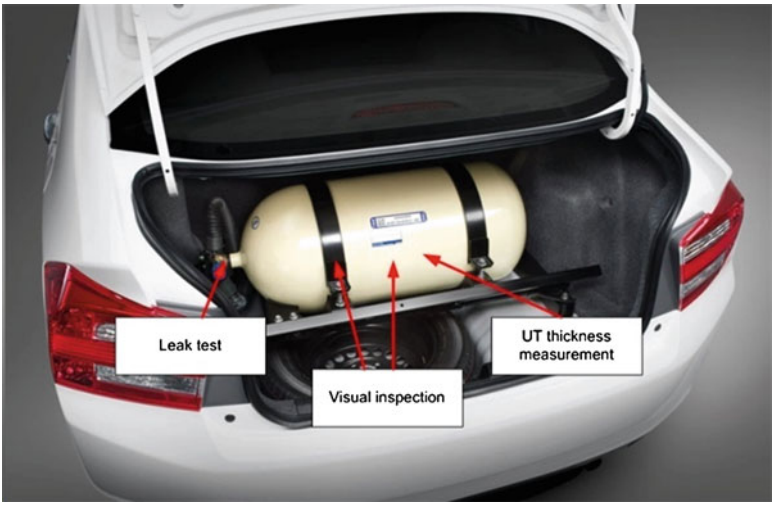

Fig. 7 External inspection point for on-board CNG cylinder

The typical external inspection point for an on-board CNG cylinder is shown in Fig. 7 [3]. Visual inspection of the cylinder's condition, UT thickness measurement, and a bubble leak test in the area of fitting should be performed.

In 2013, the National Policy Office of the Ministry of Energy announced the standard and code for testing CNG cylinders and equipment following ISO 19078

"Standard of inspection of the cylinder installation, and requalification of high pressure cylinders for the on-board storage of natural gas as a fuel for automotive vehicles." In addition, the Thai testing standard for transporting CNG cylinders was released from the Department of Energy Business to propose inspection every 5 years using effective inspection methods in order to guarantee the safe usage of gas cylinders [4]. The inspection method shall cover the inside and outside of the CNG cylinder, including

1. External/internal visual inspection,
2. Measuring wall thickness,
3. Proof pressure/volumetric expansion test,
4. Ultrasonic inspection,
5. Neck thread inspection.

Supplementary tests, including acoustic emission, can be considered for CNG cylinders constructed according to ISO 11439, ISO 9809-1, 9809-2, 9809-3, ISO 11119-3, and ISO 11120. The testing standard shall follow ISO 16148, "Gas cylinders: Refillable seamless steel–acoustic emission testing (AT) for periodic inspection" [5]. The AE testing is used to test during requalification of seamless steel cylinder capacity up to 3,000 L. The results provide only locations and indications from the AE signal or parameters that should be interpreted and evaluated by other conventional NDT methods again.

4 Status of Acoustic Emission Testing in Thailand

Acoustic emission was introduced in Thailand in the 1990s. Some academic researchers were supported by the Petroleum Institute of Thailand (PTIT) to study and train AE testing abroad. Two AE instruments and accessories (PAC) were donated for research and study to King Mongkut's University of Technology Thonburi and Chulalongkorn University, as shown in Fig. 8. Those instruments were used to conduct research and educate students and personnel. AE research into and applications of metallic deformation and fracture started during this period.

In the early 2000s, AE research was developed for other applications, such as corrosion detection and structural monitoring [6–8]. The grading of concrete structures was defined and developed by Chotickai using the Historic index following MONPAC [9]. Today, this technique is becoming the life assessment feature for AE testing of steel pressure vessels and concrete structures in Thailand. AE sensor development was also studied and constructed in this phase [10, 11]. The double-active lead zirconium titanate (PZT) elements of the AE sensor, which improved the sensitivity and frequency bandwidth, were modeled, designed, and developed for use in the lab. The sensor model is shown in Fig. 9.

In 2005, AE testing for leakage, corrosions, welding, and the pressure vessel were studied. Figure 10 displays the prototype AE instrument to detect and locate AE sources, which was designed and developed by researchers at King Mongkut's

Fig. 8 First AE instrument in Thailand (PAC: LOCAN 320)

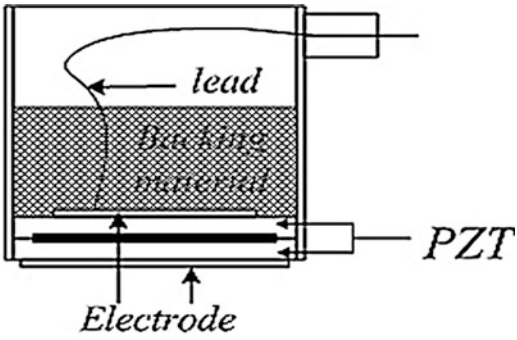

Fig. 9 Double-active PZT elements of AE sensor

Fig. 10 Prototype of AE instrument for source location

Table 2 AE services by NDT companies in Thailand

Company	AE services
Thai NDT Co. Ltd. (public)	Storage tank, pressure vessel in petrochemical industry
Qualitech Co. Ltd. (public)	Storage tank, pressure vessel in petrochemical industry
Acoustometic Co. Ltd.	Storage tank, pressure vessel in petrochemical industry, CNG cylinders
E&S NGV Co. Ltd.	CNG cylinders

Fig. 11 AE testing for leakage and cracking of drum

University of Technology Thonburi (KMUTT). The application was used for locating burst-type AE sources [12, 13]. For industry, AE testing was offered to the petrochemical industry and civil sectors. However, the technology, instrumentation, and personnel were mostly from overseas. At this time, the Thai NDT public company invested in multichannel AE equipment to introduce AE testing to industry. The main applications were storage tanks and pressure vessel testing.

As of this writing, the industry sector in Thailand is interested in rapidly applying AE for their equipment and structures. Some NDT companies provide AE testing levels such as leak monitoring, steel pressure vessel storage tank, and CNG cylinders to various industries. There are four ASNT AE Level III companies that support the development of testing procedures and training in Thailand. The NDT service personals that provide AE services and applications are listed in Table 2.

The actual AE works are mainly being conducted in petrochemical plants. For example, as in Fig. 11, the chemical plant is required to verify the possible location of leaks and cracking of the inside drum or drum paddle. The AE testing was conducted by KMUTT researchers. The drum was tested as a pressure vessel by filling air at 1.1 time of operating pressure. Then AE was utilized to monitor the character of leakage and cracking. The key of this AE testing was to find the source of leakage of the double wall drum with two materials (3-mm SS304 liner on carbon steel thickness of 46 mm). Moreover, the 54 paddles made by SS304 were installed on the drum shell. The AE was done using the zone location technique together with amplitude attenuation characteristics.

For academic work, four main universities have activities in AE research in Thailand:

1. King Mongkut's University of Technology Thonburi (KMUTT);
2. King Mongkut's University of Technology North Bangkok;
3. Chulalongkorn University;
4. Mahanakorn University.

The research fields include mechanical fractures, corrosion, metallurgy, composite materials, welding, and especially CNG cylinder testing. More than 50 scientific publications have been published in national and international proceedings and journals.

5 Conclusion

There are two summaries in this review. First, the status of using natural gas in Thailand is rapidly increasing in the transportation sector. CNG cylinders have been installed in more than 500,000 units, some of which need to be tested and inspected. The Thai standard for testing in-service CNG transport cylinders was proposed by the Department of Energy Business to occur every 5 years and to include the AE method. Second, the status and history of AE in Thailand were reviewed in this chapter. The demand for AE is increasing, especially in the oil, gas, and petrochemical sectors. Their objectives are to reduce the cost of maintenance and to plan maintenance schedules. AE testing of CNG cylinders will be an issue in the next few years in Thailand. In education publications, research in AE topics is also related to the increasing requirements of industry.

Acknowledgment We would like to thank PTT Public Company Ltd., NGV Logistics Planning and Management Division, for providing supporting information.

References

1. PTT NGV website, NGV statistics and NGV activities & news in Thailand, http://pttweb2.pttplc.com/webngv/en
2. ISO 11439: 2013 (E), *High pressure cylinders for the on-board storage of natural gas as a fuel for automotive vehicles*. (ISO/EN, Geneva, Switzerland, 2013)
3. Honda Automobile Thailand Website, Honda city CNG 2012 specification (2012), http://www.honda.co.th/en/citycng
4. Department of Energy Business of Thailand, Announcement: standard for testing and inspection of compressed natural gas cylinder (2013), Bangkok, Thailand
5. ISO/ FDIS 16148: 2006 (E), *Gas cylinders: refillable seamless steel-acoustic emission testing (AT) for periodic inspection*, (ISO/FDIS, Geneva, Switzerland, 2006)
6. C. Jirarungsatean, A. Prateepasen, P. Thungsuk, Corrosion monitoring using acoustic emission. Sci. Mater. Technol. **2**, 152–154 (2002). Thailand

7. C. Jirarungsatean, A. Prateepasen, P. Kaewtrakulpong, Pitting corrosion monitoring of stainless steels by acoustic emission. Corrosion Control & NDT Conference, Melbourne, Australia, 23–26 November 2003
8. C. Jirarungsatian, A. Prateepasen, Pitting and uniform corrosion source recognition using acoustic emission parameters. Corrosion Sci. **52**, 187–197 (2010)
9. P. Chotickai, *Acoustic emission monitoring of prestressed bridge girders with premature concrete deterioration* (The University of Texas, Austin, 2001)
10. C. Jomdecha, A. Prateepasen, Double active elements PZT for acoustic emission sensor. 3rd National Conference on Material Sciences and Technology, Bangkok, Thailand, 2003, pp. 49–51
11. C. Jomdecha, A. Prateepasen, A resonance acoustic emission sensor using single piezoelectric ceramic (characteristic and performances). KMUTT **4**, 483–498 (2006)
12. C. Jomdecha, A. Prateepasen, P. Kaewtrakulpong, P. Thungsuk, Corrosion-source location by an FPGA-PC based acoustic-emission system, IEEE TENCON, Chiangmai, Thailand, 2004
13. C. Jomdecha, A. Prateepasen, P. Kaewtrakulpong, A study on source location using an acoustic emission system on various types of corrosion in industry. NDT & E Int. **40**, 584–593 (2007)

Research on Acoustic Emission Attenuation Characteristics and Experiments on Composite Cylinders

Guang Dai, Yunkuo Ma, Feng Qiu, and Ying Zhang

Abstract The object of our research is the 50L carbon fiber composite cylinder. Using the acoustic attenuation theory formula of a fixed emission frequency and a non-fixed emission frequency, we calculated the acoustic attenuation coefficients of the composite cylinder. We obtained the theoretical attenuation laws of acoustic waves on the composite cylinder in the longitudinal direction. The research results show that the relative errors between theory and experiment of the fixed emission frequency and the non-fixed emission frequency are 1.80 and 3.33 %, respectively, but the attenuation of a fixed emission frequency is faster than that of a non-fixed emission frequency, waves of the fixed emission frequency spread closer. Both can provide the basis for a sensor layout scheme and the acoustic source judgment of composite cylinder state detection.

1 Introduction

Whether the acoustic characteristics of a fibrous composite are good or bad affects their application directly, so accurately testing the acoustic characteristics is crucial [1]. Carbon fiber composite materials are lighter, stronger, and tougher than glass fiber–reinforced plastic materials. Different than metal materials. composite materials are anisotropic and nonlinear, and the destruction is complex and discontinuous. Thus, defect detection and safety evaluation have great particularity [2]. Acoustic emission (AE) testing technology is a dynamic nondestructive test method [3] that is used to detect a composite pressure vessel. Then, using real-time monitoring, AE testing can discover and evaluate defects, perform an analysis, and,

G. Dai (✉) • Y. Ma • F. Qiu • Y. Zhang
Northeast Petroleum University, Daqing 168813, China
e-mail: Gdai126@126.com

G. Shen et al. (eds.), *Advances in Acoustic Emission Technology: Proceedings of the World Conference on Acoustic Emission-2013*, Springer Proceedings in Physics 158,
DOI 10.1007/978-1-4939-1239-1_38,

finally, evaluate the composite material pressure vessel for safety and reliability [4]. Waves propagated in a thin structure are mainly lamb waves; the wave propagation attenuation characteristics that occur in the process are the basis of container nondestructive testing. The size of the attenuation is directly relevant to each sensor's monitoring scope and is the key factor behind the sensor space and work frequency determination in the source location [5]. Hence, there must be research on the container's wave attenuation characteristics before the application of AE detection [6]. However, the material properties of the carbon fiber composite that determine the attenuation characteristics are different from the properties of metallic materials. Voids exist in the carbon fiber composite materials inevitably, increasing the acoustic attenuation and influencing the speed of acoustic waves, the acoustic impedance of the material, the attenuation coefficient, and so forth. In order to verify the effectiveness of the AE detection technology on the composite cylinder and provide a basis for the sensor layout scheme and the acoustic source judgment of composite cylinder state detection, we have conducted a theoretical analysis of and experimental research on the composite cylinder attenuation properties.

2 Acoustic Emission Theory Attenuation Formula of the Composite Cylinder

The attenuation law of carbon fiber composite can be obtained by analyzing the acoustic source attenuation of a fixed emission frequency.

2.1 Acoustic Emission Wave Attenuation Formula of a Fixed Emission Frequency on the Composite Cylinder

According to [7], three factors affect the AE wave attenuation of a composite cylinder:

1. Acoustic emission wave attenuation of resins, $C_R f P_R$;
2. Acoustic emission wave attenuation of carbon fibers, $C_F f^3 {R_F}^2 P_F$;
3. Acoustic emission wave attenuation of pores, $C'_{V1} f^4 {P_V}^2 + C'_{V2} f^2 P_V^{\frac{4}{3}}$.

Assuming that the acoustic attenuation caused by resins, carbon fibers, and pores is independent, and that there are no other defects, the problem of acoustic attenuation can be displayed as

$$\alpha_1 = C_R f P_R + C_F f^3 {R_F}^2 P_F + C'_{V1} f^4 {P_V}^2 + C'_{V2} f^2 P_V^{\frac{4}{3}}, \tag{1}$$

where α_1 is the acoustic attenuation coefficient of a fixed emission frequency, in dB/mm; C_R is a constant related to the resin material; f is the AE frequency, in MHz;

P_R is the percentage of resin; C_F is a constant related to the carbon fiber; R_F is the carbon fiber radius, in mm; P_F is the percentage of carbon fiber; P_V is the porosity; and C'_{V1}, C'_{V2} are constants.

Equation (1) can be used when the acoustic wave propagation distance is short and the frequency of the acoustic source is fixed. Using this formula, one can see the influence of the composite cylinder composition and porosity on the attenuation coefficient. When the AE frequency of the electronic dummy source is fixed, one can use Eq. (1) to calculate the attenuation coefficient. But the lead-break dummy source is often used in attenuation tests, and AE wave frequencies of lead-break dummy sources that are not fixed are broadband.

2.2 *Acoustic Emission Wave Attenuation Formula of a Non-fixed Emission Frequency on the Composite Cylinder*

According to [8], acoustic attenuation of a non-fixed emission frequency can be shown by the following formula:

$$\alpha_2 = \frac{A_0 - A - 10\log r}{r}, \tag{2}$$

where α_2 is the acoustic attenuation coefficient of a non-fixed emission frequency, in dB/cm; A_0 is the initial amplitude of the signal, in dB; A is the amplitude of the signal when it spreads some distance r (cm), in dB; and r is the distance to the acoustic source, in cm.

We can understand that the attenuation coefficient changes with the difference in distance because α_2 is a variable related to acoustic frequency, and the frequency bands of AE signals are wide. Therefore, different frequency components have different α_2 values. When the acoustic waves spread to a certain range, a frequency component is given priority to the wave frequency; in another range, another frequency component is the wave frequency. It should be noted that the establishment of Eq. (2) must meet the following two conditions: First, because of the singularity from the cylindrical wave acoustic pressure and distance law at $r = 0$, the size of the propagation distance r_0, r in Eq. (2) must be far greater than the acoustic source. Second, r_0 is assumed to be very small in Eq. (2), that is, $r_0 \ll r$; this requires the size of r_0 to be greater than that of the acoustic source and far smaller than the propagation distance r.

The acoustic frequency and the material characteristics of the carbon fiber composite cylinder have been considered in Eq. (1), which is the acoustic attenuation formula of a fixed emission frequency; that is more careful, so the selection of frequency f is important. A_0 and A in Eq. (2), which is the acoustic attenuation formula of a non-fixed emission frequency, are obtained by experiment, and they are the comprehensive results related to the material and frequency.

3 Experimental Research on the Acoustic Emission Attenuation Characteristics of Composite Cylinders

3.1 Experimental Specimen and System

A fifty-liter carbon fiber composite cylinder is the object of our experimental research. The fiber type of the container is T700S carbon fiber, the intensity is 4.9 GPa, and the resin is C60F. Wet winding technology is used, referring to GB/T 6058–2005, "Fiber winding pressure vessel fabrication and internal pressure test method."

We are using the SAMOS system of the Physical Acoustics Corporation (PAC). The core is the PCI-8 acoustic emission function card of a parallel processing PCI bus, and the threshold value is 30 dB. Broadband sensors of WD are chosen. A 2/4/6 pre-amplifier is adopted, the filter range is 1–1,200 kHz, and the amplification value is 40 dB. The coupling agent is vacuum grease. In order to explore the carbon fiber composite cylinder attenuation law of fixed and non-fixed emission frequency dummy sources in attenuation experiments, we apply two kinds of dummy sources in the experiment. One is an electronic dummy source and the other is a lead-break dummy source. A PAC FieldCAL is chosen as the electronic dummy source; its frequency is 0.15 MHz. The diameter of the lead-break dummy source is 0.5 mm, and its hardness is 2H.

Two sensors, numbered 1 and 2, are arranged on the straight segment of the composite cylinder body. Sensor 1 is fixed at the right side of the composite cylinder's straight segment, while sensor 2 moves left. The length of the straight segment is 270 mm, so the distance between the two sensors increases from 30 to 270 mm; there are nine groups in all. The electronic dummy source and 2H(0.5) lead-break dummy source are triggered at the root of sensor 1. Figure 1 shows the experimental system.

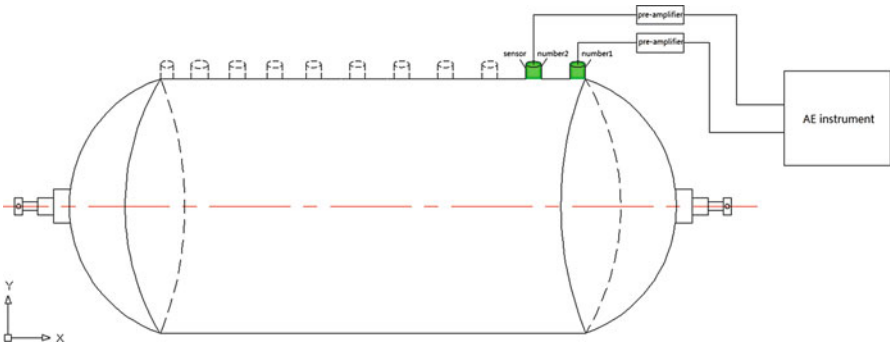

Fig. 1 Experimental system

Table 1 The amplitudes change under different distances between two sensors on a straight segment

Simulating sources	Amplitudes of different distances (dB) (distance/cm)								
	0	3	6	9	12	15	18	21	24
2H(0.5)	99	97	92	90	86	83	79	76	72
Electronic source	99	96	89	87	82	80	76	72	69

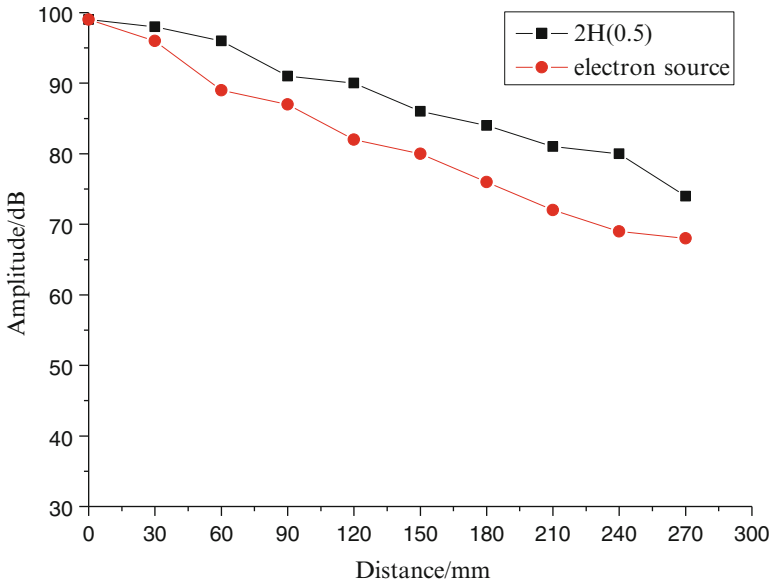

Fig. 2 Attenuation curves showing the amplitudes of two dummy sources as the distances change

3.2 Results and Analysis of Experiment

Two dummy sources trigger AE signals whose amplitudes are 99 dB at sensor 1 root. The signal amplitudes that sensor 2 receives decrease as the distance between the two sensors increases. Table 1 shows the amplitude changes under different distances between the two sensors on the straight segment. Figure 2 shows attenuation curves of the amplitudes of the two dummy sources as the distances change.

The attenuation curves in Fig. 2 show that when acoustic waves spread 270 mm, the amplitudes of electronic dummy source signals decreased from 99 to 68 dB, an attenuation loss of 31 dB. The amplitudes of lead-break dummy source signals decreased from 99 to 74 dB, an attenuation loss of 25 dB; the attenuation of the electronic dummy source is larger. In addition, the greater the distance is between sensors 1 and 2, the smaller the attenuation of amplitudes in 30 mm.

4 Contrasting Research on Attenuation Theory and Experiment of Acoustic Emission Wave in the Composite Cylinder

In order to obtain the unknown constants of C_F, C'_{V1}, and C'_{V2} in Eq. (1), we placed two sensors (sensors 3 and 4) on the straight segment of the composite cylinder body; the distance between the two sensors is 30 mm. The electronic dummy source triggers AE signals whose amplitudes are 99 dB and frequencies are 0.06, 0.15, and 0.3 MHz at the sensor 3 root, and the signal amplitudes received by sensor 4 are recorded. We repeat the test in six different places for every frequency. The average values are recorded in Table 2.

Table 2 shows that the higher the frequency of the acoustic wave is, the faster the attenuation. The attenuation of the electronic dummy source is larger than that of the 2H(0.5) lead-break dummy source because acoustic waves of the non-fixed emission frequency are composed of high- and low-frequency components. High-frequency components attenuate faster, while low-frequency components attenuate slower, so the attenuation of the non-fixed emission frequency is smaller than that of the fixed emission frequency, spread farther. Take the attenuation coefficients in Table 2 and the parameters in Table 3, substitute them in Eq. (1), and we obtain $C_F = 1.08 \times 1{,}013$ dB/(mm^2 MHz^3), $C'_{V1} = 1.35 \times 104$ dB/(mm MHz^4), and $C'_{V2} = 2.91 \times 103$ dB/(mm MHz^2).. The attenuation data of the electronic dummy source in Table 1 are fitted as the formula $y = 97.83636 - 0.11879\ x$, where the fitting error is 0.00517, the attenuation coefficient is 0.11879, and the error to the attenuation coefficient 0.1167, which is theoretically calibrated by Eq. (1), is 0.018. Because the length of the composite cylinder's straight segment is short, the attenuation curves are linear (Fig. 3).

According to the measured data and Eq. (2), when we calculate the attenuation coefficient values of different distances, we find that the average is $\overline{\alpha_2} = 0.21169$ dB / cm. The measured curve and attenuation curve according to Eq. (2) of the 50L composite cylinder when the dummy source is the 2H(0.5) lead-break is shown in Fig. 4. The theoretical curve coincides with the experimental curve well, and the average error is 0.033.

Table 2 Amplitudes of different frequencies

Frequency (MHz)	Signal amplitude received by sensor 4						Average amplitude (dB)	Attenuation coefficient (dB/mm)
0.06	97	97	96	96	95	96	96.2	0.0933
0.15	96	96	96	96	95	94	95.5	0.1167
0.30	95	95	96	94	94	95	94.8	0.1400

Table 3 Related parameters of composite cylinder

Parameters	C_R	P_R	R_F	P_F	P_V
Values	0.1 dB/(mm MHz)	41.32 %	0.8×10^{-6} mm	57.87 %	0.81 %

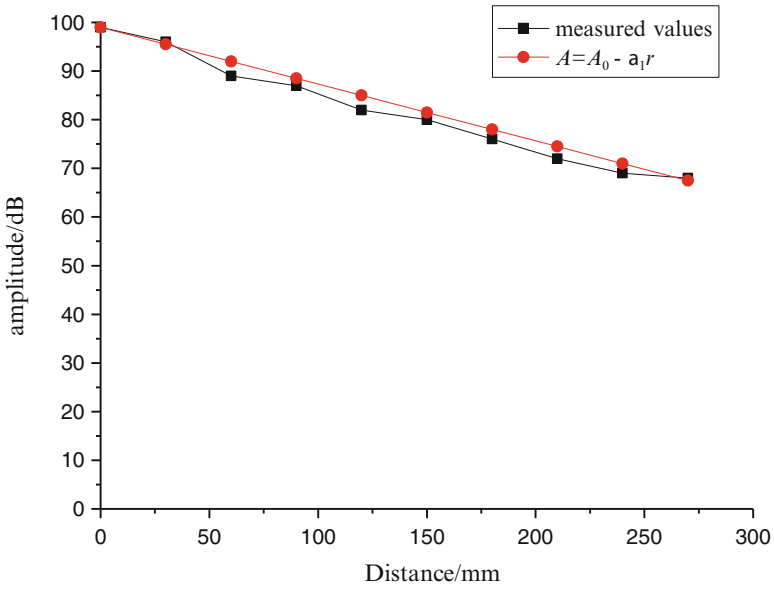

Fig. 3 The theory and measured attenuation curves of an electronic dummy source

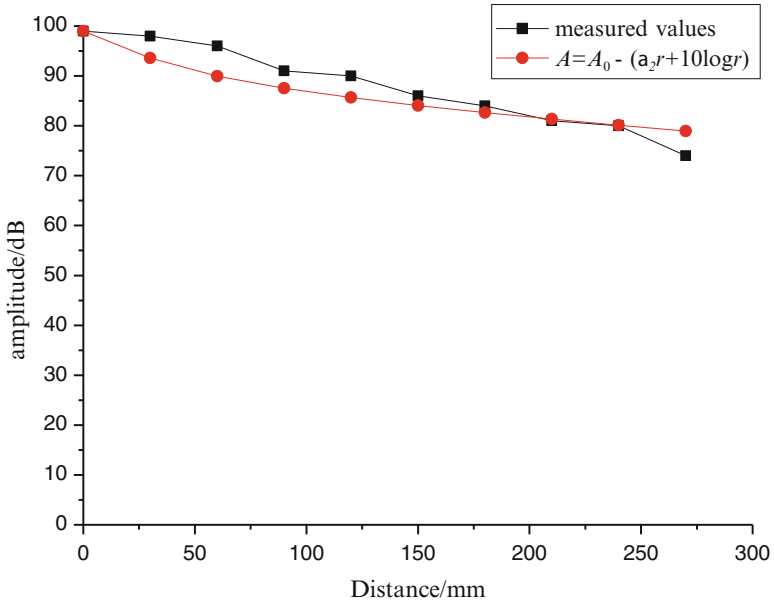

Fig. 4 The theory and measured attenuation curves of a lead-break dummy source

5 Conclusions

The attenuation of the non-fixed emission frequency is smaller than that of the fixed emission frequency, because acoustic waves of the non-fixed emission frequency are composed of both high- and low-frequency components. High-frequency components attenuate faster, while low frequency components attenuate lower and spread farther.

The relative error between theory and experiment of the fixed emission frequency is smaller than that of the non-fixed emission frequency, but both can provide the basis for a sensor layout scheme and the acoustic source judgment of composite cylinder state detection.

The higher the fixed emission frequency of the acoustic wave is, the faster the attenuation. When an attenuation experiment is conducted with a fixed emission frequency dummy source, the proper frequency should be chosen. Frequencies of no higher than 0.15 MHz are recommended.

Acknowledgment This work was supported in part by the Heilongjiang Province Natural Science Foundation of China under grant no. E201140.

References

1. J. Duan, C. Wang, B. Yu, Research on acoustic performance testing method of fiber reinforced composite [J]. J. Test. Technol. **18**(1), 39–40 (2004)
2. G. Shen, J. Li, Pressure vessel nondestructive testing—acoustic emission testing technology [J]. J. Nondestr. Test. **26**(9), 457–463 (2004)
3. G. Dai, Acoustic emission technology in China [J]. J. Nondestr. Test. **30**(7), 390–394 (2008)
4. H. Liu, H. Zhang, R. Ma, Composite NDT methods [J]. J. Nondestr. Test. **25**(12), 631–634 (2003)
5. P. Nivesrangsan, J.A. Steel, R.L. Reuben, AE mapping of engines for spatially located time series [J]. Mech. Syst. Signal. Process. **19**(5), 1034–1054 (2005)
6. J. Yu, M. Ding, Experimental research on acoustic emission signal transmission characteristics of composite materials [J]. J. Electr. Contr. **16**(8), 107–108 (2012)
7. X. Zhou, H. You, Y. Cheng, Ultrasonic attenuation model of porous carbon fiber composites [J]. Acta Materiae Compositae Sinica **14**(3), 99–105 (1997)
8. W. Guan, Y. Tao, Z. He, Acoustic wave propagation and attenuation of thick wall and thin wall components [J]. J. Pres. Ves. **8**(1), 48–49 (1991)

Research on the Acoustic Emission and Metal Magnetic Memory Characteristics of the Crane Box Beam During Destructive Testing

Zhanwen Wu, Gongtian Shen, Junjiao Zhang, and Yuntao Li

Abstract In order to achieve rapid detection and localization of defects in a crane box beam, we used acoustic emission technology (AET) and metal magnetic memory technology (MMMT) to obtain the propagating characteristics of artificial defects during destructive testing on the crane box beam. The AE sources of crack growth and plastic deformation could be located accurately on the box beam by using the AE linear location method. We analyzed the AE location event number of the AE sources; the AE location events of the crack growth were produced at a rate exceeding 85 % in the first loading process. We obtained the changing curve of the magnetic field intensity Hp value of the MMMT signals with the load; when the load was increased to 8 t, the Hp had a substantial increase, with a maximum of about 2,000 A/m. The results indicate that both the AET and MMMT could reflect the severity of the defects, but the AE is more sensitive and could provide dynamic monitoring of the structural changes.

1 Introduction

The box beam is one of the most common structures on a crane. Cracks are among familiar faults in crane structures [1]. The nondestructive testing techniques (NDT) ordinarily used in cranes include eyeballing, ultrasonic, stress testing, and so forth [2, 3].

The acoustic emission technology (AET) has many advantages in the testing of big, important, and complex structures, such as being sensitive to active defects and monitoring the whole structure or equipment in one loading test [4]. The metal

Z. Wu (✉) • G. Shen • J. Zhang • Y. Li
China Special Equipment Inspection and Research Institute, Beijing 100013, China
e-mail: wzw_1980@163.com

G. Shen et al. (eds.), *Advances in Acoustic Emission Technology: Proceedings of the World Conference on Acoustic Emission-2013*, Springer Proceedings in Physics 158,
DOI 10.1007/978-1-4939-1239-1_39,

magnetic memory technology (MMMT) is an NDT method that uses the magnetic mechanical effect of ferromagnets to determine stress-concentrated positions by inspecting the leakage magnetic field strength of a metal component and further determines welding defects in accordance with the stress concentration [5].

In order to achieve rapid detection and localization of defects in a crane box beam, the two NDT methods of AET and MMMT were used to obtain the propagating characteristics of artificial defects during destructive testing on the crane box beam. We compare and discuss in this chapter the signal characteristics of the AET and MMMT, which were conducive to assessing the structural integrity of the crane.

2 Experimental Scheme

In this test, we designed a box beam specimen for the destructive testing, and the artificial defects were made on the surface of the specimen. Also, we prepared the loading procedure for the test.

2.1 Dimension of the Box Beam

The box beam specimen was welded by Q235 steel plates, and the size of the specimen was 5,800 × 300 × 200 mm. The artificial defects were prefabricated on the bottom cover plate of the box beam. The load was put on by a three-point bend. The shape and dimensions of the specimen are shown in Fig. 1.

2.2 Instruments

The instruments used for the testing included the hydraulic pressure testing machine, the AE system, and the stress concentration TSC-1 M-4 tester. The hydraulic pressure testing machine used in the bending test was YE-5000. Its maximum capacity is 5,000 kN.

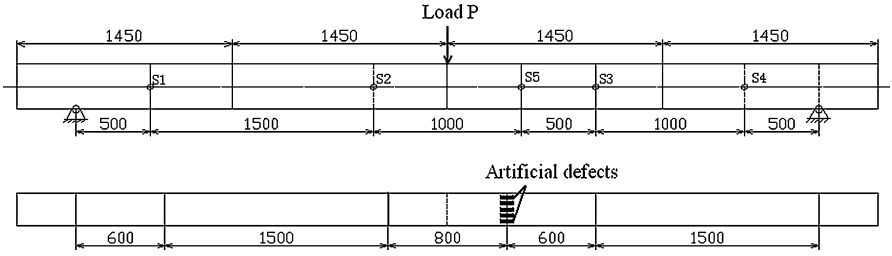

Fig. 1 Dimensions of and sensor arrangement for the box beam (mm)

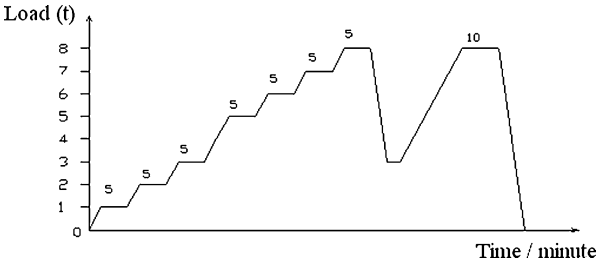

Fig. 2 Curve of the loading procedures

A fully digital multichannel AE system series AMSY-5 was used, including sensors, preamplifiers, computer software, and cables. In the test, the VS150-RIC and VS900-RIC model sensors and the AEP4 preamplifiers were used to acquire the AE signals from the specimen. The gain of the preamplifier was 34 dB. Sensors S1–S4 were arranged on the plate; their model was VS150-RIC. The arrangement of the sensors is shown in Fig. 1.

A tester of stress concentration TSC-1 M-4 was used to measure, record, and process diagnostic data about the stress–strain state of structures. The tester had four flux-gate transducers and its range of Hp measurements was ±2,000 A/m.

2.3 Loading Procedures for the Testing

The load was applied and gradually increased (see the loading procedures in Fig. 2). The AE system was used to monitor the AE signals of the box beam throughout the destructive testing, and the MMMT was applied while the load was held for 5 min.

3 Results and Discussion

During the destructive testing, we obtained the AET and MMMT characteristics of the artificial defect area on the box beam. The results of both methods are discussed next.

3.1 AE Parameters and Location Characteristics

In the test, a large number of AE signals were produced as the artificial defects propagated, and their number increased as the load was increased. Figure 3 shows the AE parameter distribution of sensor S2 throughout the load time.

From Fig. 3, we know that the maximum number of AE signals appeared during the loading process from 7 to 8 t. The AE signal energy rate and cumulative ring counts were increased as the load increased too. The maximum value 10.5 μV of the

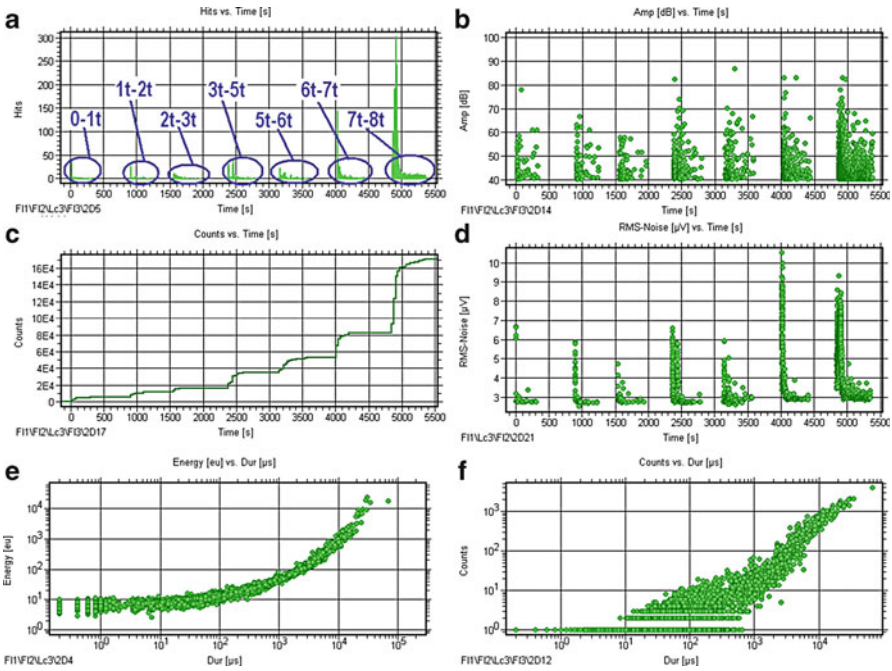

Fig. 3 AE parameter distribution of sensor S2: (**a**) distribution of AE hits vs. time; (**b**) distribution of AE amplitude vs. time; (**c**) accumulation of AE counts vs. time; (**d**) distribution of AE RMS-noise vs. time; (**e**) association graph of AE energy vs. duration; (**f**) association graph AE counts vs. duration

root-mean-square voltage (RMS) appeared during the loading process from 6 to 7 t, which indicated that the obvious yield phenomenon appeared when the load was greater than 6 t.

Mainly two AE sources appeared during the test: cracking and metal plastic deformation. Figure 4 shows the linear location of AE events both in applying the loading and in holding the load. The AE events, which were produced by the two AE sources, could be located during the test. Before the testing, the artificial defect area, which was located from 80 to 110 cm in the linear location map, was tested. According to the AE location area, the AE sources could be divided primarily into two areas: the plastic deformation area from 40 to 70 cm, and the crack growth area from 80 to 110 cm. The statistics of AE location event number in the two areas are shown in Table 1.

From the AE location events shown in Table 1, we knew that many AE source location events appeared in the crack growth area when the load was applied from 3 to 8 t the first time, but only a few AE location events appeared the second time, from 3 to 7.9 t. More than 85 % of the AE location events of the crack propagation are produced during the first loading.

When the load exceeded 7 t, many AE location events appeared in the plastic deformation area. Also, there were numerous AE location events in the second

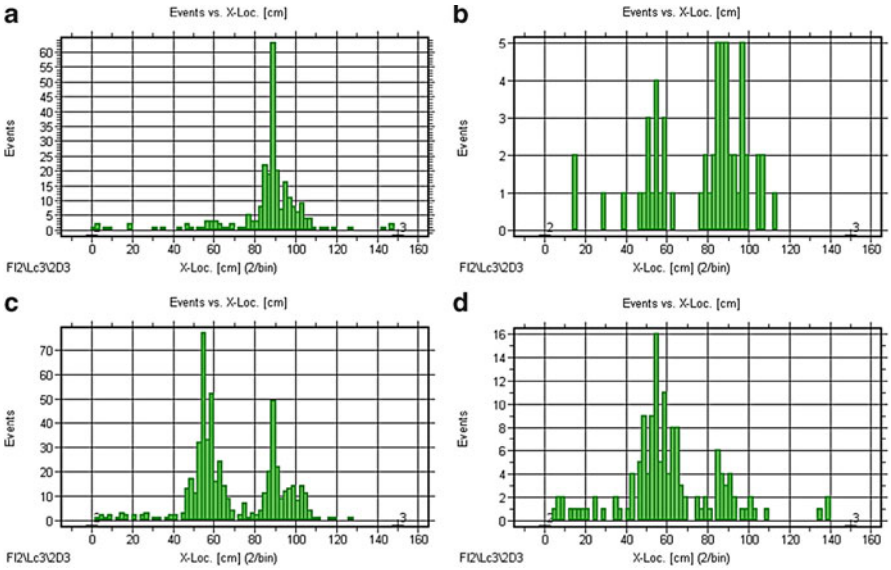

Fig. 4 Linear location of AE events: (**a**) applying the loading from 6 to 7 t; (**b**) holding the load at 7 t; (**c**) applying the loading from 7 to 8 t; (**d**) holding the load at 8 t

Table 1 Statistics of the AE location event number in the AE sources (1 t ≈ 10 kN)

	Number of location events in the AE source			Number of location events in the AE source	
Loading (*t*)	Crack growth	Plastic deformation	Holding the load (*t*)	Crack growth	Plastic deformation
0–1	10	1	1	3	2
1–2	8	1	2	2	1
2–3	11	4	3	5	1
3–5	139	9	5	12	4
5–6	133	10	6	22	4
6–7	201	20	7	34	15
7–8	197	308	8	25	88
8–3	17	5	3–7	13	4
7–7.9	63	605	7.9	73	852

loading from 7 to 7.9 t. In the testing scene, we observed that there was deformation in the side plate of the specimen when the load was applied from 7 to 8 t in the first loading. In the second loading from 7 to 7.9 t, there was obvious local buckling in the plastic deformation area. This shows that while the local buckling of elements occurred, many AE events occurred.

Figures 5 and 6 show the waveforms and frequency spectra of AE source signals for both the crack growth and plastic deformation; they were acquired by sensor S5,

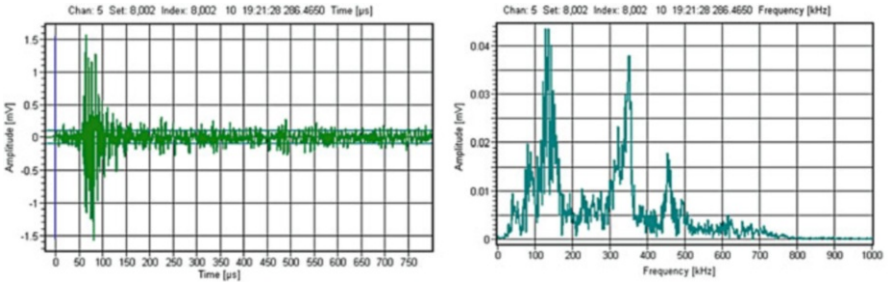

Fig. 5 Waveforms and frequency spectrum of AE signal of crack growth

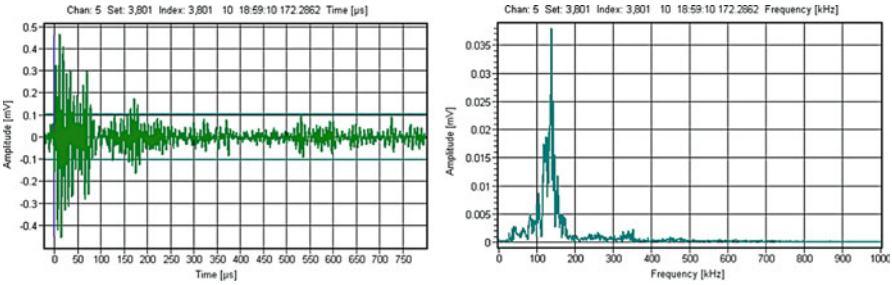

Fig. 6 Waveforms and frequency spectrum of AE signal of plastic deformation

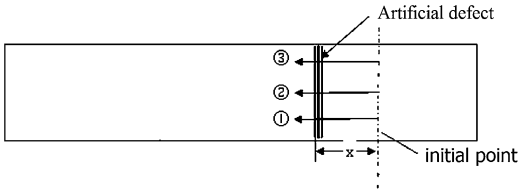

Fig. 7 Testing path for the MMMT

the VS900-RIC model sensor. For the signal of the crack growth, the frequency spectrum distributes widely from 100 to 500 kHz, which has peak values near 130, 330, and 450 kHz. For the signal of the plastic deformation, the frequency spectrum mainly distributes from 100 to 200 kHz, with the peak value near 140 kHz.

3.2 Metal Magnetic Memory Characteristics

The MMMT was applied while the load was held during the loading process, and the magnetic field intensity Hp of the artificial defect area was collected. There were three testing paths ①, ②, and ③ for the MMMT, as shown in Fig. 7. Figure 8

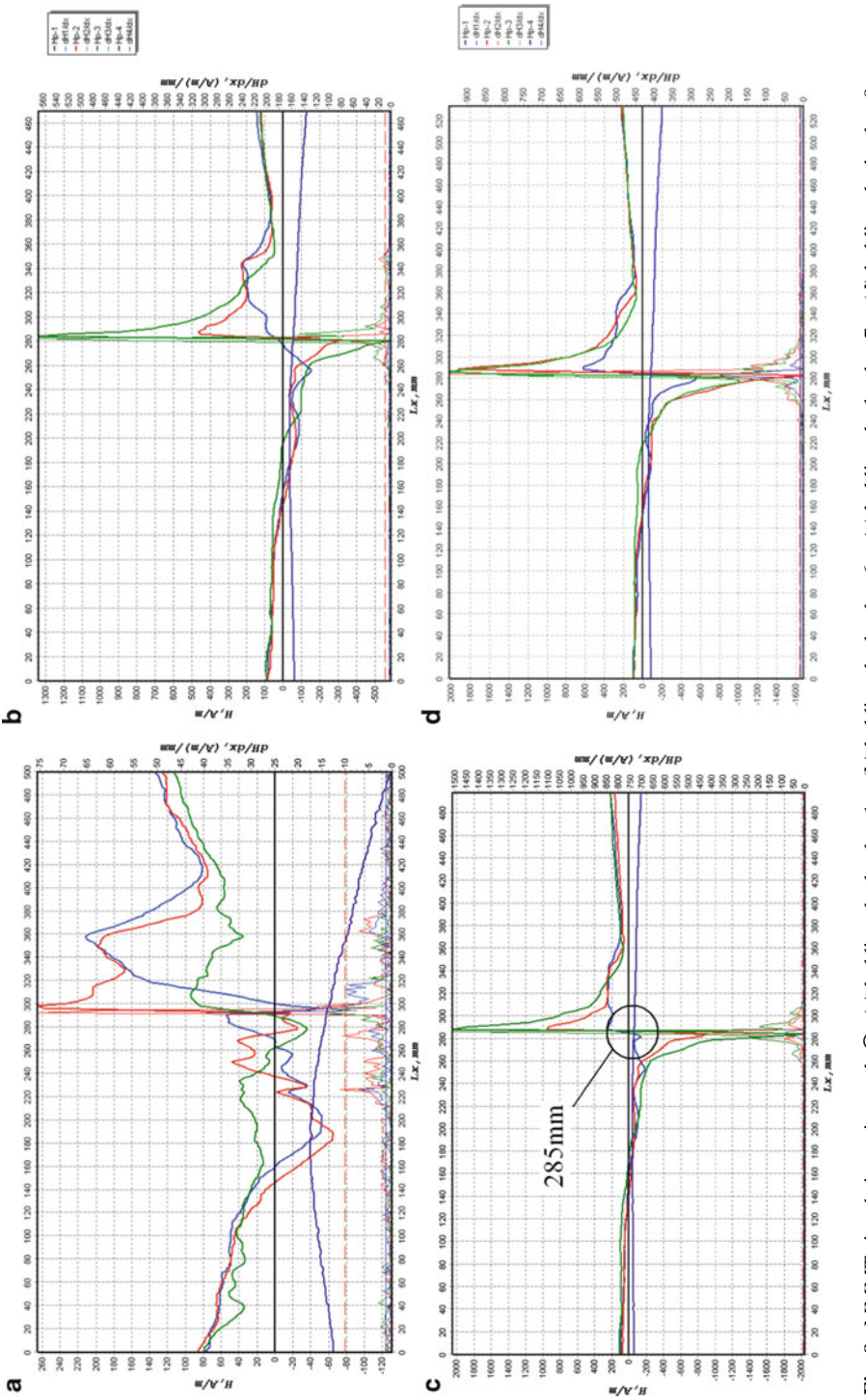

Fig. 8 MMMT signals in testing path ①: (**a**) holding the load at 1 t; (**b**) holding the load at 6 t; (**c**) holding the load at 7 t; (**d**) holding the load at 8 t

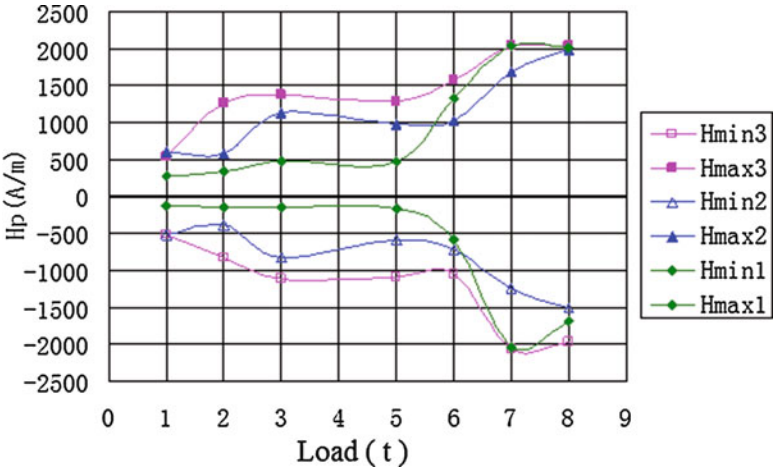

Fig. 9 Hp varies with the load in the artificial defect area

shows the MMMT signals in testing path ①, while Fig. 9 shows that the magnetic field intensity Hp varies with the load.

Hmin1 and Hmax1 respectively show the minimum and maximum values of the Hp in transducer 1. As Hp vs. load in the artificial defect area shows in Fig. 9, when the load was increased from 1 to 3 t, the Hp value rapidly increased. When the load was at 3–6 t, the Hp value was at a higher level, about 1,400 A/m. Finally, when the load was increased from 6 to 8 t, the Hp had a substantial increase, with a maximum of 2,000 A/m, which indicated the stress concentration significantly. That also showed the severity of the defects, which is similar with the AE testing results.

4 Conclusions

Our research revealed the following:

1. The results of both the AET and MMMT could reflect the severity of the defects, but the AE is more sensitive and could provide dynamic monitoring of the structural changes.
2. More than 85 % of the AE location events of the crack propagation are produced in the first loading process, which shows the importance of this stage for gathering AE data.
3. While local buckling of elements occurred, there were a large number of AE signals continually in the plastic yield area, and the AE events could be located.

Acknowledgment This study was financially supported by China's 12th Five-Year Science and Technology Supporting Project no. 2011BAK06B05.

References

1. Z. Zhao, G. Sun, Faults distribution of port cranes' metal structure [J]. J. Wuhan Transport. Univ. **23**(6), 679–680 (1999)
2. Y. Wu, G. Shen, S. Ge, Nondestructive testing of lifting appliances [J]. Nondestr. Test. **28**(7), 367–372 (2006)
3. R.D. Gordon, F.F. Kevin, et al., Assessing the structure integrity of crane booms using acoustic emission [J]. EWGAE 2002, 25th European Conference on Acoustic Emission Testing, Prague, Czech Republic, 2002, pp. 11–13
4. Z. Wu, Research on source characteristics and pattern recognition of acoustic emission for crane [*D*] (Wuhan University of Technology, 2008), pp. 1–17
5. J. Ren, J. Lin, *Metal Magnetic Memory Testing Technique* (China Electric Power, Beijing, 2000), p. 12

Research into the Possibilities for Monitoring Technical Conditions of Underground Pipelines Using Acoustic Emission

K. Paradowski, A. Zagorski, J. Plowiec, M. Ciesielski, and M. Bardadyn

Abstract Non-destructive testing (NDT) is of significant importance when it comes to safety evaluation of underground pipeline utilisation. In addition to regular NDT, an intelligent piston is used in a case of great diameter pipelines, although its usage is not always possible. In this respect, the results from monitoring underground pipeline defects with Acoustic Emission testing (AE) were presented. AE laboratory research was carried out to develop a methodology of measurements that could be applied in the real technological conditions. The obtained results prove the utility of AE testing in localization and monitoring defects in underground pipelines. A part of a research was carried out in real technological conditions. As a result, new guidelines were set up for scientific researches on detection and localization of material defects in underground pipelines in operating conditions. For the purpose of carrying out a project of the transport module for selected acoustic sensors was designed, which also had been equipped to a camera for visual inspection. The system for testing was additionally equipped with modules of alert notifications and remote desktop.

1 Introduction

The non-destructive testing (NDT) has become in the recent years an indispensable technique for assuring safe operation of pipelines. In the case of new large diameter pipelines NDT are carried out by smart pistons. In the case of small diameter and the pipelines already in service for a long period of time, the use of smart pistons is

K. Paradowski (✉) • A. Zagorski • J. Plowiec • M. Ciesielski • M. Bardadyn
Department of Materials Science and Engineering, Warsaw University of Technology, Woloska 141 Street, Warsaw 02-507, Poland
e-mail: kparadowski@inmat.pw.edu.pl

G. Shen et al. (eds.), *Advances in Acoustic Emission Technology: Proceedings of the World Conference on Acoustic Emission-2013*, Springer Proceedings in Physics 158,
DOI 10.1007/978-1-4939-1239-1_40,

difficult and sometimes impossible. In this context, the paper presents results of the research on a system utilising acoustic emission (AE) for monitoring defects in underground pipelines [1–3]. The research on the original system for AE monitoring system aimed at this stage at obtaining laboratory data providing foundations for the results of measurements carried out in industrial environment.

The results prove the possibility of AE monitoring of the defects in underground pipelines. However, the efficiency of such a method depends on the material of the pipeline, type of the transported medium and parameters such as flow, pressure and velocity. Due to the signal analysis, the ability of leakage identification and the accuracy of the location can be improved [4–6].

2 Methods

2.1 Laboratory Tests

The research work was performed in the laboratory and industry conditions. The laboratory tests were done with the pipeline shown on Fig. 1. The laboratory pipeline was constructed from parts allowing to variety of geometric structures. To simulate real conditions, artificial defects were created in the material. The plate with artificial defects [7] was located in a module which can be mounted in different positions with relation to the pipeline.

This allowed for the detection of signals passing through the liquid or the gas. The valves and the fittings allowed for filling the pipeline with liquid or inert gas. The construction allowed for the introduction of acoustic sensor into the pipe and detecting the acoustic emission signals during the test from the interior. The pipeline construction assumed the possibility of using the knees 45° and 90°. Moreover, during the study a transport module for acoustic sensors was introduced into the interior of the pipe.

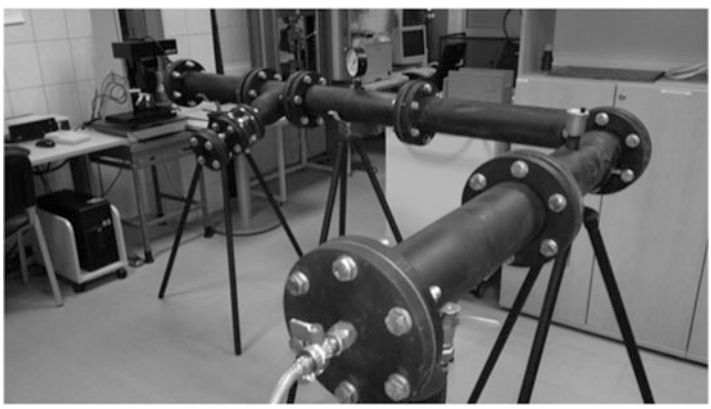

Fig. 1 The pipeline constructed for laboratory testing

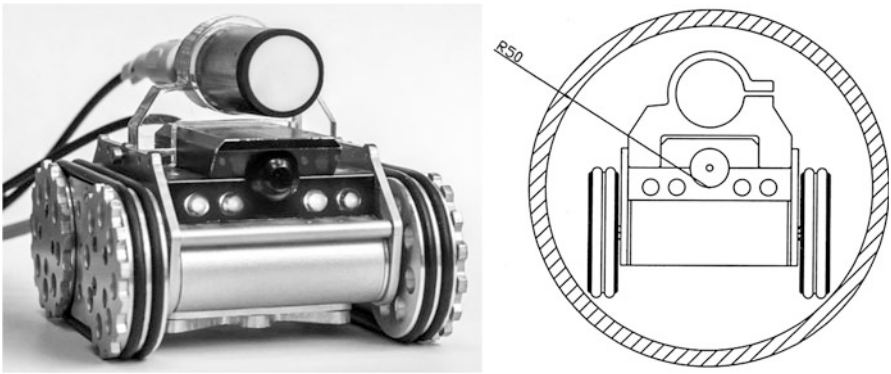

Fig. 2 PipeScan1 inspection robot with integrated AE sensor, the view in a tube with a diameter of 100 mm

For the purpose of this project, a transport module was constructed in the form of the inspection robot as shown in Fig. 2. In front of the robot, a monochrome camera and LED illuminators were placed. Choosing a monochrome camera is influenced by the conditions occurring in the pipelines. Such cameras have better contrast and higher sensitivity than colour cameras. The robot was equipped with fastening to the AE sensors used for testing pipelines. AE sensor can be mounted over the robot. The bracket was made of PMMA. The second fastening system is the system fastened to the rail screwed under the robot. Sensors can be set at different angles.

Developed for the purpose of the project, a mobile robot has electric drive and tracked chassis. The base platform has dimensions of $100.17 \times 73.71 \times 49$ mm. The clearance is 10 mm. The robot is driven by two miniature DC motors with planetary gears supplied by 12 V voltage. The 37 mm vehicle wheels are powered by engines located on both sides. Seals were arranged between the wheels and the body cover to prevent leakage of fluid to the interior of the body. The drive wheels are connected to the tensioning wheels via two O-rings with a diameter of 3 mm. This type of track drive is quiet, reliable and works well in polluted environments. Robot body was made of aluminium. Elements connections are protected with silicone technology.

Mobile base moves on four wheels with fixed geometrical arrangement. Two wheels on each side are coupled and driven by one of two DC motors, which allows differential control of the direction of motion. The base is also equipped with a camera with illumination and the image is transmitted to the control panel which makes it easy to control the robot and localise any defects.

The control panel is equipped with a set of buttons and an analogue joystick which provides smooth and precise control of speed and direction of movement of the mobile base. The text display indicates the currently set traffic speed limit, and the LCD screen shows image from the camera mounted on the robot (Fig. 3). The control panel includes connectors used for connecting to a PC. It is possible to control the movement of the robot from a computer, as well as view and record an

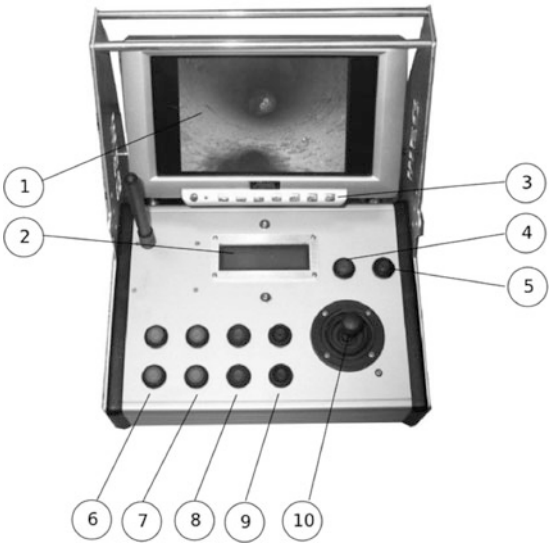

Fig. 3 Control panel: *1*—LCD monitor, *2*—panel LCD (displaying driver options), *3*—control LCD display, *4*—main control switch, *5*—robot camera switch, *6*—speed settings, *7*—controller settings, *8*—self-devices settings, *9*—additional driver options, *10*—manual control joystick

image from the camera to your computer. The recording of the camera is an additional valuable record of the conduct of the study. Robot and control panel are connected by wires that provide power to the motors, by power cables and signal camera cables. The connection with the robot by a cable is widely used because of its reliability and the ability to draw the robot from any installation in the event of failure or loss of power.

Remote Vision application for controlling the PipeScan1 is a software designed strictly and exclusively to the controller and the PipeScan1 robot. The software runs without installation on a PC Windows XP/7 with installed Microsoft .NET 3.5 or higher. The software requires a connection to the controller via serial connection (required USB/RS232 converter) and via a video capture device—USB frame grabber. When you connect two USB peripherals, it is necessary to find their ID in the system and complement CAM.txt (e.g. 0) configuration files and COM.txt (e.g. COM6) in the same way. Once the software is set correctly after you run it, the software will automatically connect and display an image.

2.2 Industrial Research

The industrial research was focused on measuring acoustic emission during normal operation of pipelines and gas pressure test. The research was carried out on the 600 m long underground pipeline. During the study different types of sensors were used, which were mounted directly on the surface of the pipeline and through the waveguide (Fig. 4).

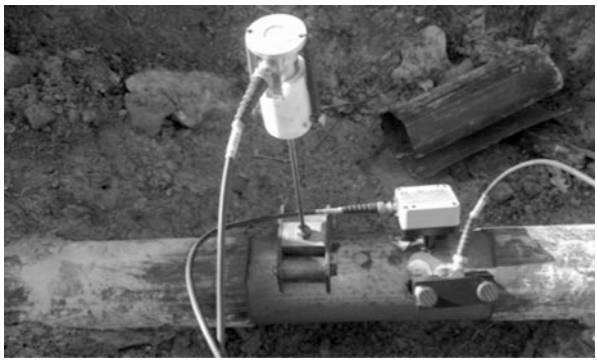

Fig. 4 The arrangement of the AE sensors on the surface of pipeline

The scope of work included the measurement of acoustic emission method in two stages. The initial test was carried out during normal operation and the next step was done during the exploitation of the pipeline during increased pressure [8]. The medium transported by the pipeline was natural gas. All AE tests were performed using measuring system, software and sensors (VS30-VBT, VS30-V, VS30-SIC) of Vallen Systeme GmbH from Germany.

3 Results

3.1 Laboratory Tests

For the study the artificial leakage defects were created, the example of which is shown in Fig. 5. The analysis of AE signals revealed the possibility of the comparison the signals generated by the air and water [9]. The results of analysis are shown on Fig. 6.

The laboratory studies showed that it is possible to detect acoustic signals with an AE sensor located inside the pipeline. The type of medium which fills the pipeline has a significant impact on the detected acoustic signals. In the case of a heterogeneous medium the proportion of filling liquid to gas phase also counts.

The analysis of the laboratory test results showed that there was no significant difference in the RMS parameters, AE amplitude and others of the signals detected by sensor inside and mounted on laboratory pipeline (Fig. 7).

3.2 Industrial Research

It was observed that during tests on real underground pipeline, in contrast to the sensors directly mounted on the pipeline for those which were mounted with the waveguides, only a small area is needed to allow sufficient contact with the surface.

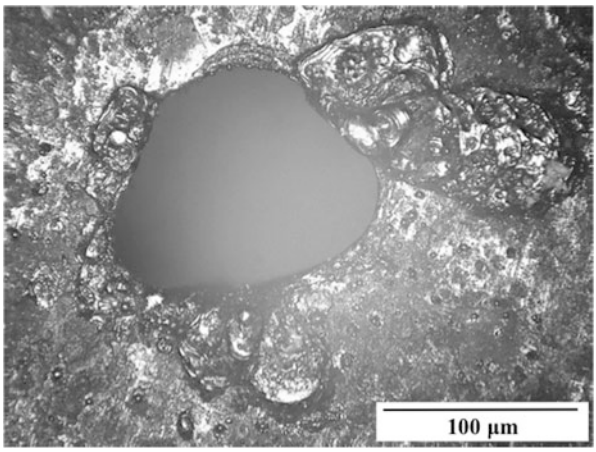

Fig. 5 The artificial defect simulating a leak in the pipeline

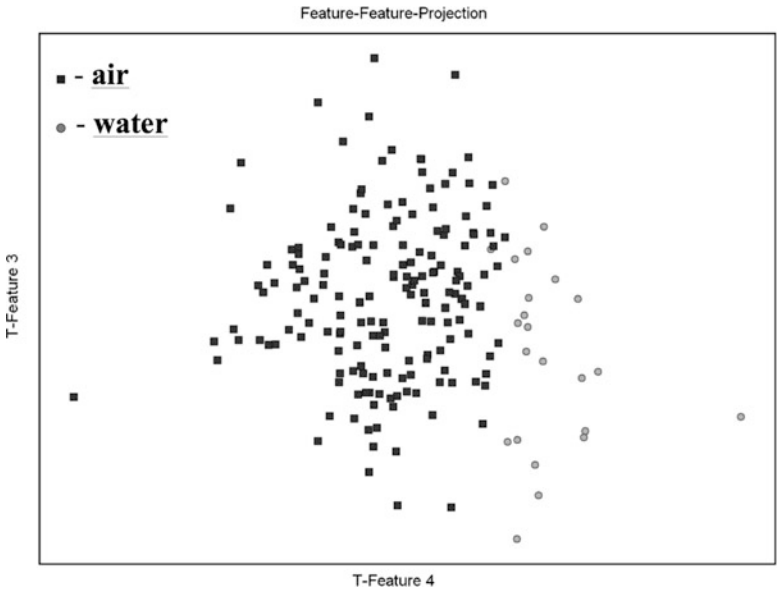

Fig. 6 The classification of AE signals identified as air leakage, compared with the signals from water

This is important when there is limited access to the test area and there is a possibility of flooding. Additionally, waveguides might be fixed to the underground pipeline (for example by welding), without further need for excavation. In order to attenuate the acoustic wave, the low frequencies sensors should be mounted about 50 m from each other. The cathodic protection should be turned off during the test. Particular attention should be paid to stray electrical currents. They have a significant impact on the acoustic noise during testing. The AE active source was located

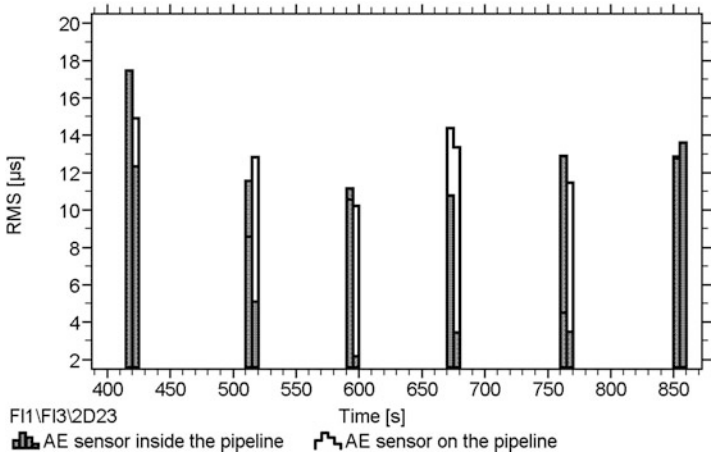

Fig. 7 The results of AE signals recorded during the subsequent simulated leakage by artificial defect. The analysis was performed for parameter comparison of RMS signals recorded by the sensor located inside the pipeline and the sensor mounted on the pipeline

as a result of the performed studies. Their verification has shown that the source of the increased acoustic activity is a thinned, due to local corrosion, pipeline wall (Fig. 8).

During the field studies, tests were carried out for different bandwidths needed to transmit remote desktop of the unit controlling measurement data acquisition. Tests have shown that the results are dependent on the degree of development of software visualising online acoustic emission measurement. In the case of using possibilities of Vallen Company VisualAE software, when the number of visually presented information is developed, to ensure efficient use of the monitoring system, a bandwidth of 1 Mbps is required. If the amount of information is small (i.e. it consists of a few basic charts allowing to slightly control the course of the study), a satisfying bandwidth level is 80–150 kbps.

Tests of the proposed software which provides the best compression and the speed of data transmission from remote desktop of control unit by measurement data acquisition had been carried out in various field conditions, where the transmission bandwidth ranged from 100 kbps to approx. 1 Mbps. The software test results were positive and satisfactory for persons performing simulated acoustic emission measurement.

It should be noted that prior to the scheduled study, it is necessary to determine the transmission capacity of data sent by the system, not downloading capacity. The transmission capacity (i.e. upload) can be many times lower than wireless data downloading capacity. This relationship was demonstrated in tests of bidirectional data transfer between remote desktop of control unit by measurement data acquisition and monitoring client.

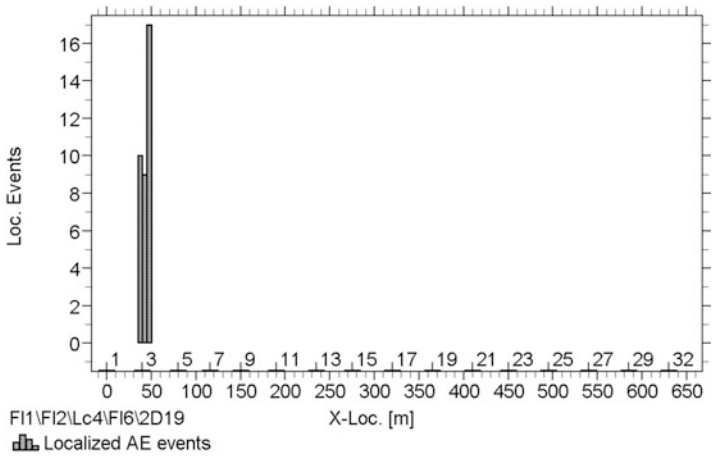

Fig. 8 Localised and verified AE active source during gas pressure test on the underground pipeline. Linear location of AE sensors

During the verification of connecting in the absence of a permanent Internet connection, it was found that the easiest way to do so is to check the bandwidth of the signal level on the mobile phone. The experience gained from the implementation of this work, inter alia, leads to the conclusion that for the measurements with no access to a permanent Internet connection it is necessary to take into account the need to use the services of various mobile operators. It should also be noted that the possibility of the combination of the wireless link is not limited to the use of mobile networks. In many places there are wired networks (for example, telephone, cable or fibre optic), or wireless services offered by local providers, which can also be used to provide communication with the AE monitoring system. If the AE monitoring system cannot be directly connected to such a network, or use the service (e.g. due to distance or lack of access to cable), it is advised to consider the possibility of making a local wireless network, installed for a specific measurement purpose. Such a network could consist of a router connected to said link or using the said wireless service through which the EA monitoring system would be connected. Particularly the use of a local network using mesh networking transmission technology which enables easy expansion of its range by adding new nodes seems to be promising. In case of nodes with its own power source (e.g. battery or generator), it is also possible to use this solution in remote areas from the telecommunication infrastructure. Global coverage can also be provided by satellite transmission.

During the tests, the correct operation of the GSM/DCS/UMTS directional reinforcement antenna was confirmed. Due to the directional antenna operation, it is helpful to know more about the directions in which transmitters are arranged in relation to the position of the reinforcement antenna. As part of the work and tests, the iMOD-9300-GPRS module was connected with the AMSY-5 system of Vallen Company for the purpose of wireless alarm notification (GSM, GPRS, e-mail). The system has the ability to wirelessly transmit alarm information on exceeding the

selected parameters of acoustic emission signals (amplitude, duration, rise time, energy). iMOD-9300-GPRS was tested with connected AMSY-5 system in field conditions, in selected locations, the results of which were positive, confirming the correct operation of the iMOD-9300-GPRS module.

4 Discussion

The study showed that it is possible, using the method of acoustic emission, to monitor the technical condition of underground pipelines. A major limitation of this method of testing is interference factor of acoustic signals generated by the transported fluid with cathodic protection or stray currents [10]. In the case of AE sensors mounted on the surface of a gas-filled underground pipeline, distance between the sensors should be about 50 m. For the pipes filled with liquid, this distance might be greater. In the study low frequency sensors were useful by using waveguides.

Laboratory tests showed that it is possible to detect leaks by sensors placed on the inside surface of the pipe. It is possible to distinguish the signals from the leakage of gas and liquid. Field studies have confirmed the correct operation of the system under condition of a good mobile network signal. In the case of a weak signal in the test site, it is necessary to use a reinforcement antenna. Before the test, it is required to learn more about the deployment of BTS stations of digital telecommunication network, in order to assess the quality of the available mobile networks.

The controller used in the transport module, which provides extensive control mechanisms, is essential to achieve full autonomy. In many tasks, the robot that should be used would be the one that could fully independently move within the system, collecting and storing measurement data and alerting external system only in specific situations. To do so, the robot must be equipped with a battery and its control system should be developed with batteries handling module. It is important to also provide wireless communication in extremely hostile conditions—in many cases, sample pipelines are made of metal and covered with a layer of soil, which considerably limits the possibility of radio communication. For this purpose, the study would be necessary for the use of long waves or other non-radio communication methods.

Acknowledgment This work was supported by The National Center Research and Development (NCBiR) under Project No. NR15 0050-10.

References

1. K. Paradowski, W.L. Spychalski, M. Ciesielski, A. Zagorski, K.J. Kurzydlowski, Acoustic emission for industrial applications. Technical Workshop VI: Operation of High-Pressure Pipelines in The Aspect of The UDT and The EU, 2005
2. S. Davoodi, A. Mostafapour, Gas leak locating in steel pipe using wavelet transform and cross-correlation method. Int. J. Adv. Manuf. Technol. **70**, 1125–1135 (2014)

3. L. Wei, Z. Laibin, X. Qingqing, Y. Chunying, Gas pipeline leakage detection based on acoustic technology. Eng. Fail. Anal. **31**, 1–7 (2013)
4. R.K. Miller, A.A. Pollock, D.J. Watts, M.J. Carlyle, A.N. Tafuri, J.J. Yezzi Jr., A reference standard for the development of acoustic emission pipeline leak detection techniques. NDE & E Int. **32**, 1–8 (1999)
5. L. Billman, R. Isermann, Leak detection methods for pipelines. Automatica **23**(3), 381–385 (1987)
6. P. Murvay, I. Silea, A survey on gas leak detection and localization techniques. J. Loss. Prev. Process. Indust. **25**, e966–e973 (2012)
7. A. Mostafapour, S. Davoudi, Analysis of leakage in high pressure pipe using acoustic emission method. Appl. Acoust. **74**, 335–342 (2013)
8. A.N. Miseinko, A.A. Sazonov, Use of the acoustic emission method for detecting corrosive damages of technological pipelines. Russ. J. Nondestr. Test. **39**(6), 453–458 (2003)
9. A.J. Brunner, M. Barbezat, Acoustic emission monitoring of leaks in pipelines for transport of liquid and gaseous media: a model experiment. Adv. Mater. Res. **13–14**, 351–356 (2006)
10. V.R. Skalskyi, P.M. Koval, *Some Methodological Aspects of Application of Acoustic Emission*. (Spolom, Lviv, 2007). 336 p

Underground Pipeline Leak Detection Using Acoustic Emission and Crest Factor Technique

Jirapong Lim

Abstract Acoustic emission (AE) technique incorporated with uncomplicated signal processing scheme has been demonstrated for underground water pipeline leakage evaluation in petrochemical industries. This technique employed two units of wide-band acoustic emission sensors that were mounted on both ends of the pipe. Various hydrostatic pressures starting from 0 to 16 bars were applied to the pipe and AE signals from both sensors were captured by a personal computer (PC) via acoustic emission system. The crest factor and AE energy are used to evaluate pipe leakage. Four sections of 20-year-old underground water pipeline in petrochemical plant were tested in the experiment. The test results presented that the proposed signal-analyzing technique, the AE energy and crest factor, can be used to evaluate a leakage pipeline sections from totally four at difference areas in the plant. The test results have been proven by visual inspection when the pipeline has been excavated. Therefore, the advantage of using this technique is that underground pipeline to be excavated for maintenance purpose can be prioritized.

1 Introduction

Underground steel pipeline is the major transportation system, for example, for water fire extinguisher in petrochemical industries. However, many old plants have had problem of pipeline corrosion on high-pressure operating condition causing leakage along the pipeline systems. This may cause jogging pump operated continuously which causes energy loss and may be risky while the plant is in

J. Lim (✉)
Department of Production Engineering, King Mongkut's University of Technology, North Bangkok, Thailand
e-mail: Jir@kmutnb.ac.th

G. Shen et al. (eds.), *Advances in Acoustic Emission Technology: Proceedings of the World Conference on Acoustic Emission-2013*, Springer Proceedings in Physics 158,
DOI 10.1007/978-1-4939-1239-1_41,

Fig. 1 Underground pipeline for fire extinguisher

operation. Therefore, several nondestructive testing methods have been applied for this application to detect and locate underground leakage before excavation for repairing (Fig. 1), due to time consumption and relatively high cost. Three conventional methods are generally used including visual inspection, electromagnetic radar detection, and long-range ultrasonic testing [1].

The early use of AE technology for steel pipeline leakage detection application was reported by R.K. Miller et al. in 1999 at Physical Acoustic Corporation (PAC), USA [2]. Small leakage on a pipe test rig as low as 0.1 g/h was successfully detected and located with 1 foot accuracy by using two different location techniques. However, the real application of industrial environment is relatively difficult to gain accurate result, due to low signal-to-noise ratio. It required high-efficiency AE equipment with complicated signal processing techniques that may not be cost effective in some cases.

Uncomplicated AE system incorporating basic signal processing scheme which has been proposed to assist conventional method is presented in this chapter. The major advantage of using AE technique is that not only it provides sufficient information to evaluate fluid leakage of underground pipeline, but also approximate leakage location can be estimated [3]. This system has been applied and tested in real industry environments. The test results have been proven by visual inspection when the pipe has been excavated.

2 Methods

The experimental setup employs two acoustic emission (AE) sensors that are attached on hydrant branches of an underground pipeline, 350 mm of diameter. Both AE sensors (AE-SS1, Holroyd Instrument, UK) provide wide-band frequency as for leakage AE signal sensing. Output signals from both sensors are amplified by 60 dB preamplifiers. Both amplified signals are transmitted to AE instruments

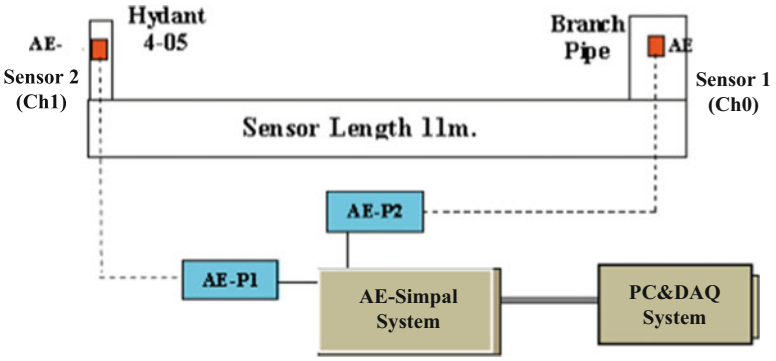

Fig. 2 AE system experimental setup

(Simpal system by Holroyd Instruments, UK) to extract AE parameters. The system is also connected to data acquisition module (NI-PCI111) which is installed in a personal computer. Time domain signals are digitized into the PC memory with the sampling rate of 2 MS/s. To investigate the AE signal generated from leakage, hydrostatic pressure of water is applied to the pipe by using a current system pressure pump. The applied pressure was varied from 0 to 16 bar with increasing step of 8 bar. In each step, the pressure is held constantly for 180 s. The experiment configuration is shown in Fig. 2.

The signals from memory were transferred to data processing software which is used to calculate AE parameters. To characterize pipe leakage, AE crest factor signal processing is applied by analyzing energy from burst period of AE signals. The AE energy (AE_{Energy}) can be calculated by the equation [4]

$$AE_{\text{Energy}}(U) = \left[\frac{1}{R}\int_0^T V^2(t)\mathrm{d}t\right]^{\frac{1}{2}}, \tag{1}$$

where R is the internal resistance of instrument, V is the voltage from AE sensor, and T is the time of the signal period. To identify the event of continuous-type AE signal that is generated by fluid flow leakage, the crest factor is utilized by the equation [5]

$$\text{Crest\_factor} = \frac{V_{\text{peak}}}{V_{\text{rms}}}, \tag{2}$$

where V_{peak} is the peak amplitude and V_{rms} is the average voltage of AE signal energy. Therefore, the proposed signal processing technique is appropriate to field test in real applications due to less complication and required short processing time.

3 Results

The experiment was applied to inspect four sections of petrochemical industry pipeline. This pipeline system has been used for over 20-year-old underground pipeline. As a result of field testing, the acoustic emission activities generated were captured by the both AE sensors which are mounted along above-ground waveguide of the underground pipeline. During the test, AE signals were detected and processed over the data acquisition and signal processing unit as for filtering and enhancement to extract the signature characteristics of the signal in order to correlate to underground pipeline condition. After the extensive calculation of inter-arrival time between sensors, the AE activities emitted during the test can be processed to conventional AE parameters such as peak value, energy of AE signal, and events. Evaluation of overall data and processed AE sources for the underground pipeline was calculated and summarized as in Table 1.

AE signal energy and crest factor can be used to identify the leakage while applying higher pressure level on pipeline system. The AE crest factor results are used to compare between normal pipe and leakage pipe, as shown in Figs. 3 and 4, good pipe and leakage pipe results, respectively.

The crest factors of pipe Nos. 2, 3, and 4 are consistent or increased at higher pressure because higher AE energy and peak may be generated from water flow in the pipeline.

From Fig. 4, the pipe No. 1 presents crest factor that is reduced dramatically at higher pressure level. The AE energy is much higher than normal operating

Table 1 Crest factor from all four pipelines

		AE crest factor	
Pipe no.	Sensor	@8 bar	@16 bar
1	Ch0	48.76	19.36
1	Ch1	8.30	7.79
2	Ch0	38.75	49.61
2	Ch1	16.97	11.84
3	Ch0	36.50	43.60
3	Ch1	7.72	5.58
4	Ch0	56.41	52.78
4	Ch1	7	8

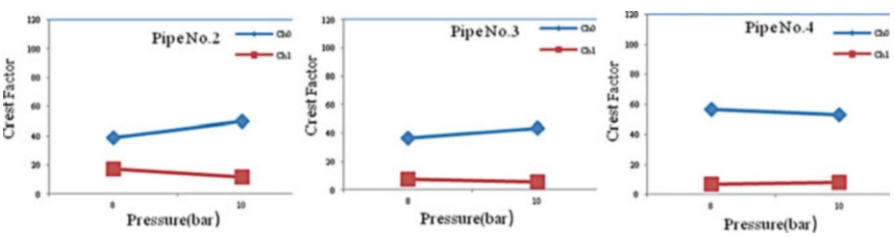

Fig. 3 AE crest factor from normal pipeline

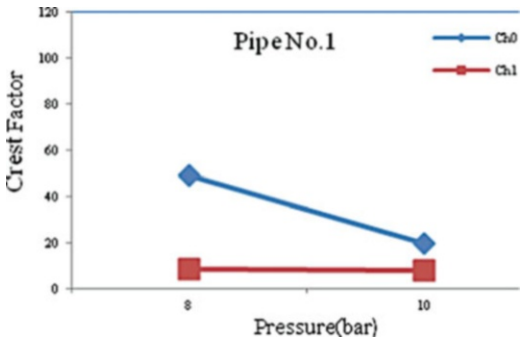

Fig. 4 AE crest factor from abnormal pipeline

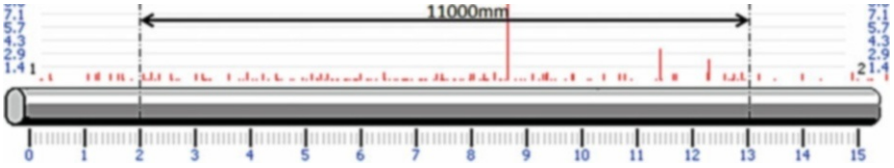

Fig. 5 AE source location plot

Fig. 6 Visual inspection of pipe defected at estimated area

pressure but the peak amplitude is unrelated to the background signal so that the ratio is reduced. The V-rms of background signal at pressure of 16 bar is higher than that of 8 bar. This implies turbulent flow of water leakage between both the sensors. The leakage location was calculated by using AE time of flight and cross-correlation signal processing technique. The results of estimate leakage location are shown in Fig. 5.

The source location plot above shows dense plot area at approximately 9 m and high amplitude at 12 m. Those location results would need to be proved by the visual inspection.

Finally, the results have been proven by excavation pipeline and compared to the AE test results which are correlated to visual inspection as shown in Fig. 6.

The pipe defected locations have been found within accuracy of 0.5 m compared to the AE source calculation plot.

4 Discussions

The acoustic emission technique provides adequate sensitivity to detect leakage of underground pipeline. The AE energy parameter and signal spectrum pattern in time domain can be used to evaluate the pipe condition relatively correctly. The crest factor is a very useful parameter to evaluate underground pipeline condition during high pipe pressure. Fluctuation characteristic of both parameters implies a number of fluid flow leakage during the test. It has been demonstrated that the proposed technique has more advantages than other conventional NDT techniques, including very high sensitivity, less complicated signal processing scheme, and cost-effective system which are relatively suitable for real industrial application.

Acknowledgment The authors would like to acknowledge Acoustomatic Co. Ltd., Thailand, for providing acoustic emission equipment and Tetsugen Jitsugyo Co. Ltd., Japan, for providing visual inspection data and photograph. The conference is financially supported by Panapong Engineering Ltd., Part, Thailand.

References

1. A.S. Reinaldo et al., Pressure wave behavior and leak detection in pipelines. J. Comput. Chem. Eng. **20**, 491–496 (1996)
2. R.K. Miller et al., A reference standard for the development of acoustic emission pipeline leak detection technique". NDT&E. Int. **32**(1999), 1–8 (1999)
3. C.B. Scruby (1987), An introduction to acoustic emission. J. Phys. Instrum. Sci. Technol. **20** 946–953 (K. Elissa, "Title of paper" unpublished)
4. A.A. Pollock, Acoustic emission2-Acoustic emission amplitudes. J. Non Destruct. Test. **10**, 264–269 (1973)
5. C. Pachaud, R. Salvetat, C. Fray, Crest factor and kurtosis contributions to identify defects inducing periodical impulsive forces". Mech. Syst. Signal Process. **11**(6), 903–916 (1997)

Comparison Between Acoustic Emission In-Service Inspection and Nondestructive Testing on Aboveground Storage Tank Floors

Huatian Xu, Xiaopeng Liu, Zhenghong Guo, Yewei Kang, and Hongyuan Chen

Abstract In-service inspection of aboveground storage tanks with acoustic emission technique is accepted by petrochemical industry more and more in the world. PetroChina Pipeline R&D Center has inspected dozens of large storage tanks with acoustic emission technology to evaluate the corrosion situation of tank floors. In this chapter our method is introduced. And the comparison between the results of acoustic emission testing and conventional NDT is described in detail in order to verify the effectiveness and reliability of AE tank floor inspection. Some typical examples are demonstrated.

1 Introduction

The floor of aboveground storage tank (AST) remains a most difficult part of the vessel to inspect for corrosion damage. For a long time, this part of the tank usually uses conventional nondestructive testing (NDT) and the costs of opening the vessel and preparing it for an internal inspection including cleaning, purging, and loss of production availability create a significant financial burden for the tank owner or operator [1]. Moreover, most of the tank floors are still in good quality when they are carried on NDT [2]. So it is important to seek for in-service inspection technologies which can reduce the period of maintenance and cost.

PetroChina Pipeline company has more than 200 ASTs. In order to adapt to the rapid development of national economy, there are more tanks that will be

H. Xu (✉) • Z. Guo • Y. Kang • H. Chen
PetroChina Pipeline R&D Center, Langfang 065000, China
e-mail: huatianxu@163.com

X. Liu
Pipeline Jinzhou Sub-Company of PetroChina Pipeline Company, Jinzhou 121013, China
e-mail: xpliujz@petrochina.com.cn

G. Shen et al. (eds.), *Advances in Acoustic Emission Technology: Proceedings of the World Conference on Acoustic Emission-2013*, Springer Proceedings in Physics 158,
DOI 10.1007/978-1-4939-1239-1_42,

constructed. If it carries on the conventional tank maintenance plan, a lot of money will be wasted. So how to evaluate the corrosion situation of tank floor and provide maintenance guidance for storage tank floors is an urgent problem.

In the late 1980s acoustic emission (AE) technology was first used to assess the corrosion of AST bottoms. From then on, it attracts great attention because it can do in-service inspection. Acoustic emissions (AE) are stress waves produced by sudden release of the elastic energy in stressed materials. When defect-related processes such as corrosion, crack growth, hydrogen blistering, and even leakage take place in and on the tank floor, stress waves will be produced [3]. By piezoelectric sensors mounted on the external surface of tank shell near tank base to detect these stress waves and output electrical waveforms that contain information about the source of emission and through some data analysis methods to analyze the information, the tank condition can be classified to prioritize its maintenance [4]. Acoustic emission testing has many advantages such as overall detection, in-service inspection, and saving money and time [5].

2 Acoustic Emission Testing on AST

PetroChina pipeline R&D center, which belongs to PetroChina Pipeline Company, begins research on AE inspection of tank floor since 2006. Now reliable AE signal acquisition and data analysis methods have been developed. The following steps are used to inspect the AST's floor:

1. Fill oil to the tank to greater than 80 % capacity; turn off all agitators, heaters, and pumps; and keep the tank at rest for a period of 12–24 h.
2. Mount sensors, the number of which depends on tank size, around the circumference of the tank approximately 0.5–1 m from the tank floor and connect them to an AE system. Guard sensors can also be employed in order to filter background noise generated in the upper section of the tank.
3. Check the monitoring conditions, and record AE data at least for 10 h.
4. Pack up equipment, and analyze the recorded data.

Our acoustic emission testing device is MicroSAMOS 24. The number of used sensors is determined by the volume or the diameter of the tank. Table 1 shows the relationship between the number of sensor and volume and diameter of the tank [6].

If the tank has insulation layer, the insulation should be removed by a certain area which is bigger than the sensor, and the anticorrosive paint on the tank shell should be removed to attach the sensor on the tank shell. The evaluation of acoustic emission testing is based on the signal activity of the tank floor and level of AE source. First the level of AE source is determined by the location results of AE events based on the arrival time differences of signals. Then the event activity of AE is determined according to the number of AE events per hour and average energy of AE events. With the above information, the final tank grade is determined. Table 2 shows the meaning of different grades in terms of severity of

Table 1 The relationship between the number of sensor and volume of the tank

TV (10^4 m^3)	1	2	3	5	10	15
TD (m)	28	40.5	45.5	60	80	90
NS	9	12	15	18	21	24

TV tank volume, *TD* tank diameter, *NS* number of sensor

Table 2 Maintenance actions corresponding to each grade

Grade	Severity of corrosion	Action	Time interval
A	Very minor	Retest	5 years
B	Minor	Retest	3 years
C	Medium	Retest	2 years
D	Serious	Open	Within 1 year
E	Very serious	Open	Immediately

corrosion, maintenance action, and the time interval [7]. In the data procession the selection of appropriate parameters according to research achievement and testing experience is very important.

3 Comparison Between Acoustic Emission Test and Nondestructive Testing

Generally our center conducts acoustic emission inspection on tank floor according to our company's tank maintenance plan. Then those storage tanks are opened to do conventional nondestructive testing such as ultrasonic thickness gauge testing. Finally, the acoustic emission test results are compared with the results of nondestructive testing to make our method reliable. Now 65 storage tanks have been inspected by acoustic emission. Statistics of the inspecting result of AE is shown in Fig. 1.

According to Fig. 1, it can be seen that ratings for class B have the largest number, which shows that the majority of inspected tanks have slight corrosion and can be inspected after 3 years later, and no maintenance is needed. The conventional nondestructive testing of tank floor is carried out by professional third party, and the results are reliable.

The comparison results between conventional nondestructive testing and acoustic emission testing are shown in Fig. 2.

Conservative evaluation represents that the results of acoustic emission detection are more serious than the actual corrosion of tank floor. And optimistic evaluation represents that the actual corrosion of tank floor is serious than the results of acoustic emission detection. The suitable evaluation represents that the two results are consistent. Comparison between these two results also includes coating condition after cleaning the tank and the corrosion of tank apparatus. The correct evaluation rate of acoustic emission is 94 %. In a word, the acoustic emission evaluation can provide proper suggestion for maintenance of storage tanks.

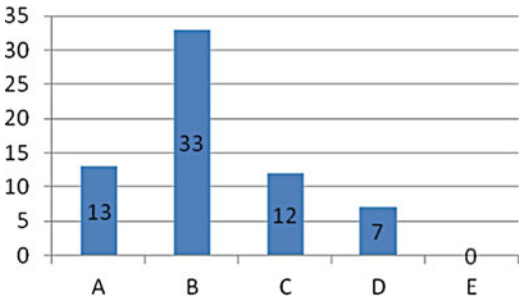

Fig. 1 Tanks rating distribution

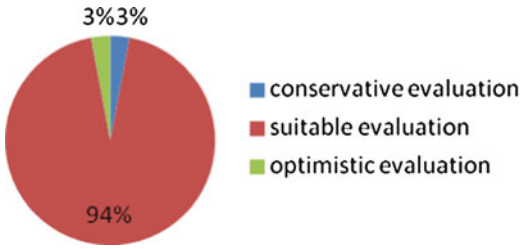

Fig. 2 The correct rate for AE testing

4 Examples of Comparison

4.1 Cases of Suitable Evaluation

1. Case one
   The tank with a capacity of 50,000 m^3 located in northeast of China has been inspected on May 9th, 2010. The grade of the result of AE is A. "A" represents a very slight corrosion of tank floor, and no maintenance should be done. It is better to have a test again 5 years later. Figure 3 shows the distribution of AE corrosion events observed during the test.

   The conventional internal inspection of tank floor is completed by independent third party after AE testing on July 20th, 2010. Its result indicates that the remaining thickness of tank floor is within safety level according to the tank maintenance standard of our company, and no repair is needed.
2. Case two
   The tank with a capacity of 10,000 m^3 located in Beijing had been inspected on June 20th, 2010. The grade of the result of AE testing is C, which means that the corrosion level of tank floor is intermediate and some maintenance should be conducted. The tank was recommended to have AE testing again 2 years later. The subsequent conventional nondestructive testing of tank floor indicates that the thickness of many inner and outer annular plates reaches about 20 % of the original thickness, and the middle plate of tank floor has some corrosion. Finally several pits are repaired.

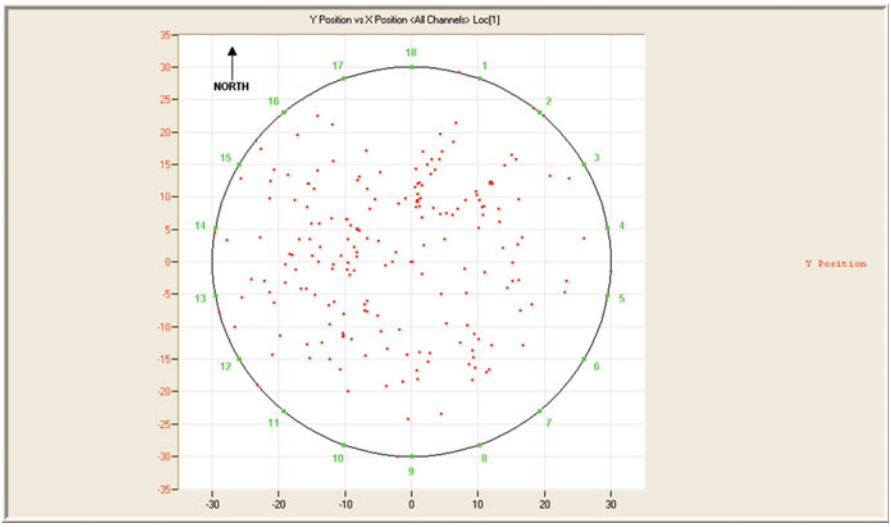

Fig. 3 AE testing result

4.2 Case of Conservative Evaluation

We had inspected a tank with a capacity of 10,000 m^3 located in northeast of China in 2009, and it got a C grade for the AE test. It indicates that the tank has intermediate damage on the tank floor, and little maintenance is needed. But the conventional nondestructive testing shows that the bottom of the tank is in good condition. The result of AE testing is more serious than the real state of the tank. However, during the field investigation after cleaning the tank, we found that the attachments of the tank have bad corrosion, such as the central drain pipes, as shown in Fig. 4. The defect signals from the coating of the central drain pipes also are regarded as the ones from tank floor for AE method. However the conventional nondestructive testing does not consider these factors because it is done after sandblast of tank floor. From this perspective, it is reasonable for the result of AE testing. Generally the conservative evaluation does not affect the safe operation of tank. It just makes the maintenance of tank in advance.

4.3 Case of Optimistic Evaluation

This tank with a capacity of 20,000 m^3 located in northeast of China has been inspected in 2010. The result of AE test of tank floor is B grade. It means minor corrosion on the tank floor and that no repair is needed. However the conventional nondestructive testing shows that tank floor has intermediate damage and one of the

Fig. 4 The coating blister of the central drain pipe

Fig. 5 Corrosion pits on the plate

plates has intense corrosive pits, as shown in Fig. 5. The maximum depth of the pit is more than 3 mm (42 % of the original thickness), and finally this plate is replaced by a new one. Obviously, the results of AE testing are inconsistent with the actual corrosion state of the tank floor. However, during field investigation thick deposition is found on the tank floor, which can decrease the strength of the signals, and have a great influence on the results of AE. When using AE method to assist the maintenance of tank, the optimistic evaluation result should be avoided. But it is a hard task. The inspector should constantly learn knowledge of AE testing and accumulate testing experience.

5 Conclusion

For AE inspection of tank floor some factors can affect the accuracy of AE inspection. The corrosion defect signals from the accessories of the AST can be regarded as from the bottom, and it will lead to a conservative evaluation. And the thick deposition on tank bottom can decrease the strength of signals and lead to an optimistic evaluation. However, keeping most AE evaluation reliable can be a reality if the inspectors have a lot of experiences; at the same time the suitable data analysis method and data acquisition method are adopted. In conclusion, acoustic emission testing has characteristics time saving, low cost, and accurate evaluation. It can evaluate the corrosion of the tank floor, and can be able to provide guidance for tank maintenance.

References

1. J.A. Mejía, J. Hay, V. Mustafa, y J.S. Fe, Aboveground storage tank floor corrosion condition assessment. Avances Investigación en Ingeniería. 12 (2010)
2. Y. Kang, W. Wang, M. Lin, et al., Factors influencing the acoustic emission inspection of aboveground storage tank floor and its counter-measures. *Proceedings of World Conference on Acoustic Emission*, Beijing, 2011
3. P.T. Cole, S.N. Gautrey, Development history of the Tankpac AE tank floor corrosion test. NDT. net **7**(9), 1–12 (2002)
4. Y. Kang, W. Wang, M. Lin, et al., Development status of in-service inspection technologies for above-ground storage tank. *Proceedings of the 2012 9th International Pipeline Conference*, 24–28 September 2012, Calgary, Canada
5. Y. Kang, M. Lin, W. Wang et al., Influencing factors of acoustic emission technique and evaluation reliability in inspection of tank floor. Oil & Gas Storage and Transportation **30**(5), 343–346 (2011)
6. Q/SY 1485–2012. Technical specification for in-service inspection and evaluation of the vertical cylindrical steel welded storage tanks. PetroChina Pipeline R&D Center, Hebei province, China (2012)
7. Y.W. Kang, M.C. Lin, W.B. Wang et al., On the technical trend at home and abroad of in-service inspection for aboveground storage tank floor. Non Destruct. Test. **32**(9), 725–729 (2010)

Acoustic Emission Application for Unapproachable Pipeline Drain Point Leakage Detection

C. Jirarungsatian and C. Jomdecha

Abstract The pipeline drain point which is at an unapproachable location is a problem to check a leakage by common techniques such as soap test and ultrasonic leak test. Acoustic emission is an advantageous technique to be applied for solution to this case. The sensitivity, acoustic attenuation, acoustic signal character, and background noise are the main factors considered in this chapter. The laboratory and field experiments were done for collection of AE signal. In laboratory, the leak rate was simulated by roughly loose an end cap of drain point for 3″ and 6″ main pipe diameter. The characteristics of acoustic signal emitted by leakage and background noise were revealed by time and frequency domain analysis. The experimental results showed that the minimum detectable atmosphere leak rate at 10 m far from a wideband AE sensor was 20 ml/s which has the frequency response at 100 kHz. The acoustic characters of drain leakage and field background noise are the benefits for development of a portable device of leak inspection in the field.

1 Introduction

The pipeline drain point at an unapproachable location, such as over 10 m high pipe bridge and high pipe rack, represents a big problem for leakage testing by frequent techniques as a soap test and ultrasonic probe. At present, scaffold is needed for approaching the drain points; however the preparation cost and time are also increased. There are other detection and monitoring techniques for this case which are the pressure or the flow change monitoring and mass balance techniques [1, 2].

C. Jirarungsatian (✉) • C. Jomdecha
Maintenance Technology Center, King Mongkut's University of Technology
Thonburi, Bangkok 10140, Thailand
e-mail: chalermkiat.jir@kmutt.ac.th

G. Shen et al. (eds.), *Advances in Acoustic Emission Technology: Proceedings of the World Conference on Acoustic Emission-2013*, Springer Proceedings in Physics 158,
DOI 10.1007/978-1-4939-1239-1_43,

However those techniques need large installation investment and time for setting up the system. Acoustic emission was an advantageous technique to be applied for solution to this case [3]. The installation needs only mounting AE sensor on the pipeline without pipe modification. The acoustic signal amplitude and background noise were the main factors considered for AE sensitivity. In addition, the acoustic attenuation and mode conversion were a function of pipe diameter, insulation, pipe material, and pipe joint [4]. The acoustic source of leakage could be assumed as cavitations (liquid media), turbulence flow, and friction [5, 6]. The shape, diameter, and depth of leak hole should be considered for analyzing a leak signal characteristic [7]. This work presents the results of laboratory and field experiments which inform the capability of AE system. The detected AE signals were sensed by wideband transducer sensor with preamplifier and then data acquisition and display on Locan320 (PAC) and spectrum analyzer. The collected AE signals in time and frequency domain were considered to study the character of leakage and background noise. The attenuation factors in the field testing were discussed by the experiments on seven varied pipelines. The benefit of obtained acoustic characters of leakage and field background noise could be used to solve a problem of leak inspection at unreachable location in the field.

2 Experimental Setup

The wideband AE sensor was used to detect a background noise and acoustic signal of leakage which were amplified by 60 dB preamplifier. The AE acquisition unit recorded AE parameters which are count, amplitude, duration, rise time, energy, and hits. The waveform and frequency spectrum were also recorded by a spectrum-analyzing device. The sensor mounting performance was checked by lead-break technique before starting and after finishing each experiment.

2.1 Experimental Setup and Procedure in Laboratory

The attenuation curve of 6″ diameter of seamless steel pipe (same as in the field) was produced to consider the attenuation efficiency. The experiment setup is shown in Fig. 1. The seamless steel pipe was pressured by an air pressure pump and then pressure is held at 5 bars. The background noise was recorded at this condition which was without leakage on pipe and branch cap. The ball valve of branch was fully opened throughout the experiment. The leak was simulated by loosening the cap. The volume leak rate was calculated by pressure drop and time. A leak signal was recorded while the air was leaking at minimum leak rate which could be detected at 10 m away from branch.

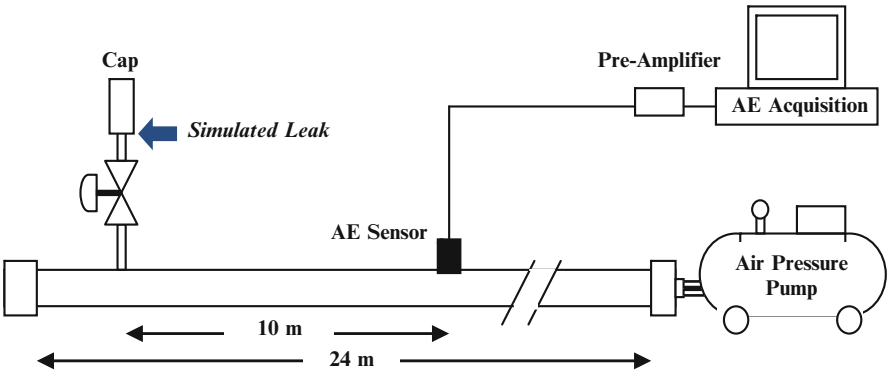

Fig. 1 Experimental setup in laboratory

2.2 Experimental Setup and Procedure in the Field

The AE system was set up the same as in the laboratory experiment on 6″ diameter of seamless steel pipe which was placed 6 m high. The background noise was detected on pipeline which ensured no leak. AE sensor was removed after background noise detection had been done and then was mounted on the pipe which had a leak at the cap for recording a leak signal. The soap test was used to check the leak on the cap.

3 Experimental Results

3.1 Leak Rate Calculations and Estimations

The minimum leak rate which was detected by AE system in the laboratory was 20 ml/s at 10 m away from branch. The leak rate was calculated by Eq. (1):

$$L = [V \times (P_1 - P_2)]/T, \tag{1}$$

where $L =$ leak rate (l/s), $V =$ volume of pipe (l), $P_1 =$ initial pressure (bar), $P_2 =$ final pressure (bar), and $T =$ experimental duration(s). The leaking condition was checked by soap test as shown in Fig. 2. Although the leak rate on the field experiment could not be measured exactly, it could be estimated by using the soap test and then comparing with the bubble size and bubble pop frequency occurrence in the laboratory result which was the same as leakage of pipe cap in the field. Therefore the leak rate in the field could be approximated as also 20 ml/s.

Fig. 2 Soap test on 20 ml/s leakage of pipe cap

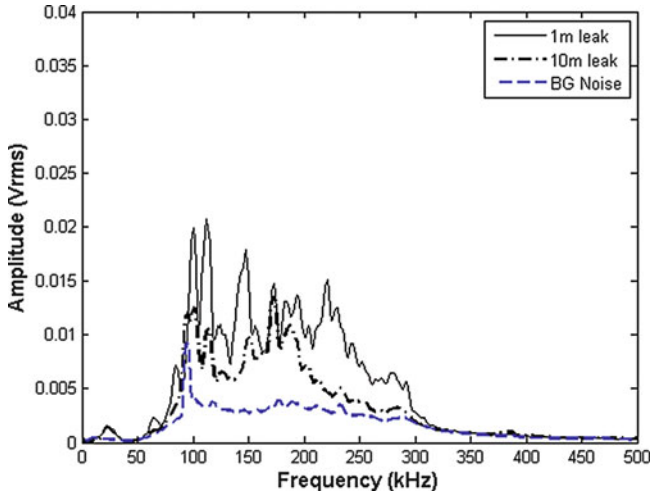

Fig. 3 Result of leak spectrum at 1 and 10 m distance and background noise in the laboratory

3.2 Effective Distance of AE Detections

Two sensor mounted locations (1 and 10 m away from 20 ml/s air-leaking pipe branch) were experimented to study the acoustic attenuation. The acoustic responded signals are shown in Fig. 3 compared with background noise. The laboratory result could be explained as that the effective detectable distance of AE system in laboratory would be 10 m for 20 ml/s leak rate.

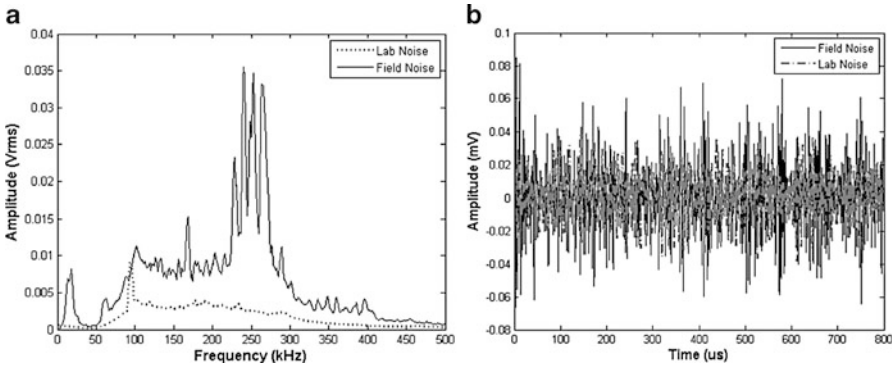

Fig. 4 (**a**) Spectrum comparison of the detected background noise from laboratory and field experiments, (**b**) time domain comparison of the detected background noise from laboratory and field experiments

3.3 Background Noise in the Laboratory and Field Experiment

The field and laboratory background noises (no leakage) were collected on the pipe as shown in the comparison in Fig. 4a, b for frequency and time domain, respectively. The peak response frequency of field was higher than laboratory in all frequency ranges that could be because the field has a mechanical vibration and fluid flow. The interested consideration of laboratory and field background noise could attend on 200–300 kHz frequency range. On the other hand, the difference cannot be seen clearly in time domain.

3.4 Leak Detection in the Field

In the field, the fluid leak rate cannot be measured by a proper device. However it can be estimated by comparison with the simulated leakage in laboratory by peak amplitude and spectrum profile, as shown in Fig. 5a. The comparison result showed that the leak rate in the field could be estimated around 20 ml/s as close to the leakage in the laboratory. The frequency spectrum characteristics of both laboratory and field were the same with 100 kHz responding frequency peak. As in Fig. 5b, frequency spectrum of leakage and background noise in the field noticed that the peak response frequencies differed which were 100 kHz for leakage and 200–300 kHz for background noise.

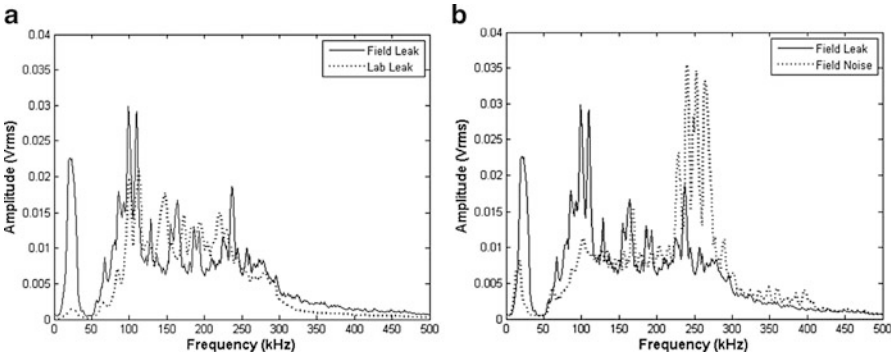

Fig. 5 (**a**) Comparison of AE spectrum from laboratory and field experiments on leak condition, (**b**) AE spectrum of leak and background noise in the field

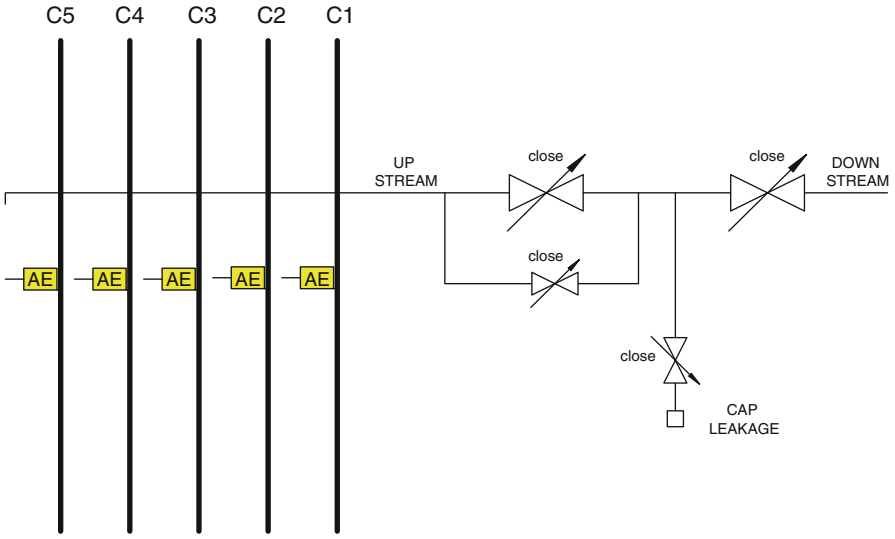

Fig. 6 Background noise detection of five low flow rate pipes in the field

3.5 Analysis of Background Noise in Field

Since the background noise in the field was the most important factor of AE sensitivity for AE application in the field, this work collected the background noise from 26 pipes for noise analysis. The 26 pipes were classified into two groups by fluid flow rate inside the pipe as low and high flow rate lower than 50,000 kg/h and around 2.6–3,000 ton/h, respectively. Figure 6 shows AE sensor locations for collection of a background noise of low flow rate from five pipes (C1, C2, C3, C4,

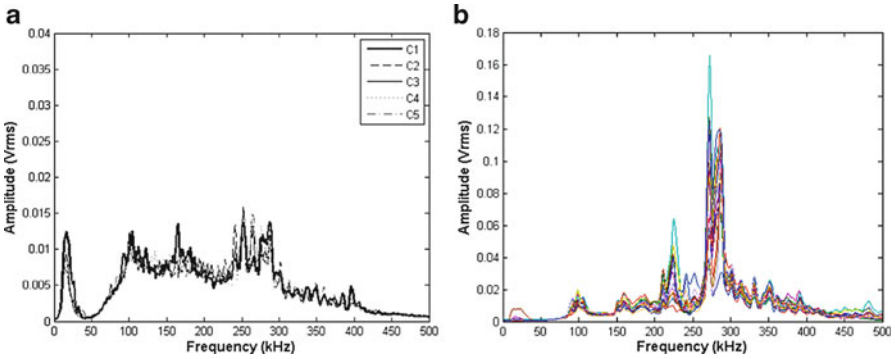

Fig. 7 (**a**) AE spectrum of background noise from five low flow rate pipes in the field, (**b**) AE spectrum of background noise from 21 high flow rate pipes in the field

and C5). These pipes were of the same material and had few differences in diameter. The background noise spectrums are shown in Fig. 7a which notices that they gave the spectrum with no difference.

The results are shown in Fig. 7b. The 21 pipes background noises with high flow rate (2.6–3,000 ton/h) in the field were collected by acoustic acquisition device which highlights the response peak around 200–300 kHz. These peaks did not appear in the case of low flow rate pipe detection and in the laboratory results (no flow). Therefore, the acoustic signals in 200–300 kHz response frequency could be an activities of media flow inside the pipe. However there were other factors which could effect to AE for leak detection.

3.6 Factors of Acoustic Attenuation

This work considered the acoustic attenuation of pipe physical in the field. These experiments were done on the pipe bridge in the field which was no leak. Three physical attenuation factors of pipe were considered as pipe diameter, elbow, and attenuation of branch and valve. The lead break tests were used to simulate the AE signal at six positions on the pipe bridge which are shown in Fig. 8. These experiments were produced on seven pipes which varied the diameter and products. The results are shown in Table 1 which explains that the large pipe diameter gave high wave attenuation. The elbow of pipe would not be effect to the acoustic attenuation which could consider the difference of detected amplitude of lead break at position 2 and 3. However a valve at the branch pipe was an effect of acoustic attenuation because of connecting joint between valve and pipe.

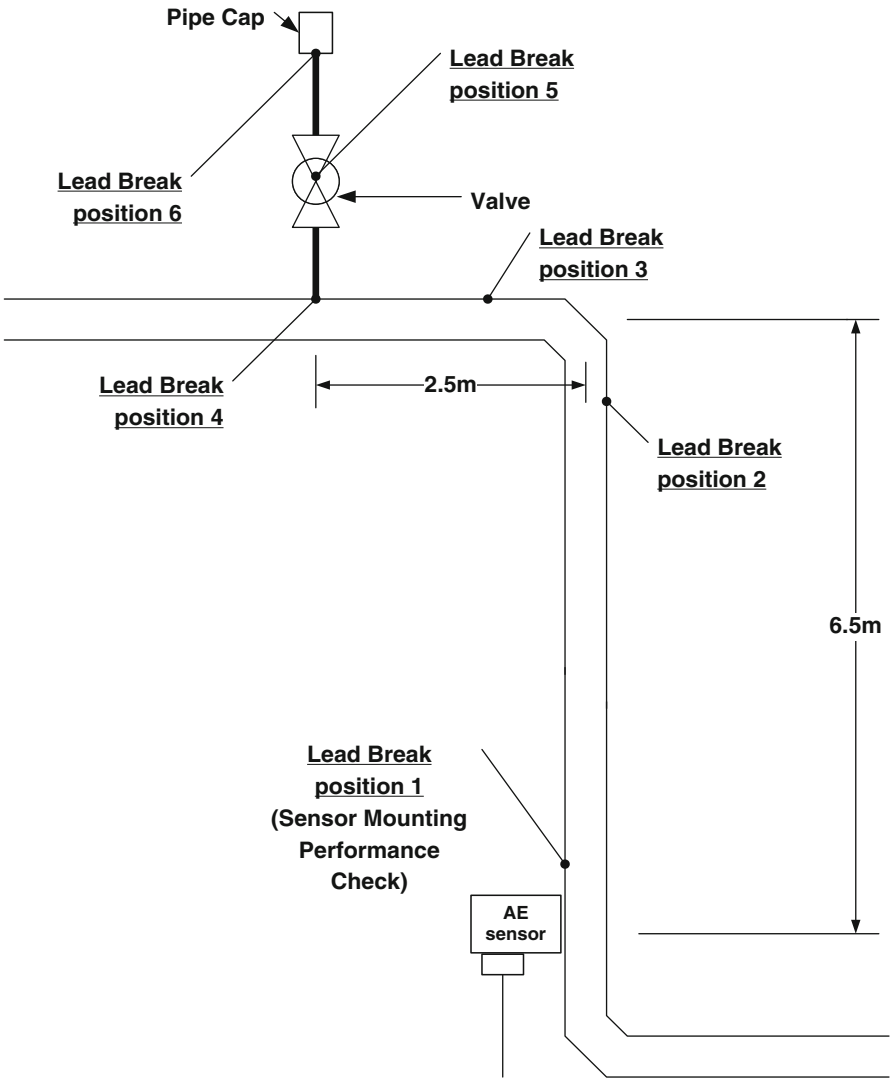

Fig. 8 AE sensor mounting location and lead-break position of attenuation factor experiment on pipe bridge in the field

4 Discussion

The experimental result acquired by the minimum detectable leak rate at 10 m far from a wideband AE sensor was 20 ml per second for atmosphere leakage. The characteristics of acoustic signal emitted by leakage and background noise were identified by frequency response of 100 kHz and 200–300 kHz, respectively, for field application.

Table 1 Results of attenuation factor experiment on seven pipes

Pipe dimension	Product	Peak amplitude (dBae)					
		Position 1	Position 2	Position 3	Position 4	Position 5	Position 6
4″ Stainless pipe	Acetic acid	99	68	67	64	–	–
30″ Steel pipe	Naphtha	98	68	–	–	–	–
8″ Steel pipe	Hydrogenated gasoline	100	72	71	68	–	–
4″ Steel pipe	Vapor	99	88	85	83	65	–
3″ Steel pipe	Octene	96	76	75	73	n/a	71
4″ Steel pipe	Tertiary butyl alcohol	98	80	74	73	66	64
6″ Steel pipe	Nitrogen	99	85	84	83	76	71

The frequency response of product flow could be also 200–300 kHz. The attenuation factors which were considered for AE application in the field were pipe diameter, joint connector, flow rate, and background noise level. In the conclusion of this work shown that AE technique could be effectively applied for leak detection of unreachable pipeline such as the pipe rack on over-head bridge instead using a scaffold. The characteristics of leak signal and background noise are the benefits of this work which could be an important data for next researches.

Acknowledgment This research was supported by the research fund by Rayong Engineering & Plant Service Co. Ltd., Thailand. The authors thank Mr. Sirichai Wijitthongreung and SCG team for the brainstorm to achieve this co-research.

References

1. J. Zhang, Designing a cost effective and reliable pipeline leak detection system. *Pipeline Reliability Conference*, Houston, USA, November 19–22 (1996)
2. M. Pal, N. Dixon, J. Flint, Detecting & locating leaks in water distribution polyethylene pipes. *Proceedings of the World Congress on Engineering 2010 Vol II*, WCE 2010, London, June 30–July 2 (2010)
3. S. Liu, L. Li, J. Cui, T. Li. Acoustic emission detection of underground pipeline leakage. *15th WCNDT*, http://www.ndt.net/article/wcndt00/papers/idn050/idn050.htm
4. W. Wichaidit, Y.H. Joe Au, Effects of the pipe-joints on acoustic emission wave propagation velocity. *The 6th International Conference on Manufacturing Research (ICMR08) Brunel University*, UK, 9–11 September (2008)
5. A.A. Pollock, S.Y.S. Hsu, Leak detection using acoustic emission. J. Acoust. Emission. **1**(4), 237–243 (1982)
6. T. Koivula, On cavitation in fluid power. *Proceeding of 1st FPNI-PhD Symposium, Hamburg*, pp. 382–371 (2000)
7. R.N. Laodeno, H. Nishino, K. Yoshida, Characterization of AE signals generated by gas leak on pipe with artificial defect at different wall thickness. Mater. Trans. **49**(10), 2341–2346 (2008)

Study of Pipeline Leak Detection and Location Method Based on Acoustic Emission

Xinying Wang, Zhiwei Jiang, Haiqun Chen, and Kaiquan Wang

Abstract Under laboratory conditions, pipeline leak detection model has been established. We studied the effect of the internal pressure, leakage flow, the propagation distance, and different pipeline characteristics on leakage acoustic emission signal attenuation, and finally used the correlation analysis method to locate the leak point. The results show that the greater the pressure inside the pipe, the stronger the acoustic emission signal energy generated. With the increase of leakage rate, the acoustic emission signal energy gradually increased. With the increase of the distance between the sensor and the leakage point, the acoustic emission signal energy decreased, resulting in acoustic emission signal attenuation gradually. Among different pipeline characteristics, the influence of the flange to the acoustic emission signal attenuation was the largest. But the influence of the tee and weld to the acoustic emission signal attenuation was not obvious. At the same time the influence of the 90° bend was very small and pipe diameter basically did not impact on signal attenuation. The signal after wavelet decomposition used the correlation analysis method; the results were more close to the real value.

1 Introduction

Yang, Zheng, Long et al. [1–3] have shown that acoustic emission is a release of strain energy in the form of an elastic wave, also known as the pressure wave emission. The following references [4–7] have shown that pipelines in the case of corrosion, crack extension, and other faults will produce a large number of acoustic

X. Wang (✉) • Z. Jiang • H. Chen • K. Wang
School of Environment & Safety Engineering, Changzhou University, Changzhou 213164, China
e-mail: wangxy@cczu.edu.cn

G. Shen et al. (eds.), *Advances in Acoustic Emission Technology: Proceedings of the World Conference on Acoustic Emission-2013*, Springer Proceedings in Physics 158,
DOI 10.1007/978-1-4939-1239-1_44,

emission signals. The following references [8–11] have shown that acoustic emission sensors used to collect signals at the ends of the pipeline and the location of the defects can be determined by analyzing the pressure wave signals. The research is a hotspot of detection of defects of pipelines based on acoustic emission in the field of nondestructive testing. Relevant experts at home and abroad have proposed many experimental schemes on crack, corrosion, and leakage of pipelines. But there are many problems in acoustic emission testing technology of pipeline. For example, Shen et al. [12] have shown accurate interpretation of characteristics of acoustic emission sources, grasp of the various factors influencing the acoustic emission signals, accurate positioning of the leakage sources, etc.

In this paper, we present the model of acoustic emission detection on pipeline leakage that was established under laboratory conditions. The influence on attenuation of leakage acoustic emission signals for different internal pressures, leakage flow, the propagation distance, and pipeline characteristics was studied. Finally, the wavelet decomposition combined with correlation analysis was used to locate leakage sources inaccurately.

2 Detection System and Detection Model

The pipeline leak acoustic emission detection system is shown in Fig. 1.

A four-channel digital testing system made by PAC Company was used in the experiment. Sensors were single-ended broadband sensor R15, frequency band range 50 kHz to 1 MHz, the ups and downs in the pass band less than 30 dB, sensitivity 120 dB. Amplifier Model S/N2462026504; filter range 20–120 kHz; an amplifier of three options 20, 40, and 60 dB.

Experimental equipment was a simulation of oil and gas pipeline system. Air was used in the experiment. It consisted of valves, pumps, tanks and 20# carbon steel metal pipe component composition, and so on. Pressure piping was rectangular and coiling four laps, 6,000 mm long, 1,500 mm wide. The pipe had a total of 15 bends, curvature radius of 65 mm. The distance of the pipeline at each lap was 320 mm, and the exit was connected with tanks. The pipeline diameter was 58 mm, while the wall thickness was 5 mm. The leaking valves were located 2,090 mm from the inlet pipe. The inlet pipeline was connected to the pump, and the pipeline work pressure was generally not more than 0.5 MPa, and the experimental pipelines were oil and gas pipelines. Pressure gauge, rotor flow meter had been installed on the pipeline; the pipeline could be installed with sensors, and they were connected with the industrial computer; the values of the change of pipeline pressure and flow rate were obtained at any time. The pressure pipeline model is shown in Fig. 2.

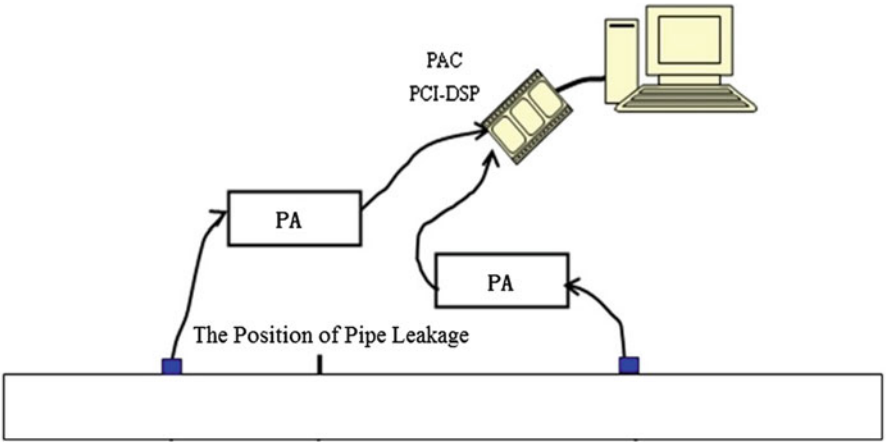

Fig. 1 AE system

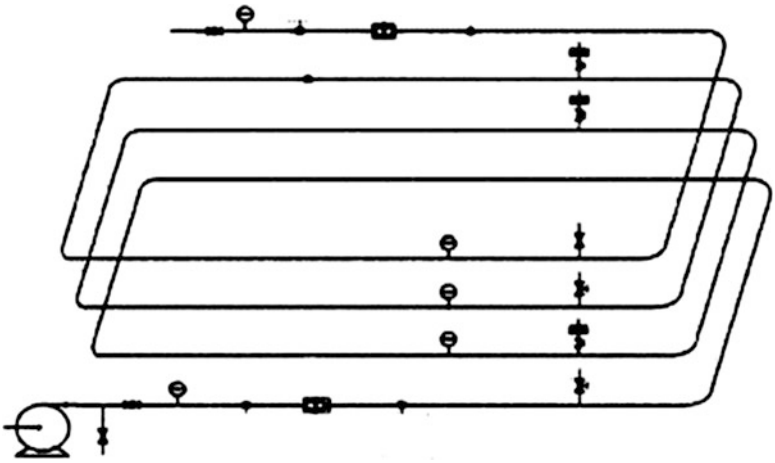

Fig. 2 Test model

3 Experimental Method

Before the test, the instrument parameters must be set and the sensitivity of channel and specific parameters be adjusted: tube length, 6,000 mm; threshold, 40 dB; gain, 40 dB; filter frequency domain, 100–400 kHz; PDT, 300 μs; HDT, 600 μs; HCT, 1,000 μs; air was adopted as the pipeline medium. The test procedures were as follows:

1. When pipe pressure was 0.05, 0.1, 02, 0.3, 0.5, and 0.5 MPa, the sensor S2 and S3 were placed at a distance of 1,000 and 1,500 mm from measuring points of leak holes on acoustic emission signal acquisition.

2. When pipe internal pressure was 0.3, 0.5 MPa, leakage rate 0.6, 1.2, 1.8, 2.4, 3.0, and 3.6 L/min, sensor S1 was placed at measuring points at a distance of 1,000 mm from leak hole on acoustic emission signal acquisition.
3. When pipe internal pressure was 0.3, 0.5 MPa, the sensors were placed at measuring points at a distance of 1, 2, 3, 4, 5, and 6 m from leak hole on acoustic emission signal acquisition.
4. The 20# carbon steel metal pipes were 6,000 mm long with different characteristics. The sensors were coupled and fixed on the location of pipe wall 100 mm from the first flange; after under a fixed pressure of 0.1 MPa, a little lead-break signal acquisition was obtained at a certain distance from the sensor. The cartridge specifications of lead-break used is HB refills of 0.5 mm diameter, each about 2.5 mm long. When the angle was about 30° between the cartridge and the surface, the lead broke. In order to simulate the acoustic emission signals of the crack for collection, 24 points were calibrated totally.

4 Experimental Result

4.1 Pipeline Pressure Effect on Leakage Acoustic Emission Signal Attenuation

Figures 3 and 4 show sensor S2 and S3 measured RMS and ASL respectively at different pressures.

Fig. 1 shows that RMS is proportional to the pressure. When the pressure is less than 0.2 MPa, the RMS value is almost a linear relationship with pressure; but when the pressure is more than 0.2 MPa, the RMS value increases very slowly. Figure 2 shows that the relationship is similar between ASL and pressure. The greater the pressure of internal pipe, the greater the energy of leakage incentive out of the acoustic emission signals; When the pressure was less than 0.2 MPa, acoustic emission signal was weak, and signals of acoustic emission were greatly impacted by the attenuation of acoustic emission at this point; When the pressure is more than 0.2 MPa, acoustic emission signal is strong, the influence of the acoustic emission signal attenuation is small.

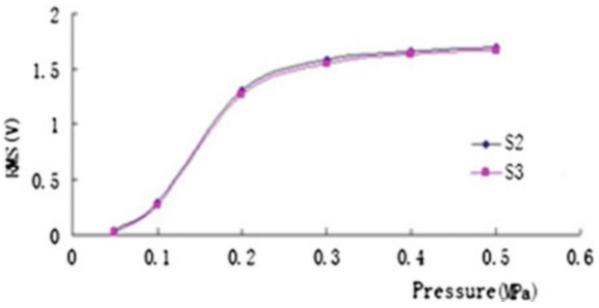

Fig. 3 The RMS along with the change of pressure

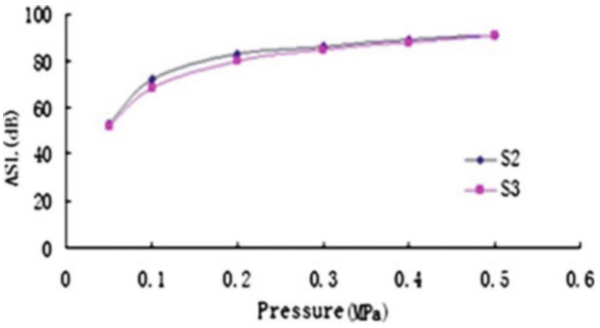

Fig. 4 The ASL along with the change of pressure

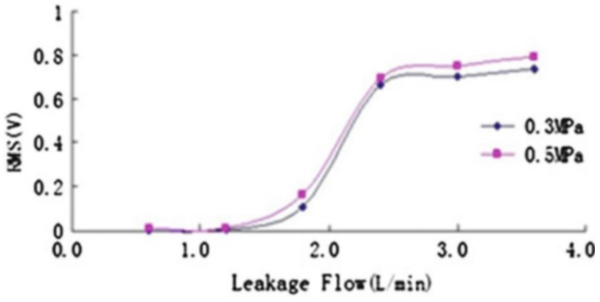

Fig. 5 The RMS along with the change of leakage flow

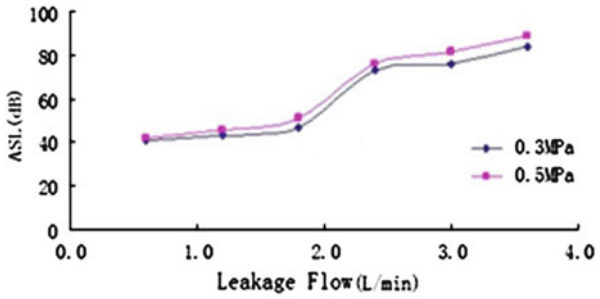

Fig. 6 The ASL along with the change of leakage flow

4.2 Leakage Flow Effect on Leakage Acoustic Emission Signal Attenuation

Figure 5 shows RMS at different leakage points measured at the pressure of 0.3 and 0.5 MPa of sensor 1; Fig. 6 shows ASL measured at different leakage points at the pressure of 0.3 and 0.5 MPa of sensor 1.

Figures 5 and 6 show that RMS and the average signal level were proportional to the leakage. When leakage rate is less than 1.0 L/min, RMS changed little, which increases rapidly when the leakage rate is in 1.0–2.5 L/min. However,

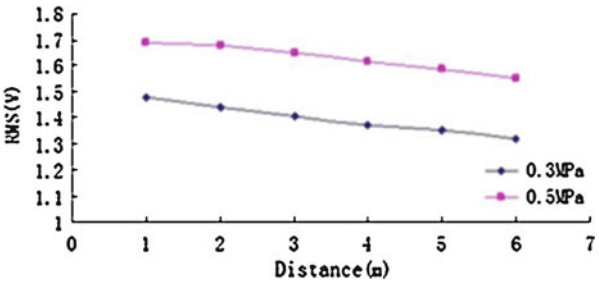

Fig. 7 The RMS along with the change of distance

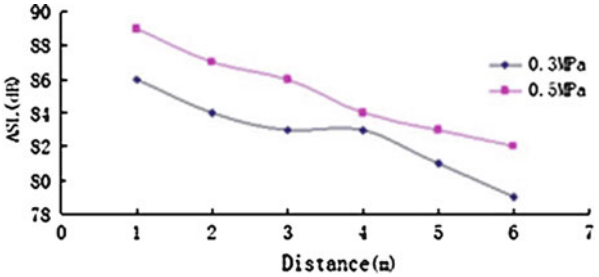

Fig. 8 The ASL along with the change of distance

when leakage is greater than 2.5 L/min, the change of RMS value is very slow. Therefore, most of the acoustic emission signals energy can disappear due to attenuation. With the increase of leakage rate, the acoustic emission signal gradually increases and the proportion of attenuation of the original signal gradually decreases. When the leakage rate increases, ratio of attenuation in original signal energy is negligible.

4.3 Propagation Distance Effect on Leakage Acoustic Emission Signal Attenuation

Figure 7 shows voltages (RMS) at different effective distance from sensor when the pressure is 0.3 and 0.5 MPa. Figure 8 shows that average signal level (ASL) when the pressure is 0.3 and 0.5 MPa.

Figure 7 shows that the effective voltage (RMS) decreases slowly with the distance. Therefore, with the increase of distance, acoustic emission signal attenuation increases. As the length of the laboratory pipeline is limited, signal attenuation of short distance is studied. The attenuation is proportional to the distance seen from the short distance attenuation curve.

Average signal level (ASL) and effective voltage (RMS) changed with the distance are very similar, which the change of attenuation with distance.

Table 1 Breakpoint location of acoustic emission signal parameters

Location	R.T (m μs)	Count	E (mV^2)	A (dB)
1	507	302.67	509.67	72.67
2	171	111	151.67	61
3	824	147.33	114.33	59.33
4	1,414.67	121.33	153.67	57.67
5	3,265.67	158.67	57.33	33.67
6	5,979.33	135.67	76	39
7	5,866.67	188	55.33	40.33
8	6,405.67	442	86	41.33
9	4,649.67	366.67	46	39.67
10	3,937	284.33	44.67	39.67
11	4,059.67	305.67	50.67	40.67
12	3,783.67	543.67	73.67	44.67
13	2,872.33	771	117.67	48.33
14	403	857	256	54.67
15	3,364.33	1,001	225	52.33
16	2,214	736	141	50
17	3,171.67	689.33	122.33	46.33
18	3,978.67	899.67	164.33	48.33
19	1,111.33	1,155.67	118.33	54
20	2,594	741	120	46
21	3,936	742	146.33	44
22	5,755.33	699.67	162.67	41.33
23	4,930.33	677	95	46.67
24	6,085.33	161	40.67	38.33

4.4 Different Pipeline Characteristics Effect on Leakage Acoustic Emission Signal Attenuation

Table 1 shows relevant parameters of acoustic emission signals collected from each breakpoint position on the different characteristics of the pipeline.

For a fixed pressure (0.1 MPa) air line, shown in Table 1:

5. The influence of flanges on the acoustic emission signal count value is obvious. The number of attenuation values after the flange at least are 190; the energy attenuation values at least are 300 mV^2; the amplitude attenuation values at least are 10 dB. And the nearer the distance to the flange, the more obvious the attenuation degree of the acoustic emission signals. The experimental results show that the count value, energy, and amplitude were attenuated to 191, 358 mV^2, and 12 dB, respectively.
6. The effect on attenuation of acoustic emission signals is not very significant at tee or weld. The experimental results show that the count value, energy, and amplitude were attenuated to 75, 40 mV^2, and 2 dB respectively.
7. The effect on attenuation of acoustic emission signals is least significant at 90° elbow.

8. The influence of variable diameter on signals attenuation can be ignored. Because of air gap within the pipeline, pipe clamp has no effect on acoustic emission signals.

5 Positioning Method

Lead-break signals were tested to simulate localization of the acoustic emission source; the following coordinates were set in the experiments: S2 (0, 0); S3 (1,500, 0); S1 (2,000, 0); lead-break point (1,100, 0). $\Delta L = 1{,}100 - 400 = 700$ mm; Wave velocity was 4117062.22 mm/s.

Amplitude data of the lead-break was collected. Figures 9 and 10 show the original signals from sensor S1 and S2.

Signal X1 and X2 were decomposed by multi-scale wavelet, then obtain five frequency bands, shown in Figs. 11 and 12.

Figures 11 and 12 show the energy after signals decomposition mainly concentrated in D3, D4 and D5, therefore, D3, D4, D5 can be used in the analysis of the original signals. Using correlation analysis method to D4 spectrum of the

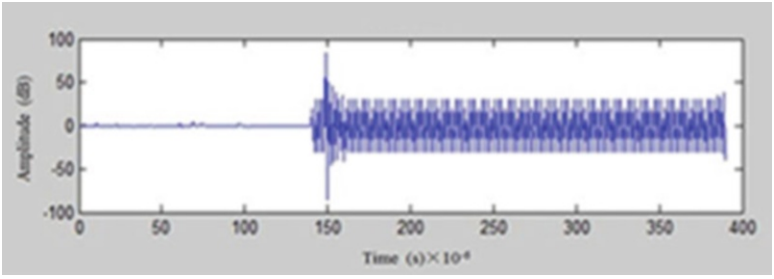

Fig. 9 The original signal X1

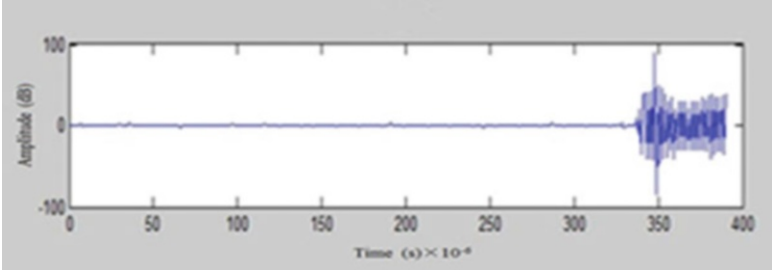

Fig. 10 The original signal X2

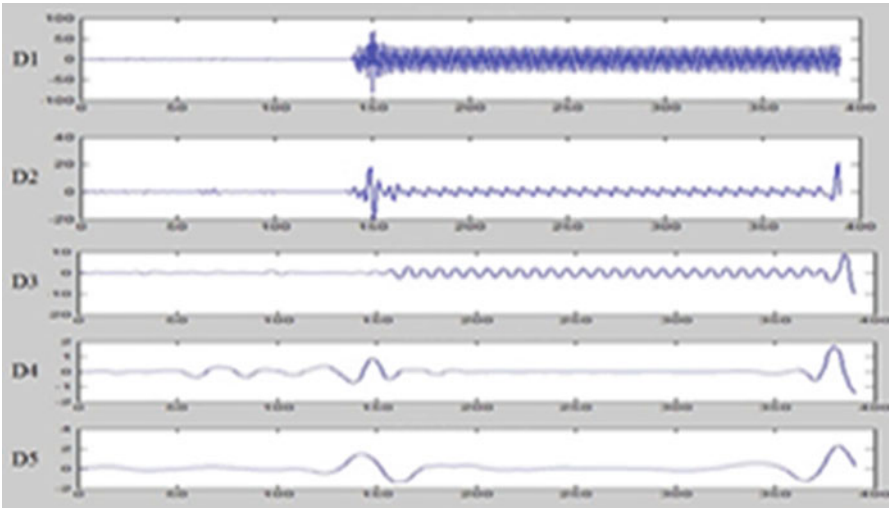

Fig. 11 Signal X1 after wavelet decomposition

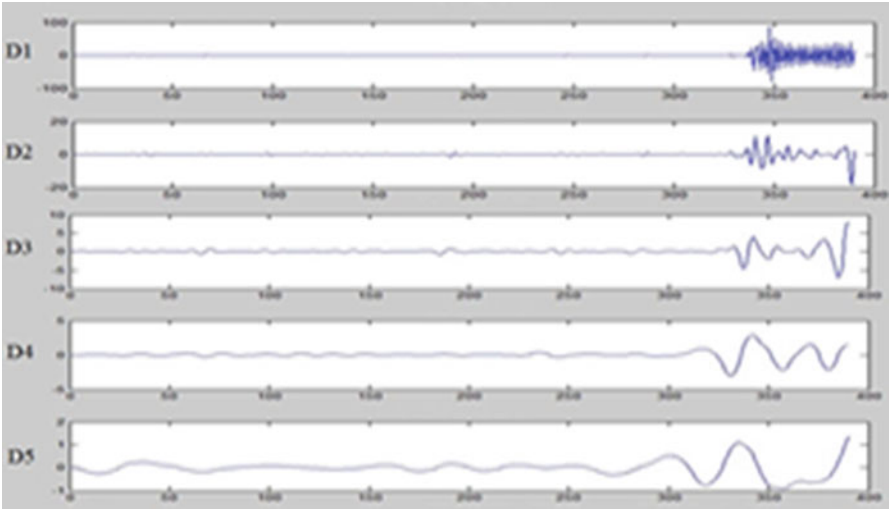

Fig. 12 Signal X2 after wavelet decomposition

signal, the following reference [13] has shown the main range of frequencies between 200 and 300 kHz. Group velocity of signals is 3259.44 m/s in the frequency band range.

Amplitude attenuation positioning method and the orientation of waveform interference method and waveform cross-correlation method were commonly

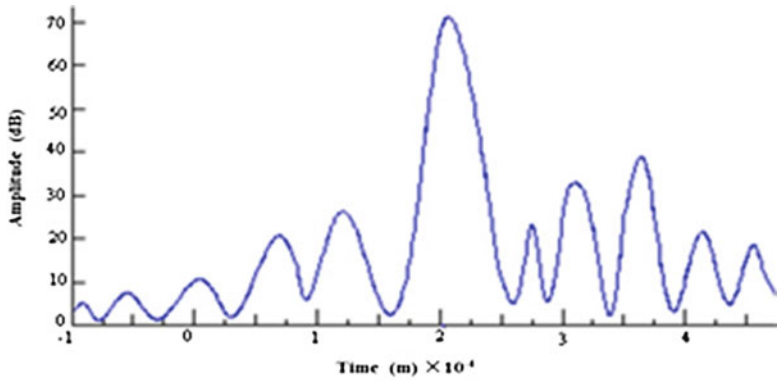

Fig. 13 Signal X2 after wavelet decomposition

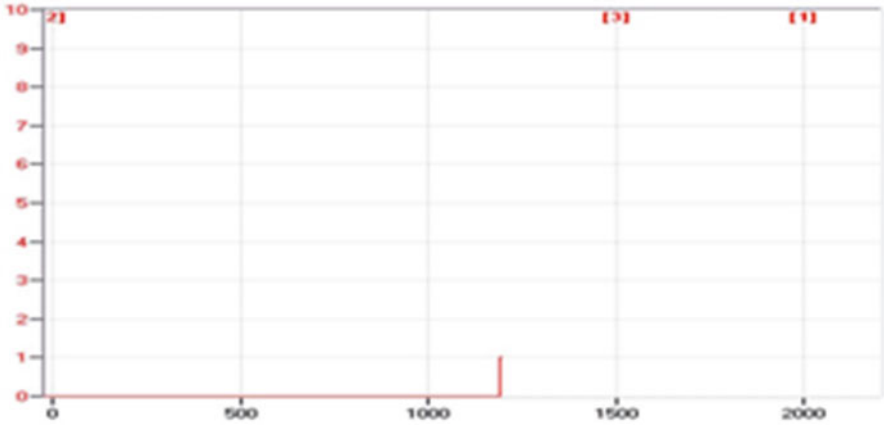

Fig. 14 Acoustic emission instrument testing location map

used in leak location. In this paper, the waveform cross-correlation method is analyzed.

The two sensors are leakage acoustic emission signal received from the same signal source; two sensor signals will generate a time lag. Figure 13 shows signal X1 and X2 related figure in size 4; ΔT is the time corresponding to amplitude maximum points.

Figure 13 shows $\Delta T \approx 0.000213$ s, the different distance:

$$\Delta L = \mathrm{L2} - \mathrm{L1} = \mathrm{Vg} \times \Delta T = 3,259.44 \times 0.210 = 684.5 \text{ mm}$$

The real different distance: 700 mm.

Relative error (after calculation): 2.21 %.

Using acoustic emission instrument to detect leak location as shown in Fig. 14, position error: 9 %.

Table 2 Data comparison before and after the wavelet decomposition

	Directly results		Results after wavelet decomposition		
No	Distance (mm)	Relative error (%)	Distance (mm)	Relative error (%)	ΔL (mm)
1	449.1	12.28	410.6	2.65	400
2	668.3	11.38	616.4	2.73	600
3	722.7	9.66	785.1	1.86	800
4	1,156.4	15.64	1,032.8	3.28	1,000
5	992.1	17.33	1,147.6	4.37	1,200
6	1,607.1	14.79	1,436.8	2.63	1,400

Six sets of data are analyzed by the above steps and compared with the experimental results; the results are shown in Table 2.

Table 2 shows that the signals are more close to the real value by relative positioning after wavelet decomposition.

6 Conclusion

This experiment studied the effect on attenuation of leakage acoustic emission signal by changing the pipeline pressure, leakage flow, propagation distance, and under the different characteristics of pipes. In addition, the correlation analysis method was used to locate the leak point. The following conclusions are drawn:

1. The greater the pressure in the pipe, the stronger the acoustic emission signal energy generated, and the stronger the acoustic emission signals. Although there is still a certain degree of attenuation, the ratio of the attenuation of original signals is lower.
2. With the increase of leakage flow, the acoustic emission signal energy gradually increases while the energy attenuation in the original signal energy decreases. When the leakage is very large, the energy attenuation in the original signal energy is very small, almost can be ignored.
3. With the increase of the distance between the sensor and the leakage point, the acoustic emission signal energy decreases but acoustic emission signal attenuation rises.
4. The influence of the acoustic emission signal attenuation is not the same for the different characteristics of the pipeline. The influence of the flange to the acoustic emission signal attenuation is the largest, and the nearer the flange, the more obvious the acoustic emission signal attenuation. The influence of the tee and weld on the acoustic emission signal attenuation is not obvious. The influence of the 90° bends on the acoustic emission signal attenuation is very small, and amplitude remains basically unchanged. When the pipeline diameter is changed, there is basically no signal attenuation.

Acknowledgment This study was supported by International Science & Technology Cooperation Project of Changzhou City, China (CZ20120015) and Industry–University Research Cooperation Joint Innovation Fund—Prospective Joint Research Project (BY2013024-04) and National Key Technology Research & Development Program of China (2011BAK03B08-01) and Science & Technology Projects for Key Technology of Production Safety Accident Prevention (Key Techniques Research of Natural Gas Pipeline Leak Detection and Risk Management System).

References

1. M.W. Yang, *Acoustic Emission Inspection* (China Machine, Beijing, 2004)
2. Z.X. Zheng, *Nondestructive Testing and Safety Assessment* (China Standards, Beijing, 2003)
3. R. Long, K. Vine, M.J.S. Lowe et al., Monitoring acoustic wave propagation in buried cast iron water pipes. Rev. Progr. Quant. Nondestr. Eval. **20**, 1202–1209 (2001)
4. G.T. Shen, D. Guang, S.F. Liu, P.E. Dodd, G.L. Hash, Acoustic emission testing technology progress in China. Nondestr. Test. **25**(6), 302–307 (2003)
5. S.H. Carpenter, M.R. Gorman, A waveform investigation of acoustic emission generated during the deformation and cracking of 7075 aluminum. Progress in Acoustic Emission VII, The Japanese Society for NDI, 1994, pp. 105–112
6. T.M. Roberts, M. Talebzadeh, Acoustic emission monitoring of fatigue crack propagation. J. Constr. Steel Res. **59**, 695–712 (2003)
7. A.A. Hill, V.K. Eric, Neural network detection of fatigue crack growth in riveted joints using acoustic emission. Mater. Eval. **53**(1), 76–82 (1995)
8. G. Chen, G.T. Shen, B.X. Li, Metal pressure vessel research of acoustic emission source characteristics. China Saf. Sci. J. **15**(1), 98–103 (2005)
9. X.Y. Li, *Oil and Gas Corrosion and Protection Technical Manuals* (Petroleum Industry, Beijing, 1999)
10. K.M. Ronnie, R.K. Miller, Tank-bottom leak detection in above-ground storage tanks by using acoustic emission. Mater. Eval. **48**(6), 822–829 (1990)
11. R. Nordstrom, Direct tank bottom leak monitoring with acoustic emission. Mater. Eval. **48**(2), 251–254 (1990)
12. G.T. Shen, R.S. Geng, S.F. Liu, Acoustic emission source location. Acta Acustica **24**(3), 114–117 (2002)
13. Z.H. Zhu, P.Z. Li, Z.G. Wang, Pipe sound propagation numerical comparison with the experimental results. Nondestr. Test. **13**(1), 1–7 (1998)

Characterization of Acoustic Emission Parameters During Testing of Metal Liner Reinforced with Fully Resin Impregnated CNG Cylinder

R. Kenok, C. Jomdecha, and C. Jirarungsatian

Abstract The aim of this paper is to study the acoustic emission (AE) parameters obtained from CNG cylinders during pressurization. AE from flaw propagation, material integrity, and pressuring of cylinder was the main objective for characterization. CNG cylinders of ISO 11439, resin fully wrapped type and metal liner type, were employed to test by hydrostatic stressing. The pressure was step increased until 1.1 time of operating pressure. Two AE sensors, resonance frequency of 150 kHz, were mounted on the cylinder wall to detect the AE throughout the testing. From the experiment results, AE can be detected from pressuring rate, material integrity, and flaw propagation from the cylinder wall. AE parameters including Amplitude, Count, Energy (MARSE), Duration and Rise time were analyzed to distinguish the AE data. The results show that the AE of flaw propagation was different in character from that of pressurization. Especially, AE detected from flaws of resin wrapped and metal liner was significantly different. To locate the flaw position, both the AE sensors can be accurately used to locate the flaw propagation in a linear pattern. The error was less than ± 5 cm.

1 Introduction

Due to a rapidly increasing demand for using natural gas, Compressive Natural Gas (CNG) cylinder is widely used in vehicles as an alternative fuel. The typical pressure of natural gas is about 200 bars. The types of CNG tubes following ISO EN 11439 include Metal (CNG-type1), Metal with hooped composite (CNG-type 2), Metal with fully wrapped composite (CNG-type 3), and fully composite

R. Kenok (✉) • C. Jomdecha • C. Jirarungsatian
Maintenance Technology Center, King Mongkut's University of Technology, Thonburi, Bangkok 10140, Thailand
e-mail: rangsan_ee36@hotmail.com; axlrosez13@hotmail.com; chalermkiat.jir@kmutt.ac.th

G. Shen et al. (eds.), *Advances in Acoustic Emission Technology: Proceedings of the World Conference on Acoustic Emission-2013*, Springer Proceedings in Physics 158,
DOI 10.1007/978-1-4939-1239-1_45,

(CNG-type 4) respectively [1]. For safe use of CNG cylinders in public utilities, accidents from natural gas cylinders must be taken care of. In-serviced CNG cylinders are commonly inspected in a standard period by external NDT methods such as visual inspection, ultrasonic, and bubble leak test. However, integrity test of cylinder is difficult to carry out if the cylinder is installed permanently in the vehicles.

Acoustic Emission (AE) is a functional method to test the onboard cylinder in vehicles. As testing with load, the benefit of AE testing is a detectability of material integrity during loading under hydrostatic test pressure. In various researches, AE testing results can be evaluated to grade the cylinder condition [2, 3]. CNG-1, metal type, was done to evaluate the acceptance of the cylinder. Composite cylinders (CNG-2, 3, and 4), were interested to study by AE during felicity effect [4, 5]. In addition, AE Standards for testing CNG cylinder were done to verify usability of the test cylinder [6–8]. Anyway, setting parameters and testing procedure are varied depending on the AE system and testing conditions. Criteria of acceptable cylinder rely on these factors.

In this research, characterization of AE parameters from flaw propagation, material integrity, and pressuring obtained from CNG-1 and 3 cylinders was the main objective. Analysis of AE energy and count showed the different characters of metallic and composite materials.

2 Methods

2.1 Types of CNG Cylinder in the Experiment

Two CNG cylinders of ISO 11439 were employed to test by AE. The first cylinder (CNG-1) was a seamless "thin wall" A6061 aluminum liner from multi-depth drawing process type. Its dimensions were 320×680 mm ($D \times L$), capacity of 60 l. The design testing pressure was 70 bars. The second cylinder (CNG-3) was a seamless "thin wall" A6061 aluminum liner with a resin fully wrapped type. Its dimensions were 340×950 mm ($D \times L$), capacity of 70 l. The design testing pressure was 240 bars.

2.2 Experiment Setup for AE Testing

Figure 1a shows the experimental setup for AE testing of CNG cylinder. Tested cylinders with full of water were connected to the fill host of hydrostatic test pump for pressurization. The cylinder was mechanically isolated to prevent any movement and contact with surface of other hardware. A pressure gauge was used to

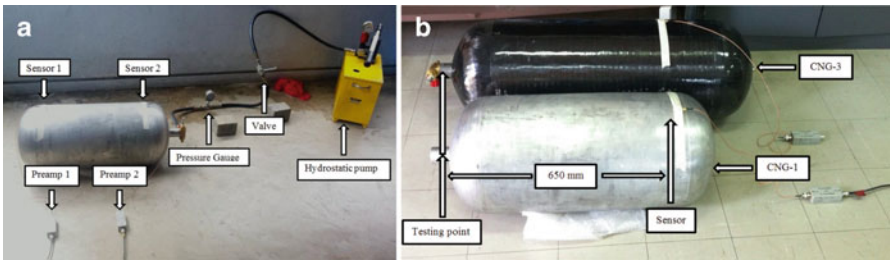

Fig. 1 (**a**) Experiment setup of AE testing for CNG cylinder, (**b**) attenuation testing of CNG-1 and CNG-3 cylinder

Table 1 Attenuation at thread of CNG-1 and CND-3

Types of CNG cylinder (mm)	10	650
CNG-1 (dB)	96.8	85.0
CNG-3 (dB)	97.0	63.6

monitor the specific loading pressure. Leaks were eliminated at any of the connections. Two AE sensors with a frequency of 150 kHz were mounted on surface of the cylinder. The sensor distances were 450 and 650 mm for CNG-1 and CNG-3 cylinders respectively. Two pre-amplifiers were connected to the sensor for increasing detecting AE signals. AE analyzer LOCAN 320 was utilized to collect and process AE data during testing.

Before testing, signal processor was adjusted for settings and checked for system performance by breaking a pencil lead on the receptacle at a distance of 100 cm from the sensors. During testing, the experiments were monitored by observing displays of pressure gauges gathering with AE data lists.

2.3 Attenuation of CNG-1 and CNG-3 Cylinders

Attenuation of AE signals was determined by pencil lead break technique. The position of testing was on the neck thread which was metal liner of both cylinders. The testing distance from mounted sensor was 650 mm as illustrated in Fig. 1b. The results are presented in Table 1. The attenuation at the neck threads of CNG-1 and CNG-3 cylinders was less than the calibration point, about 10 and 30 dB respectively. As a result, when loading the CNG-3 cylinder, noise sources from filling pressure can be ignored. On the other hand, the filling rate to the CNG-1 cylinder should be constantly loaded and low enough to reduce noise.

3 Results and Discussion

3.1 CNG-1 Cylinder (Metal Type)

Pressurization was increased and held up step by step from 0 to 94 bars. The result of AE energy vs. time is shown in Fig. 2a. Hold time of loading pressure (solid line) is plotted in the right side. The result describes that there is no AE activity during load from 0 to 65 bars (0 to 800 s). After that, High AE activities occurred from loading of 66 to 84 bars (2,100 s). The sources may be caused from cylinder wall integrity. The AE activity rose rapidly different to others. This effect can be ensured that they were caused from flaw propagation. Later, AE activities decreased during increased loading. Finally, the AE activities increase hastily again at hold pressure of 94 bars (4,900 s). At this point, the cylinder exploded at a pressure of 94 bars. To confirm the result of material integrity and flaw propagation, cumulative hits vs. time is shown in Fig. 2b. The hit rate was low at the starting period and after that, the AE hits rose rapidly at 2,100 s. Afterwards, hit rate was low again until the time of 4,900 s. The hit rate was rapidly high in the second time. This result confirmed the Kaiser's effect character of the CNG-1 metal type during pressuring. This effect refers to the absence of AE at a fixed stress level, until previously applied stress levels are exceeded.

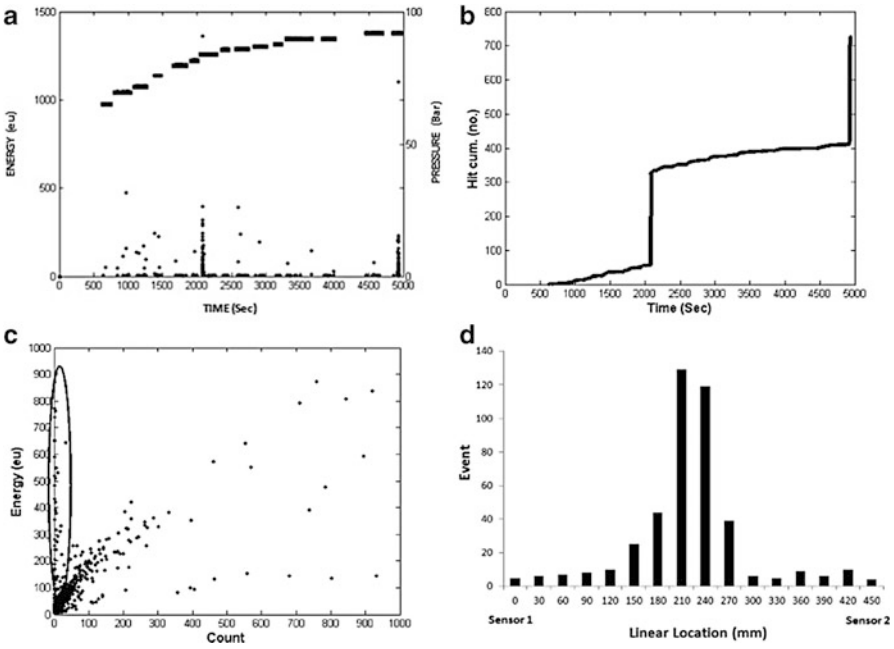

Fig. 2 (**a**) AE energy vs. time with pressurization, (**b**) AE hit cumulative vs. time, (**c**) relation between AE energy and count, (**d**) linear locations vs. number of events from CNG-1 cylinder

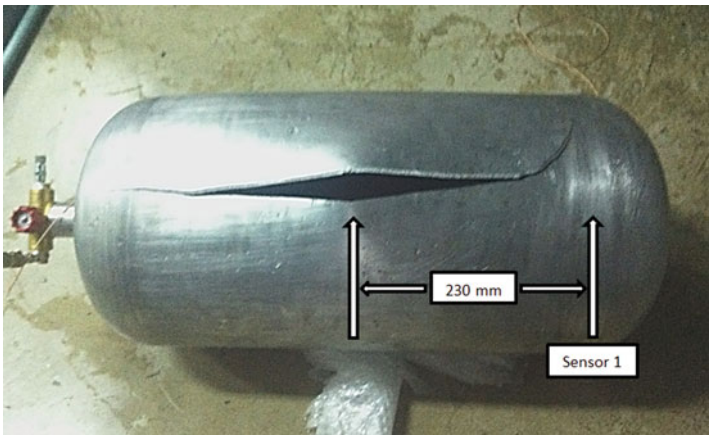

Fig. 3 Flaw propagation could be originated from CNG-1 cylinder

The relation between AE energy and count plot was done to establish the different groups of AE activities as illustrated in Fig. 2c. It is clear that the activities separated into two main groups. The first group (in the circle) has the characteristics of high energy with low count. After correlation plotted, this group can be sourced from filling flow during loading, as the flow rate of manual pump will produce low frequency with high amplitude of AE signals. On the other hand, in the second group, the relation between AE energy and count can be categorized into two clusters by observing. There are the group of high counts related to low energy, and the group of high count related to high energy. These relations could be caused by the material integrity and flaw propagations.

To determine possible material integrity and flaw growth sources, linear location technique was utilized using AE 2 sensors. The distance between both sensors was 450 mm. Result of AE locations related to number of Events was shown in Fig. 2d. Group of location was set to 30 mm/bin. Peaks of AE events were located on the cylinder at 210–240 mm. apart from sensor 1, which was the location of cylinder explosion as in Fig. 3. So flaw propagation of the cylinder could be originated from this area.

3.2 CNG-3 Cylinder (Metal with Fully Resin Wrapped Type)

AE energy plot against time with pressurization is illustrated in Fig. 4a. Pressurization was increased from 0 to 200 bars as cylinder specification. The results were totally different from the CNG-1 testing results. The AE activities were low throughout the loading period. There were some energies increased different from others. However the activity from wrapping resin activity was lower than metal. To confirm the result of resin wrapped integrity, relation plotted between cumulative hits and time is shown in Fig. 4b. Hit rate is exponentially slope throughout the

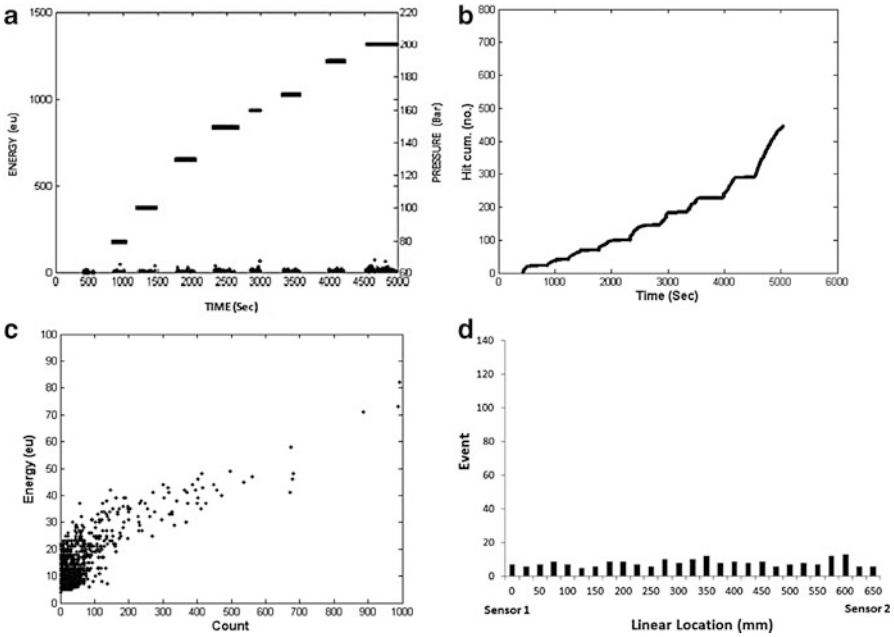

Fig. 4 (**a**) AE energy vs. time with pressurization, (**b**) AE hit cumulative vs. time, (**c**) relation between AE energy and count, (**d**) linear locations vs. number of events from CNG-3 cylinder

testing period. Due to the property of composite material, hit rate tends to be higher as the presence of detecting AE occurring at a fixed level of stress below the previous applied. This result related to the Felicity effect.

Additionally, the relation between AE energy and count showed only one trend, energy correlated to a number of counts, see Fig. 4c. There were intense group of counts less than 100 with low energy of 30 eU. This character can be used to describe the followed Felicity effect of wrapped resin. From observation of the testing CNG-3 cylinder, no indication of flaw can be detected. Therefore, the character of the relation between energy and count could be occurred from wrapped resin integrity. In contrast to the result of the CNG-1 cylinder, there was no group of high energy with low count as occurred from filling pressure due to high attenuation material of wrapped resin.

The location of AE activities during testing of the CNG-3 cylinder was determined to indicate the possibility of material integrity sources. Because the sensors were mounted on the wrapped resin material, the event hits were detected from the composite material than from an inner metal liner. Linear location technique was utilized using AE 2 sensors with 650 mm spacing. Group of location was set to 30 mm/bin. Location results of AE locations related to the number of event are shown in Fig. 4d. Event hit from both sensors was less than 20 hits throughout the length of mounted sensors. The possible AE occurrences could be caused from the fully wrapped resin integrity along the cylinder. This result was related to AE parameter analysis and visual inspection.

4 Conclusion

Analysis of AE parameters obtained from Metal (CNG-1) cylinder and metal liner with fully wrapped resin (CNG-3) cylinder was done to distinguish the character of load stressing, material integrity, and flaw propagation from the cylinder wall. The main relations of AE parameters were count, energy, cumulative hit, and event location. The results showed the different characters of AE parameters between CNG-1 and CNG-3 cylinders.

- For CNG-1, the group of material integrity and flaw growth can be separated clearly to the filling flow during loading using relation between energy and count. In addition, cumulative hit can indicate the period of flaw propagation and cylinder explosion. The results were related to the Kaiser's effect.
- For CNG-3, AE were mainly associated with the material integrity of fully wrapped resin using energy vs. count. Energy from AE activities were less than those energy obtained from CNG-1. Cumulative hit showed the pattern of hit rate related to Felicity effect.

Accordingly, the results of AE testing show that the AE of flaw propagation was different in character from that of pressurization. Especially, AE detected from flaws of resin wrapped and metal liner was significantly different. To locate the flaw position, both the AE sensors can be accurately used to locate the flaw propagation in a linear pattern. The error was less than ± 50 mm.

Acknowledgment We would like to thank METAL MATE CO., LTD. for supporting of CNG-1 and CNG-3 cylinders in experiments.

References

1. International Standard Organization, ISO EN 11439, *High pressure cylinders for the on-board storage of natural gas as a fuel for automotive vehicles*, 2nd edn. (01-06-2013)
2. D. White, Acoustic emission examination of metal pressure vessels general meeting. *The National Board of Boiler and Pressure Vessel Inspectors, 57th General Meeting*, May 1988
3. A. Akhtar, J.Y. Wong, G.S. Bhuyan, Acoustic emission testing of steel cylinders for the storage of natural gas on vehicles. NDT & E Int. **25**(3), 115–125 (1992)
4. O. Skawinski, P. Hulot, C. Binétruy et al., Structural integrity evaluation of CNG composite cylinders by acoustic emission monitoring. J. Acoust. Emis. **26**, 120–131 (2008)
5. H. Jee, J. Lee, N. Ju et al. Determinants of damage grade for vehicle CNG cylinder by the analysis of AE features during fatigue. 18th World Conference on Nondestructive Testing, 16–20 April 2012
6. International standard Organization, ISO EN 16148, *Gas cylinders: refillable seamless steel-acoustic emission testing (AT) for periodic inspection*, 1st edn. (2006)
7. American Society for Testing and Materials, ASTM-E1419, Standard practice for examination of seamless, gas-filled, pressure vessels using acoustic emission (2009)
8. American Society for Testing and Materials, ASTM-E2191M, Standard practice for examination of gas-filled filament-wound composite pressure vessels using acoustic emission (2010)

Applications of Acoustic Emission Testing in High Background Noise Environment

Yatuan Tian, Shiliang Jiang, Jie Li, and Dong Li

Abstract This article describes using Acoustic Emission Testing (AET) technology to detect and analyze the transformed parts of a gasifier online in high background noise environment, and rechecking the results of AET with conventional NDT methods. The result shows that there are well correspondences between the defects which were found by AET technology and conventional NDT methods. This conclusion speaks volumes for the feasibility and effectiveness of acoustic emission in high background noise, which provides a reference for AET to similar large-scale petrochemical equipment.

1 Introduction

Overtemp took place in a gasifier of a company while running, which led to partial cracks on the vessel wall. The manufacture treated the crack position with dig-mend method, then changed the wainscot (as shown in Fig. 1). What is more, it detected the four weld lines which were created by changing wainscot, respectively. Ultrasonic testing and TOFD (Time of Flight Diffraction Technique) testing found that there were ten inside defects on HB2, HB3 in total—six defects were on HB2, while the remaining four belonged to HB3. Without defects elimination, the deepest defect was apart from the outer wall 69.4 mm, and the longest lengthened out to

Y. Tian (✉) • S. Jiang • J. Li
SINOPEC Tianjin Petrochemical Co. Ltd., Tianjin 300271, China
e-mail: tyt8098@sina.com

D. Li
Shandong Hualu-Hengsheng Chemical Co. Ltd., Shandong 253000, China
e-mail: 13905343192@163.com

G. Shen et al. (eds.), *Advances in Acoustic Emission Technology: Proceedings of the World Conference on Acoustic Emission-2013*, Springer Proceedings in Physics 158,
DOI 10.1007/978-1-4939-1239-1_46,

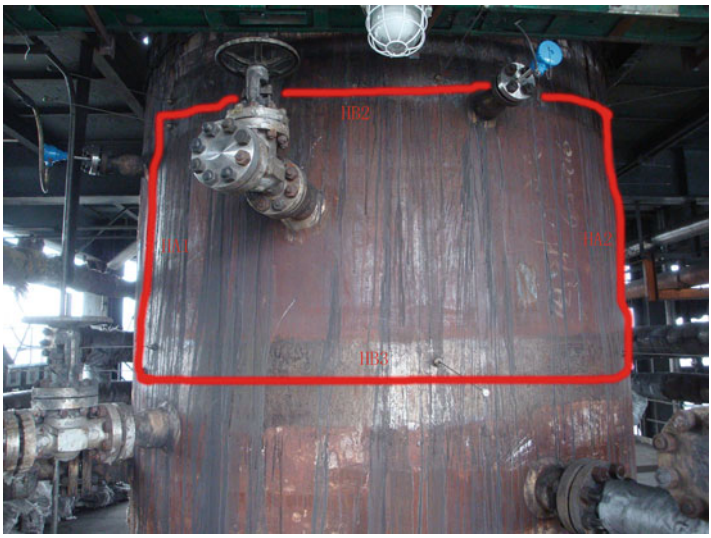

Fig. 1 Dig-mending positions of gasifier in site (identified by *red line*)

104.3 mm. To verify the activity state of these defects, the authors detected the four weld lines, which are on the repair-welding position, by online AET technology to detect four weld lines. After data handling and filtering analysis, taking repairing state of devices into account, the authors made sure that the defects of HB3 are active defects, which should be listed as key monitoring targets [1, 2].

2 Background Introduction

2.1 Device Parameter and Process of Discovering Problem

As the key device of clean-coal gasification production units, the gasifier's main material was SA387Cr11C12 + 316L (material of mending position was SA387Cr11C12 + 304L + 316L). Its format was $\varphi 2{,}820 \times 16{,}202 \times (84 + 4)$ mm (wall thickness of mending position was 80 + 4 + 4 mm). The design pressure was 6.9 MPa, while the real working pressure was 6.2–6.45 MPa; the design temperature was 425 °C, while the working temperature was 270 °C. The medium consisted of O_2, H_2, CO, H_2O, H_2S, and the cinder. Made in August, 2006, the gasifier was brought into using on January, 2007. In March, 2010, the manufacturer noticed the air leakage of vessel wall while routing inspection. After knocking out heat preservation, a 300 mm long and 20 mm wide checking was found there. Moreover, there were protrusions in the vicinity of crack position. According to the DCS log, the temperature in gasifier once raised up to 1,000 °C during work time.

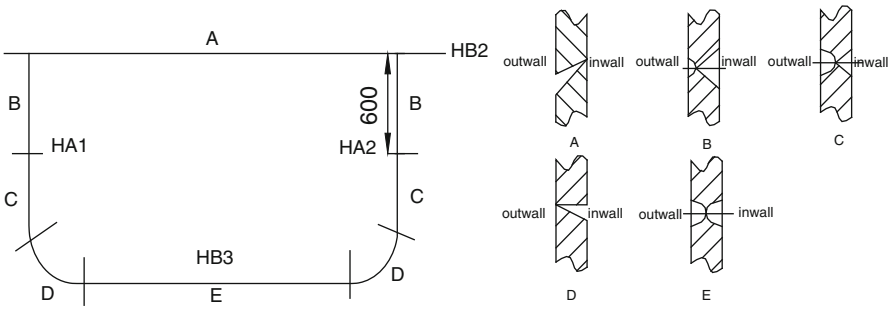

Fig. 2 Grooving method of weld lines

2.2 Process of Handling

Afterwards the manufacturer extracted some material samples in the vicinity of leakage to inspect, including tension, impinge (material ballistic work reached 280 MPa), metallographic, etc. Final analysis suggested that crack was caused by overtemp. Based on each analysis index of material and actual production, they selected dig-mend method ultimately, 3,840 mm (breadth) × 1,400 mm (height), to repair. The numbers of weld lines were HB2, HB3, HA1, HA2 (as marked in Fig. 1). Aiming at the stress distribution problem of after-mending vessel, the manufacturer adjusted the processing method of four craters correspondingly. Different positions had different grooving patterns (as shown in Fig. 2). They adopted welding inside and cleaning outside method to weld, using the welding consumable, whose grade was R307. Before welding, hydrogen elimination was implemented at former welding position of vessel, and then preheated the two sides of groove. After welding, they eliminated hydrogen again and handled vessel course by 720 °C bulk heat treatment. They put the stress test piece evenly on four welding beads while pressure testing, which suggested that stress of weld line HB2, HB3 was relatively high.

After welding, the manufacturer carried out ultrasonic test and found a number of inside defects (their positions were identified by red line in Fig. 3). Among those, six defects were on HB2, while four belonged to HB3. Refer Table 1 for the sizes of the defects; all the ten defects had not being treated until the vessel was re-brought into working in May, 2010.

3 Acoustic Emission Testing (AET)

In June, 2010, to verify the activity state of in wall defects and whether there were new defects, the manufacturer carried out online AET, aiming at the four weld lines of the vessel's mending position. This test applied the SAMOS AET system of PAC. The host model was SAMOS-MAIN-48, testing software was AE-WIN-TB-LOC, probe model was R15I-AST, and all the testing process referred to "Acoustic

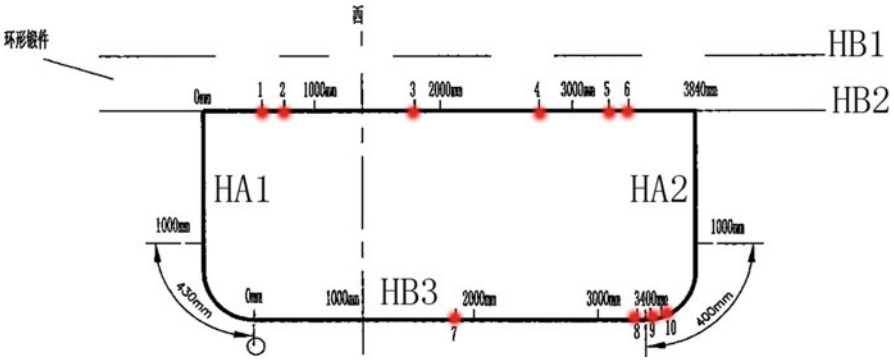

Fig. 3 Distribution map of defects in welds

Table 1 Ultrasonic testing rank table of internal defects

No.	Position	Depth of burial (mm)	Indicating length (mm)	Reflectance amplitude	Rank
1	HB2+622.3	68.7	42.0	III	III
2	HB2+870.4	31.0	53.0	II	III
3	HB2+1896.6	67.9	54.0	III	III
4	HB2+2748.3	63.5	104.3	III	III
5	HB2+3240.6	69.4	72.0	III	III
6	HB2+3389.6	65.1	71.0	III	III
7	HB3+1889.9	60.3	33.0	III	III
8	HB3+3323.6	63.0	38.0	III	III
9	HB3+3407.6	15.0	47.0	II	III
10	HA2+1345.6	28.3	43.0	III	III

P.S. (1) In the "position" column of Table 1, the antecedent means which weld line the defect belong to, the latter number means the distance between defect and zero point of weld line, unit is mm
(2) The "reflectance amplitude" column is on the basis of JB/T 4730.3-2005 defects zone; ranking refers to JB/T 4730.3-2005

emission examination and evaluation of metallic pressure vessels." As this test was an online testing, operating temperature of the device, which raised up to 270 °C, exceeded the limit of probe. So it was infeasible to place probes on vessel wall directly. Through the wave guide, their test adopted linear alignment and regional alignment to make sure where the active positions of defects are.

3.1 Placement of Probe

After mending, 600-mm-long wave guide had been placed on the vessel wall respectively by the manufacturer (as shown in Fig. 4). The probes were placed at A1, A2, A5, A6, A7, A8, A11, A12—eight positions in total of wave guide—to carry on testing. Linear testing was divided into four parts—A1, A12 aimed at weld

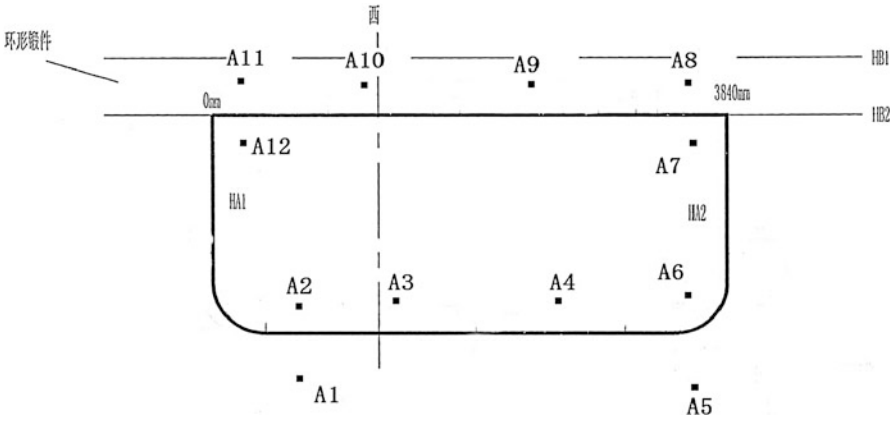

Fig. 4 Position sketch of wave guide

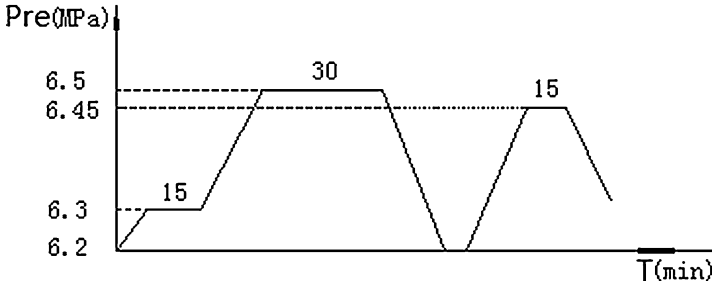

Fig. 5 AET loading process

line HA1; A2, A5 aimed at weld line HB3; A6, A8 aimed at weld line HA2; A7, A11 aimed at weld line HB2. Meanwhile, Regional testing was divided into three parts—probe of A11 aimed at defect 1/2/3; probe of A8 aimed at defect 4/5/6; probe of A5 aimed at defect 7/8/9/10.

3.2 Process of Testing

The process of testing referred to GB/T18182-2000 "Acoustic emission examination and evaluation of metallic pressure vessels." Background noise, which once reached 80 dB, was far higher than the routine detection value (under 40 dB) before testing. To get the signal characteristic value of background noise, we collected 15-minute-signal as standard analytical data before formal test. For the purpose of more testing-process data, the threshold of apparatus was set to 35 dB, in which way complete data bank could be provided for later analysis.

The test adopted system twice pressure circulate method. The detection curve is shown in Fig. 5.

Table 2 Results and rank of ultrasonic recheck

No.	Position	Depth of burial (mm)	Indicating length (mm)	Reflectance amplitude	Rank
1	HB3-125	34.3	17.0	III	III
2	HB3-275	56.5	50.0	III	III
3	HB3-410	45.0	25.0	III	III
4	HB3-890	22.5	30.0	II	III
5	HB3-2183	56.4	15.0	II	III

4 Ultrasonic Recheck

In order to judge the validity of AET's data, the position of ex-check was tested again through ultrasonic flaw detection during shutdown maintenance in July. Results of recheck are shown in Table 2.

5 Data Analysis

The signal amplitude of background noise peaked at 80 dB, which is higher than the request of routine inspection. Therefore conventional method could not be carried out to analyze. Data analysis filtered background noise by data filtering technology. Referring to the GB18182-2000 "Acoustic emission examination and evaluation of metallic pressure vessels," we ranked the detection signal.

The analysis to the collected background noise signal showed characteristics of signature as follows [3, 4]:

1. Average frequency of most signal $<$30 kHz;
2. Peak frequency of most signal $<$10 kHz;
3. Energy of most signal $<$20.

After filtering the above characteristic parameter, the concrete conditions of the analysis to acoustic emission testing are as follows:

The first stage was pressure boosting, from 6.2 to 6.5 Mpa, then maintained it.

Generated from weld line HB3 during the first loading, a large quantity of source signal mostly centralized at 1,000, 2,000, and 3,000 mm, while the crest amplitude reached 82 dB. A few valid source signals generated from weld line HB2, yet no valid signal from weld line HA1, HA2 (Figs. 6 and 7).

Generated from weld line HB3 during the first maintaining, a large quantity of source signal mostly centralized at 1,200, 2,200, and 3,800 mm, while the crest amplitude reached 82 dB. A few valid source signals generated from weld line HA2, HB2, yet there were still no signal generated from weld line HA1 (Figs. 8 and 9).

The second stage was pressure boosting, from 6.3 to 6.45 Mpa, then maintained it.

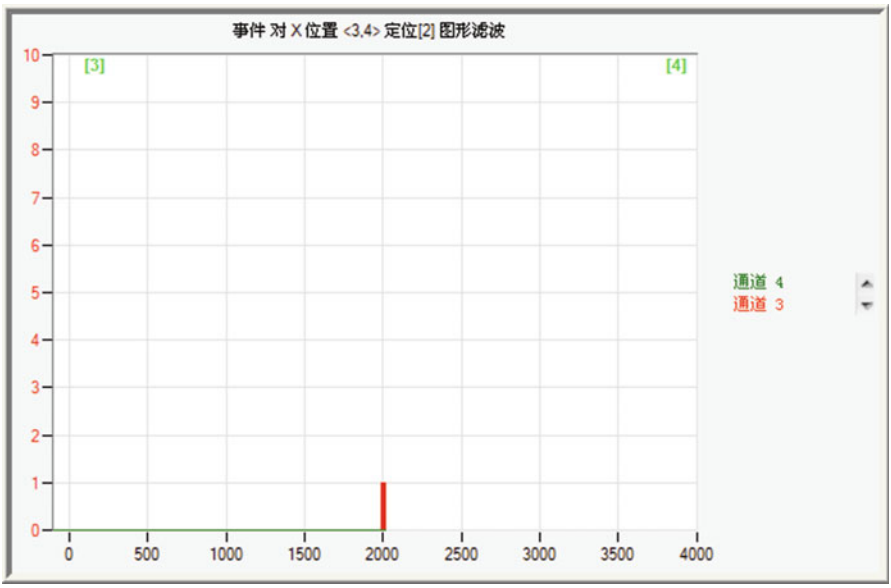

Fig. 6 Linear alignment map of HB2's detection signal during first loading

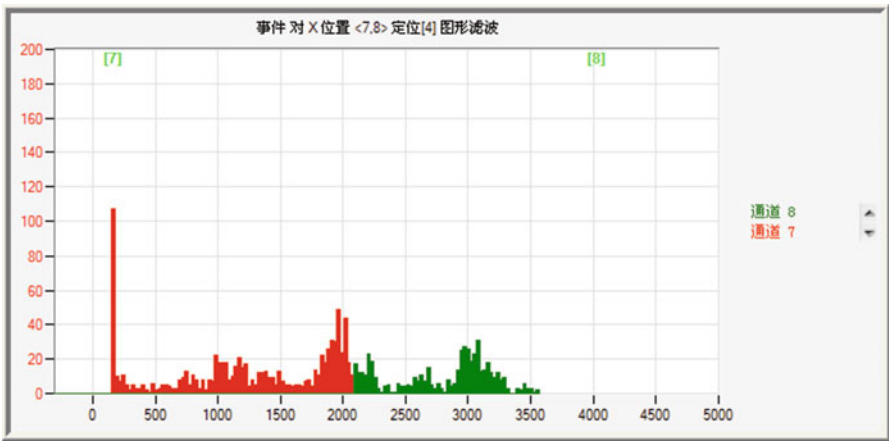

Fig. 7 Linear alignment map of HB3's detection signal during first loading

Generated from weld line HB3 during the second loading, a large quantity of source signal mostly centralized at 2,000, 2,300, and 3,800 mm, while the crest amplitude reached 81 dB. But there were no valid source signal generated from weld line HA1, HA2, HB2 (Figs. 10 and 11).

Generated from weld line HB3 during second maintaining, a large quantity of source signal mostly centralized at 1,000, 2,000, 2,400, 3,000, and 3,800 mm, while

Fig. 8 Linear alignment map of HA2's detection signal during first retaining

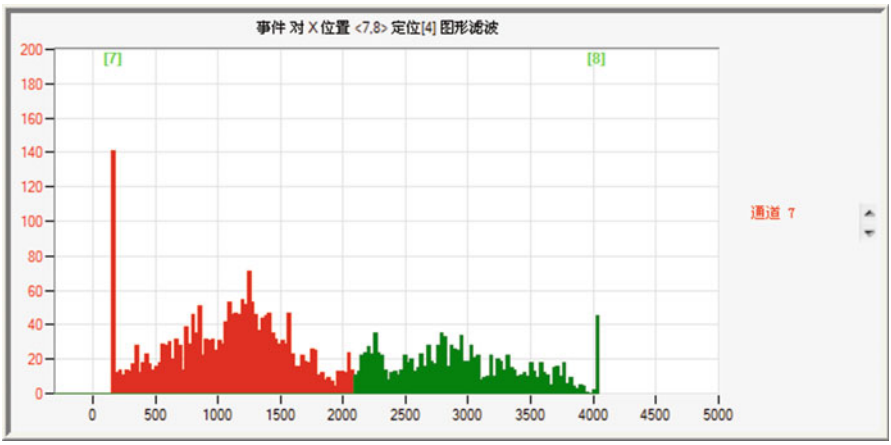

Fig. 9 Linear alignment map of HB3's detection signal during first retaining

the crest amplitude reached 78 dB. Still, no valid source signal generated from weld line HA1, HA2, HB2.

According to the GB18182-2000 "Acoustic emission examination and evaluation of metallic pressure vessels," source within 1,000 mm of weld line HB3 was active and of mid-strength, ranked D-level source; source within 2,000 mm was strongly active and of mid-strength, ranked E-level source; source within 3,000 mm was active and of mid-strength, ranked D-level source; source within 3,800 mm was weakly active and of mid-strength, ranked C-level source. Above data proved that active source existed in all four positions. Due to the limitation of system process debugging, the pressure, which had not reached maximum at full capacity, merely

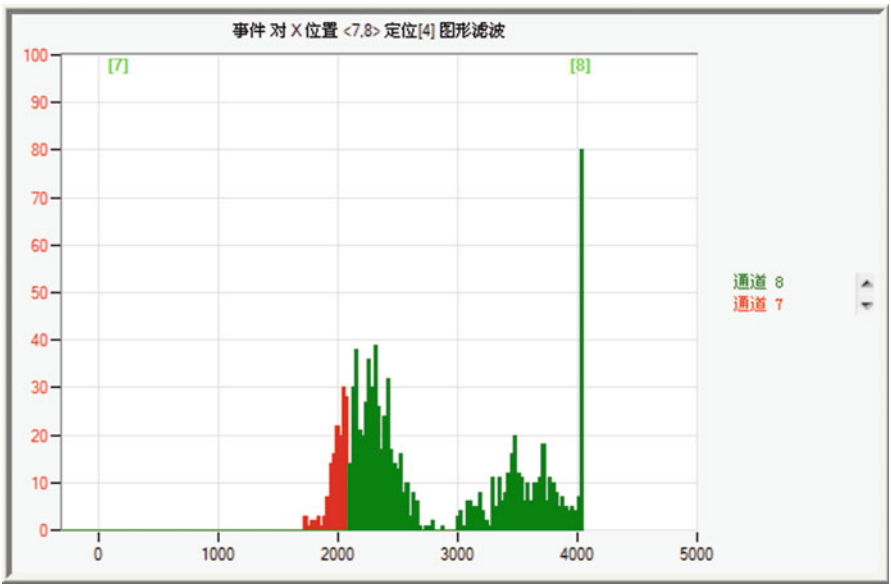

Fig. 10 Linear alignment map of HB3's detection signal during second loading

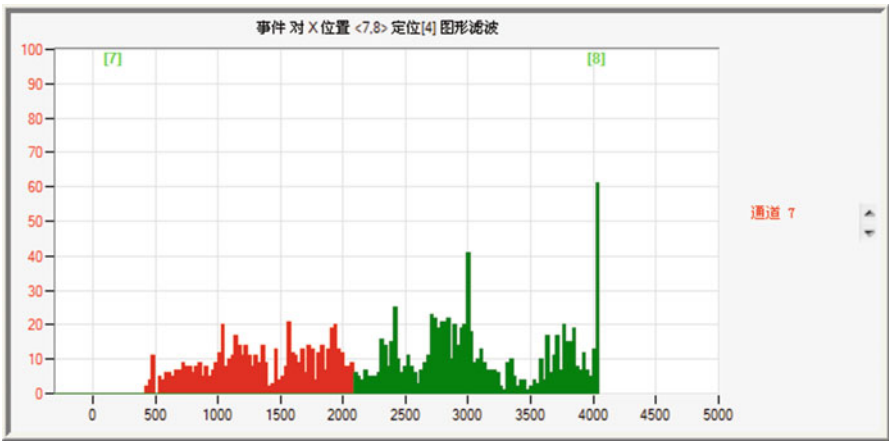

Fig. 11 Linear alignment map of HB3's detection signal during second retaining

raised up to 6.5 MPa. Continual loading might lead to the extension of the three sources of active defects, or generating new sources of active defects.

Compared with original testing data, results of ultrasonic recheck showed a number of differences (contrast is shown as Table 3). As the testing methods differ, it was reasonable to see the difference in numerical values. A new defect, whose position agreed well with acoustic emission source area, was found during the

Table 3 Contrast between data of the two ultrasonic testing

Data of recheck					Data of former manufacturer			
No.	Position	Depth of burial (mm)	Indicating length (mm)	Reflectance amplitude	Position	Depth of burial (mm)	Indicating length (mm)	Reflectance amplitude
1	HB3-125	34.3	17	III	HA2+1345.6	28.3	43.0	III
2	HB3-275	56.5	50	III	HB3+3407.6	15.0	47.0	II
3	HB3-410	45	25	III	HB3+3323.6	63.0	38.0	III
4	HB3-890	22.5	30	II	–	–	–	–
5	HB3-2183	56.4	15	II	HB3+1889.9	60.3	33.0	III

P.S. In the two data, different marking outset led to the difference in position marking

recheck. So we could come to the conclusion—active defects of HB3, discovered by AET, were mostly formed by those untreated inside defects. It was also suggested that it is operable to test defects of similar devices in a high background noise environment through AET. For the purpose of verifying the feasibility of AET, further contrastive detection was necessary to get an accurate appraisement.

According to the above analysis, periodic online AET should be carried out while the gasifier is running. Weld line HB3 was supposed to be key monitored; moreover, overpressure was strictly forbidden in service—maximum working pressure ought not to exceed 6.45 MPa. In order to track the extension state of inherited defects, the manufacturer should make good use of shutdown maintenance or choose another moment to recheck the corresponding part of the vessel by ultrasonic.

6 Summary

As a practical application of acoustic emission in high background noise environment, this test created a new endeavor indeed. The mending positions of vessel are supposed to be tested by online AET under operating conditions, each quarter of later operation. Meanwhile building data files of gasifier's regular online AET, more detailed contrastive analysis on the data of regular examination, mastering the working condition of gasifier, all can ensure gasifier's safe operation more effectively. In addition, they can help accumulate more valuable data of online AET, under similar operating conditions.

References

1. C. Wang, W. Zhu, Based on acoustic emission testing and ultrasonic TOFD online technology research and application [J]. Petro. Chem. Equip. **3**, 20–22 (2009)
2. Y. Zhang, G. Dai, W. Li, Research and application of the periodical on-line inspection method of acoustic emission of adsorption towers [J]. Chem. Eng. Mach. **36**(2), 144–149 (2009)
3. Z. Zhang, J. Gong, H. Liang, The application of acoustic emission technology on coke tower inspection [J]. Nondestr. Test. **32**(2), 143–148 (2010)
4. L. Sun, J. Shen, G. Mao, X. Wang, Several false defect signals in acoustic emission testing of pressure vessels [J]. Nondestr. Test. **30**(8), 550–552 (2008)

Part V
Condition Monitoring and Diagnosis

Acoustic Emission: An Indispensable Structural Health Monitoring Means for Aircraft

Rongsheng Geng and Peng Jing

Abstract In the past 10 years, full scale fatigue tests were undertaken for two types of aircraft groups, and correspondently, the acoustic emission based integrated non-destructive testing means was used for the early detection of fatigue damages throughout the test. What accompanied the full scale fatigue test was eventually a health monitoring process for the aircraft. During the test, researchers needed to know when the aircraft "got ill" and what remedy measure was required to make the aircraft "recover." A variety of techniques have found important applications in the structural monitoring. Studies were made of various means and the role of health monitoring of aircraft structures and of some special problems to be solved for each method. Comparisons were made for various monitoring methods and the most suitable one was chosen for the full scale aircraft under test. A carefully designed NDT scheme plus AE monitoring was eventually selected as the first choice to complete the task and was shown rather effective in early damage detection for the aircraft under fatigue test although very high risk was confronted throughout the test.

1 Introduction

The health monitoring is not a new concept and it comes from the "periodic physical examination" or "the clinic observation for a patient." The same exists for the aircraft structure, and the prerequisite for its safety and possible life-extension is the capability of detecting early damages in key parts before being not too late for their recovery repairing or replacement [1, 2].

R. Geng (✉) • P. Jing
Beijing Aeronautical Technology Research Centre, Beijing 100076, China
e-mail: gengrs@sohu.com

G. Shen et al. (eds.), *Advances in Acoustic Emission Technology: Proceedings of the World Conference on Acoustic Emission-2013*, Springer Proceedings in Physics 158,
DOI 10.1007/978-1-4939-1239-1_47,

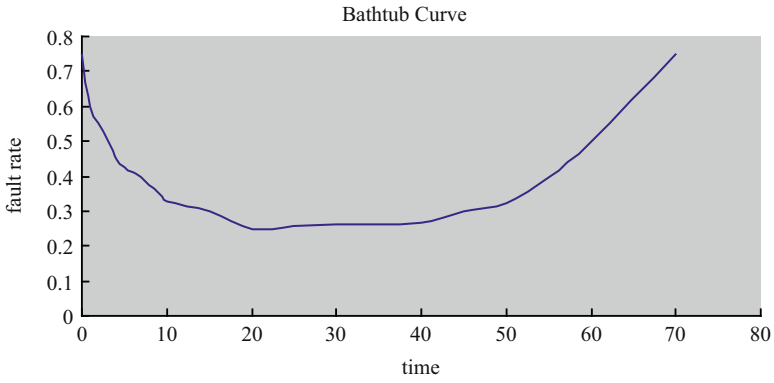

Fig. 1 The bathtub curve of fault (or hazard) rate

The traditional method of maintenance is the so-called aftermath repairing following the occurred accident or breakage of a component. The second stage of maintenance concept is so-called periodic or cyclic repairing system, the base of which is the "bathtub curve" of fault rate of a mechanical product, Fig. 1, where the fault rate experiences three stages of fast falling in the early stage (infant mortality), stable (random failure) and abruptly rising till failure (wearout). This maintenance system is not outdated as it sounds and till now it still acts as the main system of maintenance for many industrial products, such as aircrafts and car vehicles, and more importantly the effectiveness of SHM is more or less for the second stage only.

The newly developed maintenance system is the so-called condition based maintenance performed according to the "health condition" of the structure referred. This system sounds as the best maintenance system but it is extremely difficult to realize it completely. Some questions must be answered before its realization and they are: (1) what is the concept of "health" and which parameters are needed to describe the "health?" (2) how to quantify the extent of health? (3) how to evaluate the risk if condition based maintenance system is to be performed and which kind of measures need to be taken in order to safeguard the integrity of the structure, and so on. The periodic maintenance system shall therefore play a dominant role and the structural health monitoring can only play a subsidiary role before a clear answer is given for the above-mentioned questions.

In the past 10 years, fatigue tests were undertaken for two types of aircraft groups and the main goal of the test was to determine the service life of the related aircraft group of which the aircraft under test was its typical representative. One of the key factors in guaranteeing the success of the test was to find and locate the fatigue cracks and damages of critical structures in an earliest possible stage in order for these damages repaired in time without causing the breakage or failure of the structure. The role of a single monitoring means or single NDT means is absolutely limited and the integrated or multi-means monitoring of multi-parameters should be the most effective health monitoring method. Theoretically,

any NDT means can be used as the health monitoring means if a continuous testing is carried out for some parts of the structure. For the reality, some pre-buried sensor strips in the structure can make the monitoring realistic. In any cases, the knowing of the structure itself and the understanding of the engineering project itself is the key factor in performing the so-called health monitoring.

2 Review of Existing Health Monitoring Methods

There are many available methods for health monitoring and in some extent any nondestructive testing means can be employed as the one to achieve the same aim so long as it is used constantly. These methods include strain measurement, optical fiber/optical grate strain measurement, emburied smart sensors, comparative vacuum sensors, structure response evaluation, resistance measurement, ultrasonic guided waves, acousto-ultrsonic testing, vibration analysis and acoustic emission, etc. Theoretical analysis and engineering experience showed that any one single SHM method only was difficult, if not impossible, to acomplish the health evaluation task for aircraft and aircraft structures.

2.1 Strain Measurement

The strain gage measurement is probably the simplest medium for health monitoring and the newly developed optical fiber/optical grate strain gage might be the best replacement for the traditional type gage. The remaining question is the relationship between strain variation and the damage of the structure and so far only quantitative relation between the two is known.

2.2 Comparative Vacuum Monitoring (CVM) Technique

This technique was first developed by SMS (Structural Monitoring System) company of Australia and it made use of the principle that a steady-state vacuum maintained within a small volume was extremely sensitive to any leakage [3, 4]. In Fig. 2 is shown its work principle, where the red ones represent capillaries maintaining vacuum whereas the blue ones represent the capillaries of normal air pressure. The two types of capillaries are alternatively lined together to maintain a fixed pressure difference. If there is no crack crossing the sensor, the pressure difference shall be steady, whereas the pressure difference shall be abruptly increased if there is a crack under the sensor lines. The greatest advantage of the CVM is its insensitive to the background noise and this makes it a very good alternative choice of acoustic

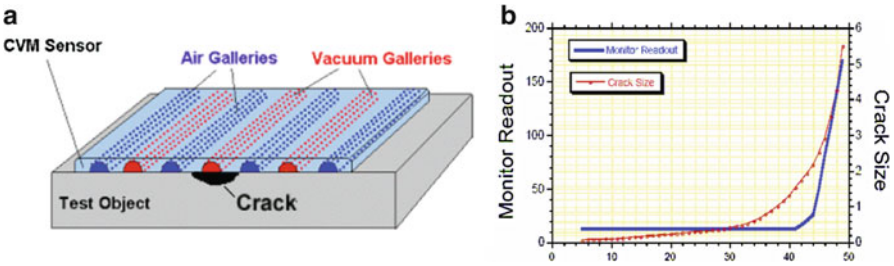

Fig. 2 Principle of CVM. (**a**) CVM sensor composition, (**b**) CVM readout vs. crack size

emission. The CVM was used for the monitoring of the right side wall of the aircraft during its fatigue test.

2.3 Embedded Smart Sensor

The key factor of the technique is to develop the smart sensors of light weight and tiny size so that they can be pre-buried inside the structures. The Acellent Technologies of the USA declared the success of realizing this technique and it has already been used in the SHM.

2.4 Monitoring of CFRP (Carbon Fiber Reinforced Polymers) by Resistance Measurement

Carbon fiber reinforced polymer (CFRP) has found wide applications in aeronautical engineering materials due to its very high specific strength (ratio of strength against weight for unit volume) and are used for aircraft wings and air foils. The shortcomings of this material are the possible sudden breakage without precautions. The monitoring of the CFRP during its service is therefore extremely important. The CFRP, which is conductive, can be monitored by its changes in electrical resistance with time. The changes in electrical resistance of CFRP composites are related to the changes in the micro structure in the materials.

The resistance monitoring is to use the material itself as the sensors and to use the special integrated processing method to allocate the electric polar inside the material to have the resistance change signal out. Tests have shown that the longitudinal resistance change is a good signature of fiber breakage and the transverse resistance change is to some extent related with the damage extent of the material, and therefore a combination of changes of longitudinal and transverse resistances shall be a very good indicator of the material damage [5, 6].

2.5 Acousto-Ultrasonic Method (AU)

It is an active monitoring means as compared with the AE because it actively stimulates the object under test by emitting an acoustic wave to it or knocking at the object and then to watch the change of received stimulated signals. Strictly speaking this method is only a variate of acoustic emission or merely a type of vibration monitoring. A major draw of this method is the trasmission efficience of the transmitted stress wave and the stress wave factor (SWF) can be used as an evaluation parameter for the structural integrity of the object under test:

$$\mathrm{SWF} = RTC \tag{1}$$

where, R—the repetition frequency of input waveform, T—preset time interval, and C—ring down count of acoustic emission signal over the threshold voltage.

There are definitely many limitations in using the AU to characterize the structural damages although some successes were reported.

2.6 SHM Based on Vibration Signal Analysis

Structural health monitoring by vibration is the most popularly and widely used method, especially for rotating machinery and bearings. A machine shall produce vibration signal whenever the machine is in run. The vibration signal shall show changes when early damages or failures occur in the rotating elements, and through monitoring these changes one can find or locate the early damages.

There are some commonly used methods for characterizing the vibration signals, which are: (a) low frequency analysis, whose main frequency ranges are between tens Hz and several kHz, decided by shaft rotating speed and the numbers of bearings. The main advantage of this range is the abundant information about the fault and ease with the diagnosis schemes, but the disadvantage is the serious noise interference and the main frequency being related with the shaft rotating speed; (b) high frequency range analysis, whose main frequency ranges are in several tens kHz, decided by the inherent vibrations of bearings; (c) resonant-demodulation (R-D) method, whose working principle is based on that any fault in the bearings shall produce impulse signal and the impulse in return behaves like an exciting source to stimulate the resonant vibrations of the sensor. One can use the resonant signal to obtain its envelope through demodulation and the envelope shall contain the fault information about the bearings. The R-D method is widely used because it has the highest sensitivity compared with other vibration means by using the resonant characteristics of the sensor and enhancing the signal to noise ratio.

In addition to using the effective vibration level in certain frequency range, the gradient (the differential) of the vibration signal and the sound signal both can be used to diagnose the state of the machine. The integral use of several parameters can

effectively raise the fault diagnostic rate and reduce the rate of false alarm and undetected faults. The key point is to choose the correct frequency range and define the permissive limit of vibration parameters for normal state, which relies on results by well designed experiments and statistically averaged vibration parameters through field test or test bench. It was reported that the intermediate-axial bearing of certain fight aircraft and the inter-axial bearing gap were effectively monitored by two types of bearing fault testers.

2.7 SHM Based on Ultrasonic Guided Waves

For some layered and plate structures of aircraft, such as the wings, ultrasonic guided waves can play important role in monitoring their structural changes. One of the comparatively effective means is to have the sensors embedded in the structures under monitoring, whereas the most difficult is to choose the correct wave modes sensitivity of which is related to the faults. The other means is to use a pair of sensors, one of which is to emit the stress wave into the structure, and the other is to receive the transmitted wave to observe any changes of the wave signature against time during service [7]. Although some partial successes were reported in the past, there is still a long way to go before one can realize the genuine structural health monitoring.

2.8 Acoustic Emission (AE)

AE is one of the passive testing means, which need not inject any signals or stimulus to the object under observation. The AE sensors are sitting on the structures to listen to the changes in the structural and therefore AE is characteristic of condition monitoring and of exerting the least effect on the structures themselves. The other advantage of AE as compared with other NDT means is the larger areas covered by every one sensor, which is important for large structures, such as aircraft. For those inaccessible structures by conventional NDT means, AE shows a convincible advantage because it needs only an effective path for sound wave, but not actually physically approaching the parts under monitoring. For key aircraft structures, which are almost in the hidden places, the accessibility is very important for realizing the test. The main difficulties for AE monitoring are the background noise interference and the way to identify fatigue crack or damage related AE signals from the noises. The other one is the lack of effective means to quantify the damages.

3 Full Scale Aircraft Fatigue Test: SHM from Cradle to Grave

A breakthrough of SHM in application for the key engineering project is the AE based integrated NDT means for two consecutive full aircraft fatigue tests. The role of fatigue test of a full scale aircraft is to determine the service life of the related aircraft group, of which the aircraft under test is its typical representative. Well designed effective NDT schemes and procedures, including acoustic emission fatigue damage monitoring for key structures of the aircraft are the key factors to guarantee the fulfillment of the fatigue test. The major purpose of using AE is to find and locate the fatigue cracks and damages of critical structures in an earliest possible stage in order for these damages repaired in time without causing breakage or failure of the structure. For one type of aircraft under test, due to the early detection of fatigue cracks in some key structures and hence resulting in an effective repairing measure, the life of the aircraft group was increased by more than half of the originally designed one, creating enormous economic and social benefit. Also, so obtained results were used to guide the repairing measures in the repair depot. It is possibly the first ever AE work of real time and in-time monitoring of fatigue cracks in such a long period and for a full scale aircraft, to the author's knowledge. Recent experience of fatigue test for another full scale aircraft showed again the significance of AE-based integrated NDT means for aircraft life evaluation.

3.1 Main Features of AE Based SHM

The following are the main characteristics of the AE based SHM during full scale fatigue test.

1. Full time monitoring-from cradle to grave, i.e., from the new aircraft to the termination of the life of the aircraft;
2. All direction monitoring, any structures relating with the life of the aircraft must be under monitoring;
3. AE centered integrated NDT means;
4. Endurable repairing measures based on testing results.

3.2 Background Knowledge and Background Noise

It was definitely reasonable to assume that the aircraft under test was in good conditions in the early stage of the test, and hence the collected data during that stage was the so-called background noise and it did not contain information related with damages. The assumption was important and realistic, but it could give us

much information about the background of AE monitoring. It was therefore extremely significant to draw as much information as possible from the background because the work was the basis for the trend analysis and correlation work in later stages.

3.3 Basic Approaches to Signal Processing

The random signals obtained during test must be disintegrated into different sub-data sets of being stationary random signal or pseudo-stationary random signals, whose statistically averaged data sets can show meaningful trend for the aircraft structures under monitoring. A correct strategy for the analysis of the recorded data was therefore needed. The load spectrum was random, but it was characteristic of periodic nature in the long run, because it could be resolved into different loading states and each of them could repeat itself in a specified period. For example, the loading states for the main landing gear were composed of taking off, landing on, taxiing operation, braking, turning a corner, etc., and each of them should repeat itself in a specified time period. Therefore, if we dissolve the loading spectrum into different states, especially those main states, then we could take out all the data corresponding to the same loading state and view so-obtained data (so-called sub-data set) as that due to periodic loading state.

Suppose the AE data can be divided into a series of sub-data and the latter forms a time series data, then the dissolution of the data can be expressed as following:

$$\begin{gathered}\left[a_{ij}\right]_t = [\mathbf{A}_{mn}]_t (i = 1, 2, \ldots, m; j = 1, 2, \ldots, n; \text{at time of } t) \\ a_{11}, a_{12}, a_{13}, \ldots, a_{1n} \\ a_{21}, a_{22}, a_{23}, \ldots, a_{2n} \\ a_{31}, a_{32}, a_{33}, \ldots, a_{3n} \\ \ldots \\ \ldots \\ a_{m1}, a_{m2}, a_{m3}, \ldots, a_{mn}\end{gathered} \tag{2}$$

The AE data thus form a tensor $[\mathbf{A}_{mn}]_t$ and can be divided into a series of sub-data, i.e., n vectors, such as $A_1(a_{11}, a_{21}, a_{31}, \ldots, a_{m1})$, $A_2(a_{12}, a_{22}, a_{32}, \ldots, a_{m2})$, $A_n(a_{1n}, a_{2n}, a_{3n}, \ldots, a_{mn})$, with each being corresponding to a specified loading state. The subscript t means that the above mentioned process was carried out at a specific point of time scale for the test, say t moment. It therefore must be noted that every element in so specified sub-data, the vector A_i, was a statistically averaged data, and also it is not a static process, but a dynamic process, which means each vector A_i only stands for the obtained data for the specific loading state in a specific time period, and it shall change and give a series data of A_{it}, and here t stands for the time elapse process.

By doing so, what we need to do is to watch the change tendency of A_{it} or to calculate its correlation coefficient and related changes. Therefore, two methods

could be used. One is to statistically average the sub-data set in a specified time period and to observe its trend of change. The other is to use correlation analysis to view the change trend of the statistically averaged sub-data. Other data processing parameter, like entropy or maxim entropy, also could be used to show the trend of change of AE activity, but we shall not discuss it here. The correlation coefficient γ as we know is a factor to evaluate the similarity of a function with itself after some time lapse has passed. If γ is close to the unit, that means the function does not change very much while time passes by, and for the aircraft structure, it means the area of concern varies a little during the test. More than often, the value of $(1-\gamma)$, the non-correlation coefficient is more sensitive to the state change than γ, but they describe the same thing and give the same result.

3.4 Outcomes

The following are the main achievements for the full scale aircraft fatigue test monitored by AE centered integrated NDT means.

1. Prolonging life of aircraft group
   The life of aircraft group was effectively prolonged. The life of the first aircraft group was extended by more than 50 %, while the second one was over 75 %. The significance of this life prolonging program is not difficult to image.
2. Compiling atlas of aircraft fatigue cracks
   The compiling of aircraft fatigue crack atlas has even more important significance than the life prolonging itself. The atlas can give one clear idea of when and where the fatigue cracks appear and what repairing measures should be taken, which are extremely helpful for the correct operation and correct maintenance of the aircraft.
3. Guiding rule for repairing cycle and repairing method
   All information obtained during the fatigue test shall supply guidance for the repair cycle and repair method, and also the information shall give important guidance for the in-service aircrafts to guarantee their safety flight.
4. Improvement of aircraft design and technology quality
   The comparison of performances of key structures of the two types of aircraft during fatigue test can draw some conclusions for the fatigue behavior of corresponding structures. The difference of fatigue behavior is due to the minor changes of design and technology although the two have almost the same key structures. The second type of aircraft has shown superior fatigue characteristics in many key structures compared to the first one. Understanding these minor structure and technology changes of the second type of aircraft can leave much information for the aircraft designers to learn about.

4 Conclusions

The SHM of aircraft and aerostructures is of significance for their safety during service; its realization is however a very tough task and needs much effort in a long time period. The combination of various SHM methods and the fusion of their resulted data should give much better outcomes compared with any single one SHM means. The application of AE based integrated NDT methods in full scale fatigue test of two types of aircrafts and the successful prolonging of the fatigue lives of the aircraft group showed once again the importance of SHM and implied the possibility of realizing the genuine SHM with the help of advanced NDT techniques and advanced data processing measures.

References

1. W.J. Staszewski, C. Boiler, P.R. Tomlison, *Health Monitoring of Aerospace Structures* (John Wiley & Sons, West Sussex, 2004)
2. R.S. Geng, P. Jing, Identification of acoustic emission signals due to fatigue crack initiation of aircraft bulkhead. Acta Aeronautica Et Astronautica Sinica (in Chinese) **17**(3), 368–372 (1996)
3. P.K. Sharp, G. Clark, *Evaluation of A Novel NDE Technique for Surface Monitoring Using Laboratory Fatigue Specimens*. (Airframes and Engines Division, Defence Science and Technology Organisation, Melbourne, Australia)
4. D.P. Barton, G. Wheatley, Comparative vacuum monitoring (CVM) in fatigue prone areas of in-service aircraft. Aerospace Technology Seminar 2002, Structural Monitoring Systems Ltd., Po. Box. 2067, Churchlands 6018, Australia
5. Y.Q. Mao, D.Z. Wu, X.P. Yang, The development of structural health monitoring for CFRP composite by electrical resistance method. Polym. Mater. Sci. Eng. (in Chinese) **21**(3), 16–20 (2005)
6. Y.Q. Mao, Y.H. Yu, R.C. Zhang et al., Tensile damage behavior study for CFRP composite by electrical resistance measurement. Polym. Mater. Sci. Eng. (in Chinese) **21**(4), 248–251 (2005)
7. H. Lei, G.J. Qi, P. Jing et al., Recent development of ultrasonic guided wave sensor array in aircraft structural health monitoring. Global Chinese Forum on Nondestructive Testing Proceedings, Xiamen, China, November 2011, pp. 132–136

Differentiating Signals from Different Sources of Acoustic Emission for Structural Health Monitoring Purposes

Manindra Kaphle and Andy C.C. Tan

Abstract Though possessing a number of advantages is an effective structural health monitoring tool for engineering infrastructures, a major challenge in practical use of acoustic emission (AE) technique is the presence of sources of AE other than crack related, such as rubbing and impacts between different components of a structure. These spurious AE signals often mask the signals from the crack activity; hence discrimination of signals to identify the sources is very important. This chapter explores this issue in detail and also explores how different signal-processing tools such as cross-correlation, magnitude squared coherence, and energy distribution in different frequency bands can be accurately used for differentiating signals from different simulated AE sources.

1 Introduction

Acoustic emission is the phenomenon where high-frequency stress waves are generated by rapid release of energy within a material by sources such as crack initiation or growth. AE is one of the several nondestructive testing (NDT) techniques currently used for structural health monitoring (SHM) of engineering structures. Some of its advantages include the ability to provide continuous in situ monitoring and high sensitivity to crack activity. However, a major problem in practical use of AE technique is the presence of sources of AE other than crack related, such as rubbing and impacts between different components of a structure. These spurious AE signals often mask the signals from the crack activity; hence discrimination of signals to identify the sources is very important. This chapter

M. Kaphle (✉) • A.C.C. Tan
Queensland University of Technology, Brisbane, QLD 4000, Australia
e-mail: m.kaphle@qut.edu.au

G. Shen et al. (eds.), *Advances in Acoustic Emission Technology: Proceedings of the World Conference on Acoustic Emission-2013*, Springer Proceedings in Physics 158,
DOI 10.1007/978-1-4939-1239-1_48,

explores the use of different signal-processing tools such as cross-correlation, magnitude squared coherence, and energy distribution in different frequency bands for accurately differentiating signals from different simulated AE sources.

1.1 Signal Uniqueness and Similarity

Comparing similarity of signals can be used as a tool for signal discrimination. As manual checking of similarity can be tedious and in cases of large number of signals can be impossible, in this study the following tools are used to check if two signals are similar or not: the cross-correlation coefficients in time domain and magnitude squared coherence (MSC) in frequency domain. The cross-correlation coefficients give a measure of the similarity of two time series shifted along each other, with the maximum value indicating the maximum correlation of the two signals at a certain time shift [1, 2]. Mathematically, the cross-correlation function relating two signals $f_1(t)$ and $f_2(t)$ can be written as

$$r_{xy}(\tau) = \int_{-\infty}^{\infty} f_1(t) \cdot f_2(t+\tau) \cdot dt \tag{1}$$

where τ is a time shift imposed upon one of the signals and cross-correlation function r_{xy} is a continuous function of the imposed time shift τ [3].

Similarly, MSC of two signals is calculated using power spectral densities (P_{xx} and P_{yy}) and cross power spectral density (P_{xy}) of the signals as follows [4, 5]:

$$C_{xy}(f) = \frac{\left|P_{xy}(f)\right|^2}{P_{xx}(f) \cdot P_{yy}(f)} \tag{2}$$

For two identical signals, MSC value of 1 is obtained over the whole frequency range, while lower values occur for unrelated signals.

1.2 Energy Distribution in Different Frequency Bands

Performing short-time Fourier transform (STFT) on recorded signal results in a matrix of coefficients, $C(\omega_i,\tau_j)$, by discretization in both frequency (ω) and time (τ) domains. $|C(\omega_i,\tau_j)|^2$ can then be used to represent energy contents (spectral density) of the signal in joint time and frequency domains, with the resulting plot known as spectrogram. To study energy distribution with frequency, energies across the total time can be then summed and the values normalized with respect to the total energy across all times and frequencies, as follows:

$$E(\omega) = \frac{\sum_{j=1}^{N} C(\omega_i, \tau_j)}{\sum_{i=1}^{M}\sum_{j=1}^{N} C(\omega_i, \tau_j)} \tag{3}$$

where M and N are the number of discretization in frequency and time domains, respectively. $E(\omega)$, representing the energy ratios against frequencies, can then be used to study the energy distribution in different frequency bands. Though energy–frequency analysis can be done using Fourier transform alone, it is noted that the study of simultaneous time–frequency distribution conveys important information regarding signal discrimination.

2 Experiments

2.1 Experiment A

For first set of experiments, two sources of AE signals were generated by (a) breaking 0.5 mm pencil leads (PLB) and (b) dropping steel balls (6 mm diameter) from a height of 15 cm on a 4 m long steel beam (BD). Breaking pencil lead is a standard method for simulating acoustic emission signals as it provides a fast rise time or step function like transient force similar to real AE sources and easily reproducible signal waveforms [6]. Ten sets of each experiment were performed. Four-channel micro-disp PAC (Physical Acoustics Corporation) system was used for data acquisition. An R15α sensor (manufactured by PAC, resonant at 150 kHz) was used to collect AE signals. The sensor was coupled to the test specimen using vacuum grease and magnetic holders. Preamplifiers were used with gain set at 40 dB and the signals were band-pass filtered between 20 and 400 kHz using the software control of the data acquisition system, as most signals were expected in this range. A value of 60 dB was set as the threshold value for recording.

2.2 Experiment B

For second set of experiments, AE signals from real growing crack were collected from three-point bending test of a rectangular steel specimen—300 mm long, 25 mm wide, and 10 mm thick, with a small 45° through cut notch in the middle to initiate the crack growth, using an INSTRON tensile machine with a 50 kN load cell (at a loading rate of 2 mm/min); see Fig. 1.

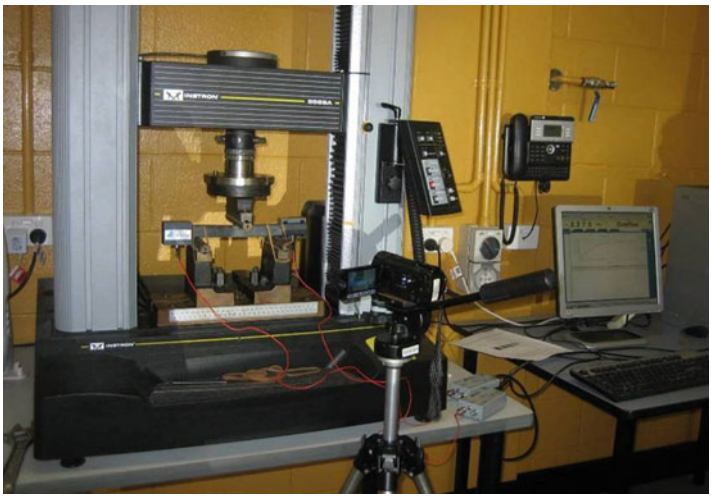

Fig. 1 Experimental setup for three-point bending tests

The same data acquisition system as described in Experiment A was used in this case. Two R15α sensors were placed at two ends of the specimen to collect AE signals and were coupled to the test specimen using vacuum grease and magnetic holders. Preamplifiers were used with gain set at 40 dB. To set the threshold value for recording and ensure that sensors were performing correctly, pencil lead breaks (5 mm, HB leads) were carried out near the crack tip and recorded signals were observed. The value of 60 dB was decided as this value was found to prevent the recording of lower amplitude reflected signals from the pencil lead break tests as well as remove low-amplitude signals generated at the loading point from the roller directly above the crack during a trail test.

Impact signals were simulated by dropping steel balls (6 mm diameter) from a height of 15 cm on the middle of a thin steel beam (4 m long, 75 mm wide, and 5 mm thick). An R15α sensor was placed at a distance of 1 m from the impact location to record the signals. Rubbing was simulated by allowing a steel piece ($200 \times 135 \times 12$ mm^3) to slide along an inclined steel beam, with two sensors (R15α) placed underneath the inclined beam. Other instrumentation and settings used were same as described previously.

3 Results and Discussion

3.1 Experiment A

To study signal uniqueness, the first generated PLB signal was used as a template signal to perform cross-correlation and magnitude squared coherence with rest of the simulated signals. The results are shown in Fig. 2a, b, respectively.

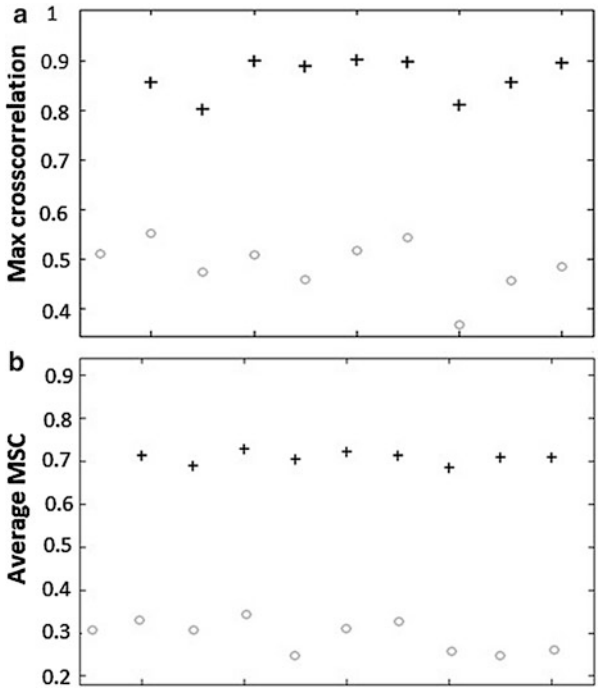

Fig. 2 (**a**) Maximum cross-correlation coefficients, (**b**) average magnitude squared coherence values between the template PLB and rest of the signals

Two clusters are clearly visible—the cluster with higher values (indicated by "+") corresponds to the values from comparison of the template PLB with other PLBs while smaller values (indicated by "o") correspond to the comparison with the BD signals. Summarizing the results, cross-correlation of the template PLB signal with the remaining nine PLB tests gave an average maximum value of 0.87 (in the range between 0.80 and 0.91) while the value for cross-correlation between the PLB and ten BD signals was 0.48 (in the range between 0.38 and 0.54). Further, the average MSC values of the template PLB with the other PLB signals lie in the range of 0.71–0.75, while mean MSC values of the PLB signal with other ten BD signals recorded by S1 lie in the much smaller range of 0.25–0.35 with a mean value of 0.29.

Thus, very distinct differences in maximum cross-correlation and average magnitude squared coherence values are seen between signals from like and unlike sources. It proves the suitability of using these parameters as criteria for signal discrimination when a signal from a known source is available as template for comparison.

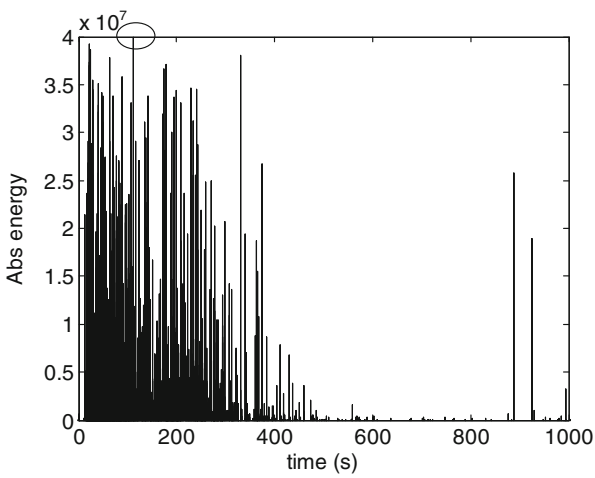

Fig. 3 Absolute energy versus time

3.2 Experiment B

The variation in absolute energies of hits with time for one sensor during three-point bending test is shown in Fig. 3. Absolute energy is derived from the integral of the squared voltage signal divided by the reference resistance (10 k-ohm) over the duration of the AE waveform packet [7]. Signals with highest energy can be attributed to crack growth, while those with very low energies are likely to have occurred due to reflections of the signals from the edges and can be neglected.

An AE crack signal (occurring around 150 s, indicated in Fig. 3) is shown in Fig. 4a. To study the distribution of signal energy in time and frequency domains, short-time Fourier transform was carried out using time–frequency toolbox [8]. Typical impact and rubbing signals obtained from the experiments are also shown in Fig. 4b, c, respectively. In all plots, the energy values (in z-axis) are in logarithmic scale for clarity and indicated by color scale.

To study energy distribution with frequency, ten random signals of each type recorded by one sensor were collected. Energies across the total time (squared STFT coefficients) were summed and the values normalized with respect to the maximum energy as described in Sect. 1. The distribution of energy against frequencies (averaged for ten signals of each type) is shown in Fig. 5.

Rubbing signals were seen to be of continuous type compared to transient nature of crack signals. Impact signals were also transient but reflections persist and continue for longer duration compared to the crack signals. From energy distribution plot in Fig. 5, impact signal is found to have frequencies of around 60 kHz. For rubbing signals, two peaks of frequencies of round 70 and 120 kHz are visible. However, in addition to frequency components of 70 and 120 kHz, another peak of around 200 kHz is present for the crack signal. Thus, distinct distribution of energies with frequencies is found for the three main types of AE source signals; hence, this can act as an effective source differentiation criterion. However, care is

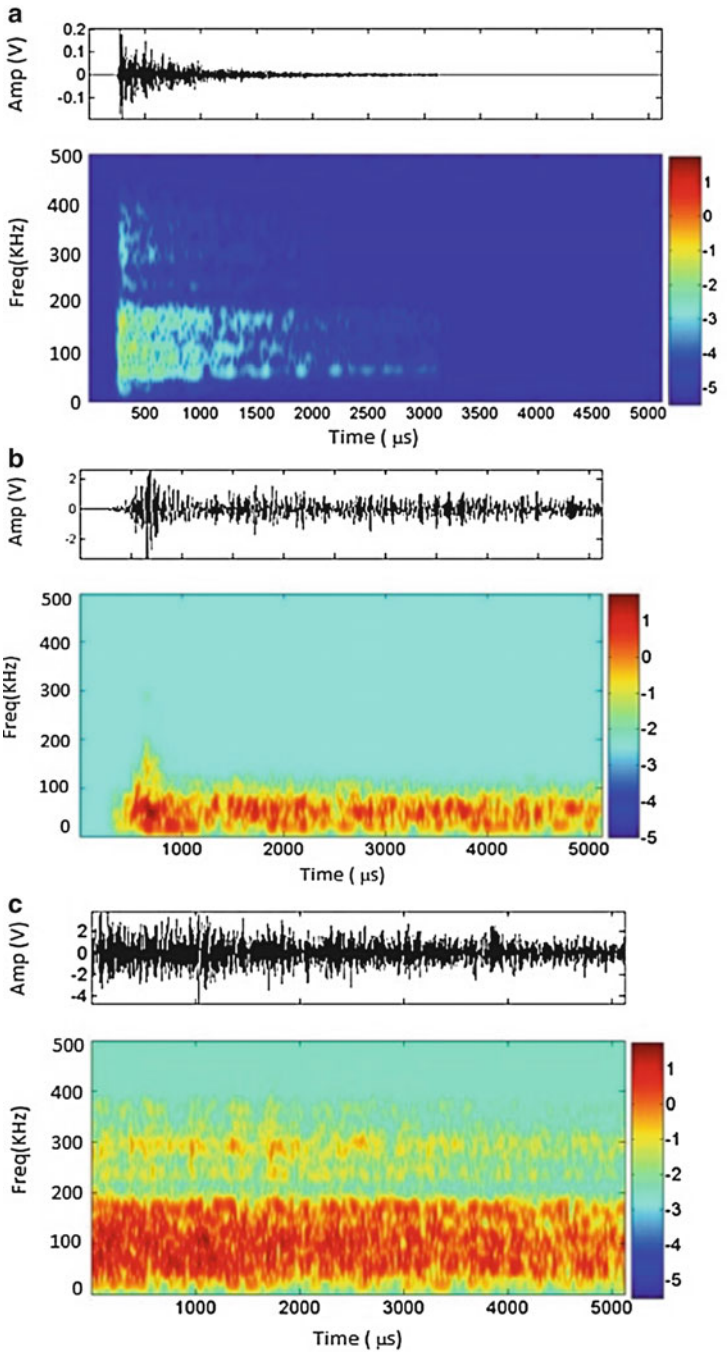

Fig. 4 (**a**) Typical crack signal and its STFT analysis, (**b**) typical impact signal along with its STFT analysis, (**c**) typical rubbing signal along with its STFT analysis

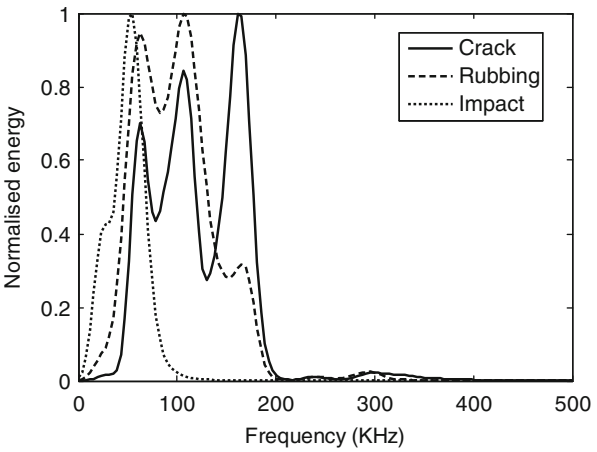

Fig. 5 Energy distribution in different frequency bands for three different signal types

needed to interpret results as there are numerous factors that can affect AE signal waveforms, such as dimensions of the medium, the paths the signals travel, signal reflections, and mode conversions. It is very difficult to take every factor into account; nevertheless, it is believed that energy distribution with frequency can still convey information about the nature of the source.

4 Conclusion

Source differentiation is an important component of AE monitoring. This study explored the use of different signal-processing tools such as cross-correlation, coherence, and energy distribution in frequency domain for the purpose of signal differentiation from AE sources and found encouraging results. Further research is being carried out to simulate more accurate crack, impact, and rubbing signals and explore newer techniques for signal discrimination.

References

1. M. Eaton, R. Pullin, K. Holford, S. Evans, C. Featherston, A. Rose, Use of macro fibre composite transducers as acoustic emission sensors. Rem. Sens. **1**, 68–79 (2009)
2. J.H. Kurz, F. Finck, C.U. Grosse, H.W. Reinhardt, Similarity matrices as a new feature for acoustic emission analysis of concrete. 26th European Conference on Acoustic Emission Testing, Berlin, 2004
3. P.A. Lynn, *An Introduction to the Analysis and Processing of Signals* (Macmillan, London, 1973)
4. C.U. Grosse, F. Finck, J.H. Kurz, H.W. Reinhardt, Improvements of AE technique using wavelet algorithms, coherence functions and automatic data analysis. Construct. Build Mater. **18**, 203–213 (2004)

5. M.A. Natick (ed.), Mathworks, *MATLAB Users Guide* (Mathworks Inc, Natick, MA, 2009)
6. W.H. Prosser, Acoustic Emission, in *Non-destructive Evaluation, Theory, Techniques and Applications*, ed. by P.J. Shull (Marcel Dekker, New York, NY, 2002)
7. Physical Acoustics Corporation, *PCI-2 Based AE System User's Manual* (Physical Acoustics Corporation, Princeton Junction, NJ, 2007)
8. F. Auger, P. Flandrin, P. Goncalves, O. Lemoine, Time–Frequency Toolbox: For Use with MATLAB (CNRS, France and Rice University, USA, 1996)

Application of Acoustic Emission Technology for Rolling Bearing Condition Monitoring on Passenger Ropeway

Junjiao Zhang, Heying Wang, Gongtian Shen, Zhanwen Wu, and Yilin Yuan

Abstract As one of the most important parts on the passenger ropeway, the rolling bearing is difficult to be disassembled for in-service inspection. Online monitoring of rolling bearing on passenger ropeway could be carried out by acoustic emission technology. This chapter presents two tests of acoustic emission detection of rolling bearing on a ropeway. The AE characteristics of the normal rolling bearing are investigated using comparative analysis of AE statistical parameters, AE parameter courses, waveform, and spectrum. The results prove that the AE technology has great potential for the condition monitoring and fault diagnosis of rolling bearings on passenger ropeway.

1 Introduction

Passenger ropeway is a mechanical transport facility which uses aerial rope and delivery vehicles to transport passengers. With the rapid development of tourism, 860 passenger ropeways have put into passenger transport in China. Rolling bearing is an important stress part of passenger ropeway; its failure will lead to accidents and casualties. There is no mature and effective method of bearing testing due to difficulty to disassemble and its extremely low speed, which brings a huge risk to the safe running of ropeway. Therefore, it is urgent to find an in-service nondestructive testing method for the rolling bearings. Acoustic emission

J. Zhang (✉) • G. Shen • Z. Wu • Y. Yuan
China Special Equipment Inspection and Research Institute, Beijing 100013, China
e-mail: zhangjj1000@163.com

H. Wang
Institute of Quality and Technology Supervision, Hebei University, Baoding 071002, China
e-mail: 2418985388@qq.com

G. Shen et al. (eds.), *Advances in Acoustic Emission Technology: Proceedings of the World Conference on Acoustic Emission-2013*, Springer Proceedings in Physics 158,
DOI 10.1007/978-1-4939-1239-1_49,

(AE) technique not only can meet the requirement but also has the potential for prediction of early failure.

There are numerous investigation reports about rolling bearing condition monitoring and fault diagnosis based on AE technology which are mainly about AE parameter analysis, waveform analysis, fault location, and pattern recognition [1, 2]. However, most of the detect objects are high-speed rolling bearings [3, 4]. For the low-speed rotating machinery, acoustic emission online detection has been successfully applied on the rolling bearing of giant wheel [5]. Also, the AE signal characteristics were acquired through parameter analysis, spectrum analysis, etc.

In this chapter, we sum up the analysis methods for AE signals of low-speed rolling bearing which were obtained in previous studies. Then, the AE signals of rolling bearing on a ropeway acquired from two tests were analyzed using the methods above. The results of this research establish an important foundation for the condition monitoring and fault diagnosis of rolling bearings on passenger ropeway.

2 AE Signal Analysis Method of Low-Speed Rolling Bearing

2.1 Statistical Analysis of AE Parameters

The statistical analysis method can extract the useful information from a large quantity of AE signals which were collected during the long-term online monitoring of the low-speed rolling bearings.

An acoustic emission signal can be described by most widely used parameters such as amplitude, rise time, duration, root-mean-square voltage (RMS), counts, energy, and hits. The AE parameters are calculated according to the operating circles of rolling bearing. For each circle, the sum of hits and the mean value of other AE parameter are defined as the statistical parameters. Then fitting curves of the statistical parameters with running circles are obtained by MATLAB. By observing the trend of the fitting curves, the abnormal condition of rolling bearing can be discovered during its operation.

By means of statistical analysis of AE parameters, the abnormal signals of rolling bearing on giant wheel have been discovered in the fitting curve of the mean value of RMS [6].

2.2 Observation of AE Parameter Courses

The AE source activity and its trend can be reflected intuitively by the changes of AE parameters with time. Therefore, observation of parameter courses is most commonly used in AE signal processing. The periodic regularity of AE signals or signals with high amplitude can be directly observed in parameter courses during the operation of rolling bearing. It will be possible to realize fault prediction.

2.3 Waveform and Spectrum Analysis

We can obtain a gross evaluation and description of the AE signal by parameter analysis methods and in detail with the waveform analysis methods. The fast Fourier transform (FFT) has been used extensively for the waveform analysis of AE signals. The spectrum obtained by the FFT shows the frequency distribution characteristic of the AE signal. According to the changes of frequency distribution and its energy of AE signals, the health status of rolling bearing can be reflected to some extent.

In the study of rolling bearing with an artificial defect on giant wheel, there is a new peak frequency appearing compared to the frequency distribution of the rolling bearing with no defect [7].

3 AE Signal Characteristics of Rolling Bearing on Passenger Ropeway

AE online monitoring of rolling bearing on a ropeway was carried out in 2008 and 2012. The test object is a continuous circulating passenger ropeway in a park at Henan province; see in Fig. 1. The model of rolling bearing of the ropeway is GB297-64 7536E. The bearing operating cycle is 12.17 s; see in Fig. 2. An AMSY-6 digital multichannel acoustic emission instrument was used in the test. The sensors VS150-RIC were used to detect the AE signals which main frequency range is from 100 to 450 kHz.

A large number of AE signals were collected in the process of normal operation of the ropeway. In order to obtain the AE characteristics of rolling bearing on passenger ropeway, the signals collected from one test are analyzed first using the method described above.

3.1 AE Statistical Parameters

The AE signals are acquired continuously for about 310 s in one test. According to the bearing operating cycle, the acquisition time is about 25 running cycles. For each operating cycle signals, the sum of hits and the mean value of other AE parameters are calculated using the statistical analysis method. Then the fitting curves of the statistical parameters with running cycles are obtained. Observing the statistical results of AE parameters, we found that all the fitting curves fluctuate within a certain range without obvious change in the amplitude. Figure 3 shows the fitting curves of hit sum and RMS mean.

Fig. 1 The test passenger ropeway

Fig. 2 The test rolling bearing

3.2 AE Parameter Courses

Observing the AE parameter courses of 25 running cycles, there is no periodic regularity of peaks. All the AE parameters irregularly changed with time. See the courses of hits-time, RMS-time, counts-time, and energy-time in Fig. 4.

3.3 Waveform and Spectrum

Three signals are randomly selected in the figure of RMS-time which are named A, B, and C; see in Fig. 4b. Observing the waveform and frequency spectrums of the three signals in Fig. 5, we found that the typical AE signal covers a wide frequency range of 50–180 kHz with two peaks of 80 and 165 kHz.

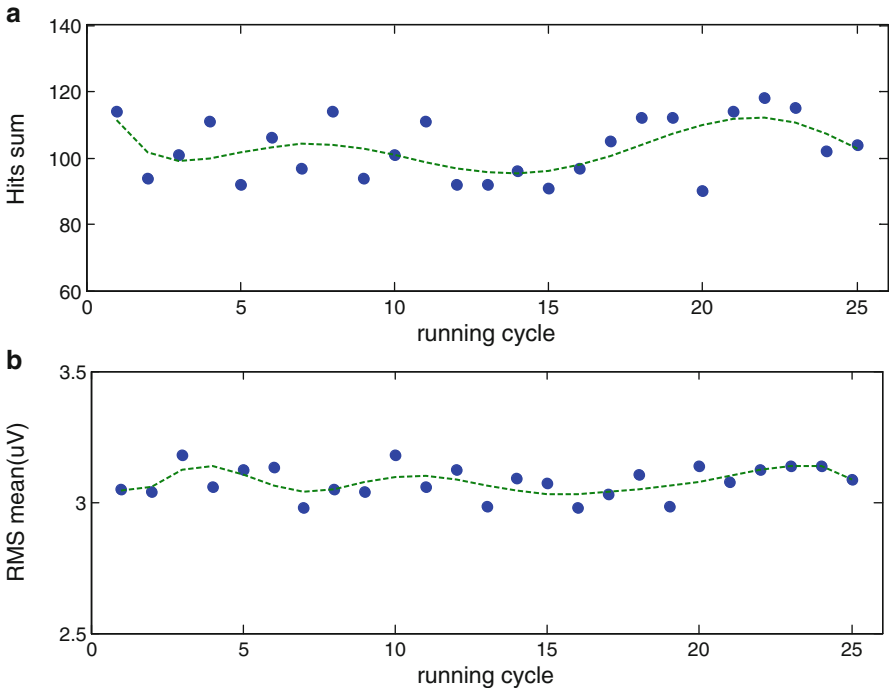

Fig. 3 The trends of AE statistical parameters, (**a**) hits sum, (**b**) RMS mean

4 Data Comparison of the Two Tests

Through the comparative analysis of AE signals collected from the two tests, we can find the changes of AE characteristics when the rolling bearing runs for a long time. Five operation cycle signals of rolling bearing were taken out, respectively, from the data obtained in the two tests. Then the AE signals were analyzed using the method described above.

4.1 AE Statistical Parameters

For each of the five operation cycle signals, the fitting curves of all the statistical parameters with running cycles are obtained. In contrast to the statistical results of the two tests, we found that all the statistical parameters have not obvious change in amplitude. Figure 6 shows the fitting curves of hits sum and RMS mean of the two tests.

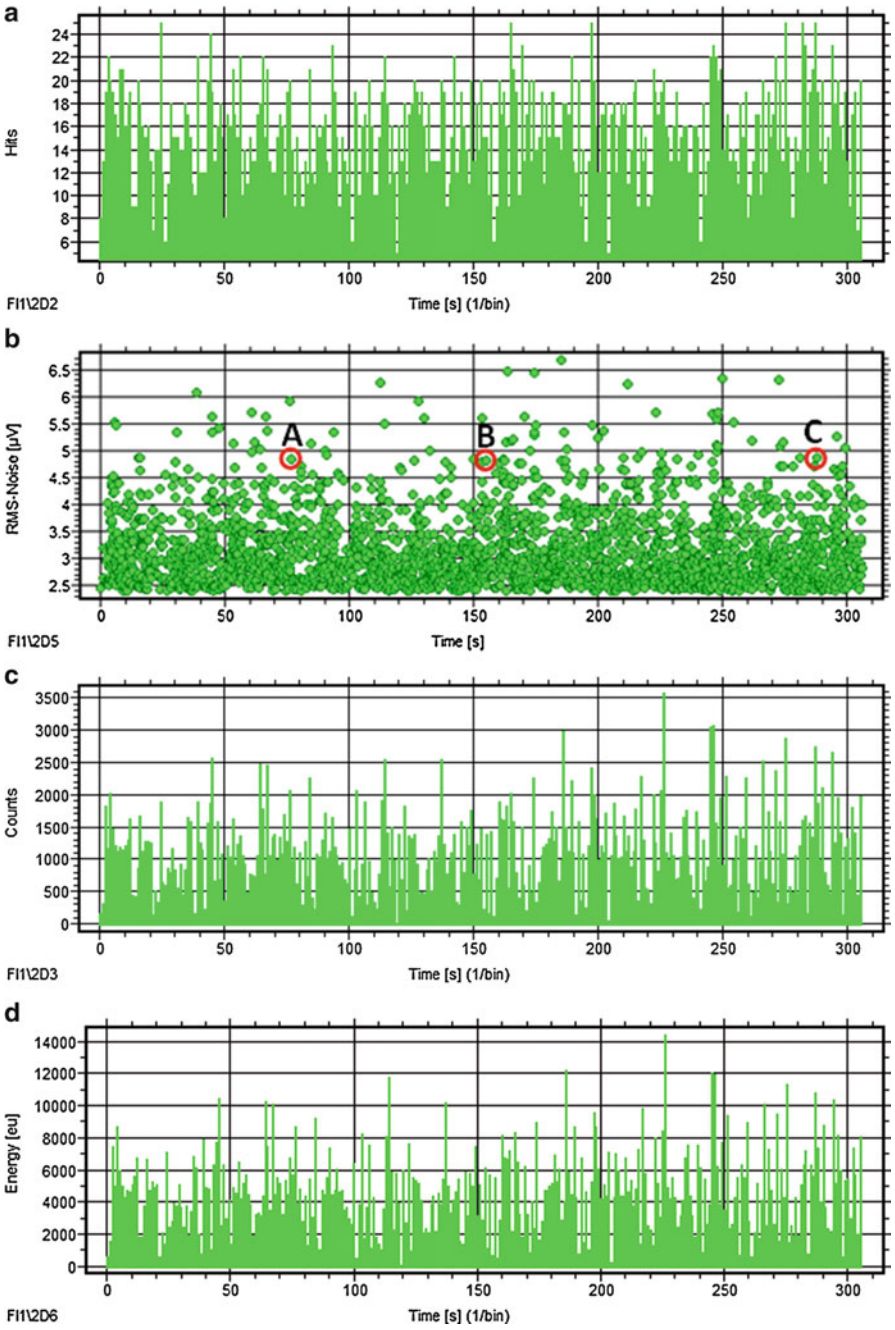

Fig. 4 (**a**) Hits-time, (**b**) RMS-time, (**c**) counts-time, (**d**) energy-time

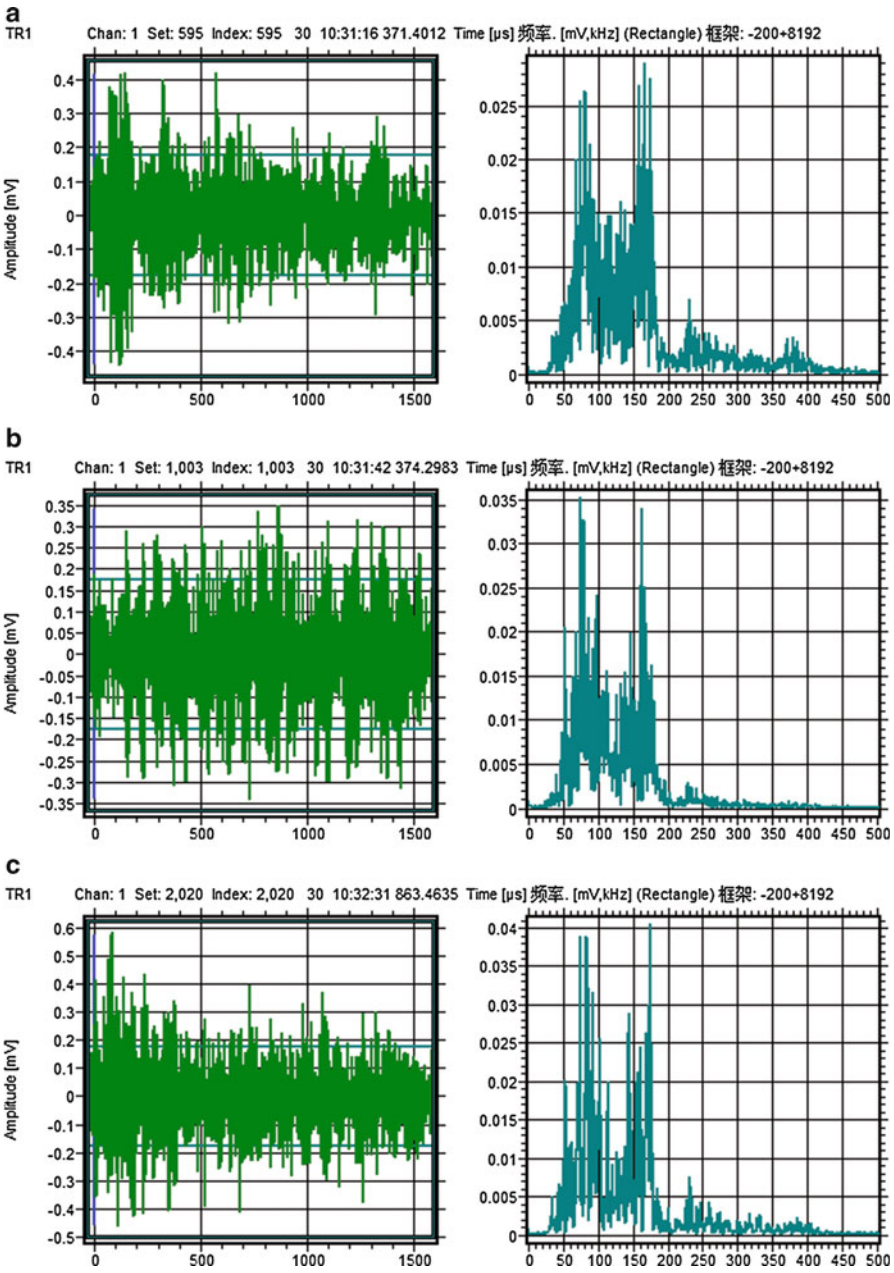

Fig. 5 Waveform and spectrum analysis of AE signals, (**a**) signal A, (**b**) signal B, (**c**) signal C

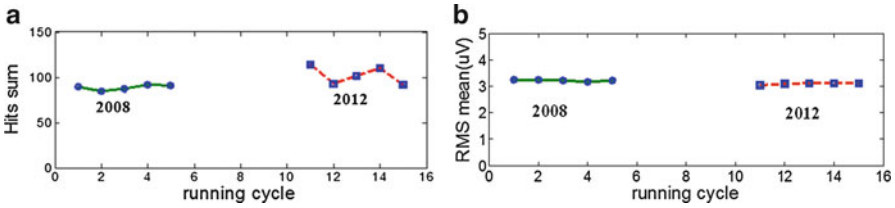

Fig. 6 (**a**) Fitting curves of hits sum, (**b**) fitting curves of RMS mean

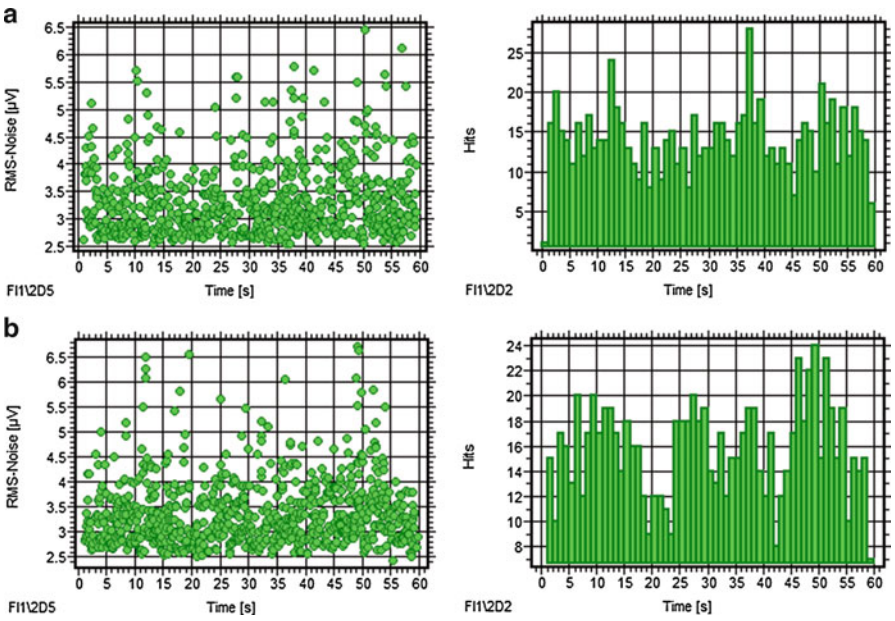

Fig. 7 (**a**) AE parameter courses of 2008, (**b**) AE parameter courses of 2012

4.2 AE Parameter Courses

Observing the AE parameter courses of five running cycles, there is no periodic regularity of peaks in the two tests. Comparing the AE parameter courses of the two tests, the signals are irregularly distributed and have similar distribution of all the AE parameters. See the RMS courses and hits courses in Fig. 7.

4.3 Waveform and Spectrum

Figure 8 shows waveform and spectrums of the typical AE signals of the two tests. The spectrums have no significant difference of the two tests. The frequency distributes in the range of 50–180 kHz with two peaks of 80 and 165 kHz.

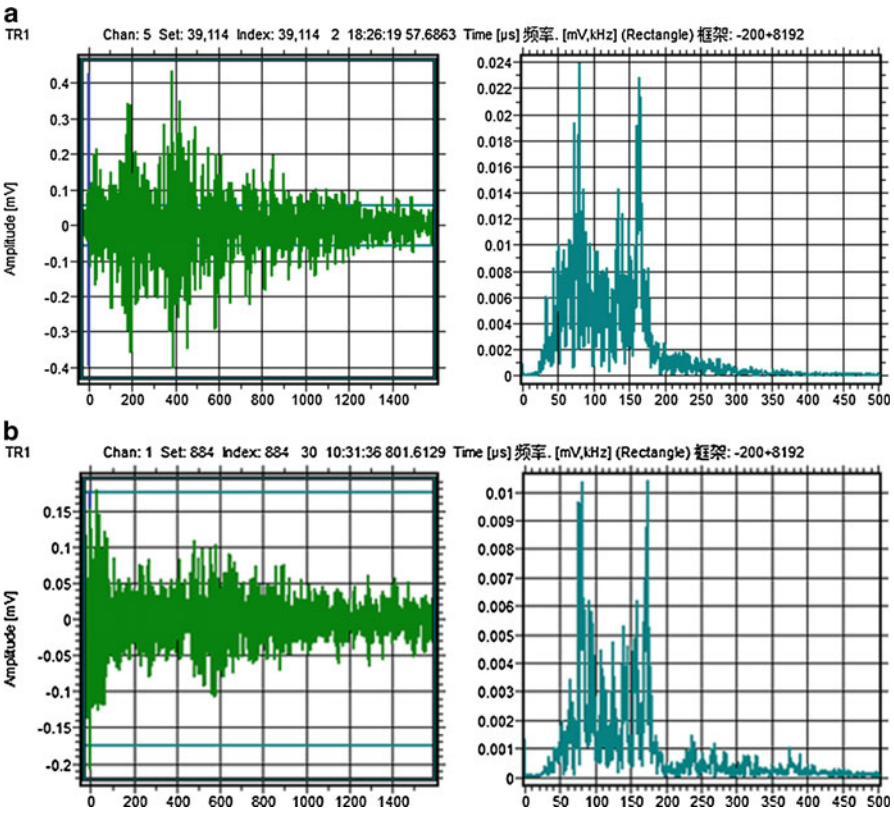

Fig. 8 (**a**) AE signal waveform and spectrum of 2008, (**b**) AE signal waveform and spectrum of 2012

Through the comparative analysis using the three methods above, it can be concluded that the AE signals acquired in 2008 and 2012 have the same AE characteristics. Also, there is no obvious change in health status of the rolling bearing.

5 Conclusion

The testing results show that the AE technique could be used as an effective means for the health condition monitoring and detection of rolling bearing on passenger ropeway.

Through the analysis of AE signals of rolling bearing collected in the process of ropeway operation, the AE characteristics of normal rolling bearing are obtained.

1. The amplitudes of acoustic emission statistical parameters have no obvious change with the increase of the year.

2. There is no cyclical peak characteristic in the AE parameter courses.
3. The spectrum of typical signals is mainly concentrated in the range of 50–180 kHz.

Acknowledgment This study was financially supported by Chinese 12th 5-year science and technology supporting project No. 2011BAK06B05.

References

1. Y.Y. He, X.M. Zhang, M.I. Friswell, Observation of time-frequency characteristics of the acoustic emission from defects in rolling element bearings. Insight **52**(8), 412–418 (2010)
2. R.J. Hao, W.X. Lu, F.L. Chu, Mathematical morphology extracting method on roller bearing fault signals. Proc. CSEE **28**(26), 65–70 (2008)
3. X.J. Zhang, C.X. Li, The application of acoustic emission in fault diagnosis of locomotive wheel set bearing. Bearing **6**, 25–27 (2007)
4. Y.H. Lu, Z.Y. Yin, Fault diagnosis of aero-engine rolling-element bearing based on the wavelet packet analysis. Gas Turbine Exp. Res. **18**(1), 35–44 (2005)
5. Z.W. Wu, G.T. Shen, J. Yuan, Y. Wang, Application of acoustic emission technique in detection of giant wheel main spindle [J]. NDT **33**(5), 39–42 (2011)
6. C.F. He, J.J. Zhang, G.T. Shen, Z.W. Wu, J. Yuan, Acoustic emission characteristics of rolling bearings for giant wheel [J]. J. Beijing Univ. Technol. **39**(5), 653–659 (2013)
7. Z.W. Wu, G.T. Shen, J.J. Zhang, Characteristics of acoustic emission signals in the rolling bearing on giant wheel [J]. Proceedings of the 30th European Conference on Acoustic Emission Testing and 7th International Conference on Acoustic Emission

Wireless AE Event and Environmental Monitoring for Wind Turbine Blades at Low Sampling Rates

Omar M. Bouzid, Gui Y. Tian, K. Cumanan, and J. Neasham

Abstract Integration of acoustic wireless technology in structural health monitoring (SHM) applications introduces new challenges due to requirements of high sampling rates, additional communication bandwidth, memory space, and power resources. In order to circumvent these challenges, this chapter proposes a novel solution through building a wireless SHM technique in conjunction with acoustic emission (AE) with field deployment on the structure of a wind turbine. This solution requires a low sampling rate which is lower than the Nyquist rate. In addition, features extracted from aliased AE signals instead of reconstructing the original signals on-board the wireless nodes are exploited to monitor AE events, such as wind, rain, strong hail, and bird strike in different environmental conditions in conjunction with artificial AE sources. Time feature extraction algorithm, in addition to the principal component analysis (PCA) method, is used to extract and classify the relevant information, which in turn is used to classify or recognise a testing condition that is represented by the response signals. This proposed novel technique yields a significant data reduction during the monitoring process of wind turbine blades.

O.M. Bouzid (✉)
Faculty of Engineering, Al-Jabel Al-Garbi University, LYGH 200 Gharian, Libya
e-mail: bouzidom@yahoo.com

G.Y. Tian • K. Cumanan • J. Neasham
School of Electrical and Electronic Engineering, Newcastle University,
Newcastle upon Tyne NE1 7RU, UK
e-mail: g.y.tian@ncl.ac.uk

G. Shen et al. (eds.), *Advances in Acoustic Emission Technology: Proceedings of the World Conference on Acoustic Emission-2013*, Springer Proceedings in Physics 158,
DOI 10.1007/978-1-4939-1239-1_50,

1 Introduction

Offshore wind turbines (OWTs) should be combined with structural health monitoring (SHM) systems to reduce the cost of the operation and maintenance (O&M) of safety-critical components and systems [1, 2]. This chapter investigates the use of an in situ wireless inspection system in monitoring the structural health of the wind turbine blades (WTBs) in conjunction with monitoring the environmental conditions. This scheme is developed based on the employment of a novel concept of using low sampling rates in acquiring acoustic emission (AE) signals discussed in Bouzid et al. [3, 4] so that a significant reduction of data can be achieved during the monitoring process of WTBs.

To validate the developed wireless SHM system and use of AE features extracted from the aliased versions in providing a robust SHM system for WTBs, field studies are conducted. This is shown by conducting in situ experiments in which AE events, such as wind, rain, strong hail, and bird strike, are detected and discriminated among different environmental conditions in conjunction with artificial AE sources. The intention of using such sound sources is to emulate impact damage or audible cracks caused by different objects such as tools or bird strikes. Time feature extraction algorithm, in addition to the principal component analysis (PCA) method, is used under low sampling rates to extract and classify the relevant information, which in turn is used to classify or recognise a testing condition that is represented by the response signals.

2 Methods

2.1 Experimental Setup

An in situ wireless SHM system has been implemented on the top of a 300 W wind turbine as shown in Fig. 1a. Furthermore, Fig. 1b shows the hardware components which are used in developing this wireless system, including MICAz motes equipped with the sensor board (MTS310) [2]. The omnidirectional microphone sensor of the MTS310 board is replaced by a BNC connector for AE sensors. The AE sensor is the BII-7070 from "Benthowave Instrument Inc." (www.benthowave.com) and operates at a usable frequency range of 0.1 Hz to 400 kHz with a size of $\phi \times L = 18.6 \times 20$ mm. It is characterised by relatively small mass and low cost. The wind turbine is installed on the roof of the School of Electrical and Electronic Engineering (EEE) as illustrated in Fig. 2. This wind turbine has three blades made of carbon with a diameter of 1.5 m.

All of the sensing units communicate with a PC base station via an RF interface and are programmed in a TinyOS environment [5]. The PC base station includes an MIB510 gateway board incorporating a MICAz mote which is used to forward the

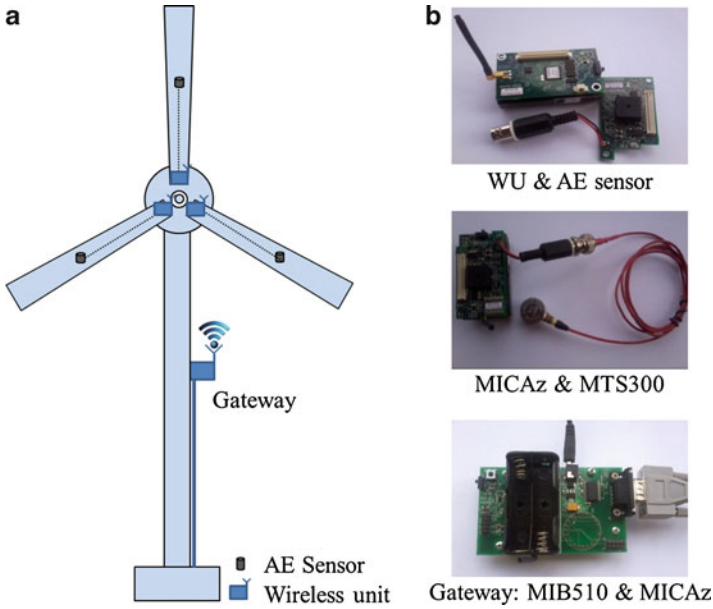

Fig. 1 (**a**) Wireless monitoring network installed on the top of a 300 W wind turbine, (**b**) hardware components used

Fig. 2 System installation on the school's roof for field studies and the PC base station in the lab

extracted features or the raw data to the PC for monitoring and processing. The PC runs a software package which consists of a Java application and MATLAB scripts to provide a user-friendly graphical user interface which allows operators to control the monitoring process.

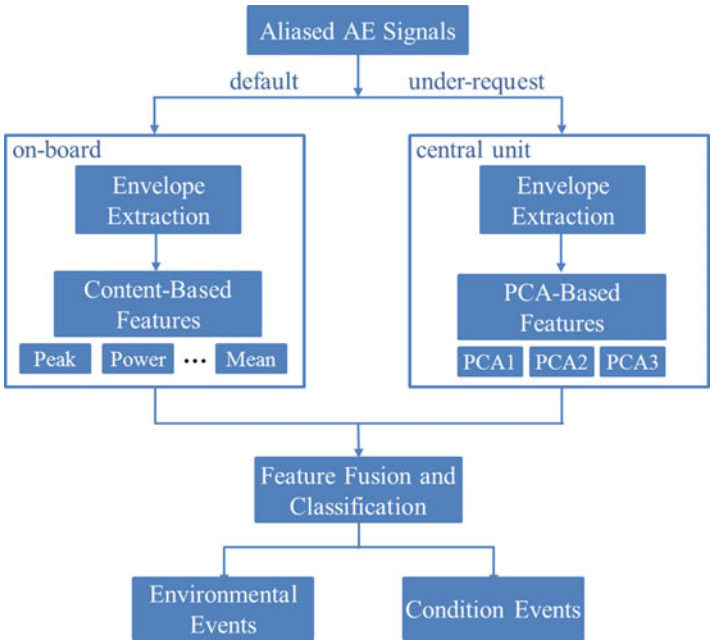

Fig. 3 AE feature extraction and classification scheme

2.2 AE Feature Extraction and Classification Algorithms

For field study and continuous monitoring, the relevant AE aliased signals captured should be locally pre-processed on-board the wireless units, so that only the results of evaluation and other meaningful features are transmitted to the remote control room, which reduce the amounts of data captured. As the wireless system developed here is based on the use of MICAz platforms, which have limited power resources and memory size as well as low processing capabilities, computationally expensive algorithms which are based on spectral and statistical approaches cannot be considered. Therefore, relatively simple signal processing algorithms are considered for on-board AE feature extraction.

In addition, for better analysis and classification results, content-based features should be extracted from the envelope of the received AE aliased versions rather than from the amplitude values of the time domain signal, since the envelope optimises the signal shape and minimises the ambiguity in the signal caused by lowering the sampling rate. Figure 3 summarises the steps of the proposed feature extraction and classification algorithm utilised in this wireless SHM system.

In this algorithm, the envelope is extracted from band-pass filter outputs by full-wave rectification and low-pass filtering. To do this, a one-pole filter with a smoothing parameter β is applied to the full rectified AE aliased version shown in Eqs. (1) and (2) [6]:

$$y(t) = \left|x(t)\right| \tag{1}$$

$$y(t) = (1 - \beta)x(t) + \beta y(t - 1) \tag{2}$$

where $x(t)$ is the aliased AE signal, and $t = 1, 2, \ldots, N$ where N is the number of samples.

After the envelope of the aliased version is extracted, AE features, including peak value, arrival time, mean value, and power value, are extracted as shown in Fig. 3. These features have the advantage that they can be computed while the sensing process is in progress without the need to have acquired the whole signal first. The extracted features are assembled in vectors named "acoustic vector properties" (AVPs) which are transferred to the control unit where they are characterised and used to distinguish different AE events.

The extracted features are then used for AE classification as well as monitoring the structural health of the blades under different environmental conditions, as illustrated in Fig. 3.

As seen in Fig. 3, the proposed method provides two possible options for the extraction of AE features: either on-board the wireless units or in the central unit. The former option represents the default case and it is implemented for a continuous monitoring approach where a simple content-based feature algorithm is applied. On the other hand, the latter is used for off-line techniques or for cases where more investigation, data fusion, and mining are requested using advanced feature extraction PCA-based approach. For more information about PCA technique refer to [7, 8].

3 Results and Discussions

3.1 AE Event and Environmental Monitoring

Leaving the WTB system to rotate under different environmental conditions is likely to result in different AE events. These events could occur based on these conditions as well as on the structural health of the blades. Therefore, for a robust SHM system it is very important to be able to distinguish and characterise these events in order to specify the main causes of such events. The motivation was that if this abnormality could be successfully detected and classified by the SHM approach developed here, then damage could also be detected and discriminated. In this regard, waveforms of various relevant environmental conditions were recorded during this type of in situ experiment under wind and rain conditions. The experiments were conducted while the wind turbine was installed on the school roof with the wireless monitoring system on top of it as shown in Fig. 2. Each reading consists of 500 samples, all of which were initiated by a simple threshold crossing condition which was below 100 mV in order to allow the wireless units to detect such waveforms even if they were weak.

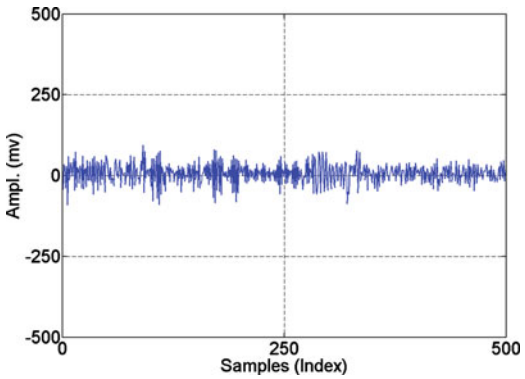

Fig. 4 *Wind condition* waveform detected

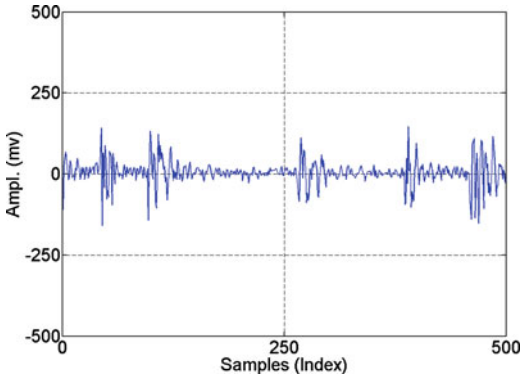

Fig. 5 *Rainfall condition* waveform detected

Figure 4 depicts an example of waveforms detected while the blades rotated due to the wind, i.e., the *wind condition*. Such types of waveforms are caused by the sound produced as a result of blade rotation. These signals are characterised as noisy signals whose variance and power increase with wind speed. However, raising the detection threshold value of the wireless units will lead to the filtering of such signals.

The second environmental condition waveforms were signals caused during the *rainfall condition*. These signals were recorded while the blades were stationary and then when the blades were rotating. Figure 5 shows an example of the waveform recorded in the former case. This type of signal is characterised by a random sequence of repetitive AE pulses whose peak and repetition values depend on the density and speed of the rainfall.

In contrast, a waveform of *rain* and *wind conditions* is shown in Fig. 6. This type of waveform was recorded during light rainfall while the blades were spinning under the wind load. As a result of blade rotation the collected rain waveform was contaminated with the noise caused by the spinning of the blades. This type of waveform appears as a sum of the two waveforms of the *rain* and *wind conditions*.

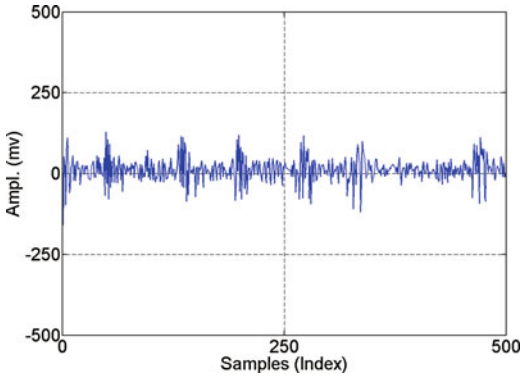

Fig. 6 *Rainfall* and *wind condition* waveform detected

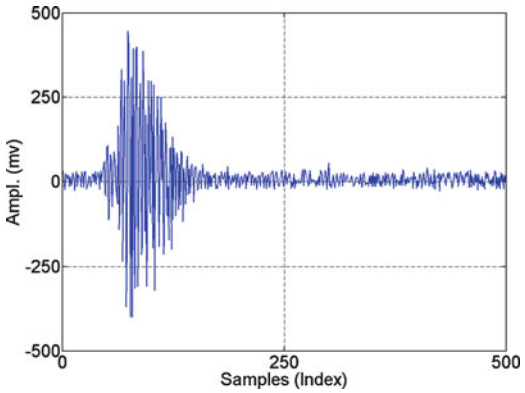

Fig. 7 *Hit condition* waveform detected

In addition, the blades were also hit with a plastic stick, which has a diameter and length of 15 mm and 500 mm, respectively, while the blades were stationary and then during the rain test in order to capture both an abnormal signal and a *rainfall condition* waveform. Figures 7 and 8 show an example of waveforms obtained from such experiments for *impact* as well as *rain* and *impact conditions*, respectively. Based on the results of the experiments conducted, these types of signals can be usually characterised by the differences in amplitude and shape between the hit event and the rainfall signals.

Furthermore, by comparing the signals received from all wireless units for the measurements in the *rainfall condition*, it is noticeable that there is a high correlation between these signals in terms of the amplitude and width of the individual pulses, as shown in Fig. 9a. This is because they were caused by the same condition, i.e., rainfall. This makes the features extracted from such signals among wireless units almost the same. In contrast, if one of the blades encountered a hit during the *rainfall condition*, the received signals will be similar to the signals shown in Fig. 9b. In addition to the *rainfall condition* waveforms, this figure shows the signals caused by the emulated impact damage of one of the wind turbine blades.

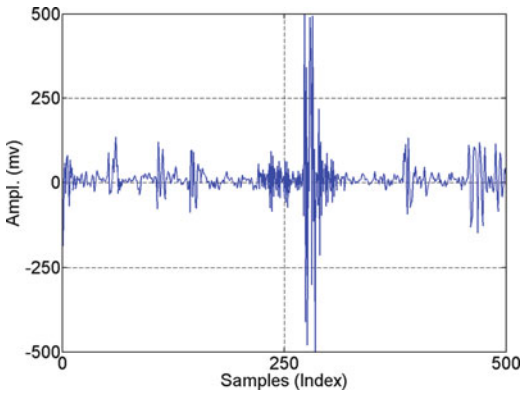

Fig. 8 *Rainfall* and *hit condition* waveform detected

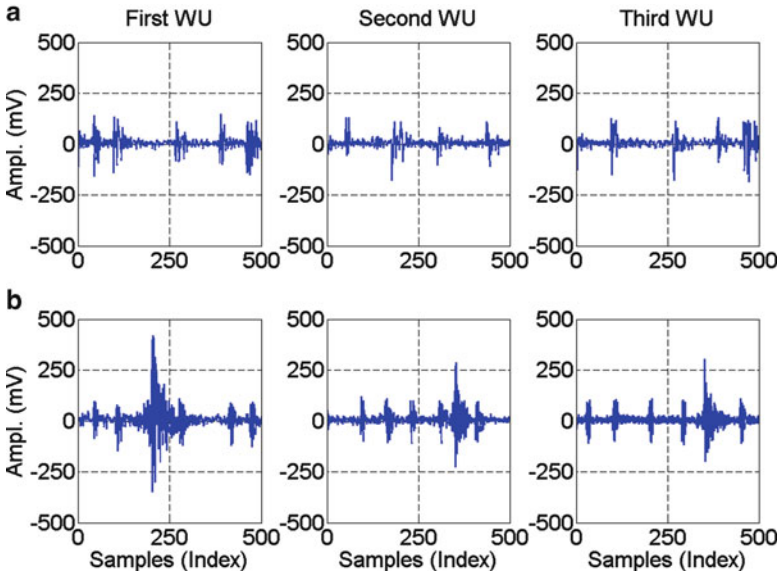

Fig. 9 AE events received at three wireless units (WU), (**a**) for rain, (**b**) rain and hit measurements

The impact signal propagated from this blade to the other two blades, which are then captured by other two wireless units, can be clearly seen in the last two plots in Fig. 9b.

The above-mentioned in situ wireless experiments were conducted several times and a sequence of AE aliased waveforms was recorded under the aforementioned conditions. In addition, waveforms of the steady case at a very low wind speed were also recorded. These waveforms were further analysed and classified as discussed next.

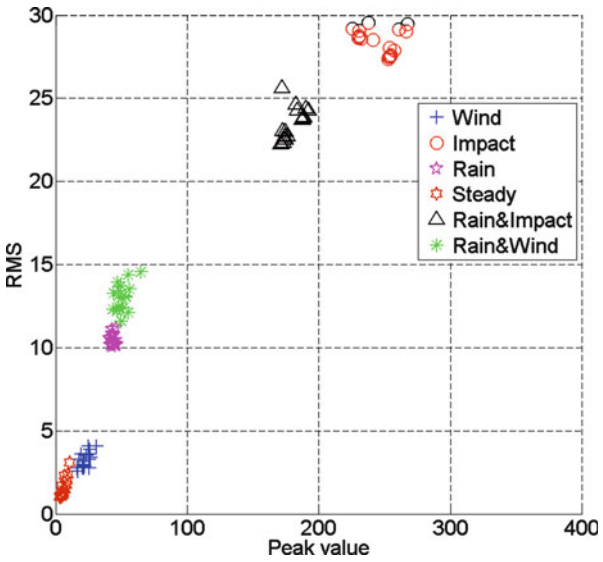

Fig. 10 Classification of received events under different environment conditions using time domain features

Figure 10 illustrates the results using time domain features, including peak value and RMS features as a combination to lead to the signals recorded being distinguished. From the captured waveforms discussed above, it is noticeable that those relevant only to the *wind condition* have values of RMS greater than those in waveforms for the *steady condition* case. This difference was increased by increasing the speed of rotation of the WTBs. In contrast, the difference in peak values due to raindrops hitting the blades between the waveforms of the former condition and the *rainfall condition* led to the two cases being distinguishable, and as the strength of the rainfall increased this difference increased as well. In addition, the waveforms relevant to the *rain and wind conditions* were distinguished by their relatively large RMS values compared to the *rainfall condition* due to the difference in noise levels.

Finally, for the cases where the blades were manually hit, in order to generate artificial sounds which emulated audible cracks or impact damage due to different objects, the AE events produced gave the highest peak values as shown in Fig. 10. These values made the discrimination of these events from the waveforms discussed above very easy. The signals resulting from the propagation of the emulated impact damage to the other blades are not considered in Fig. 10 since they show the same features as the main signals, but with relatively low values.

In addition to the time domain features which were used in the above classification of AE events under different environment conditions, the PCA features have also been applied to a similar set of such events collected at the remote unit. Figure 11 illustrates the discrimination results of this process. In this figure, to ensure better representation of this classification, the first PCA features have been integrated with the time domain features (average of peak values) of the AE events

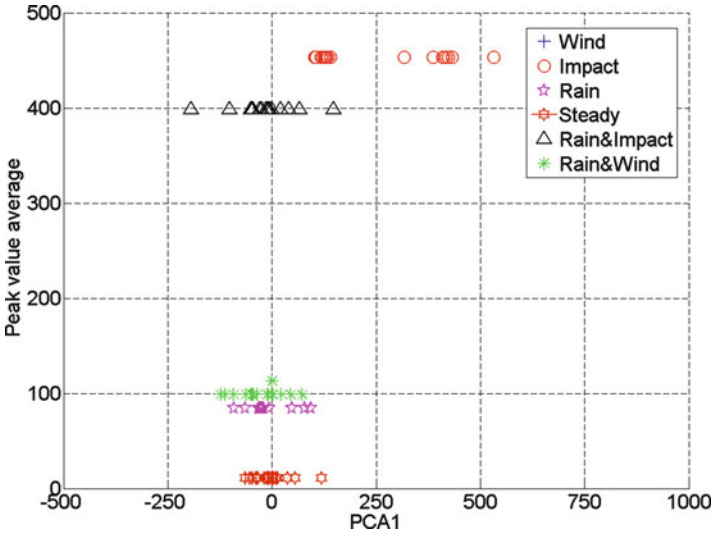

Fig. 11 Classification of received events under different environment conditions using the integration of time domain and PCA features

captured. As seen in this figure, it was found that this integration has the potential to discriminate between these AE events, where they are clearly classified into six non-overlapping clusters based on this combination.

In the last two figures, it can be seen that waveforms relative to the impact damage emulated are obviously separated from the rest of waveforms discussed above. To obtain better identification and classification of such impact or crack AE events, more emulated impact measurements were conducted and feature extraction algorithms applied, as discussed next.

3.2 Discrimination and Classification of Emulated Impact Damage

Monitoring of the emulated impact damage is also carried out on WTBs through the developed wireless SHM system. The impact was emulated by hitting the blades while they were static, by three metallic balls of different sizes, as shown in Fig. 12. The smallest ball (SB) has a diameter and mass of 5 mm and 1 g, respectively, whereas the medium ball (MB) is 9 mm and 3 g and the largest ball (LB) 13 mm and 9 g. The balls were thrown to the blades at the same speed and from the same height and at the same distance from the AE wireless units.

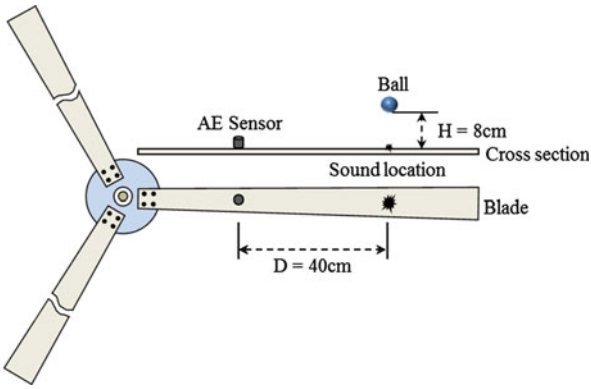

Fig. 12 Emulated impact damage setup

As a result of this emulated impact damage three different aliased AE signals were generated, as illustrated in Fig. 13. It can be seen in this figure that the duration and power parameters of these signals are proportional to the size of the ball used, where the largest ball caused the longest signal duration and maximum power. These experiments were repeated several times and in each case the AE parameters or features discussed in Sect. 2 were extracted on-board the wireless unit and sent to the control unit in the form of APVs. These APVs were used in the control unit to discriminate between the three cases.

To identify the three cases, it was found that the AE parameters such as power and duration features are sensitive to the type of impact damage emulated. These parameters were used to discriminate between the different ball impacts, as shown in Fig. 14. This figure shows that the AE aliased signals caused by the smallest ball were characterised by small values of the selected parameters. These parameters increased as the size of the ball increased, leading to a clear separation between the three cases.

In addition to the time domain features, the PCA features have been applied to a similar set of such events collected at the remote unit. Figure 15 illustrates the discrimination results of this process. AE signals caused by the largest ball are separated from the others as the PCA1 values are all positive. In addition, the PCA3 values are all negative for the smallest ball which distinguishes them from the signals caused by the medium ball, whereas the PCA2 values are positive for all cases. The values of PCA3 are almost linearly proportional to the strength of these signals which increased as the effect of the impact source increased. From the above, it can be seen that the three cases of impacts can be classified via PCA-based features.

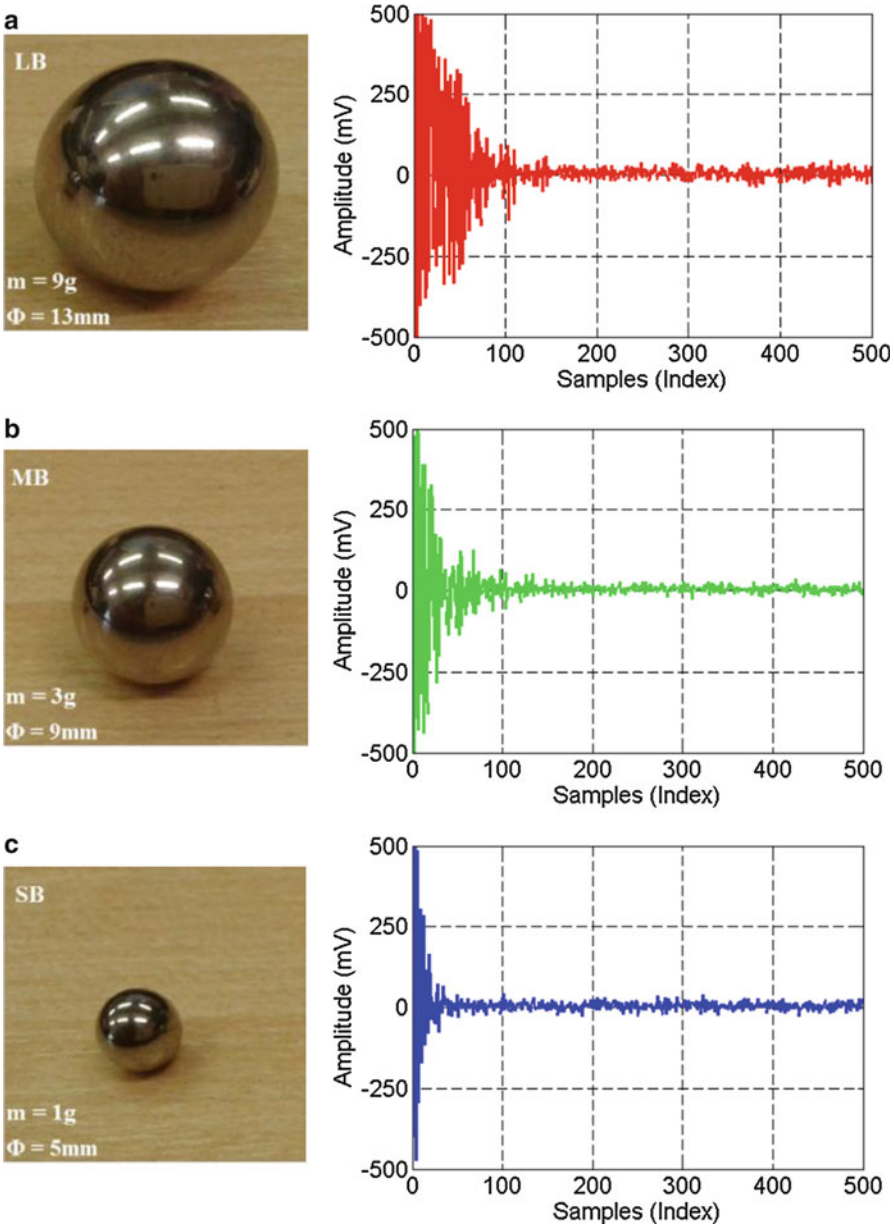

Fig. 13 Aliased AE signals caused by the emulated impact damages by the three balls, (**a**) LB, (**b**) MB, (**c**) SB

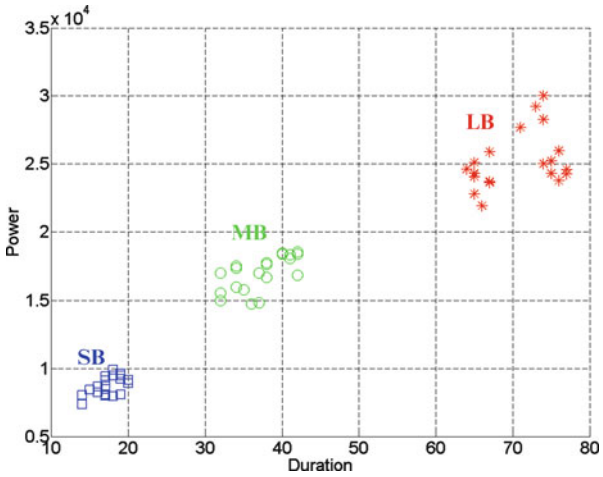

Fig. 14 Discrimination between impact signals caused by the three balls using time domain features

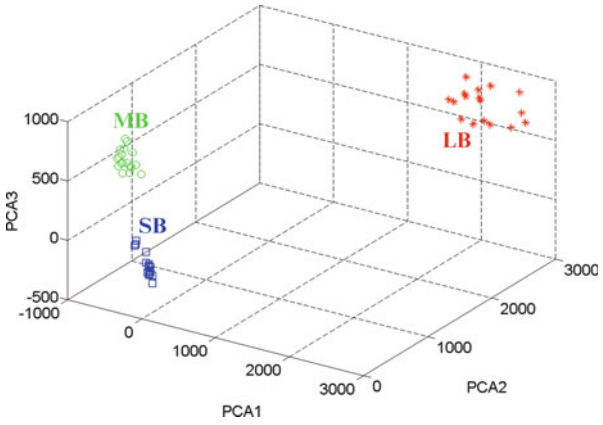

Fig. 15 Discrimination of impact signals caused by the three balls using PCA features

4 Conclusions

Throughout this study AE events and environmental monitoring measurements were carried out in which each waveform was captured several times. The results of separating and clustering the individual groups based on the extracted AE features confirm the novelty of using AE in monitoring environmental conditions. These results were confirmed using time features in addition to the PCA features. This also showed that working under the utilization of low sampling rates to extract AE features from aliased AE waveforms can help in fulfilling the requirements of wireless SHM systems for WTBs, including reduction of sensing data and preserving the communication bandwidth of wireless sensor networks (WSNs). Future work will extend the study to field studies including noise handling in the industrial environment, e.g., offshore environment.

References

1. P.J. Schubel, R.J. Crossley, E.K.G. Boateng, J.R. Hutchinson, Review of structural health and cure monitoring techniques for large wind turbine blades. Elsevier Renew. Energ. **51**, 113–123 (2013)
2. Z. Hameed, Y.S. Hong, Y.M. Cho, S.H. Ahn, C.K. Song, Condition monitoring and fault detection of wind turbines and related algorithms: a review. Renew. Sustain. Energy Rev. **13**, 1–39 (2009)
3. O.M. Bouzid, G.Y. Tian, J. Neasham, B. Sharif, Investigation of sampling frequency requirements for acoustic source localisation using wireless sensor networks. Elsevier Appl. Acoust. **74**, 269–274 (2013)
4. O.M. Bouzid, G.Y. Tian, J. Neasham, B. Sharif, Envelope and wavelet transform for sound localisation at low sampling rates in wireless sensor networks. Journal of Sensors **2012** (2012)
5. P. Levis, D. Gay, *TinyOS Programming* (Cambridge University Press, New York, NY, 2009)
6. G. Tzanetakis, P. Cook, Musical genre classification of audio signals. IEEE Trans. Speech. Audio. Process. **10**, 293–302 (2002)
7. A. Sophian, G.Y. Tian, D. Taylor, J. Rudlin, A feature extraction technique based on principal component analysis for pulsed Eddy current NDT. NDT & E Int. **36**, 37–41 (2003)
8. M.J. Eaton, R. Pullin, J.J. Hensman, K.M. Holford, K. Worden, S.L. Evans, Principal component analysis of acoustic emission signals from landing gear components: an aid to fatigue fracture detection. Strain **47**, 588–594 (2011)

Experimental Study on Acoustic Emission Detection for Low Speed Heavy Duty Crane Slewing Bearing

Yang Jiao, Guanghai Li, Zhanwen Wu, Chen Chen, and Shangyan Mi

Abstract By use of the custom-built crane model, AE instrument and loads, a large amount of experiments have been done. For all AE signals acquired from the slewing bearing with no defect and with defect on different operation mode, AE signal parameter distribution analysis, AE signal parameter correlation analysis, AE signal frequency spectrum analysis have been achieved. The AE parameter distribution range for signals acquired from the slewing bearing with defect is much wider than that for those from the slewing bearing with no defect. By observing energy–duration correlation diagram, the defect signal can be identified evidently. Through frequency spectrum analysis, it can be found that the defect will lead to high frequency signal. In addition, the statistical analysis method is used to investigate the AE characteristics of the non-defective slewing bearing and defective slewing bearing. The statistical results of AE parameters are obtained respectively under different load and rotation speed of slewing bearing. Hits sum and energy sum of AE signal acquired from the slewing bearing with defect are much higher than the values acquired from the slewing bearing with no defect, and they increase with loads increasing. The maximum amplitude, hits sum, energy sum of AE signal acquired from slewing bearing with defect are all higher than those acquired from the slewing bearing with no defect regardless of rotation speed.

Y. Jiao (✉) • C. Chen • S. Mi
Hebei university of science and technology, Hebei 050018, China
e-mail: jyang939@163.com

G. Li • Z. Wu
China special equipment inspection and research institute, Beijing 100013, China
e-mail: liguanghai@netease.com

G. Shen et al. (eds.), *Advances in Acoustic Emission Technology: Proceedings of the World Conference on Acoustic Emission-2013*, Springer Proceedings in Physics 158,
DOI 10.1007/978-1-4939-1239-1_51,

1 Introduction

Heavy duty slewing bearing is the key component of gantry crane, tower crane, and arm crane. These hoisting equipment run in low speed, heavy load, and intermittent operation. In operation a large impact load is supported by them. Their operational status directly affects the performance of the whole system. If they get out of order, the production efficiency of the whole equipment can be influenced, and the safety of personnel and equipment is threatened.

For the scientific research project "The key technology research on slewing bearing condition monitoring of low speed heavy duty crane," a crane model is made specially. A large amount of experimental study has been done.

The acoustic emission (AE) detection [1] for crane slewing bearing is discussed in this paper. The acoustic emission detection on the slewing bearing with no defect (ND), the slewing bearing with roller defect (RD), and the slewing bearing with outer race defect (ORD) is done respectively. The result show that fault detection for crane slewing bearing in low speed and heavy load is feasible.

2 Experimental Set-Up and Plan

The experimental setup consists of crane model, loads, testing instrument, computer, and sensors. The main part of the crane model and loads are shown in Fig. 1a. The crane model consists of foundation, slewing bearing, control cabinet, etc. Four loads which each weight 2.2 t are made. The sensors layout is shown in Fig. 1b. The German Vallen AMSY-6 is used as the testing instrument. The VS150-RIC resonant sensors are adopted.

By increasing or decreasing load we can change crane load. Using control cabinet, we can adjust crane speed. In addition, the roller defect and the outer race defect are made to simulate the actual defect. The two defects are shown in Fig. 2.

The AE signal in the slewing bearing with ND, the slewing bearing with RD, and the slewing bearing with ORD is acquired at three loads and three speeds.

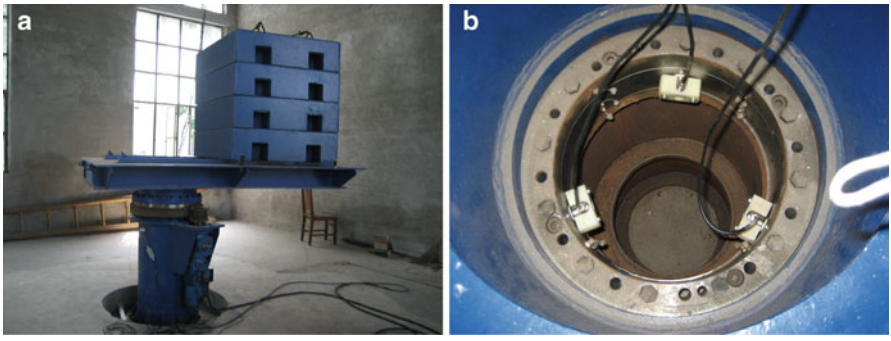

Fig. 1 The crane model, loads, and sensors. (**a**) The crane model and loads, (**b**) sensors layout

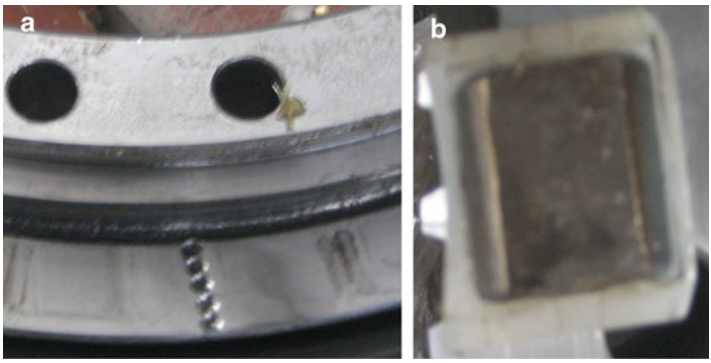

Fig. 2 The outer race defect and roller defect. (**a**) The outer race defect, (**b**) The roller defect

3 Acoustic Emission Signal Feature Analysis

3.1 AE Signal Parameter Distribution Analysis

The crane model carrying 4.4 t of loads rotates in a circle at a moderate speed. For the slewing bearing with ND, or the slewing bearing with RD, or the slewing bearing with ORD, AE signal is acquired respectively. The AE parameter distribution of defect free slewing bearing and defective slewing bearing is shown in Table 1. Comparing with defect free slewing bearing, the AE parameter distribution range of defective slewing bearing increase significantly, and it is obvious especially for the slewing bearing with ORD.

For example, the energy course of RMS is shown in Fig. 3. When the slewing bearing with ND is running, the energy varies from 1–1,000 eU. The maximum is 1,000 eU. When the slewing bearing with RD is running, the energy varies from 1–1,800 eU. The maximum is 1,800 eU. When the slewing bearing with ORD is running, the energy varies from 1–3,400 eU. The maximum is 3,400 eU.

3.2 AE Signal Parameter Correlation Analysis

The AE signal acquired from three kinds of slewing bearing was observed. AE parameter correlation analysis [2] is made respectively. It is discovered that energy–duration correlation diagram has obvious characteristics. It is shown in Fig. 4. From the correlation diagram of defective slewing bearing, two kinds of AE signal that were recorded as A and B can be distinguished.

Table 1 AE parameter distribution range of defect free slewing bearing and defective slewing bearing

Parameter distribution	ND	RD	ORD
A (dB)	40–59	40–79	40–72
Hits	1–7	1–46	1–108
Energy (eU)	1–530	1–2,300	1–2,500
RMS (μV)	5–52	5–450	5–940
Risetime (μs)	1–582	1–915	1–2,670
Dur (μs)	1–3,549	1–8,826	1–5,510

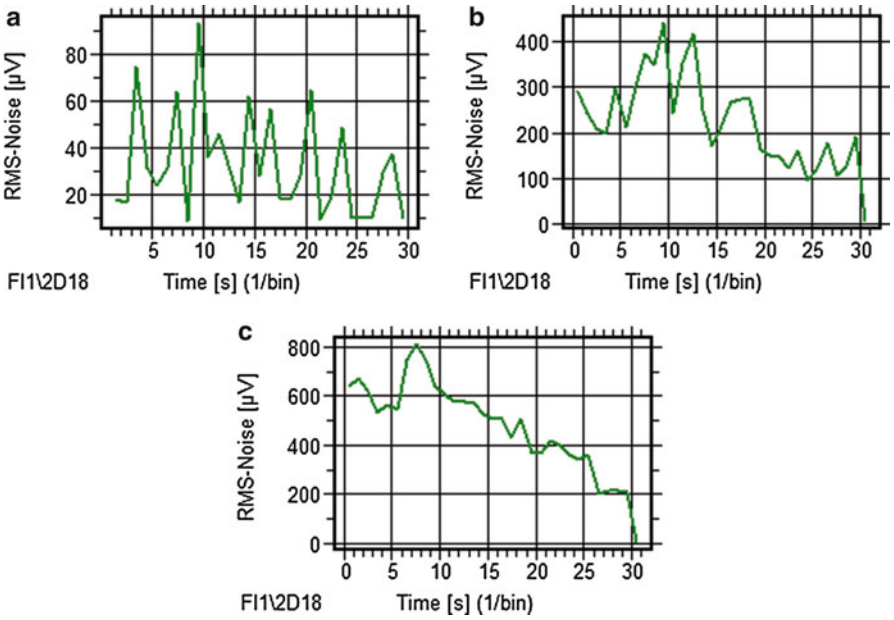

Fig. 3 RMS course. (**a**) Slewing bearing with ND, (**b**) slewing bearing with RD, (**c**) slewing bearing with ORD

3.3 AE Signal Frequency Spectrum Analysis

AE signal acquired from defect free slewing bearing and defective slewing bearing, carrying 4.4 t load and rotating one circle, was observed; frequency spectrum analysis [3] is done respectively. All frequency spectrums are shown in Fig. 6. The frequency spectrum of slewing bearing with ND is shown in Fig. 5a. Its frequency range is 30–280 kHz.

The frequency spectrum of slewing bearing with RD is shown in Fig. 5b, c. Figure 5b is the frequency spectrum corresponding to A signal shown in Fig. 4b. Figure 5c is the frequency spectrum corresponding to B signal shown in Fig. 4b. It can be found that the frequency spectrum of A signal is same as the frequency spectrum of slewing bearing with ND. The frequency range of B signal is 30–950 kHz. It is a defect signal.

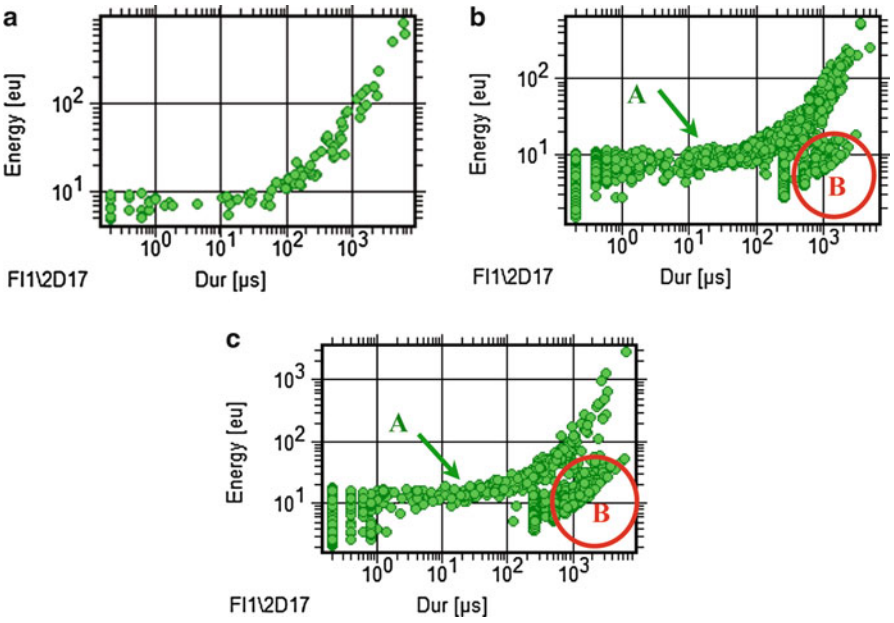

Fig. 4 Energy–duration correlation diagram. (**a**) Slewing bearing with ND, (**b**) Slewing bearing with RD, (**c**) Slewing bearing with ORD

The frequency spectrum of slewing bearing with ORD is shown in Fig. 5d, e. Figure 5d is the frequency spectrum corresponding to A signal shown in Fig. 4c. Figure 5e is the frequency spectrum corresponding to B signal shown in Fig. 4c. It can be found that the frequency spectrum of A signal is same as the frequency spectrum of slewing bearing with ND. The frequency range of B signal is 30–950 kHz. It is a defect signal.

4 The Effect of Load and Rotation Speed on Statistical Results of AE Parameters

4.1 Load Change

The crane model carrying 4.4 t of loads rotates in a circle at a moderate speed. The parameter statistical analysis [4] for acquired AE signal is done. The curve of relationship between AE parameters and loads can be obtained. In all statistical parameters, hits sum, energy sum, COUNTS sum, duration sum, and rise time sum have obvious change tendency. Only statistical curves of hits sum and energy sum are shown in Figs. 6 and 7.

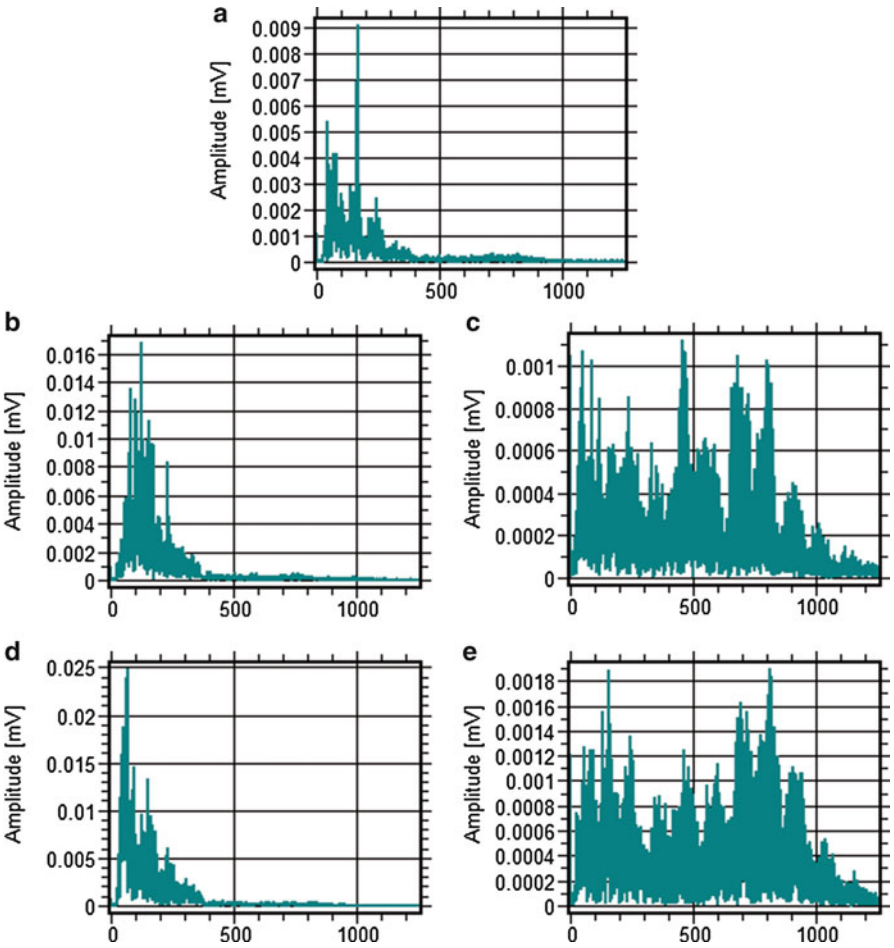

Fig. 5 AE signal frequency spectrum. (**a**) Slewing bearing with ND, (**b**) A signal of slewing bearing with RD, (**c**) B signal of slewing bearing with RD, (**d**) A signal of slewing bearing with ORD, (**e**) B signal of slewing bearing with ORD

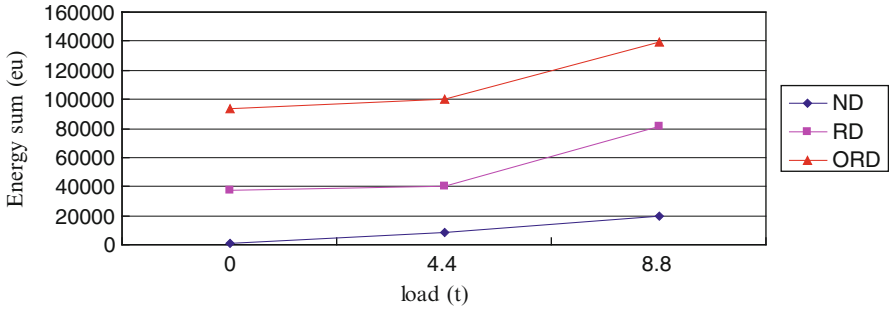

Fig. 6 The statistical curve between hits sum and load

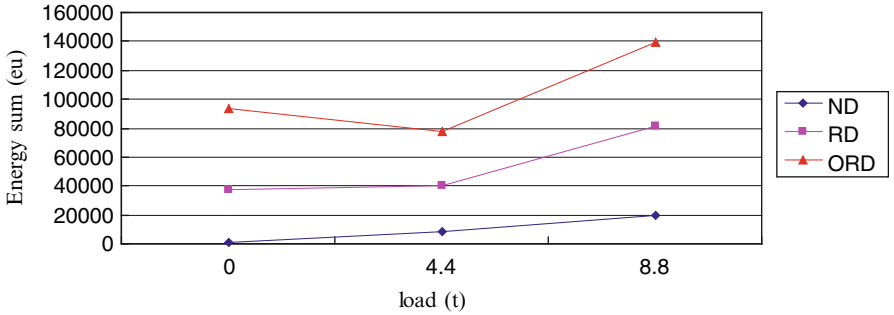

Fig. 7 The statistical curve between energy sum and load

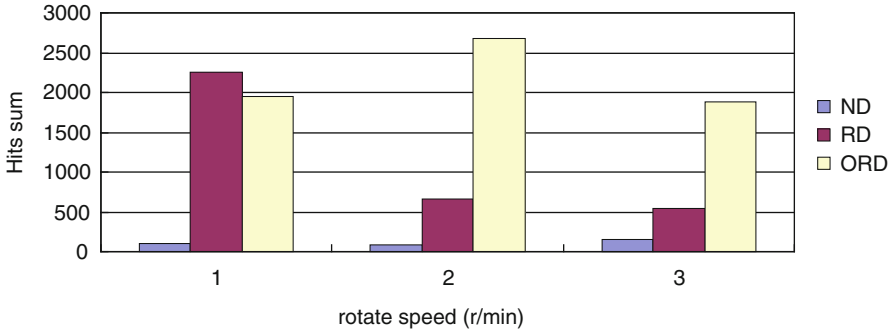

Fig. 8 The statistical curve between hits sum and speed

As shown in Figs. 6 and 7, for all kinds of loads, hits sum and energy sum of AE signal acquired from the slewing bearing with RD and with ORD are much higher than the values acquired from the slewing bearing with ND. And hits sum and energy sum increase with loads increasing.

4.2 Rotation Speed Change

The crane model carrying 4.4 t of loads rotates in a circle at different speeds. The parameter statistical analysis for acquired AE signal is done. The curve of relationship between AE parameters and rotation speed can be obtained. They are shown in Figs. 8, 9, and 10.

In general, the maximum amplitude, hits sum, energy sum of AE signal acquired from slewing bearing with defect are all higher than those acquired from the slewing bearing with no defect regardless of rotation speed. Specifically, hits sum and energy sum from the slewing bearing with defect are much higher than those from the slewing bearing with no defect. And the values from the slewing bearing with ORD are much higher than the values from the slewing bearing with RD

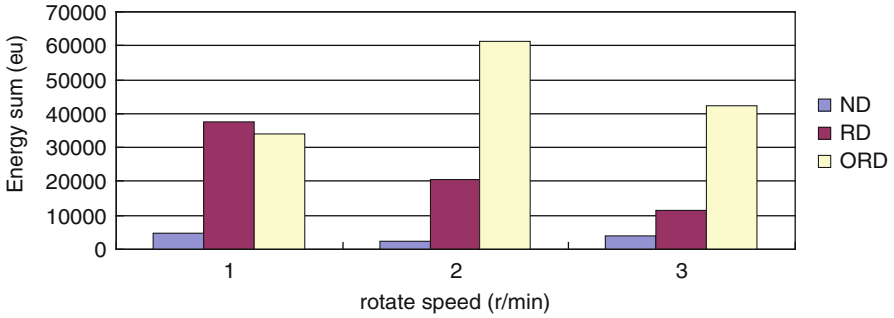

Fig. 9 The statistical curve between energy sum and speed

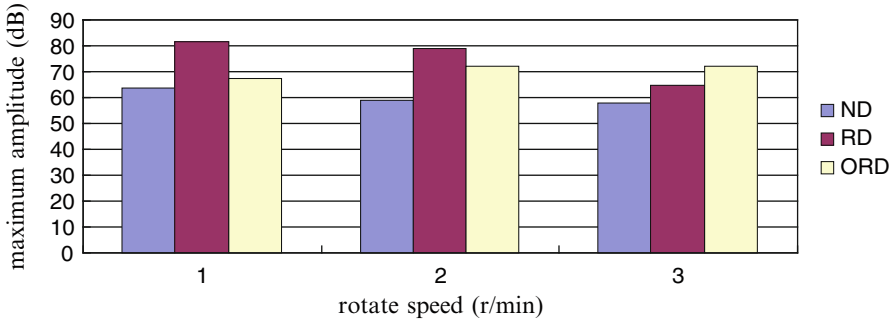

Fig. 10 The statistical curve between maximum amplitude and speed

except the crane running in low speed. For the maximum amplitude, the values from the slewing bearing with RD are much higher than the values from the slewing bearing with ORD except the crane running in high speed.

5 Conclusion

A large amount of field experiment on the slewing bearing with ND, the slewing bearing with RD, and the slewing bearing with ORD has been done. Parameter analysis for AE signal acquired on every slewing bearing has been carried out. The conclusion is as follows.

1. Compared with the slewing bearing with ND, parameter distribution range of AE signal acquired on defective slewing bearing increases obviously.
2. By observing the energy–duration correlation diagram, the defect signal can be identified evidently.

3. Through signal frequency spectrum, the frequency range of defect free signal is 30–280 kHz, and the frequency range of defective signal is 30–950 kHz. The defect will lead to high frequency signal.
4. When the loads change, the AE statistical parameters have obvious change tendency. Hits sum and energy sum increase obviously with loads increasing, and the values acquired from the slewing bearing with defect are much higher than the values acquired from the slewing bearing with no defect.
5. When rotation speed changes, AE parameters have different change tendency. The maximum amplitude, hits sum, energy sum of AE signal acquired from slewing bearing with defect are all higher than those acquired from the slewing bearing with no defect regardless of rotation speed.

Through the experimental study, it can be observed that fault detection for crane slewing bearing in low speed and heavy load is feasible.

Acknowledgment The research work was supported by AQSIQ Public Welfare Industry Scientific Research Project No. 201110032.

References

1. J. Yuan, G. Shen, Z. Wu et al., Acoustic emission testing technology in diagnosis of bearing failure [J]. NDT **33**(4), 5–11 (2011)
2. G. Shen, R. Geng, S. Liu, Parameter analysis of acoustic emission signals [J]. NDT **24**(2), 72–77 (2002)
3. Z. Wu, G. Shen, J. Yuan et al., Application of acoustic emission technique in detection of giant wheel main spindle [J]. NDT **33**(5), 39–42 (2011)
4. C. He, J. Zhang, G. Shen et al., Acoustic emission characteristics of rolling bearings for giant wheel [J]. J. Beijing Univ. Technol. **39**(5), 653–659 (2013)

Interlaminar Shear Properties and Acoustic Emission Monitoring of the Delaminated Composites for Wind Turbine Blades

Wei Zhou, Yajuan Li, Zhiyuan Li, Xiaomin Liang, Yanrong Pang, and Fang Wang

Abstract In this study, tensile tests have been carried out to investigate interlaminar shear properties of the delaminated composite materials for wind turbine blades. Acoustic emission (AE) technique was used to monitor the damage and failure progress of the specimens and the shear failure mechanisms of the delaminated composites have been discussed. The results show that the size of strip delamination has little effect on the failure load of the composite specimens when these defects are located at the center of interlaminar shear region. The main damage evolution approaches the extremities of the shear plane. The AE relative energy, amplitude distribution, and duration were connected with the damage process of the specimens. Finally, the initiation and propagation of damage has been proved by linear AE source location results.

1 Introduction

Glass fiber reinforced composites with its high specific strength, high modulus, good fatigue resistance, etc. have become the most commonly used materials for wind turbine blades [1, 2]. However, inevitable inner defects such as delamination may result in the damage and bulk failure of wind turbine blades [3, 4]. Recent investigations show that ultrasonic and radiographic techniques are capable of reliably detecting inner defects of the blades [5–7]. Acoustic emission (AE) testing, which is sensitive to dynamic defects, has become the primary method of testing glass fiber reinforced composites [8]. But few studies concern the AE

W. Zhou (✉) • Y. Li • Z. Li • X. Liang • Y. Pang • F. Wang
College of Quality and Technology Supervision, Hebei University, Baoding, 071002, China
e-mail: zhouweihy@126.com

G. Shen et al. (eds.), *Advances in Acoustic Emission Technology: Proceedings of the World Conference on Acoustic Emission-2013*, Springer Proceedings in Physics 158,
DOI 10.1007/978-1-4939-1239-1_52,

characteristic of delamination damages of composites for wind turbine blades are reported.

In this study, tensile tests have been carried out to investigate interlaminar shear properties of the delaminated composite materials. Acoustic emission technique was used to monitor the damage and failure progress of the specimens and the shear failure mechanisms of the delaminated composites have been discussed.

2 Methods

2.1 Materials and Specimens

The delaminated composites for wind turbine blades were manufactured using unidirectional E-glass fiber epoxy prepreg. Ten layers of each composite laminate were laid manually and teflon inserts with different widths (0, 10, 20, and 40 mm) were introduced during the hand lay up process. Then, the composites with simulated delaminations were formed by the hot-press at 120 °C for about 90 min. In order to obtain the shear plane, the prepreg were pre-cut. The thickness of the composite laminates was about 1.8 mm. Finally, rectangular specimens were cut from each laminate using a high-speed diamond saw and the width of each specimen was about 25 mm. Aluminum end tabs were bonded on all specimens in order to prevent grip failure of the composite specimens. A total of five specimens of each type composites were employed.

2.2 Experimental Procedures

The tensile tests of the specimens were carried out to research the interlaminar shear properties of the delaminated composites and the damage process of the specimens was recorded using AE technology. The unidirectional tensile tests were performed with a crosshead speed of 1 mm/min via an electronic universal testing machine (CMT5305). The loading–unloading tensile tests were dominated with a speed of 500 N/s by program and the load history is $0 \rightarrow 3 \rightarrow 1 \rightarrow 5 \rightarrow 2 \rightarrow 7 \rightarrow 2 \rightarrow 8 \rightarrow 2 \rightarrow 9 \rightarrow 2 \rightarrow 12$ kN. Furthermore, the lowest load was kept for 5 s under unload conditions. AMSY-5 system from Vallen Corporation was used for acquisition of AE signals.

Experimental setup for AE monitoring during the interlaminar shear tests is shown in Fig. 1. Two VS150-RIC AE transducers were used, whose output was amplified by 34 dB at the preamplifiers. In order to eliminate electric and mechanical noises, the threshold was fixed to 46 dB. The transducers were mounted on the specimen surface using a tape and the distance between them was 80 mm. Silicone grease was used as coupling agent between the sensor and the specimen surface.

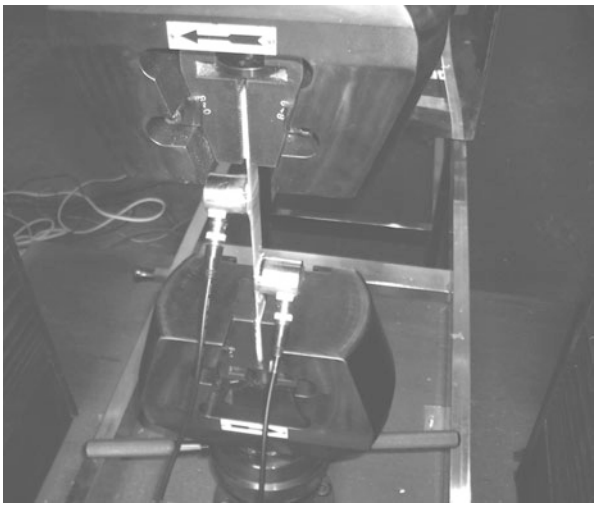

Fig. 1 Experimental setup for AE monitoring during the tensile tests

AE parameters (event, relative energy, amplitude, etc.) were obtained during the load process. These event data correspond to one AE sensor was discussed. In order to obtain the linear AE source location, the pencil breakage tests were conducted. According to the difference of the arrival times and the distance of the two AE transducers, the velocity of the wave was computed. As a result, the precise AE source could be determined.

3 Results and Discussion

3.1 Mechanical Properties of the Composites

According to a series of experiments, the average failure load and interlaminar shear properties were obtained. The standard deviation of failure load and interlaminar shear stress is less than 0.5 kN and 0.25 MPa, respectively. The load–time curves of the four types of composite specimens are shown in Fig. 2. Compared to Fig. 2a–d, similar linear relationships between load and time and failure load of the specimens are observed. As the length of the delamination defect increases from 0 to 10, 20, and 40 mm, the average failure load is 10.1, 10.2, 10.1, and 10.3 kN, the interlaminar shear stress is 5.05, 5.83, 6.73, and 10.3 MPa, respectively. From Fig. 2d, 40 mm in length was introduced into the specimen by inserting teflon and the minimum area of the interface is obtained. That is why no load drops and less AE activity are induced. Therefore, the size of strip delaminations has little effect on the failure load of the composite specimens when these defects lie in the middle of interlaminar shear region. The damage evolutions may approach the extremities of the shear plane.

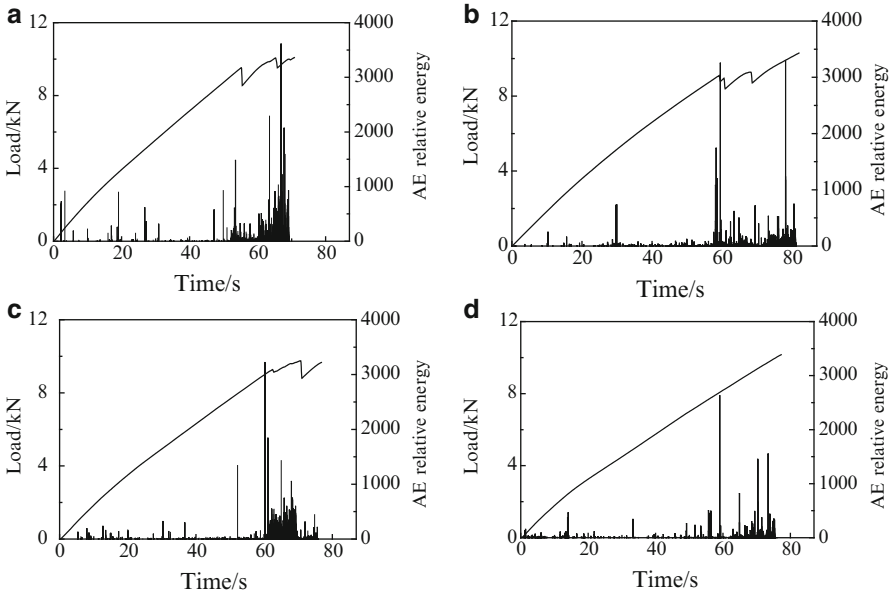

Fig. 2 Load, AE relative energy vs. time for specimens without defects (**a**) and with delaminations at the length of 10 mm (**b**), 20 mm (**c**), and 40 mm (**d**)

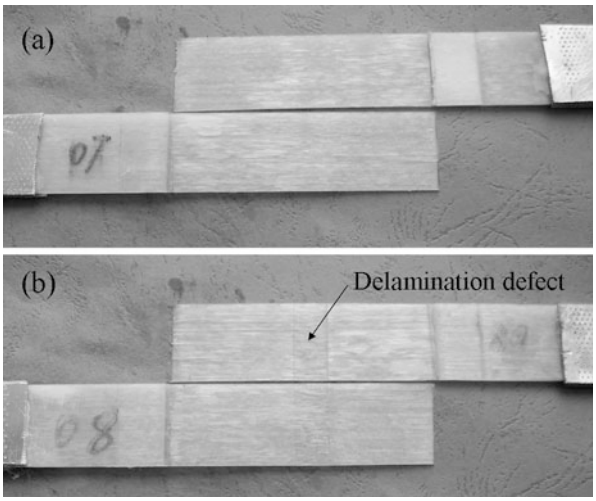

Fig. 3 Photograph of the fractured specimens without defects (**a**) and with typical delamination defects (**b**)

Figure 3 shows the photograph of the fractured specimens. In the case of specimen without delamination defects in Fig. 3a, interlaminar crack is main failure mode and no obvious fibers fracture is observed. Under the loaded condition, the specimen experiences shear stress and crack propagations are induced along the shear plane.

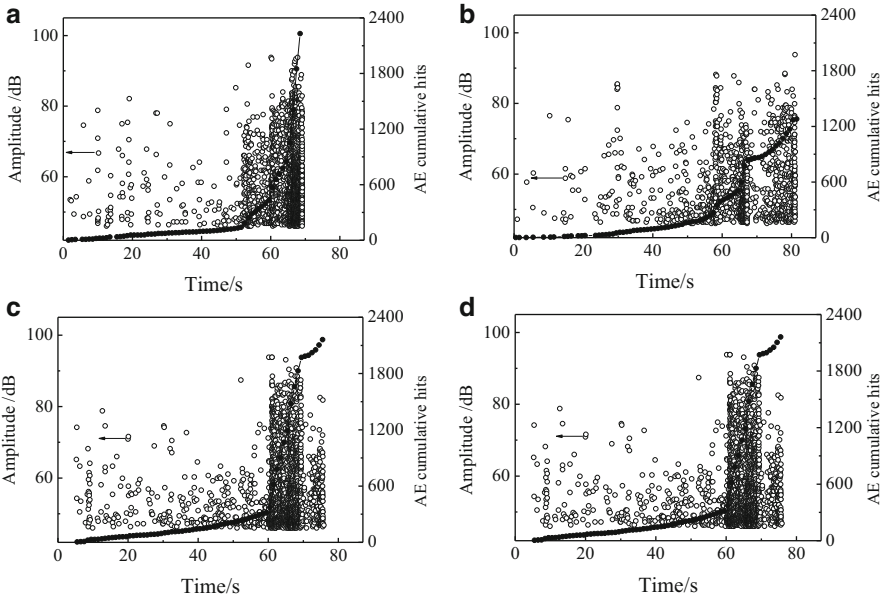

Fig. 4 Amplitude, cumulative hits vs. time for specimens without defects (**a**) and with delaminations at the length of 10 mm (**b**), 20 mm (**c**), and 40 mm (**d**)

Compared to Fig. 3a, similar failure mode of the specimen with delamination defect is obtained in Fig. 3b. Furthermore, the surface of delamination defect is smoother than other parts on the shear plane and shows that delamination propagations are not induced along a flat plane.

3.2 AE Characteristics of the Composites

The interlaminar damage process and microscopic failure mechanism of the composites were investigated by considering the corresponding AE signal characteristics. The damage and failure process of the composite specimens could be divided into two stages, the evolution and failure stages. The AE relative energy in the four types of composite specimens is shown in Fig. 2. It can be seen that less damage and low AE relative energy are obtained in the initial load stage. As the load increases, the value of AE relative energy increases gradually. The appearance of AE signals whose relative energy is about 3,000 will lead to the failure of the shear plane. Compared to Fig. 2a, because of the presence of delamination defect, AE signals, the value of relative energy is about 3,000, are observed earlier in Fig. 2b–d. As the area of delamination defect increases, the bearing area of the shear plane is decreased. A small region of damage evolution result in the early emergence of AE signals which are connected with delamination growth. Figure 4 shows the characteristics of AE amplitude and cumulative hits in the specimens.

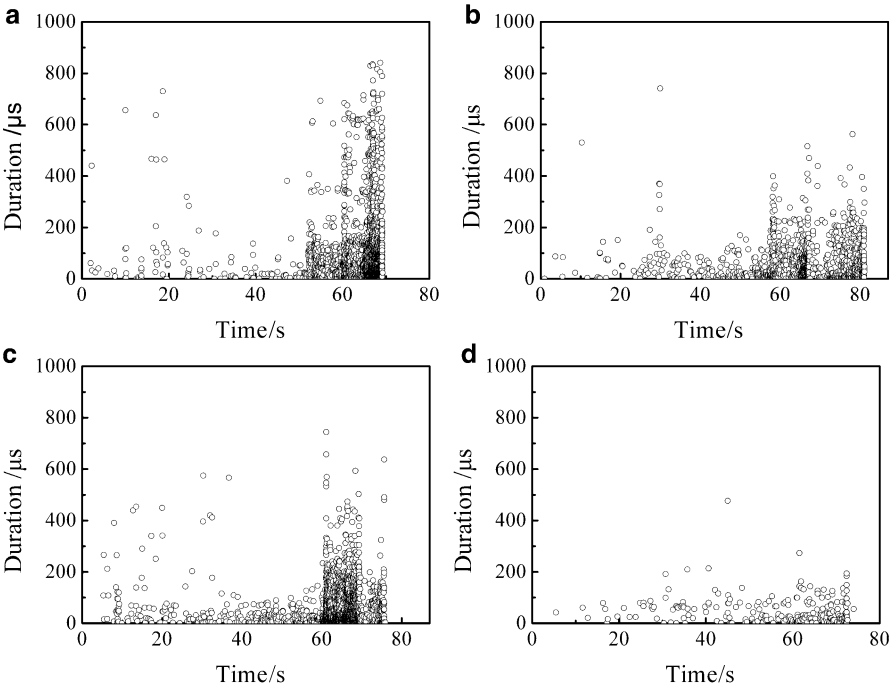

Fig. 5 Duration vs. time for specimens without defects (**a**) and with delaminations at the length of 10 mm (**b**), 20 mm (**c**), and 40 mm (**d**)

As shown in Fig. 4a, few AE signals were generated at the evolution stage of the composites without delamination defects. As the load increases, the subsequent macro-cracking generates fewer signals, especially the number of AE hits which have an amplitude form 60 to 80 dB increases at the evolution stage. Compared to Fig. 4a–c, as the length of delamination defect increases from 0 to 10 and 20 mm, the total AE signals decreases. From Fig. 4d, it would be observed that there were less AE signals and cumulative hits were recorded when the length of delamination defect increased to 40 mm. This phenomenon could be attributed to the decrease of the actual bearing area.

Figure 5 shows the characteristics of AE duration time produced in four kinds of specimens. With regard to the composites without delamination defects, the duration time of AE signals was mostly distributed in a range under 200 μs at the evolution stage. As the load increases, the AE signals which have long duration time were generated. Compared to Fig. 5a–d, as the length of the delamination defect increases from 0 to 10, 20, and 40 mm, the number of AE hits with the duration time above 200 μs is 370, 95, 157, and 5, respectively. It has been found that the decrease of the actual bearing area along the shear plane contributes to the decrease of AE signals with long duration time. According to the AE signals in experiments, the failure of the shear plane is connected to the AE signals whose

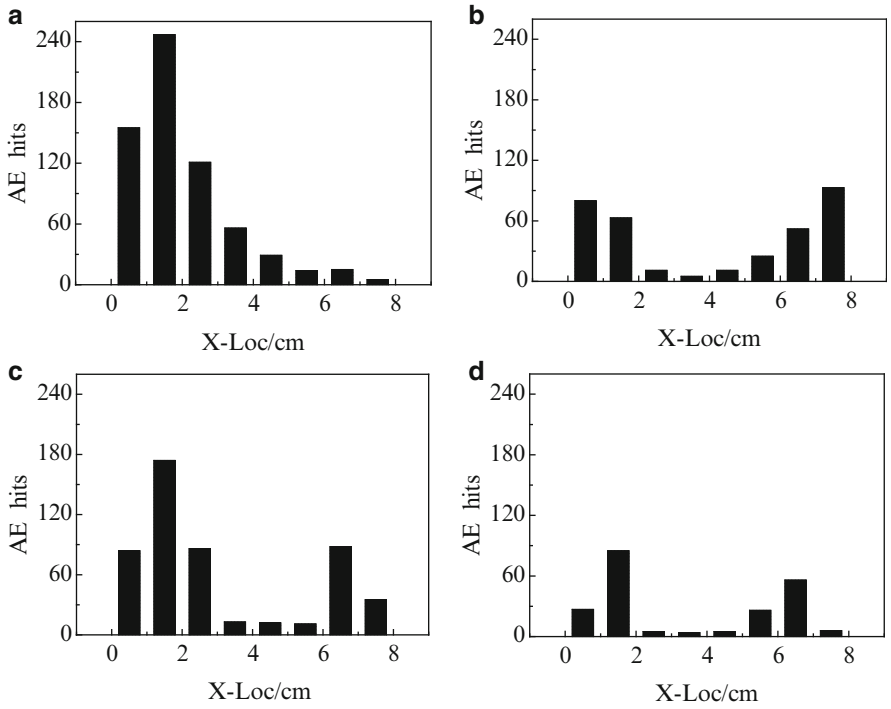

Fig. 6 AE source location for specimens without defects (**a**) and with delaminations at the length of 10 mm (**b**), 20 mm (**c**), and 40 mm (**d**)

relative energy is about 3,000. The decrease of the actual shear area results in the decrease of the total AE signals, especially when the duration time is above 200 μs.

3.3 Effect of Delamination on the Composites

According to the experimental results, the average wave velocities along longitudinal direction in unidirectional composites is 4,640 m/s. Figure 6 shows the results of the linear AE source location for the four kinds of specimens. From Fig. 6a, 642 AE sources are observed and most AE sources approach the extremities of the shear plane, whereas few AE sources are generated at the center of the shear plane. In the case of the composites without delamination defects, the damage propagates along the entire shear plane. As shown in Fig. 6b–d, as the length of the delamination defect increases from 10 to 20 and 40 mm, the number of AE sources is 340, 503, and 214, respectively. Compared to Fig. 6a–d, most AE sources approach

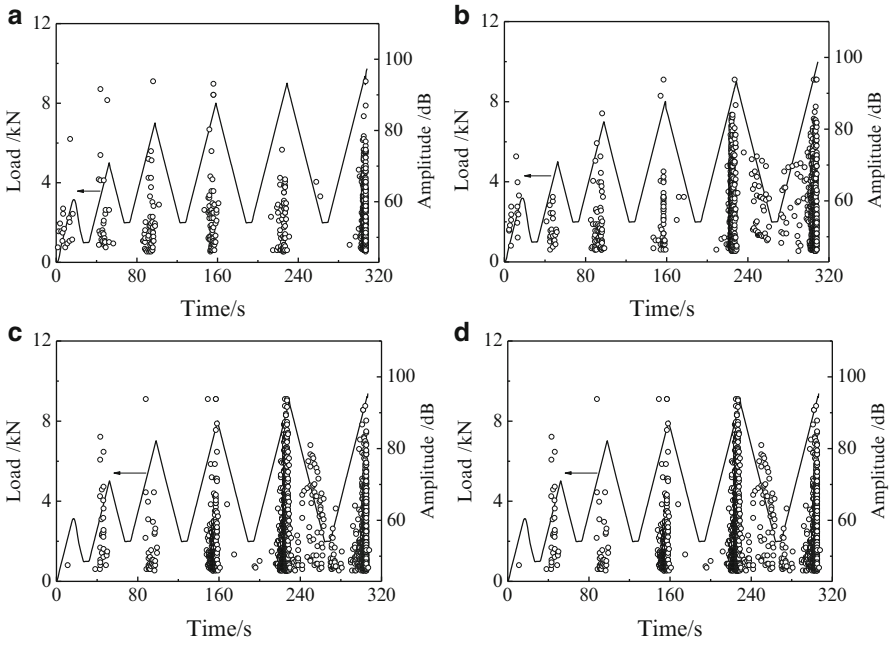

Fig. 7 Load, amplitude vs. time history graph for specimens without defects (**a**) and with delaminations at the length of 10 mm (**b**), 20 mm (**c**), and 40 mm (**d**) under unloading and reloading condition

the extremities of the shear plane and the damage evolutions mostly focus on these interlaminar shear regions has been proved.

Related research by Moura et al. [9] has reported the stress analysis of composite bonded joints containing strip defects. It has been verified that stress distributions are not markedly altered relative to the centered defect and stress concentrations are more important when the defect approaches the extremities of the overlap. In the case of the delaminated composite, lower stress values are obtained near the center of the interlaminar shear plane when delamination defects are located at the center of the shear plane. Therefore, the strip delamination defects which lie in these low stress regions have little effect on the interlaminar damage and evolution of the composite specimen.

Figure 7 shows the AE amplitude response of the four kinds of specimens under unloading and reloading condition. As shown in Fig. 7a, no obvious damages are induced and low AE amplitudes are obtained in the initial load stage. Furthermore, no AE signals are generated during the unload conditions. As the load increases, the high amplitude signals are present. Compared to Fig. 7a, in the failure stages of the interlaminar shear plane, a few AE signals are generated during the unload conditions in Fig. 7b, c. It can be attributed to the effect of delamination defects and is agree well with the earlier damage evolution in Fig. 2b–d. From Fig. 7d, as the

length of the denomination increases to 40 mm, the number of AE signals decreases, resulting in no signals are generated during the unload conditions. Generally, significant information about the interlaminar damage state can be extracted form AE parameters. As the load increases, micro damage in the interlaminar interface appears and generate small amount of AE signal. The micro damages progressively accumulate by increasing load and macroscopic crack occurs. Then rapid crack propagation and a drop in the load are obtained.

4 Conclusion

In summary, a study on the interlaminar shear properties of the delaminated composite materials for wind turbine blades has been conducted. AE response properties during the damage and evolution of the four kinds of specimens with various delamination defects are obtained. The results show that the size of strip delaminations has little effect on the failure load of the composite specimens when these defects lie in the middle of interlaminar shear region, and the main damage evolution approaches the extremities of the shear plane. The failure of the shear plane is connected to the AE signals whose relative energy is about 3,000. The decrease of the actual bearing area along the shear plane results in the decrease of the total AE signals, especially when the duration time is above 200 μs. The linear AE source location results agree well with the initiation and propagation of interlaminar damage.

Acknowledgment This work was supported by the Natural Science Foundation of Hebei Province, P. R. China (under grant no. E2012201084) and National University Students' innovative training program (under grant no. 201310075013).

References

1. P. Brøndsted, H. Lilholt, A. Lystrup, Composite materials for wind power turbine blades. Annu. Rev. Mater. Res **35**, 505–538 (2005)
2. H.G.M. Joselin, S. Iniyan, E. Sreevalsan, S. Rajapandian, A review of wind energy technologies. Renew. Sust. Energ. Rev **11**(6), 1117–1145 (2007)
3. M.H. Thomas, M. Dharmaraj, E.L. James, Post buckling analysis of a wind turbine blade substructure. J. Sol. Energy. Eng **127**(4), 544–552 (2005)
4. M.S. Mahmood, R. Roham, Simulation of fatigue failure in a full composite wind turbine blade. Compos. Struct **74**(3), 332–342 (2006)
5. E. Jasiūnienė, R. Raišutis, R. Šliteris, A. Voleišis, M. Jakas, Ultrasonic NDT of wind turbine blades using contact pulse-echo immersion testing with moving water container. Ultrasound **63** (3), 28–32 (2008)
6. R. Raišutis, E. Jasiūnienė, E. Žukauskas, Ultrasonic NDT of wind turbine blades using guided waves. Ultragarsas (ultrasound) **63**(1), 7–11 (2008)

7. E. Jasiūnienė, R. Raišutis, NDT of wind turbine blades using adapted ultrasonic and radiographic techniques. Insight **51**(9), 477–483 (2009)
8. A.G. Beattie, Acoustic emission, principles and instrumentation. J. Acoust. Emis. **2**(1/2), 95–128 (1983)
9. M.F.S.F. Moura, R. Daniaud, A.G. Magalhães, Simulation of mechanical behaviour of composite bonded joints containing strip defects. Int. J. Adhes. Adhes. **26**, 464–473 (2006)

Condition Monitoring of Shaft Crack with Acoustic Emission

Li Lin, Yong Zhou, Fulei Chu, and Wenxiu Lu

Abstract A cracked shaft is one of the most catastrophic failures in any rotating machine such as the axle of a railway vehicle with increasing speed which is usually working in a hazardous environment. This paper describes an experimental investigation in which Acoustic Emission technology was applied to monitor the presence of a naturally fatigued crack in an operating high speed shaft. A test rig was built for generating natural rotating fatigue crack on a shaft. The experiments show that the classical AE parameters, such as energy, hit, and amplitude can indicate the cracked shaft failure process.

1 Introduction

The testing and inspection of shaft, which is one of the rotating machine's main components, plays an important role in the safe operation, especially for the axle of trains [1]. Fatigue cracking is one main [2] type of failure mode [1]. The Acoustic Emission (AE) technique has been widely researched for the in situ monitoring and has the potential to provide cost-effective condition monitoring [3–5].

Shigeishia et al. [6] demonstrate that acoustic emission technique can be applied to condition assessment of bridges and show that AE is useful in detecting crack

L. Lin (✉)
Dalian Jiaotong University, Dalian 116023, China
e-mail: julandalili@126.com

Y. Zhou
Dalian University of Technology, Dalian 116023, China
e-mail: kevinzh@dlut.edu.cn

F. Chu • W. Lu
Tsinghua University, Tsinghua 100089, China

G. Shen et al. (eds.), *Advances in Acoustic Emission Technology: Proceedings of the World Conference on Acoustic Emission-2013*, Springer Proceedings in Physics 158,
DOI 10.1007/978-1-4939-1239-1_53,

growth and determining the position of the crack tips at a much earlier stage in their development, before they are noticed during visual inspection. Thakkar et al. [7] present a laboratory study on the physical processes of impact and wear Acoustic Emission (AE) generated during railway wheel–rail track interaction, with a view to developing methods of in situ rail–wheel interaction monitoring using rail-mounted sensors. Gu et al. [8] develop a new signal processing method which uses envelope analysis with discrete wavelet transforms for application in an early fault detection system for AE signals caused by crack growth on a rotating shaft. It has been shown that the crack growth in rotating machinery can be detected and energy can be used in the early detection of the crack.

Mohan et al. [3] indicate that acoustic emission energy can be used to indicate the onset of ply and inter laminar failure. D. Mba et al. [9, 10] demonstrate the results of an investigation for detecting and monitoring natural crack initiation and propagation in slow-speed rotating machinery with the AE technology and concluded that crack initiation and propagation on slow-speed bearings and shafts can be detected with the AE technology.

Schumacher et al. [11] present a detection methodology using acoustic emission techniques to identify vehicles operating with studded tires and found that using relatively simple detection algorithms such as mean AE hit amplitude, vehicles with studded tires could be discriminated reliably. D. Mba et al. [12] present an experimental investigation in which several technologies such as Acoustic Emission, vibration and motor current signature analysis were applied to identify the presence of a naturally fatigued pinion shaft in an operating gearbox and concluded that the combination of these methods could offer good diagnostic information though successful diagnosis is very dependent on the diagnostic path taken by the investigator.

In this work, we have investigated shaft crack growth in specially built test rigs that allowed continuous monitoring of AE throughout the life span of rotating shaft. The classical AE parameters, such as energy, hit, and amplitude were applied to detect the crack growth.

2 Experimental Setup

In this work, the experiment setup is the same as the test rig of the author's article "HHT-based AE characteristics of natural fatigue cracks in rotating shafts" [13].

The test rig consisted of four bearings, an electrical reduction geared motor (reduction ratio is 3:1), a coupling at the driving end, and a rotating shaft with 25 mm diameter and 600 mm long. The diameter of the shaft was produced to decrease to 6 with 2 mm long in the middle of the shaft and between the two deep groove ball bearings which were used to transmit the hydraulic load onto the shaft to accelerate fatigue crack initiation and growth as shown in Fig. 1a. The test rig rotational speed was kept constant at 400 RPM. Two deep groove ball bearings were employed to support the shaft on both sides.

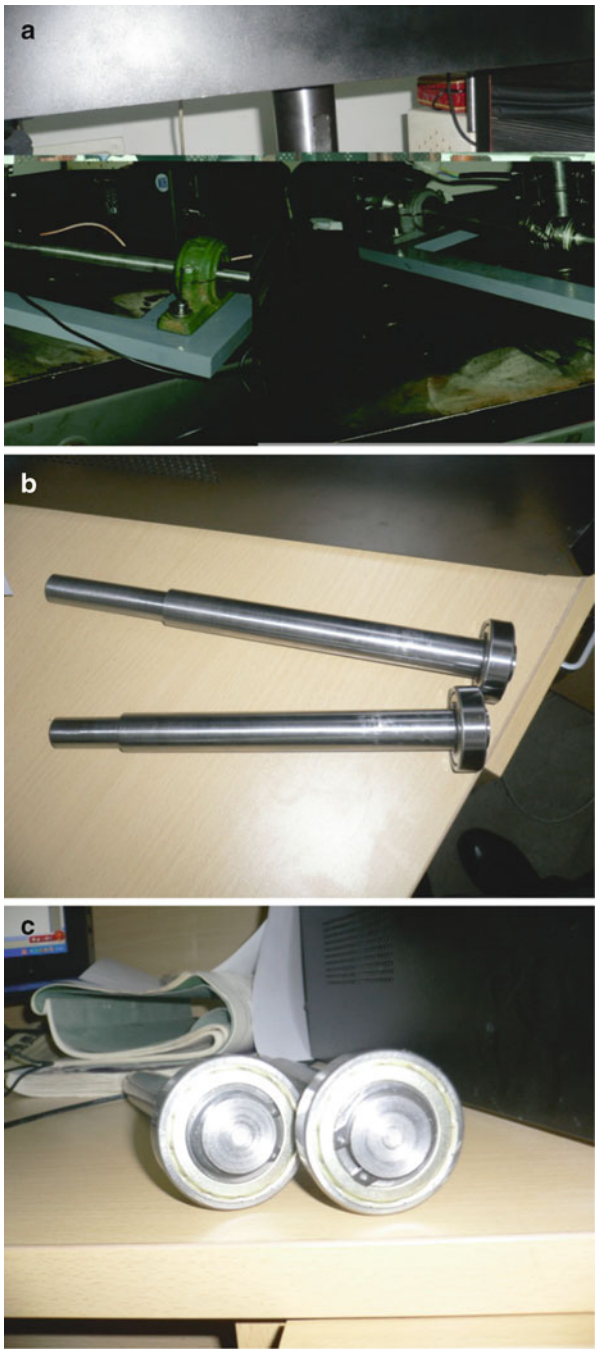

Fig. 1 Test rig

It is expected that natural fatigue cracks will be initiated in the site of the diameter sharp change due to the high bending stress concentration. The test shaft was tested from the fatigue crack initiation; the fatigue crack grows until the shaft completely fractured into two in the site of the diameter sharp change at loads 100 N. The damage for this test condition is observed in Fig. 1b, c.

Two Physical Acoustics Corporation R15a transducers were employed to detect the fatigue crack. The AE sensors were attached to the outer ring surface of the two middle bearings and connected to variable gain preamplifiers 20, 40, and 60 dB, which were in turn connected to a ruggedized PC, containing Physical Acoustics Corporation PCI-2 acquisition cards. The preamplifiers were set at a gain of 40 dB. The system was also continuously set to acquire AE waveforms at a sampling rate of 1 MHz.

Reference [13] addressed an application of recently developed Hilbert–Huang transform (HHT) signal processing technique on AE feature extraction of natural fatigue cracks in rotating shafts providing an energy–frequency–time distribution with adaptable precision. This paper addresses an application of the classical AE parameters, such as energy, hit, and amplitude on the same AE signal of natural fatigue cracks in rotating shafts providing the cracked shaft failure process.

3 Test Results and Discussion

Acoustic Emission is "the class of phenomena whereby transient elastic stress waves are generated by the rapid release of energy from localized sources within a material" defined by the American Society for the Testing of Materials. Weavers define AE as "Acoustic Emission is a naturally occurring phenomenon within materials and the term acoustic emission is used to define the resulting transient elastic waves when the strain energy is released suddenly from a material due to the occurrence of micro-structural changes in a material" [14].

Figure 2 shows the AE waveform in which the information of the source can be derived. Acoustic emission at the source of a test piece originates, propagates, and hits a piezoelectric crystal transducer's output voltage which is amplified and passed to a data acquisition and analysis computer.

Amplitude is the important feature of an AE signal that passes through the threshold as shown in Fig. 2, and is the highest voltage on the waveform. Amplitude is described on a decibel (dB) scale in practice as:

$$A(\mathrm{dB_{AE}}) = 20\ \log \frac{V_\mathrm{p}}{V_\mathrm{ref}} \tag{1}$$

where V_p is the peak voltage at the transducing element's output, with respect to the reference voltage, $\mathrm{V_{ref}}$.

A hit due to AE signals hitting the transducer is the waveform shown in Fig. 2.

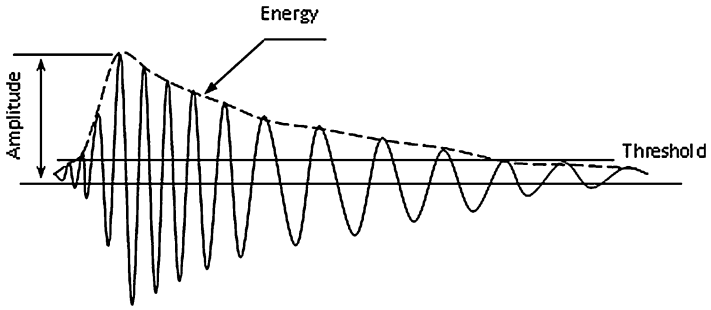

Fig. 2 Acoustic emission waveform

Fig. 3 Amplitude (dB) versus time (s)

Energy shown in Fig. 2 is the power energy of AE waveform that passes through threshold and within duration period.

In this work, the shafts were tested and natural fatigue cracks would be initiated and propagate in the site of the diameter sharp change which was produced to decrease to 6 with 2 mm long in the middle of the shaft due to the high bending stress concentration until the shaft completely fractured into two. These cracks would be detected by the AE sensors. The test rig rotational speed was 400 RPM and radial load was 100 N employed for this particular test.

Traditional AE parameters of continuous monitoring of the AE levels, such as amplitude are presented in Fig. 3. The test lasted only 250 s and was terminated due to the fracture of the shaft. Figure 3 shows trends of amplitude which is one of the important traditional AE parameter. AE activity was noted from 108 s of operation. Relatively high levels of AE activity were noted between 235 and 250 s of operation. The value of the amplitude ranged mostly from about 30 to 50 dB between 108 and 235 s. And it was observed that at approximately 235 s significant increase in AE amplitude which ranged from 30 to 85 dB was shown until the test was terminated.

It can be believed by the authors that increased AE activity between 108 and 235 s is attributed to crack initiation and the large transient AE events towards the end of the tests are due to the rapid propagation of the crack.

Fig. 4 Energy versus time (s)

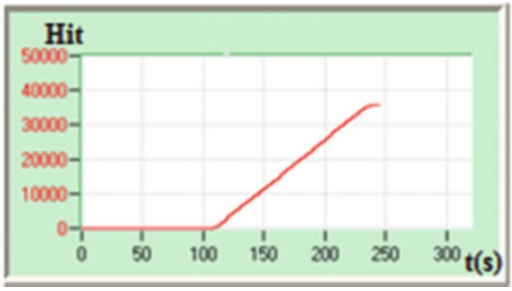

Fig. 5 Hit versus time (s)

Interestingly observations of AE energy which is also one of the conventional AE parameters, showed changing characteristics as a function of time. This is presented in Fig. 4. Observations of continuous monitoring of the AE levels for 250 s of shaft operation did not show any considerable rise early during testing. During the start of the test steady AE activity was noted. Figure 4 shows the results for the test run until damage after approximately 250 s of operation.

On the initial stage of the test, the measured AE energy remained constant of 0. And this AE activity gradually increased after 110 s and the measured AE energy remained constant. After approximately 235 s a large transient rise in AE energy level was observed and this AE activity kept until the test was terminated.

Hit which is another classical AE parameter recorded over the duration of the test is detailed in Fig. 5, where it was noted that high levels of AE activity were observed at the end of the test, also observed was hit going up in a straight line with time.

The early AE activity (108–235 s) was attributed to crack initiation. The crack had initiated at the edge where the diameter of the shaft was produced to decrease from 25 mm to 6 with 2 mm in the middle of the shaft and which is between the two deep groove ball bearings used to transmit the hydraulic load onto the shaft to accelerate fatigue crack initiation and growth. And the crack propagated at the edge after 235 s to a rapid rise until failure of the shaft and the duration between propagation to the final crack fracture was clearly noted and lasted only 15 s. In the test where low load (100 N) was applied there was a clearly defined region where crack initiation can be identified. This is attributed to the fact that the time between initiation and accelerated crack propagation lasted 27 s (108–235 s).

4 Conclusion

The results of this experiment presented here demonstrate that classical AE parameters such as amplitude, energy, and hit are sensitive to the detection of natural incipient crack initiation and propagation in high speed shafts. AE is reliable in detecting crack growth at a much earlier stage in their development before they are noticed during visual inspection on shafts whilst in operation. Crack initiation and propagation on rotating shafts could be detected due to its release of much of AE energy and resulting in a rapid increase of AE parameters such as amplitude, energy, and hit. D. Mba et al. [10] found that there is a clear correlation between increasing AE energy levels and the natural propagation and formation of shaft defects in low speed shafts which was also found in higher speed shafts in this paper. Therefore there is the potential to apply this AE technique in detecting crack initiation and propagation on an operating shaft.

Acknowledgment The authors acknowledge the facilities of Tsinghua University. The financial support of National Natural Science Foundation of China is gratefully acknowledged. The first author gratefully acknowledges Department of Precision Instruments, Tsinghua University for the research collaboration. The authors thank Physical Acoustics Corporation for help.

References

1. X. Wei, L. Jia, H. Liu, A comparative study on fault detection methods of rail vehicle suspension systems based on acceleration measurements. Vehicle Syst. Dynam. **51**(5), 700–720 (2013)
2. A. Daadbin, J. Rosinski, D. Smurthwaite, Online monitoring of essential components helps urban transport management and increases the safety of rail transport. WIT Trans. Built Environ. **128**, 541–552 (2012)
3. R. Mohan, G. Prathap, An acoustic emission energy analysis and its use to study. J. Nondestr. Eval. **1**, 225–233 (1980)
4. S. Soua et al., Determination of the combined vibrational and acoustic emission signature of a wind turbine gearbox and generator shaft in service as a pre-requisite for effective condition monitoring. Renew. Energy **51**, 175–181 (2013)
5. A.V. Kappatos, S.E. Dermatas, Feature extraction for crack detection in rain conditions. J. Nondestr. Eval. **26**(2–4), 57–70 (2007)
6. M. Shigeishia et al., Acoustic emission to assess and monitor the integrity of bridges. Construct. Build Mater. **15**, 35–49 (2001)
7. N.A. Thakkar, J.A. Steel, R.L. Reuben, Rail–wheel interaction monitoring using acoustic emission: a laboratory study of normal rolling signals with natural rail defects. Mech. Syst. Signal. Process. **24**(1), 256–266 (2010)
8. D. Gu et al., Evaluation of the use of envelope analysis and DWT on AE signals generated from degrading shafts. Mater. Sci. Eng. B. **177**(19), 1683–1690 (2012)
9. M. Elforjani, D. Mba, Condition monitoring of slow-speed shafts and bearings with acoustic emission. Strain **47**, 350–363 (2011)
10. M. Elforjani, D. Mba, Detecting natural crack initiation and growth in slow speed shafts with the acoustic emission technology. Eng. Fail. Anal. **16**(7), 2121–2129 (2009)

11. T. Schumacher, C.C. Higgins, S.C. Lovejoy, Detection of vehicles with studded tires using acoustic emission sensors mounted to highway bridges. J. Transport. Eng. Asce. **136**(5), 480–487 (2010)
12. B. Eftekharnejad, A. Addali, D. Mba, Shaft crack diagnostics in a gearbox. Appl. Acoust. **73**(8), 723–733 (2012)
13. L. Lin, F. Chu, HHT-based AE characteristics of natural fatigue cracks in rotating shafts. Mech. Syst. Signal. Process. **26**, 181–189 (2012)
14. G. Drummond, J.F. Watson, P.P. Acarnley, Acoustic emission from wire ropes during proof load and fatigue testing. NDT. E. Int. **40**(1), 94–101 (2007)

Studies on Automobile Clutch Release Bearing Characteristics with Acoustic Emission

Guoliang Chen and Xiaoyang Chen

Abstract Automobile clutch release bearings are important automotive driveline components. For the clutch release bearing, early fatigue failure diagnosis is significant, but the early fatigue failure response signal is not obvious, because failure signals are susceptible to noise on the transmission path and to working environment factors such as interference. With an improvement in vehicle design, clutch release bearing fatigue life indicators have increasingly become an important requirement. Contact fatigue is the main failure mode of release rolling bearing components. Acoustic emission techniques in contact fatigue failure detection have unique advantages, which include highly sensitive nondestructive testing methods. In the acoustic emission technique to detect a bearing, signals are collected from multiple sensors. Each signal contains partial fault information, and there is overlap between the signals' fault information. Therefore, the sensor signals receive simultaneous source information integration is complete fragment rolling bearing fault acoustic emission signal, which is the key issue of accurate fault diagnosis. Release bearing comprises the following components: the outer ring, inner ring, rolling ball, cage. When a failure occurs (such as cracking, pitting), the other components will impact damaged point to produce acoustic emission signal. Release bearings mainly emit an acoustic emission waveform with a Rayleigh wave propagation. Elastic waves emitted from the sound source, and it is through the part surface bearing scattering. Dynamic simulation of rolling bearing failure will contribute to a more in-depth understanding of the characteristics of rolling bearing failure, because monitoring and fault diagnosis of rolling bearings provide a theoretical basis and foundation.

G. Chen (✉) • X. Chen
Department of Mechatronics Engineering and Automation, Shanghai University, Shanghai 200072, China
e-mail: guoliang.chen@zf.com

G. Shen et al. (eds.), *Advances in Acoustic Emission Technology: Proceedings of the World Conference on Acoustic Emission-2013*, Springer Proceedings in Physics 158,
DOI 10.1007/978-1-4939-1239-1_54,

1 Introduction

Automobile clutch release bearings are important automotive driveline components. The active part (and the driven part) of the clutch passes through the friction force between the contact surfaces, or uses a liquid as a transmission medium (torque converter), or uses a magnetic drive (electromagnetic clutch) to transmit torque. Currently, spring-loaded friction clutches (referred to as a friction clutch) are in wide use in commercial vehicles. Engine torque is first sent through the flywheel and pressure plate and then passed or driven through the disc, producing contact surface friction. Commercial vehicles' clutch release bearing structure, shown in Fig. 1, has some common principles, described next.

In the automotive power transmission process, the role of the clutch release bearing is to connect or disconnect the power transmission between the transmission and the engine via axial displacement of the bearing, thus completing the smooth start of the car, or to suspend and/or transform gear operations. As the vehicle design to raise the level of the clutch release bearing noise indicators are increasingly high requirement.

For the clutch release bearing, early fatigue failure diagnosis is significant, but conveying the release bearing's early fatigue failure response signal is not obvious, because it is susceptible to noise along the transmission path and to working environment factors such as interference. Early fatigue failure between signal excitation and a dynamic response of the intrinsic relationship that is not obvious, based on acoustic emission (AE) signal processing and feature extraction of fault diagnosis technology encountered new challenges. In the diagnosis of rolling bearing faults, domestic and foreign scholars have conducted significant long-term research about the development of AE signal fault detection and diagnosis techniques.

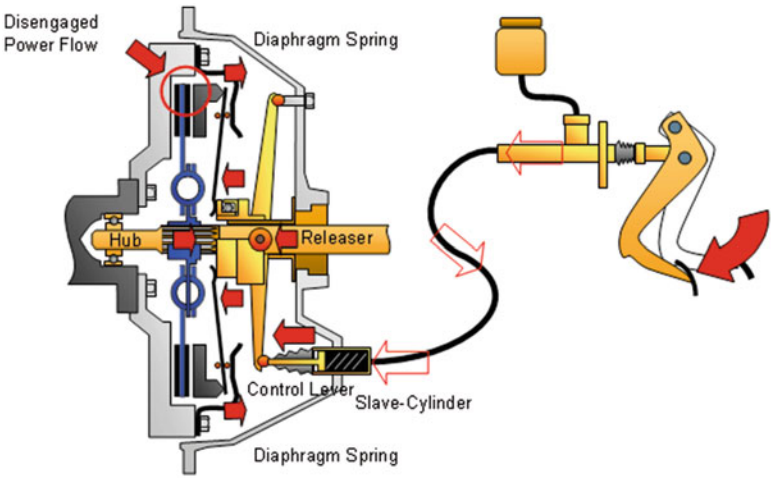

Fig. 1 Clutch state diagram

However, compared with bearing fault diagnosis technology, bearing failure and failure mechanisms of modeling theory are particularly inadequate. The following research on the dynamic simulation of rolling bearing faults should help give a better understanding of the characteristics of bearing failure:

1. A nonlinear time-varying bearing model was created. It had simulated local spalling and damage to the bearings.
2. A rolling–stator coupling model was created, which could be studied as a rolling dynamic model of a rotor with the outer ring, the inner ring, and the rolling injury.
3. A rolling nonlinear dynamics model was created, which was used for the mathematical description of the inner ring, outer ring, and rolling elements of the local damage.
4. A 6-DOF dynamic model of bearing failure was established. The model took into account the influence of factors of variable stiffness and nonlinear rolling slide caused by the bearing clearance time and, after the introduction of the analog unit resonator frequency, of the natural vibration of faulty bearing components.

Dynamic simulation of a rolling bearing fault study will contribute to a better understanding of the mechanism and characteristics of bearing failure, which will provide a theoretical basis and foundation for monitoring and fault diagnosis of rolling bearings.

2 Methods

A rolling bearing, which is a core component of rotating machinery, is the main failure mode of contact fatigue rolling such parts. Acoustic emission technology has developed rapidly in recent years, [1] and its advantages include its high sensitivity of nondestructive testing methods. The AE technique has unique advantages in detecting contact fatigue failure. In recent years, domestic and international researchers have studied in depth metal parts in contact fatigue damage process to understand the characteristic parameters and mechanism of damage [2]. Furthermore, researchers have also studied other AE signal amplitude fatigue. In both areas, they have made progress. However, there is little research on AE signal characteristics during contact fatigue damage on the wear-resistant coating of such a nonhomogeneous material system. The study of AE signals reveals that understanding of the mechanism of contact fatigue damage is still in its infancy, where theamplitude, "energy counts, and average frequency" are commonly used to analyze the characteristics of important parameters of fatigue damage. Amplitude is the sound of a crash in the emission's maximum amplitude, which is directly related to the degree of damage, and there is a hit with the AE amplitude's square root of the mean squared. The amplitude of the AE threshold's operating frequency and the propagation characteristics of the coating may well reflect that the degree of fatigue

damage is the energy of a crash in the integral value of the amplitude of the AE's duration.

Bearing fault detection shows its complexity. Failure of rolling bearing work is accompanied by abnormal noise generation under the broad category of AE, and thus it can be applied to detect an AE technique. The AE technique for detection of the bearing is mostly of the contact type [3], which is mainly to detect the fixed shaft rotary bearing. For non-contacting type acoustic emission testing, must consider removing noise [4]. In this detection state, each signal contains fault information that is not complete, and there is an overlap between each signal's fault information. Therefore, how the sensor receives simultaneous source signal segment information and then integrates signals into a complete acoustic signal of rolling bearing fault is the key issue behind accurate fault diagnosis.

The fault signal processing method appears in the frequency characteristic. Rolling work is accompanied by a failure to produce abnormal noise, which is a broad category of AE, so one can use it to detect the AE technique [5]. For a long time the fault bearings collected by AE signals at different speeds (0.5–0.85 rpm), that the use of "the impact of the number of times per second" may reflect fault information, but by the background noise interference is very serious. As the system of rotating machinery is complex, collected bearing AE signals are complex and noisy. A collision frequency based on a typical rolling bearing failure, and multi-sensor while the time difference between when the source signal, establish time-related rules [6]. When the rolling bearing's outer ring, inner ring, cage, and other components fail (such as from cracks, pitting, etc.), the other parts impact the damaged points and generate AE signals. Depending on the defect portion, the contact point is not the same frequency throughout the defect.

Rolling bearing damage analysis shows that rolling failure occurs during the rolling part's operation. Characteristics of the vibration signal can be divided into different classes of wear and surface damage fault. Generally, bearing surface wear failure experience working longer, which is a gradual failure, and therefore it has a low degree of harm [7]. Fault surface damage includes fatigue pitting, spalling formation, cracks, and so on, and the bearing point of damage, when in contact with other components, produces an altered impulse force and causes the system resonance, which leads to vibration and increases the noise. Under normal operating conditions, the failure is most likely to occur in the form of rolling elements or inner and outer raceway contact stress points to withstand cyclic changes due to the emergence of fatigue pitting, leading to the cited rolling failure.

MM3A310 is a low-power, high-performance, three-axis, linear capacitive accelerometer and is the development of micromachining technology (Fig. 2). The high-performance silicon micro-accelerometer sensing element's composition appears in a ($3 \times 3 \times 1$)-mm ASIC land grid array (LGA) package. It which ensures that the sensor operates within the range from -40 to +85 °C, sealed from the environment. The device has a user-selectable full scale of a ± 2 g/± 4 g/± 8 g/s;16 g measurement range and a data output rate from 1 Hz to 4 KHz of signal conditions, temperature compensation, self-test, and 96 free-fall detection-level embedded data output FIFO. Two independent and flexible interrupts provide greatly simplify the algorithm for

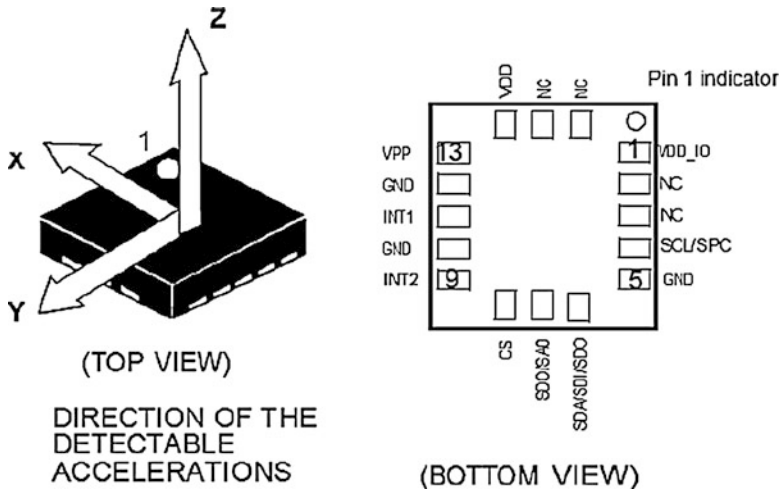

Fig. 2 MM3A310 outline

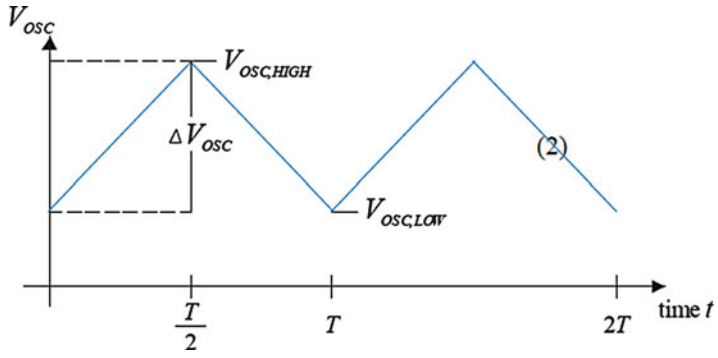

Fig. 3 The voltage output of the oscillator

various motion status detection. It features standard I2C and SPI interface chip communication.

The MM3A310 has a supply voltage of 1.71–3.6 V, a $(3 \times 3 \times 1)$-mm LGA-16 package, 10,000 g of high-impact viability, factory-programmable offset and sensitivity, and digital temperature output.

The capacitive proportional voltage signal converter output interface integrated circuit CAV424 works as follows: An through the capacitor COSC adjustable-frequency reference oscillator drives two symmetrical integrators that are in time and phase synchronization (see Fig. 3). Two capacitors CR and CM are controlled by the amplitude of the integrator. Since the integrator has a high common-mode rejection ratio and resolution, the difference between the two amplitude signals provided by the two capacitors CM and CR reflects the voltage difference. This

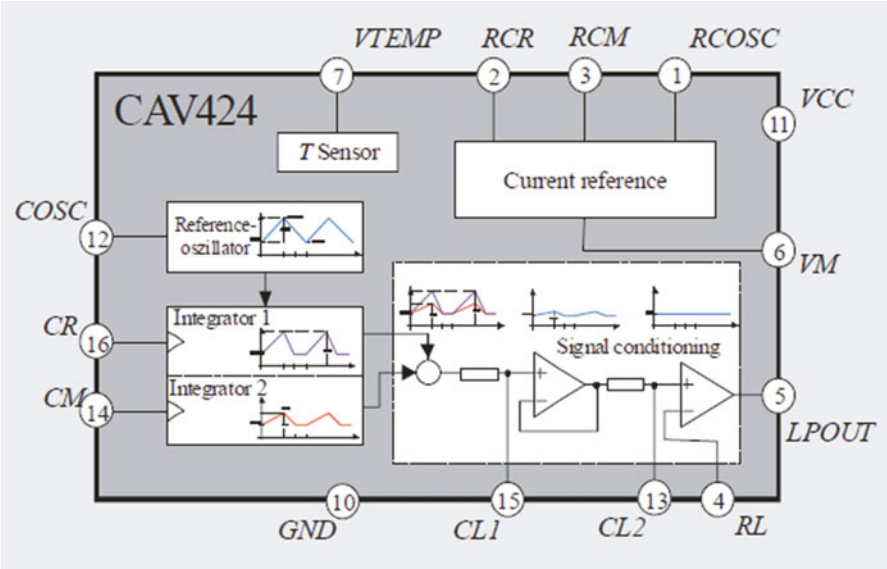

Fig. 4 With a signal processing block

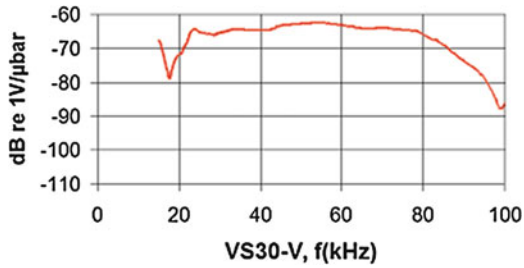

Fig. 5 Frequency-response curves of the VS30-V

voltage difference is filtered through the back of the active filter DC power signal (rectifying effect), fed to the variable amplifier, and then adjusted to the desired output voltage. If the CM and CR capacitors' signals are the same, then when rectified and filtered, the obtained DC voltage signal is zero (see Fig. 4). If the measured capacitance CM changed ΔCM, then the resulting output voltage changes proportionally. If the CM and CR capacitances are not identical, then when $\Delta CM = 0$, the output terminal is obtained by an offset value, which is always superimposed on the DC voltage signal.

A diagram showing a schematic of the current appears in Fig. 5. The frequency-response curves are like those of standard environment AE sensors. High-sensitivity, low-frequency AE sensors are optimized for testing tank floors and other civil structures as well as for leak detection. An RG 178/0.3-m cable is used. VS30-V has 6 dB less sensitivity if used with a 1.2-m-long cable (see Fig. 5).

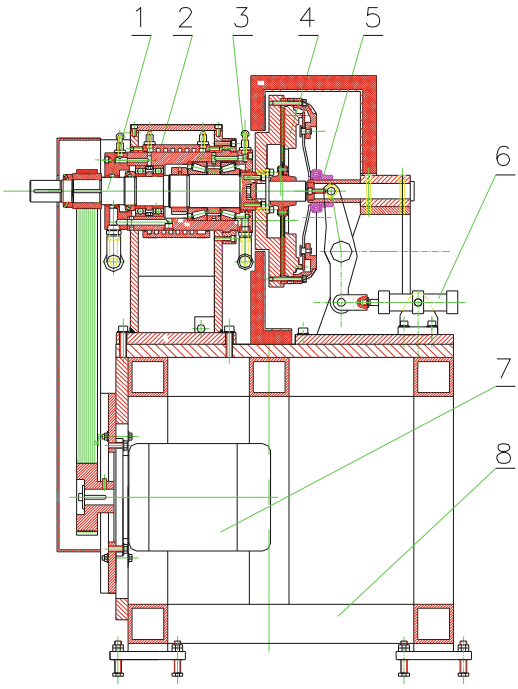

Fig. 6 Schematic diagram of new testing device

Contact fatigue simulation experiment applied to performance testing of new materials and processing technology. The quality of steel and advanced heat treatment technology equipment is essential to the life of steel materials and their reliability. The bearing raceway surface needs coating or laser quenching treatment. Maintenance-free bearings are used in nonmetallic materials such as glass fiber–reinforced polyamide (PA), silicon nitride (Si_3N_4), silicon carbide (SiC), nitrile rubber, acrylonitrile, glass fiber– reinforced nylon, and grease. Bearing tests and a measurement and control system in the assessment and validation analysis results are essential in that vehicle clutch bearings bear the load, displacement, clutch frequency, speed, and temperature and must be the main parameters of a simulation test. Figure 6 shows the schematic diagram of the structure's new testing device. In the figure, (1) is the spindle, (2) is the spindle cooling system, (3) is the spindle lubrication system, (4) is the clutch,(5) is the testing release bearing, (6) is the cylinder, (7) is the electric motor, and (8) is the frame.

Calculating the contact stiffness between the contact stress and contact deformation is based on a separation of the design parameters of the bearing's internal structure. Because these are very important parameters, one must design as accurately as possible test equipment and a measurement and control system for verifying the theory and basic experiments.

3 Results

1. The count and average frequency energy are used to analyze the characteristics of fatigue damage. An important characteristic parameter is the amplitude of an impact; that is, the degree of damage is directly related to the AE's maximum amplitude.
2. The morphological filtering is applied to the signal in the frequency domain, in order to eliminate colored noise.
3. The results show that the method handle obtained by the integration of the source signal and the rolling bearing fault signal similarly had a higher degree than the corresponding state of the simultaneous source signal received by the sensor chip information.

4 Discussion

Release bearing AE waves are generally sharp pulses with wideband. The AE sensor used in communication between media is affected by frequency. Its waveform is measured relative to a certain difference in the AE source waveform. A release bearing AE wave is mainly from a Rayleigh wave transmit. Elastic waves emitted from the source through parts of the surface of the isolation bearings undergo resonance, filtering, and contact surface scattering. A sound detection sensor measures the sound intensity; the accuracy affected by the installation position sensor measurements.

When the release bearing is subjected to alternating cycles of stress, the bearing of the wave propagates along the surface, called a Rayleigh wave. A Rayleigh wave propagates on the surface of the bearing. It is a wave for elliptical motion on the surface of particles and can be regarded as the synthesis of a longitudinal wave and a transverse wave motion. Therefore, a Rayleigh wave may travel only through a solid medium. The attenuation of AE waves can be divided into three main aspects:

1. An increase in propagation distance diffusion attenuation: With increased elastic wave propagation distance, the unit area of the acoustic energy and pressure decreases, leading to diffusion attenuation.
2. Absorption and attenuation due to dielectric friction: Elastic waves come from the viscous medium itself, and the heat conduction is caused by energy loss due to absorption and attenuation.
3. Acoustic emission is a scattering wave in the medium: The material itself contains impurities; the discontinuities in the porosity medium's impedance are mainly caused by scattering attenuation.

Separation bearing by alternating contact stress in operation, bearing parts and components of the contact defects produced acoustic emission. On a crack isolation bearing surface, scratches and other problems will lead to attenuation of Rayleigh waves. In studies on the acoustic emission of various causes of decay, emitting waves can be used to distinguish among different sound sources, whether it is separated from the bearing detection performance.

References

1. D. Guang, L. Wei, Z. Ying, L. Feifei, An acoustic emission method for the in service detection of corrosion in vertical storage tanks [J]. Am. Soc. Nondestr. Test. Mater. Eval. **60**(8), 976–978 (2002)
2. D. Mba, R.B.K.N. Rao, Development of acoustic emission technology for condition monitoring and diagnosis of rotating machines; bearings, pumps, gearboxes, engines and rotating structures [J]. Shock Vib. Digest. **38**(1), 3–16 (2006)
3. B. Eftekharnejad, M.R. Carrasco, B. Charnley, D. Mba, The application of spectral kurtosis on acoustic emission and vibrations from a defective bearing [J]. Mech. Syst. Signal Process. **25**(1), 266–284 (2011)
4. N. Jamaludin, D. Mba, Monitoring extremely slow rolling element bearings: part I [J]. NDT. E. Int. **35**(6), 349–358 (2002)
5. J. Miettinen, P. Pataniitty, Acoustic emission in monitoring extremely slowly rotating rolling bearing [C]. In: Proceedings of COMADEM'99. Oxford, Coxmoor Publishing Company. 1999. ISBN 1-901892-13-1. pp. 289–297.
6. A.M. Al Ghamd, D. Mba, A comparative experimental study on the use of acoustic emission and vibration analysis for bearing defect identification and estimation of defect size [J]. Mech. Syst. Signal Process. **20**(7), 1537–1571 (2006)
7. N.G. Nikolaou, I.A. Antoniadis, Application of morphological operators as envelope extractors for impulsive type periodic signals [J]. Mech. Syst. Signal Process. **17**(6), 1147–1162 (2003)

Research Based on the Acoustic Emission of Wind Power Tower Drum Dynamic Monitoring Technology

Penglin Zhang, Yuan Sang, Yaxing Xu, and Zhiqiang Zhao

Abstract Wind power tower drum is one of the key components of the wind power equipment. Whether the wind tower drum performs safety directly affects the efficiency, life, and performance of wind power equipment. Wind power tower drum in the process of manufacture, installation, and operation may lead to injury, and the wind load and gravity load and long-term factors such as poor working environment under the action of crack initiation or distortion, which eventually result in the instability or crack of the wind power tower drum and cause huge economic losses. Thus detecting the wind power tower drum crack damage and instability is especially important. In this chapter, acoustic emission is used to monitor the whole process of wind power tower drum material Q345E steel tensile test at first, and processing and analysis tensile failure signal of the material. And then based on the acoustic emission testing technology to the dynamic monitoring of wind power tower drum, the overall detection and evaluation of the existence of active defects in the whole structure, and the acoustic emission signals collected for processing and analysis, we could preliminarily master the wind tower drum mechanism of acoustic emission source. The acoustic emission is a kind of online, efficient, and economic method, which has very broad prospects for work. The editorial committee of nondestructive testing qualification and certification of personnel teaching material of science and technology industry of national defense, "Acoustic emission testing" (China Machine Press, 2005.1).

P. Zhang (✉) • Y. Sang • Y. Xu • Z. Zhao
Lanzhou University of Technology, Lanzhou 730050, China
e-mail: 524284980@qq.com

G. Shen et al. (eds.), *Advances in Acoustic Emission Technology: Proceedings of the World Conference on Acoustic Emission-2013*, Springer Proceedings in Physics 158,
DOI 10.1007/978-1-4939-1239-1_55,

1 Introduction

Because of the characteristics of wind power, including renewable, wide distribution and no pollution, wind power has become an important direction of the world renewable energy development; modern wind turbines are also developing in the direction of light, high efficiency, high reliability, and upsizing. In the design of large- and medium-sized wind turbine, the higher tower drum is used to capture more wind power. Tower drum is mainly used for supporting impeller and engine room, which can lift the impeller and engine room to the desired height in order to obtain enough wind power and make the generator run properly. Tower drum should have not only a certain height to make wind turbine operate in the ideal position, but also enough strength and stiffness to ensure that wind turbine will not collapse in the bad environment. Thus ensuring that the tower drum under different circumstances will be safe and reliable is the premise for normal operation of the wind generator.

The structure of wind power tower drum is conical cylinder made of Q345E steel plate which belongs to the low carbon alloy steel. Its parent material metallographic is ferrite and pearlite presenting zonal distribution. It adds some trace metal elements on the basis of 16Mn alloy steel, and strictly controls phosphorus and sulphur elements in order to improve the low temperature impact performance [2]. On the basis of ensuring the tensile properties, Q345E steel is focused on improving the impact toughness of steel. Research on damage and fracture characteristics of this kind of steel plate has vital significance on its equipment fault diagnosis.

Longitudinal weld joint and annular weld joint of wind power tower drum are welded by union melt welding; T-type weld joint between the cylinder and flange is also welded by union melt welding. Flanges are connected by a bolt. Surface defects of Q345E steel in welding process are mainly crater arc crack, delay crack caused by repair welding without preheating, etc. Internal defects are slag inclusion caused by incomplete cleaning up and pores caused by incomplete drying potions. So nondestructive testing plays a vital role to guarantee the quality and security of tower drum.

In the detection of the wind turbine, the acoustic emission system can be used for real-time monitoring of wind power tower drum, which can detect and evaluate the existence of active defects in the whole structure, and can dynamically monitor and predict early damage of the wind power tower drum in the operation process, and also prevent catastrophic failure of the system caused by unknown discontinuous and the maximum working load of limit system.

2 Testing Programs and Parameters

2.1 Test 1

The specimen in the test 1 was processed by 10 mm thick Q345E weld steel plate. The test content was monitoring the whole process of tensile test by using acoustic emission technique till the specimen fracture. In the test, we used displacement to

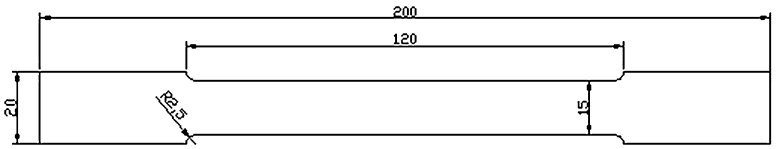

Fig. 1 Shape of the tensile test specimen (Group A)

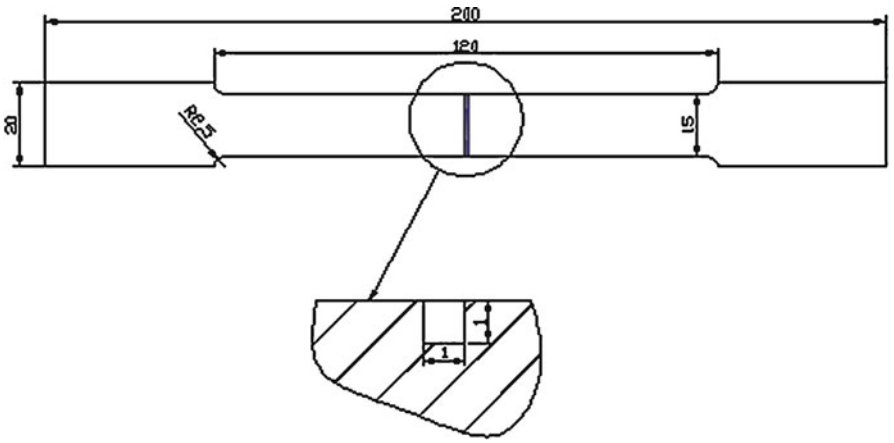

Fig. 2 Shape of the tensile test specimen (Group B)

control loading; the loading rate of tensile testing machine was 5 mm/min and loading force was 10,000KGF, adopting uniform velocity and uniaxial tension. Figures 1 and 2 show the shape and size of the specimens.

The specimens were divided into two groups to test; group A was two intact specimens, group B was two specimens with an artificial defect which was a rectangular groove in the middle of the specimens, and SAEU2S Acoustic Emission System of Soundwel Technology Co. Ltd was used to monitor the whole process of tensile test. Using an empirical approach the following settings were selected for the succeeding tests (shown in Table 1).

2.2 Test 2

On the basis of test 1, we designed the test 2. This test was conducted in Jiuquan city, Gansu province, Yumen Town CNOOC wind farm, the 11th wind generator. By west wind and wind force of six grades, diameter of the bottom of the tower drum was 4 m. Acoustic emission instrument adopted SAEU2S Acoustic Emission System of Soundwel Technology Co. Ltd (eight channels). Distribution of sensor is shown in Fig. 3.

Table 2 shows the acoustic emission system parameter settings. Sensors were placed in the bottom of the tower drum between bolt links and the first line of girth

Table 1 Settings for the recorder software of test 1

Parameters	Setting value
Preamp	40 dB
Sampling rate	10,000 kHz
Sampling length	4,000 μs
HDT	600 μs
HLT	1,000 μs
PDT	300 μs
Poisoning lockout time	1,000 μs
Spacing of sensors	70 mm
Band-pass filter	100–400 k

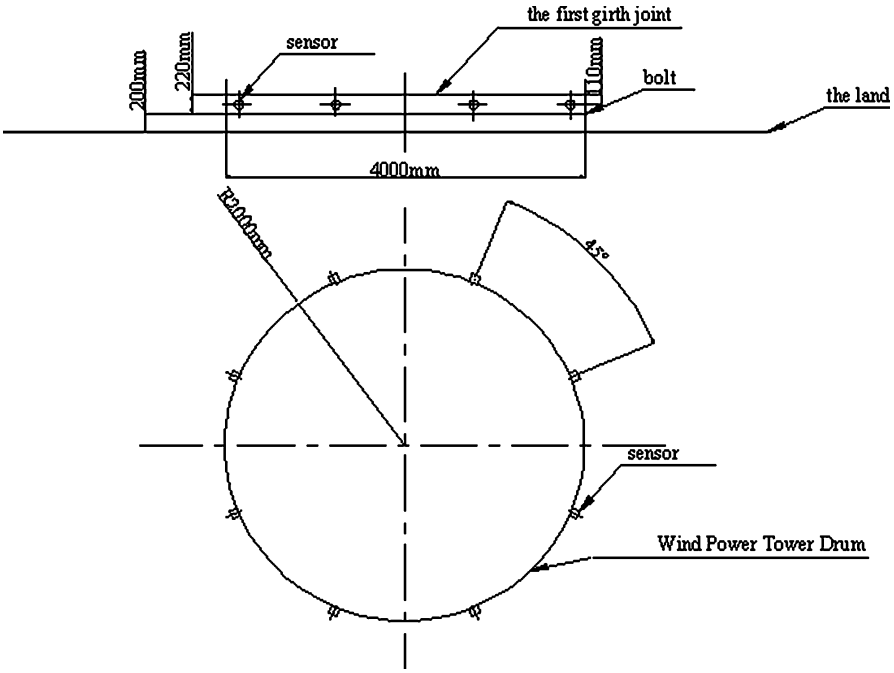

Fig. 3 Distribution of sensor of test 2

Table 2 Settings for the recorder software of test 2

Parameters	Setting value
Preamp	50 dB
Sampling rate	2,857 kHz
Sampling length	2,048 μs
HDT	1,000 μs
HLT	2,000 μs
PDT	800 μs
Poisoning lockout time	1,000 μs
Spacing of sensors	1,570 mm
Band-pass filter	100–400 k

weld, using line positioning; the first sensor was put on the due north direction, and seven other sensors uniformly distributed along the counterclockwise.

After the completion all attachments, breaking a 2H 0.5 mm pencil as trigger signal of the experiment to test the sensitivity of the eight sensors. Simultaneous determination propagation velocity of sound waves in the wind power tower drum was 3,200 m/s. And then we could start to run the wind tower drum acoustic emission dynamic monitoring test.

After completion of acoustic emission testing, magnetic memory testing method was used for the reinspection.

3 Test Results and Analysis

3.1 Acoustic Emission-Associated Figure Analysis

After replaying, filtering, and preliminarily analyzing AE signals collected from the test, various parameter-associated diagrams were obtained. Some electromagnetic interference signals usually have high amplitude and low energy, which can be distinguished through the energy-amplitude association diagram. As Fig. 4 shows, those plots close to the *x*-axis are mostly electromagnetic interference signals which have low energy, and cracks signal and fracture signal have high amplitude and energy.

As can be seen from Fig. 4, the amplitude of crack signal of the intact specimen distributes between 80 and 94 dB, the amplitude of fracture signal is 97 dB which is the highest, the amplitude of crack signal of the defective specimen distributes between 80 and 90 dB, and the amplitude of fracture signal is 92 dB, which is lower than that of the intact specimen. Meanwhile, amplitude of the crack signal is very high, but the corresponding energy is not always high. The highest energy of AE signals of the intact specimen reached 100,000 (mv*μs), and that of the defective specimen reached 120,000 (mv*μs), but these are not crack signals or fracture signals; they may be friction signal caused by the relative displacement occurred between the specimen and tensile machine or sensors.

Figure 5 shows that most of the signals are concentrated in the range between 40 and 60 dB. For intact specimen, there are a number of signals between 90 and 100 dB; they have high amplitude and short duration, which conform to the characteristic of the crack signal, and for detective specimen, signals which have the same characteristics distribute between 80 and 90 dB, and their amplitude is obviously less than that of intact specimen. In Fig. 5 we can see some high-amplitude and long-duration signals, which may be mechanical rubbing and electromagnetic interference.

Figures 4 and 5 are associated diagrams that show acoustic emission signal parameters of crack propagation of the specimens in the tensile process, which are about energy-duration and ringing counts-duration. From these four diagrams, as a result, in the case of equal energy and ringing counts, the duration of the fracture signal is much bigger than the duration of the crack propagation.

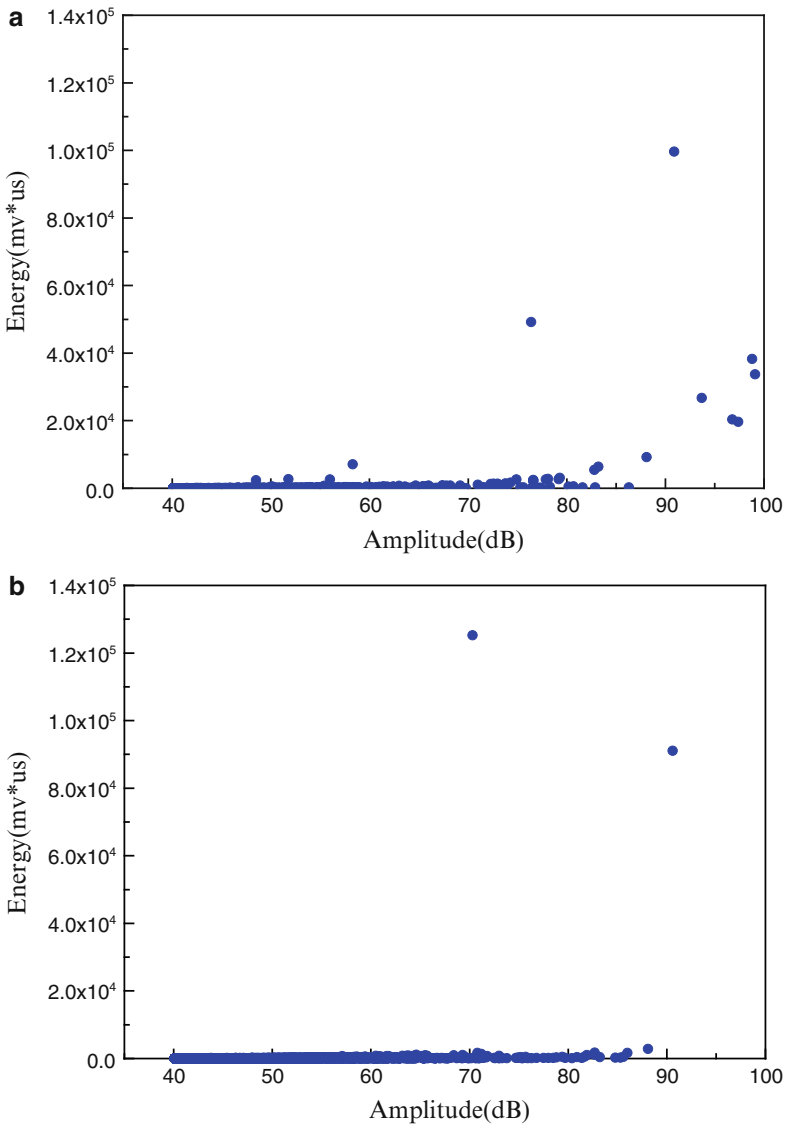

Fig. 4 Energy-amplitude-associated diagrams in test 1, (**a**) specimen A, (**b**) specimen B

Also, time-energy and time-ringing count diagrams could reflect how the acoustic emission signal changed with time. Figures 6 and 7 show the acoustic emission process of the test 1; the tensile process of intact specimen lasted for 282 s and that of the defective specimen lasted for 240 s. Energy of acoustic emission signal and ringing counts basically changed the same trend with time in the tensile process of specimen. Acoustic emission process of Q345E steel specimen tensile could be

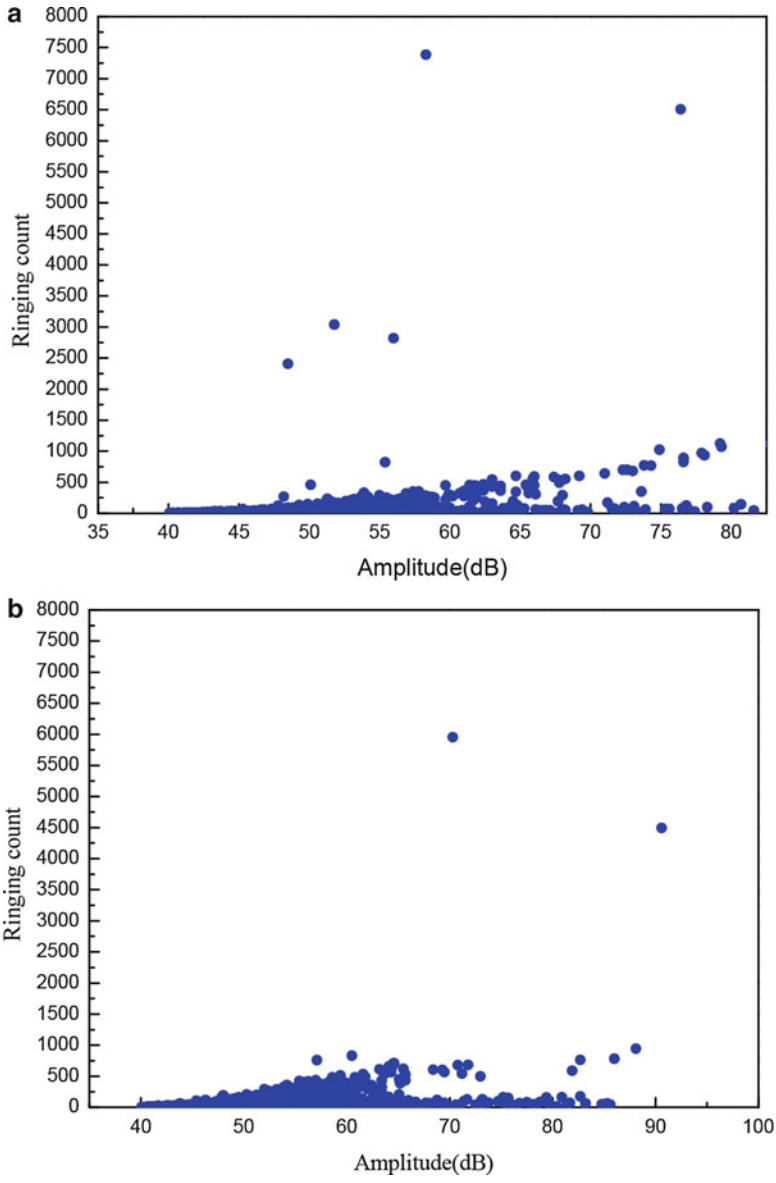

Fig. 5 Ringing counts-amplitude-associated diagrams in test 1, (**a**) specimen A, (**b**) specimen B

roughly divided into three stages, including linear elastic stage, plastic deformation stage, and fracture stage. It could be seen from Fig. 6 that the degree of failure of specimen was growing with the continuous increase of tensile load. Change of acoustic emission parameters in the steel tensile fracture process reflected the fracture process of the material. In the early part of the specimen tensile, the

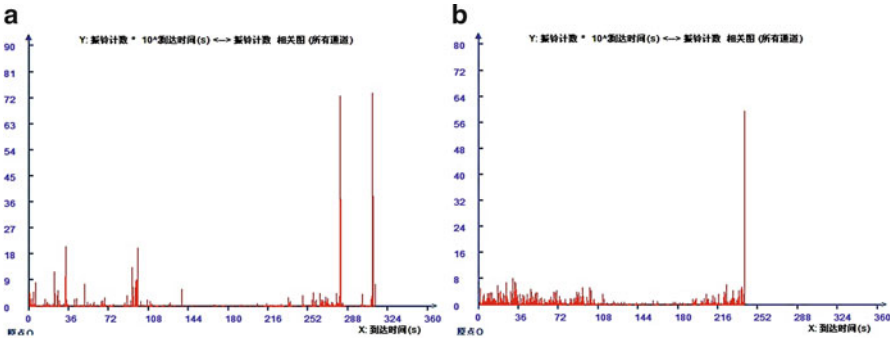

Fig. 6 Time-ringing count-associated figure of specimen A in test 1, (**a**) specimen A, (**b**) specimen B

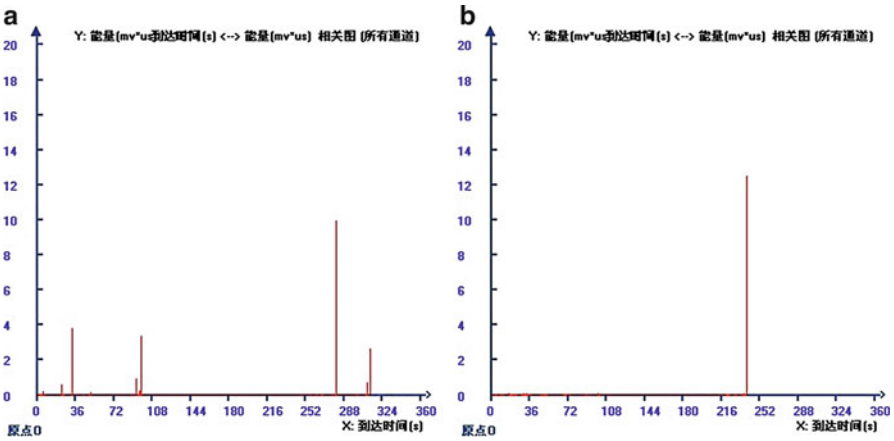

Fig. 7 Time-energy-associated figure of specimen A in test 1, (**a**) specimen A, (**b**) specimen B

material was basic in the elastic deformation stage with little dislocation movement and no obvious yield point. In this stage amplitude value of a single acoustic emission wave strike signal was less than 80 dB, ringing counts were less than 25, and energy was less than 20 (mv*μs). And these parameters of defective welding plates were obviously slightly below those of the intact welding plates.

As shown in Fig. 6, ringing count of the intact specimen suddenly increased to 7 from the 230th second approximately and ringing count of the defective specimen suddenly increased to 7 from the 200th second approximately; this kind of situation lasted before specimen fracturing, which illustrate that necking occurred to the specimens in this period and dislocation produced uneven slip inside the material, and thus some acoustic emission signal was generated. However, the material has entered the instability stage in this time, cross-sectional area of the specimen reduced sharply, and the load which the specimen required was also reduced, so the acoustic emission signals were not strong.

Table 3 Relationship between acoustic emission burst energy and loading

	Breaking point 1		Breaking point 2		Breaking point 3	
Groups	Time (s)	Loading (Mp)	Time (s)	Loading Mp	Time (s)	Loading Mp
A	34.41	345	98.63	350	313.10	230
B	19.86	315	32.38	335	242.07	225

In elastic stage, plastic deformation stage, and necking stage, acoustic emission energy of the specimens is released with burst peak instead of uniform energy, which could clearly be observed. In addition, the peak energy of the intact specimen is greater than the peak energy of the defective specimen. As shown in Table 3, with the continuous increase of tensile load, tiny cracks begin to expand, which cause stress concentration and accumulate a lot of energy; the energy releases with the form of elastic waves; there appears a few burst points in the process of energy release.

Figures 6 and 7 show that the material produced a high-intensity acoustic emission signal at the time of fracture. The amplitude, ringing count, and energy of the defective specimen and the intact specimen, respectively, suddenly increased from the 280th and the 280th second; the amplitude was up to 90 dB but not in excess of 100 dB, the highest ringing count was 75, and the highest energy was 117 (mv*μs). It shows that there has been a long time of energy accumulation before this energy was intensively released; when cracks of the specimen sharply changed, this higher intensive energy was intensively released. That is to say, at the critical load point in which cracks of the specimen extended to the next stage, acoustic emission signal energy increased dramatically.

By comparing and analyzing those above figures, they can well describe the fracture process of the material and show strong regularity in the whole process of the tensile test. Different types of acoustic emission sources will produce different acoustic emission signal characteristics. In fact in the process of specimen tensile acoustic emission signal source was very complicated; in each stage the acoustic emission source type was not sole, and it should be a variety of acoustic emission source overlay.

The active defect was closely related with acoustic emission parameters. We could comprehensively consider parameters such as energy, amplitude, ringing counts into monitoring wind power tower drum, and predicting the early damage. In test 2, because the northwest and the north wind is in the majority in the northwest district, cracks on the tower drum or looseness of bolts may generally occur in the position of the wind blowing. On that day test 2 was conducted by the west wind. By sorting out and analyzing the acoustic emission parameters collected at the scene, the signal amplitude of other channels was mostly concentrated on 50 dB, but the signal amplitude of channel 8 was concentrated on 60–70 dB. Also we found that there were many high-amplitude signals near the channel 8, whose amplitude was greater than 65 dB, and those parameters such as ringing count, energy, and rising count value were very high; we preliminarily considered that there exists active acoustic emission source near the channel 8 which was in the east position; Fig. 8 shows the AE signal parameter-associated diagrams of the channel 8 of the wind power tower drum in service.

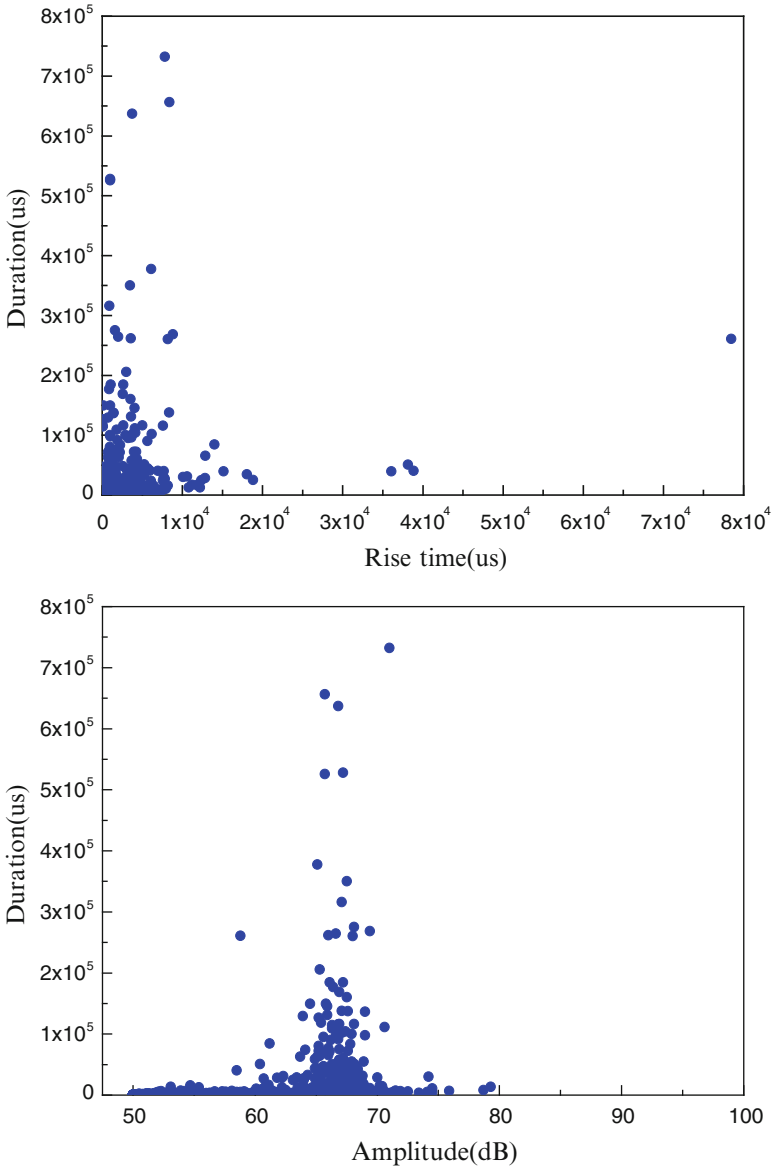

Fig. 8 AE signal parameter-associated diagrams of the channel 8 in test 0032

3.2 Acoustic Emission Source Localization

Acoustic emission source of tensile process of the Q345E weld steel plate is mainly from dislocation movement, macroscopic crack propagation, and so on; under each damage mode developing in the process plenty of acoustic emission signals could be generated, which could accurately reflect damage information of the material,

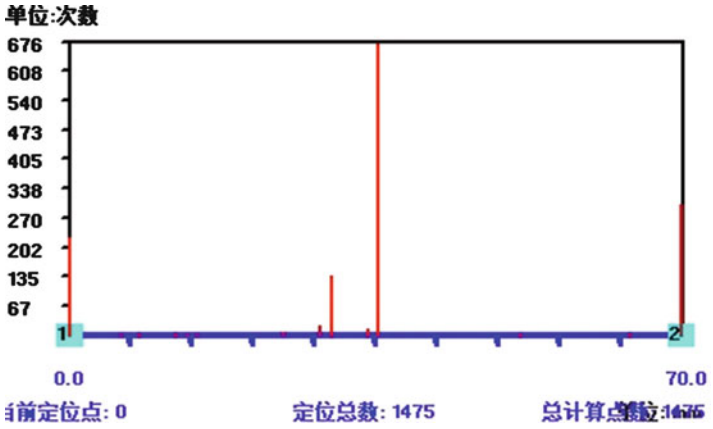

Fig. 9 Linear positioning diagram of specimen A in test 1

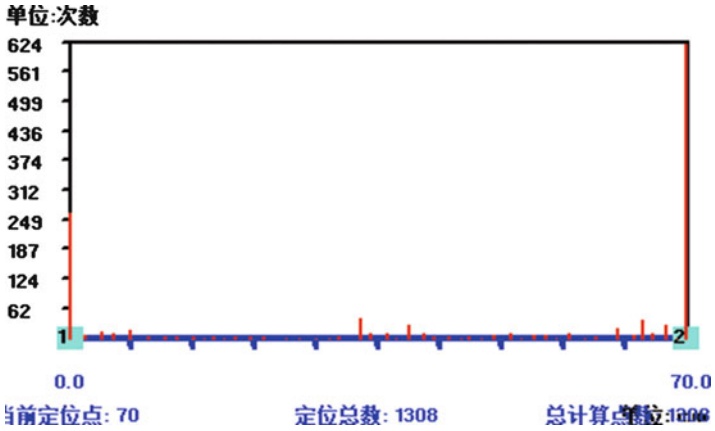

Fig. 10 Linear positioning diagram of specimen B in test 1

and its measurability is good. Figures 9 and 10, respectively, show the linear positioning figures of specimens A and B in test 1, using line positioning to arrange two sensors with 70 mm spacing.

Acoustic emission is not accurate positioning; due to uneven material and sensors and other inconsistencies, there is an error of 10 % of sensor maximum distance. Thus there is a need to conduct reinspection with other NDT methods.

Figure 9 shows that positioning count of the No.1 sensor is 210 times and positioning count of the No. 2 sensor is 290 times, at a distance of 36 mm from No. 1 sensor, positioning number reached 676 which is the most, the acoustic positioning accords well with the actual fracture location. The positioning total number of the intact specimen is 1,475 times. Figure 10 shows that positioning number at the No. 1 sensor is 260 times and positioning number at the No. 2 sensor is 624 times; there appears some positioning points at a distance of 34–38 mm from

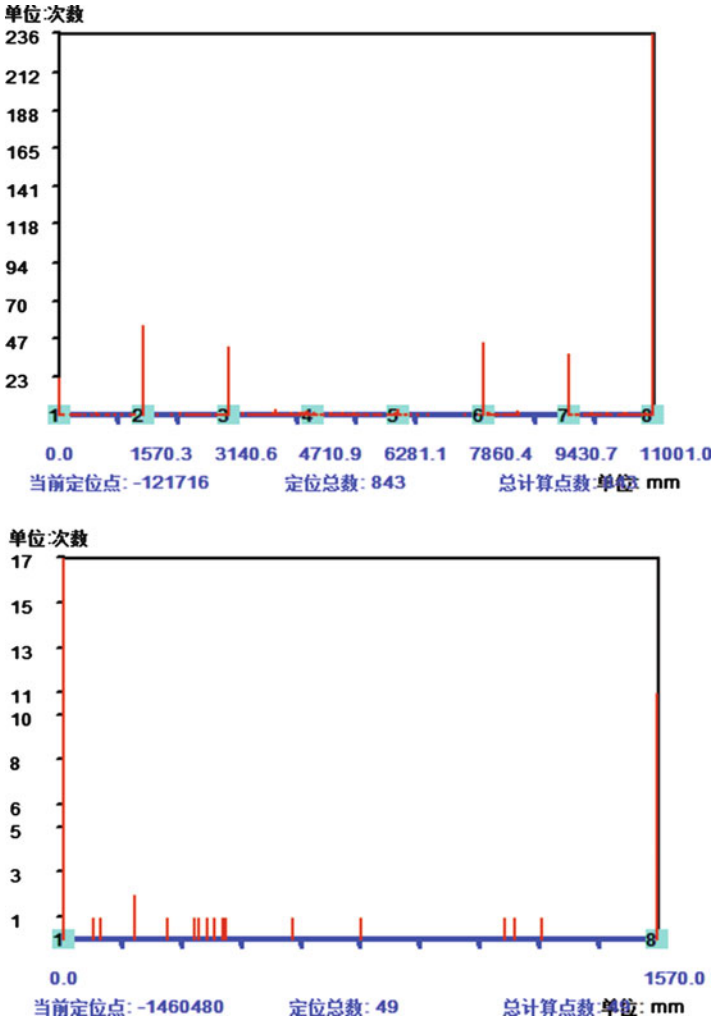

Fig. 11 Linear positioning diagrams of 8 channels in test 2

No. 1 sensor, because an artificial crack was made at a distance from No. 1 sensor, and the acoustic emission events are active. Also there appear some positioning points at a distance of 2–8 mm from No. 2 sensor, the actual fracture location is at a distance of 5 mm from No. 2 sensor, and the acoustic positioning accords well with the actual fracture location. The positioning total number of the defective specimen is 1,308 times which is slightly less than that of the intact specimen. Acoustic emission source location shown in the figures is in conformity with the actual fracture location of specimens; it illustrates that location accuracy is higher.

Fig. 11 shows the dynamic monitoring of linear positioning diagram for wind power tower drum. There are many signals among channels 1–7, the signal amplitude

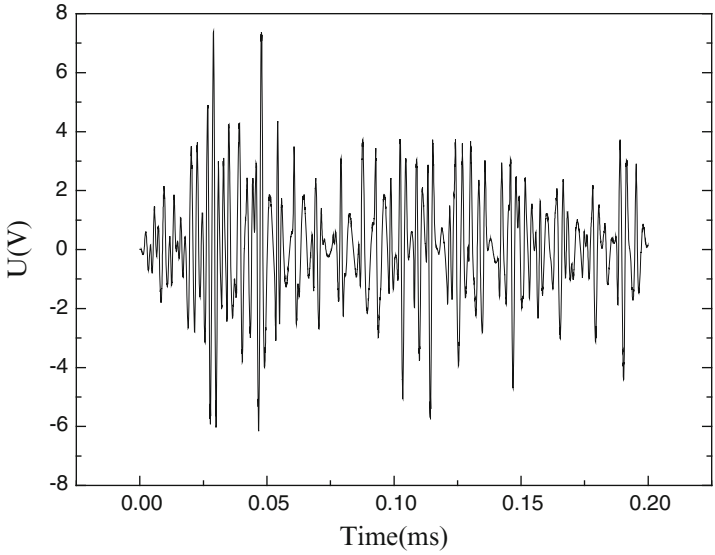

Fig. 12 Crack waveform diagram of specimen A

is very low, the energy is very small, and between channel 1 and channel 8 appeared more signals; especially in the location of the channel 8, there appear most acoustic emission events. Through the comparative analysis of the acoustic emission parameters in channel 8 position, there exists active acoustic emission source. In order to further determine the accuracy of judgment, we used magnetic memory testing for the position to recheck, which confirmed the existence of stress concentration and confirm the accuracy of the method of acoustic emission testing results.

Acoustic emission is not accurate positioning; due to uneven material and sensors and other inconsistencies, there is an error of 10 % of sensor maximum distance. Thus there is a need to conduct reinspection with other NDT methods.

3.3 Waveform Analysis

Frequency spectrum analysis technology is widely used as an important auxiliary analysis method to study acoustic emission signals because it is relatively simple and practical. FFT algorithm quickly transforms the digital signal to its corresponding spectrum, which will be able to get on the characteristics of various signals from the spectrum. By analyzing AE signal parameter-associated diagrams, we screen out some crack signals and obtained their waveforms that were recorded by the software of Soundwel. In addition, the response frequency range of the acoustic emission sensor is 60–250 kHZ, and the collected signals amount to signal after the band-pass filter, which filter out most of the low-frequency and high-frequency noise-jamming signal. Figures 12, 13, 14, and 15 show crack waveform

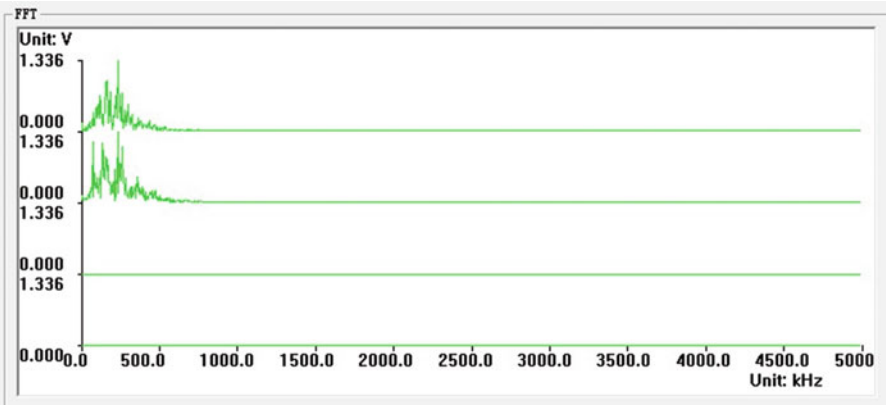

Fig. 13 Crack FFT analysis diagram of specimen A in test 1

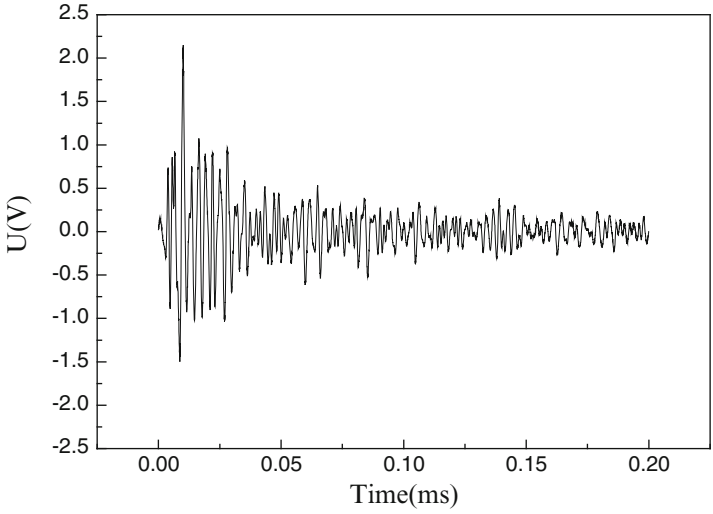

Fig. 14 Crack waveform diagram of specimen B

diagrams and crack FFT analysis diagrams of specimens in the test 1. By Figs. REF Fig. 12 and 14 it can be seen that the amplitude of acoustic emission signal of the intact specimen is greater than that of the defective specimen.

By FFT analysis of acoustic emission signal spectrum analysis diagram it can be found that the spectrum distribution range of the two kinds of specimens is mainly between 0 and 500 kHz, and acoustic emission signal amplitude of the intact specimen fluctuates greatly, the largest peak is 1.336 V, spectral distributes intensively and the total energy increases greatly. It is obvious that the crack is rapidly expanding. Because of its flaws, acoustic emission signal amplitude of the defective

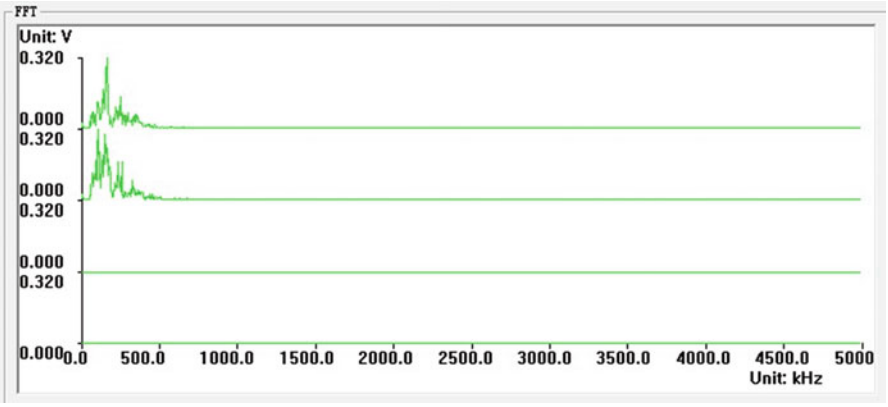

Fig. 15 Crack FFT analysis diagram of specimen B in test 1

specimen fluctuates slightly, the largest peak is 0.320 V, and spectral distributes dispersedly. Comparing two kinds of signal spectrum after careful observation, energy on frequency distribution has obvious difference. High-frequency component and low-frequency component of energy of the intact specimen are higher than those of the defective specimen. Obviously, how the existence of defects on specimens influences the acoustic emission signal could be reflected in the spectrum analysis. It is beneficial to summarize the feature information of acoustic emission signal spectrum domain for identifying whether there are defects on wind power tower drum.

For test 2, some improvements were made to test parameters; we got the waveform diagram of dynamic monitoring as shown in Fig. 16 and its FFT analysis diagram as shZwn in Fig. 17. The spectrum distribution range is mainly between 100 and 500 kHz, and acoustic emission signal amplitude of the intact specimen fluctuates greatly; the largest peak is 0.034 V. The frequency components of the various modal components of the fault signal are more than the frequency components of the various modal components of the normal signal, and its amplitude is higher than that of normal signal amplitude of each modal component, which can verify that there are some problems on the tower drum.

3.4 Noise Signal

In dynamic monitoring for wind power tower drum, noise signal mainly includes electromagnetic noise and mechanical noise. In the process of wind power tower drum dynamic monitoring, the main sources of noise signal are the fittings, bolt force caused by deformation, and friction between the bolt load redistribution caused by unevenness. In the two tests, we just adopted frontier identification and

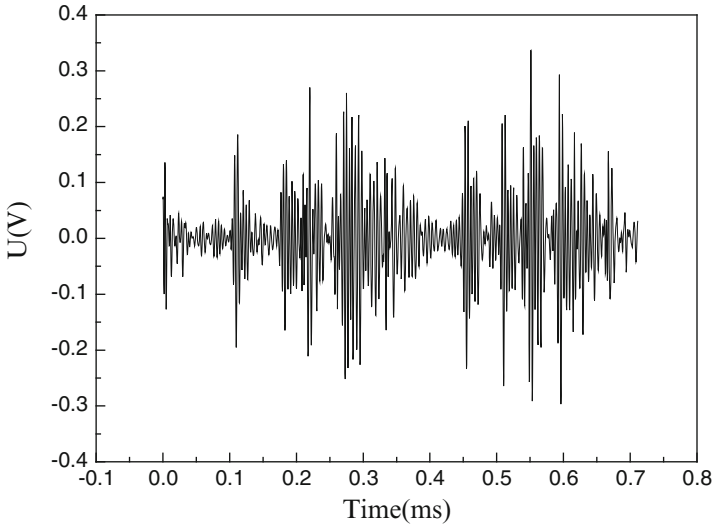

Fig. 16 Acoustic emission waveform diagram in test 2

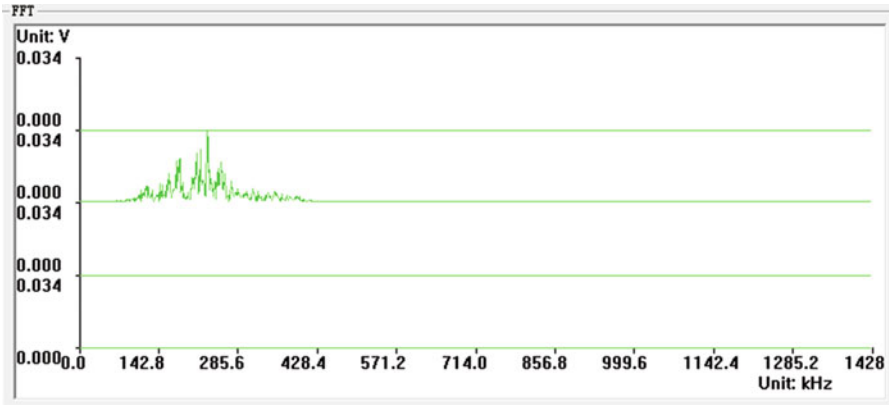

Fig. 17 FFT analysis diagram in test 2

data filtering to filter out the noise. Since wind generator working environment is bad, the external interference is inevitable, and the acoustic emission signal contained more electrical and mechanical noise, which needs further research to eliminate acoustic emission signal noise and extract the typical defects in the development of acoustic emission signals that could reflect the status of defects such as qualitative and quantitative indicators.

4 Conclusions

This chapter has demonstrated the applicability of acoustic emission to wind power tower drum dynamic monitoring. Acoustic emission line positioning method was adopted to realize the defect source of accurate positioning, combined with feature parameters and frequency spectrum analysis method to realize the accurate classification of typical defect signal and noise signal. Through the magnetic memory testing and the reinspection, we found that magnetic memory testing results and acoustic emission detection results fit very well. Acoustic emission system is able to collect the weak fault signal, which is more suitable for early detection of the failure, and to avoid the failure of deteriorating even further. We have drawn the following three conclusions.

1. Q345E steel internal damage process of ductile fracture and acoustic emission parameters and associated graphs has a direct corresponding relationship. The cumulative changes of acoustic emission parameters can reflect the damage inside the material. Acoustic emission source of tensile fracture process is mainly from the dislocation motion, macroscopic crack extension, etc. Each injury pattern in its development has rich obvious acoustic emission signal, and these acoustic emission signals can timely and accurately reflect the damage information; its measurability is good.
2. In elastic stage, plastic deformation, and creep fracture stages, necking stage of the tensile test acoustic emission energy is released with sudden peak energy instead of uniform energy. In addition, in tensile failure process energy peak of the intact specimen is greater than the defective specimen. As a result, the acoustic emission time-energy-associated diagram of the failure mechanism analysis of wind power tower drum has the vital significance.
3. Acoustic emission detection without additional downtime and shutdown, compared with the conventional nondestructive testing method, is simpler, convenient, and economical; provides environmental protection; and can effectively change the traditional way of wind power tower drum test. Since wind generator working environment is bad, the external interference is inevitable, and the acoustic emission signal contained more electrical and mechanical noise, which needs further research to eliminate acoustic emission signal noise and extract the typical defects in the development of acoustic emission signals that could reflect the status of defects such as qualitative and quantitative indicators.

References

1. The editorial committee of nondestructive testing qualification and certification of personnel teaching material of science and technology industry of national defense, “Acoustic emission testing” (China Machine Press, 2005.1)
2. J. Che, Wind power tower drum of Q345E steel welding. Gansu. Sci. Technol. **26**(24), 66–69 (2010)

3. Y Wu, Z Liang, Acoustic emission technology and its application in composite steel plate detection, Association for science and technology BBS (the second half of the month), 2008 (10), pp.43–45
4. G. Shen, G. Dai, S. Liu, Acoustic emission testing technology progress in China. Nondestr. Test. **25**(6), 32–35 (2003)
5. H. Kwun, K.A. Bartels, Mannetostrictive sensor technology and its applications [J]. Ultrasonics **36**, 171–178 (1998)
6. Y. Ma, Metal material crack acoustic emission signals based on wavelet feature. Nondestr. Test. **34**(6), 8–11 (2012)
7. J. Zheng, Y. Liu, D. Cui, The finite element analysis of megawatt wind turbine tower drum. Mach. Des. Manufact. **12**, 26–27 (2010)
8. P. Zhang, K. Shi, R. Geng, Wavelet transform in the application of acoustic emission testing. Nondestr. Test. **24**(10), 436–442 (2002)
9. W. Guanghui, W. Liang, H. Wang, Crack detection based on acoustic emission technique of turbine runner blades. Grid Clean Energ. **25**(4), 58–60 (2009)
10. R.K. Miller, P. Melntire. Acoustic Emission Testing, Nondestructive Testing Handbook. (American Society for Nondestructive Testing, 1987)
11. Z. Pan, P. Chen, C. Cao, X. Zhang, Acoustic emission in the fine blanking abrasive blade under the application of on-line detection. Nondestr. Test. **34**(9), 30–33 (2012)
12. J. Yang, B. Zhang, L. Li, Rotor crack acoustic emission monitoring research. China Plant Eng. **8**, 51–52 (2007)
13. R. Geng, G. Shen, S. Liu, Acoustic emission signal processing and analysis technology. Nondestr. Test. **24**(1), 23–28 (2002)

Part VI
Miscellaneous

Acoustic Emission and Digital Image Correlation as Complementary Techniques for Laboratory and Field Research

Rami Carmi, P.A. Vanniamparambil, J. Cuadra, K. Hazeli, S. Rajaram, U. Guclu, Arrie Bussiba, I. Bartoli, and Antonios Kontsos

Abstract This article presents the advantages of combining Acoustic Emission (AE) and Digital Image Correlation (DIC) in nondestructive testing (NDT) applications focusing on in situ damage monitoring. This data-fusion approach is used herein to characterize the mechanical and damage behavior of a fiber metal laminate (Glare 1A) tested in both tension and fatigue. Furthermore, the approach is used to investigate the structural behavior of partially grouted reinforced masonry walls. The obtained AE datasets were post-processed, in combination with DIC and mechanical information, using signal processing and pattern recognition techniques to investigate progressive failure of the Glare 1A. In the case of the masonry wall specimens, DIC clearly identified critical damage areas as a function of applied loading, while AE was capable to monitor the damage process and reveal changes in the overall behavior. The presented analysis demonstrates the potential of integrating AE and DIC in data-driven damage mechanics investigations at multiple time and length scales.

1 Introduction

Acoustic Emission (AE) and Digital Image Correlation (DIC) are two Nondestructive Testing (NDT) techniques that are rarely used simultaneously, although the combined information has shown that it can greatly assist material characterization

R. Carmi • A. Bussiba
NRCN-Negev, P.O.B. 9001, Beer Sheva 84190, Israel
e-mail: carmo_nm@netvision.net.il

P.A. Vanniamparambil • J. Cuadra • K. Hazeli • S. Rajaram • U. Guclu
I. Bartoli • A. Kontsos (✉)
Drexel University, Philadelphia, PA 19104, USA
e-mail: prashanth288@gmail.com; AKontsos@coe.drexel.edu

G. Shen et al. (eds.), *Advances in Acoustic Emission Technology: Proceedings of the World Conference on Acoustic Emission-2013*, Springer Proceedings in Physics 158,
DOI 10.1007/978-1-4939-1239-1_56,

from deformation, fracture, and damage evolution aspects, as demonstrated in this article.

AE can be used to monitor an entire component using a relatively small number of sensors capable to detect transient elastic waves generated due to sudden microstructural changes in the material [1]. In addition to real time extracted AE parameters with relevance to the deformation and damage process, postmortem analyses can be used to separate the signals into clusters that contain AE information from various failure mechanisms activated during loading.

The application of the DIC method can be achieved with one camera (for 2D) or two cameras (for 3D measurements) [2]. The method is based on tracking gray scale light intensity on the surface of the tested item as loading is applied, which is then used to compute tensorial components of in and out of plane strains. The final result is typically a full field strain map of the loaded structure developing with time [3–5]. This technique has the potential of visualizing defects or strain evolution on the surface with a very high accuracy (~100 με).

These NDT techniques have been considered by the authors as complementary ones and have been already applied for understanding fundamental plasticity as well as crack initiation and growth in light metal alloys, progressive damage development in fiber-reinforced polymer composites and failure of structural components used in civil engineering applications [6–8]. The fundamental reason for this integration is that AE can monitor the structure in terms of both volumetric and surface effects, though without the capability to visualize them, whereas DIC detects defects and provides full field strain maps, though only on the surface of the monitored specimen or component. Therefore the integration of these two NDT techniques by definition has the potential to lead to more quantitative and comprehensive results compared to the stand-alone use of each method as also demonstrated in this article.

The research work presented herein first illustrates the capabilities of the combined AE-DIC method in investigating the tensile and fatigue behavior of a fiber-reinforced metal laminate (FML). Specifically, Glare 1A (registered trademark of ALCOA) is a type of hybrid composite consisting of alternating thin layers of metal sheets and fiber-reinforced epoxy prepregs [9, 10]. This composite is used as shielding material against debris and meteors in space stations, and as aircraft skin [11]. Second, larger scale testing was conducted on partially grouted masonry wall specimens to examine their structural behavior for different types of reinforcement architectures.

The results of the research work in this paper are discussed with emphasis on the AE response by using relevant DIC information that focuses on providing a better and more quantitative understanding of the damage progress.

2 Materials, Structures, and Methods

2.1 FML Glare 1A

The characterized FML composite was Glare 1A with 1.4 mm in thickness. This material has a stacking sequence of three layers (each 0.3 mm in thickness) of Al-7475T76 alloy, and two prepreg (containing a mold-mat chemical thickening agent) layers of S2-glass fibers (each 0.25 mm in thickness) in an epoxy resin (designated FM-94 [10, 12]) with a 0.6 volume fraction of unidirectional fibers. At the final stage of processing, the FML was post-stretched by 0.4 % in order to achieve residual compressive stress in the metal and residual tensile stress in the fiber–resin interface. More details on the manufacturing process can be found elsewhere [9, 10]. A metallographic cross section of the composite with unidirectional fibers is illustrated in Fig. 1.

The mechanical behavior of flat Glare 1A specimens was characterized using both quasi-static and cyclic loading in a MTS computerized servo-hydraulic system with a load capacity of 100 KN. The commercially available Micro II AE system (manufactured by MISTRAS) was operated by using the AEwin software and by mounting on the specimens' surface two resonant sensors (Pico) with 2/4/6 AST preamplifiers and band-pass filters between 20 kHz and 1 MHz. An amplitude threshold of 32 dB was selected in accordance with measured background noise levels. AE signals and post-processing data were analyzed using the NOESIS software (MISTRAS). Prior testing, both the sensors' sensitivity and material wave speeds were measured.

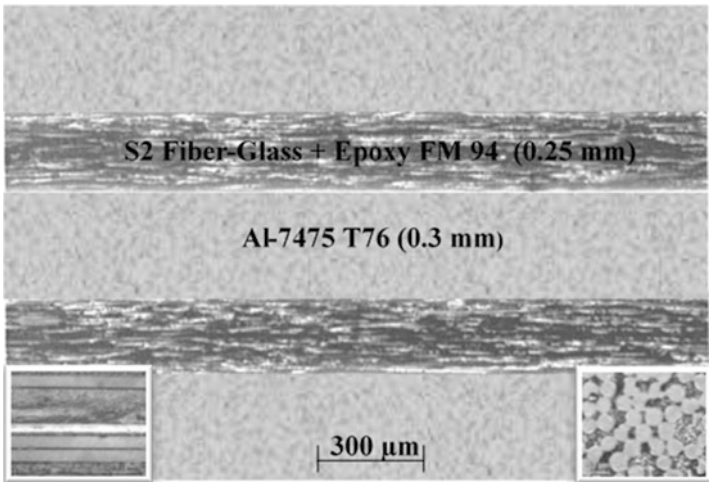

Fig. 1 The layup of Glare 1A containing unidirectional glass fibers in an epoxy matrix as well as aluminum alloy layers; longitudinal and perpendicular cross sections of the sample located in *lower left* and *right images*, respectively. Fiber diameter was 10 µm

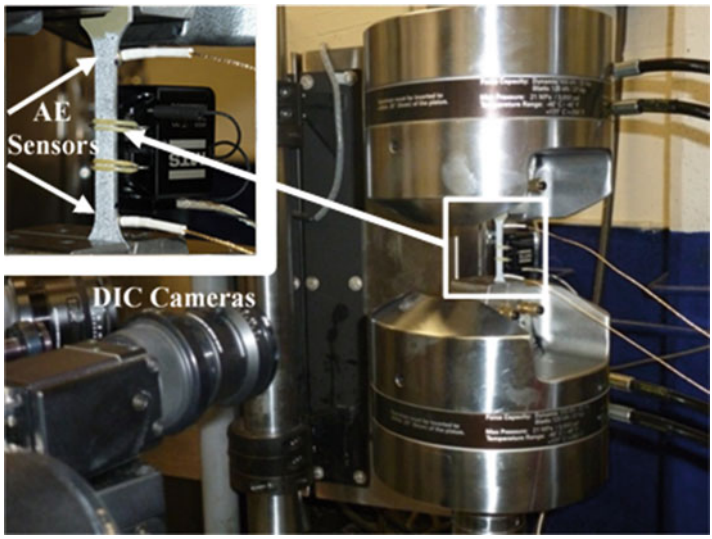

Fig. 2 Experimental setup focusing on the speckle painted specimen and the location of the AE sensors and the extensometer

A 5 megapixel GOM 3D DIC system (distributed by Trilion Quality Systems) was used in parallel to the AE system to acquire DIC data. The cameras were calibrated for a field of view (FOV) of 55 × 44 mm and were positioned 40 cm away from the specimen to capture the required FOV. A random speckle pattern (black dots on white paint) was applied on the specimen surface to track the deformation process with a strain sensitivity of about 60 με. For the monotonic tests, the images were recorded at a rate of 1 Hz, while in the fatigue tests a rate of 22 Hz was used.

For quantitative understanding of the mechanical behavior of the FML, a comprehensive study was conducted on its constituents, namely, S2-glass fibers, Al-alloy, epoxy resin, and interface matrix/fibers. To this aim, besides the flat Glare specimens used for the uniaxial tensile and fatigue tests, special specimens were designed for fiber and matrix/fiber characterization. Furthermore, and although DIC was used, an extensometer (manufactured by MTS) with a gauge length of 10 mm was additionally used. A constant displacement rate of 0.5 mm/min was selected for the quasi-static tests, while a sinusoidal wave loading profile with frequency equal to 5 Hz and a load ratio of 0.1 was used for the fatigue tests with different maximum stresses related to the measured yield stress. Metallographic and fractographic studies were also performed in order to track micro-cracking, delamination, other deformation and fracture features, as well as to assist the AE classification process.

Figure 2 illustrates the experimental setup that includes the combined AE and DIC systems. A closer view of the speckle painted specimen for DIC measurements, as well as the attached AE sensors and used extensometer is given in the upper left corner of Fig. 2.

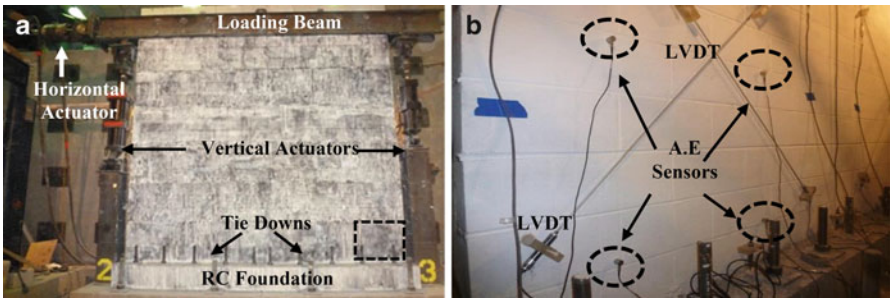

Fig. 3 Experimental setup of the tested masonry wall; (**a**) front view with coating for DIC measurements, (**b**) rear view showing the AE sensors and LVDTs for displacement measurements

2.2 Partially Grouted Reinforced Masonry Walls

The tested structure consisted of partially grouted masonry wall specimens reinforced with steel beams in different configurations for comparison of their response. The wall was base-fastened and loaded by a hydraulic actuator mounted (Fig. 3a) in the upper left corner of the wall in displacement control using a triangle wave at a frequency of 0.02 Hz. The wave amplitude was increased every two cycles until significant damage or final fracture was observed. The damage evolution was monitored simultaneously by DIC, AE, several LVDTs and was assisted by visual inspections. For the DIC measurements, a FOV of approximately 3,700 × 4,000 mm was used with the cameras positioned 6 m from the wall. The distance between the two lenses was 1.92 m. A random speckle pattern was created on the surface using spray paint and perforated sheets. The sampling rate was 1–2 frames per second depending on the overall duration of each test. The noise level for strain measurement was measured 50 μm/m. For AE measurements, four resonant R15 sensors (MISTRAS) were mounted on the back side of the wall near the lower right corner using hot-glue (Fig. 3b). In order to obtain appropriate signals for representative source localization, a square configuration with AE sensors placed 1 m apart was selected. The same AE system and software were used; a threshold of 44 dB was chosen. Pretests of 0.3 mm pencil lead break (PLB) [13] were performed in order to determine values for appropriate AE parameters in the system.

3 Experimental Results

3.1 Glare 1A Constituent

Figure 4 illustrates the mechanical and acoustic responses of Al-Alloy specimens in terms of AE counts and cumulative AE energy. As shown, significant AE activity initiates near yielding at ~1 % true strain. The sudden increase in AE activity was

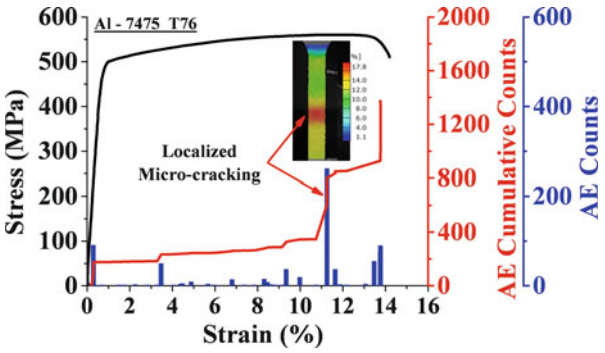

Fig. 4 Mechanical and acoustic responses combined with DIC measurements of Al-7475 T76 specimens in quasi-static tensile tests

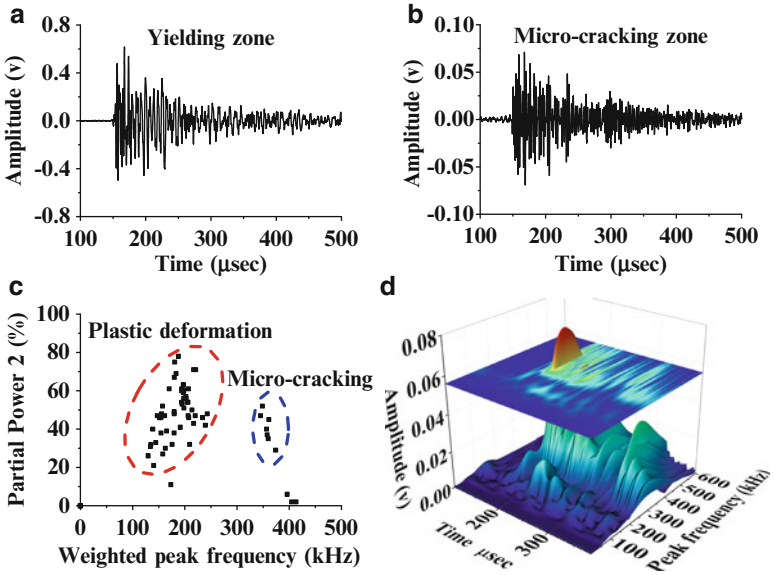

Fig. 5 AE results obtained by testing Al alloy samples: (**a**) representative AE waveform obtained near yielding, (**b**) waveform corresponding to micro-cracking, (**c**) weighted peak frequency versus partial power for several AE waveforms, (**d**) wavelet analysis of the waveform shown in (**b**) indicating a dominant peak frequency of 400 kHz

followed by a stage of moderate AE recordings up to ~11 % strain at which point DIC confirmed (see arrows) the onset of micro-cracking in the middle of the gauge area. This pronounced activity was followed by another stage of slow AE recordings until a final burst at the fracture point. The results in Fig. 4 clearly indicate dominant stages of plastic deformation and micro-cracking initiation/evolution. The existence of the aforementioned micro-mechanisms can be further seen by the different AE waveforms as depicted in Fig. 5a, b. The waveform in Fig. 5a was

Table 1 Frequency features and their definition

Feature	Definition
Peak frequency [kHz]	Maximum of frequency spectrum f_{peak}
Weighted peak frequency	$f_{wpf} = \sqrt{f_{peak} \cdot f_{centroid}}$
Frequency centroid	$f_{centroid} = \frac{\int f \cdot A(f) df}{\int A(f) df}$ $A(f)$ = Amplitude at frequency f
Partial power [%]	Fraction of frequency spectrum
Partial power 1 [%]	0–150 kHz
Partial power 2 [%]	150–300 kHz
Partial power 3 [%]	300–450 kHz
Partial power 4 [%]	450–600 kHz

collected in the quasi-plateau region following the macroscopically observed yielding, while the waveform in Fig. 5b was recorded right at the transition point (~11 % strain).

A pattern recognition technique [14–16] was applied using the k-means algorithm. The classification procedure was based on the weighted peak frequency and is described elsewhere [17], and therefore it will not be repeated here. Table 1 summarizes the features which were used to classify the AE data.

AE data in Fig. 5c are displayed in terms of the weighted peak frequency (PF) and a partial power defined by FFT analysis. This two-dimensional feature projection reveals two dominant groups of AE signals, one in the 150–200 kHz range (plastic deformation) and the second between 350 and 400 kHz (micro-cracking). A representative wavelet analysis of the micro-cracking waveform in Fig. 5b is shown in Fig. 5d; a PF of around 400 kHz is clearly identified.

Results from a similar study performed on fiber bundle specimens are shown in Fig. 6. It should be emphasized based on the waveform of Fig. 6a that AE from a fiber breakage exhibits a rapid decay as compared to the more moderate decay shown in Fig. 5a for the Al-alloy specimen. Figure 6b, c show results from both frequency and time domain analysis; a dominant frequency of 450 kHz and AE amplitude between 50 and 90 dB (Fig. 6c) were found. Finally wavelet analysis shows in 3D display the measured PF of the fiber fracture.

To complete the constituent's characterization, matrix/fiber specimens were also tested and the results are shown in Fig. 7. For the waveform in Fig. 7a, three characteristic frequencies appeared in the wavelet analysis as shown in Fig. 7b. The 450 kHz one was already attributed to fiber breakage, while the other two of approximately 50 and 150 kHz are related to matrix and interface cracking, respectively. This conclusion is also based on AE waves recorded at early stages of loading (Fig. 7c) which have one characteristic frequency of ~100 kHz (Fig. 7d) associated with matrix cracking.

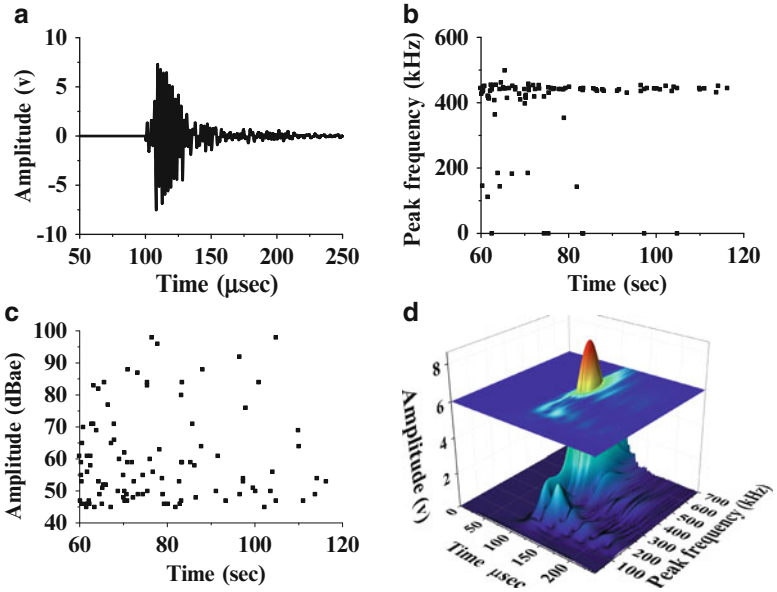

Fig. 6 AE results obtained by testing fiber bundle specimen; (**a**) AE waveform from fiber breakage, (**b**) PF, (**c**) amplitude, (**d**) wavelet analysis

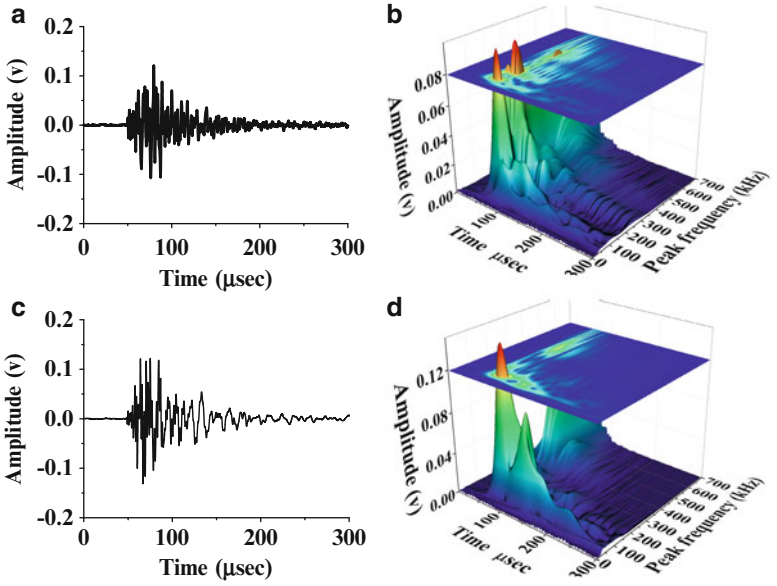

Fig. 7 AE results obtained by testing fiber-glass/matrix specimens; (**a**) a typical waveform of matrix cracking with fiber breakage, (**b**) wavelet analysis of the waveform at (**a**); (**c**) AE waveform possibly due to matrix cracking, (**d**) wavelet analysis of the waveform at (**c**)

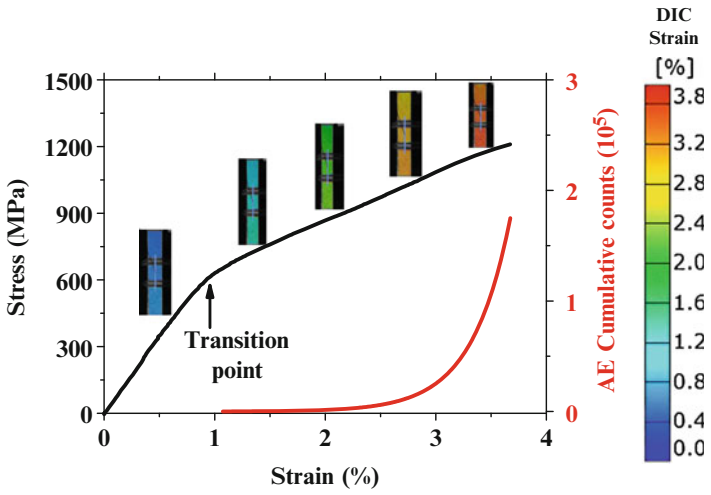

Fig. 8 Stress and AE cumulative counts versus strain as obtained in tensile test of Glare 1A

3.2 Glare 1A Quasi-Static Mechanical Behavior

Figure 8 illustrates the applied stress and cumulative AE counts versus strain obtained simultaneously by DIC (full field inserts) and the extensometer (*X*-axis values) for a representative uniaxial tensile test of Glare 1A. As shown, good agreement was found between the strain measurements provided by DIC (notice the DIC colorbar scale) and by the extensometer. The mechanical response of the FML is characterized by bilinear behavior, as also previously reported [18]. Significant AE activity initiated at the transition point between the elastic and plastic response (see arrow). The damage evolution during testing can be represented by both the exponential profile of the cumulative AE counts and the changes of the full field DIC strain maps.

To further quantify the fracture process of the tested Glare tensile specimen, AE data are displayed in Fig. 9a in terms of AE amplitude (*Y*-axis), PF (color range) and versus strain (obtained by the DIC method). Three peak frequencies are well emphasized by the used color range. The first one is around 50–150 kHz, the second between 200–300 kHz, and the highest one in the range between 400 and 450 kHz. To eliminate frequency range overlap and to identify the corresponding dominant failure mechanism and the sequence of their appearance, separated AE cumulative counts are shown in Fig. 9b. The lowest PF which was attributed to both plastic deformation (based on Fig. 5) and matrix cracking (based on Fig. 7) was extracted from AE signals recorded near the macroscopically observed yielding, while Fig. 9b shows that this group of AE signals continued to increase up to the final fracture. The second PF appeared mostly at and past the elastic plastic transition, while Fig. 9b shows that it saturates before the final fracture. The AE waveforms with these intermediates PFs are possibly correlated with interfacial micro-cracking

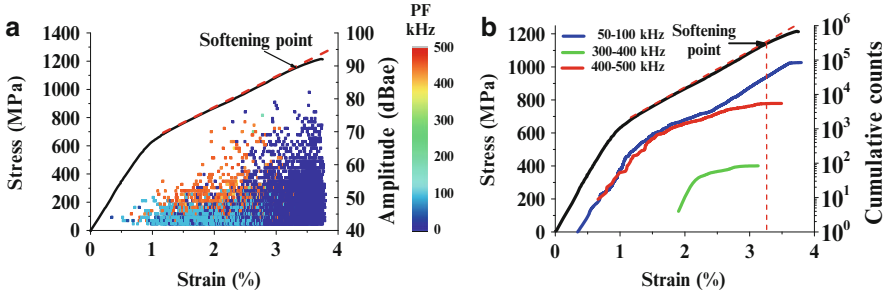

Fig. 9 (**a**) Stress and amplitude versus strain with peak frequency scale (**b**) stress and amplitude in cumulative manner at various peak frequencies

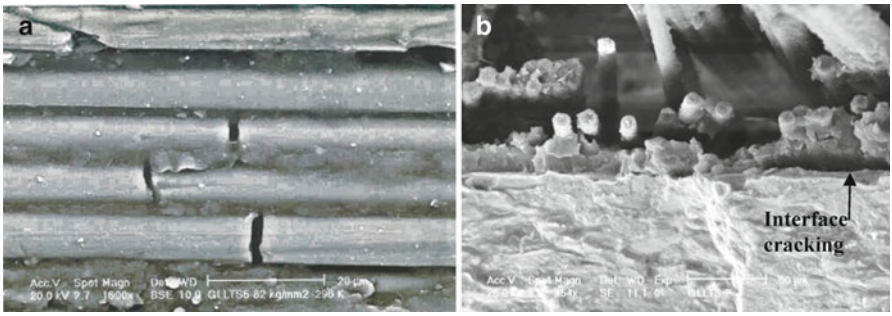

Fig. 10 Dominant fracture modes of Glare 1A tested in tension; (**a**) fiber breakage, (**b**) mixed mode fracture of Al-Alloy and S2-fiberglass layers

which appeared in later stages of deformation but ended near the softening zone shown by the arrows, and indicates the point past which the overall hardening rate appears to decrease. This quantitative description of the sequence of damage events based on AE information indicates that the contribution of the fibers, matrix, and interfaces reduces during the final stages of deformation which is dominated by Al-alloy micro-cracking as shown in Fig. 5.

Finally, Fig. 10 shows relevant microscopic images of the main fracture modes in Glare 1A tested in tension. Figure 10a demonstrates the fiber breakages mainly perpendicular to the loading axis. The fracture surface further revealed the ductile behavior of the Al-Alloy, de-bonding of the matrix–Al-layer interface, matrix cracking, and fractured fibers and the matrix–fiber interface.

3.3 Glare 1A Fatigue Behavior

Figure 11a. illustrates obtained results in terms of PFs as well as mechanical information (maximum strain per cycle, residual stiffness defined by the slope of the line defined by the line that connects the endpoints of each loop and energy

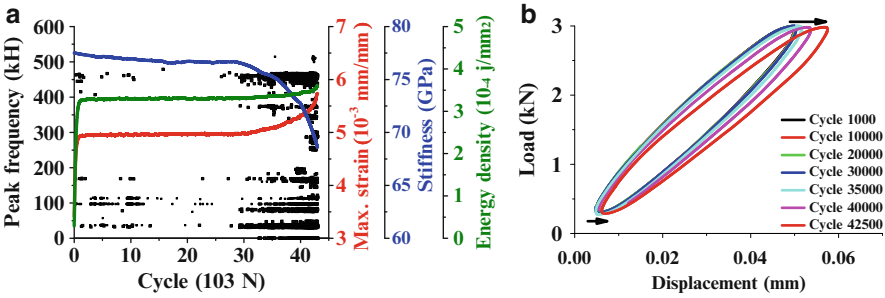

Fig. 11 Fatigue results of Glare 1A tested at cycling conditions of $\sigma_{max} = 0.6\sigma_y$ with load ratio of 0.1; (**a**) PF and loop properties versus fatigue cycles, (**b**) the change of loop cycle during fatigue experiment

density defined as the enclosed area in each loop) extracted by the hysteretic cyclic behavior of a selected fatigue test with $\sigma_{max} = 0.6\sigma_y$ and load ratio of 0.1. As the number of cycles increases the limits of the hysteresis loops and their enclosed area also increase (Fig. 11b). Up to ~15,000 cycles a moderate increase in the maximum strain and energy density occurs, accompanied by a same trend in the residual stiffness. In addition, both low and high PF values appear indicating matrix, matrix/interface, and fiber breakage together with plastic deformation mechanisms. From this point and up to ~30,000 cycles a relative silence in the AE activity is observed. This behavior may be attributed to crack arrest phenomena of the micro-cracks (mainly de-bonding delaminations at the interfaces) due to the laminate nature of this composite. Beyond this region dramatic changes are observed in the mechanical properties, namely, sudden decrease in the stiffness due to the massive cumulative damage accompanied by increasing maximum strain and energy density. These variations are further associated with a significant change in the AE activity due to development of several damage mechanisms. Fiber breakages occur just after the plateau region (PFs of around 450 kHz), followed by matrix micro-cracking (PFs about 50–100 kHz) and after that simultaneous activation of several damage mechanisms is possibly occurring: interface cracking with PFs of 100, 150 kHz, plastic deformation around 200 kHz, and micro-cracking at 400 kHz.

The mentioned damage mechanisms were also analyzed using FFT and relevant results displayed in terms of weighted peak frequency (Fig. 12a). The main peak frequencies are depicted and the dominant ones as defined by their intensity include fiber breakage and matrix cracking. Only for comparison to the quasi-static behavior, a wavelet analysis of an AE waveform possibly from fiber breakage is illustrated in Fig. 12b.

At the end of the fatigue loading the specimen was removed for damage characterization purposes and images were obtained by looking at the pre-polished thickness and the cross section normal to the applied load. Figure 13a demonstrates the characteristic breakage of the fibers which shows micro-cracking at different orientations. This damage is completely different from the one observed in quasi-static mode (see Fig. 10a) which appeared to consist of discrete cracks perpendicular to the applied loading direction. Figure 13b demonstrates interface cracking between the metal and

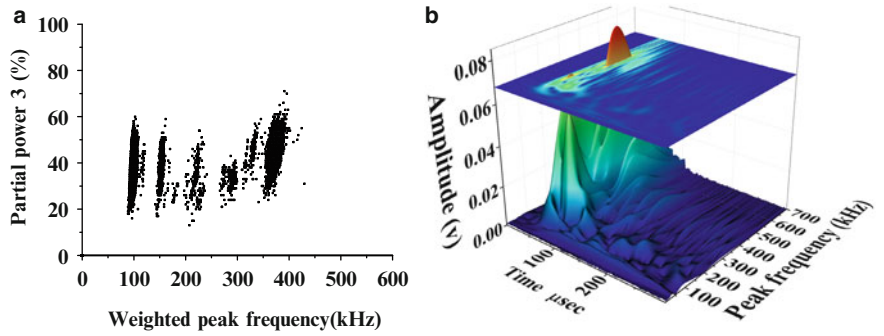

Fig. 12 (**a**) Weighted peak frequency results from partial power of AE signals at the end of fatigue test, (**b**) wavelet analysis of AE wave represent fiber breakage

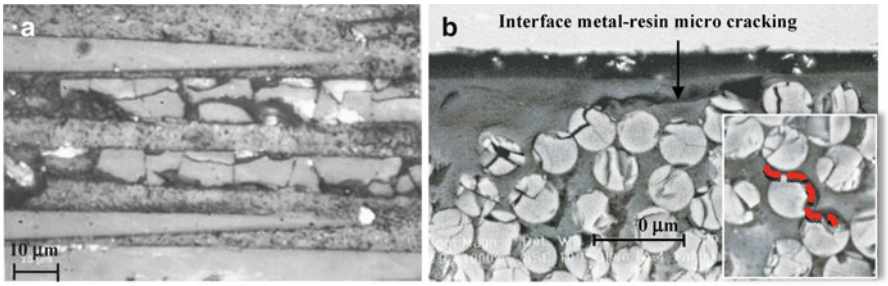

Fig. 13 Characteristic damage patterns during fatigue in two different views: (**a**) fiber fragmentation parallel to the loading direction, (**b**) fiber fragmentation at metal–resin interface, as well as fiber-matrix micro-cracking (see *curved dot line*) perpendicular to the loading direction

fiber/resin layer. As shown the micro-cracks occurred adjacent to interface as also observed in the quasi-static case (see Fig. 10b). The occurrence of cracks in this area may be attributed to the stress distribution resulting from the post-stretching at the final stage of the manufacturing process, namely, compressive stresses at the metal and tensile residual stresses at the fiber/resin layer.

3.4 Masonry Wall Damage Characterization

Figure 14a shows the loading history up until the end of the second cycle combined with the distribution of AE amplitude and the average strain that was measured by DIC at the bottom right area (see highlighted box in Fig. 14b). As one can notice, significant AE activity starts from the first loading cycle. This preferred site of damage is to be expected since this region transfers the horizontal applied load by the actuator to the wall foundation in a cyclic mode. As a consequence massive deformation and cracking occurs as the load changes from tensile to compression mode.

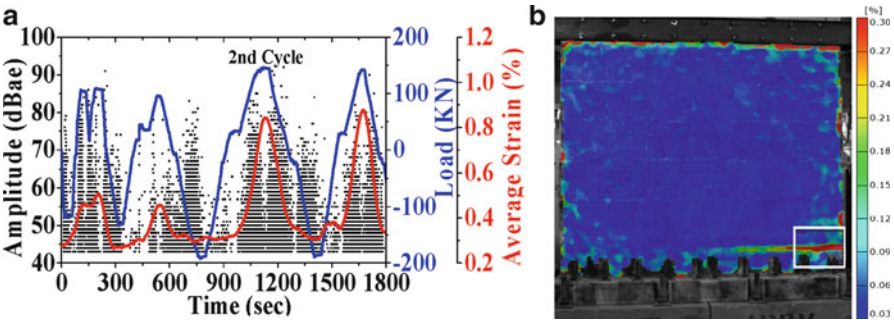

Fig. 14 Continuous monitoring results up to the second cycle of the loaded masonry wall: (**a**) AE activity combined with load and DIC average strain as measured in the square area shown on the *bottom right corner*, (**b**) full field DIC principal strain at the peak load of the second cycle

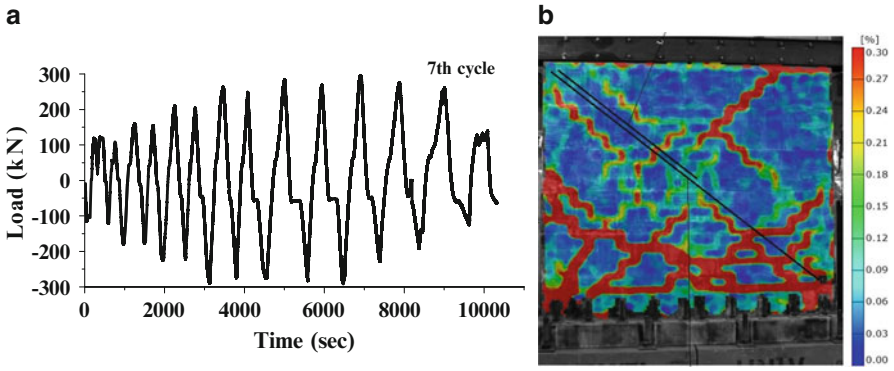

Fig. 15 Final stage of the loaded wall; (**a**) the load history up to fracture, (**b**) DIC strain mapping indicating extensive macro-cracks network

At the first cycle, a good correlation exists between AE activity and DIC measurements. High AE amplitude values were detected accompanied by high local deformation indicated by a pronounced damage development at this area. Increasing the load by 50 %, increases significantly the localized measured strain by DIC. In addition, the AE amplitude increases from 80 dBae to more than 95 dBae (at the peak load) which can be mostly attributed to interface cracking as shown by the DIC pictures. Post loading visual inspection assessed those results and revealed a micro-crack in the form of hairline cracks along the mortar. It is also worth mentioning that both AE and DIC provided early signs of cracking far before visual inspection could detect those hairline cracks. This mutual correlation between AE and DIC has significant importance in terms of validating real AE signals and filtering noise due to friction, vibration, hydraulic flow, and mechanical impact, among other reasons.

Finally, Fig. 15 displays the last stage of the loaded wall which manifests catastrophic damage. Figure 15a shows the loading history of the entire test. As it

can be noticed the seventh load cycle shows a decrease in the load amplitude due to significant accumulated damage. The latter is being well reflected by the DIC measurements, revealing an extended a micro-crack network (Fig. 15b).

4 Discussion

The present study accentuates the great potential of using a variety of advanced techniques together with common ones in order to understand in a comprehensive way fundamental aspects related to plastic deformation, micro-cracking, evolution of damage and its profile quantified in both monotonic and cyclic loading conditions. With respect to structural durability, the integration of both techniques illustrates in real time the damage progression and highlights the preferential sites of intensified damage.

The comprehensive work on the Glare-1A with its complicated structure emphasizes the potential of the combination of the AE and DIC methods to reveal its deformation and fracture behavior. The mechanical response of this hybrid composite is characterized by bilinear behavior with a secondary low modulus (E_p) at the plastic regime as compared to the higher one at the elastic region. The observed E_p is a consequence of the competitive activation of several damage mechanisms. The evolving plasticity of the Al-alloy contributes to the overall strain hardening (similar to monolithic Al-Alloy) whereas the other damage mechanisms of the resin/fiber layers, the fiber breakages, and the matrix cracks contribute to softening. This competition appears to end (see the softening point in Fig. 9b) when the damage in the resin/fiber layer is substantial as compared to strain hardening contributions, which leads to localized "necking" followed by a decrease in the stress and causes the final fracture. This argument is based on the fracture sequences revealed by the NDT measurements in this paper which visually show the localized strain regions in the Al-Alloy.

Damage evolution can be represented by the exponential growth of the cumulative AE energy. In addition, significant AE activity initiates at a characteristic threshold strain. From practical/engineering point of view, it is important to know this value in cases where no damage can be tolerated for proper functioning (fail-safe approach). The exponential profile of the damage modeled in terms of AE information is very similar to a micro-mechanical damage model suggested by Talreja [19], for inter-laminar cracking in composite laminates such as the tested FML. Talreja proposed the use of a damage tensor defined as:

$$D_{ij} = \frac{k \cdot t_c^t}{s \cdot t \cdot \cos\theta} n_i \cdot n_j \tag{1}$$

where t is the thickness of the specimen, t_c is the ply thickness, s the crack spacing, θ the angle between the fiber direction and the transverse direction, and $n = (\cos h, \sin h, 0)$. By using a thermodynamic framework for the description of the

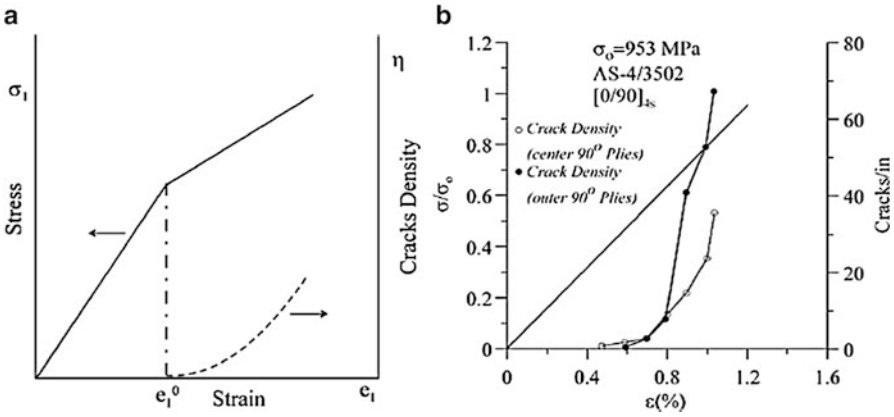

Fig. 16 (**a**) A bilinear stress–strain behavior with associated transverse crack density and (**b**) experimental stress–strain curve and associated transverse rack density of a graphite–epoxy (0, 90) [20]

material response, Talreja further determined D_1 for a bilinear stress–strain curve in the following form:

$$\log \frac{D_1}{D_1^0} = \frac{E_t}{\eta}\left[d_4\left(e_1 - e_0^1\right)\right] + \left[A\left\{e_0^2 - \left(e_0^1\right)^2\right\} + B\left\{e_1^3 - \left(e_1^0\right)^3\right\}\right] \tag{2}$$

where D_1^0 is the initial damage (initial crack density) that begins to grow at threshold strain e_1^0 and E_t the tangent modulus beyond the initiation of damage growth. Combining Eq. (1) for the non-zero component of damage tensor and Eq. (2) with $g = 1\ \mathrm{s}^{-1}$, gives the crack density as an exponential function of strain, as shown schematically in Fig. 16a by the dashed curve. The predicted profile is in agreement with experimental results such as the ones obtained by Kistner et al. [21] in graphite–epoxy composites shown in Fig. 16b. The exponential behavior of the crack density vs. strain was also viewed in NCF cross-ply laminates up to the transition point where damage coalescence is operating [20]. These observations strengthen the argument that AE is a powerful tool in damage characterization especially when used in combination with other complementary NDT methods, such as the DIC presented in this paper.

The field work on a reinforced masonry wall contributed decisively in determining the optimum reinforcing steel beam pattern (consisting mainly by reinforced beams in appropriate distance from each other, and all perpendicular to the applied load) to withstand earthquake-type loads. The findings of both NDT techniques used in this paper are relatively straightforward. In other words the current results emphasize the potential of these characterization tools for appropriate engineering decisions. Furthermore, it is well known that shear forces are responsible for major damage modes during applied loading. When these forces cause a major damage, a

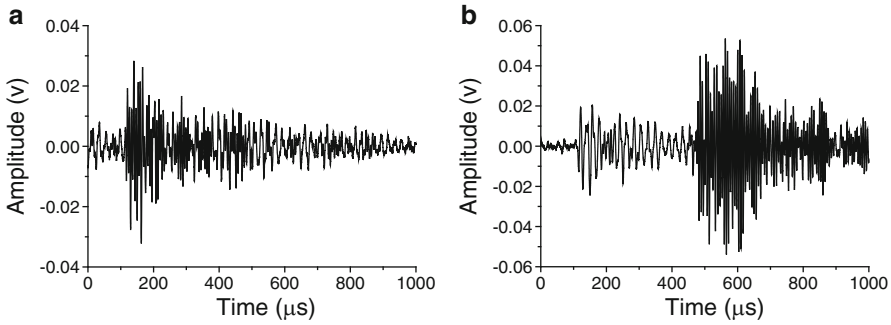

Fig. 17 Typical AE waves that were recorded during different stages of loading; (**a**) Mode I early stages, (**b**) mode II at cycle 2 and beyond

shear wave is emitted due to pertinent movement in the damaged area. The AE wave typically composed of a longitude and transverse wave, when the shear mode is dominant shows a relatively late arrival of its peak amplitude [22]. Therefore by analyzing the shear component of recorded AE waves one can predict the damage severity of a structure [23]. On these experiments a good correlation between AE and DIC achieved using shear wave analysis. In this context, Fig. 17 illustrates typical longitudinal and shear waves that were analyzed during different stage in the experiment.

5 Conclusions

Application and research results from integrating of DIC and AE are presented in this article. Combined data can assist the characterization of the mechanical behavior of fiber metal laminates. As for the wall, the AE-DIC combined data can serve to form an important basis for engineering considerations that can ensure structural performance in extreme conditions. The following conclusions can be drawn from the recent work:

1. The bilinear mechanical behavior of Glare 1A is a consequence of the competitive activation of several damage mechanisms, including plastic deformation and micro-cracking coalescence at the Al-Alloy, as well as fiber breakage and interfacial de-bonding at metal/resin layer in addition to fiber/matrix and matrix cracking. The softening behavior occurs as the balance of these mechanisms is interrupted.
2. The obtained AE data highlight the operated damage mechanisms and their sequence appearance in terms of characteristics PF and damage evolution with exponential profile. This AE activity follows the same trend with suggested micro-mechanical models for damage development in terms of crack density for laminated composites.

3. The AE-DIC data reveal critical damage areas of the loaded wall as a function of applied loading, providing in this way early signs of deterioration that can be implemented in structural health monitoring applications.

Acknowledgment The authors wish to thank Prof. Ahmad Hamid and Prof. Frank Moon from the Civil engineering Dept. at Drexel University, for assistance in conducting the tests on the masonry wall.

References

1. R.K. Miller, P. McIntire, *Nondestructive Testing Handbook, Vol 6: Acoustic Emission Testing* (American Society for Nondestructive Testing, Columbus, OH, 2005), p. 447
2. M. Sutton et al., Application of an optimized digital correlation method to planar deformation analysis. Image. Vision. Comput. **4**(3), 143–150 (1986)
3. T. Chu, W. Ranson, M. Sutton, Applications of digital-image-correlation techniques to experimental mechanics. Exp. Mech. **25**(3), 232–244 (1985)
4. B. Pan et al., Two-dimensional digital image correlation for in-plane displacement and strain measurement: a review. Meas. Sci. Technol. **20**(6), 062001 (2009)
5. M.A. Sutton, J.J. Orteu, H.W. Schreier, *Image Correlation for Shape, Motion and Deformation Measurements: Basic Concepts, Theory and Applications* (Springer, New York, 2009)
6. J. Cuadra et al., Damage quantification in polymer composites using a hybrid NDT approach. Compos. Sci. Technol. **83**, 11–21 (2013)
7. E. Schwartz et al., *The Use of Digital Image Correlation for Non-destructive and Multi-scale Damage Quantification. In SPIE Smart Structures and Materials + Nondestructive Evaluation and Health Monitoring* (International Society for Optics and Photonics, Bellingham, WA, 2013)
8. P.A. Vanniamparambil et al., An integrated structural health monitoring approach for crack growth monitoring. J. Intel. Mat. Syst. Struct. **23**(14), 1563–1573 (2012)
9. T. Beumler, Flying Glare, A contribution to aircraft certification issues on strength properties in non-damaged and fatigue damaged GLARE® structures. Dissertation, Faculty of Aerospace Engineering, Technical University Delft, 2004
10. A. Vlot, *Glare: History of the development of a New Aircraft Material* (Kluwer, New York, 2001)
11. C. Vermeeren et al., Glare design aspects and philosophies. Appl. Compos. Mater. **10**(4–5), 257–276 (2003)
12. G. Wu, J.M. Yang, The mechanical behavior of GLARE laminates for aircraft structures. JOM **57**(1), 72–79 (2005)
13. ASTM E976, *Standard Guide for Determining the Reproducibility of Acoustic Emission Sensor Response* (ASTM, West Conshohocken, PA, 2005)
14. A. Anastassopoulos, T. Philippidis, Clustering methodology for the evaluation of acoustic emission from composites. J. Acoustic. Emission. **13**(1–2), 11–22 (1995)
15. M. Sause et al., Quantification of failure mechanisms in mode-I loading of fiber reinforced plastics utilizing acoustic emission analysis. Compos. Sci. Technol. **72**(2), 167–174 (2012)
16. M. Kempf, O. Skrabala, V. Altstädt, Acoustic emission analysis for characterisation of damage mechanisms in fibre reinforced thermosetting polyurethane and epoxy. Compos. B Eng. **54**, 289–299 (2013)
17. P.A. Vanniamparambil, R. Carmi, F. Khan, I. Bartoli, A. Kontsos, Novel optico-acoustic sensing system for cross-validated structural health monitoring, in *ICOSSAR 2013 – the 11th International Conference on Structural Safety & Reliability* (Columbia University, New York, NY, 2013)

18. A. Bussiba et al., Damage evolution and fracture events sequence in various composites by acoustic emission technique. Compos. Sci. Technol. **68**(5), 1144–1155 (2008)
19. R. Talreja, Damage development in composites: mechanisms and modelling. J. Strain Anal. Eng. Des. **24**(4), 215–222 (1989)
20. F. Edgren et al., Formation of damage and its effects on non-crimp fabric reinforced composites loaded in tension. Compos. Sci. Technol. **64**(5), 675–692 (2004)
21. M.D. Kistner, J.M. Whitney, C.E. Browning, First-ply failure of graphite/epoxy laminates. Recent Adv. Compos. US Jpn ASTM STP **864**, 44–61 (1985)
22. K. Ohno, M. Ohtsu, Crack classification in concrete based on acoustic emission. Construct. Build Mater. **24**(12), 2339–2346 (2010)
23. A. Farhidzadeh, S. Salamone, P. Singla, A probabilistic approach for damage identification and crack mode classification in reinforced concrete structures. J. Intel. Mat. Syst. Struct. **24** (14), 1722–1735 (2013)

Integral Thickness Measuring

D.A. Terentyev

Abstract The method of integral thickness measuring has been developed. It is realizable on the basis of standard AE systems and AE sensors. On the object at a distance of several meters or tens of meters apart two AE sensors are placed. They are used as a transmitter and a receiver of the acoustic signals. On the spectrogram of received signals the dispersion curves are extracted. The arithmetic mean thickness, the thickness dispersion, and the estimation of the minimum thickness can be calculated.

1 Introduction

Most of the acoustic emission (AE) systems operate within the frequency range from 30 to 500 kHz. This frequency range is used for AE testing, since only within this range the following two requirements are satisfied at the same time: first, the acoustic signal attenuation is so small that the useful signals can cover distances of several meters; and second, the noise level is low in comparison with the useful signals.

The unique properties of the above frequency range allow for fast and complete testing of the large areas of the object using a small number of sensors. It would be useful not only for the AE techniques, but also for the active acoustic testing [1]. The combination of two said techniques in a single device is particularly promising.

One of the most pressing problems of nondestructive testing (NDT) is detection of corrosion damage of the object and determination of its extent. Generally, values

D.A. Terentyev (✉)
INTERUNIS LLC, Myasnitskaya St., 24/7, Building 3-4, Moscow 101000, Russia
e-mail: tyev@interunis.ru

G. Shen et al. (eds.), *Advances in Acoustic Emission Technology: Proceedings of the World Conference on Acoustic Emission-2013*, Springer Proceedings in Physics 158,
DOI 10.1007/978-1-4939-1239-1_57,

of residual wall thickness and areas of corrosion damage are used as a quantitative characteristic of the degree of damage. To determine these parameters, ultrasonic thickness gauges are commonly used which allow for making local measurements of the wall thickness.

The disadvantages of this method are the high labor content of testing of large-area objects, the necessity to remove insulation on the whole tested area, and the impossibility to measure thickness of the object areas to which there is no physical access. These disadvantages lead to that the thickness is usually measured on a small part of area of the tested object as a result of which the degree of corrosion damage is determined with low accuracy; there is a probability of missing a corrosion defect, and the degree of subjectivity of testing increases. In addition, the object parts of large area remain nontested at all. It should be also mentioned that arrangement of monitoring of the large-area objects by the methods of ultrasonic thickness measuring is a complicated problem.

Thus, the urgent problem is the development of the method that permits to carry out an integral measuring of thickness, i.e., to receive data on the wall thickness between the sensors mounted on the object some distance apart.

2 Integral Thickness Measuring

To solve the assigned task by the acoustic methods, it is necessary to transmit the signal through a few meters of the object wall. This requires changing frequency range from the region of above 1 MHz that is typical for the conventional ultrasonic thickness gauges to the range from 30 to 500 kHz that is typical for AE testing.

"INTERUNIS" company has developed the method of integral thickness measuring and monitoring, which is based on the phenomenon of dependence of the Lamb wave group velocity on the product of frequency and wall thickness, and realizable on the basis of standard AE systems and AE sensors [2].

The work scheme is as follows. On the object at a distance of several meters or tens of meters apart two AE sensors are placed (Fig. 1). They are used as a transmitter and a receiver of the acoustic signals. At the transmitter an electrical δ pulse is fed with the result that this AE sensor radiates a wideband impulse with a length of about 1 μs.

The spectrogram of the received signal is calculated (Fig. 2). In this spectrogram we extract the dispersion curves of various Lamb waves [2]. Since the arrival times of different frequency components $t(f)$ in a complicated way depend on the plot of thickness $h(x)$ at the section between the sensors

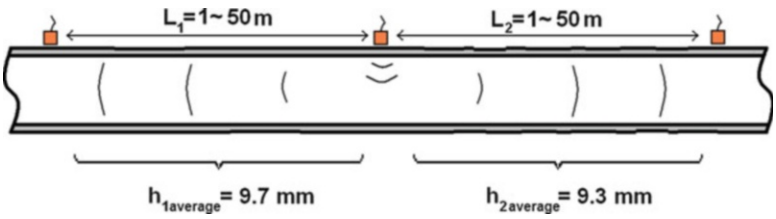

Fig. 1 Emitter and receiver arrangement on the testing object and the arithmetic mean thickness values between them

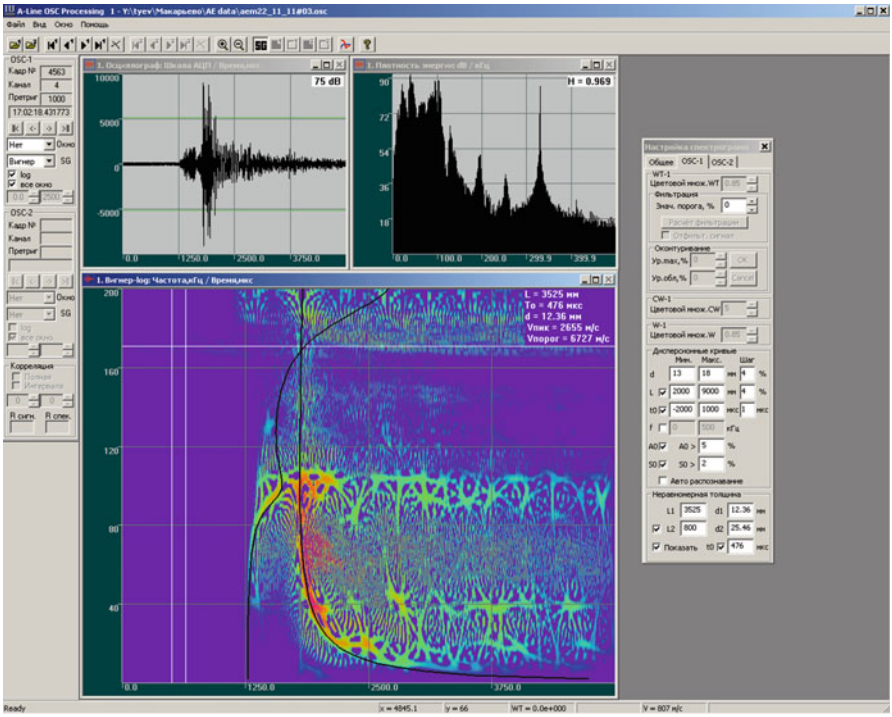

Fig. 2 A waveform, spectrum, and spectrogram calculated using a specialized software "A-Line OSC Processing"

$$t(f) = t_{\mathrm{RAD}} + \int_0^L \frac{dx}{v_i(f \cdot h(x))}, \tag{1}$$

analysis of the frequency dependence of Lamb wave arrival times enables to get information about the thickness values at the segment between sensors. Here, v_i is a group velocity of i-th mode of Lamb wave, t_{RAD} is a time point of radiation, and L is the distance between sensors.

3 Experiments on Objects with Uniform-Thickness Wall

To test the method operation, at first we have conducted a series of experiments on pipelines with a uniform-thickness wall. In such cases Eq. (1) is simplified to

$$t(f) = t_{\mathrm{RAD}} + \frac{L}{v_i(f \cdot \ h)}. \tag{2}$$

It has been found that the accuracy of thickness measuring can reach 1 %. It has also been found that this method is operable at least within the thickness range from 4 to 40 mm. It has been revealed that the present method is operative only when the distances between AE sensors are more than 1 m, because in this case the different portions of dispersion curves are sufficiently separated from each other along the time axis. Furthermore, it has been revealed that the maximum distance can amount up to 12 m on pipes with the insulation and up to 56 m on pipelines with the insulation removed (Fig. 3). The experiments have shown that welded seams have no effect on measurements.

To automate the process of extraction of dispersion curves from the spectrogram and determine the wall thickness in cases when the thickness is uniform, a modification of the Hough transform has been developed. This extraction method has been added to the specialized software "A-Line OSC Processing" developed by "INTERUNIS" company, which is applied for manual and automatic processing of waveforms and spectrograms of AE signals [3].

Since the group velocity of Lamb waves depends on the product of frequency and thickness, the plots of dispersion curves on spectrograms (2) corresponding to

Fig. 3 An experiment on the section of pipeline of length 56 m

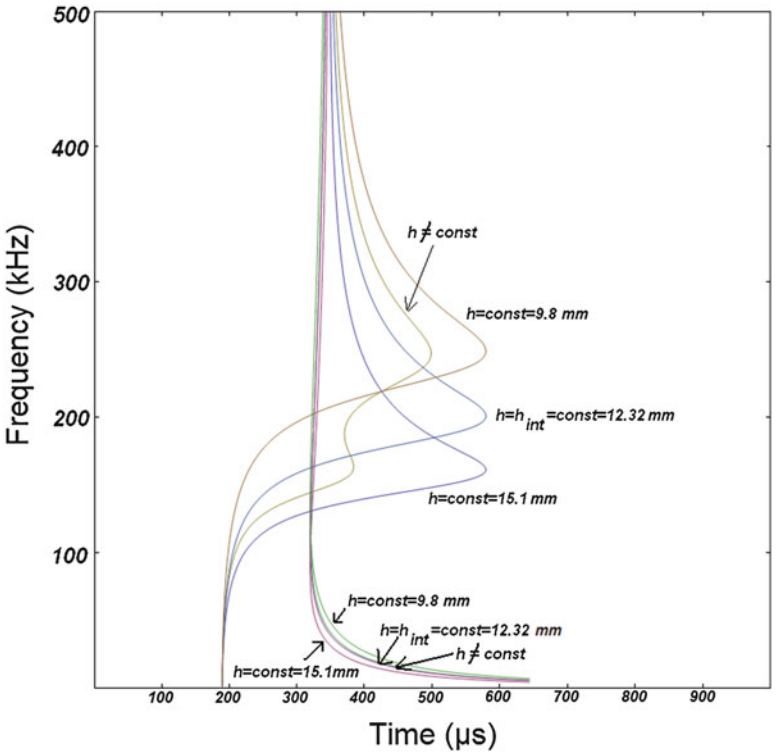

Fig. 4 The plots of dispersion curves on spectrograms corresponding to objects with uniform thicknesses and to objects with thickness variations

any distances between sensors and to any objects of the same material with uniform thicknesses are related to one another by an affine transformation (Fig. 4). Therefore, theoretically any Lamb mode and any frequency range can be used for extraction on such objects—the result is supposed to be the same. However, the most preferred selection is an operation using zero-order Lamb waves, S_0 and A_0, because only waves of this type can propagate at any frequencies that enables to select frequencies rather low to ensure low signal attenuation. In this situation an emitted signal can cover the sufficiently great distances between sensors. Furthermore, for decreasing errors of determination of thickness, the frequency regions are preferable, within which the derivative of the group velocity with respect to frequency is sufficiently high.

It was found that the pipe curvature had no significant effect on the values of group velocity and this made it possible to use the model of Lamb waves instead of the more complicated Pochhammer-Chree model [4]. However, when analyzing the spectrograms, the substantial problem was in signals arriving not by the shortest routes, but by helixes, once or several times rounding the pipe. Existence of such

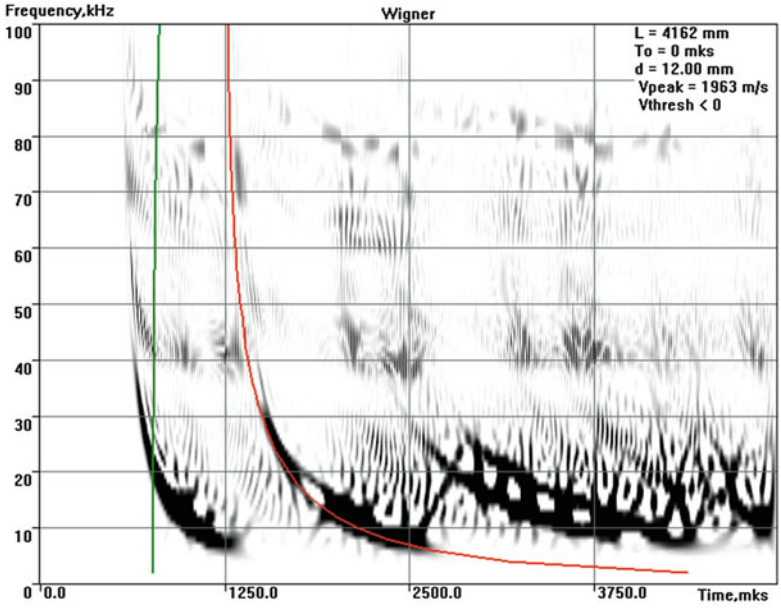

Fig. 5 Signals propagating by the helixes are indistinguishable from signals propagating by the shortest routes

signals resulted in occurrence of one or several additional curves on the spectrogram which in contrast to electromagnetic interferences or other noises are not always distinguishable in their shape from the true dispersion curves (Fig. 5).

4 Experiments on Objects with Wall Thickness Variations

Later, a series of experiments was conducted on the objects with wall thickness variations.

First experiment was set up on a pipeline which firstly had a uniform-thickness wall; the thickness was reduced up to 50 % of its original value by means of an angle grinder aside of the segment between the sensors (Fig. 6). As a result, it has been found that the region, wherein the thickness values affect the measurement results, is a narrow elongated area with a width of no more than 6 % of the distance between the sensors along the segment connecting the sensors.

In another experiment, on a pipeline which firstly had a uniform-thickness wall, a thickness profile in the form of the step function was made. To do this, using an angle grinder the thickness was reduced up to 50 % of its original value at the portion of the segment between the sensors (Fig. 7). The dispersion curves obtained by experiment (Fig. 2) coincided with the curves calculated for the corresponding geometry of the object by (1).

Fig. 6 A pipeline whose thickness was reduced up to 50 % of its original value aside of the segment between the sensors

Fig. 7 A pipeline with the thickness profile in the form of the step function

It should be noted that plots of dispersion curves on the objects with significant variations of wall thickness are no longer related to one another by an affine transformation, and differ from the previously discussed case of the objects with the uniform thickness (Fig. 4). As the first approximation, it is possible to consider

that the time of arrival at any frequency is equal to the time of arrival, which would be observed on some object with thickness being anywhere equal to the arithmetic mean value $M[h]$ of thickness on a real object, summarized with a correction, which depends on the product of the variation σ^2 of thickness values on a real object, and the second derivative of reciprocal of the group velocity with respect to the product of thickness and frequency:

$$t_i(f) = t_{\mathrm{RAD}} + \frac{L}{v_i(f \cdot \ M[h])} + \frac{1}{2}\left(\left.\frac{\partial^2\left(v_i^{-1}(f \ \cdot h)\right)}{\partial(f \ \cdot h)^2}\right|_{f \cdot M[h]}\right) f^2 \cdot L \cdot \sigma^2.$$

For this reason, when applying the extraction method developed for the simpler geometry of objects, a mismatch appears among the results obtained using different frequency ranges and different Lamb modes. For example, when using the portion of mode S_0, corresponding to the low-frequency part of the slope of the group velocity plot, the obtained effective values of thickness fall in the range between the arithmetic mean value and the maximum value of thickness. When using the portion of mode S_0, corresponding to the essentially linear part of the group velocity plot, the obtained effective values of thickness coincide with the arithmetic mean value of thickness. At the same time, when using the low-frequency portion of mode A_0, corresponding to the rapid growth of the group velocity with increasing frequency, the obtained effective values of thickness fall in the range between the minimum value and the arithmetic mean value of thickness.

The mathematical simulation shows that in case when the arithmetic mean value of thickness is determined with the use of the linear portion of the plot of the dispersion curve of mode S_0, it becomes also possible to determine the variation. For this purpose, the mismatching value between the arithmetic mean value of thickness and the effective thickness values obtained with the use of the low-frequency portion of mode A_0 is used. For example, we have applied the following formula:

$$\sigma^2 = \frac{t(f) - L \cdot v_i^{-1}(f \cdot M[h]) - t_{\mathrm{RAD}}}{\left(\frac{1}{2}\left.\frac{\partial^2\left(v_i^{-1}(f \cdot h)\right)}{\partial(f \cdot h)^2}\right|_{f \cdot M[h]}\right) f^2 L.}$$

In turn, the arithmetic mean value of thickness and the value of variation of the thickness allow estimation of the minimum thickness of the object, for example, by the formula

$$h_{\min} = M[h] - k\sigma,$$

where k is a safety factor within the range from 0.5 to 3.

Now, work is under way on experimental estimate of determination accuracy of the arithmetic mean thickness value and the minimum thickness value between the sensors. It should be mentioned that these two parameters are widely used for NDT of objects exposed to corrosion and erosion [5].

Fig. 8 Portable universal device "UNISCOPE"

The procedure of data acquisition for the integral thickness measuring has been added to capabilities of the portable universal device "UNISCOPE" (Fig. 8), intended for AE testing, leak detection, and vibration control [6]. It has enabled to combine the benefits of active and passive methods of acoustic testing in a single device.

5 Conclusions

1. The method of integral thickness measuring and monitoring is developed. It allows us to measure thickness values in the area between two AE sensors installed on an object some distance apart.
2. The experiments show that the method is operable within the thickness range from 4 to 40 mm and within distances from 1 to 56 m.
3. The region, wherein the thickness values affect the measurement results, is a narrow elongated area with a width of no more than 6 % of the distance between the sensors.
4. The use of the portion of mode S_0, corresponding to the essentially linear part of the group velocity plot, makes it possible to determine the arithmetic mean value of the thickness between two sensors.
5. Work is under way on experimental estimate of determination accuracy of the arithmetic mean thickness value and the minimum thickness value between two sensors.

References

1. T. Kundu (ed.), *Advanced Ultrasonic Methods for Material and Structure Inspection*. (ISTE, London, 2007), 393 pp
2. S. Elizarov, A. Bukatin, M. Rostovtsev, D. Terentyev, New developments of software for A-line family AE systems. J. Acoust. Emission **26**, 311–317 (2008)
3. D.A. Terentyev, V.A. Barat, K.A. Bulygin, The extraction method for dispersion curves from spectrograms using Hough transform. J. Acoust. Emission **29**, 232–242 (2011)
4. F. Seco, A.R. Jiménez, Modelling the generation and propagation of ultrasonic signals in cylindrical waveguides, in *Ultrasonic Waves*, ch. 1, (Intech Open Access Publisher, 2012), pp. 1–28
5. *ASME Standard API 579-1/ASME FFS-1*, 5 June 2007, 1128 pp
6. S.V. Elizarov, A.L. Alyakritskiy, V.G. Koltsov, V.A. Barat, P.N. Trofimov, *Portable NDT Instrument UNISCOPE, Proceedings of the 30th European Conference on Acoustic Emission Testing & 7th International Conference on Acoustic Emission EWGAE 30/ICAE 7*, Granada, 12–15 Sept 2012

Separation of the Elastic and Plastic Wave in Electromagnetically Induced Acoustic Emission Testing

Zhichao Cai, Suzhen Liu, Qingxin Yang, and Chuang Zhang

Abstract In this chapter, a developed electromagnetically induced acoustic emission technique (EMAE) which can be used for nondestructive flaw detection is introduced. This method is different from traditional acoustic emission testing (AET) in the behalf of locally electromagnetic force, which has a big advantage of contactless load. Based on the principle of electromagnetic acoustic transducers (EMAT), it causes the dynamic locally elastic vibration in the area of eddy current during the process of loading at the same time. Acoustic emission sensors receive the stress wave signal, which is the superposition of plastic wave and elastic wave. It is very meaningful to separate the elastic and plastic wave in EMAE. The results could enhance detection accuracy of small crack properties and acoustic emission signal.

1 Introduction

The brittle and fatigue fracture caused by micro-crack and fatigue damage often happens suddenly in the thin aluminum plate surface in the extreme condition, and even leads to a catastrophic accident. Electromagnetically induced acoustic emission (EMAE) is considered as a nondestructive testing method by electromagnetic induction; the electromagnetic force in crack area, which is induced by exciting coil, stimulates the deformation at the tip of crack and produces acoustic emission signal [1–3]. Therefore, it fixes the tiny defects or crack position. Meanwhile, the

Z. Cai (✉) • S. Liu • C. Zhang
Hebei University of Technology, Tianjin 300130, China
e-mail: czchebut@foxmail.com

Q. Yang
Tianjin Polytechnic University, Tianjin 300160, China
e-mail: qxyang@tjpu.edu.cn

G. Shen et al. (eds.), *Advances in Acoustic Emission Technology: Proceedings of the World Conference on Acoustic Emission-2013*, Springer Proceedings in Physics 158,
DOI 10.1007/978-1-4939-1239-1_58,

eddy current inside the material interacts with the biasing magnetic field, causes body forces, and then generates elastic waves. The characteristics of acoustic emission parameters contain the abundant information of defects. Analyzing acoustic emission signal parameters has better ability to judge crack growth and predicate mechanical life.

This chapter embarks on the electromagnetic-stress coupling theory and analyzes the wave propagation characteristics of electromagnetic load. A finite element (FE) model of electromagnetic acoustic emission is established in this chapter, and the deformation of precrack under electromagnetic load is studied. Fast Fourier transform (FFT) is used to analyze stress wave signal. This study reveals the defect characteristics of plastic deformation and elastic deformation signal, which can be used to identify the features of true acoustic emission.

2 Source of EMAE

2.1 Principle of EMAE

EMAE is considered to be a "passive" nondestructive technique, which usually identifies cracks only while loading specimen during the test. Unlike regular stress load, a local load due to electromagnetic force replaced the whole load. Meanwhile, EMAE has a wide application prospect based on its contactless load.

The previous literature mostly studied the collection and analysis of acoustic emission signal [4–6]. However, there are less scholars undertaking research on the source of acoustic emission. Figure 1 shows the principle of acoustic emission.

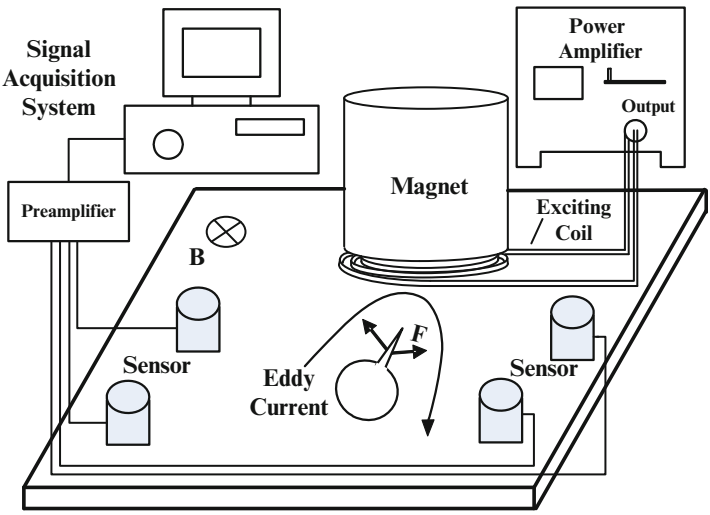

Fig. 1 Acoustic emission under electromagnetic load

Effective current density at defect tips is higher than other areas by several orders of magnitudes. The eddy current flows in opposite directions along the crack tip. Meanwhile, an external static magnetic field is perpendicular to the detection area, and produces localized electromagnetic force with the opposite direction. The AE signal has low amplitude and wide frequency band, which is excited by elastic-plastic deformation and interfacial friction. So EMAE signals are produced by plastic wave.

2.2 Electromagnetic Load Limit

Even though acoustic emission testing (AET) is classified as a nondestructive method, AE is more strongly dependent on dislocation. So this method is only capable of detecting the progression of existing crack, friction process, and the formation of new cracks. As a local load, EMAE should be considered as internal mechanical or thermal effects. Therefore, it is essential to set the appropriate loading time and incentive amplitude to avoid additional mechanical or thermal damage in the existing crack.

Taking aluminum sheet for example, most of the aluminum sheets have ductile fracture. Crack opening displacement (COD) portrays as the main parameter of the crack tip field. For penetrating mode I crack in aluminum sheet, the critical displacement is 0.09 mm [7]. In the following experiments and simulations, the frequency of excitation current is 500 kHz and the amplitude is 5 A; the loading time is two cycles. The maximum displacement of crack tip is 3.41×10^{-7} mm under eddy excitation. Due to the exciting current amplitude and cycle being too small, the temperature is far from the crack tip metal melt (the melting point of the aluminum is 660 °C). So the influence of temperature can be negligible during the analysis. Therefore, we can conclude that EMAE of local electromagnetic excitation does not cause additional damage to the component.

2.3 Comparison with EMAT

The AE wave is generated as the electromagnetic acoustic emission by the electromagnetic load, which is an electromagnetic-stress coupling process. EMAE and electromagnetic acoustic transducers (EMAT) exist at the same time during electromagnetic excitation in the crack. Compared with EMAT [8], the mechanisms of loading condition and coupling process are similar, while the mechanisms of transduction are discrepant. In general, due to the effect of the instantaneous electromagnetic force on the crack, load of EMAE can be considered as completely plastic medium. While in the study of EMAE, the approximate assumption is inappropriate to analyze acoustic emission mechanism by theory of elastic vibration. The elastic deformation in EMAT is essentially different from plastic deformation in EMAE.

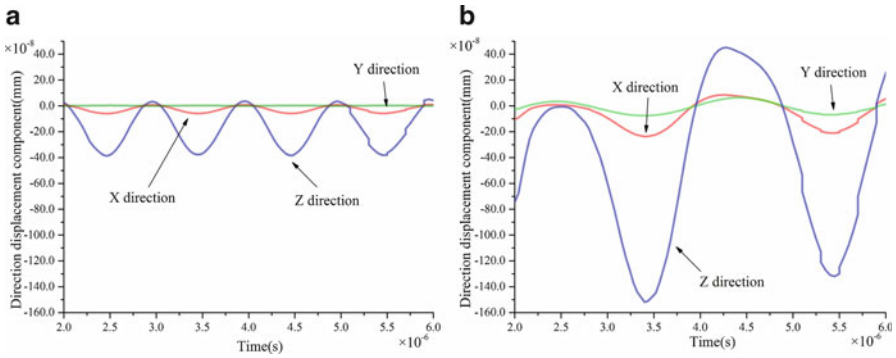

Fig. 2 (**a**) Three directions of fixed-point displacement under alternating magnetic field. (**b**) Three directions of fixed-point displacement under static magnetic field

The electromagnetic load is conducive to the spread of the acoustic emission signal. AE signal modulates ultrasonic signal which is motivated by EMAT. The modulation process for ultrasonic is controllable. The spread improves transmission distance of acoustic emission signal and ensures the acoustic emission signal integrity during the transmission.

Different from the traditional nonlinear ultrasonic technique, the ultrasonic is modulated by the interactions between the ultrasonic wave and AE signal which is from the closed-crack defect itself.

EMAT is based on the electromagnetic-stress coupling. The acoustic wave equation of the isotropic elastic medium is as follows:

$$(\lambda + G)\nabla\nabla \cdot u + G\nabla^2 u + f = \rho \frac{\partial^2 u}{\partial t^2} \tag{1}$$

where λ is Lame constants, G is Shear modulus, ρ is the mass density, u is the displacement, and f denotes electromagnetic force per unit volume.

$$f = J_e \times (B_0 + B_d) \tag{2}$$

where J_e is eddy current density, B_d is alternating magnetic field, and B_0 is static magnetic field.

Figure 2 shows the displacement of elastic wave under alternating magnetic field at a fixed point, which is on the elastic wave transmission path. The displacement of z direction is significantly larger than the other two directions, because of the electromagnetic force mainly along the z direction. The frequency of the electromagnetic force generated by excitation is twice as large as the exciting current frequency. So the frequency of the elastic wave is twice as large as the exciting current frequency. Comparing (a) with (b), it indicates that the displacement due to static magnetic field is about five times larger than that due to alternating magnetic field. The frequency of the latter is twice than the former. In both cases, z direction displacements are stronger

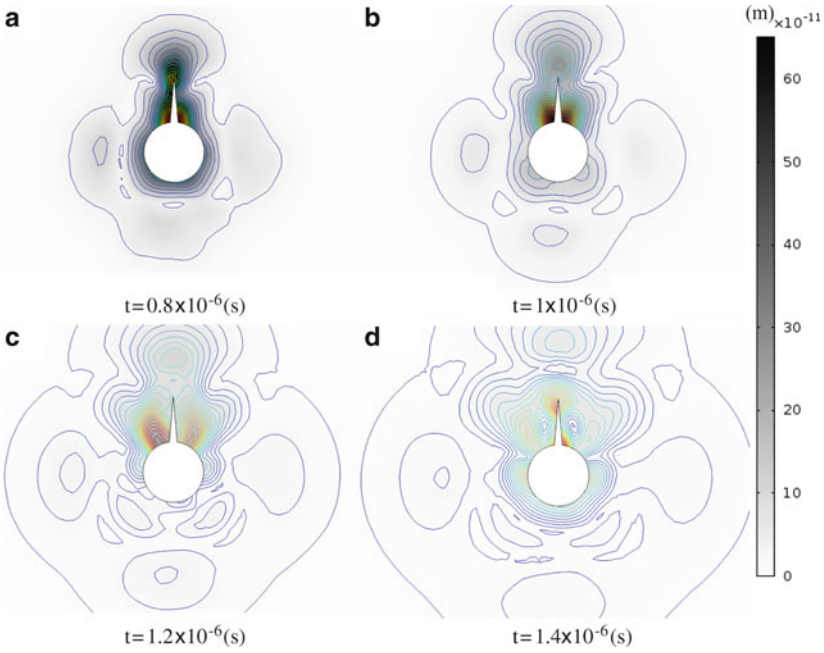

Fig. 3 Crack displacement contour

than the other two directions. The amplitude of z-direction displacements has a 1/7 period advance than x direction and 1/20 period advance than y direction.

The crack deformation contours and stress wave propagation over time are shown in Fig. 3. Gradient of the deformation around the defect is along its tangential direction. The changes of deformation are very sensitive to the position of coil and permanent magnet. The spread diffusion of stress wave is mainly related to the length and angle of crack.

Differences of the deformation will be reflected in the intensity of elastic wave signal, and AE signal is due to the expansion or the vibration of cracks.

3 Stress Wave Propagation in Solids

3.1 Angle of Elastic Wave

Different from the plastic wave, the elastic wave has certain directivity in EMAT. And the directivity of the elastic wave should start from the source. The areas of defect tip concentrate on the electromagnetic force mentioned above. The effective area is the main elastic wave source which has the similar shape with the triangular area of defect tip. And depth of the area is skin depth. The elastic source is thus simplified to the two

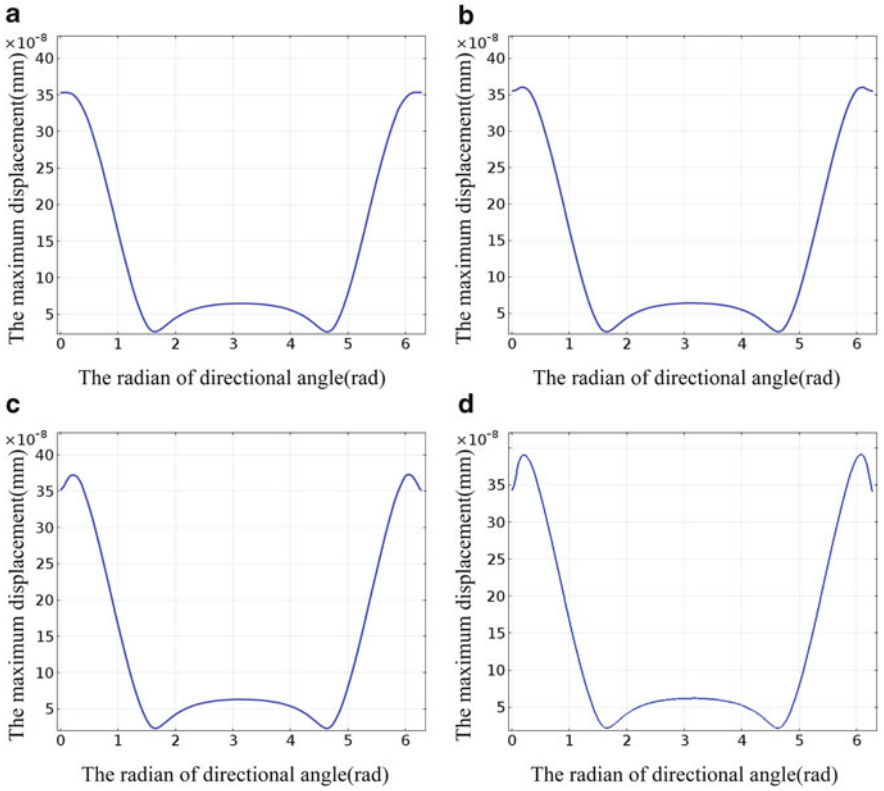

Fig. 4 The maximal displacement curve on circular path

rectangular sources between the couple sides of defect tip. The directional coefficient of the material plane is as follows:

$$D_{\mathrm{r}} = \frac{\sin\left(kd\sin\theta\right)}{kd\sin\theta} \tag{3}$$

where k is the wavelength, θ is the directional angel, and d is the effective crack length.

The following equation can be launched by using Eq. (3):

$$\sin\theta = \pi/kd \tag{4}$$

The directional angle of elastic wave is determined by wavelength and effective crack length. The directional angles under different effective crack length are compared. Using the finite element analysis, it can be calculated by taking the maximum displacement of circular path. The center of the circle is the center of the precrack, which creates a circular path with 7 mm radius. Directional angle can be calculated from the curve, and the value can be decided by the cutoff displacement. The value of cutoff displacement is 1/5 period advance than the maximal displacement. As shown in Fig. 4,

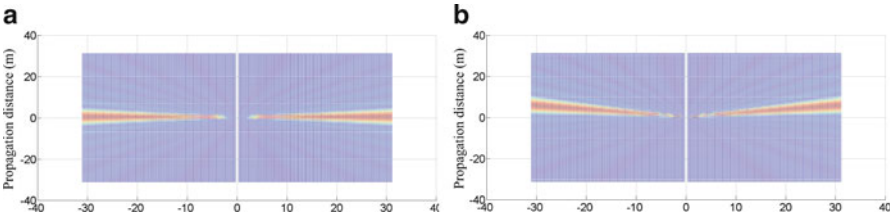

Fig. 5 (**a**) The normalized distribution of undamped elastic wave at closed defect. (**b**) The normalized distribution of undamped elastic wave at 20° defect

with the increase of the effective crack length, directional angle decreases significantly, and the directivity of elastic wave is better.

Diffusion coefficient decides spread angle and the crack angle decides the direction of diffusion as shown in Fig. 5, which has a referential meaning for setting the AE sensors. This arrangement should avoid the position of elastic wave propagation path.

3.2 Stress Wave Propagation Mode

Electromagnetic excitation stress wave propagation through the whole solid under the material thickness is less than the wavelength of the stress wave, so in the propagation of plate waveguide is mainly Lamb wave. According to its transmission mode, Lamb wave can be divided into symmetric mode and the antisymmetric mode. And the dispersion equation of symmetry mode and antisymmetric mode can be obtained by solving the wave equation. It is difficult to distinguish collected signals characteristic of multi-mode. With guided wave propagation distance increasing, the signal will gradually lengthen along the time axis and overlap the stress wave signal. So it is hard to distinguish the types of waves from time-domain signals.

4 Experiment and Discussion

A hole with a diameter of 13.14 mm analogue simulates fixed bolt hole in the aluminum sheet metal, and a precrack with a length of 25.5 mm is made by repeated bending. The dimension of the sheet is 0.5 m × 0.2 m × 0.0013 m. Motivate probe is composed of a cylindrical permanent magnet and an exciting coil. Permanent magnet provides a magnetic field of 0.1 T. And the drive coil with bigger size can produce a larger area of eddy current. However, electromagnetic load should consider the size of crack and permanent magnet. In order to meet the requirements of experiment, a 100-turns coil with an outer diameter of 26 mm is designed, which is supported by 500 kHz alternating current. The Physical Acoustic Company's

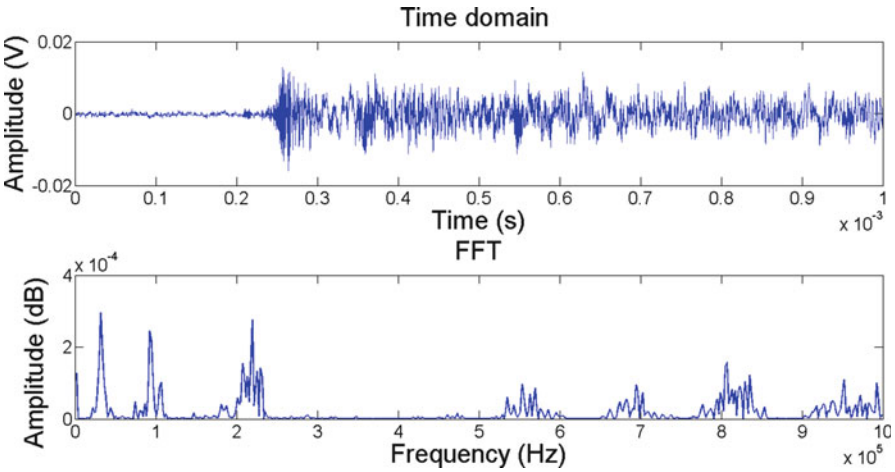

Fig. 6 Frequency domain and time domain before filtering

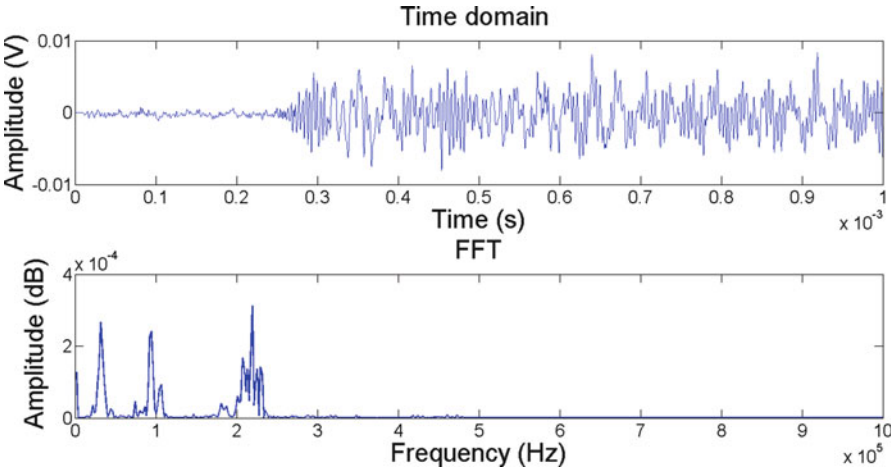

Fig. 7 Frequency domain and time domain after filtering

WSA acoustic emission sensor is selected in the experiment, which has a wide frequency response, and the arrangement follows the principle mentioned above.

The signal of EMAE is transient acoustic emission, selecting first crash signal. The time of transient acoustic emission acquisition is 750 μs. As shown in Fig. 6, the stress wave signal is gathered by AE sensors with a wide spectrum distribution. The composition of high-frequency signal is mainly produced by the EMAT. The signals also have corresponding change in frequency spectrum from 500 kHz to 1 MHz, which is due to the signal modulation. The signals shown in Fig. 7 are traditional AE signals after low-pass filtering, and the AE signals contain three

frequency bands generated from the loaded crack itself and have broadband frequency characteristics of acoustic emission.

The separation of the elastic and plastic wave is the demodulation and filtering process, which helps to acquire the true AE signal. Thus the characteristics of emission signal are effective in detecting the defects and can enhance the detection capability for small cracks.

5 Conclusion

Acoustic emission load is no longer needed for the whole load. In the process of passive monitoring, just a transient external electromagnetic field actively is applied to a defect, which can excite the stress wave by the vibration of the defect itself. Meanwhile, electromagnetic load produces ultrasonic. In this chapter, the following work has been done:

1. In the process of electromagnetic load, the AE signal is interfered by ultrasonic wave caused by elastic vibration.
2. According to amplitude-frequency characteristic, directional angle, and propagation mode, this chapter distinguished the differences between acoustic emission plastic wave and elastic wave.
3. The elastic and plastic waves are separated by low-pass filtering and reasonable sensor arrangement, which has a good effect.

The future work will focus on the rigorous implementation of the elastic wave control. And EMAE can be developed to evaluate the decentralized structure caused by microscopic discontinuities.

Acknowledgment This work was supported by the National Natural Science Foundation of China (Grant No. 51077036, No. 51207105), the Natural Science Foundation of Hebei Province (Grant No. E2012202026, E2012202048), and the research and development project of science and technology of Hebei Province (Grant No. 11215648).

References

1. C.U. Grossp, M. Ohtu et al., *Acoustic Emission Testing Basics for Research-Application in Civil Engineering* (Springer, Germany, 2008), pp. 3–6
2. P. Finkel, V. Godinez, Numerical simulations of an electromagnetic of the ultrasonic signal for nondestructive detection of ferromagnetic inclusions and flaws. IEEE Trans. Magn. **40**, 2179–2181 (2004)
3. P. Finkel, V. Godinezl, R. Miller et al., Electromagnetically induced acoustic emission – novel NDT technique for damage evaluation. Proc. Am. Inst. Phys. Conf. **20**, 1747–1754 (2001)
4. Liu Suzhen, Yang Qingxin, Jin Liang, et al., Application of electromagnetic acoustic emission technology in non-destructive testing. Trans. China Electrotech. Soc. **24**(1), 23–27, (2009)

5. Liu Suzhen, Jin Liang, Zhang Chuang, et al., Eddy current exciting method for electromagnetically induced acoustic emission detecting technique. Trans. China Electrotech. Soc. **27**(7), 153–158, (2012)
6. Zhang Chuang, Liu Suzhen, Jin Liang, et al., Experimental study of electromagnetically induced acoustic emission. Based on high current loading directly. Trans. China Electrotech. Soc. **28**(1), 101–105, (2013)
7. Niu Liping, Yang Bangcheng, Xu Lei, et al., Numerical analysis of stable crack tearing in aluminum alloy. Sci. Technol. Eng. **7**(19), 4842–4845, (2007)
8. M. Hirao, H. Ogi, *EMATs for science and industry: noncontacting ultrasonic measurements* (Kluwer Academic, Boston, MA, 2003)

Correlation Between Acoustic Emission and Induced Hydrogen of Shield Metal Arc Welding

P. Homsawat, C. Jirarungsatian, and I. Phung-On

Abstract This chapter presents a study on detecting acoustic emission (AE) of hydrogen diffusion after shield metal arc welding (SMAW) process. Technique to detect hydrogen which diffused from steel, gas, or other elements is performed. A correlation between occurred AE and induced hydrogen in weldment after welding is determined. In the experiment, a broadband AE sensor and welded specimens were mounted on a wave guide plate which has 250 mm of separate distance for monitoring and recording AE activity of hydrogen diffusion. The specimens are prepared according to the welding standard (JIS Z 3113). The specimen sizes were 25 mm width, 130 mm length, and 12 mm thickness. Four types of electrodes were used for welding to vary hydrogen amount. The welding current was lower than the manufacturer's specification of 15 amperes. The specimens were quenched in 5 s after welding process. The results showed that the AE technique can be used to detect hydrogen diffusion after weld. The emitted AE signals were analyzed to determine the relation with the amount of hydrogen. The method for measurement of hydrogen referred to the welding standard (JIS Z 3113). The correlation plot between AE and diffused hydrogen amount can be shown as 0.8 of R^2 linearity. The benefit of this study will be applied to monitor the weldment before cold crack occurs.

P. Homsawat (✉) • C. Jirarungsatian • I. Phung-On
Maintenance Technology Center, King Mongkut's University of Technology Thonburi, Bangkok 10140, Thailand
e-mail: nitrous_mce@hotmail.com; chalermkiat.jir@kmutt.ac.th; isa_ceo@yahoo.com

G. Shen et al. (eds.), *Advances in Acoustic Emission Technology: Proceedings of the World Conference on Acoustic Emission-2013*, Springer Proceedings in Physics 158,
DOI 10.1007/978-1-4939-1239-1_59,

1 Introduction

Nowadays, the business of fabrication industries has been expanded to support an increasing market demand. The welding process has also been developed continuously by advanced technique [1, 2]; however the inspection technique must be developed to ensure the weld quality after welding process. The cold cracking is one of the failure types which could occur on welds after welding process. The amount of hydrogen diffusion on welds is a cause of this case which could induce a crack any time after welding process is done.

Indeed, the procedure of shield metal arc welding (SMAW) process allows inspecting a discontinuity after 72 h of welding process by using NDT techniques. If a crack is found, the repairing will be done and then wait for another 72 h for inspection. The advanced inspection technique is required for monitoring a crack during the waiting period to solve this problem. Acoustic emission (AE) is the advanced technique which is frequently applied for welding process monitoring [3]. However, there are two possible acoustic sources on welds after welding process which are crack and induced hydrogen in the welds. Therefore, the characteristic of AE source should be studied to use in AE analyzing process.

In this work, acoustic emission was applied for studying a correlation between acoustic emission characteristic and induced hydrogen of SMAW. The result of this work could be used as the AE source identification and signal conditioning process for the AE application of cold cracking monitoring.

2 Methods

The procedure of this work is illumined in Fig. 1 as a flow diagram. Three preparation conditions of 3.2 mm diameter low-hydrogen (E7016) electrodes were used in the experiment to produce the difference of hydrogen amount in the welds for studying a relation with AE activity. From Fig. 1, a specimen was A36 steel plate which was $25 \times 130 \times 12$ mm. The specimen was cleaned to be free of dirt and oil before welding process. The welding electrodes were left in the humidity container overnight for saturation and then they were baked in the oven which was kept at 300 °C. The baking duration differed which were 10, 35, and 60 min for producing three electrode conditions. For the convenience of reference and explanation of the results, the three different welding conditions were called welding conditions A, B, and C (welded by 10-, 35-, and 60-min baked electrode weld condition, respectively).

After electrode had been baked, two specimens were welded by SMAW (120A) on one surface of each which controlled the weld length as about 115 mm. Two specimens were welded: one specimen was dipped into a cold water to stabilize a

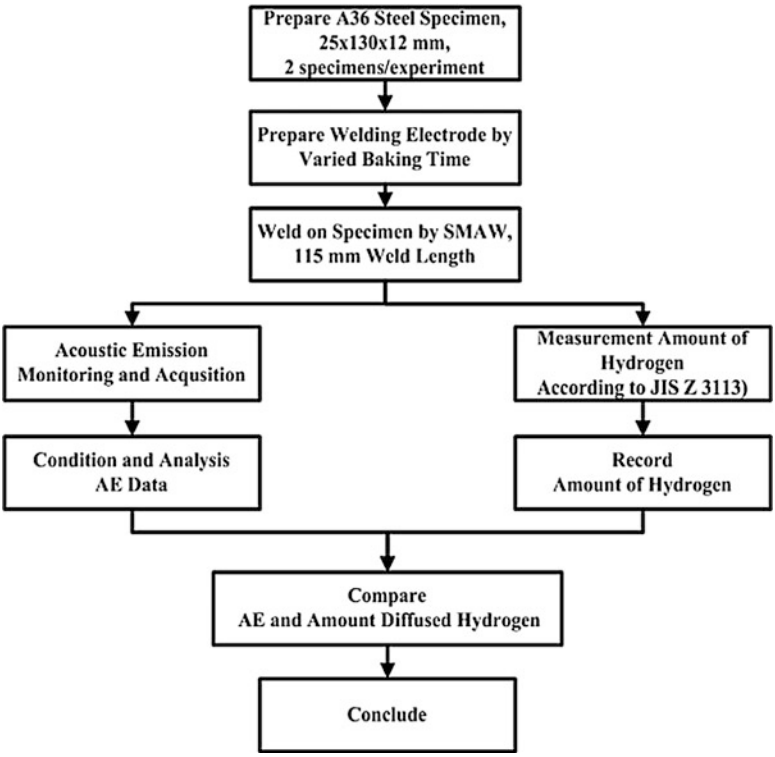

Fig. 1 Schematic of the experiments

microstructure and grain and then used as the specimen for acoustic emission monitoring experiment, and the other was dipped into cold water for 5 s and then cleaned before immersed in 45 °C glycerin with gas collector for 48 h as shown in Fig. 2a. After 48 h, measure the amount of hydrogen gas and then record and calculate a unit to volume per 100 g of weld weight (ml/100 g). The method of measurement for hydrogen evolved from deposited metal refers to JIS Z 1331 (1991).

The acoustic emission setup is shown in Fig. 2b. The wide-band AE sensor was used to detect an acoustic activity of welds. The activities were amplified by 60 dB preamplifier. The AE acquisition unit (LOCAN320) recorded AE parameters which are count, amplitude, duration, rise time, energy, and hits. The waveform and frequency spectrum were also recorded by a spectrum-analyzing device. The sensor was mounted on A36 guide wave plate ($250 \times 350 \times 16$ mm) away from the specimen about 250 mm. The performance of sensor mounting was performed by lead-break technique before start and after finish of each experiment. An acoustic couplant was used for coupling AE signal between specimen and guide wave plate.

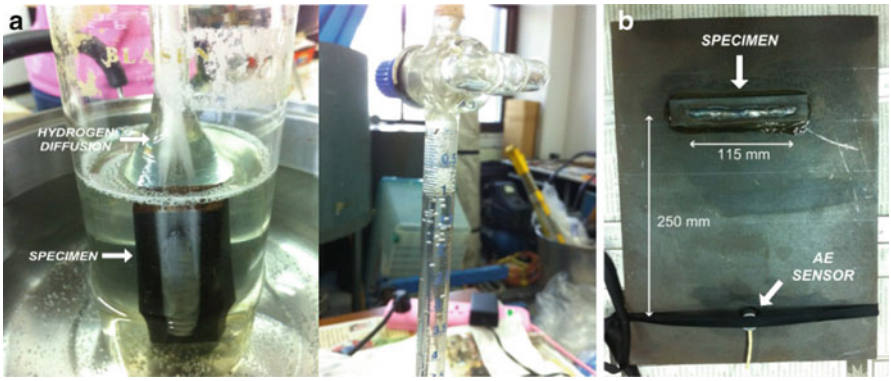

Fig. 2 (**a**) Apparatus of H_2 measurement, (**b**) specimen and sensor mounting on wave guide plate

3 Results

3.1 Hydrogen Gas Measurement

The hydrogen amounts of three weld conditions after 48-h hydrogen gas-evaluated measurement were 6.06 ml of condition A, 5.24 ml of condition B, and 5.05 ml of condition C which confirmed that the amount of hydrogen gas related to the baking duration of welding electrode.

3.2 Acoustic Emission Analysis

The analysis considered only the initial 2 h of AE data acquisition because after that the amount of AE activity was decreased and then no activity detected. The collected AE signals of three weld conditions were conditioned and filtered out unwanted signals which are background noise, electrical noise, and mechanical signal. The AE activities of the first 5 min of each acquisition were neglected to avoid a mechanical noise of sensor mounting and water evaporation on the specimen.

The remained signals were analyzed by the AE parameter correlation plot technique to characterize the signals. Count, duration, and energy were plotted wherein the result showed that the trend of each correlation plot is the same. Thus, this chapter presented only the correlation plots between count and energy (Fig. 3a–c) as a sample for three weld conditions.

Figure 3a shows the AE result of welding condition A which had the trend line of AE activities longer than the result of welding conditions B and C in Fig. 3b, c. This comparison could describe that the higher hydrogen creation would emit a high energy and count of AE signal.

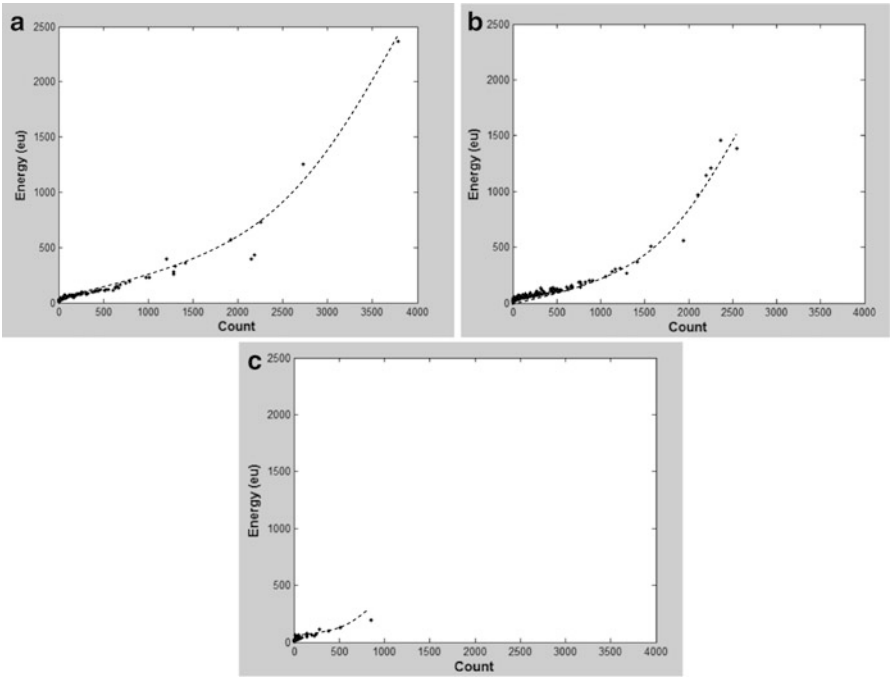

Fig. 3 (**a**) AE correlation plot and a trend line of welding condition A: welded by 10-min baked electrode (6.06 ml of hydrogen); (**b**) AE correlation plot and a trend line of welding condition B: welded by 35-min baked electrode (5.24 ml of hydrogen); (**c**) AE correlation plot and a trend line of welding condition C: welded by 60-min baked electrode (5.05 ml of hydrogen)

When considering the history plot of energy, the notice points were the amount of total AE activities (total hits) and amount of decay by time of each condition as shown in Fig. 4a–c.

The total hits of each condition in 2 h did not have a trend and repeatability. The condition A could produce hits as highest or lowest from each experiment. Thus the total hits could not be considered to relate with the amount of hydrogen gas evolution. However considering the hits decay line of each condition, we found that weld condition A presented a highest slope when compared with other weld conditions. These results could be described by consideration of a behavior of hydrogen gas escaping from weld. If high amount of gas was stuck in the weld, the weld structure would be with more cavities than low amount of gas. Thus the gas could escape quickly from weld for high hydrogen gas stuck. The high energy would be also released which presented as high slope of decay line as in Fig. 4a–c.

However the parameter of energy could be related to the amount of hydrogen by description of energy/hits. This comparison could describe that the higher hydrogen creation would emit a high energy and count of AE signal as shown in Fig. 5 which showed the correlation of AE parameters and hydrogen gas amount from welds. The R-square values of them were beyond 80 % which ensure the correlation results.

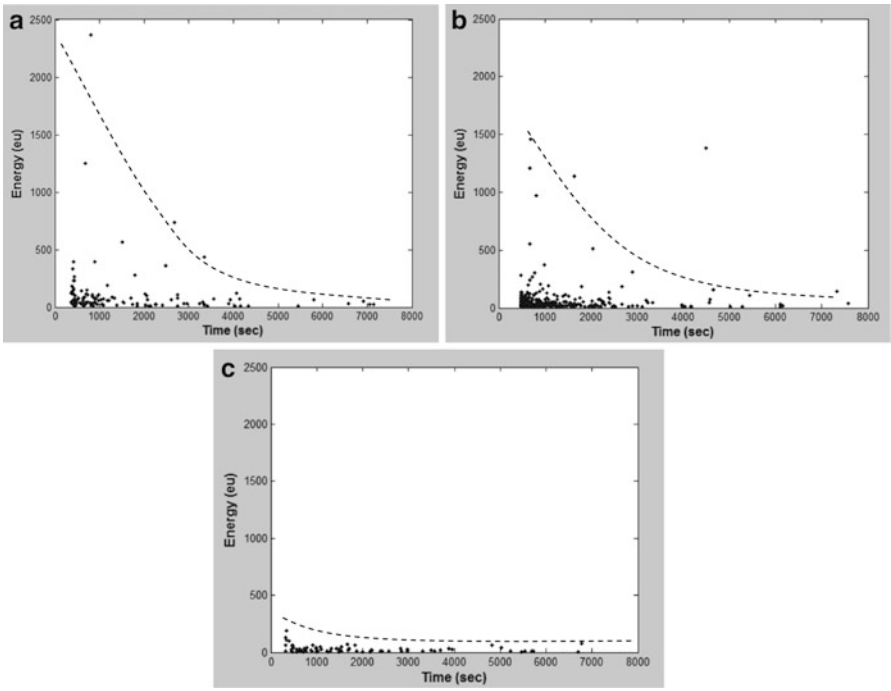

Fig. 4 (**a**) AE history plot of welding condition A and decay line, (**b**) AE history plot of welding condition B and decay line, (**c**) AE history plot of welding condition C and decay line

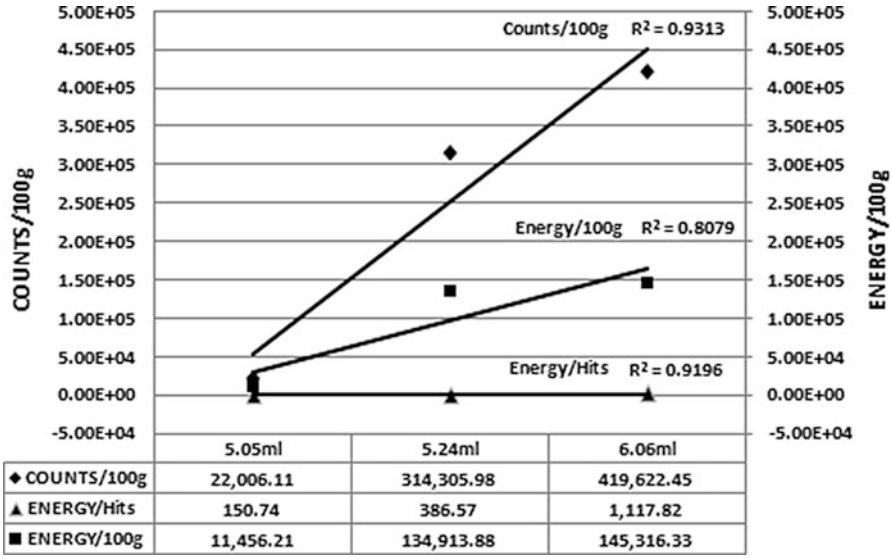

Fig. 5 Comparison of AE parameters with the amount of hydrogen gas

4 Discussion

The results showed that the AE technique can be used to detect hydrogen diffusion after weld. The emitted AE signals were analyzed to determine the relation with the amount of hydrogen gas by AE parameters which were counts and energy. The characteristic of hydrogen gas was described in correlation plot technique which can be used for identification of AE source of other weld inspection. The benefit of this study will be applied to monitor the welds after welding process for detecting cold cracking to reduce the time and cost of production.

References

1. Y.F. Sun, H. Fujii, N. Takaki, Y. Okitsu, Microstructure and mechanical properties of dissimilar Al alloy/steel joints prepared by a flat spot friction stir welding technique. Mater. Des. **47**, 350–357 (2013)
2. X. Qi, L. Liu, Fusion welding of Fe-added lap joints between AZ31B magnesium alloy and 6061 aluminum alloy by hybrid laser-tungsten inert gas welding technique. Mater. Des. **33**, 436–443 (2012)
3. S. Charunetratsamee, B. Poopat, C. Jirarungsatean, Feasibility study of acoustic emission monitoring of hot cracking in GTAW weld. Key Eng. Mater. **545**, 236–240 (2013)

Numerical Simulation Study on Propagation Law of Acoustic Emission Signal of Slewing Ring

Xinhua Wang, Jun Liang, Kai Qi, and Guanghai Li

Abstract Based on the explicit dynamic analysis method, finite element model of acoustic emission signal propagation of slewing ring is created by using ANSYS/LS-DYNA software, processing acoustic emission signal as a kind of high frequency stress wave. The propagation law of acoustic emission signal of slewing outer ring is respectively studied from four aspects: amplitude, frequency, energy, and propagation path. The results show that time-domain waveform of acoustic emission signal is distorted through propagating due to the complexity of the propagation path, and frequency components of the signal are dispersed and energy is attenuated at the same time. Compared with the upper and lower surfaces of slewing outer ring, the form of signal energy attenuation of outer surface is relatively simple and can be described as an exponential decay. Therefore, the outer surface is suitable for installing sensors and signal acquisition in the course of acoustic emission testing; however, taking the impact of signal distortion into account, the number of the sensors used in acquisition should not be less than three.

1 Introduction

Acoustic emission testing, as a dynamic nondestructive testing technique, achieves the detection, location, and evaluation of severity on damage source by receiving and analyzing transient elastic waves arising from the rapid release of energy of

X. Wang (✉) • J. Liang • K. Qi
Guangzhou Academy of Special Equipment Inspection and Testing, Guangzhou GD 20, China
e-mail: wangnewhua@163.com

G. Li
China Special Equipment Inspection and Research Institute, Beijing BJ 10, China
e-mail: liguanghai@tsinghua.org.cn

G. Shen et al. (eds.), *Advances in Acoustic Emission Technology: Proceedings of the World Conference on Acoustic Emission-2013*, Springer Proceedings in Physics 158,
DOI 10.1007/978-1-4939-1239-1_60,

damage source in the structure [1, 2]. Compared with other NDT techniques, acoustic emission signal directly carries the comprehensive information including the activity, intensity, and other aspects of damage source. Therefore, acoustic emission testing is easy for the real-time online damage monitoring, and it has broad application prospect in the structural health monitoring [3].

Slewing ring has a complex structure and poor working condition, so it is difficult for routine vibration monitoring, oil analysis, and other methods to realize the online monitoring of the fault especially weak fault [4, 5]. But acoustic emission testing is sensitive to the active defect, L.M. Rogers applied acoustic emission technique to the crack detection of slewing ring for the first time in 1979, and succeed in detecting the fatigue crack difficult to be diagnosed with the vibration method [6, 7]. Based on the study of acoustic emission testing on the low-speed bearing, Mba D. and Jamaludin N. monitored the integrity of slewing ring mounting bolts using the acoustic emission technology and thought that acoustic emission parameters could provide valuable information for condition recognition [8]. But the structure of slewing ring is complex; acoustic emission signal will cause attenuation, reflection, mode conversion, etc. in the process of propagation, making the difference between the original signal and the received signal of the acoustic emission source when testing and affecting the accuracy of the acoustic emission testing result. Therefore, it is necessary to research on the propagation law of acoustic emission signal in the slewing ring.

Based on the theory of fluctuation dynamics, this paper established the numerical analysis model of acoustic emission signal propagation of slewing ring to simulate the acoustic emission signal propagation in the interior of slewing ring using the large-scale dynamic finite element software ANSYS/LS-DYNA. Through analyzing the simulation results, the propagation law of acoustic emission signal on the time-domain waveform, frequency spectrum, and others is studied.

2 Acoustic Emission and Finite Element Simulation

2.1 Acoustic Emission Signal and Signal Analysis

Acoustic emission is a phenomenon that stress and strain energy is released in the form of elastic wave by damage source of material or component under the action of external force or internal force. The elastic wave released by damage source carries the status information of acoustic emission source, and the information propagate from the inside to the surface or within the structure along with the elastic wave, converted to an electrical signal by the acoustic emission sensor. Then, after amplified by the pre-amplifier, the electrical signal is converted to digital signal by the acoustic emission acquisition system, which is the acoustic emission signal. Acoustic emission signal is the numerical expression of acoustic

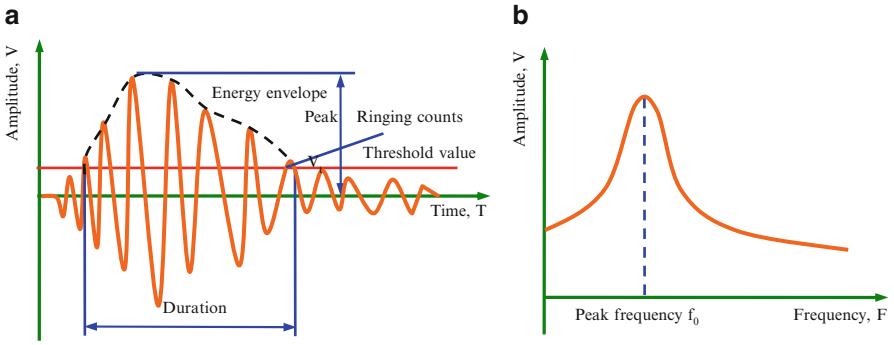

Fig. 1 Time-domain waveform and frequency spectrum of burst-type acoustic emission signal. (**a**) Time-domain waveform. (**b**) Frequency spectrum

emission phenomenon, it can be divided into continuous signal and burst-type signal based on the waveform characteristics. Continuous signal is formed by a series of burst-type signals, the typical burst-type acoustic emission signal is similar to exponential decay signal, shown as Fig. 1a, and the Fourier transform of the signal was shown as Fig. 1b.

The acoustic emission signal carries the status information of acoustic emission source, so we can identify the state of acoustic emission source through analyzing and processing the acoustic emission signal. These analysis methods of acoustic emission signal are mainly divided into parametric analysis and waveform analysis. Parametric analysis achieves the evaluation of acoustic emission source by artificially defining time and frequency domain parameters such as amplitude, energy, ringing counts, rise time, peak frequency, and others. Therefore, parametric analysis only uses the part information of acoustic emission signal, making it difficult to accurately evaluate the acoustic emission source. Waveform analysis is considered to be the most accurate analysis method of acoustic emission signal. Recently, with the extensive application of wavelet analysis, modern spectral analysis, neural network, and other new analysis technology, the waveform analysis of acoustic emission signal has been applied well and achieved good results.

2.2 Explicit Dynamics and Finite Element Method

Acoustic emission wave belongs to the category of mechanical wave. For infinite or semi-infinite ideal medium, the propagation of acoustic emission wave could be processed as the propagation of elastic wave. According to the wave equation:

$$\begin{cases} \rho \dfrac{\partial^2 \xi}{\partial t^2} = (\lambda + \mu) \dfrac{\partial \Delta}{\partial x} + \mu \nabla^2 \xi \\ \rho \dfrac{\partial^2 \eta}{\partial t^2} = (\lambda + \mu) \dfrac{\partial \Delta}{\partial y} + \mu \nabla^2 \eta \\ \rho \dfrac{\partial^2 \zeta}{\partial t^2} = (\lambda + \mu) \dfrac{\partial \Delta}{\partial z} + \mu \nabla^2 \zeta \end{cases} \tag{1}$$

Where, $\Delta = \varepsilon_{xx} + \varepsilon_{yy} + \varepsilon_{zz}$, $\nabla^2 = \frac{\partial^2}{\partial x^2} + \frac{\partial^2}{\partial y^2} + \frac{\partial^2}{\partial z^2}$. By solving the formula (1), the propagation situation of acoustic emission wave can be obtained in the ideal medium. But in the practical engineering, the formula (1) is often difficult to obtain analytical solution because the diversity of the boundary conditions, so an approximate solution should be worked out by using numerical method such as the finite element method. In the explicit dynamics, the general system equation of structure could be expressed as:

$$KD + C\dot{D} + M\ddot{D} = F \tag{2}$$

Where, D is vector formed by the displacement components, K is stiffness matrix, C is the damping coefficient matrix determined by the testing, M is mass matrix, F is external load vector. The formula can be changed into:

$$\ddot{D} = M^{-1}\left[F - \left(C\dot{D} + KD\right)\right] = M^{-1}\left[F - F^{\text{int}}\right] = M^{-1}F^{\text{residual}} \tag{3}$$

Where, F is external force vector, F^{int} is internal force vector, F^{residual} is residual force vector, Acceleration vector $\ddot{D}$ is often used to form the lumped mass of a diagonal mass matrix to solve it, generally not need to solve the matrix equation, so it is not difficult to be solved.

3 Numerical Simulation Research

3.1 Establishment of FEM Model

In order to study the propagation law of acoustic emission signal of slewing ring, the slewing outer ring is used as an example. Finite element model of acoustic emission signal propagation of slewing outer ring is created in the ANSYS/LS-DYNA software, and the physical dimension of finite element model is shown in Fig. 2 (units: mm). According to the characteristics of axial symmetry of slewing ring, the 1/40 of the finite element model is created firstly, and the material parameters used in the model is as, the density: $\rho = 7{,}800$ kg/m^3, the elasticity

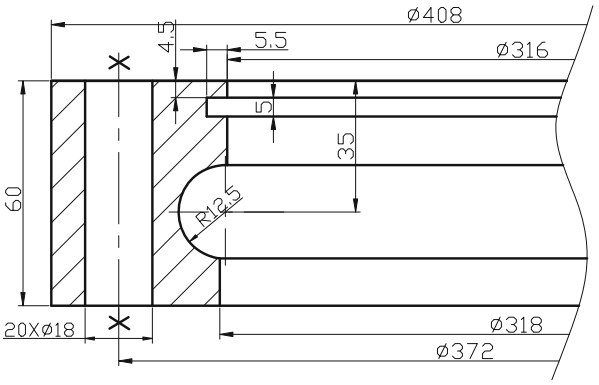

Fig. 2 Physical dimensions of slewing outer ring

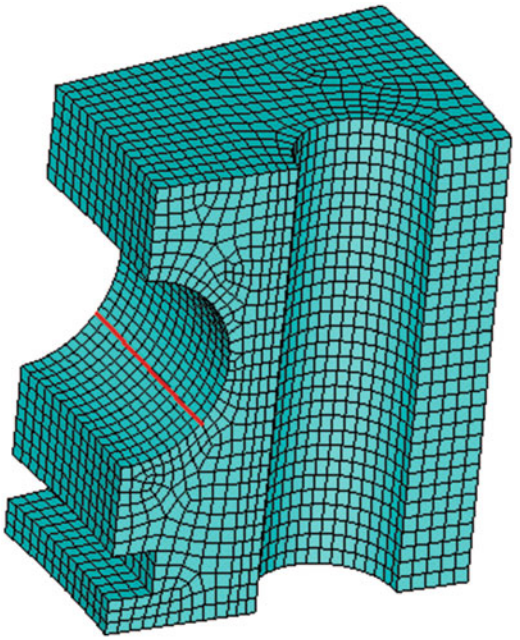

Fig. 3 1/40 of finite element model of slewing outer ring

modulus: $E = 207$ GPa, the Poisson's ratio: $\mu = 0.27$. To call the explicit algorithm, the explicit element of 3D solid 164 is selected for mesh generation, but the selection of mesh size and time step need to simultaneously satisfy the two requirements: accuracy and stability. Therefore, when meshing the geometry model, the element dimensions should not be greater than 2 mm, and time step is automatically calculated for the analysis by the software based on the minimum element size. The 1/40 of the finite element model is shown in Fig. 3, and the

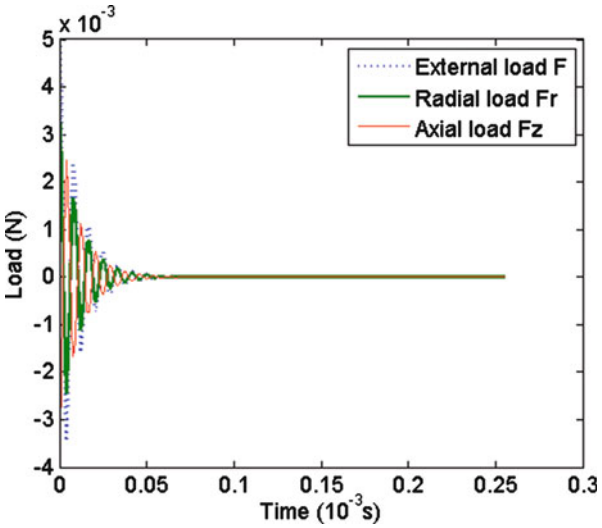

Fig. 4 Load–time curves of incentive external load

integral finite element model of acoustic emission signal propagation of slewing outer ring could be created through extending the created 1/40 of the finite element model.

3.2 Loading and Boundary Conditions

Initial contact fatigue crack often appears in the rolling element and the raceway contact area of slewing ring. Considering the weakest situation, acoustic emission source should be located on the position near the bolt hole, as shown in Fig. 3. In order to study the propagation of acoustic emission signal, we ignore the generation mechanism of acoustic emission signal, and acoustic emission signal was induced to generate by applying an exponential decay-type external load [9]. The applied external load is as (units: N):

$$F(t) = \begin{cases} 5 \times 10^{-3} \times \mathrm{e}^{-4.5t/0.00005} \cos(2\pi ft) & t \geq 0 \\ 0 & t < 0 \end{cases} \tag{4}$$

So the applied radial load component and axial load component is as:

$$\begin{cases} F_r(t) = F(t) \cos\alpha \\ F_z(t) = -F(t) \sin\alpha \end{cases} \tag{5}$$

For this type of slewing ring, contact angle $\alpha = 45°$, so when $f = 120$ kHz, $F(t)$, $F_r(t)$, $F_z(t)$ load–time curves are shown in Fig. 4.

Table 1 Position parameters of path

Path no.	R/m	Z/m
1	0.1590	0.060
2	0.1687	0.060
3	0.1770	0.060
4	0.1860	0.060
5	0.1950	0.060
6	0.1986	0.060
7	0.2040	0.060
8	0.0600	0.048
9	0.0600	0.036
10	0.0600	0.024
11	0.0600	0.012
12	0.2040	0
13	0.1986	0
14	0.1950	0
15	0.1860	0
16	0.1770	0
17	0.1673	0
18	0.1580	0

3.3 Selection of Analysis Path

Eighteen paths, situated on the upper surface, the outer surface, and the lower surface of slewing outer ring, are selected to analyze the propagation law of acoustic emission signal. The position parameters of each path are shown in Table 1. Analyzed points are uniformly distributed on the whole 0°–180° area of each path of slewing outer ring, and these points are either in the middle section or in the same section of the bolt hole, as shown in Fig. 5.

4 Results and Discussion

4.1 Dynamic Response

Under the excitation of exponential decay external load, $F(t)$, displacement–time history curves of acoustic emission source in the radial, circumferential, and axial direction are shown in Fig. 6a, which show the exponential type decay. After the source signal is transmitted, the displacement–time response curves of node 2046 ($r = 0.204$ m, $\theta = 0°$, $z = 0.024$ m), node 60058 ($r = 0.204$ m, $\theta = 45°$, $z = 0.024$ m), and node 118178 ($r = 0.204$ m, $\theta = 90°$, $z = 0.024$ m) are shown as Fig. 6. The waveform of acoustic emission signal has changed significantly when the signal propagates outwards, and the changed waveform is difficult to describe the acoustic emission source in a simple form.

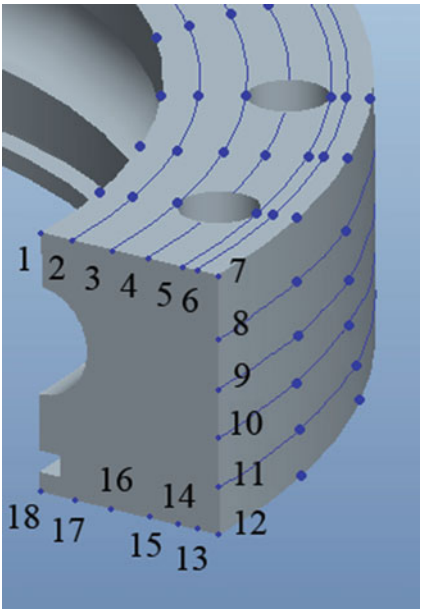

Fig. 5 Positions of analyzed points of slewing outer ring

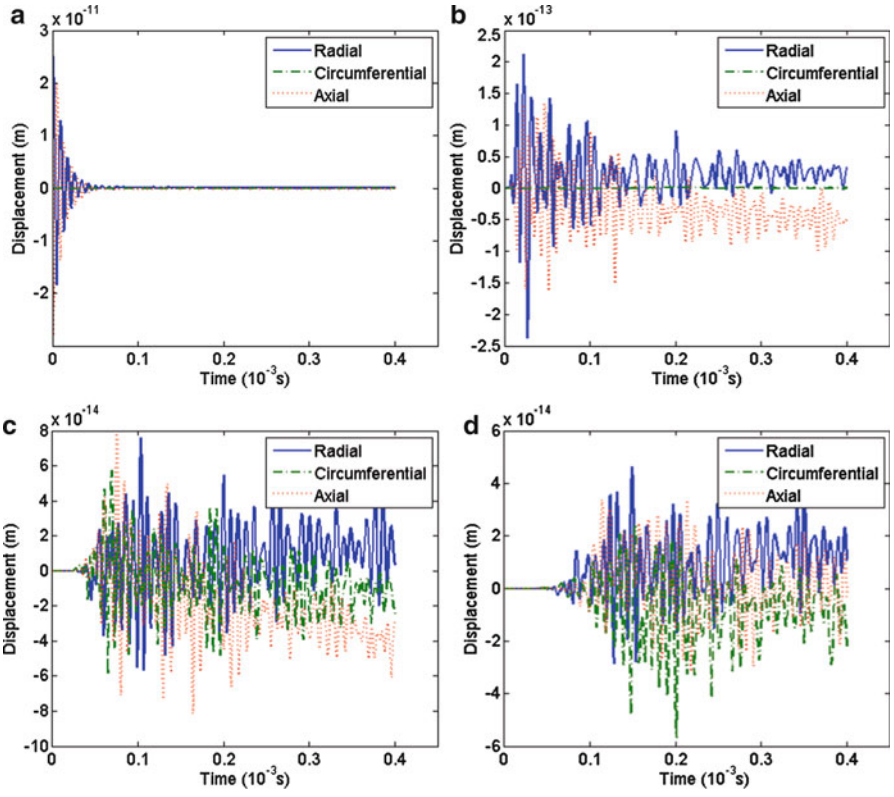

Fig. 6 Displacement–time response curves of typical nodes. (**a**) Acoustic emission source, Node 8922 ($r = 0.16766$ m, $\theta = 0°$, $z = 0.02707$ m). (**b**) Node 2046 ($r = 0.204$ m, $\theta = 0°$, $z = 0.024$ m) (**c**) Node 60058 ($r = 0.204$ m, $\theta = 45°$, $z = 0.024$ m). (**d**) Node 118178 ($r = 0.204$ m, $\theta = 90°$, $z = 0.024$ m)

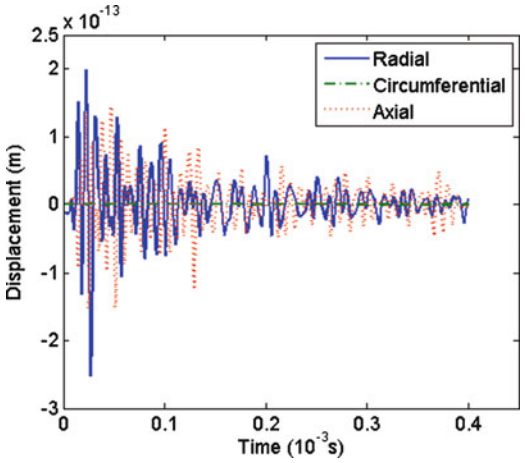

Fig. 7 Displacement–time response curves of Node 2046 after eliminating trend term

Exponential decay oscillation, $F(t)$, is different from simple harmonic oscillation. When it is loaded into the node as an initial condition, the asymmetric load will inevitably lead to an asymmetric node displacement. In addition, this trend is not constrained by boundary condition, the asymmetric displacement increases gradually after accumulation, finally leads node to deviate from the equilibrium position, as shown in Fig. 6. When the asymmetric vibration of acoustic emission source spreads to other nodes with the stress wave, it will also lead other nodes to deviate from equilibrium position. But in the practical engineering, this deviation is not possible, mainly because that the boundary in actual is always affected by various constraints. These constraints allow high frequency stress wave to propagate forward, but will limit the rigid body displacement of nodes. To highlight the changes of acoustic emission signal in the propagation process, firstly it should eliminate the signal trend, deviating from the zero point, before the signal for further processing. After eliminating the trend item, the displacement–time history curves of node 2046 are shown in Fig. 7. The signal eliminated the trend rules out the influence of the trend term, and it roughly presents exponential decay oscillation around zero point.

4.2 Amplitude Variation

Amplitude is one of the main parameters for the acoustic emission signal. For the piezoelectric acoustic emission sensor, it often acquires the acoustic emission signal by obtaining displacement component perpendicular to the surface. Therefore, for the upper and lower surface of slewing outer ring, axial displacement could be selected as analysis parameter, but for the outer surface, radial displacement is selected. Figure 8 shows the changes of the amplitude of the acoustic emission wave regarded as acoustic emission signal over the path.

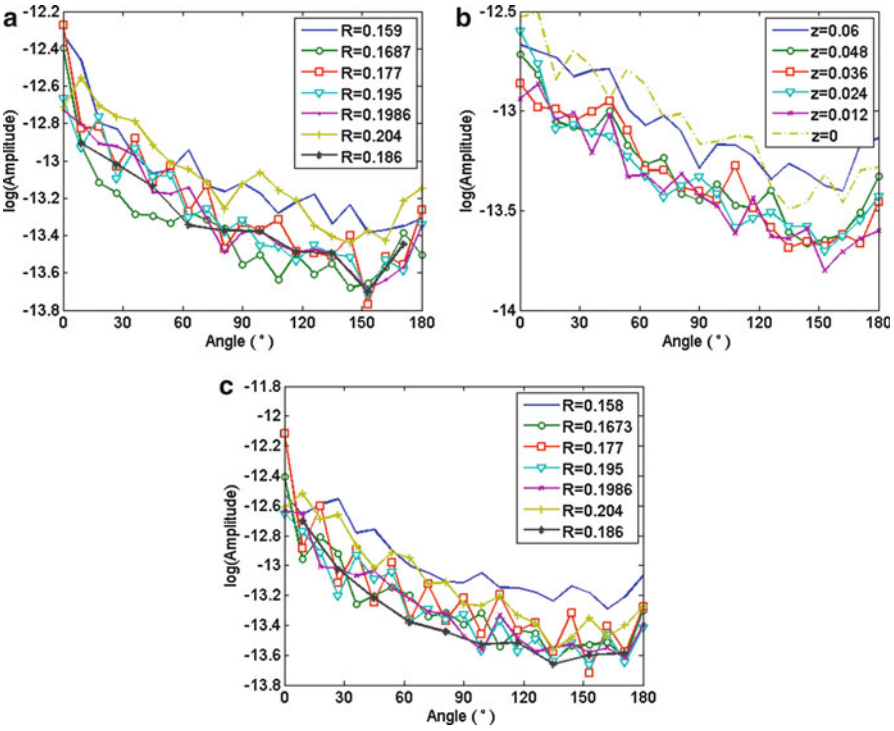

Fig. 8 Amplitude–path curves of acoustic emission signals. (**a**) Upper surface ($z = 0.06$). (**b**) Outer surface ($R = 0.204$). (**c**) Lower surface ($z = 0$)

Overall, whether the upper surface, or the outer surface or the lower surface, as the selected point is gradually moving away from acoustic emission source, the amplitude of obtained signal exponentially declines in the overall trend. But for the nodes whose radial angle away from the source point is 155°–180°, the amplitude of the obtained signal slightly increases because acoustic emission waves interfere with each other in this space. Considering a single path, the signal amplitude declines like a wave. But for the different paths, the oscillation amplitudes are diverse from each other when the displacement amplitudes decline, not exhibiting uniform regularity.

4.3 Frequency Spectrum Variation

The changes of time domain signal only reflect the changes of signal over the time, and do not reflect the signal components in the frequency domain. Using fast Fourier transform to analyze the frequency spectrum of signal eliminated the trend terms, the signal frequency domain components of node 8922, node 2046,

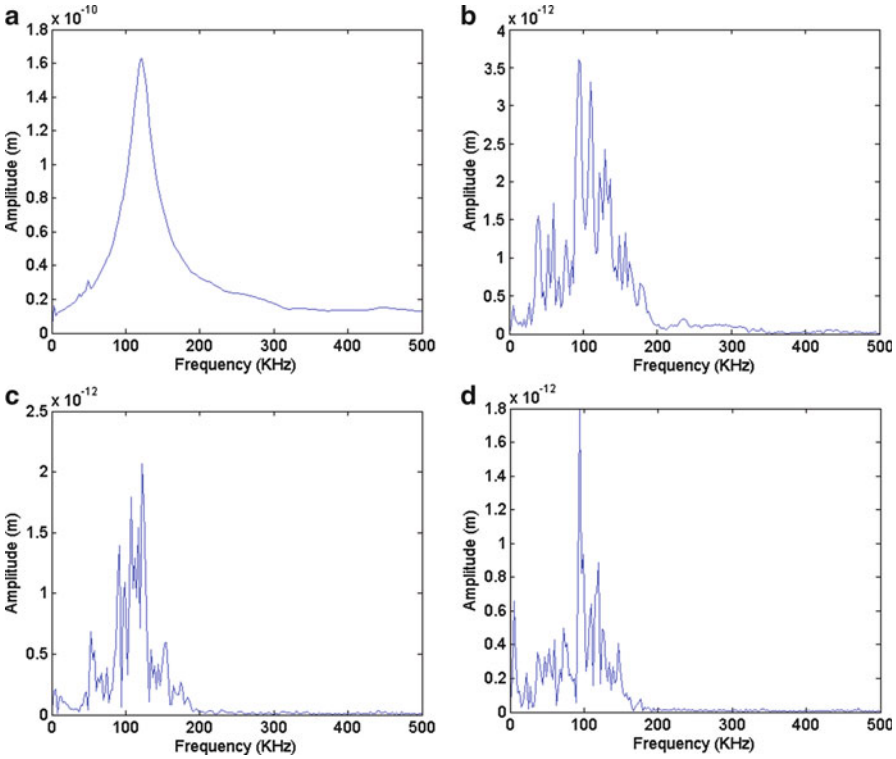

Fig. 9 Frequency spectrum of acoustic emission signals. (**a**) Acoustic emission source, Node 8922. (**b**) Node 2046. (**c**) Node 60058. (**d**) Node 118178

node 60058, and node 118178 are shown in Fig. 9. Compared with the signal of acoustic emission source (node 8922), the frequency spectrum of the acoustic emission signal after propagation undergoes significant change. The frequency component distribution is more scattered, and the maximum amplitude of the frequency domain decreases with the increase of propagation distance, while the distribution band gradually widens, appearing more "glitches" in the low frequency area. The signal is equivalent to via a low-pass filter in the propagation process, and high frequency signal is filtered to some extent. But its essence is that high frequency signal is easier to attenuate, and the longer the transmitted distance, the more obvious this attenuation. This indicates that the frequency components of acoustic emission signal will change in the propagation process. That change is relevant with the signal propagation distance and the signal propagation path, the more complex the path and the longer propagation distance, the more obvious this change.

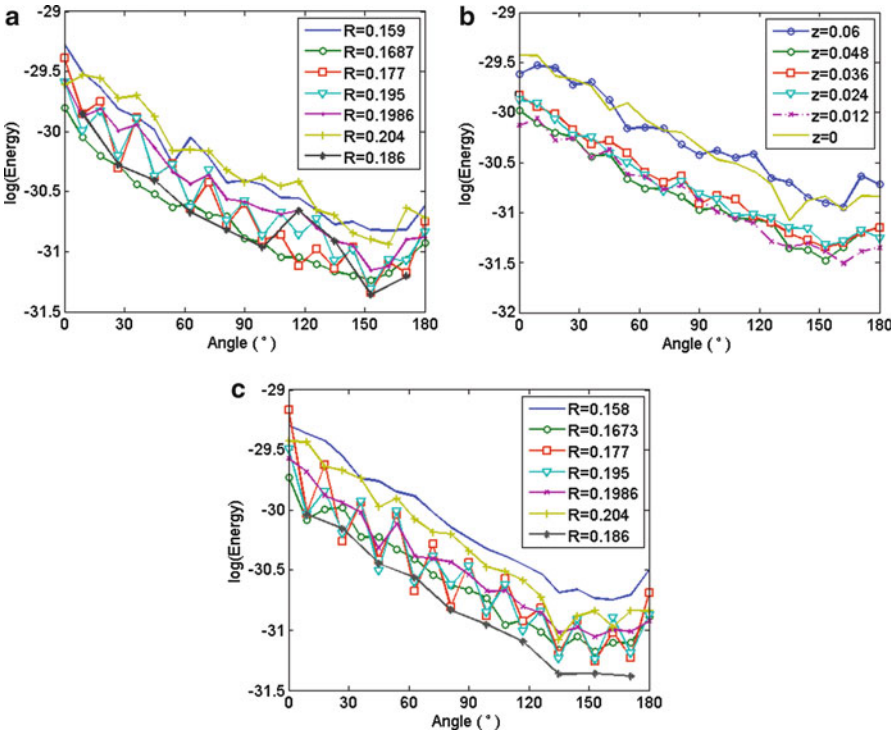

Fig. 10 Total energy–path curves of acoustic emission signals. (**a**) Upper surface ($z = 0.06$). (**b**) Outer surface ($R = 0.204$). (**c**) Lower surface ($z = 0$)

4.4 Energy Attenuation

The carried energy of the signal may be defined as:

$$E = \int_0^t s^2(t)dt \tag{6}$$

For the total displacement, $s(t)$ could be expressed as the vector sum of the radial, circumferential, and axial displacement. That is:

$$s^2(t) = s_r^2(t) + s_\theta^2(t) + s_z^2(t) \tag{7}$$

So, the total energy of the node signal in slewing outer ring can be expressed as:

$$E = E_r + E_\theta + E_z \tag{8}$$

Selecting the same nodes as the analysis object, the change curves of total energy of nodes with the path are shown in Fig. 10. The change curves of total energy are

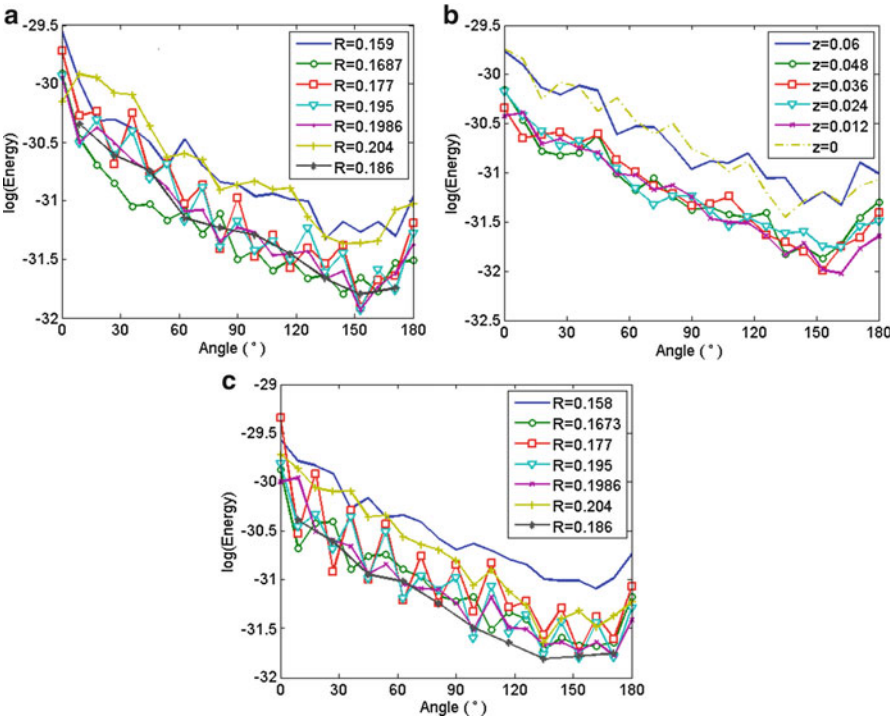

Fig. 11 Energy–path curves of acoustic emission signals received by sensors. (**a**) Upper surface ($z = 0.06$). (**b**) Outer surface ($R = 0.204$). (**c**) Lower surface ($z = 0$)

more similar to the change curves of the amplitude with the path. In the circumferential region whose radial direction angle is 0°–155° from the acoustic emission source, the common logarithm of the total energy shows in the form of gradual decline that is particularly evident for the outer surface. For the upper and lower surfaces, the total energy gradually decays in general, but the specific forms of the attenuation are different each other for the different paths, for example, two paths of $R = 0.177$, $R = 0.195$ show up the wave-like attenuation, which indicates that the signal energy presents uneven distribution due to the existence of the bolt hole and the energy near the bolt hole is higher than other area. Similar to the changes of the maximum amplitude of the displacement with the path, total energy is firstly attenuated and then rebounded in the circumferential region whose radial direction angle away from the acoustic emission source is 155°–180°, mainly because that acoustic emission signals spread to this region along both sides of the slewing outer ring and interfere with each other.

For the upper and lower surface, axial signal energy (z director) is selected as the analysis parameter, and for outside surface, the radial signal energy (r director) is considered. The part of energy can be received by the piezoelectric acoustic emission sensors, as shown in Fig. 11. And compared with the total energy

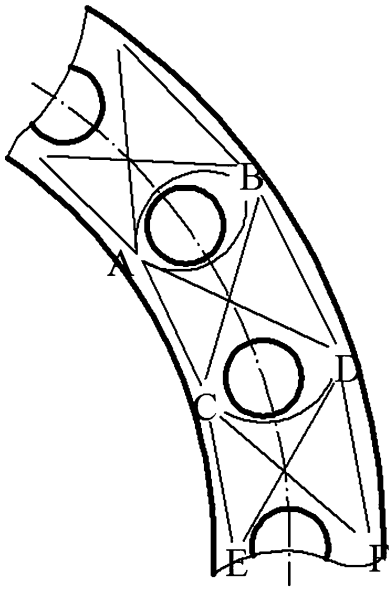

Fig. 12 Diagram of propagation paths of acoustic emission signal

distribution with the path, the curves of received energy do not have significant change along the path. Using least-square method, the data of four paths, $z = 0.048$, 0.036, 0.024, 0.012, lying on the area before 155° on the outer surface, could be fitted to a straight line, which is:

$$\log_{10}\widetilde{E}_x(\theta) = -0.5528\theta - 30.3919 \tag{9}$$

Where, the units of θ is rad. That shows the energy attenuates in accordance with exponential decay form.

4.5 Propagation Path

Assuming acoustic emission signal does not occur to reflection when encountering the boundary in the propagation process. In accordance with Huygens' principle, the diagram of propagation paths of acoustic emission signal in the slewing outer ring could be given, shown as Fig. 12. For the acoustic emission source in the A point, by which the acoustic emission signal caused would transmit forwards along the path AB, AC, and AD. At the same time, B, C, and D will become new wavelet sources, the wavelets excited by the B, C wavelet sources would transmit forwards along the path BD, CD, and is superimposed onto the wave from the source A. Similarly, C will not only receive the wave from source A, but also will be affected by two wavelet of source B and D. The signal received by E or F could still

be analysed according to the above ideas. The above analysis shows that propagation path of acoustic emission signal in the slewing ring is greatly affected due to the existence of the bolt hole, this effect increases along with the increase of propagation distance, while the complexity of this path will lead to the rapid attenuation of wave energy and the complication of wave components.

The above analysis is based on non-reflective boundary assumption. But when the acoustic emission signal propagates to the boundary, reflection would occur to varying degrees and further enhance the complexity of wave propagation path, making time domain waveform and frequency domain components of the received signals further distortion. The complexity of wave propagation path and some reflection on the boundary are the main factors of signal distortion when acoustic emission signal propagates inside the slewing ring. In order to reduce the influence of the signal interference, the number of acoustic emission sensors should not be less than three when the acoustic emission testing is performed, the installation position should give preference to the outer surface for installation.

5 Conclusion

By establishing the finite element model of acoustic emission signal propagation in the slewing ring, the propagation rule of acoustic emission signal in the slewing outer ring is studied; the following conclusions could be drawn:

Firstly, acoustic emission signal propagation in the slewing ring would produce the dispersion of the frequency components and energy attenuation, causing the time domain waveform and frequency domain signal distortion. So the acoustic emission signal obtained by sensor is often the distorted signal, and it has a certain deviation with the actual when using it to analyze the acoustic emission source.

Secondly, compared with the upper and lower surfaces of slewing outer ring, the energy attenuation form of the outer surface signal is relatively single and simple. On the outer surface, especially the several paths near to the raceway, the relationship between the common logarithm of signal energy and the path could be simply described as the linear relationship. That is to say, the energy of acoustic emission signal attenuates like an exponential decay.

Thirdly, the complexity of signal path and some reflection on the boundary are the main factors of signal distortion. When the acoustic emission testing is performed, the number of acoustic emission sensors should not be less than three in order to reduce the influence of signal distortion. At the same time, the outer surface should be selected to install the sensors as a matter of priority.

Acknowledgment This work was supported in part by the Special Fund for Quality Inspection Research in the Public Interest of China under Grant No. 201110032, and the Science and Technology Project of AQSIQ under Grant No. 2011QK323.

References

1. D. Mba, R.B.K.N. Rao, Development of acoustic emission technology for condition monitoring and diagnosis of rotating machines; bearings, pumps, gearboxes, engines and rotating structures. Shock Vib. Digest **38**(1), 3–16 (2006)
2. M. Kaphle, A.C.C. Tan, D.P. Thambiratnam, T.H.T. Chan, Identification of acoustic emission wave modes for accurate source location in plate-like structures. Struct. Contr. Health Monit. **19** (2), 187–198 (2012)
3. B. Muravin, G. Muravin, L. Lezvinsky, The Fundamentals of Structural Health Monitoring by the Acoustic Emission Method, Proceedings of the 20th International Acoustic Emission Symposium, November 17-19, 2010, Kumamoto, Japan, pp. 253–258
4. X.Q. Bai, H.L. Xiao, L. Zhang, The condition monitoring of large slewing bearing based on oil analysis method. Key Eng. Mater. **474–476**, 716–719 (2011)
5. N. Jamaludin, D. Mba, Monitoring extremely slow rolling element bearings: part I. NDTE Int. **35**(6), 349–358 (2002)
6. L.M. Rogers, The application of vibration signature analysis and acoustic emission source location to on-line condition monitoring of anti-friction bearings. Tribol. Int. **12**(2), 51–58 (1979)
7. L.M. Rogers, Detection of incipient damage in large rolling element bearings. Adv. Mater. Res. **13–14**, 37–44 (2006)
8. D. Mba, Applicability of acoustic emissions to monitoring the mechanical integrity of bolted structures in low speed rotating machinery: case study. NDTE Int. **35**(5), 293–300 (2002)
9. D. Mitraković, I. Grabec, S. Sedmak, Simulation of AE signals and signal analysis systems. Ultrasonics **23**(5), 227–232 (1985)

Three-Dimensional Finite Element Simulation of Signal Detection Transducer for Electromagnetically Induced Acoustic Emission

Guangchao Zhang, Qingxin Yang, and Liang Jin

Abstract Electromagnetically induced acoustic emission technique is a new nondestructive testing technology. By electromagnetically induced high density eddy current pulse, we can get a strong signal which can be used to locate small flaws in a thin-walled structure nondestructively. The strength of the acoustic emission signal determines the accuracy of the signal detection. This paper presents two three-dimensional finite element models for signal detection electromagnetic ultrasonic transducer, and the analysis based on three-dimensional finite element simulation on sensitivity of models with different coil shapes has been performed, and the matching problem between permanent magnet and coil size is also considered.

1 Introduction

The further industrialization and modernization of China is greatly increasing the demand for aluminum alloy sheets; from the perspective of manufacture and application, a high-performance, high-efficiency detection technique is in great need. Dynamic nondestructive detection can be performed by electromagnetically induced acoustic emission detection technique without coupling agent and pretreatment to specimens. Thus it not only can detect the flaws in the aluminum sheet in the production process but also can inspect specific areas without loading the whole structure [1–3]. In this paper, we applied the electromagnetic ultrasonic transducer to the signal detection of electromagnetically induced acoustic emission, and performed simulation analysis about the influence of the coil shape, size on the transducer' detection capability.

G. Zhang (✉) • Q. Yang • L. Jin
Tianjin Polytechnic University, Tianjin 300387, China
e-mail: chyzwb1314@sina.com

G. Shen et al. (eds.), *Advances in Acoustic Emission Technology: Proceedings of the World Conference on Acoustic Emission-2013*, Springer Proceedings in Physics 158,
DOI 10.1007/978-1-4939-1239-1_61,

2 Mechanism of Signal Detection Transducer

Electromagnetically induced acoustic emission technique is mainly used in sheet metal, the eddy current will concentrate at the tip of the defect, the defect in the sheet metal will vibrate and even crack at the tip, generating acoustic emission signal. The spreading of signal in the sheet metal fits the general law of a sound wave. When the frequency of the alternating electromagnetic field ranges is in KHz range, the alternating electromagnetic field in the aluminum sheet can be considered as magnetoquasistatic (EQS), Under the effect of the alternating electromagnetic field, the eddy current in the aluminum sheet will produce the Lorentz force, which is the power load to stimulate the acoustic emission phenomenon, where the acoustic wave equation of the isotropic elastic medium is shown below [4]:

$$F = J_e \times B_d \tag{1}$$

$$\frac{E}{2(1+\mu)}\left[\nabla^2 u + \frac{2\mu}{(1-2\mu)}\nabla(\nabla \cdot u)\right] + F = m\frac{\partial^2 u}{\partial t^2} \tag{2}$$

In Eq. (1), F is the Lorentz force, B_d and J_e are the alternating electromagnetic field and eddy current, respectively.

In Eq. (2), E and μ are the material elastic modulus and Poisson's ratio, m and u is the material density and the displacement, respectively.

The units of equation above are SI.

The acoustic wave in the metal sheet is a kind of vibration by the lattice collision and other physical effects in the metal. When the vibration spread to the field which under the signal detection electromagnetic ultrasonic transducer, eddy currents will be induced by the effect of magnetostatic field. The induced eddy currents will produce the alternating magnetic field, which will further induce the electromotive force in the coil of the signal detection transducer, and the electromotive force is the voltage signal that we need [5, 6]. The mechanism of the signal detection transducer is opposite to the signal excitation transducer [7–9]. According to observation of the difference of the stress wave that excited by different signal excitation transducer, we can analyze the sensitivity of the signal detection transducer to different stress wave.

3 Simulation Analysis of Signal Detection Transducer

The efficiency of signal detection electromagnetic ultrasonic transducer is mainly decided by the shape of the coil. Commonly, the coil is designed as snakelike or spiral. We build the three-dimensional models that are based on the two different coil shape mentioned above, and analyze the characteristics of the two models. Figure 1 shows the concrete three-dimensional models. Figure 2 shows the finite element three-dimensional models that hide the air far-field.

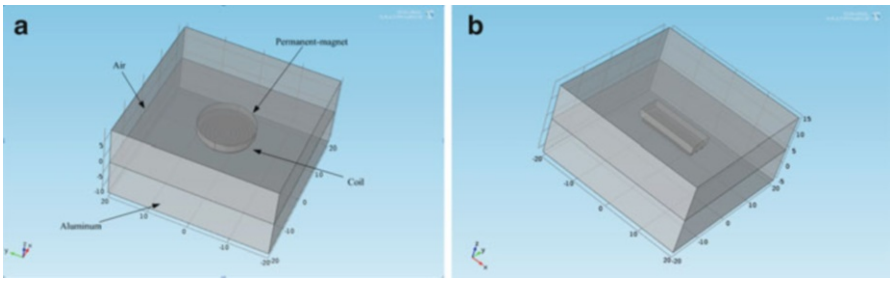

Fig. 1 Concrete three-dimensional transducer models with different coil. (**a**) Transducer model based on spiral coil. (**b**) Transducer model based on snakelike coil

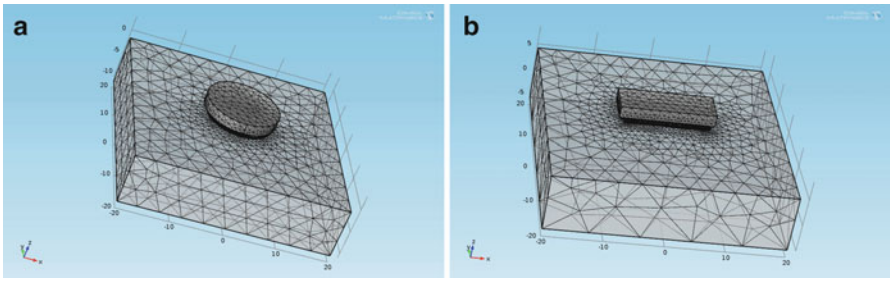

Fig. 2 Finite element three-dimensional model of signal detection transducer with air far-field hidden. (**a**) Finite element model based on spiral coil. (**b**) Finite element model based on snakelike coil

Considering the permanent magnet domain, we set the material as air, and the constitutive relation as remnant flux density with the downward direction, and it's value is 2[T]. To get the sensitivity of the two kinds of transducer to different stress wave, we excite the coil with current at first, then we observe the stress waves excited by the two kinds of transducer. The way we excite the coil is by boundary feed, and the excitation function is $\sin(2 \times \pi \times f_0 \times t) \times 1[\mathrm{A}](t < T_0)$, in which the value of f_0 is 1 MHz, and $T_0 = 1 \times 10^{-6}$ s. The body load of the aluminum sheet is Lorentz force contribution. This model is the coupling of magnetic fields and solid mechanics; the mesh of the different domains of the models are generated in different sizes, and the way we study the models is time dependent and the step is $T_0/20$, stop at $6 \times T_0$.

Figure 3a, b show the stress nephograms of the snakelike coil model at different time. We can observe the stress mainly concentrate on the directions that are perpendicular to the long side of the snakelike coil, the stress-deformation perpendicular to the surface of the aluminum sheet. That is to say, snakelike coil signal detection transducer model is sensitive to transverse wave that perpendicular to the long side of the snakelike coil.

Figure 4a, b show the stress nephograms of the spiral coil model at different times. It can be seen that the stress is radial distribution from the spiral coil.

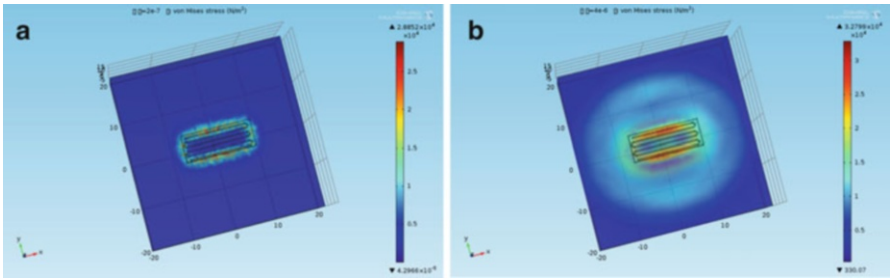

Fig. 3 The stress nephogram of snakelike coil model at different times. (**a**) Stress nephogram at $t = 2 \times 10^{-7}$ s. (**b**) Stress nephogram at $t = 4 \times 10^{-6}$ s

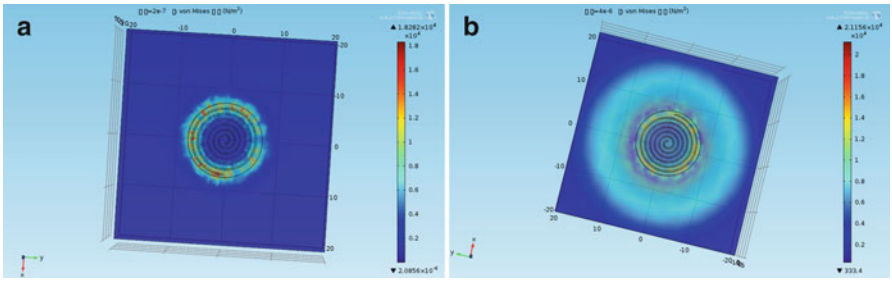

Fig. 4 The stress nephogram of spiral coil model at different times. (**a**) Stress nephogram at $t = 2 \times 10^{-7}$ s. (**b**) Stress nephogram at $t = 4 \times 10^{-6}$ s

The stress-deformation is perpendicular to the surface of the aluminum sheet. That is, spiral coil signal detection transducer model is sensitive to transverse wave from every direction.

Comparing the stress nephograms of the two models, the stress excited by snakelike coil has good directivity, while spiral coil has no directivity. What is more, the stress wave excited by the snakelike coil is more energy-intensive and has higher amplitude. Considering that the acoustic emission signal is generated by subtle crack shock or further crack of the tip, then radiate to the surrounding, thus we draw the conclusion that the coil of the acoustic emission signal detection electromagnetic ultrasonic transducer should be designed to spiral shape.

Figure 5 shows the magnet flux density norm in permanent magnet of different models at different times. Figure 5a, b show the magnetic flux density distribution in the permanent magnet of the snakelike coil at $t = 2 \times 10^{-7}$ s and $t = 4 \times 10^{-6}$ s, Fig. 5c, d show the magnetic flux density distribution in the permanent magnet of the spiral coil at $t = 2 \times 10^{-7}$ s and $t = 4 \times 10^{-6}$ s. We can see the magnetic flux density in the permanent magnet mainly concentrated near the boundary; the closer it is to the boundary, the higher the norm value. Thus we can conclude that we will get the maximum utilization when the permanent magnet coverage area equals the coil size.

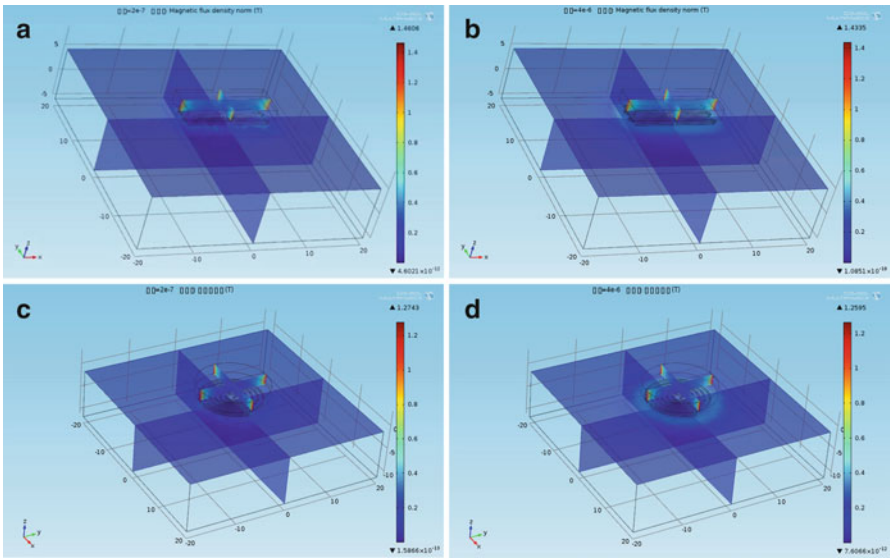

Fig. 5 Magnetic flux density norm in permanent magnet of different models at different time. (**a**) The magnet flux density norm of snakelike coil at $t = 2 \times 10^{-7}$ s. (**b**) The magnet flux density norm of snakelike coil at $t = 4 \times 10^{-6}$ s. (**c**) The magnet flux density norm of spiral coil at $t = 2 \times 10^{-7}$ s. (**d**) The magnet flux density norm of spiral coil at $t = 4 \times 10^{-6}$ s

4 Conclusion

We analyzed the mechanism of detection transducer of acoustic emission signal, built and analyzed the three-dimensional finite element models of snakelike coil and spiral coil. Because the signal of acoustic emission has no directivity, the detection transducer with spiral coil can more easily catch the acoustic emission signal. The magnetic flux density in the permanent magnet mainly concentrated near the boundary; the closer it is to the boundary, the higher the norm value. Thus we will get the maximum utilization of permanent magnet when the coverage area of permanent magnet equals the coil size.

References

1. Liu Suzhen, Yang Qingxin, Jin Liang et al., Application of electromagnetic acoustic emission technology in non-destructive testing. Trans. China Electrotech. Soc. **24**(1), 23–27, (2009)
2. Jin Liang, Yang Qingxin, Liu Suzhen, Electromagnetic stimulation of the acoustic emission for fatigue crack detection of the sheet metal. IEEE Trans. Appl. Supercond. **20**(3), 1848–1854, (2010)
3. Zhang Chuang, Liu Suzhen, Yang Qingxin et al., Signal processing of electromagnetically induced acoustic emission based on FFT and wavelet packet. Trans. China Electrotech. Soc. **25**(4), 24–28, (2010)

4. G. Rongsheng, S. Gongtian, L. Shifeng, Acostic emission signal processing and analysis technique. Nondestr. Test. **24**(1), 23–28 (2002)
5. H. Ogi, Field dependence of coupling efficiency between electromagnetic field and ultrasonic bulk waves. J. Appl. Phys. **82**(8), 3940–3949 (1997)
6. X. Zhao, K. Venugopal, G. Mei, In-line nondestructive inspection of mechanical dents on pipelines with guided shear horizontal wave electromagnetic acoustic transducers. J. Pressure Vessel Technol. **127**, 304–309 (2005)
7. X. Jian, S. Dixon, K. Grattan et al., A model for pulsed Rayleigh wave and optimal EMAT design. Sensor. Actuator. **128**, 296–304 (2006)
8. X. Jian, S. Dixon, Enhancement of EMAT and eddy current using a ferrite back-plate. Sensor. Actuator. **131**, 57–61 (2006)
9. B. Dutton, S. Boonsang, R. Dewhurst, Modeling of magnetic fields to enhance the performance of an in-plane EMAT for laser-generated ultrasound. Ultrasonics **44**, 657–665 (2006)

Name Index

G. Shen et al. (eds.), *Advances in Acoustic Emission Technology: Proceedings of the World Conference on Acoustic Emission-2013*, Springer Proceedings in Physics 158,
DOI 10.1007/978-1-4939-1239-1,

Subject Index

G. Shen et al. (eds.), *Advances in Acoustic Emission Technology: Proceedings of the World Conference on Acoustic Emission-2013*, Springer Proceedings in Physics 158,
DOI 10.1007/978-1-4939-1239-1, © Springer Science+Business Media New York 2015